Nanoarchitectonics: bottom-up creation of functional materials and systems
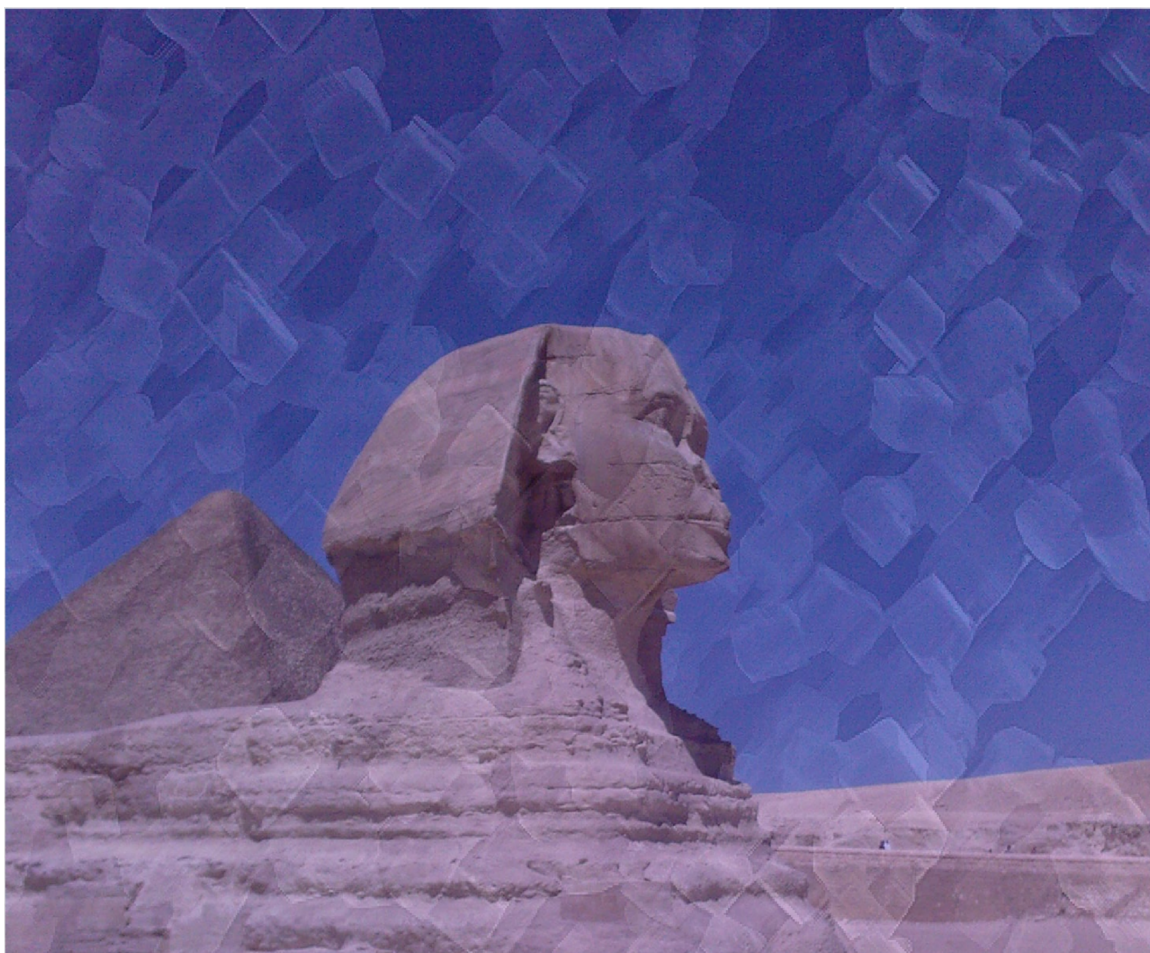
Edited by Katsuhiko Ariga

Imprint

Nanoarchitectonics: bottom-up creation of functional materials and systems

Katsuhiko Ariga[1,2]

Editorial

Address:
[1]WPI-MANA, National Institute for Materials Science, 1-1 Namiki, Tsukuba 305-0044, Japan and [2]Department of Advanced Materials Science, Graduate School of Frontier Sciences, The University of Tokyo, 5-1-5 Kashiwanoha, Kashiwa 277-8561, Japan

Email:
Katsuhiko Ariga - ARIGA.Katsuhiko@nims.go.jp

Given the significant and time-critical problems of energy shortage, environmental protection, and biomedical issues, the creation of new functional materials and systems for efficient energy production and storage [1,2], environmental remediation with sensitive pollutant detection [3,4], and biological and biomedical applications [5,6] is a crucial matter. In addition to the intrinsic functionality of bulk materials, control of their internal structure on the nanometer-scale is realized to be increasingly important to obtain high efficiency and specificity in their functions. For this general demand, the bottom-up creation of functional materials and systems from nanometer-scale and molecular units using nanotechnology principles is necessary. This can be accomplished by the conceptual fusion of nanotechnology with the other research fields such as atom/molecular manipulation, organic synthesis, supramolecular chemistry, and bio-related technology. This task is assigned to an emerging concept, nanoarchitectonics (Figure 1) [7-9].

The nanoarchitectonics concept was initially proposed by Masakazu Aono [10,11] who envisioned the production of functional materials with the following principles: (i) construction

Figure 1: Outline of the nanoarchitectonics concept.
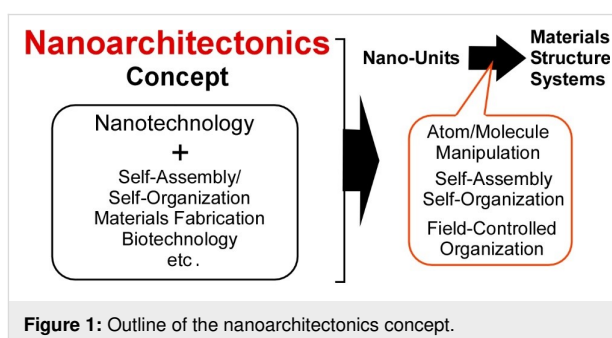
of functional materials and systems by organizing nanometer-scale structures (nanounits) even with some unavoidable unreliability; (ii) the properties of the structures may differ from those of the individual nanounits, whereby their interactions may synergistically create new functionalities; (iii) unexpected functionality may be included through assembling or organizing a very large number of nanounits; (iv) new theories and computational approaches are developed to support these fabrication processes. Because the features of the nanoarchitectonics concept are general and applicable to most materials systems,

this concept can be applied to many research targets. In fact, the nanoarchitectonics concept has already been applied in various fields, including materials production [12,13], structural fabrication [14,15], sensing [16,17], catalysis [18], energy [19], environmental [20], devices [21,22], and bio-related [23,24] applications.

Accordingly, the goal of the thematic issue "Nanoarchitectonics: bottom-up creation of functional materials and systems" was to collect leading research examples that employ the nanoarchitectonics concept. These examples range from fundamental studies on structural formation and control to application-oriented approaches in biology, physical science, and device technology.

As examples of some fundamental studies on the formation and control of nanounits, in one work, the chiral structure was found to control the self-assembly of nitrocinnamic amide amphiphiles [25]. Works related to the formation of higher-dimensional materials included, for example, the self-assembly of crystalline cellulose oligomers that resulted in nanoribbon networks [26], silicon nanowires that were formed by metal-assisted chemical etching (MACE) [27], and the formation of high-tolerance crystalline hydrogels from cyclic dipeptides upon self-assembly [28]. In addition, a review on the use of DNA as the fundamental material building block for molecular and structural engineering [29] gives insight into this interesting field of research which has great potential.

The nanoarchitectonics concept has been applied for various bio-related applications, for example, in the small-protein-induced cellular uptake of complex nanohybrids [30], the controlled drug release from layered double hydroxide/sepiolite hybrids [31], and cell surface engineering with halloysite-doped silica cell imprints for shape recognition of human cells [32]. In another example, magnetic nanoparticles were attached to microbubble shells for enhanced biomedical imaging [33]. In a final example, the detection of the prostate-specific antigen biomarker was expedited by application of advanced data processing and computational tools [34]. The molecular architecture plays a crucial role for obtaining high sensitivity and specificity in immunosensors, thus tools which speed up the ability to analyze the large amounts of data produced could significantly contribute to the field of immunosensing.

Some terrific examples of the application of the nanoarchitectonics concept for engineering applications and the physical sciences include a report by Ruiz-Hitzky et al., where they summarize how photoactive clays incorporating TiO_2 and ZnO nanoparticles exhibit distinct and useful properties [35]. Other examples include a self-assembled MoS_2-based composite that

was developed for energy conversion and storage purposes [36], a silver-nanoparticle/cellulose-nanofiber composite that was applied for surface-enhanced Raman spectroscopy [37], bio-nanocomposites with clay nanoarchitectures for electrochemical devices [38], a biomimetic nanofluidic diode with polymeric carbon nitride nanotubes [39], and a unique Janus-micromotor applied as a luminescence sensor for sensitive TNT detection [40].

The variety of nanoarchitectonics approaches collected in this thematic issue strikingly demonstrates the wide-range application of this concept. In addition to the bottom-up creation of new functional materials and systems, the inclusion of several additional factors, such as biocompatibility [41] and connection with wet ionic systems [42] that are low cost and emission-less in nature, would facilitate the development for practical usage in the near future.

Katsuhiko Ariga

Tsukuba, February 2020

ORCID® iDs

Katsuhiko Ariga - https://orcid.org/0000-0002-2445-2955

References

1. Guo, D.; Shibuya, R.; Akiba, C.; Saji, S.; Kondo, T.; Nakamura, J. *Science* **2016,** *351,* 361–365. doi:10.1126/science.aad0832
2. Miyasaka, T. *Bull. Chem. Soc. Jpn.* **2018,** *91,* 1058–1068. doi:10.1246/bcsj.20180071
3. Shak, K. P. Y.; Pang, Y. L.; Mah, S. K. *Beilstein J. Nanotechnol.* **2018,** *9,* 2479–2498. doi:10.3762/bjnano.9.232
4. Rodlamul, P.; Tamura, S.; Imanaka, N. *Bull. Chem. Soc. Jpn.* **2019,** *92,* 585–591. doi:10.1246/bcsj.20180284
5. Sung, B.; Kim, M.-H. *Beilstein J. Nanotechnol.* **2018,** *9,* 205–215. doi:10.3762/bjnano.9.22
6. Kobayashi, J.; Okano, T. *Bull. Chem. Soc. Jpn.* **2019,** *92,* 817–824. doi:10.1246/bcsj.20180378
7. Ariga, K.; Ji, Q.; Nakanishi, W.; Hill, J. P.; Aono, M. *Mater. Horiz.* **2015,** *2,* 406–413. doi:10.1039/c5mh00012b
8. Ariga, K.; Minami, K.; Ebara, M.; Nakanishi, J. *Polym. J.* **2016,** *48,* 371–389. doi:10.1038/pj.2016.8
9. Ariga, K.; Yusuke, Y. *Chem. – Asian J.*, in press. doi:10.1002/asia.202000106r1
10. Ariga, K.; Ji, Q.; Hill, J. P.; Bando, Y.; Aono, M. *NPG Asia Mater.* **2012,** *4,* e17. doi:10.1038/am.2012.30
11. Aono, M.; Ariga, K. *Adv. Mater. (Weinheim, Ger.)* **2016,** *28,* 989–992. doi:10.1002/adma.201502868
12. Ariga, K.; Matsumoto, M.; Mori, T.; Shrestha, L. K. *Beilstein J. Nanotechnol.* **2019,** *10,* 1559–1587. doi:10.3762/bjnano.10.153
13. Ariga, K.; Mori, T.; Kitao, T.; Uemura, T. *Adv. Mater. (Weinheim, Ger.)*, in press. doi:10.1002/adma.201905657

14. Rydzek, G.; Ji, Q.; Li, M.; Schaaf, P.; Hill, J. P.; Boulmedais, F.; Ariga, K. *Nano Today* **2015,** *10,* 138–167. doi:10.1016/j.nantod.2015.02.008
15. Ariga, K.; Mori, T.; Li, J. *Langmuir* **2019,** *35,* 3585–3599. doi:10.1021/acs.langmuir.8b01434
16. Ariga, K.; Makita, T.; Ito, M.; Mori, T.; Watanabe, S.; Takeya, J. *Beilstein J. Nanotechnol.* **2019,** *10,* 2014–2030. doi:10.3762/bjnano.10.198
17. Komiyama, M.; Mori, T.; Ariga, K. *Bull. Chem. Soc. Jpn.* **2018,** *91,* 1075–1111. doi:10.1246/bcsj.20180084
18. Abe, H.; Liu, J.; Ariga, K. *Mater. Today* **2016,** *19,* 12–18. doi:10.1016/j.mattod.2015.08.021
19. Azhar, A.; Li, Y.; Cai, Z.; Zakaria, M. B.; Masud, M. K.; Hossain, M. S. A.; Kim, J.; Zhang, W.; Na, J.; Yamauchi, Y.; Hu, M. *Bull. Chem. Soc. Jpn.* **2019,** *92,* 875–904. doi:10.1246/bcsj.20180368
20. Ariga, K.; Ishihara, S.; Abe, H.; Li, M.; Hill, J. P. *J. Mater. Chem.* **2012,** *22,* 2369–2377. doi:10.1039/c1jm14101e
21. Ariga, K.; Watanabe, S.; Mori, T.; Takeya, J. *NPG Asia Mater.* **2018,** *10,* 90–106. doi:10.1038/s41427-018-0022-9
22. Ariga, K.; Ito, M.; Mori, T.; Watanabe, S.; Takeya, J. *Nano Today* **2019,** *28,* 100762. doi:10.1016/j.nantod.2019.07.001
23. Ariga, K.; Leong, D. T.; Mori, T. *Adv. Funct. Mater.* **2018,** *28,* 1702905. doi:10.1002/adfm.201702905
24. Zhao, L.; Zou, Q.; Yan, X. *Bull. Chem. Soc. Jpn.* **2019,** *92,* 70–79. doi:10.1246/bcsj.20180248
25. Jiang, H.; Fan, H.; Jiang, Y.; Zhang, L.; Liu, M. *Beilstein J. Nanotechnol.* **2019,** *10,* 1608–1617. doi:10.3762/bjnano.10.156
26. Hata, Y.; Fukaya, Y.; Sawada, T.; Nishiura, M.; Serizawa, T. *Beilstein J. Nanotechnol.* **2019,** *10,* 1778–1788. doi:10.3762/bjnano.10.173
27. Carapezzi, S.; Cavallini, A. *Beilstein J. Nanotechnol.* **2019,** *10,* 2094–2102. doi:10.3762/bjnano.10.204
28. You, Y.; Xing, R.; Zou, Q.; Shi, F.; Yan, X. *Beilstein J. Nanotechnol.* **2019,** *10,* 1894–1901. doi:10.3762/bjnano.10.184
29. Ghosh, D.; Datta, L. P.; Govindaraju, T. *Beilstein J. Nanotechnol.* **2020,** *11,* 124–140. doi:10.3762/bjnano.11.11
30. Merkl, J.-P.; Safi, M.; Schmidtke, C.; Aldeek, F.; Ostermann, J.; Domitrovic, T.; Gärtner, S.; Johnson, J. E.; Weller, H.; Mattoussi, H. *Beilstein J. Nanotechnol.* **2019,** *10,* 2477–2482. doi:10.3762/bjnano.10.238
31. Rebitski, E. P.; Darder, M.; Aranda, P. *Beilstein J. Nanotechnol.* **2019,** *10,* 1679–1690. doi:10.3762/bjnano.10.163
32. Rozhina, E.; Ishmukhametov, I.; Batasheva, S.; Akhatova, F.; Fakhrullin, R. *Beilstein J. Nanotechnol.* **2019,** *10,* 1818–1825. doi:10.3762/bjnano.10.176
33. Shi, D.; Wallyn, J.; Nguyen, D.-V.; Perton, F.; Felder-Flesch, D.; Bégin-Colin, S.; Maaloum, M.; Krafft, M. P. *Beilstein J. Nanotechnol.* **2019,** *10,* 2103–2115. doi:10.3762/bjnano.10.205
34. Proença, C. A.; Freitas, T. A.; Baldo, T. A.; Materón, E. M.; Shimizu, F. M.; Ferreira, G. R.; Soares, F. L. F.; Faria, R. C.; Oliveira, O. N., Jr. *Beilstein J. Nanotechnol.* **2019,** *10,* 2171–2181. doi:10.3762/bjnano.10.210
35. Ruiz-Hitzky, E.; Aranda, P.; Akkari, M.; Khaorapapong, N.; Ogawa, M. *Beilstein J. Nanotechnol.* **2019,** *10,* 1140–1156. doi:10.3762/bjnano.10.114
36. Zoller, F.; Luxa, J.; Bein, T.; Fattakhova-Rohlfing, D.; Bouša, D.; Sofer, Z. *Beilstein J. Nanotechnol.* **2019,** *10,* 1488–1496. doi:10.3762/bjnano.10.147
37. Lu, Y.; Luo, Y.; Lin, Z.; Huang, J. *Beilstein J. Nanotechnol.* **2019,** *10,* 1270–1279. doi:10.3762/bjnano.10.126
38. Lo Dico, G.; Wicklein, B.; Lisuzzo, L.; Lazzara, G.; Aranda, P.; Ruiz-Hitzky, E. *Beilstein J. Nanotechnol.* **2019,** *10,* 1303–1315. doi:10.3762/bjnano.10.129
39. Xiao, K.; Kumru, B.; Chen, L.; Jiang, L.; Schmidt, B. V. K. J.; Antonietti, M. *Beilstein J. Nanotechnol.* **2019,** *10,* 1316–1323. doi:10.3762/bjnano.10.130
40. Yuan, Y.; Gao, C.; Wang, D.; Zhou, C.; Zhu, B.; He, Q. *Beilstein J. Nanotechnol.* **2019,** *10,* 1324–1331. doi:10.3762/bjnano.10.131
41. Stauss, S.; Honma, I. *Bull. Chem. Soc. Jpn.* **2018,** *91,* 492–505. doi:10.1246/bcsj.20170325
42. Nishizawa, M. *Bull. Chem. Soc. Jpn.* **2018,** *91,* 1141–1149. doi:10.1246/bcsj.20180064

Photoactive nanoarchitectures based on clays incorporating TiO$_2$ and ZnO nanoparticles

Eduardo Ruiz-Hitzky[*1], Pilar Aranda[1], Marwa Akkari[1,2], Nithima Khaorapapong[3] and Makoto Ogawa[4]

Address:
[1]Materials Science Institute of Madrid, CSIC, C/ Sor Juana Inés de la Cruz 3, Cantoblanco, 28027 Madrid, Spain, [2]Laboratory of Nanomaterials and Renewable Energy Systems. Research and Technology Center of Energy, Borj-Cedria Science and Technology Park, BP 95, 2050 Hammam-Lif, Tunisia, [3]Materials Chemistry Research Center, Department of Chemistry and Center of Excellence for Innovation in Chemistry, Faculty of Science, Khon Kaen University, Khon Kaen 40002, Thailand and [4]School of Energy Science and Engineering, Vidyasirimedhi Institute of Science and Technology (VISTEC), 555 Moo 1 Payupnai, Wangchan, Rayong 21210, Thailand

Email:
Eduardo Ruiz-Hitzky[*] - eduardo@icmm.csic.es

* Corresponding author

Keywords:
clays; nanoarchitectures; photocatalysts; titanium dioxide; zinc dioxide

Abstract

Thought as raw materials clay minerals are often disregarded in the development of advanced materials. However, clays of natural and synthetic origin constitute excellent platforms for developing nanostructured functional materials for numerous applications. They can be easily assembled to diverse types of nanoparticles provided with magnetic, electronic, photoactive or bioactive properties, allowing to overcome drawbacks of other types of substrates in the design of functional nanoarchitectures. Within this scope, clays can be of special relevance in the production of photoactive materials as they offer an advantageous way for the stabilization and immobilization of diverse metal-oxide nanoparticles. The controlled assembly under mild conditions of titanium dioxide and zinc oxide nanoparticles with clay minerals to give diverse clay–semiconductor nanoarchitectures are summarized and critically discussed in this review article. The possibility to use clay minerals as starting components showing different morphologies, such as layered, fibrous, or tubular morphologies, to immobilize these types of nanoparticles mainly plays a role in i) the control of their size and size distribution on the solid surface, ii) the mitigation or suppression of the nanoparticle aggregation, and iii) the hierarchical design for selectivity enhancements in the catalytic transformation and for improved overall reaction efficiency. This article tries also to present new steps towards more sophisticated but efficient and highly selective functional nanoarchitectures incorporating photosensitizer elements for tuning the semiconductor–clay photoactivity.

Review

Introduction: immobilization of nanoscale TiO$_2$ and ZnO on clay minerals

Nanoarchitectonics is a term coined by Japan's National Institute for Materials Science (NIMS), which refers to the nanoscale design of complex materials through a deep and detailed understanding of the interactions between individual nanostructures and their organization [1-3]. 2D nanoarchitectures have been recently reviewed by Ariga and collaborators [4-6]. Among 2D solids, clay minerals have been widely studied as versatile components for the preparation of functional nanoarchitectures by means of their assembly with diverse active compounds including nanoparticles (NPs) of variable nature, such as metal-oxide NPs, which is of great interest for many diverse applications [7-11]. As it is well known, clay minerals are a big family of silicates showing diverse structural arrangements and morphologies (Figure 1) with topologies able to accommodate a variety of NPs of semiconductors such as TiO$_2$ and ZnO. TiO$_2$ and, to a minor extent, ZnO NPs in the form of anatase and wurtzite phases (Figure 1E and 1F, respectively), are semiconducting materials that have been assembled at the nanometer scale with clay silicates and deeply investigated due to their useful properties for various applications, including heterogeneous photocatalysis, antibacterial activity, and water splitting [12-20]. Both semiconducting solids are more efficient as photocatalysts than the corresponding bulk TiO$_2$ and ZnO

powders when they are present as NPs. This fact could be simply explained by the fact that the smaller particles normally have a larger surface-to-volume ratio.

Many studies have focused on the photocatalytic activities of TiO$_2$ and ZnO supported on clays, clay minerals and related solids that include layered double hydroxides, such as hydrotalcite, and layered polysilicates, such as magadiite. However, this article will focus only on materials based on clay minerals. The emphasis of these studies has been the photodegradation of diverse organic compounds, including the photodecolorization of dyes such as methylene blue (MB), methyl green (MG), acid red G, acid yellow 11, acid orange 11, and Congo red, in water, as well as other photo-applications, for instance, water splitting under UV or visible/solar light irradiation (Table 1). Among the 2D clay-based solids (layered silicates), montmorillonite and other smectites used for assembly with diverse NPs exhibit excellent adsorption, rheological, ion-exchange, and swelling properties as well as a large relative surface area for incorporating the NPs. Kaolinite clay presents lower values of ion-exchange capacity and a smaller relative surface area as, in general, the interactions only involve its external surface. However, the latter aluminosilicate shows a chemical inertness that

Figure 1: Schematic representation of the crystal structures of the following clay minerals: kaolinite (A), montmorillonite (B), sepiolite (C), halloysite nanotubes (HNT) (D), and the metal oxides, anatase (E) and wurtzite (F), obtained by applying the VESTA software using the following color codes: silicon oxide tetrahedron – blue: Si, red: O. In kaolinite and halloysite – aluminium oxide-hydroxide octahedron: green, red: O; magnesium oxide octahedron: brown, red: O. In montmorillonite – Al,Mg octahedron: pale blue; Ti: pink; Zn: gray. Panel D shows the nanotubular morphology of HNT resulting from the rolling of layers of 1:1 aluminium phyllosilicate with the same structural arrangement as kaolinite. TEM images of (G) montmorillonite and (H) sepiolite clay minerals.
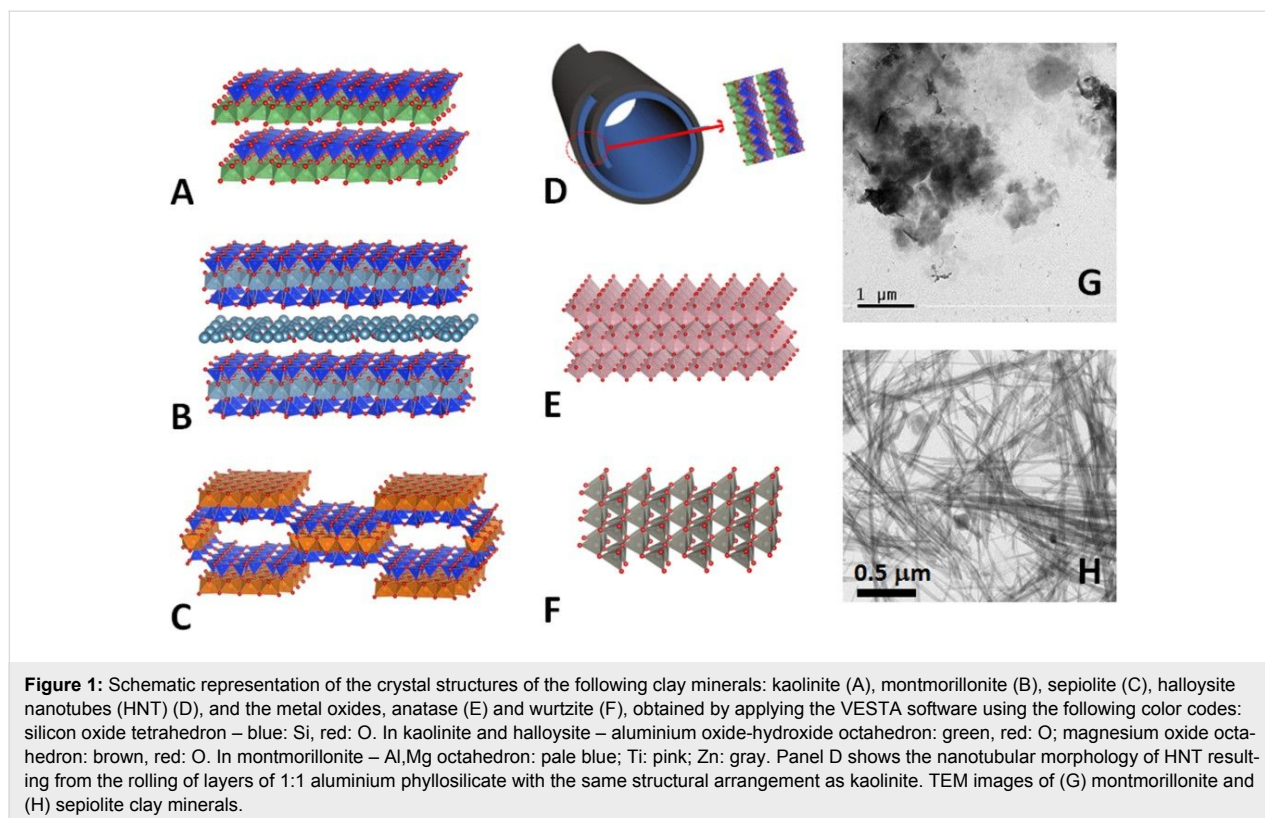
Table 1: Selected examples of catalytic applications of TiO_2@clay and ZnO@clay nanoarchitectures.

clay-based nanoarchitectures		photodegradation	other applications
clay component	semiconductor component		
kaolinite	TiO_2	Kutláková et al. (2011) [94]; Zhang et al. (2011) [95]; Chong et al. (2009) [96]; Barbosa et al. (2015) [98]	CO_2 reduction, Kočí et al. (2011) [97]
kaolinite	ZnO	M. Kutláková et al. (2015) [172]	antibacterial activity, Dědková et al. (2016) [173]
halloysite	TiO_2	Papoulis et al. (2013) [174]; Wang et al. (2011) [123]; Li et al. (2015) [175]; Du et al. (2014) [176]; Papoulis et al. (2010) [114]	—
hectorite	TiO_2	Ma et al. (2009 & 2010) [103,108], Kibanova et al. (2009) [101]; Belessi et al. (2007) [102]	—
Laponite®	TiO_2	Zhu et al. (2002) [177]	—
Ce–Ti-pillared Laponite®	TiO_2	Lin et al. (2010) [178]	—
Zr–Ti-pillared Laponite®	TiO_2	Lin et al. (2011) [179]	—
stevensite	TiO_2	Bouna et al. (2014) [180]	—
beidellite	TiO_2	Rhouta et al. (2015) [99]	—
Ti-pillared beidellite	TiO_2	—	cracking of cumene, Swarnakar et al. (1996) [181]
TiO_2-pillared saponite	TiO_2	—	degradation of NO_x gas, Nikolopoulou et al. (2009) [182]
montmorillonite, bentonite and related smectites	TiO_2	Sun et al. (2015) [105]; Manova et al. (2010) [106]; Rossetto et al. (2010) [104]	—
montmorillonite, bentonite and related smectites	ZnO	Fatimah et al. (2011) [89]; Khumchoo et al. (2016) [46]; Ye et al. (2015) [120]; Akkari et al. (2016) [118]; Xu et al. (2014) [124]	
montmorillonite and related smectites	TiO_2/ZnO	Bel Hadjltaief et al. (2016) [158]; Tobajas et al. (2017) [159]	
montmorillonite (CTA-organoclay)	ZnO	—	antibacterial activity, Gu et al. (2015) [117];
lightweight expanded clay aggregates (LECA)	TiO_2/ZnO	—	removal of ammonia from wastewater; Mohammadi et al. (2016) [161]
montmorillonite–kaolinite	TiO_2	—	removal of Pb(II), Cu(II), Zn(II), and Cd(II); Đukić et al. (2015) [183]
bentonite	TiO_2	—	Degradation of volatile organic compounds (VOCs); Mishra et al.(2018) [184]
rectorite	TiO_2	Bu et al. (2010) [185]; Zhang et al. (2011) [186]; Yang et al. (2012) [187]	—
rectorite	ZnO	Li et al. (2014) [188]	—
rectorite	TiO_2/ZnO	Wang et al. (2018) [163]	—
sepiolite	TiO_2	Aranda et al. (2008) [109];Suárez et al. (2008) [112]; Ökte & Sayınsöz (2008) [113]; Du et al. (2015) [189][a]; Zhou et al. (2017) [190]	photoreforming of methanol, Pérez-Carvajal et al. (2016) [131][b]
sepiolite	ZnO	Xu et al. (2010) [90]; Akkari et al. (2016) [118]	removal of H_2S by chemisorption, Portela et al. (2015) [122]
sepiolite	TiO_2/ZnO	Vaizoğullar (2017) [160]	
palygorskite	TiO_2	Zhang et al. (2011) [191][c]; Bouna et al. (2011) [111]; Papoulis et al. (201) [115] Stathatos et al. (2012) [116]	degradation of NO_x gas, Papoulis et al. (2010) [114]
palygorskite	ZnO	—	antibacterial activity, Huo and Yang (2010) [121]

[a]containing Ag_2O/TiO_2; [b]Pt- or Pd-doped TiO_2; [c]containing SnO_2/TiO_2.

is useful for its use as support of the semiconducting NPs considered here.

According to the "Web of Science" (WoS) [21] around 10,000 papers have been published in the last decade in connection with the topic of TiO$_2$ NPs used as photocatalysts, indicating the high interest in the use of these materials for this type of applications. In fact, titanium dioxide (anatase phase) can be considered the most extensively studied solid among the diverse transition-metal oxides and transition-metal chalcogenides investigated with that focus over the last decades. However, TiO$_2$ has disadvantages such as limited activity together with a reduced sensitivity to sunlight. Hence, alternative semiconductors such as ZnO are increasingly investigated for processes concerning environmental remediation, antibacterial activity and chemical technologies for hydrogen production and synthesis of organic compounds [22]. Anyway, according to WoS, in the given period TiO$_2$ NPs appear to be cited ten times more often than ZnO NPs regarding their use as photocatalysts.

One of the main applications of clay–semiconductor materials is the mineralization of organic pollutants, which represents an ideal solution for the remediation of wastewater contaminated with diverse organic species. This process consists in the oxidative decomposition of organic pollutants to non-toxic inorganic species such as carbon dioxide, avoiding the formation of any kind of residual sludge [23]. In fact, advanced oxidation processes (AOP) might be considered as promising technologies for the sustainable removal of pollutants from urban, industrial and agricultural wastewater. They are based on the in situ generation of reactive species as hydroxyl radicals (OH$^\bullet$) with high oxidizing capability [24]. AOP include Fenton and photo-Fenton reactions based on the combination of chemical oxidants, e.g., hydrogen peroxide, and UV irradiation, and other photocatalytic reactions assisted by semiconductor photocatalysts. The use of TiO$_2$ and ZnO NPs, particularly the anatase and wurtzite phases, as heterogeneous photocatalysts attracted great attention over the last years. Atmospheric oxygen is used as oxidant to achieve complete mineralization of harmful organic compounds, such as pesticides, phenols, dyes, and pharmaceuticals drugs to water, CO$_2$, and non-toxic inorganic residues under solar light or UV irradiation. Advantages such as low cost and chemical stability are essential requirements of this type of photocatalysts [25,26]. In addition, highly toxic heavy metals such as Cr(VI) and Hg(II) can be removed from aqueous environments by photoreduction employing NPs as heterogeneous photocatalysts leading to insolubilization [23,27-29].

Based on the redox and photoactive properties, TiO$_2$ and ZnO are the most commonly reported nanoparticulated materials for photocatalytic applications as they can be considered to be chemically stable and easily available (inexpensive commercial products) [12,13,30-33]. In this context, ZnO appears as a better candidate for water cleaning compared to the more commonly used TiO$_2$. In fact, ZnO shows a wider absorption in the visible-wavelength region than TiO$_2$, which is advantageous [34-43].

A possible higher catalytic activity of ZnO compared to TiO$_2$ has also been discussed. However, contradictory arguments and results have been reported [20]. The origin of the experimentally observed differences in the photoactivity are not yet clear due to the effect of complex parameters including light absorption, charge recombination, changes in the available surface area and chemical reactivity [44,45]. Another characteristic of ZnO is its lower chemical stability compared to TiO$_2$, particularly in acidic solution, which can be a drawback for practical applications [46,47].

By changing morphology, doping, and conformation, i.e. as films, of the nanoparticles the intrinsic opto-electronic properties of the semiconductor as well as its chemical stability and surface reactivity can be modified [48,49]. TiO$_2$ and ZnO NPs with different shapes, sizes and exposed crystal facets were assembled to yield hollow particles, fibers, nanosheets, nanowires, nanorods, nanoflowers and nanobelts through various synthesis routes including template synthesis [50-53]. Controlling the NP morphology can be advantageous for the following purposes: i) to increase the available surface area for the reactant access, ii) to obtain stable aqueous suspensions for efficient light transmission (or to suppress light scattering), and iii) to expose specific catalytically active facets. Synthesis strategies of hierarchically designed TiO$_2$ and ZnO nanoarchitectures with controlled morphology, crystallinity, anisotropic shape, and composition have been investigated recently. The aim was to obtain accessible and interconnected porous networks with increased specific surface area for the adsorption of reactants and diffusion of the products [54].

Photocatalysts need to be removed and recovered from the suspension after use. When the photocatalysts are present as nanoscale particles, their aqueous suspensions become more stable, reducing unfavorable effects such as scattering. However, the recovery of the NPs, e.g., through filtration, can be very difficult, which may add substantial costs to industrial processes involving these materials. In addition, the tendency of the particles to aggregate, especially at high concentrations, may cause changes in the transparency and viscosity of the suspensions.

To overcome these drawbacks, the development of active photocatalysts based on supported NPs appears as a promising

solution to these problems. Hence, the development of efficient nanoarchitectured clay–semiconductor NP materials is an attractive option.

TiO$_2$ and ZnO NPs assembled with different inorganic solids (substrate or matrix components) are advantageous not only for photocatalytic purposes but also for applications as pigments and cosmetics, where colloidal and surface characteristics play a significant role. TiO$_2$ and ZnO NPs have been prepared in the presence of inorganic matrices by in situ formation in the available nanoscale spaces of the solid substrates, resulting in controlled size and shape of the supported TiO$_2$ and ZnO NPs. The involved inorganic matrices can be of very diverse nature such as silica and silicates (mesoporous silicas, zeolites, clays, and clay minerals), carbonaceous materials (carbon nanotubes, graphene, graphene oxide, and activated carbon), layered double hydroxides, layered polysilicates (magadiite and kenyaite), and metal organic frameworks. The role of the inorganic matrices in the assembly of the semiconductor NPs [55-59] is: i) to control the particle size and the size distribution of the growing NPs; ii) to immobilize the NPs either on the external surface or within nanoscale spaces, e.g., pores and intracrystalline cavities; iii) to diminish/to avoid NPs aggregation; iv) to suppress the NPs dissolution; v) to yield stable suspensions more suitable for photocatalytic reactions; vi) to facilitate percolation in membrane or column designs for the easier separation and collection of products; and vii) to enable molecular recognition in photocatalysis through the well-defined nanopores in the inorganic component.

Well-defined nanoporous solids such as zeolites and mesoporous silicas have been used as templates in the growth of NPs with precisely controlled particle size and shape replicating size and shape of the pores. Thus, a novel class of nonlinear optical materials based on host–guest composites has been prepared using zeolites as inorganic crystalline hosts [60-66]. Nanoarchitectures composed of zeolites and mesoporous silica and TiO$_2$ or ZnO NPs have been reported as efficient photocatalysts as well as photoluminescent materials [67-69]. The formation of TiO$_2$ and ZnO NPs on the external surface, in addition to the NPs confined in the nanopores, is still an important challenge. Recently, the size-controlled synthesis of TiO$_2$ NPs within mesoporous silica (SBA-15) has been reported, where, according to Vibulyaseak and co-workers [70], the NPs formation occurred exclusively in the mesopores.

The aim of this work is to summarize and critically discuss the different experimental options in the use of TiO$_2$ and ZnO NPs, assembled with clay minerals and related solids, emphasizing on their structural and textural characteristics in relation to their photocatalytic activity.

Synthetic strategies for the preparation of TiO$_2$ and ZnO nanoarchitectures: modulation of their physical and chemical characteristics

As introduced above, different functional nanoarchitectures for various applications have been synthesized from clay minerals taking advantage of their natural abundance and eco-friendly nature, as well as their unique structural and textural features. It is well known that these silicates show different nanostructures and particle shapes, such as lamellar (smectites and kaolinites), fibrous (sepiolite and palygorskite), and tubular (halloysite) morphologies (Figure 1). Mainly on the basis of the ion-exchange of their interlayer inorganic cations and to the presence of reactive hydroxyl groups at their external surfaces, it is possible to modify in a controlled manner the surface characteristics of clay minerals introducing new suitable functions leading to hierarchically structured nanoarchitectures [8,10,11].

A useful strategy to enhance the photocatalytic activity of metal-oxide NPs considered here consists in their distribution as homogenously as possible on the surface of clay minerals acting as supports and provided with large specific area and porosity. Among the clay materials (Figure 1), layered silicates such as smectites are of particular interest as they have been largely used in adsorption and catalysis applications due to their valuable properties as expandable interlayer space, low cost and environmentally friendly nature [71]. Similarly, fibrous silicates, i.e., palygorskite and sepiolite, are characterized by a large specific surface area and microporosity, as well as the presence of external silanol groups, which can immobilize species including NPs of diverse nature [11,72]. Halloysite (Figure 1D) is a layered aluminosilicate with a silica/alumina composition similar to that of kaolinite that can be present as a tubular clay (halloysite nanotubes, HNTs) with diameters of 50–80 nm (external) and 10–15 nm (internal), and a typical length of ca. 1000 nm [73-75]. The external surface of HNTs is composed of siloxane groups (Si–O–Si) while the internal surface is covered by aluminol groups (Al–OH) with a structural arrangement similar to that of the kaolinite 1:1 phyllosilicate (Figure 1D). These groups able to interact with diverse compounds entering the cavities, facilitating their immobilization [76-79]. The morphology of HNTs yields some advantages with regard to the development of new architectures, including the immobilization of TiO$_2$ and ZnO NPs.

Semiconductor NP–clay nanoarchitectures prepared from natural or synthetic clay minerals have been extensively investigated, involving both the assembly of already formed metal-oxide particles as well as the in situ formation of NPs [80-83]. The assembly of TiO$_2$ and ZnO NPs with clays of different

characteristics takes place mainly on the external surfaces. However, in materials produced from layer silicates of the smectite group, the interlayer space may also be involved. In this case, it is important to control the synthesis procedures in order to obtain the desired surface properties of the NPs, as well as suitable size and shape and nanopore characteristics in the resulting pillared layered structures.

The formation of house-of-cards-like structures during the preparation of ZnO NPs in the presence of smectites as a result of the re-stacking of the exfoliated nanosheets has been reported [84]. Due to the variety of hierarchical structures and particle locations (at the external surface or in the interlayer space), the resulting particle size distribution of ZnO NPs can be very wide, affecting the physio-chemical characteristics of the resulting clay-based nanoarchitectures [85-87].

Nanotubular halloysite and microporous fibrous silicates such as sepiolite and palygorskite can be also considered as good candidates for the size-controlled growth of NPs, due to their well-defined nanopore structure and other surface characteristics. However, in the case of sepiolite and palygorskite, the sizes of the available nanospaces are too small for the generation of TiO_2 and ZnO NPs within the nanopores [72]. In this case, mesopores, which can be ascribed to inter-fibre regions, could facilitate the growth of the semiconductor NPs. This happens in the same way as that occurring at the external surface of the fibrous clay minerals with the participation of surface Si–OH groups for anchoring the TiO_2 and ZnO NPs.

The assembly of TiO_2 and other types of semiconducting NPs takes place very often on the external surface of clay minerals [8,11]. The particle shape and size have been evaluated by transmission electron microscopy (TEM) and X-ray diffraction (XRD) using the Scherrer equation, in addition to the spectroscopic information obtained from the shift of the UV–vis absorption band to a shorter wavelength region, showing quantum-size effects. The advantages of clay minerals acting as supports for TiO_2 and ZnO NPs are the presence of surface electrical charge and/or the elevated concentration of hydroxy groups on the available surface, which can have an important influence on the NPs immobilization as well as on the structural stability during the photocatalytic reactions. In addition, the immobilization of NPs on clay surfaces is a key advantage for the easier recovery of the photocatalyst from the reaction medium compared to bare NPs [88-93].

Clay-based nanostructured materials prepared by in situ formation of NPs can be achieved by applying various procedures such as impregnation by precipitation, sol–gel, solvothermal and microwave-assisted rea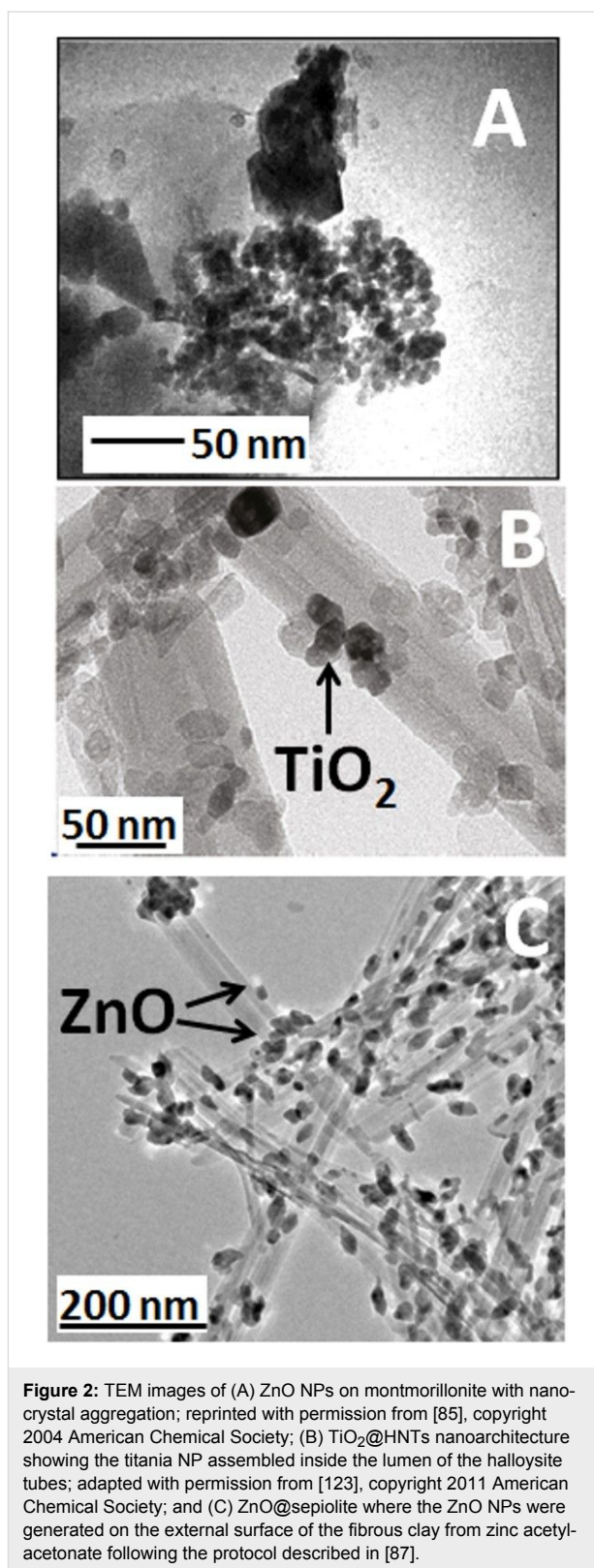ctions. As already indicated, clay-based nanoarchitectures containing TiO_2 NPs (anatase phase) are currently the most extensively studied clay–semiconductor systems for photocatalysis applications. Various procedures have been reported to produce kaolinite clay mineral fully coated with TiO_2 NPs [94-98]. An example of these methods is the in situ formation of titanium dioxide and its anchorage on the external kaolinite surface through sol–gel methods as, for instance, one based on the controlled hydrolysis titanium(IV)-*n*-butoxide in ethanol, resulting in heterocoagulation with kaolinite in aqueous suspensions [96]. However, kaolinite can be expanded by the intercalation of polar molecules such as urea, dimethyl formamide and dimethyl sulfoxide (DMSO), which could facilitate the access of other compounds to the interlayer region of this phyllosilicate. Németh and co-workers [85] claimed the generation of ZnO NPs in the interlamellar space of kaolinite following an alkaline hydrolysis of the clay treated with a solution of Zn-cyclohexanebutyrate dihydrate in DMSO. From the XRD patterns, it has been found that at low ZnO loading confined NPs of a very small size (1–2 nm) are produced, whereas at high ZnO loading, a part of the ZnO NPs grew at the external surface of kaolinite. The absorption onset of ZnO in layered clay minerals showed a strong blue-shift compared to bare ZnO prepared at the same precursor concentrations. In kaolinite, the particle size of ZnO was larger and the intercalation ratio was smaller than in montmorillonite 2:1 (a typical smectite clay mineral). In this last case, the average particle size of ZnO (2.6–13.0 nm) obtained from the same concentration of the precursor was affected by the cation-exchange capacity of the clay minerals [85].

Layered clay minerals belonging to the smectite group, such as montmorillonite, hectorite, stevensite and beidellite [99-108], as well as fibrous silicates such as sepiolite and palygorskite [109-116] have been also assembled with TiO_2 NPs yielding various clay-based nanoarchitectures with photocatalytic activity (Table 1). For instance, a method to develop TiO_2@hectorite as multilayer films using layer-by-layer self-assembly has been reported by Ma and co-workers [103]. TiO_2 NPs have been also precipitated in the presence of layered silicates such as montmorillonite and hectorite using Ti alkoxides or $TiCl_4$ and $TiCl_3$ as precursors. Similarly, ZnO NPs have been assembled with diverse smectites [46,89,117-120] and fibrous clay minerals [87,90,118,121,122].

The characteristics of the NPs on clay minerals vary depending on the preparation conditions. For instance, in the case of TiO_2@clays formed by the hydrolysis at 90 °C of titanium(IV) oxysulfate in a kaolinite suspension, anatase NPs of 18 nm size were formed. In this case, a preferential growth at the edges of platy aluminosilicate particles was observed [94,97]. This preference can be tentatively ascribed to the anchorage of TiO_2 NPs

through the aluminol groups located at the kaolinite edges. These NPs grew from 6 to 18 nm during calcination at 500–700 °C with a phase transition from anatase to rutile taking place at ca. 650 °C [96]. Layered silicates, such as kaolinite and montmorillonite, also stabilize the formation of ZnO NPs (Figure 2A) from zinc cyclohexanebutyrate hydrolyzed in dimethyl sulfoxide. The particle size is clearly influenced by the nature of the clay [85]. In the case of HNTs, TiO_2 NPs of 5–15 nm size were formed inside the halloysite tubes (lumen) as observed by TEM (Figure 2B) [123]. Moreover, Papoulis and co-workers [114] have been reported that the particle size of TiO_2 NPs is about 3–15 nm in the macropores of the clay, which corresponds to the central hole in HNTs, leading to the blockage of the lumen. The particle size of titania NPs homogeneously deposited on the external surface of palygorskite fibrous clay was 10–30 nm as detected by SEM [114]. In another example, ZnO NPs from zinc acetate ca. 20 nm were exclusively located at the external surface of the palygorskite silicate fibres [121]. ZnO can be also directly formed on the external surface of sepiolite fibres (Figure 2C), using zinc acetylacetonate as precursor [87].

As reported by Fatimah et al. [89], ZnO@montmorillonite materials can be synthesized from a Zn solution and cetyltrimethylammonium (CTA)-montmorillonite organoclays. In these materials, the bandgap energy of ZnO is decreased compared to bare ZnO NPs, which results in a faster photodegradation of MB. In experiments to prepare ZnO@clay nanoarchitectures using smectites such as natural montmorillonite, synthetic saponite, as well as the corresponding CTA-smectites, Khaorapapong and co-workers [46,92,93] synthesized diverse photocatalysts where the ZnO NPs were formed on the inner and/or outer surfaces of the CTA-smectites. The photoluminescence at visible wavelengths (blue and green emission at around 436–438 nm and 544–548 nm) of ZnO hybridized with CTA-smectites varies depending on the ZnO loading. This was attributed to defects, such as oxygen vacancies in ZnO, and trapped surface charges. The photoluminescence intensity of ZnO in saponite and CTA-saponite was stronger than in montmorillonite and CTA-montmorillonite, suggesting that the iron atoms in montmorillonite play a significant role through the quenching of excited states. In the photodegradation experiments, the ZnO–smectite nanoarchitectures show a longer life time at low pH values than bare ZnO. This was attributed to the dissolution of ZnO in acidic solution, which is suppressed by the hybridization with smectites [46,92,93]. CTA-smectites treated with a hydrothermal solution intercalation method at 70 °C for 10 h lead to ZnO@CTA-montmorillonite where the ZnO NPs are either embedded in the interlayer space of the organoclays or dispersed on its external surface. These nanomaterials can be applied as antibactericide. It has been observed that they destroy

Figure 2: TEM images of (A) ZnO NPs on montmorillonite with nanocrystal aggregation; reprinted with permission from [85], copyright 2004 American Chemical Society; (B) TiO_2@HNTs nanoarchitecture showing the titania NP assembled inside the lumen of the halloysite tubes; adapted with permission from [123], copyright 2011 American Chemical Society; and (C) ZnO@sepiolite where the ZnO NPs were generated on the external surface of the fibrous clay from zinc acetylacetonate following the protocol described in [87].

the cellular surface structure of *Microcystis aeruginosa,* and also inhibit the physiological activity of *M. aeruginosa,* when exposed to UV light [117]. Other alternative approaches include

the direct precipitation of the ZnO from Zn salts in presence of bentonite dispersed in ethanol [124] or the association of ZnO NPs with Laponite® using poly(vinyl alcohol) as binder agent [125]. In both cases, the resulting materials show photocatalytic activity and are easily recoverable from the reaction medium.

The so-called "organoclay colloidal route" [71,109,126] represents an innovative approach to prepare, under mild conditions, porous nanoarchitectures from alkylammonium-exchanged smectite clays combined to metal-oxide NPs already synthesized or formed in situ by incorporation of the corresponding precursors (alkoxides, salts in alkaline medium and metal complexes) as schematized in Figure 3. Of particular relevance is the irreversible delamination of the 2:1 charged layered silicates, e.g., smectite clay minerals, taking place during the heterocoagulation of hydrolyzed alkoxides previously incorporated in the surfactant–clay interface, as it was first reported by Letaïef and Ruiz-Hitzky [126,127]. In the same way, organoclays dispersed in an organic solvent can facilitate the incorporation of already formed metal-oxide nanoparticles, leading to a loss of the stacking order in the silicate layers due to the assembly with ZnO NPs [118].

The protocol schematized in Figure 3A, a very convenient pathway to produce functional nanoarchitectures by using alkylammonium-exchanged layered clays, has been applied to produce TiO_2@clay and ZnO@clay materials. Following this approach, micro- and mesoporous clay–semiconductor nanoarchitectures with high pore volume and increased specific sur-

face area due to clay delamination have been obtained. In some of these materials, the TiO_2 and ZnO NPs generated from the corresponding alkoxides, salts or coordination complexes, remain associated with the delaminated clay sheets, resulting in stable and efficient photoactive catalysts of particular interest for the removal of organic pollutants from wastewater [84,87,89,106,107,118,128]. Akkari and co-workers [118] have recently applied this procedure to assemble ZnO NPs, previously synthesized by hydrolysis of Zn acetate, with organoclays derived from two different smectites (Figure 3A), leading to ZnO@smectite nanoarchitectures in which the delaminated silicate remains associated with ZnO NPs of 7–10 nm size. The specific surface area values are of the order of 50–100 m^2/g whereas the ZnO NPs alone exhibit values below 15 m^2/g. The mesoporosity (ca. 0.25 cm^3/g total porosity) together the photoactivity of the ZnO NPs make these materials suitable photocatalysts for the removal of organic dyes from water [118]. ZnO–clay nanoarchitectures have been prepared by in situ generation of ZnO NPs using Zn acetylacetonate precursor in isopropanol under reflux in the presence of the organoclays, leading to intermediate ZnO@clay organo-heterostructures. After calcination, the organic matter (alkyl groups from the organoclay) is eliminated and the ZnO NPs remain assembled to the clay surface [83]. These materials exhibit good photoactivity useful for the removal of organic pollutants such as pharmaceutical drugs from water.

In recent years, fibrous clays are attracting increasing interest as supports for the assembly with a large variety of nanoparticles
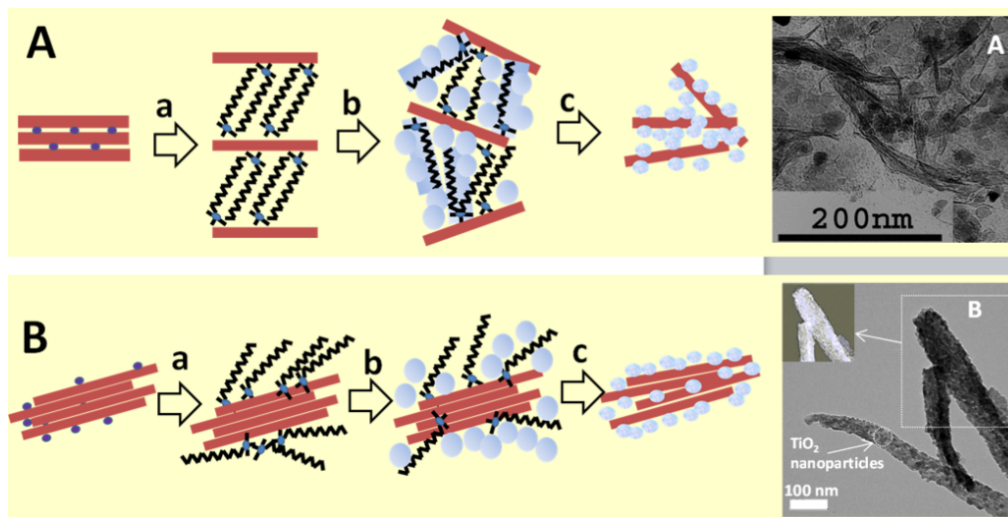

Figure 3: Synthesis of clay–semiconductor nanoarchitectures by the "organoclay colloidal route" involving either smectites (A) or fibrous clays (B) in the following steps: a) replacement of inorganic cations by alkylammonium ions forming the intermediate organoclay, which is treated with metal-oxide precursors being transformed (b) into intermediate compounds that after calcination (c) finally yield the nanoarchitecture containing the photoactive semiconductor. TEM Images (on the right) of A: ZnO@smectite from Gafsa, where ZnO NPs were previously prepared from Zn acetate [118], and B: TEM of TiO_2@sepiolite, where TiO_2 NPs were prepared from titanium isopropoxide; reprinted with permission from [109], copyright 2008 American Chemical Society.

in the search of new functional and multifunctional nanostructured materials [11]. The procedures used to assemble TiO_2 and ZnO NPs with sepiolite and palygorskite include the in situ generation from salts [90,122,129] or alkoxide precursors in presence of organoclays [109,111], directly on the clay surface from precursors dispersed with surfactants [116] or without [129,130], as well as the direct attachment of already formed particles to the clay [118,122]. The characteristics of the resulting materials are strongly influenced by the preparation conditions as the generated NPs show significant differences in size, degree of self-agglomeration as well as dispersion on the surface of the clay, which may influence the resulting properties of the materials.

The principle of using the interfaces in layered clays is also applicable to fibrous clays with the generation of NPs homogeneously distributed on the surface of sepiolite or palygorskite [109,111,118]. Figure 3 also shows TEM images of TiO_2 produced in a controlled sol–gel process on the external surface of sepiolite modified with cetyltrimethylammonium ions. A coverage of the silicate surface by small NPs (4–8 nm diameter) suitable for photocatalytic applications is clearly seen [109]. An advantage of the organoclay colloidal route is the possibility to incorporate NPs of different nature, in one or multiple steps, which can be of interest for the introduction of diverse functionalities in the resulting nanoarchitectures [131,132]. The incorporation of various types of NPs using neat clay and applying a two-step synthesis has been reported. A recent example of this refers to the incorporation of ZnO nanoparticles to a Fe_3O_4-sepiolite nanoarchitecture previously prepared by in situ formation of superparamagnetic iron-oxide nanoparticles on the external surface of sepiolite fibres. The resulting ZnO–Fe_3O_4@sepiolite nanoarchitecture exhibits photoactivity due to the ZnO NPs, and the presence of magnetite NPs facilitates the recovery by the use of a magnet (Figure 4) [133]. Moreover, the presence of iron oxide could be useful also to profit from possible Fenton processes improving the overall photocatalytic efficiency. This opportunity would be of interest for future developments of multifunctional nanoarchitectured photocatalysts.

Tuning the photoactivity of TiO_2–clay and ZnO–clay nanoarchitectures: catalytic applications and perspectives

Nanoparticulated TiO_2 has almost the same bandgap characteristics than ZnO, with bandgap energies of 3.20 eV and 3.37 eV, respectively [48,134-136]. Therefore, the photocatalytic capability of both types of NPs should be quite similar. Apart from these large bandgap energy values, both metal oxides exhibit a large exciton binding energy, large piezoelectric constants and strong photoluminescence. This is of interest not only for applications as photocatalysts but also as sensors, solar cell devices, disinfectants, and cosmetics [137,138].

As discussed above, the dispersion of the semiconducting NPs on inert porous solids of large specific surface area is considered to be beneficial for the photocatalytic activity. Recently, strategies have been reported to improve the performance of photocatalysts via doping, or the introduction of semiconductor heterojunctions by combining them with transition metals or with other semiconductors. Among them, semiconductor heterojunctions have attracted great attention [139]. The doping of TiO_2 and ZnO NPs with the aim to conveniently tuning the bandgap energy values can be a suitable option. In this context, it has been verified for both types of NPs, a decrease in the bandgap values by doping with Ag, Pd and other transition metals such as Zr, W, Ce, Sn, Sb and In improve the photoactivity efficiency [140]. Alternatively, combination of TiO_2 and ZnO with other metal oxides leads to mixed oxide NPs, including the TiO_2–ZnO compositions, which exhibit alternative interesting semiconductor–semiconductor heterojunctions. Finally, another approach to increase the photo-efficiency of the consid-
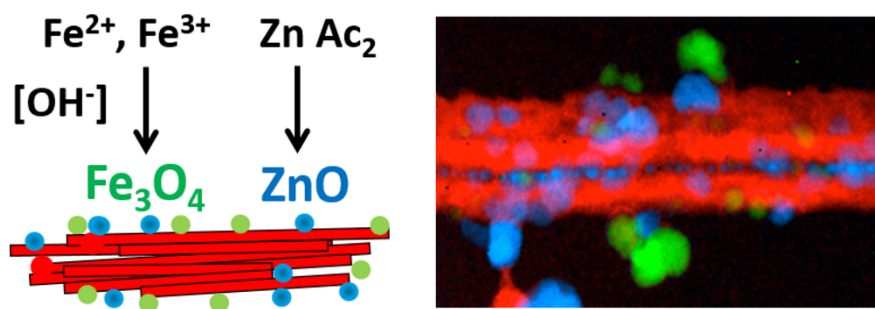

Figure 4: ZnO-Fe_3O_4@sepiolite nanoarchitecture prepared in two steps: First, the fiber clay is modified by assembly of magnetite NPs. After that, the ZnO NPs are added yielding a magnetic photocatalyst. The STEM images on the right shows the silicate component (red), the magnetite NPs (green) and the ZnO NPs (blue) analyzed with an EDAX detector and a Gatan Tridiem energy filter; reprinted with permission from [133], copyright 2017 Elsevier.

ered systems is the photosensitization of TiO_2 and ZnO NPs to obtain visible-light responsive photocatalysts as well as solar-cell components [93,141,142]. These approaches to control the intrinsic characteristics of the NPs with the aim of modulating and improving their photoactivity are discussed below.

Li and co-workers [143] have prepared ZnO@kaolinite doped with Pd(II) following a soft chemistry procedure that involves the use of $PdCl_2$ and polyvinylpyrrolidone as starting reagents. Interestingly, they reported a considerable increase of the photocatalytic activity in the degradation of methylene blue (MB) in water solution under UV irradiation for Pd–ZnO@kaolinite compared to Pd@ZnO, ZnO@kaolinite, and pure ZnO under equivalent experimental conditions. Pd- and Pt-doped TiO_2@clay nanoarchitectures based on sepiolite and montmorillonite have been also prepared by applying two different strategies: i) in situ incorporation of the noble-metal precursor (typically acetylacetonate) in the suspension of commercial organoclays (e.g., Cloisite®30B and sepiolite Pangel B20, prepared by modification of montmorillonite and sepiolite with cationic surfactants, respectively) during sol-gel process, and ii) selective photodeposition of the noble metal in the previously formed TiO_2@clay nanoarchitecture [131]. The good dispersion of the noble-metal NPs, clearly revealed by TEM (Figure 5A), leads to efficient nanostructured materials for the photocatalytic production of hydrogen tested in methanol photoreforming. Herein, montmorillonite-based nanoarchitectures are less efficient as hydrogen production catalyst than nanoarchitectures derived from sepiolite. Higher rates of hydrogen production are obtained with the Pt-doped TiO_2@sepiolite nanoarchitectures obtained by photodeposition (Figure 5B).

Photocatalysts based on Ag-doped ZnO@montmorillonite reported by Sohrabnezhad and Seifi [144] are another example for the enhancement of photocatalytic activity through doping.

Silver metal NPs (Ag) were prepared from $AgNO_3$ and deposited over ZnO@montmorillonite following a green approach for the Ag^+ reduction. Here again, the doped nanoarchitecture (Ag–ZnO@montmorillonite) exhibited a better efficiency than the corresponding ZnO@montmorillonite and Ag@ZnO samples, in this case tested in the MB removal from water solutions.

Belver and co-workers [145-147] have recently reported that doping of TiO_2@clay nanoarchitectures with elements such as W, Zr and Ce leads to enhanced solar photocatalytic activity for the removal of organic pollutants such as pharmaceutical drugs, organic dyes, and phenols in aqueous solution. The single-step synthesis yields W–TiO_2, Zr–TiO_2 and Ce–TiO_2 immobilized on the surface of delaminated layered clay derived from montmorillonite. The resulting doped TiO_2@clay materials showed high specific surface area values and a slight reduction of the TiO_2 bandgap leading to improved efficiency in the degradation of antipyrine, atrazine, rhodamine B and phenol using solar-light irradiation.

Chen and co-workers [148] have also studied the doping of TiO_2@montmorillonite introducing heteroelements such as C and V. A bandgap reduction to 2.25 eV, corresponding to a light wavelength of 550 nm suitable for a photocatalyst responsive to visible light was reported. The co-doping of N and S [149] and Cu, Ag, and Fe on TiO_2@bentonite has also been reported [150]. Other authors also reported the modification of the photoactivity characteristics by the deposition of metallic particles such as Ag, V, and Pt on TiO_2@montmorillonite [151-157].

Novel TiO_2–ZnO@clay nanoarchitectures have been recently prepared from diverse clay minerals with improved photoactivity in the resulting materials [158-161]. Probably the first contribution was introduced by Bel Hadjltaief and co-workers
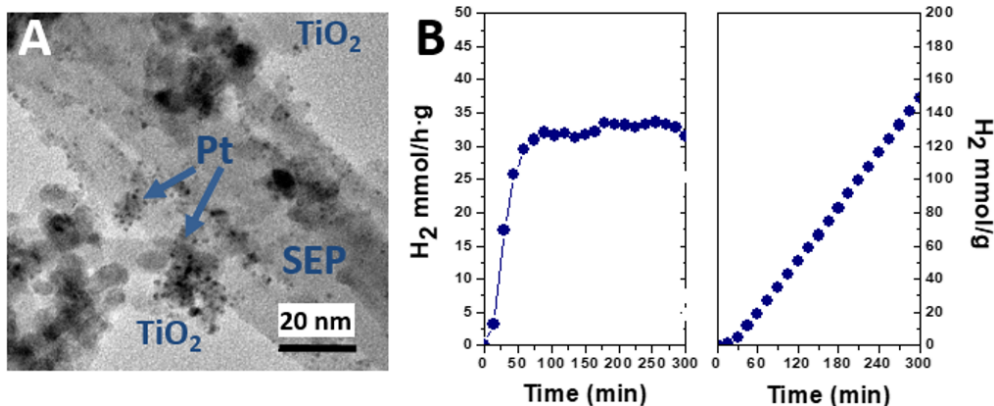

Figure 5: (A) TEM image of the Pt–TiO_2@sepiolite clay nanoarchitectures prepared by a photodeposition procedure, reprinted with permission from [131], copyright 2015 Elsevier; (B) hydrogen production in methanol photoreforming using this Pt-doped clay nanoarchitecture as catalyst [131].

[158], using a Tunisian Na$^+$-smectite treated with titanium(IV) isopropoxide and zinc acetate. This ZnO–TiO$_2$@clay material shows that a rapid and complete mineralization of methyl green dye in water can be achieved with the additional of ZnO providing a higher photocatalytic activity to the starting clay or the TiO$_2$@clay nanoarchitecture. Related ZnO–TiO$_2$@clay materials based on commercially available expanded clay aggregates (LECA), apparently belonging to the smectite family, have been also positively tested as photocatalyst for the removal of ammonia from wastewater (Table 1) [161]. Also, TiO$_2$–ZnO@clay nanoarchitectures derived from a smectite (Cloisite®30B) have been also prepared by sol–gel reactions involving the delamination of the silicate. The resulting materials show good photocatalytic activity for the photodegradation of pollutants such as the pharmaceutical drugs acetaminophen and antipyrine and the pesticide atrazine [147,159,162]. TiO$_2$–ZnO@clay materials have been also prepared from fibrous clay minerals such as sepiolite, as recently reported by Vaizoğullar [160]. The TiO$_2$–ZnO@sepiolite nanoarchitecture shows good catalytic activity (ca. 85%) in the photodegradation of the antibiotic flumequine in aqueous solution. Interestingly, the sepiolite nanoarchitecture shows better degradation efficiency than the semiconducting components alone according to the following sequence [160]: TiO$_2$–ZnO@sepiolite > TiO$_2$–ZnO > TiO$_2$ > ZnO.

It can be summarized that this type of nanostructured materials prepared from diverse clay minerals constitutes a promising way to enhance the photoactivity of the semiconductors. The idea can be extended to structurally more complex clays, as it is the case of rectorite, a 1:1 regular interstratification of two phyllosilicates (mica/montmorillonite), and the commercial clay aggregates named as LECA. Both, silicates involved in the assembly of TiO$_2$–ZnO lead to photocatalysts useful for the removal of pollutants in wastewater [161-163].
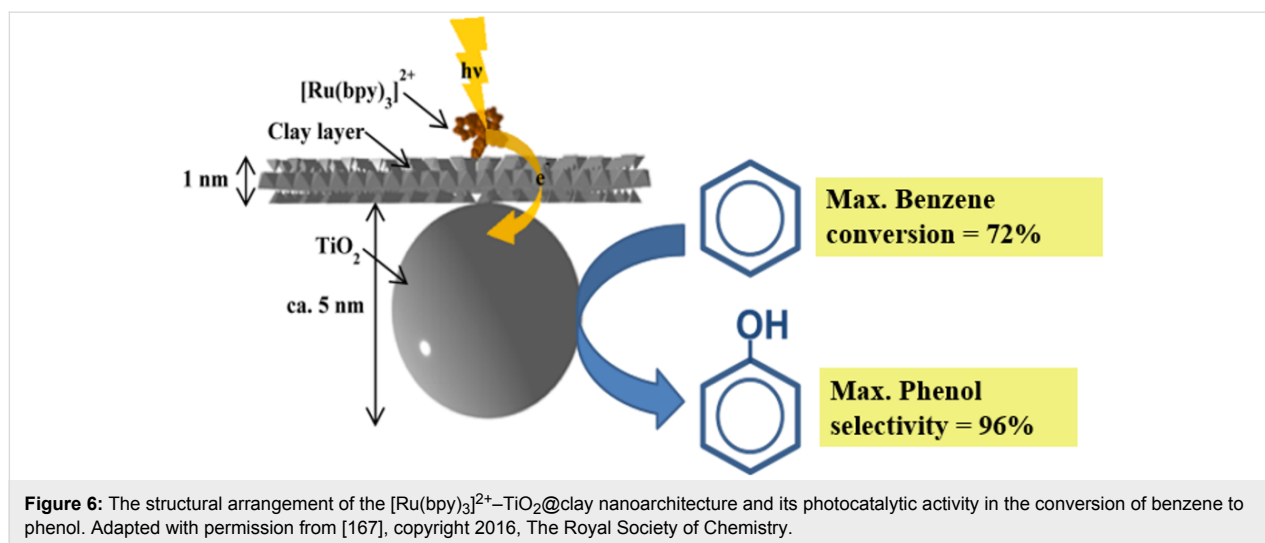
Due to the abundance of clay minerals in nature, these results are relevant for the production at large scale of eco-friendly materials for depollution of water using light as energy source. Additional investigations to ascertain the observed photoactivity and to explain the involved mechanisms are still needed. Regarding possible future contributions in the use of mixed-oxide NPs, it would be also of interest to explore new synthetic procedures for the preparation of nanoparticulated TiO$_2$–ZnO solids. See for instance the recent and systematic studies developed by Bachvarova-Nedelcheva et al. [164], which could be used for the assembly of diverse types of clay minerals.

According to the Encyclopedia Britannica, the term "photosensitization" is defined as "the process of initiating a reaction through the use of a substance capable of absorbing light and transferring the energy to the desired reactants" [165]. Therefore, photosensitization represents an additional improvement of the photoactivity tuning of semiconductor–clay nanoarchitectures. For instance, tris(2,2′-bipyridine)ruthenium(II) has been used as photosensitizer for titania, being further applied to TiO$_2$@clay nanoarchitectures. In this way, a synthetic saponite containing tris(2,2′-bipyridine)ruthenium(II) intercalated in the interlayer space was complexed with TiO$_2$ NPs [166]. The resulting material shows enhanced stability toward visible-light irradiation, if compared with the TiO$_2$ (P25) standard material photosensitized by an analogous commercially available photosensitizer (tris(2,2′ -bipyridine-4,4′-dicarboxylic acid)ruthenium(II) dichloride, abbreviated as Ru470). The stability of the two samples was compared by measuring the color change after visible-light irradiation from a solar simulator. The colour of the clay nanoarchitecture (hereafter abbreviated as [Ru(bpy)$_3$]$^{2+}$–TiO$_2$@clay) did not change after irradiation for 4 h, while bleaching of Ru470 on P25 was observed. The superior stability of [Ru(bpy)$_3$]$^{2+}$–TiO$_2$@clay upon the irradiation was explained as follows: [Ru(bpy)$_3$]$^{2+}$ was separated from the TiO$_2$ surface by the clay nanosheet, while the photoexcited complex can still interact with TiO$_2$ due to the hybrid structure (at an appropriate distance). The [Ru(bpy)$_3$]$^{2+}$–TiO$_2$@clay induced the direct oxidation of aqueous benzene to phenol under visible-light irradiation (Figure 6). The oxidation of aqueous benzene to phenol was very efficient (the maximum yield of benzene conversion and the selectivity of phenol are 72 and 96%, respectively) after visible-light irradiation for 5 h. The photocatalytic reaction efficiency on the oxidation of benzene (referred to both benzene elimination yield and the selectivity of the formation of phenol) was substantially changed when the reactions were conducted in the presence of phenol (starting from a benzene/phenol mixture in water). There is a demand for an alternative to the commonly used cumene process in the production of phenol. A photocatalytic reaction with high yields and selectivity of phenol can be highly suitable for mass production [167]. The difficulties in the application to continuous-flow systems has been solved by processing the [Ru(bpy)$_3$]$^{2+}$–TiO$_2$@clay nanoarchitecture as a film to be mounted in a flow reactor [168]. The film of the [Ru(bpy)$_3$]$^{2+}$TiO$_2$–@clay photocatalyst is stable and can be reutilized, which is a very important advantage for the flow system. A simpler continuous-flow reactor was designed by Meshram and co-workers [169].

Conclusions and Future Perspectives

Clay minerals are abundant, low-cost and benign materials that can be advantageous over other kinds of inorganic solids used in heterogeneous catalysis. They represent a source of components easily applicable to the development of new photocatalysts based on these silicates. We have above examined how

Figure 6: The structural arrangement of the [Ru(bpy)$_3$]$^{2+}$–TiO$_2$@clay nanoarchitecture and its photocatalytic activity in the conversion of benzene to phenol. Adapted with permission from [167], copyright 2016, The Royal Society of Chemistry.

titanium oxide and zinc oxide NPs can be assembled to diverse type of clay minerals of variable topologies leading to nanoarchitectured materials with more or less tunable photoactivity.

Optimization and streamlining of synthetic processes must be achieved in order to tailor the physical and chemical characteristics of those materials. For instance, efforts have been made to combine TiO$_2$ NPs with clays and clay minerals by a simple mixing to obtain a modified catalytic activity of titanium dioxide in aqueous clay suspensions [170]. In addition, mechanochemical methods [171] seem to be applicable to the complexation of TiO$_2$ with clays and clay minerals as alternative synthetic route.

Doping of TiO$_2$@clay and ZnO@clay photocatalysts with different metals, particularly noble metals, as well as the use of semiconducting mixed oxides, e.g., TiO$_2$/ZnO, are promising approaches, necessary to deeply study the correlations between electronic configuration, bandgap energy and photochemical efficiency. Improvements could be expected by controlled modification of the electronic characteristics, or by adding conducting polymers with different degrees of transparency, or black electronic collectors such as graphene and CNT components to the nanoarchitectured clay-based materials.

Photosensitization using organic components is a potential way to improve the photo-efficiency of these systems, which can, coupled to the beneficial effect provided by the metal doping of both semiconducting oxides, further improve the photoactivity of these new nanomaterials.

Nowadays, the main application is the removal of organic pollutants from contaminated wastewater. However, new challenges are developments regarding applications related to antibacterial activity and uses in the production of fine chemicals through photo-assisted organic syntheses. The use as films and membranes appears as a valuable alternative for industrial processes. Moreover, the clays can be used as substrates for the incorporation of additional active species, e.g, NPs or organic and biological species, for the production of multifunctional nanoplatforms as components of sensing devices and solar cells.

Acknowledgements

ORCID® iDs
Eduardo Ruiz-Hitzky - https://orcid.org/0000-0003-4383-7698
Pilar Aranda - https://orcid.org/0000-0003-2196-0476
Makoto Ogawa - https://orcid.org/0000-0002-3781-2016

References
1. Ariga, K.; Aono, M., Eds. *Supra-Materials Nanoarchitectonics;* Elsevier: Amsterdam, Netherlands, 2017. doi:10.1016/c2014-0-03535-6
2. Aono, M.; Bando, Y.; Ariga, K. *Adv. Mater. (Weinheim, Ger.)* **2012,** *24,* 150–151. doi:10.1002/adma.201104614
3. Ariga, K., Ed. *Manipulation of Nanoscale Materials: An Introduction to Nanoarchitectonics;* Royal Society of Chemistry: Cambridge, United Kingdom, 2012. doi:10.1039/9781849735124
4. Khan, A. H.; Ghosh, S.; Pradhan, B.; Dalui, A.; Shrestha, L. K.; Acharya, S.; Ariga, K. *Bull. Chem. Soc. Jpn.* **2017,** *90,* 627–648. doi:10.1246/bcsj.20170043
5. Fujii, K.; Hashizume, H.; Shimomura, S.; Ariga, K.; Ando, T. *Appl. Clay Sci.* **2015,** *104,* 88–95. doi:10.1016/j.clay.2014.11.013

6. Vinokurov, V. A.; Stavitskaya, A. V.; Chudakov, Y. A.; Ivanov, E. V.; Shrestha, L. K.; Ariga, K.; Darrat, Y. A.; Lvov, Y. M. *Sci. Technol. Adv. Mater.* **2017,** *18,* 147–151. doi:10.1080/14686996.2016.1278352

7. Ruiz-Hitzky, E.; Aranda, P.; Darder, M.; Ogawa, M. *Chem. Soc. Rev.* **2011,** *40,* 801–828. doi:10.1039/c0cs00052c

8. Ruiz-Hitzky, E.; Aranda, P.; Belver, C. Nanoarchitectures Based on Clay Materials. In *Manipulation of Nanoscale Materials: An Introduction to Nanoarchitectonics;* Ariga, K., Ed.; Nanoscience & Nanotechnology Series; Royal Society of Chemistry: Cambridge, United Kingdom, 2012; pp 87–111. doi:10.1039/9781849735124-00087

9. Aranda, P.; Belver, C.; Ruiz-Hitzky, E. Nanoarchitectures by Sol-Gel from Silica and Silicate Building Blocks. In *The Sol–Gel Handbook: Synthesis, Characterization, and Applications;* Levy, D.; Zayat, M., Eds.; Wiley-VCH Verlag GmbH: Weinheim, Germany, 2015; pp 443–470. doi:10.1002/9783527670819.ch14

10. Aranda, P.; Ruiz Hitzky, E. Nanoarchitectures based on sepiolite: assembly of nanoparticles. In *Surface Modification of Clays and Nanocomposites;* Beall, G.; Powell, C. E., Eds.; CMS Workshop Lectures Series, Vol. 20; The Clay Minerals Society: Chantilly, VA, U.S.A., 2016; pp 87–100. doi:10.1346/cms-wls-20.7

11. Aranda, P.; Ruiz-Hitzky, E. *Chem. Rec.* **2018,** *18,* 1125–1137. doi:10.1002/tcr.201700113

12. Linsebigler, A. L.; Lu, G.; Yates, J. T., Jr. *Chem. Rev.* **1995,** *95,* 735–758. doi:10.1021/cr00035a013

13. Fujishima, A.; Rao, T. N.; Tryk, D. A. *J. Photochem. Photobiol., C* **2000,** *1,* 1–21. doi:10.1016/s1389-5567(00)00002-2

14. Zhang, X.; Wang, F.; Huang, H.; Li, H.; Han, X.; Liu, Y.; Kang, Z. *Nanoscale* **2013,** *5,* 2274–2278. doi:10.1039/c3nr34142a

15. Gupta, M.; Sharma, V.; Shrivastava, J.; Solanki, A.; Singh, A. P.; Satsangi, V. R.; Dass, S.; Shrivastav, R. *Bull. Mater. Sci.* **2009,** *32,* 23–30. doi:10.1007/s12034-009-0004-1

16. Klingshirn, C. *Phys. Status Solidi B* **2007,** *244,* 3027–3073. doi:10.1002/pssb.200743072

17. Liangyuan, C.; Zhiyong, L.; Shouli, B.; Kewei, Z.; Dianqing, L.; Aifan, C.; Liu, C. C. *Sens. Actuators, B* **2010,** *143,* 620–628. doi:10.1016/j.snb.2009.10.009

18. Krunks, M.; Katerski, A.; Dedova, T.; Oja Acik, I.; Mere, A. *Sol. Energy Mater. Sol. Cells* **2008,** *92,* 1016–1019. doi:10.1016/j.solmat.2008.03.002

19. Kou, J.; Li, Z.; Guo, Y.; Gao, J.; Yang, M.; Zou, Z. *J. Mol. Catal. A* **2010,** *325,* 48–54. doi:10.1016/j.molcata.2010.03.029

20. Barnes, R. J.; Molina, R.; Xu, J.; Dobson, P. J.; Thompson, I. P. *J. Nanopart. Res.* **2013,** *15,* 1432. doi:10.1007/s11051-013-1432-9

21. Web of Science. https://apps.webofknowledge.com/ (accessed Feb 20, 2019).

22. Hernández-Alonso, M. D.; Fresno, F.; Suárez, S.; Coronado, J. M. *Energy Environ. Sci.* **2009,** *2,* 1231–1257. doi:10.1039/b907933e

23. Kabra, K.; Chaudhary, R.; Sawhney, R. L. *Ind. Eng. Chem. Res.* **2004,** *43,* 7683–7696. doi:10.1021/ie0498551

24. Vilhunen, S.; Sillanpää, M. *Rev. Environ. Sci. Bio/Technol.* **2010,** *9,* 323–330. doi:10.1007/s11157-010-9216-5

25. Hoffmann, M. R.; Martin, S. T.; Choi, W.; Bahnemann, D. W. *Chem. Rev.* **1995,** *95,* 69–96. doi:10.1021/cr00033a004

26. Sudha, D.; Sivakumar, P. *Chem. Eng. Process.* **2015,** *97,* 112–133. doi:10.1016/j.cep.2015.08.006

27. Chen, D.; Ray, A. K. *Chem. Eng. Sci.* **2001,** *56,* 1561–1570. doi:10.1016/s0009-2509(00)00383-3

28. López-Muñoz, M. J.; Aguado, J.; Arencibia, A.; Pascual, R. *Appl. Catal., B* **2011,** *104,* 220–228. doi:10.1016/j.apcatb.2011.03.029

29. Liu, X.; Pan, L.; Zhao, Q.; Lv, T.; Zhu, G.; Chen, T.; Lu, T.; Sun, Z.; Sun, C. *Chem. Eng. J.* **2012,** *183,* 238–243. doi:10.1016/j.cej.2011.12.068

30. Weibel, A.; Bouchet, R.; Boulc, F.; Knauth, P. *Chem. Mater.* **2005,** *17,* 2378–2385. doi:10.1021/cm0403762

31. Chen, X.; Mao, S. S. *Chem. Rev.* **2007,** *107,* 2891–2959. doi:10.1021/cr0500535

32. Fröschl, T.; Hörmann, U.; Kubiak, P.; Kučerová, G.; Pfanzelt, M.; Weiss, C. K.; Behm, R. J.; Hüsing, N.; Kaiser, U.; Landfester, K.; Wohlfahrt-Mehrens, M. *Chem. Soc. Rev.* **2012,** *41,* 5313–5360. doi:10.1039/c2cs35013k

33. Laxman, K.; Al Rashdi, M.; Al Sabahi, J.; Al Abri, M.; Dutta, J. *Appl. Surf. Sci.* **2017,** *411,* 285–290. doi:10.1016/j.apsusc.2017.03.139

34. Daneshvar, N.; Rasoulifard, M. H.; Khataee, A. R.; Hosseinzadeh, F. *J. Hazard. Mater.* **2007,** *143,* 95–101. doi:10.1016/j.jhazmat.2006.08.072

35. Daneshvar, N.; Salari, D.; Khataee, A. R. *J. Photochem. Photobiol., A* **2004,** *162,* 317–322. doi:10.1016/s1010-6030(03)00378-2

36. Dindar, B.; Içli, S. *J. Photochem. Photobiol., A* **2001,** *140,* 263–268. doi:10.1016/s1010-6030(01)00414-2

37. Lizama, C.; Freer, J.; Baeza, J.; Mansilla, H. D. *Catal. Today* **2002,** *76,* 235–246. doi:10.1016/s0920-5861(02)00222-5

38. Tang, Q.; Zhou, W.; Shen, J.; Zhang, W.; Kong, L.; Qian, Y. *Chem. Commun.* **2004,** 712–713. doi:10.1039/b313387g

39. Djurišić, A. B.; Chen, X.; Leung, Y. H.; Man Ching Ng, A. *J. Mater. Chem.* **2012,** *22,* 6526–6535. doi:10.1039/c2jm15548f

40. Jang, E. S.; Won, J.-H.; Hwang, S.-J.; Choy, J.-H. *Adv. Mater. (Weinheim, Ger.)* **2006,** *18,* 3309–3312. doi:10.1002/adma.200601455

41. Ghosh, A.; Deshpande, N. G.; Gudage, Y. G.; Joshi, R. A.; Sagade, A. A.; Phase, D. M.; Sharma, R. *J. Alloys Compd.* **2009,** *469,* 56–60. doi:10.1016/j.jallcom.2008.02.061

42. Mclaren, A.; Valdes-Solis, T.; Li, G.; Tsang, S. C. *J. Am. Chem. Soc.* **2009,** *131,* 12540–12541. doi:10.1021/ja9052703

43. Bian, S.-W.; Mudunkotuwa, I. A.; Rupasinghe, T.; Grassian, V. H. *Langmuir* **2011,** *27,* 6059–6068. doi:10.1021/la200570n

44. Fatin, S. O.; Lim, H. N.; Tan, W. T.; Huang, N. M. *Int. J. Electrochem. Sci.* **2012,** *7,* 9074–9084.

45. Kou, J.; Lu, C.; Wang, J.; Chen, Y.; Xu, Z.; Varma, R. S. *Chem. Rev.* **2017,** *117,* 1445–1514. doi:10.1021/acs.chemrev.6b00396

46. Khumchoo, N.; Khaorapapong, N.; Ontam, A.; Intachai, S.; Ogawa, M. *Eur. J. Inorg. Chem.* **2016,** *2016,* 3157–3162. doi:10.1002/ejic.201600252

47. Kosmulski, M. *J. Colloid Interface Sci.* **2009,** *337,* 439–448. doi:10.1016/j.jcis.2009.04.072

48. Hariharan, C. *Appl. Catal., A* **2006,** *304,* 55–61. doi:10.1016/j.apcata.2006.02.020

49. Pauporté, T.; Rathouský, J. *J. Phys. Chem. C* **2007,** *111,* 7639–7644. doi:10.1021/jp071465f

50. Sang, L.; Zhao, Y.; Burda, C. *Chem. Rev.* **2014,** *114,* 9283–9318. doi:10.1021/cr400629p

51. Chen, X.; Mao, S. S. *J. Nanosci. Nanotechnol.* **2006,** *6,* 906–925. doi:10.1166/jnn.2006.160

52. Gomez, J. L.; Tigli, O. *J. Mater. Sci.* **2013,** *48,* 612–624. doi:10.1007/s10853-012-6938-5

53. Spanhel, L. *J. Sol-Gel Sci. Technol.* **2006,** *39,* 7–24. doi:10.1007/s10971-006-7302-5

54. Li, X.; Yu, J.; Jaroniec, M. *Chem. Soc. Rev.* **2016,** *45,* 2603–2636. doi:10.1039/c5cs00838g

55. Liu, S.; Li, C.; Yu, J.; Xiang, Q. *CrystEngComm* **2011,** *13,* 2533–2541. doi:10.1039/c0ce00295j

56. Gunjakar, J. L.; Kim, I. Y.; Lee, J. M.; Jo, Y. K.; Hwang, S.-J. *J. Phys. Chem. C* **2014,** *118,* 3847–3863. doi:10.1021/jp410626y

57. Zhan, Z.; Zheng, L.; Pan, Y.; Sun, G.; Li, L. *J. Mater. Chem.* **2012,** *22,* 2589–2595. doi:10.1039/c1jm13920g

58. Zhu, L.-P.; Liao, G.-H.; Huang, W.-Y.; Ma, L.-L.; Yang, Y.; Yu, Y.; Fu, S.-Y. *Mater. Sci. Eng., B* **2009,** *163,* 194–198. doi:10.1016/j.mseb.2009.05.021

59. Yuan, S.; Li, Y.; Zhang, Q.; Wang, H. *Colloids Surf., A* **2009,** *348,* 76–81. doi:10.1016/j.colsurfa.2009.06.040

60. Kim, H. S.; Jeong, N. C.; Yoon, K. B. *J. Am. Chem. Soc.* **2011,** *133,* 1642–1645. doi:10.1021/ja109126w

61. Herron, N.; Wang, Y.; Eddy, M. M.; Stucky, G. D.; Cox, D. E.; Moller, K.; Bein, T. *J. Am. Chem. Soc.* **1989,** *111,* 530–540. doi:10.1021/ja00184a021

62. Moller, K.; Eddy, M. M.; Stucky, G. D.; Herron, N.; Bein, T. *J. Am. Chem. Soc.* **1989,** *111,* 2564–2571. doi:10.1021/ja00189a031

63. Stucky, G. D.; Mac Dougall, J. E. *Science* **1990,** *247,* 669–678. doi:10.1126/science.247.4943.669

64. Brigham, E. S.; Weisbecker, C. S.; Rudzinski, W. E.; Mallouk, T. E. *Chem. Mater.* **1996,** *8,* 2121–2127. doi:10.1021/cm960045s

65. Terasaki, O.; Yamazaki, K.; Thomas, J. M.; Ohsuna, T.; Watanabe, D.; Sanders, J. V.; Barry, J. C. *Nature* **1987,** *330,* 58–60. doi:10.1038/330058a0

66. Sun, T.; Seff, K. *Chem. Rev.* **1994,** *94,* 857–870. doi:10.1021/cr00028a001

67. Wang, F.; Song, H.; Pan, G.; Fan, L.; Dai, Q.; Dong, B.; Liu, H.; Yu, J.; Wang, X.; Li, L. *Mater. Res. Bull.* **2009,** *44,* 600–605. doi:10.1016/j.materresbull.2008.07.002

68. Shao, Y.-F.; Yan, B.; Jiang, Z.-Y. *RSC Adv.* **2012,** *2,* 9192–9200. doi:10.1039/c2ra21605a

69. Lu, Q.; Wang, Z.; Li, J.; Wang, P.; Ye, X. *Nanoscale Res. Lett.* **2009,** *4,* 646–654. doi:10.1007/s11671-009-9294-x

70. Vibulyaseak, K.; Bureekaew, S.; Ogawa, M. *Langmuir* **2017,** *33,* 13598–13603. doi:10.1021/acs.langmuir.7b03252

71. Ruiz-Hitzky, E.; Aranda, P. *J. Sol-Gel Sci. Technol.* **2014,** *70,* 307–316. doi:10.1007/s10971-013-3237-9

72. Ruiz-Hitzky, E. *J. Mater. Chem.* **2001,** *11,* 86–91. doi:10.1039/b003197f

73. Lvov, Y.; Abdullayev, E. *Prog. Polym. Sci.* **2013,** *38,* 1690–1719. doi:10.1016/j.progpolymsci.2013.05.009

74. Cavallaro, G.; Lazzara, G.; Milioto, S.; Parisi, F.; Sanzillo, V. *ACS Appl. Mater. Interfaces* **2014,** *6,* 606–612. doi:10.1021/am404693r

75. Takahara, A.; Higaki, Y. Design and physicochemical characterization of novel organic-inorganic hybrids from natural aluminosilicate nanotubes. In *Functional Polymer Composites with Nanoclays;* Lvov, Y.; Guo, B.; Fakhrullin, R., Eds.; RSC Smart Materials, Vol. 22; Royal Society of Chemistry: Cambridge, United Kingdom, 2017; pp 131–156. doi:10.1039/9781782626725-00131

76. Lvov, Y.; Panchal, A.; Fu, Y.; Fakhrullin, R.; Kryuchkova, M.; Batasheva, S.; Stavitskaya, A.; Glotov, A.; Vinokurov, V. *Langmuir* **2019,** in press. doi:10.1021/acs.langmuir.8b04313

77. Suner, S. S.; Demirci, S.; Yetiskin, B.; Fakhrullin, R.; Naumenko, E.; Okay, O.; Ayyala, R. S.; Sahiner, N. *Int. J. Biol. Macromol.* **2019,** *130,* 627–635. doi:10.1016/j.ijbiomac.2019.03.025

78. Micó-Vicent, B.; Martínez-Verdú, F. M.; Novikov, A.; Stavitskaya, A.; Vinokurov, V.; Rozhina, E.; Fakhrullin, R.; Yendluri, R.; Lvov, Y. *Adv. Funct. Mater.* **2018,** *28,* 1703553. doi:10.1002/adfm.201703553

79. Cavallaro, G.; Lazzara, G.; Milioto, S.; Parisi, F.; Evtugyn, V.; Rozhina, E.; Fakhrullin, R. *ACS Appl. Mater. Interfaces* **2018,** *10,* 8265–8273. doi:10.1021/acsami.7b19361

80. Liu, J.; Zhang, G. *Phys. Chem. Chem. Phys.* **2014,** *16,* 8178–8192. doi:10.1039/c3cp54146k

81. Ding, Z.; Kloprogge, J. T.; Frost, R. L.; Lu, G. Q.; Zhu, H. Y. *J. Porous Mater.* **2001,** *8,* 273–293. doi:10.1023/a:1013113030912

82. Szczepanik, B. *Appl. Clay Sci.* **2017,** *141,* 227–239. doi:10.1016/j.clay.2017.02.029

83. Centi, G.; Perathoner, S. *Microporous Mesoporous Mater.* **2008,** *107,* 3–15. doi:10.1016/j.micromeso.2007.03.011

84. Hur, S. G.; Kim, T. W.; Hwang, S.-J.; Hwang, S.-H.; Yang, J. H.; Choy, J.-H. *J. Phys. Chem. B* **2006,** *110,* 1599–1604. doi:10.1021/jp0543633

85. Németh, J.; Rodríguez-Gattorno, G.; Díaz, D.; Vázquez-Olmos, A. R.; Dékány, I. *Langmuir* **2004,** *20,* 2855–2860. doi:10.1021/la035097s

86. Xu, X.-x.; Zhong, L.-h.; Xie, X. *Polym. Compos.* **2014,** *35,* 1023–1030. doi:10.1038/aps.2014.51

87. Akkari, M.; Aranda, P.; Amara, A. B. H.; Ruiz-Hitzky, E. *J. Nanosci. Nanotechnol.* **2018,** *18,* 223–233. doi:10.1166/jnn.2018.14613

88. Körösi, L.; Mogyorósi, K.; Kun, R.; Németh, J.; Dékány, I. Preparation and photooxidation properties of metal oxide semiconductors incorporated in layer silicates. In *From Colloids to Nanotechnology;* Zrinyi, M.; Horvolgyi, Z. D., Eds.; Progress in Colloid and Polymer Science, Vol. 125; Springer Berlin: Berlin, Germany, 2004; pp 27–33. doi:10.1007/978-3-540-45119-8_5

89. Fatimah, I.; Wang, S.; Wulandari, D. *Appl. Clay Sci.* **2011,** *53,* 553–560. doi:10.1016/j.clay.2011.05.001

90. Xu, W. G.; Liu, S. F.; Lu, S. X.; Kang, S. Y.; Zhou, Y.; Zhang, H. F. *J. Colloid Interface Sci.* **2010,** *351,* 210–216. doi:10.1016/j.jcis.2010.07.052

91. Peng, H.; Liu, X.; Tang, W.; Ma, R. *Sci. Rep.* **2017,** *7,* 2250. doi:10.1038/s41598-017-02501-w

92. Khumchoo, N.; Khaorapapong, N.; Ogawa, M. *Appl. Clay Sci.* **2015,** *105–106,* 236–242. doi:10.1016/j.clay.2015.01.001

93. Khaorapapong, N.; Khumchoo, N.; Ogawa, M. *Mater. Lett.* **2011,** *65,* 657–660. doi:10.1016/j.matlet.2010.11.052

94. Mamulová Kutláková, K.; Tokarský, J.; Kovář, P.; Vojtěšková, S.; Kovářová, A.; Smetana, B.; Kukutschová, J.; Čapková, P.; Matějka, V. *J. Hazard. Mater.* **2011,** *188,* 212–220. doi:10.1016/j.jhazmat.2011.01.106

95. Zhang, Y.; Gan, H.; Zhang, G. *Chem. Eng. J.* **2011,** *172,* 936–943. doi:10.1016/j.cej.2011.07.005

96. Chong, M. N.; Vimonses, V.; Lei, S.; Jin, B.; Chow, C.; Saint, C. *Microporous Mesoporous Mater.* **2009,** *117,* 233–242. doi:10.1016/j.micromeso.2008.06.039

97. Kočí, K.; Matějka, V.; Kovář, P.; Lacný, Z.; Obalová, L. *Catal. Today* **2011,** *161,* 105–109. doi:10.1016/j.cattod.2010.08.026

98. Barbosa, L. V.; Marçal, L.; Nassar, E. J.; Calefi, P. S.; Vicente, M. A.; Trujillano, R.; Rives, V.; Gil, A.; Korili, S. A.; Ciuffi, K. J.; de Faria, E. H. *Catal. Today* **2015,** *246,* 133–142. doi:10.1016/j.cattod.2014.09.019

99. Rhouta, B.; Bouna, L.; Maury, F.; Senocq, F.; Lafont, M. C.; Jada, A.; Amjoud, M.; Daoudi, L. *Appl. Clay Sci.* **2015,** *115,* 266–274. doi:10.1016/j.clay.2015.04.025

100. Mishra, A.; Mehta, A.; Sharma, M.; Basu, S. *J. Alloys Compd.* **2017,** *694,* 574–580. doi:10.1016/j.jallcom.2016.10.036

101. Kibanova, D.; Trejo, M.; Destaillats, H.; Cervini-Silva, J. *Appl. Clay Sci.* **2009,** *42,* 563–568. doi:10.1016/j.clay.2008.03.009

102. Belessi, V.; Lambropoulou, D.; Konstantinou, I.; Katsoulidis, A.; Pomonis, P.; Petridis, D.; Albanis, T. *Appl. Catal., B* **2007,** *73,* 292–299. doi:10.1016/j.apcatb.2006.12.011

103. Ma, J.; Jia, Y.; Jing, Y.; Yao, Y.; Sun, J. *Appl. Clay Sci.* **2010,** *47,* 433–437. doi:10.1016/j.clay.2009.12.020

104. Rossetto, E.; Petkowicz, D. I.; dos Santos, J. H. Z.; Pergher, S. B. C.; Penha, F. G. *Appl. Clay Sci.* **2010,** *48,* 602–606. doi:10.1016/j.clay.2010.03.010

105. Sun, H.; Peng, T.; Liu, B.; Xian, H. *Appl. Clay Sci.* **2015,** *114,* 440–446. doi:10.1016/j.clay.2015.06.026

106. Manova, E.; Aranda, P.; Angeles Martín-Luengo, M.; Letaïef, S.; Ruiz-Hitzky, E. *Microporous Mesoporous Mater.* **2010,** *131,* 252–260. doi:10.1016/j.micromeso.2009.12.031

107. Belver, C.; Bedia, J.; Rodriguez, J. J. *Appl. Catal., B* **2015,** *176–177,* 278–287. doi:10.1016/j.apcatb.2015.04.004

108. Ma, J.; Jia, Y.; Jing, Y.; Sun, J.; Yao, Y. *Appl. Clay Sci.* **2009,** *46,* 114–116. doi:10.1016/j.clay.2009.07.011

109. Aranda, P.; Kun, R.; Martín-Luengo, M. A.; Letaïef, S.; Dékány, I.; Ruiz-Hitzky, E. *Chem. Mater.* **2008,** *20,* 84–91. doi:10.1021/cm702251f

110. Zhang, Y.; Wang, D.; Zhang, G. *Chem. Eng. J.* **2011,** *173,* 1–10. doi:10.1016/j.cej.2010.11.028

111. Bouna, L.; Rhouta, B.; Amjoud, M.; Maury, F.; Lafont, M.-C.; Jada, A.; Senocq, F.; Daoudi, L. *Appl. Clay Sci.* **2011,** *52,* 301–311. doi:10.1016/j.clay.2011.03.009

112. Suárez, S.; Coronado, J. M.; Portela, R.; Martín, J. C.; Yates, M.; Avila, P.; Sánchez, B. *Environ. Sci. Technol.* **2008,** *42,* 5892–5896. doi:10.1021/es703257w

113. Ökte, A. N.; Sayınsöz, E. *Sep. Purif. Technol.* **2008,** *62,* 535–543. doi:10.1016/j.seppur.2008.03.011

114. Papoulis, D.; Komarneni, S.; Nikolopoulou, A.; Tsolis-Katagas, P.; Panagiotaras, D.; Kacandes, H. G.; Zhang, P.; Yin, S.; Sato, T.; Katsuki, H. *Appl. Clay Sci.* **2010,** *50,* 118–124. doi:10.1016/j.clay.2010.07.013

115. Papoulis, D.; Komarneni, S.; Panagiotaras, D.; Stathatos, E.; Christoforidis, K. C.; Fernández-García, M.; Li, H.; Shu, Y.; Sato, T.; Katsuki, H. *Appl. Catal., B* **2014,** *147,* 526–533. doi:10.1016/j.apcatb.2013.09.025

116. Stathatos, E.; Papoulis, D.; Aggelopoulos, C. A.; Panagiotaras, D.; Nikolopoulou, A. *J. Hazard. Mater.* **2012,** *211–212,* 68–76. doi:10.1016/j.jhazmat.2011.11.055

117. Gu, N.; Gao, J.; Wang, K.; Yang, X.; Dong, W. *Water, Air, Soil Pollut.* **2015,** *226,* 136. doi:10.1007/s11270-015-2407-5

118. Akkari, M.; Aranda, P.; Ben Rhaiem, H.; Ben Haj Amara, A.; Ruiz-Hitzky, E. *Appl. Clay Sci.* **2016,** *131,* 131–139. doi:10.1016/j.clay.2015.12.013

119. Xu, H.; Zhang, D.; Xu, A.; Wu, F.; Cao, R. *Int. J. Photoenergy* **2015,** No. 750869. doi:10.1155/2015/750869

120. Ye, J.; Li, X.; Hong, J.; Chen, J.; Fan, Q. *Mater. Sci. Semicond. Process.* **2015,** *39,* 17–22. doi:10.1016/j.mssp.2015.04.039

121. Huo, C.; Yang, H. *Appl. Clay Sci.* **2010,** *50,* 362–366. doi:10.1016/j.clay.2010.08.028

122. Portela, R.; Rubio-Marcos, F.; Leret, P.; Fernández, J. F.; Bañares, M. A.; Ávila, P. *J. Mater. Chem. A* **2015,** *3,* 1306–1316. doi:10.1039/c4ta04440a

123. Wang, R.; Jiang, G.; Ding, Y.; Wang, Y.; Sun, X.; Wang, X.; Chen, W. *ACS Appl. Mater. Interfaces* **2011,** *3,* 4154–4158. doi:10.1021/am201020q

124. Xu, H.; Yu, T.; Liu, J. *Mater. Lett.* **2014,** *117,* 263–265. doi:10.1016/j.matlet.2013.12.022

125. Joo, J. C.; Ahn, C. H.; Jang, D. G.; Yoon, Y. H.; Kim, J. K.; Campos, L.; Ahn, H. *J. Hazard. Mater.* **2013,** *263,* 569–574. doi:10.1016/j.jhazmat.2013.10.017

126. Letaief, S.; Ruiz-Hitzky, E. *Chem. Commun.* **2003,** 2996–2997. doi:10.1039/b310854f

127. Letaïef, S.; Martín-Luengo, M. A.; Aranda, P.; Ruiz-Hitzky, E. *Adv. Funct. Mater.* **2006,** *16,* 401–409. doi:10.1002/adfm.200500190

128. Chmielarz, L.; Gil, B.; Kuśtrowski, P.; Piwowarska, Z.; Dudek, B.; Michalik, M. *J. Solid State Chem.* **2009,** *182,* 1094–1104. doi:10.1016/j.jssc.2009.02.017

129. Vahidhabanu, S.; Karuppasamy, D.; Adeogun, A. I.; Babu, B. R. *RSC Adv.* **2017,** *7,* 5669–5678. doi:10.1039/c6ra26273b

130. Uğurlu, M.; Karaoğlu, M. H. *Chem. Eng. J.* **2011,** *166,* 859–867. doi:10.1016/j.cej.2010.11.056

131. Pérez-Carvajal, J.; Aranda, P.; Obregón, S.; Colón, G.; Ruiz-Hitzky, E. *Microporous Mesoporous Mater.* **2016,** *222,* 120–127. doi:10.1016/j.micromeso.2015.10.007

132. Akkari, M.; Aranda, P.; Ben Haj Amara, A.; Ruiz-Hitzky, E. *Beilstein J. Nanotechnol.* **2016,** *7,* 1971–1982. doi:10.3762/bjnano.7.188

133. Akkari, M.; Aranda, P.; Mayoral, A.; García-Hernández, M.; Ben Haj Amara, A.; Ruiz-Hitzky, E. *J. Hazard. Mater.* **2017,** *340,* 281–290. doi:10.1016/j.jhazmat.2017.06.067

134. Welte, A.; Waldauf, C.; Brabec, C.; Wellmann, P. J. *Thin Solid Films* **2008,** *516,* 7256–7259. doi:10.1016/j.tsf.2007.12.025

135. Wang, Z. L. *J. Phys.: Condens. Matter* **2004,** *16,* R829–R858. doi:10.1088/0953-8984/16/25/r01

136. Ong, C. B.; Ng, L. Y.; Mohammad, A. W. *Renewable Sustainable Energy Rev.* **2018,** *81,* 536–551. doi:10.1016/j.rser.2017.08.020

137. Lee, K. M.; Lai, C. W.; Ngai, K. S.; Juan, J. C. *Water Res.* **2016,** *88,* 428–448. doi:10.1016/j.watres.2015.09.045

138. Mohd Adnan, M. A.; Julkapli, N. M.; Abd Hamid, S. B. *Rev. Inorg. Chem.* **2016,** *36,* 77–104. doi:10.1515/revic-2015-0015

139. Wang, H.; Zhang, L.; Chen, Z.; Hu, J.; Li, S.; Wang, Z.; Liu, J.; Wang, X. *Chem. Soc. Rev.* **2014,** *43,* 5234–5244. doi:10.1039/c4cs00126e

140. Pasang, T.; Namratha, K.; Parvin, T.; Ranganathaiah, C.; Byrappa, K. *Mater. Res. Innovations* **2015,** *19,* 73–80. doi:10.1179/1433075x14y.0000000217

141. Hagfeldt, A.; Boschloo, G.; Sun, L.; Kloo, L.; Pettersson, H. *Chem. Rev.* **2010,** *110,* 6595–6663. doi:10.1021/cr900356p

142. Grätzel, M. *J. Photochem. Photobiol., C* **2003,** *4,* 145–153. doi:10.1016/s1389-5567(03)00026-1

143. Li, X.; Yang, H. *Appl. Clay Sci.* **2014,** *100,* 43–49. doi:10.1016/j.clay.2014.05.007

144. Sohrabnezhad, S.; Seifi, A. *Appl. Surf. Sci.* **2016,** *386,* 33–40. doi:10.1016/j.apsusc.2016.05.102

145. Belver, C.; Bedia, J.; Álvarez-Montero, M. A.; Rodriguez, J. J. *Catal. Today* **2016,** *266,* 36–45. doi:10.1016/j.cattod.2015.09.025

146. Belver, C.; Bedia, J.; Rodriguez, J. J. *J. Hazard. Mater.* **2017,** *322,* 233–242. doi:10.1016/j.jhazmat.2016.02.028

147. Belver, C.; Han, C.; Rodriguez, J. J.; Dionysiou, D. D. *Catal. Today* **2017,** *280,* 21–28. doi:10.1016/j.cattod.2016.04.029

148.Chen, K.; Li, J.; Wang, W.; Zhang, Y.; Wang, X.; Su, H.
Appl. Surf. Sci. **2011,** *257,* 7276–7285.
doi:10.1016/j.apsusc.2011.03.104

149.Zhang, G.; Ding, X.; Hu, Y.; Huang, B.; Zhang, X.; Qin, X.; Zhou, J.;
Xie, J. *J. Phys. Chem. C* **2008,** *112,* 17994–17997.
doi:10.1021/jp803939z

150.Tomul, F.; Turgut Basoglu, F.; Canbay, H. *Appl. Surf. Sci.* **2016,** *360,*
579–593. doi:10.1016/j.apsusc.2015.10.228

151.Liu, J.; Li, X.; Zuo, S.; Yu, Y. *Appl. Clay Sci.* **2007,** *37,* 275–280.
doi:10.1016/j.clay.2007.01.008

152.Kaliyamoorthy, S.; Mari, A.; Rengasamy, V.; Meenakshisundaram, S.
Bull. Chem. Soc. Jpn. **2010,** *83,* 831–837. doi:10.1246/bcsj.20090319

153.Wu, T.-S.; Wang, K.-X.; Li, G.-D.; Sun, S.-Y.; Sun, J.; Chen, J.-S.
ACS Appl. Mater. Interfaces **2010,** *2,* 544–550.
doi:10.1021/am900743d

154.Sahel, K.; Bouhent, M.; Belkhadem, F.; Ferchichi, M.; Dappozze, F.;
Guillard, C.; Figueras, F. *Appl. Clay Sci.* **2014,** *95,* 205–210.
doi:10.1016/j.clay.2014.04.014

155.Krishnan, B.; Mahalingam, S. *Adv. Powder Technol.* **2017,** *28,*
2265–2280. doi:10.1016/j.apt.2017.06.007

156.Bineesh, K. V.; Kim, S.-Y.; Jermy, B. R.; Park, D.-W.
J. Ind. Eng. Chem. (Amsterdam, Neth.) **2009,** *15,* 207–211.
doi:10.1016/j.jiec.2008.10.006

157.Ding, X.; An, T.; Li, G.; Zhang, S.; Chen, J.; Yuan, J.; Zhao, H.;
Chen, H.; Sheng, G.; Fu, J. *J. Colloid Interface Sci.* **2008,** *320,*
501–507. doi:10.1016/j.jcis.2007.12.042

158.Bel Hadjltaief, H.; Ben Zina, M.; Galvez, M. E.; Da Costa, P.
J. Photochem. Photobiol., A **2016,** *315,* 25–33.
doi:10.1016/j.jphotochem.2015.09.008

159.Tobajas, M.; Belver, C.; Rodriguez, J. J. *Chem. Eng. J.* **2017,** *309,*
596–606. doi:10.1016/j.cej.2016.10.002

160.Vaizoğullar, A. İ. *Chem. Eng. Commun.* **2017,** *204,* 689–697.
doi:10.1080/00986445.2017.1306518

161.Mohammadi, Z.; Sharifnia, S.; Shavisi, Y. *Mater. Chem. Phys.* **2016,**
184, 110–117. doi:10.1016/j.matchemphys.2016.09.031

162.Belver, C.; Hinojosa, M.; Bedia, J.; Tobajas, M.; Alvarez, M.;
Rodríguez-González, V.; Rodriguez, J. *Materials* **2017,** *10,* 960.
doi:10.3390/ma10080960

163.Wang, H.; Zhou, P.; Wang, J.; Wang, Y.; Wei, J.; Zhan, H.; Guo, R.;
Zhang, Y. *J. Wuhan Univ. Technol., Mater. Sci. Ed.* **2018,** *33,*
729–735. doi:10.1007/s11595-018-1885-x

164.Bachvarova-Nedelcheva, A. D.; Iordanova, R. S.; Stoyanova, A. M.;
Gegova, R. D.; Dimitriev, Y. B.; Loukanov, A. R. *Cent. Eur. J. Chem.*
2013, *11,* 364–370. doi:10.2478/s11532-012-0167-2

165.Photosensitization | chemistry.
https://www.britannica.com/science/photosensitization (accessed Sept
25, 2018).

166.Ogawa, M.; Sohmiya, M.; Watase, Y. *Chem. Commun.* **2011,** *47,*
8602–8604. doi:10.1039/c1cc12392k

167.Goto, T.; Ogawa, M. *RSC Adv.* **2016,** *6,* 23794–23797.
doi:10.1039/c5ra25430b

168.Goto, T.; Ogawa, M. *ACS Appl. Mater. Interfaces* **2015,** *7,*
12631–12634. doi:10.1021/acsami.5b03128

169.Meshram, S.; Limaye, R.; Ghodke, S.; Nigam, S.; Sonawane, S.;
Chikate, R. *Chem. Eng. J.* **2011,** *172,* 1008–1015.
doi:10.1016/j.cej.2011.07.015

170.Ide, Y.; Matsuoka, M.; Ogawa, M. *ChemCatChem* **2012,** *4,* 628–630.
doi:10.1002/cctc.201200043

171.Intasa-ard, S. G.; Imwiset, K. J.; Bureekaew, S.; Ogawa, M.
Dalton Trans. **2018,** *47,* 2896–2916. doi:10.1039/c7dt03736h

172.Mamulová Kutláková, K.; Tokarský, J.; Peikertová, P. *Appl. Catal., B*
2015, *162,* 392–400. doi:10.1016/j.apcatb.2014.07.018

173.Dědková, K.; Kutláková, K. M.; Matějová, K.; Kukutschová, J.
Adv. Sci. Lett. **2016,** *22,* 695–698. doi:10.1166/asl.2016.6904

174.Papoulis, D.; Komarneni, S.; Panagiotaras, D.; Stathatos, E.; Toli, D.;
Christoforidis, K. C.; Fernández-García, M.; Li, H.; Yin, S.; Sato, T.;
Katsuki, H. *Appl. Catal., B* **2013,** *132–133,* 416–422.
doi:10.1016/j.apcatb.2012.12.012

175.Li, C.; Wang, J.; Guo, H.; Ding, S. *J. Colloid Interface Sci.* **2015,** *458,*
1–13. doi:10.1016/j.jcis.2015.07.025

176.Du, Y.; Zheng, P. *Korean J. Chem. Eng.* **2014,** *31,* 2051–2056.
doi:10.1007/s11814-014-0162-8

177.Zhu, H. Y.; Orthman, J. A.; Li, J.-Y.; Zhao, J.-C.; Churchman, G. J.;
Vansant, E. F. *Chem. Mater.* **2002,** *14,* 5037–5044.
doi:10.1021/cm0205884

178.Lin, Y.; Pi, P.; Zheng, D.; Yang, Z.; Wang, L. *J. Rare Earths* **2010,** *28,*
732–736. doi:10.1016/s1002-0721(09)60190-3

179.Lin, Y.; Pi, P.; Yang, Z.; Wang, L.
J. Wuhan Univ. Technol., Mater. Sci. Ed. **2011,** *26,* 852–856.
doi:10.1007/s11595-011-0324-z

180.Bouna, L.; Rhouta, B.; Maury, F.; Jada, A.; Senocq, F.; Lafont, M.-C.
Clay Miner. **2014,** *49,* 417–428. doi:10.1180/claymin.2014.049.3.05

181.Swarnakar, R.; Brandt, K. B.; Kydd, R. A. *Appl. Catal., A* **1996,** *142,*
61–71. doi:10.1016/0926-860x(96)00061-0

182.Nikolopoulou, A.; Papoulis, D.; Komarneni, S.; Tsolis-Katagas, P.;
Panagiotaras, D.; Kacandes, G. H.; Zhang, P.; Yin, S.; Sato, T.
Appl. Clay Sci. **2009,** *46,* 363–368. doi:10.1016/j.clay.2009.09.007

183.Đukić, A. B.; Kumrić, K. R.; Vukelić, N. S.; Dimitrijević, M. S.;
Baščarević, Z. D.; Kurko, S. V.; Matović, L. L. *Appl. Clay Sci.* **2015,**
103, 20–27. doi:10.1016/j.clay.2014.10.021

184.Mishra, A.; Mehta, A.; Kainth, S.; Basu, S. *Appl. Clay Sci.* **2018,** *153,*
144–153. doi:10.1016/j.clay.2017.11.040

185.Bu, X.-Z.; Zhang, G.-K.; Gao, Y.-Y.; Yang, Y.-Q.
Microporous Mesoporous Mater. **2010,** *136,* 132–137.
doi:10.1016/j.micromeso.2010.08.009

186.Zhang, Y.; Guo, Y.; Zhang, G.; Gao, Y. *Appl. Clay Sci.* **2011,** *51,*
335–340. doi:10.1016/j.clay.2010.12.023

187.Yang, Y.; Zhang, G.; Xu, W. *J. Colloid Interface Sci.* **2012,** *376,*
217–223. doi:10.1016/j.jcis.2012.03.003

188.Li, S.-q.; Zhou, P.-j.; Zhang, W.-s.; Chen, S.; Peng, H.
J. Alloys Compd. **2014,** *616,* 227–234.
doi:10.1016/j.jallcom.2014.07.102

189.Du, Y.; Tang, D.; Zhang, G.; Wu, X. *Chin. J. Catal.* **2015,** *36,*
2219–2228. doi:10.1016/s1872-2067(15)61015-4

190.Zhou, F.; Yan, C.; Wang, H.; Zhou, S.; Komarneni, S. *Appl. Clay Sci.*
2017, *146,* 246–253. doi:10.1016/j.clay.2017.06.010

191.Zhang, L.; Liu, J.; Tang, C.; Lv, J.; Zhong, H.; Zhao, Y.; Wang, X.
Appl. Clay Sci. **2011,** *51,* 68–73. doi:10.1016/j.clay.2010.11.003

A silver-nanoparticle/cellulose-nanofiber composite as a highly effective substrate for surface-enhanced Raman spectroscopy

Yongxin Lu[‡1], Yan Luo[‡2], Zehao Lin[1] and Jianguo Huang[*1]

Full Research Paper

Address:
[1]Department of Chemistry, Zhejiang University, Hangzhou, Zhejiang 310027, P. R. China and [2]Shaoxing Test Institute of Quality and Technical Supervision, Shaoxing, Zhejiang 312071, P. R. China

Email:
Jianguo Huang[*] - jghuang@zju.edu.cn

* Corresponding author   ‡ Equal contributors

Keywords:
cellulose nanofiber; composites; nanoarchitectonics; silver nanoparticle; surface-enhanced Raman spectroscopy

Abstract

A highly active surface-enhanced Raman scattering (SERS) substrate was developed by facile deposition of silver nanoparticles onto cellulose fibers of ordinary laboratory filter paper. This was achieved by means of the silver mirror reaction in a manner to control both the size of the silver nanoparticles and the silver density of the substrate. This paper-based substrate is composed of a particle-on-fiber structure with the unique three-dimensional network morphology of the cellulose matrix. For such a SERS substrate with optimized size of the silver nanoparticles (ca. 70 nm) and loading density of silver (17.28 wt %), a remarkable detection limit down to the sub-attomolar (1×10^{-16} M) level and an enhancement factor of 3×10^6 were achieved by using Rhodamine 6G as the analyte. Moreover, this substrate was applied to monitor the molecular recognition through multiple hydrogen bonds in between nucleosides of adenosine and thymidine. This low-cost, highly sensitive, and biocompatible paper-based SERS substrate holds considerable potentials for the detection and analyses of chemical and biomolecular species.

Introduction

In the last decades, impressive advances have been made in nanoscience and nanotechnology both in fundamental research and practical applications. The basis for nanoscience and nanotechnology, the construction of functional materials with specific structural features at the nanoscale, is now stepping up from "nanofabrication" to "nanoarchitectonics" [1]. Nanoarchitec-tonics as a novel paradigm to create specific materials by assembling the corresponding nanoscale building blocks was first proposed by M. Aono and co-workers in the year 2000 [2,3]. The concept has been recently extended extensively and deepened systematically by K. Ariga and his colleagues [4-14]. Various functional units ranging from atoms and molecules to

polymers, biomacromolecules and nanoscale objects are employed for the construction of specific nanoarchitectures by various chemical methodologies such as self-organization and layer-by-layer self-assembly [7,15-17]. In particular, layer-by-layer self-assembly holds significant potentials for the fabrication of a large variety of functional nanoarchitectures [18-25]. It has been demonstrated that the different nanoarchitectures developed so far have prominent application potentials in the areas of sensors and devices [26-30], catalysts [17,31,32], energy materials [16,32,33], as well as bio-oriented applications [34-42]. In the current work, a functional nanoarchitecture composed of silver nanoparticles anchored on cellulose nanofibers was fabricated, which is shown to be a highly effective substrate for surface-enhanced Raman spectroscopy (SERS).

SERS, a powerful molecular spectroscopy method, is widely used in the trace detection and characterization of various chemical and biological substances where the substrates are crucial for obtaining an enhanced Raman signal [43-45].

The Raman signal of SERS is enhanced remarkably in the "hot spots" that are generated in the nanogaps of plasmonic metal nanoparticles (e.g., Au, Ag and Cu) through the amplification of the electromagnetic field caused by localized surface plasmon resonance [46]. In order to create more nanogaps and to generate more hot spots to improve the SERS effect, a number of nanostructures based on metal particles were prepared by different methods, such as thermal evaporation [47], electrospray [48], inject printing [49], successive ionic layer absorption and reaction (SILAR) [50], and photochemical methods [51]. However, there are still challenges regarding the facile fabrication of the SERS substrates with high spectroscopic performance.

Regarding SERS substrates, the choice of the substances employed on which the metal nanoparticles are deposited influences both the collection efficiencies and detection sensitivities. Cellulose, such as laboratory filter paper and bacterial nanocellulose, have been considered as superior candidates for the fabrication of SERS substrates with silver nanoparticles, due to their low cost, wide availability, as well as flexibility, portability and biodegradability [52-54]. The high surface density of hydroxy groups in cellulose results in a sufficient stability of the deposited silver nanoparticles via Ag–O bonding [52]. Moreover, the unique three-dimensional cross-linked porous structure and the hierarchical morphologies at micro- and nanoscale of bulk cellulose lead to the creation of more hot spots by the loaded silver nanoparticles, and therefore, to higher SERS enhancement. Furthermore, cellulose materials such as filter paper are structurally porous, physically flexible and hydrophilic, which allows for a facile and efficient collection of the

analytes from solution media. Hence, a number of works have been reported concerning the fabrication of SERS substrates by deposition of silver particles onto cellulose filter paper by means of the silver mirror reaction [55-59]. In order to ensure the effective loading of silver particles on the cellulose fiber surfaces, relatively high reaction temperatures (above 45 °C) [55-58] or strong reducing agents (such as formaldehyde) [59] were applied in the reactions, which resulted in rather large sizes and excessive loading densities of the silver particles. Eventually this led to somewhat low sensitivities of the substrates, because detection limits at the sub-attomolar level could not be achieved.

In the present work, a SERS substrate was fabricated by the deposition of silver nanoparticles (Ag-NPs) onto the surfaces of the cellulose nanofibers (NFs) in ordinary laboratory filter paper by means of the one-step silver mirror reaction. Both size and density of the of the silver nanoparticles on the substrates could be controlled. This paper-based silver-nanoparticle/cellulose-nanofiber (Ag-NP/cellulose-NF) showed a very good SERS performance. In the optimized case, the detection limit of Rhodamine 6G (R6G) was as low as 1×10^{-16} M (sub-attomolar level) with just a small droplet of solution needed (10 µL). This is superior to some of the reported works mentioned above [55-59]. The SERS substrate was also applied to monitor the molecular recognition through multiple hydrogen bonds between adenosine and thymidine. This paper-based SERS substrate could hold potential in the detection of trace amounts of analytes and for the spectroscopic study of biomolecules.

Results and Discussion
Characterization of the Ag-NP/cellulose-NF composite

The silver-nanoparticle/cellulose-nanofiber SERS substrates were fabricated by deposition of silver nanoparticles onto the surfaces of the cellulose nanofibers of ordinary laboratory filter paper by the silver mirror reaction. As described in the Experimental section, the sizes of the silver nanoparticles and the final silver densities of the substrates were adjusted by varying the deposition time. The substrates obtained after deposition times of 2, 4, 6, 8, and 10 min are denoted as sample Ag-NP/cellulose-NF–A, B, C, D, and E, respectively.

The field-emission scanning electron microscopy (FE-SEM) images of the Ag-NP/cellulose-NF composite sheets in Figure 1 show that the surfaces of the cellulose fibers are decorated with silver particles. The comparison with SEM images of bare filter paper (Supporting Information File 1, Figure S1) shows that the structural integrity of the filter paper was not affected by the deposition process. With increasing reaction time, the particle

size increased gradually; and excessive reaction time resulted in much larger particle sizes and obvious aggregation of the silver particles, as seen for the samples Ag-NP/cellulose-NF–D (Figure 1g,h) and –E (Supporting Information File 1, Figure S2), where the cellulose fibers are fully coated with silver layers. In the samples Ag-NP/cellulose-NF–A, –B and –C (Figure 1a–f), silver nanoparticles with an average size of 46.5, 70.2, and 75.8 nm (Supporting Information File 1, Figure S3a,c,e), respectively, are uniformly anchored on the cellulose

fibers. According to energy-dispersive X-ray (EDX) analyses, the silver contents of the corresponding samples were 0.49, 9.61, and 17.28 wt % respectively (Supporting Information File 1, Figure S3b,d,f). As demonstrated in Figure 1f, more nanogaps between the silver nanoparticles exist in the substrate Ag-NP/cellulose-NF–C, which would be beneficial for the enhanced SERS effect.

Figure 2a shows the transmission electron microscopy (TEM) image of the sample Ag-NP/cellulose-NF–C showing the silver nanoparticles anchored on the cellulose fibers. The amount of the silver nanoparticles observed is much less than that of the FE-SEM image (Figure 1f), which is because some nanoparticles were apparently lost from the as-prepared sample during the preparation procedure of the specimen, as noted in the Experimental section. The high-resolution TEM (HR-TEM) image of an individual silver nanoparticle is displayed in Figure 2b, the lattice spacing of 0.236 nm observed is corresponding to the (111) plane of metallic silver [60], confirming the formation of the silver nanoparticles.

Figure 1: FE-SEM micrographs of the paper-based SERS substrates Ag-NP/cellulose-NF–A (a,b), B (c,d), C (e,f), and D (g,h), which were fabricated with reaction times of 2, 4, 6, and 8 min, respectively.

Figure 3a shows the X-ray diffraction (XRD) patterns of the prepared Ag-NP/cellulose-NF composites. Two series of diffraction peaks were observed. The ones located at 2θ = 15.0°, 16.5°, 22.8°, and 34.1° are ascribed to the $(10\bar{1})$, (101), (002), and (040) planes of crystalline cellulose, respectively [61]; and the other ones located at 2θ = 38.1°, 44.3°, and 64.4° are assigned to the (111), (200), and (220) planes of metallic silver phase, respectively [60]. It is noticed that the diffraction peak intensities of metallic silver increased along with the increment of the silver content in the samples, which agrees well with the FE-SEM results. The reflectance UV–vis spectra of the samples are presented in Figure 3b. No obvious absorption band was observed for the bare cellulose filter paper (Supporting Information File 1, Figure S4). For sample Ag-NP/cellulose-NF–A, the strong surface plasmon resonance absorption band of silver nanoparticles was observed at around 400 nm. With increasing size of the silver nanoparticles, this band gradually
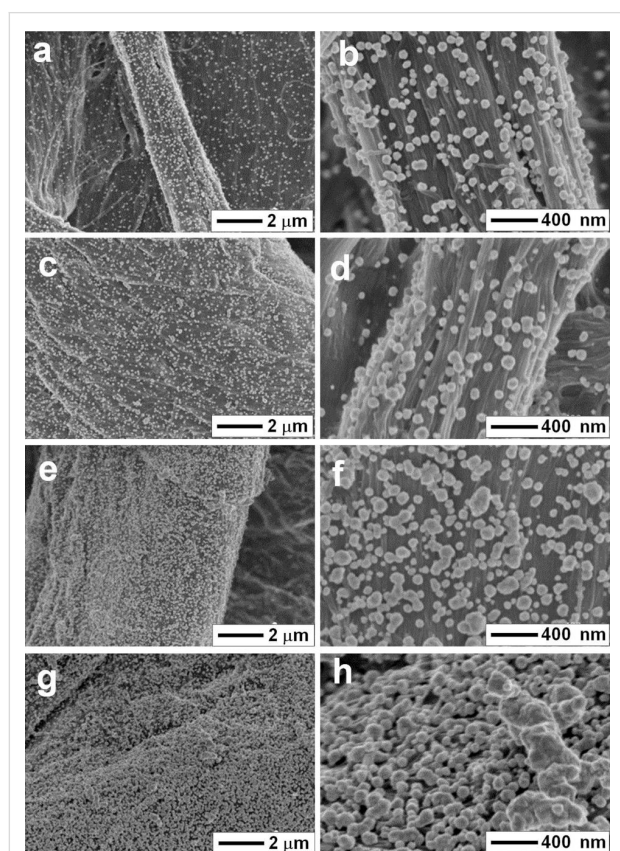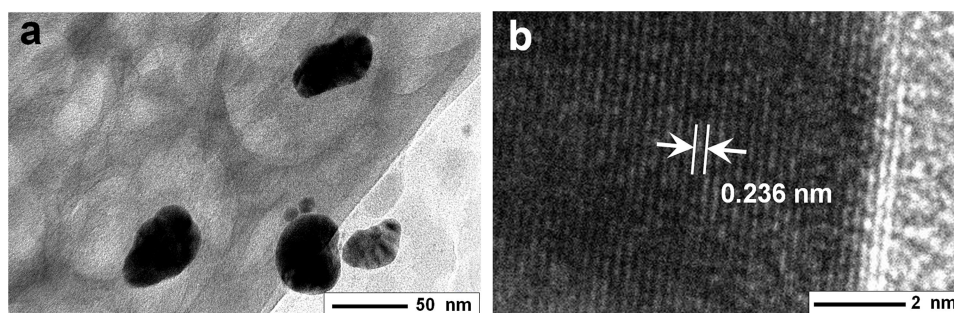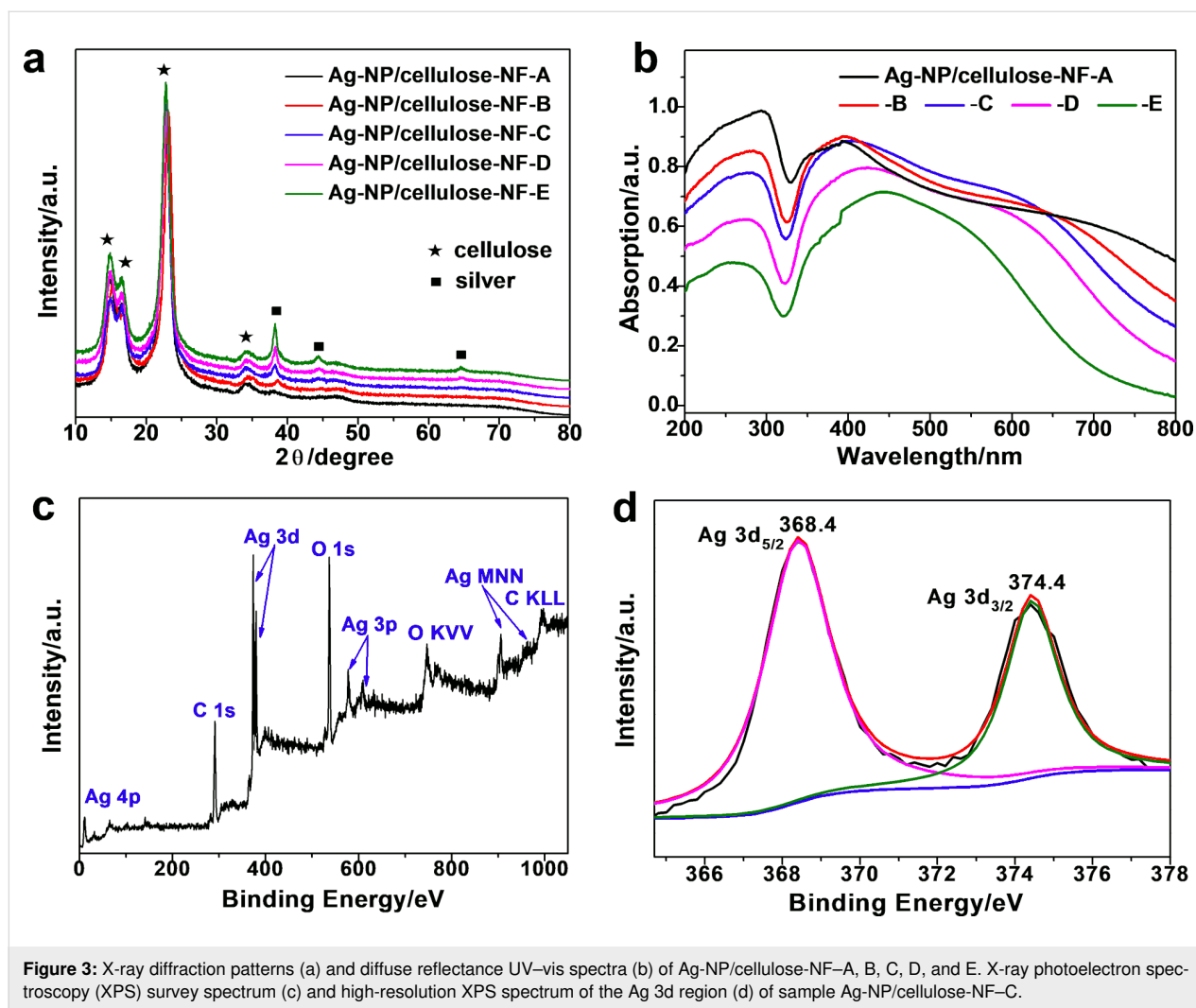

Figure 2: TEM image of Ag-NP/cellulose-NF–C (a), and HR-TEM image of an individual silver nanoparticle showing the lattice of metallic silver (b).

Figure 3: X-ray diffraction patterns (a) and diffuse reflectance UV–vis spectra (b) of Ag-NP/cellulose-NF–A, B, C, D, and E. X-ray photoelectron spectroscopy (XPS) survey spectrum (c) and high-resolution XPS spectrum of the Ag 3d region (d) of sample Ag-NP/cellulose-NF–C.
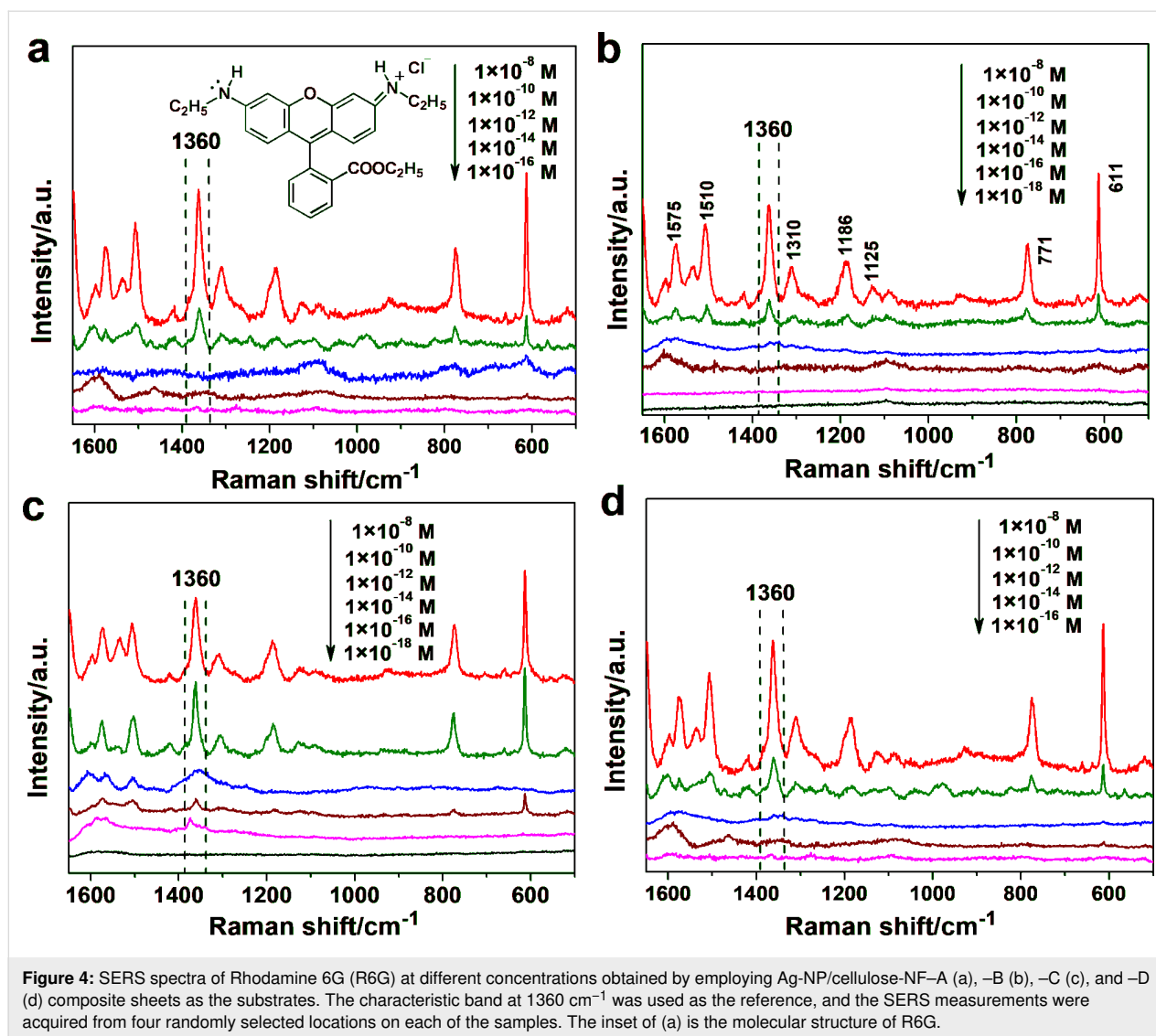
broadened and red-shifted to 450 nm for sample Ag-NP/cellulose-NF–E. It is known that, along with the increment of the silver nanoparticle sizes, the corresponding surface plasmon resonance band red-shifts to higher wavelengths [62]. It is also seen that every spectrum shows a shoulder band between 350 and 400 nm, which becomes more prominent with increasing silver nanoparticle size. This is because multipole transitions of surface plasmons become more prominent with the increment of the particle size [62]. These results are in accordance with the electron microscopy observations discussed above.

The X-ray photoelectron spectroscopy (XPS) survey spectrum of sample Ag-NP/cellulose-NF–C is shown in Figure 3c, showing the distinct peaks of carbon, oxygen and silver. Figure 3d shows the corresponding high-resolution spectrum of the Ag 3d region, where the two peaks located at 368.4 and 374.4 eV are attributed to the binding energies of Ag $3d_{5/2}$ and Ag $3d_{3/2}$ of metallic silver, respectively [60]. This result indicates metallic silver in the as-prepared paper-based SERS sub-

strate, which is in good agreement with the afore-mentioned characterizations.

SERS performance of the Ag-NP/cellulose-NF substrate

The performance of the Ag-NP/cellulose-NF composite sheets as SERS substrates was investigated by using Rhodamine 6G (R6G, inset of Figure 4a) as probe molecule. Neither the filter paper itself nor the pure Ag-NP/cellulose-NF substrate gave any spectral peak in the wavenumber region measured (Supporting Information File 1, Figure S5). R6G is employed as the model analyte due to its strong affinity to silver particles and its distinct Raman fingerprint [53]. All samples gave the characteristic Raman scattering bands of R6G at relatively high concentrations (Figure 4; Supporting Information, Figure S6). As marked in Figure 4b, the bands located at 611, 771, and 1125 cm^{-1} are assigned to the C–C–C ring in-plane, out-of-plane bending, and C–H in-plane bending vibrations, respectively; and those at 1186, 1310, 1360, 1510, and 1575 cm^{-1} are

Figure 4: SERS spectra of Rhodamine 6G (R6G) at different concentrations obtained by employing Ag-NP/cellulose-NF–A (a), –B (b), –C (c), and –D (d) composite sheets as the substrates. The characteristic band at 1360 cm^{-1} was used as the reference, and the SERS measurements were acquired from four randomly selected locations on each of the samples. The inset of (a) is the molecular structure of R6G.

associated with the totally symmetric modes of in-plane C–C–C stretching vibrations [63,64].

It is seen from the spectra in Figure 4a that the intensities of the Raman signals decreased along with the decrement of the concentrations of R6G. The most intense Raman band at 1360 cm^{-1} was adopted to compare the detection limit of the series of substrates.

The substrate Ag-NP/cellulose-NF–C exhibited the highest SERS enhancement, a detection limit as low as 1×10^{-16} M was achieved (Figure 4c). It is known that the SERS signals mainly result from the plasmon coupling of the metal particles, which depends considerably on the density and morphology of the particles. For substrates Ag-NP/cellulose-NF–A and –B, the detection limits are 1×10^{-10} M and 1×10^{-12} M, respectively (Figure 4a,b), which is due to the large distance between the

neighboring silver nanoparticles. And, as for the samples Ag-NP/cellulose-NF–D and –E, the corresponding detection limits are 1×10^{-12} M (Figure 4c) and 1×10^{-10} M (Supporting Information File 1, Figure S6), respectively. This is because, as seen from the FE-SEM images of the two substrates (Figure 1h; Supporting Information File 1, Figure S2), large aggregates of silver particles were formed during the prolonged reaction time, which resulted in a reduced number of hot spots. It can thus be concluded that, sample Ag-NP/cellulose-NF–C possesses the optimal loading density and morphology of the silver nanoparticles for SERS application. This SERS substrate is usable for the trace detection of the analyte.

In order to better understand the high SERS activity of the substrate Ag-NP/cellulose-NF–C, finite element method (FEM) modeling was performed to investigate the localized electric field intensity (E_{max}) of the silver nanoparticles (diameter

70 nm) with different inter-particle spacings. The obtained electric field intensity distributions are shown in Figure 5. The maximum values of the electric field intensities for inter-particle spacings of 15, 5, and 1 nm are 5.7, 9.2, and 40.7 V/m, respectively, and the value for the aggregated nanoparticles is 4.8 V/m. This result indicates that a smaller inter-particle distance of the silver nanoparticles leads to stronger electric fields. The sample Ag-NP/cellulose-NF–C shows a small inter-particle distance and, therefore, exhibits the best SERS activity. According to the fourth-power dependence of the enhancement factor on the electric field intensity, the enhancement factor of this substrate was estimated to be ca. 3×10^6.

Compared with previously reported cellulose-based SERS substrates, our current substrate shows a better SERS activity. For example, the bacterial nanocellulose adsorbed with gold nanoparticles in the form of a hydrogel had a detection limit of 1×10^{-9} M for R6G [54], the Au–Ag bimetallic microfluidic SERS sensor had a detection limit of 1×10^{-13} M for the same analyte [64]; and a detection limit of 1×10^{-6} M was offered by a hybrid substrate composed of cellulose nanofibrils and silver nanoprisms [65]. Two further examples are the silver dendrite decorated filter membrane and the silver nanoparticle decorated plasmonic paper, which both had a detection limit for R6G of 1×10^{-11} M [56,66]. The current paper-based Ag-NP/cellulose-NF SERS substrate achieved a remarkable detection limit at the sub-attomolar (1×10^{-16} M) level, which offers an outstanding potential for the detection and analyses of trace amounts of analytes.

This active paper-based SERS substrate was employed to detect the molecular recognition through multiple hydrogen bonds between nucleosides to test its potential in monitoring biomolecules. Figure 6 shows the Raman spectra obtained from adenosine and thymidine, measured before and after the molecular recognition between the two nucleosides on the substrate. Compared to the Raman spectra of the powder samples of adenosine and thymidine (Supporting Information File 1, Figure S7), different spectral features were observed. For adenosine (Figure 6, black curve), the strong scattering band located at 731 cm^{-1} is attributed to the ring breathing vibration of the adenine moiety, and the band at 1326 cm^{-1} is assigned to the stretching vibration of C–N and the bending vibration of C–H [67]. For thymidine (Figure 6, red curve), the weak bands at 799 and 1194 cm^{-1} are due to the ring breathing vibration and C–CH$_3$ stretching vibration of the thymine moiety, respectively [68]. It was noticed that the signal intensities of thymidine are much weaker than those of adenosine. This is because the amino group contained in the adenine moiety of adenosine leads to a much stronger interaction between the molecule and the surface of the silver nanoparticle. After the molecular recognition process occurred for the two nucleosides, similar spectra
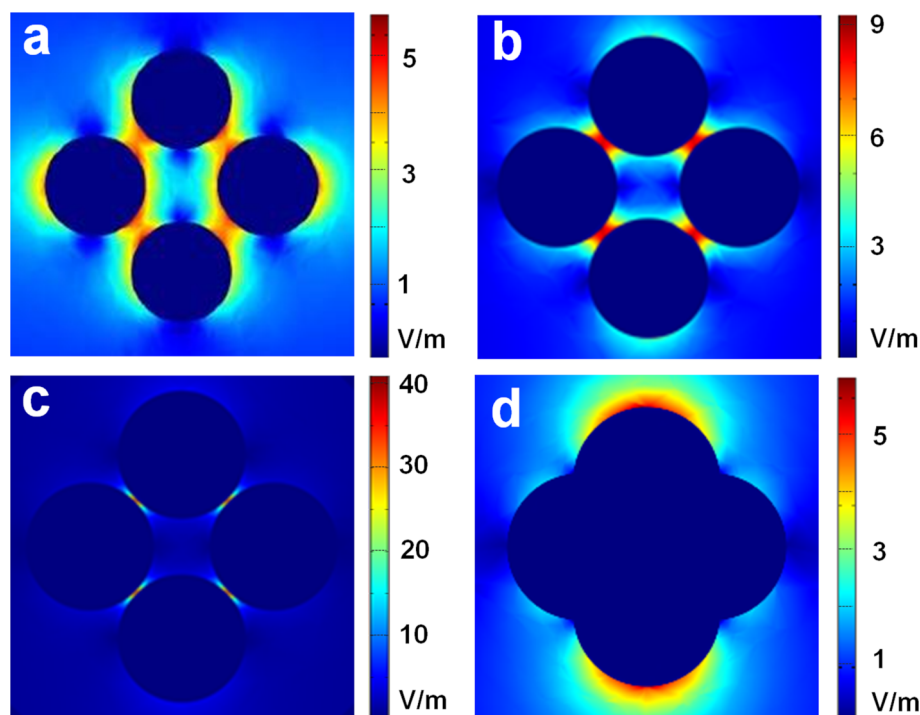

Figure 5: Electric field intensity distributions (indicated by the color bar) of the silver nanoparticles (diameter 70 nm) with different inter-particle spacings of 15 nm (a), 5 nm (b), 1 nm (c), and aggregated particles (d) at an excitation wavelength of 514 nm.
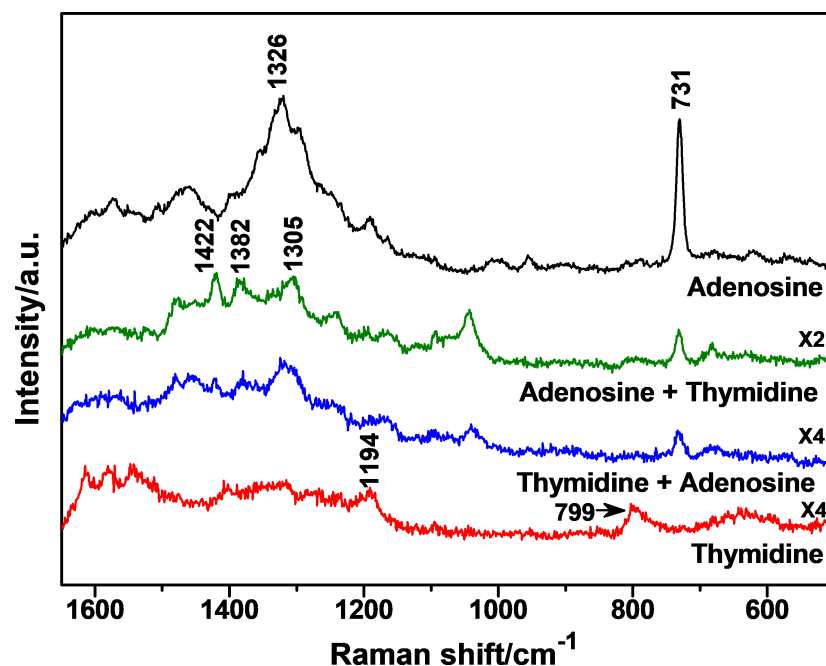
Figure 6: SERS spectra of adenosine and thymidine (both 10 µM), and the surface mixture of adenosine and thymidine obtained by employing the paper-based substrate Ag-NP/cellulose-NF–C.

(Figure 6, green and blue curves) were observed for both addition sequences (see Experimental section). The relative intensity of the band at 731 cm^{-1} of adenosine decreased, the band at 799 cm^{-1} of thymidine disappeared, and the initial band at 1326 cm^{-1} of adenosine became much weaker and red-shifted to 1305 cm^{-1}. Moreover, two new bands at 1382 and 1422 cm^{-1} attributed to the ring breathing vibrations of the thymine moiety of thymidine raised. These spectral features, which depend on the specific molecular orientation of the analyte on the silver surface, indicate the formation of complementary hydrogen bonds between the adenine and thymine moieties of the two nucleosides. This result demonstrates the potential of the SERS substrate for biomolecular analyses.

Conclusion

In summary, a paper-based SERS substrate with high activity was fabricated by the facile deposition of silver nanoparticles onto the cellulose fibers of laboratory filter paper. That is, the substrate exhibits a silver-nanoparticle/cellulose-nanofiber nanoarchitecture. Because of the optimized loading density and morphology of the deposited silver nanoparticles, as well as the unique structure of the cellulose matrix, this substrate exhibits a high SERS activity. A sub-attomolar-level detection limit is achieved for the detection of Rhodamine 6G. The substrate may be applicable for facile and sensitive analyses of chemical and biomolecular substances using Raman spectroscopy.

Experimental
Chemicals

Silver nitrate (AgNO$_3$), β-D-glucose and concentrated ammonia were bought from Sinopharm Chemical Reagent Co., Ltd. (Shanghai, China); sodium hydrate (NaOH) was purchased from Shanghai Titanchem Co., Ltd. (Shanghai, China); Rhodamine 6G (R6G, 98.5%) was obtained from J&K Chemical Ltd. (Shanghai, China); adenosine and thymidine were purchased from Fluorochem Ltd. (Derbyshire, UK). All the chemicals were guaranteed reagents and were used without further purification. Commercial laboratory filter paper (quantitative ashless) was purchased from Hangzhou Xinhua Paper Industry Co., Ltd. (China). The water used in all the experiments was purified by using a Milli-Q Advantage A10 system (Millipore, Bedford, MA, USA) with a resistivity higher than 18.2 MΩ·cm.

Fabrication of the paper-based Ag-NP/cellulose-NF composites

The silver nanoparticles (Ag-NPs) were deposited onto the surface of the cellulose nanofibers (NFs) of the filter paper by means of the silver mirror reaction. Briefly, 2.50 mL of fresh aqueous NaOH solution (5.0 wt %) was added into 50.0 mL ice-bath cooled fresh aqueous AgNO$_3$ solution (3.0 wt %), whereupon the brown AgOH precipitate was formed; afterwards, concentrated aqueous NH$_3$ solution was added dropwise under swift stirring into the mixture until the precipitate dissolved.

Then, 15.0 mL of aqueous β-ᴅ-glucose solution (10 wt %) was added into the prepared Tollens' reagent under continuous stirring. The solution obtained was immediately poured into a Petri dish where 5 pieces of filter paper (size 1 × 1 cm^2) were placed. In order to control the size and final density of the deposited silver nanoparticles, the filter paper pieces were left in the solution for different periods of time (2, 4, 6, 8, and 10 min). The corresponding piece of filter paper was the removed from the solution, thoroughly washed with water and ethanol, and dried in nitrogen flow. The corresponding silver-nanoparticle/cellulose-nanofiber (Ag-NP/cellulose-NF) composites obtained were denoted as Ag-NP/cellulose-NF–A, B, C, D, and E, respectively.

Characterizations

Direct surface observations of the Ag-NP/cellulose-NF composite sheets by field-emission scanning electron microscopy (FE-SEM) were carried out in a Hitachi SU-70 electron instrument with an EDAX HORIBA X-Max 80006 equipment working at accelerating voltages of 3.0 kV. To prepare the samples for transmission electron microscopy (TEM) measurements, a small piece of the corresponding sample was cut from the sheet and stirred in 5.0 mL of ethanol overnight to yield a suspension, which was dripped onto a carbon-coated copper grid followed and dried in air. TEM and high-resolution TEM (HR-TEM) images were acquired using a Hitachi HT-7700 instrument working at an acceleration voltage of 100 kV and a JEM 2100F electron microscope operated at an accelerating voltage of 200 kV, respectively. To obtain the size distributions of the silver nanoparticles in the samples, the size of 100 randomly selected particles in a TEM images was measured manually. Powder X-ray diffraction (XRD) patterns were acquired on a Philips X'Pert Pro diffractometer with a Cu Kα (λ = 0.15405 nm) radiation source. Diffuse reflectance UV–vis spectra were recorded by using a Shimadzu UV-2450 spectrophotometer in the diffuse-reflectance mode using an integrating sphere accessory with BaSO$_4$ as reference. X-ray photoelectron spectra were acquired by using a VG Escalab Mark 2 spectrophotometer equipped with a Mg Kα X-ray source (*h*ν = 1253.6 eV), the peak positions were internally referenced to the C 1s peak at 285.50 eV.

SERS measurements

The Ag-NP/cellulose-NF composite sheets were used as SERS substrates, and aqueous solutions of R6G with different concentrations (from 1 × 10^{-6} M to 1 × 10^{-18} M) were used as the test samples. 10 μL R6G solution with the given concentration was dripped onto the Ag-NP/cellulose-NF substrate using a pipette; after the solvent was volatilized, the sample was put on a glass slide to carry out the SERS measurement. The spectra were acquired using a Jobin Yvon LabRam HR UV Raman spec-

trometer, which was operated at an excitation wavelength of 514 nm with a maximum power of 250 mW. The SERS signals were recorded from four randomly selected points on the paper substrate with an integration time of 5 s for each spectrum. To monitor the molecular recognition between adenosine and thymidine, 10 μL aqueous solution (10 μM) of each nucleoside was dripped separately onto two pieces of the paper substrates; after the evaporation of the solvent, 10 μL aqueous solution of the complementary nucleoside was dripped onto the corresponding paper substrate, and then the SERS spectra were measured after drying under the same experimental conditions as noted above. The finite element method (FEM) modeling of the plasmonic properties of the silver nanoparticles of the Ag-NP/cellulose-NF–C substrate was conducted by employing the RF module of Comsol Multiphysics, and the parameters adopted were based on the silver nanostructures from the FE-SEM observation, together with the excitation at 514 nm. The optical constants of metallic silver were acquired from the literature [69].

Supporting Information

FE-SEM micrographs of the paper-based SERS substrate Ag-NP/cellulose-NF–E; histograms of the silver nanoparticle size distribution and EDX spectra of the samples Ag-NP/cellulose-NF–A, –B, and –C; SERS spectra of R6G at different concentrations obtained by using substrate Ag-NP/cellulose-NF–E.

Supporting Information File 1
Additional figures.
[https://www.beilstein-journals.org/bjnano/content/supplementary/2190-4286-10-126-S1.pdf]

ORCID® iDs
Yongxin Lu - https://orcid.org/0000-0002-5220-6209
Jianguo Huang - https://orcid.org/0000-0001-6862-8118

References

1. Malgras, V.; Ji, Q.; Kamachi, Y.; Mori, T.; Shieh, F.-K.; Wu, K. C.-W.; Ariga, K.; Yamauchi, Y. *Bull. Chem. Soc. Jpn.* **2015,** *88,* 1171–1200. doi:10.1246/bcsj.20150143
2. Ariga, K.; Ji, Q.; Hill, J. P.; Bando, Y.; Aono, M. *NPG Asia Mater.* **2012,** *4,* e17. doi:10.1038/am.2012.30
3. Ariga, K.; Aono, M. *Jpn. J. Appl. Phys.* **2016,** *55,* 1102A6. doi:10.7567/jjap.55.1102a6

4. Ariga, K.; Lee, M. V.; Mori, T.; Yu, X.-Y.; Hill, J. P.
   Adv. Colloid Interface Sci. **2010,** *154,* 20–29.
   doi:10.1016/j.cis.2010.01.005

5. Sakakibara, K.; Hill, J. P.; Ariga, K. *Small* **2011,** *7,* 1288–1308.
   doi:10.1002/smll.201002350

6. Ariga, K.; Mori, T.; Hill, J. P. *Langmuir* **2013,** *29,* 8459–8471.
   doi:10.1021/la4006423

7. Ramanathan, M.; Shrestha, L. K.; Mori, T.; Ji, Q.; Hill, J. P.; Ariga, K.
   Phys. Chem. Chem. Phys. **2013,** *15,* 10580–10611.
   doi:10.1039/c3cp50620g

8. Shrestha, L. K.; Ji, Q.; Mori, T.; Miyazawa, K.; Yamauchi, Y.; Hill, J. P.;
   Ariga, K. *Chem. – Asian J.* **2013,** *8,* 1662–1679.
   doi:10.1002/asia.201300247

9. Ariga, K.; Ji, Q.; Nakanishi, W.; Hill, J. P.
   J. Inorg. Organomet. Polym. Mater. **2015,** *25,* 466–479.
   doi:10.1007/s10904-015-0179-4

10. Ariga, K.; Malgras, V.; Ji, Q.; Zakaria, M. B.; Yamauchi, Y.
    Coord. Chem. Rev. **2016,** *320–321,* 139–152.
    doi:10.1016/j.ccr.2016.01.015

11. Ariga, K.; Mori, T.; Nakanishi, W.; Hill, J. P. *Phys. Chem. Chem. Phys.*
    2017, *19,* 23658–23676. doi:10.1039/c7cp02280h

12. Komiyama, M.; Mori, T.; Ariga, K. *Bull. Chem. Soc. Jpn.* **2018,** *91,*
    1075–1111. doi:10.1246/bcsj.20180084

13. Ariga, K.; Mori, T.; Shrestha, L. K. *Chem. Rec.* **2018,** *18,* 676–695.
    doi:10.1002/tcr.201700070

14. Ariga, K.; Mori, T.; Li, J. *Langmuir* **2018,** *35,* 3585–3599.
    doi:10.1021/acs.langmuir.8b01434

15. Ariga, K.; Yamauchi, Y.; Rydzek, G.; Ji, Q.; Yonamine, Y.;
    Wu, K. C.-W.; Hill, J. P. *Chem. Lett.* **2014,** *43,* 36–68.
    doi:10.1246/cl.130987

16. Rydzek, G.; Ji, Q.; Li, M.; Schaaf, P.; Hill, J. P.; Boulmedais, F.;
    Ariga, K. *Nano Today* **2015,** *10,* 138–167.
    doi:10.1016/j.nantod.2015.02.008

17. Ariga, K.; Ishihara, S.; Abe, H. *CrystEngComm* **2016,** *18,* 6770–6778.
    doi:10.1039/c6ce00986g

18. He, Q.; Cui, Y.; Ai, S.; Tian, Y.; Li, J. *Curr. Opin. Colloid Interface Sci.*
    2009, *14,* 115–125. doi:10.1016/j.cocis.2008.09.005

19. He, Q.; Cui, Y.; Li, J. *Chem. Soc. Rev.* **2009,** *38,* 2292–2303.
    doi:10.1039/b816475b

20. Yan, X.; Zhu, P.; Li, J. *Chem. Soc. Rev.* **2010,** *39,* 1877–1890.
    doi:10.1039/b915765b

21. Chen, C.; Liu, K.; Li, J.; Yan, X. *Adv. Colloid Interface Sci.* **2015,** *225,*
    177–193. doi:10.1016/j.cis.2015.09.001

22. Jia, Y.; Li, J. *Chem. Rev.* **2015,** *115,* 1597–1621.
    doi:10.1021/cr400559g

23. Feng, X.; Du, C.; Li, J. *Chem. Rec.* **2016,** *16,* 1991–2004.
    doi:10.1002/tcr.201600051

24. Cui, W.; Li, J.; Decher, G. *Adv. Mater. (Weinheim, Ger.)* **2016,** *28,*
    1302–1311. doi:10.1002/adma.201502479

25. Xuan, M.; Zhao, J.; Shao, J.; Du, C.; Cui, W.; Duan, L.; Qi, W.; Li, J.
    J. Colloid Interface Sci. **2017,** *487,* 107–117.
    doi:10.1016/j.jcis.2016.10.018

26. Ariga, K.; Ji, Q.; Mori, T.; Naito, M.; Yamauchi, Y.; Abe, H.; Hill, J. P.
    Chem. Soc. Rev. **2013,** *42,* 6322–6345. doi:10.1039/c2cs35475f

27. Ariga, K.; Yamauchi, Y.; Ji, Q.; Yonamine, Y.; Hill, J. P. *APL Mater.*
    2014, *2,* 030701. doi:10.1063/1.4868177

28. Ishihara, S.; Labuta, J.; Van Rossom, W.; Ishikawa, D.; Minami, K.;
    Hill, J. P.; Ariga, K. *Phys. Chem. Chem. Phys.* **2014,** *16,* 9713–9746.
    doi:10.1039/c3cp55431g

29. Ariga, K.; Minami, K.; Shrestha, L. K. *Analyst* **2016,** *141,* 2629–2638.
    doi:10.1039/c6an00057f

30. Jackman, J. A.; Cho, N.-J.; Nishikawa, M.; Yoshikawa, G.; Mori, T.;
    Shrestha, L. K.; Ariga, K. *Chem. – Asian J.* **2018,** *13,* 3366–3377.
    doi:10.1002/asia.201800935

31. Ariga, K.; Vinu, A.; Yamauchi, Y.; Ji, Q.; Hill, J. P.
    Bull. Chem. Soc. Jpn. **2012,** *85,* 1–32. doi:10.1246/bcsj.20110162

32. Abe, H.; Liu, J.; Ariga, K. *Mater. Today* **2016,** *19,* 12–18.
    doi:10.1016/j.mattod.2015.08.021

33. Khan, A. H.; Ghosh, S.; Pradhan, B.; Dalui, A.; Shrestha, L. K.;
    Acharya, S.; Ariga, K. *Bull. Chem. Soc. Jpn.* **2017,** *90,* 627–648.
    doi:10.1246/bcsj.20170043

34. Ariga, K.; Ji, Q.; McShane, M. J.; Lvov, Y. M.; Vinu, A.; Hill, J. P.
    Chem. Mater. **2012,** *24,* 728–737. doi:10.1021/cm202281m

35. Nakanishi, W.; Minami, K.; Shrestha, L. K.; Ji, Q.; Hill, J. P.; Ariga, K.
    Nano Today **2014,** *9,* 378–394. doi:10.1016/j.nantod.2014.05.002

36. Ariga, K.; Kawakami, K.; Ebara, M.; Kotsuchibashi, Y.; Ji, Q.; Hill, J. P.
    New J. Chem. **2014,** *38,* 5149–5163. doi:10.1039/c4nj00864b

37. Ariga, K. *Anal. Sci.* **2016,** *32,* 1141–1149. doi:10.2116/analsci.32.1141

38. Ariga, K. *ChemNanoMat* **2016,** *2,* 333–343.
    doi:10.1002/cnma.201600053

39. Ariga, K.; Naito, M.; Ji, Q.; Payra, D. *CrystEngComm* **2016,** *18,*
    4890–4899. doi:10.1039/c6ce00432f

40. Komiyama, M.; Yoshimoto, K.; Sisido, M.; Ariga, K.
    Bull. Chem. Soc. Jpn. **2017,** *90,* 967–1004. doi:10.1246/bcsj.20170156

41. Ariga, K.; Jackman, J. A.; Cho, N.-J.; Hsu, S.-h.; Shrestha, L. K.;
    Mori, T.; Takeya, J. *Chem. Rec.* **2018,** in press.
    doi:10.1002/tcr.201800103

42. Ariga, K.; Leong, D. T.; Mori, T. *Adv. Funct. Mater.* **2018,** *28,* 1702905.
    doi:10.1002/adfm.201702905

43. Zhang, K.; Zhao, J.; Xu, H.; Li, Y.; Ji, J.; Liu, B.
    ACS Appl. Mater. Interfaces **2015,** *7,* 16767–16774.
    doi:10.1021/acsami.5b04534

44. Hwang, J.; Lee, S.; Choo, J. *Nanoscale* **2016,** *8,* 11418–11425.
    doi:10.1039/c5nr07243c

45. Satheeshkumar, E.; Karuppaiya, P.; Sivashanmugan, K.; Chao, W.-T.;
    Tsay, H.-S.; Yoshimura, M. *Spectrochim. Acta, Part A* **2017,** *181,*
    91–97. doi:10.1016/j.saa.2017.03.040

46. Ko, H.; Singamaneni, S.; Tsukruk, V. V. *Small* **2008,** *4,* 1576–1599.
    doi:10.1002/smll.200800337

47. Park, M.; Jung, H.; Jeong, Y.; Jeong, K.-H. *ACS Nano* **2017,** *11,*
    438–443. doi:10.1021/acsnano.6b06196

48. Ke, Y.; Meng, G.; Huang, Z.; Zhou, N. *J. Mater. Chem. C* **2017,** *5,*
    1402–1408. doi:10.1039/c6tc04579k

49. Yu, W. W.; White, I. M. *Analyst* **2013,** *138,* 1020–1025.
    doi:10.1039/c2an36116g

50. Kim, W.; Lee, S. H.; Ahn, Y. J.; Lee, S. H.; Ryu, J.; Choi, S. K.; Choi, S.
    Biosens. Bioelectron. **2018,** *111,* 59–65.
    doi:10.1016/j.bios.2018.04.003

51. Rajapandiyan, P.; Yang, J. *J. Raman Spectrosc.* **2014,** *45,* 574–580.
    doi:10.1002/jrs.4502

52. Meng, Y.; Lai, Y.; Jiang, X.; Zhao, Q.; Zhan, J. *Analyst* **2013,** *138,*
    2090–2095. doi:10.1039/c3an36485b

53. Lee, C. H.; Hankus, M. E.; Tian, L.; Pellegrino, P. M.; Singamaneni, S.
    Anal. Chem. (Washington, DC, U. S.) **2011,** *83,* 8953–8958.
    doi:10.1021/ac2016882

54. Tian, L.; Jiang, Q.; Liu, K.-K.; Luan, J.; Naik, R. R.; Singamaneni, S.
    Adv. Mater. (Weinheim, Ger.) **2016,** *3,* 1600214.
    doi:10.1002/admi.201600214

55. Cheng, M.-L.; Tsai, B.-C.; Yang, J. *Anal. Chim. Acta* **2011,** *708,* 89–96. doi:10.1016/j.aca.2011.10.013

56. Li, Y.; Zhang, K.; Zhao, J.; Ji, J.; Ji, C.; Liu, B. *Talanta* **2016,** *147,* 493–500. doi:10.1016/j.talanta.2015.10.025

57. Sallum, L. F.; Soares, F. L. F.; Ardila, J. A.; Carneiro, R. L. *Spectrochim. Acta, Part A* **2014,** *133,* 107–111. doi:10.1016/j.saa.2014.04.198

58. Lin, C.-C.; Lin, C.-Y.; Kao, C.-J.; Hung, C.-H. *Sens. Actuators, B* **2017,** *241,* 513–521. doi:10.1016/j.snb.2016.09.183

59. Zhu, Y.; Li, M.; Yu, D.; Yang, L. *Talanta* **2014,** *128,* 117–124. doi:10.1016/j.talanta.2014.04.066

60. Luo, Y.; Li, J.; Huang, J. *Langmuir* **2016,** *32,* 12338–12343. doi:10.1021/acs.langmuir.6b01556

61. Pang, Q.; Wang, L.; Yang, H.; Jia, L.; Pan, X.; Qiu, C. *RSC Adv.* **2014,** *4,* 41212–41218. doi:10.1039/c4ra05520a

62. Bhui, D. K.; Bar, H.; Sarkar, P.; Sahoo, G. P.; De, S. P.; Misra, A. *J. Mol. Liq.* **2009,** *145,* 33–37. doi:10.1016/j.molliq.2008.11.014

63. Nie, S.; Emory, S. R. *Science* **1997,** *275,* 1102–1106. doi:10.1126/science.275.5303.1102

64. Qu, L.-L.; Song, Q.-X.; Li, Y.-T.; Peng, M.-P.; Li, D.-W.; Chen, L.-X.; Fossey, J. S.; Long, Y.-T. *Anal. Chim. Acta* **2013,** *792,* 86–92. doi:10.1016/j.aca.2013.07.017

65. Jiang, F.; Hsieh, Y.-L. *Biomacromolecules* **2014,** *15,* 3608–3616. doi:10.1021/bm5011799

66. Zhao, B.; Lu, Y.; Zhang, C.; Fu, Y.; Moeendarbari, S.; Shelke, S. R.; Liu, Y.; Hao, Y. *Appl. Surf. Sci.* **2016,** *387,* 431–436. doi:10.1016/j.apsusc.2016.06.128

67. Qiu, H. W.; Xu, S. C.; Chen, P. X.; Gao, S. S.; Li, Z.; Zhang, C.; Jiang, S. Z.; Liu, M.; Li, H. S.; Feng, D. J. *Appl. Surf. Sci.* **2015,** *332,* 614–619. doi:10.1016/j.apsusc.2015.01.231

68. Datta, D.; Bera, R. K.; Jana, S.; Manna, B.; Roy, D.; Anoop, A.; Raj, C. R.; Pathak, T. *Chem. – Asian J.* **2015,** *10,* 1554–1560. doi:10.1002/asia.201500045

69. Johnson, P. B.; Christy, R. W. *Phys. Rev. B* **1972,** *6,* 4370–4379. doi:10.1103/physrevb.6.4370

Multicomponent bionanocomposites based on clay nanoarchitectures for electrochemical devices

Giulia Lo Dico[1,2], Bernd Wicklein[1], Lorenzo Lisuzzo[2], Giuseppe Lazzara[2], Pilar Aranda[1] and Eduardo Ruiz-Hitzky[*1]

Abstract

Based on the unique ability of defibrillated sepiolite (SEP) to form stable and homogeneous colloidal dispersions of diverse types of nanoparticles in aqueous media under ultrasonication, multicomponent conductive nanoarchitectured materials integrating halloysite nanotubes (HNTs), graphene nanoplatelets (GNPs) and chitosan (CHI) have been developed. The resulting nanohybrid suspensions could be easily formed into films or foams, where each individual component plays a critical role in the biocomposite: HNTs act as nanocontainers for bioactive species, GNPs provide electrical conductivity (enhanced by doping with MWCNTs) and, the CHI polymer matrix introduces mechanical and membrane properties that are of key significance for the development of electrochemical devices. The resulting characteristics allow for a possible application of these active elements as integrated multicomponent materials for advanced electrochemical devices such as biosensors and enzymatic biofuel cells. This strategy can be regarded as an "a la carte" menu, where the selection of the nanocomponents exhibiting different properties will determine a functional set of predetermined utility with SEP maintaining stable colloidal dispersions of different nanoparticles and polymers in water.

Introduction

In recent years, the "nanoarchitectonics" concept has helped to develop a large variety of materials with new functionalities [1-6]. Among them, different types of functional materials based on clay minerals have been also prepared; pillared clays and polymer–clay nanocomposites are the best-known examples [7]. Besides classical layered silicates, clays showing other morphologies, such as fibrous (sepiolite and palygorskite) and tubular (halloysite and imogolite) clays, could also be interest-

ing nanoparticulated solids in this context [8-11]. Sepiolite (SEP) and palygorskite are attracting increasing attention in the development of nanoarchitectured materials in applications such as catalysis or biomedicine [8]. The presence of silanol groups at the external surface of the clay fibers allows for the easy assembly with different species facilitating the design and the build up of functional materials. On the other hand, tubular nanoclays, such as halloysite nanotubes (HNTs), are interesting containers for the controlled chemical reactions at nanoscale interfaces and the delivery of active compounds thanks to their unique nature [12], which could be advantageous when integrated as component in nanoarchitectured materials.

Halloysite nanotubes are aluminosilicates of cylindrical shape with the length ranging between 500 and 1000 nm and a lumen diameter between 15 and 70 nm [13]. The lumens represent an ideal nanospace for the uptake and preservation of diverse functional species including drugs, proteins, and enzymes [14-18], even serving as nanoreactor for chemical processes [19]. Of particular interest is the use of HNTs for the uptake of enzymes in an approach for the development of (bio)electrochemical devices like biosensors and enzymatic biofuel cells (EBCs) [20,21]. However, one of the main problems limiting the preparation of HNT-based nanoarchitectured materials is the low colloidal stability of HNTs in aqueous media. This ultimately leads to inhomogeneous and badly performing nanocomposites in spite of the different approaches that have been developed to obtain homogeneous dispersions within different polymeric matrices [22-24]. Therefore, other and more efficient colloidal stabilizers are needed to fully exploit the potential of HNTs.

It has been recently observed that fibrous sepiolite clay mineral of rheological grade (see Experimental section) develops highly stable and viscous suspensions after sonomechanical treatment in water. Dispersions of disaggregated sepiolite can efficiently suspend nanoparticles of different topologies and hydrophobic nature such as graphene nanoplatelets (GNPs) and multiwalled carbon nanotubes (MWCNTs) in water [25,26]. In fact, following this approach it was possible to prepare multifunctional and homogeneous nanocomposite materials such as self-supported sepiolite–nanocarbon hybrid buckypapers [25] and conducting bionanocomposites [26]. Therefore, the present study explores the potential of sepiolite for stabilizing aqueous HNT suspensions.

SEP is a microcrystalline hydrated magnesium silicate with fibrous morphology and dimensions depending on the geological environment of its origin [27]. For instance, an aspect ratio of up to 100 and diameters ranging from 10 to 50 nm are usually observed in sepiolite samples from Taxus basin (Spain) deposits [28]. The unique property of this nanofibrous clay is its

ability to largely disaggregate in water after ultrasound treatment, creating thus a rigid, percolated network that can sustain co-dispersed compounds or reinforce polymer matrices [25,26,29]. Interestingly, HNTs are known to maintain their ability to act as nanocontainers even when dispersed in a multicomponent system included in polymer matrices [22]. It has been observed that positively charged polymers such as chitosan (CHI) can electrostatically incorporate the previously loaded halloysite through interactions with its external surface, leaving the lumen unaffected. This offers interesting possibilities for further inclusion of diverse guest species [30,31]. In addition, the role of the polymer matrix is crucial to process advanced bionanocomposite materials either as films or as foams [32-34]. This type of hybrid material offers the advantage of a large interface improving the contact efficiency between the entrapped active molecules and the external environment allowing for the development of promising devices for biosensing [35,36] and enzymatic biofuel cells (EBCs) [37,38].

In this work, conducting multicomponent nanoarchitectured materials involving HNTs, GNPs, MWCNTs, and a CHI matrix were prepared and processed as films and foams from aqueous suspensions of the components dispersed through ultrasound irradiation as schematized in Figure 1. The incorporation of glucose oxidase (GOx) into the lumen of HNTs has been chosen here as an example for the immobilization of bioactive species, which can be crucial to design (bio)electrochemical devices with high performance and long life-time. The SEP, GNP, and MWCNT components are also expected to behave as polymer nanofillers to ensure the mechanical strength and electrical conductivity of the prepared bionanocomposite films and
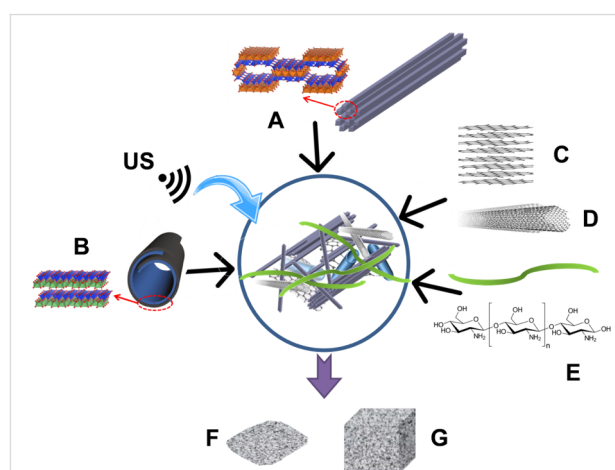

Figure 1: Schematic representation of the different components integrated in the bionanocomposite materials, i.e., (A) sepiolite fibrous clay, (B) halloysite nanotubes, (C) graphene nanoplatelets, (D) multiwalled carbon nanotubes, and (E) chitosan biopolymer, prepared in aqueous media under ultrasound irradiation (US). The resulting nanoarchitectured materials can be formed into films (F) or foams (G).

foams [26]. Moreover, MWCNTs are supposed to act as nano-wires improving the contact between the active site of the immobilized enzymes and an electrode surface via direct electron transfer [39].

The resulting multicomponent systems have advantages such as high electrical conductivity and flexibility that make the bio-nanocomposite films appropriate components for biosensors [35,40] for glucose detection, while the relatively high porosity of the bioactive foams enhances the power density and operational stability of EBCs [37,41].

Herein, the performance of the biosensor was evaluated by cyclic voltammetry exploiting the mediated electron transfer (MET) mechanism and the power density of the assembled biofuel cell is examined through polarization curves obtained with linear sweep voltammetry in the direct electron transfer (DET) mode.

Results and Discussion
Preparation of bionanocomposite films and foams

The preparation of multicomponent nanoarchitectured materials used as functional nanofiller in the further preparation of bioactive and conducting nanocomposites was carried out by mixing of SEP and HNT nanoclays with GNPs and MWCNTs in aqueous media assisted by sonomechanical treatment as schematized in Figure 1. The generation of homogeneous and stable multicomponent dispersions in water (Figure 2) can only be accomplished thanks to the rheological properties of the SEP fibrous clay (Pangel® S9) under ultrasound irradiation.
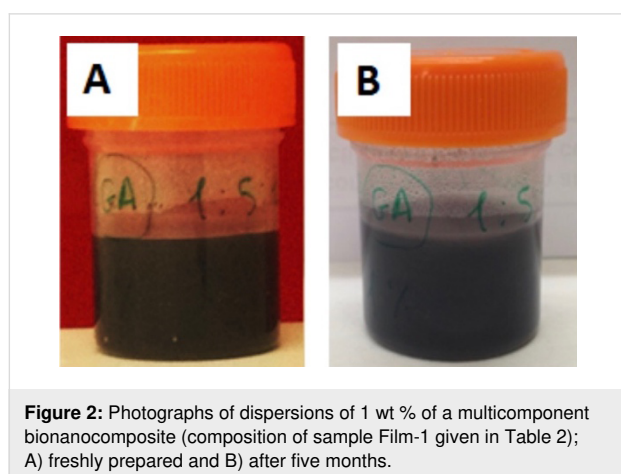

Figure 2: Photographs of dispersions of 1 wt % of a multicomponent bionanocomposite (composition of sample Film-1 given in Table 2); A) freshly prepared and B) after five months.

The incorporation of these components into a polymeric CHI matrix results in composite materials that can be processed either as films or as foams. In agreement with previous works [25,26], the ultrasound treatment of this type of sepiolite in

aqueous medium promotes the homogeneous dispersion of diverse nanoparticulated components. It can be inferred that the disaggregated fibres of sepiolite form an interpenetrated network representing, in the present case, a steric hindrance for GNPs, MWCNTs, and HNTs to aggregate. This avoids phase segregation and particle sedimentation. These dispersions remained stable for more than five months (Figure 2B) and proved to be suitable for preparing self-supported, flexible films by solvent-casting (Figure 3B) as well as foams by freeze-casting (Figure 3C).
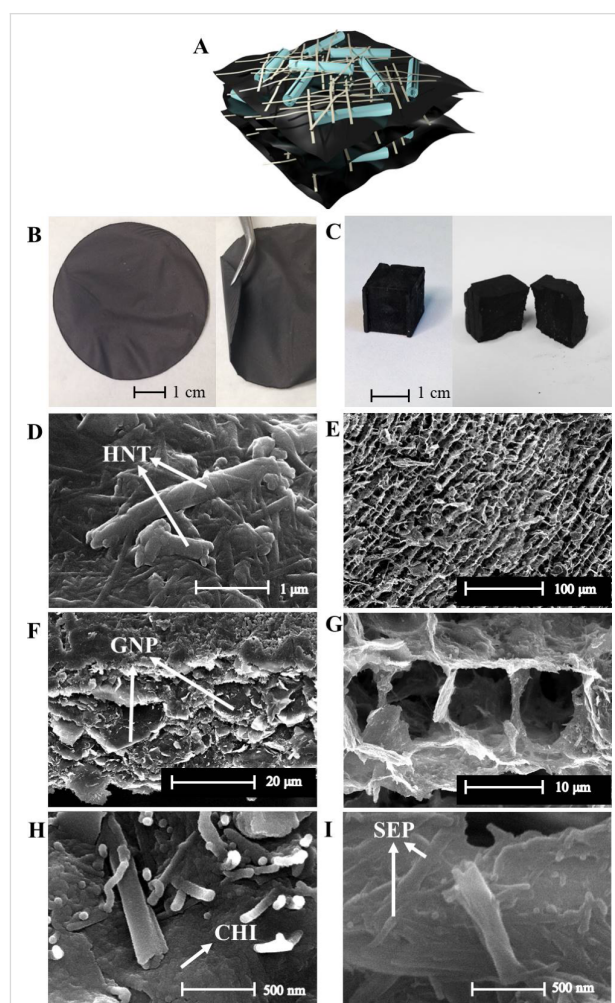

Figure 3: Schematic representation of particle assembly in the multicomponent bionanocomposites: A) cross section of processed materials: HNTs and SEP are represented as tubes and fibres, while chitosan, GNPs and MWCNTs are depicted in the black matrix. Photographs of B) Film-1 and C) Foam-1. SEM micrographs of the film: D) upper surface, F) and H) cross section; SEM micrographs of the foam: E) and G) pore architecture, I) cell walls.

The lamellar arrangement of the bionanocomposite films is schematized in Figure 3A, while SEM images (Figure 3D,F) reveal that the components are uniformly distributed throughout the film and are organized as a compact particle assembly

within the chitosan matrix. Furthermore, the film cross section (Figure 3F) displays the typical layered structure of films solvent-cast from fibre dispersions [26,29,42]. Importantly, the access to the lumen of the HNTs appears to remain unblocked despite the assembly with the other components (Figure 3H), which is crucial for the effective use of HNTs as nanocontainers for bioactive molecules. The presence of MWCNTs was not detected in the SEM images given their small size and low concentration (2–5%) in the bionanocomposites.

Freeze-casting rendered foams of high uniformity and shape fidelity (Figure 3C). The foams display open, cell-like pores (Figure 3E,G) with a pore diameter of 13 ± 4 μm and a cell wall thickness of 0.2–0.4 μm (Figure S1, Supporting Information File 1), comparable to similar freeze-cast clay nanocomposite foams [43,44]. Halloysite nanotubes are visible on the surface of the cell walls with free access to the lumen (Figure 3I).

The porosity of the foams was estimated from their relative density values (Table 1). It was found that foams with a high content of chitosan showed the lowest porosity, i.e., 89%. The porosity of films with low chitosan content was 96%. In fact, by reducing the chitosan content (and concomitantly increasing the clay and GNP content) the apparent density slightly decreases, while the skeletal density increases due to the higher density of the solid components. Consequently, the relative density decreases and the porosity increases. It is interesting to note that the foam structure does not seem to collapse after reducing the polymer content, which would otherwise lead to higher apparent density values. The increased apparent density of the foams at higher chitosan content might be attributed to the tendency of the polymer matrix to create a more compact assembly of the particulate components [44,45]. The high porosity is also reflected in the nitrogen adsorption/desorption isotherms (Figure S2a,b in Supporting Information File 1). The BET specific surface area of the samples Film-1 and Foam-1 was 5 and 58 $m^2 \cdot g^{-1}$, respectively.

The microstructure of the films was characterized by X-ray diffraction (XRD). The diffractogram of Film-1 displays the main reflections of both nanoclays and GNPs without 2θ displacement (Figure S3, Supporting Information File 1). This suggests that, in contrast to other polymer–HNT composites, no intercalation of chitosan into the halloysite interlayer spacing occurred, and thus, halloysite still remains in its dehydrated form (Figure S4, Supporting Information File 1) [30,34]. Furthermore, a change in the relative intensity of the main halloysite reflections is observed as a typical consequence of a preferential in-plane orientation of the nanotubes in the film architecture (Figure S4, Supporting Information File 1) [46].

The mechanical properties of the bionanocomposite materials were evaluated in stress–strain measurements (Figure S5, Supporting Information File 1), analysing the influence of the nanofiller content on the elastic behaviour as it has been described in related biopolymer-based nanocomposites [26]. The results show that the Young's modulus of the films (Figure 4A) increases with the clay nanofiller content from 5 GPa for pure chitosan up to 11 GPa for the sample Film-4, which contains 40% of clay components.

These findings are in good agreement with the mechanical properties of similar composite materials based on sepiolite, MWCNTs and poly(vinyl alcohol) [25], sepiolite, graphene nanoplatelets, and biopolymers (e.g., alginate, gelatine) [26] and cellulose or foams of microfibrillated cellulose and starch [47], which exhibit Young's moduli in the range from 0.1 to 9 GPa. The high stiffness of these materials has been previously attributed to the sepiolite fibres that strongly interact with chitosan chains and may also interlock hindering physical movement and sliding of the other particulate components [48].

The mechanical test (Figure 4B) of the bionanocomposite foams confirmed the crucial role of the chitosan matrix conferring robustness to these systems as the Young's modulus of

Table 1: Apparent, skeletal, and relative density together with the corresponding porosity of the bionanocomposite foams.

sample	NC[a] (wt %)	GNP[b] (wt %)	CHI (wt %)	ρ_{app}[c] (g·mL^{-1})	ρ_{sc}[d] (g·mL^{-1})	ρ_{rel}[e]	porosity (%)
Foam-1	18	55	15	0.071	1.9	0.04	96
Foam-2	12	36	45	0.072	1.4	0.05	95
Foam-3	10	30	54	0.076	1.2	0.06	94
Foam-4	6	18	72	0.080	0.7	0.1	89
Foam-5	2	6	91	0.081	0.4	0.21	79

[a]NC = total amount of nanoclays; the ratio between both clay minerals (SEP/HNTs) was kept at 1:1. [b]The ratio between both nanocarbons (GNPs/MWCNTs) was kept at 5:1. [c]ρ_{app} denotes the apparent density. [d]ρ_{sc} denotes the skeletal density. [e]ρ_{rel} denotes the relative density calculated as ρ_{app}/ρ_{sc}.
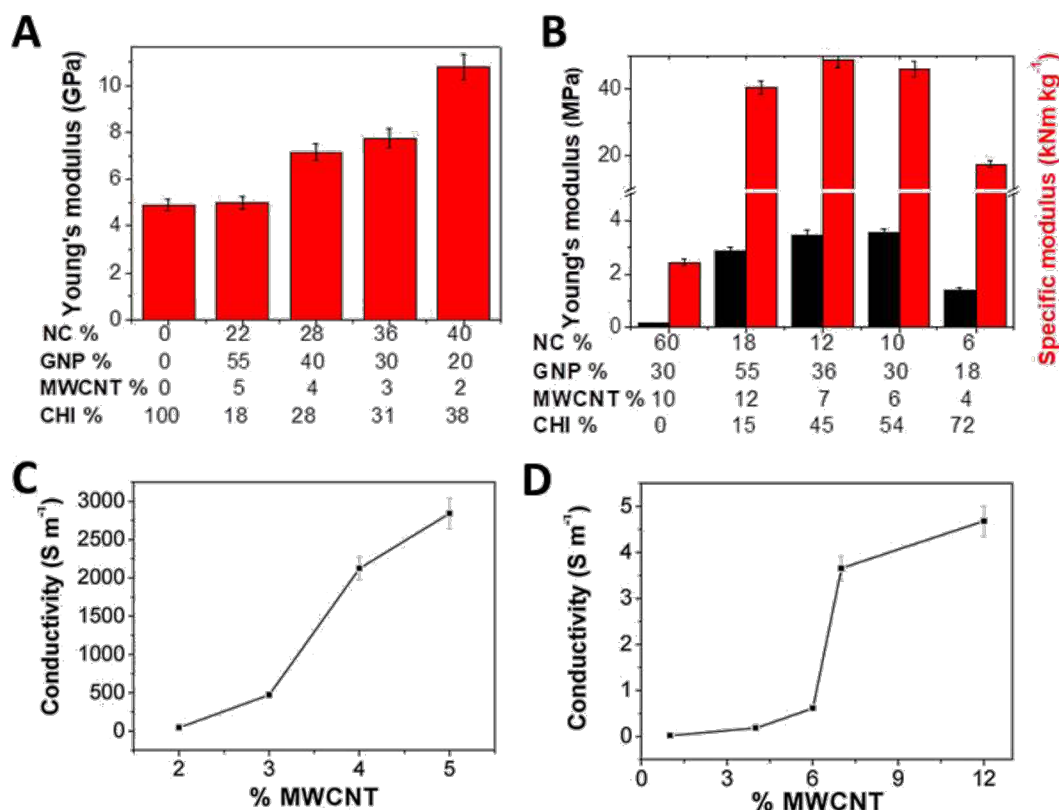
Figure 4: Young's moduli and electrical conductivity of HNTs/SEP/GNPs/MWCNTs/CHI films (A, C) and foams (B, D), respectively.

0.2 MPa for a foam without chitosan (with the composition of 1:1:1:0.3 in HNTs/SEP/GNPs/MWCNTs) increases to 3.5 MPa after incorporation of the biopolymer (45 wt %). This increase can be correlated to the strong interaction between the chitosan matrix and the sepiolite fibres as well as to an increase in the relative density that produces a decrease in porosity, commonly related to a smaller pore size and a lower tendency to collapse than in the case of larger macropores [48,49]. In contrast, a decrease in the compression modulus (1.4 MPa) was found for the sample with a higher content of chitosan (72%), suggesting a synergic effect of both clays as reinforcing fillers of the polymer and as adhesive agent, which is required to improve the mechanical properties of the designed samples [50,51]. The obtained compression modulus is comparable to values measured for other chitosan/clay foams (1.4 MPa) [51] and significantly higher than those of self-assembled graphene hydrogels (0.03–0.3 MPa) [52]. Notably, the specific modulus of the bionanocomposite foams was 50 kNm·kg^{-1}, which is considerably higher than values reported for silica aerogels (5–20 kNm·kg^{-1}) [53] and is on par with polystyrene foams (10–100 kNm·kg^{-1}) [49] and other bionanocomposite graphene–clay foams (77 kNm·kg^{-1}) [43].

A high electrical conductivity of the bionanocomposite films and foams is crucial for their application in electrochemical devices. The conductivity was therefore assessed by the van der Pauw method based on the four-point technique [26]. This method is useful to accurately measure the surface properties of a sample of arbitrary shape. Figure 4C displays the in-plane electrical conductivity of the films as a function of the MWCNT content (composition of samples in Table 2).

A remarkable value of 2900 S·m^{-1} is obtained at 5 wt % of carbon nanotubes, while the percolation threshold for electrical conductivity is at 4 wt % MWCNT content. The conductivity values are higher than the values reported previously for sepiolite–nanocarbon–polymer bionanocomposites (1000–2500 S·m^{-1} [14,15]). The high in-plane conductivity found here can be attributed to a synergic effect of MWCNTs and the lamellar assembly of graphene nanoplatelets in the plane of the film as observed by SEM (see Figure 3F). The MWCNTs act as nanowires connecting the GNPs, which facilitates the electron percolation across the insulating network of polymer and clay components [26,29]. In addition, the polymer matrix appears to have a significant influence on the electrical

Table 2: Composition and nomenclature of the prepared samples.[a]

	sample	NC[c] (wt %)	GNP[d] (wt %)	CHI (wt %)
films	Film-1[b]	22	55	18
	Film-2	28	40	28
	Film-3	36	30	31
	Film-4	40	20	38
foams	Foam-1[b]	18	55	15
	Foam-2	12	36	45
	Foam-3	10	30	54
	Foam-4	6	18	72
	Foam-5	2	6	91

[a]The sepiolite (SEP)/halloysite (HNTs) ratio was kept at 1:1. [b]GOx loaded into HNTs for biosensor and EBC assays. [c]NC = total amount of nanoclays. The ratio between both clay minerals (SEP/HNT) was kept at 1:1. [d]In the film composition the ratio between both nanocarbons (GNPs/MWCNTs) was kept at 10:1, whie in the foam it was 5:1.

conductivity. While having a similar GNP/MWCNT content bionanocomposites with different polymer matrices showed different conductivity values, i.e., 2700 S·m^{-1} for alginate, 900 S·m^{-1} for gelatin, and 300 S·m^{-1} for poly(vinyl alcohol), and the chitosan matrix discussed here yielded conductivity of 2900 S·m^{-1} [26]. The increase of the conductivity in chitosan films can tentatively be ascribed to the presence of physically adsorbed water not only on the nanoclay surfaces. it might also be associated with the polymer matrix enhancing electrical conductivity trough ionic species and proton diffusion [54,55].

The electrical conductivity of the bionanocomposite foams is presented in Figure 4D. The foams displayed conductivity values of ca. 4.5 S·m^{-1}, which is significantly lower than that of films of similar composition. This is attributable to the higher porosity and separation of the charge carriers. However, the electrical conductivity of these foams is considerably higher than that of other related graphene-based foams (0.5 S·m^{-1} [52]). The electrical percolation threshold of the foams was around 6.5 wt % MWCNT content. The higher value in foams reflects a poorer connectivity between carbon nanoparticles dispersed in the clay–polymer matrix probably due to the high porosity, requiring a larger amount of GNPs/MWCNTs to form a conducting network within the matrix of the bionanocomposite. In any case, the percolation threshold is on par or slightly lower than the values for related MWCNT–polymer composites, which are in the range of 4–9 wt % [56,57].

The bionanocomposite sample Film-1 was used to evaluate the stability of these multicomponent hybrid materials in water showing a mass loss of only 3.2 wt % over the course of two months. This excellent stability, together with the good electrical and mechanical properties, suggest that the prepared

multicomponent bionanocomposite can be suitable as electrode material in aqueous media. Moreover, the successful incorporation of HNTs as nanoreactor prompted the use of these bionanocomposite materials in bioelectrocatalysis applications (see below).

Immobilization of glucose oxidase in the lumen of HNTs

The developed multicomponent bionanocomposites were used for the immobilization of the enzyme glucose oxidase in the search of multifunctional properties of interest in bioelectrochemical applications. GOx was chosen as a prototypic bioactive component because of its properties and compatibility with HNTs, i.e., an appropriate size (5.4 nm) as well as an appropriate isoelectric point (at pH 4.0–4.5) for inclusion and immobilization at the surface of the halloysite lumen. Then, HNTs were exploited as nanocontainers for GOx, avoiding the direct interaction the protein with the sepiolite fibres that may lead to enzymatic inactivity [58,59]. In fact, assays showed a drastic loss of enzymatic activity when GOx was incorporated in the film without previous immobilization within HNTs. Hence, GOx was immobilized in the HNT clay prior to its incorporation into the multicomponent mixture. The uptake of GOx was 7.7 ± 0.2 wt % according to CHN elemental analysis. The enzyme immobilization was also confirmed by FTIR spectroscopy (Figure S6 and Table S1, Supporting Information File 1). The HNT–GOx spectrum clearly shows the presence of bands assigned to the symmetric stretching of C–H aliphatic groups and the amide groups of GOx [60]. In particular, there is no significant variation in the amide I and amide II vibrations of the immobilized GOx enzyme with respect to unsupported GOx. This observation strongly supports that the adsorption of GOx in HNTs occurs via non-deteriorating electrostatic interactions [57]. This physical entrapment, in contrast to immobilization via covalent bonding is essential for the preservation of the enzyme structure and bioactivity [38,58].

The presence of GOx in the lumen of HNTs was also evidenced by measuring nitrogen adsorption/desorption isotherms (Figure S7, Supporting Information File 1). Compared to pristine HNTs, a notable decrease of the specific surface area from 25 to 19 m^2·g^{-1} for HNT–GOx could be observed. The volume of the mesopores was also reduced after GOx uptake (Table S2, Supporting Information File 1) in agreement with a partial pore blockage, supporting the hypothesis that the majority of GOx was loaded into the lumen of HNTs [24].

With the GOx-loaded HNTs a multicomponent bionanocomposite film (Film-GOx) and foam (Foam-GOx) were prepared with the composition of Film-1 and Foam-1, respectively (see Table 2). The enzymatic activity of Film-GOx was confirmed in

a test with peroxidase and 2,2'-azino-bis(3-ethylbenzothiazo-line-6-sulphonic acid (ABTS), indicating that the preparation procedure did not affect the response of the entrapped GOx towards glucose (Figure S8, Supporting Information File 1).

Detection of glucose with a film-GOx biosensor

The GOx-loaded bionanocomposite film (Film-GOx) was tested as biosensor for the detection of glucose (Figure 5A).

The performance of the biosensor was studied by cyclic voltammetry (CV) in the presence of potassium ferricyanide as mediator, relying on the mediated electron transfer (MET) mechanism. Figure 5B shows the CV curve of the biosensor in response to 50 mM glucose in phosphate-buffered solution (PBS). The intensity of the oxidation and reduction peaks of $Fe(CN_6)^{4-}$ at 0.19 and 0.33 V, respectively, increases significantly in presence of glucose. Together with the change of the CV curve shape this confirms the catalytic behaviour of the
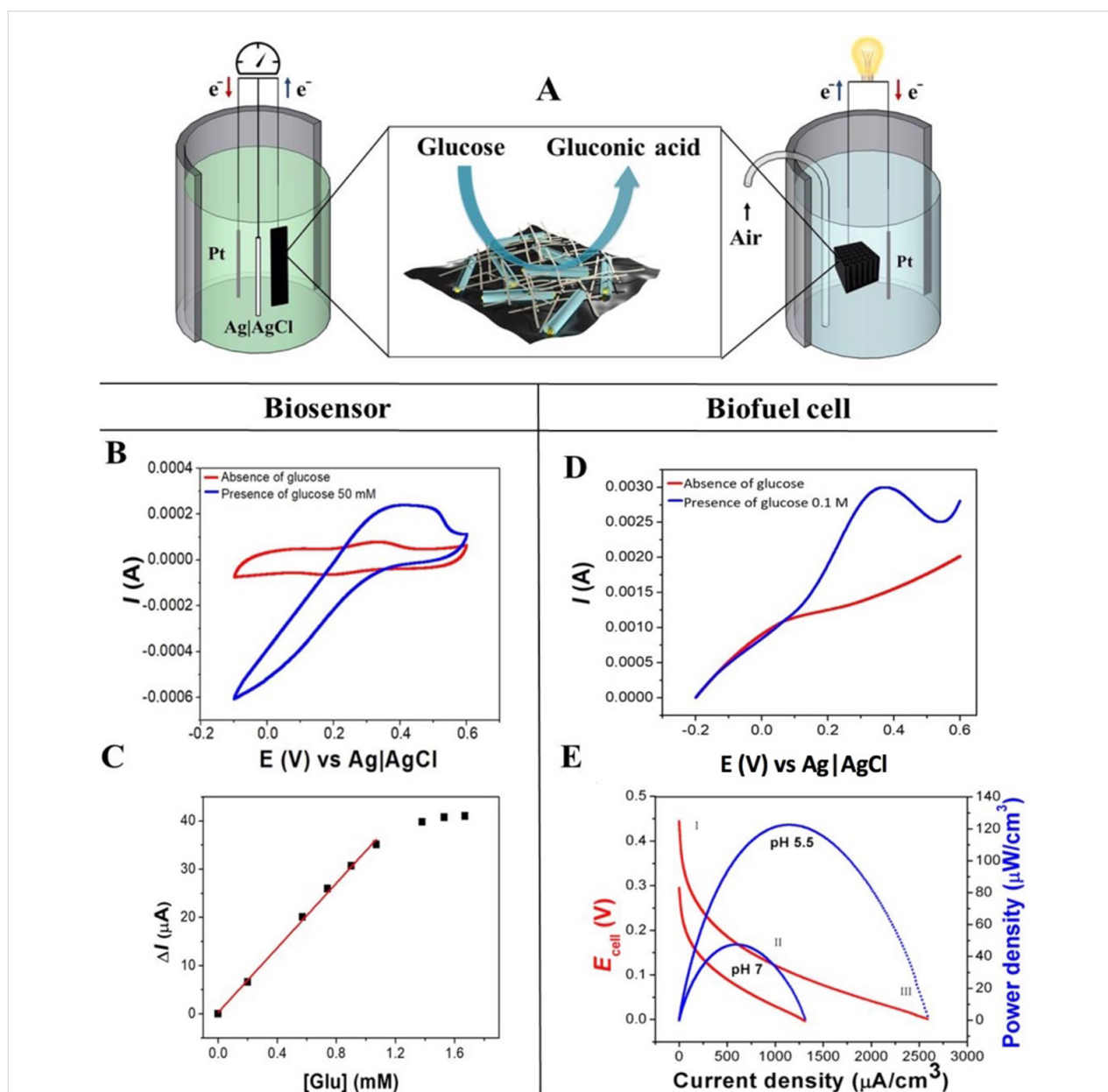
Figure 5: A) Scheme of an EBC (left) and a biosensor (right) with the electrode microstructure and biocatalytic oxidation of glucose at the bioactive nanocomposite interface. B) Effect of glucose on the Film-GOx sample in CV measurement in PBS, pH 7 and 0.1 mM of potassium ferricyanide at a scan rate of 5 mV·s⁻¹. C) Sensor response as a function of the glucose concentration. The red line is a linear fit. Δ*I* = steady-state current at 0.45 V. D) LSV measurement of Foam-GOx immersed in PBS at pH 7 and in the presence of 0.1 M glucose in PBS at the same pH vaue. E) Polarization curve obtained by LSV measurements at a scan rate of 1 mV·s⁻¹. The medium is PBS with 1 M glucose at pH 7 and pH 5.5.

immobilized enzyme [61,62]. The steady-state current as a function of the glucose concentration is depicted in Figure 5C showing Michaelis–Menten behaviour, i.e., an effect of the substrate concentration on the rate of the enzyme-catalysed reaction. The use of potassium ferricyanide as mediator enabled a fast electron transfer between the enzyme and the electrode surface. In fact, a fit of the curve with the Lineweaver–Burk plot (Figure S9, Supporting Information File 1) rendered a Michaelis–Menten constant (K_m) of 9.3 mM, which is smaller than those reported for GOx in solution (33 mM) [62] and GOx immobilized in mesopores of Al_2O_3 membranes (10–30 mM) [63], sol–gel-derived composite films (14 mM) [64], and similar devices based on graphene and carbon nanotubes (4–15 mM) [65,66]. The low K_m value is indicative of an excellent performance attributed to strong substrate binding and high enzymatic activity of the immobilized GOx [65].

The linear range of the biosensor was 0–1.1 mM glucose and the sensitivity was as high as 34 $\mu A \cdot mM^{-1}$. These results also reflect the stronger response of the designed biosensor to low amounts of glucose with respect to other devices based on immobilized GOx on, for instance, graphene, CNTs, and buckypapers (10–25 $\mu A \cdot mM^{-1}$) [46,66,67], the external surface of functionalised HNTs (5.2 $\mu A \cdot mM^{-1}$) [20], a polymeric matrix (5 $\mu A \cdot mM^{-1}$) [68] or a chitosan-modified matrix (1.2 $\mu A \cdot mM^{-1}$) [69].

The crucial role of HNTs as protective containers for the enzymes was underlined by immobilizing GOx directly on bionanocomposite films prepared without the incorporation into halloysite, where the enzyme was directly integrated in the system after the ultrasonication treatment. The CV curves of these films showed no response to glucose (Figure S10, Supporting Information File 1), suggesting the inactivity of the entrapped enzyme. This is probably due to the direct interaction of the enzyme with sepiolite and shows the necessity to load the enzyme into the clay nanotubes. It is well known that the electrostatic interaction of proteins with the external surface of sepiolite can be very strong and, in some cases, might cause the loss of the biological functionality [60].

Application of foam-GOx as anode in a membrane-less and open-air biofuel cell

It is well known that redox mediators are required for most of the GOx-based bioelectrocatalysis applications to guarantee an efficient electron transfer process from the enzyme to the electrode interface [70]. Therefore, in a preliminary assay, Foam-GOx was tested in the presence of $Fe(CN_6)^{4-}$ as mediator and separated from the cathode chamber by a Nafion® membrane. A power density of 565 $\mu W \cdot cm^{-3}$ and 31 $\mu W \cdot cm^{-2}$ was generated (Figure S11, Supporting Information File 1). Next, the
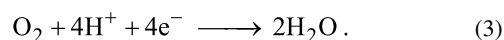
EBC performance was evaluated under open-air conditions and in the absence of any mediator or expensive proton exchange membranes. Figure 5A illustrates the EBC designed as a one-pot cell. The GOx enzyme catalyses the conversion of glucose in gluconic acid as follows [71]:

$$FAD\text{-}GOx + glucose \longrightarrow FADH_2\text{-}GOx + gluconic\ acid\ . \quad (1)$$

The reaction occurring on the anode surface is:

$$FADH_2\text{-}GOx \longrightarrow FAD\text{-}GOx + 2H^+ + 2e^-\ , \quad (2)$$

while the Pt cathode catalyses the reaction:

$$O_2 + 4H^+ + 4e^- \longrightarrow 2H_2O\ . \quad (3)$$

Linear sweep voltammetry (LSV) experiments were carried out to evaluate the electrocatalytic properties of the bionanocomposite Foam-GOx as 3D bio-anode. Figure 5D displays the catalytic behaviour during the oxidation of glucose. In fact, with the addition of 0.1 M glucose, a clear increase (blue line) of the anodic current appears compared to that in PBS without glucose. For the here designed mediator-less cell, this behaviour is correlated to a direct electron transfer mechanism at the interface between the active site (FAD) of the enzyme and the conducting elements of the electrode surface [72,73]. The current increase occurs at a voltage of 0.35 V, which is higher than the typical $FAD/FADH_2$ standard voltage (−0.460 V at pH 7.0 and 25.8 °C) probably because of the presence of carbon nanotubes that can influence the electrochemical response [60].

The polarization measurements were carried out in a concentrated glucose solution (1 M) to estimate the maximum power density regardless of the glucose content [70,71]. The polarization curves for the described biofuel cell working at two different pH values are shown in Figure 5E. The polarization curves show the common behaviour of microbial fuel cells (MFCs) and EBCs and can be divided into three zones as shown in Figure 5E, commonly called the activation zone (I), ohmic losses (II), and the mass-transport zone (III) [72,73].

The open-circuit potential (OCP) of the cell at pH 5.5 was 0.442 V, while at pH 7 the OCP was 0.298 V. This finding can be correlated to the combination of effects such as a more suitable working pH value for glucose oxidase (the optimal working pH value of GOx is close to 5) and a faster oxygen reduction at the cathode surface. The presence of the acidic medium, in fact, can favour the proton migration from the anode to the cathode surface leading to an increase of the half-cell potential [70]. The power output of the EBC was different for the two pH values. Compared to pH 7 the cell working at pH 5.5 exhib-

its an increase in volumetric power density from 47.8 $\mu W\cdot cm^{-3}$ at 0.081 V to 120 $\mu W\cdot cm^{-3}$ at 0.116 V and in current density from 1.3 $mA\cdot cm^{-3}$ to 2.6 $mA\cdot cm^{-3}$, respectively, as well as a rise in surface power density from 2.6 $\mu W\cdot cm^{-2}$ to 6.5 $\mu W\cdot cm^{-2}$. These values are in good agreement with other EBC systems, indicating a good performance the Foam-GOx bionanocomposite (Table 3).

The decrease of power density compared to the cell working in presence of redox mediator is associated with a slower electron transfer at the enzyme–electrode interface. Nevertheless, the confined GOx in halloysite nanotubes was able to operate even in the DET mechanism, allowing for a use in physiological environments [72,74].

Furthermore, the high surface area promotes a better contact between glucose and the active sites of the enzyme, but at the same time the high porosity of 96% of the bio-anode helps to delay the leaching of bioactive components. Before being released into the surrounding medium, the enzyme must take a tortuous path through the pore system of the foam, resulting in a good stability over time. A preliminary evaluation of this effect was carried out by repeating the test after a period of five days of storage in PBS at 30 °C, after which 93% of the initial power was retained.

Conclusion

This work reports a preliminary study showing the viability to integrate nanoclays, biopolymers, and graphene-based conducting components into homogeneous multifunctional nanoarchitectured materials. The presence of sepiolite fibrous clay, together with ultrasonication, is the key to disperse all these components in water. The resulting stable colloids can be processed as films and foams displaying acceptable mechanical properties, good electrical conductivity, and controlled porosity useful for diverse applications at the nanoscale. HNTs were efficiently loaded with 7.7 wt % of the model enzyme glucose oxidase that retained high enzymatic activity inside the halloysite lumens. This allows for the exploration of the multicomponent bionanocomposites as functional components of electrochemical devices such as biosensor and as 3D bio-anode in a biofuel cell. The latter revealed a volumetric power density of 120 $\mu W\cdot cm^{-3}$ and a good stability over time at elevated temperatures (the power density decreased by only 7% after five days of storage at 30 °C). These bioelectrocatalysis results are representative for an incipient development that could be sextended in the future to other fields of interest, especially considering the versatility of halloysite as nanocontainer of various bioactive species [17]. The possibility to introduce additional functionalities by modification of sepiolite, for instance, by incorporating magnetic or photoactive nanoparticles [8], could pave the way to further applications of these multicomponent functional bionanocomposites in the near future.

Experimental
Materials

Sepiolite (SEP) from the Vallecas-Vicálvaro clay deposits (Madrid, Spain) was provided by TOLSA S.A. (Spain) as a commercial, rheological grade product (Pangel® S9). This microfibrous clay has a low cationic exchange capacity (ca. 15 $meq\cdot(100~g)^{-1}$) and high specific surface area (ca. 300 $m^2\cdot g^{-1}$). Dehydrated halloysite nanotubes (HNTs) from the New Zealand China Clays deposits were provided by Imerys (France). Before use, HNTs were ground and sieved through a 250 µm mesh. Glucose oxidase (GOx; type VII-S, 181,500 $U\cdot g^{-1}$ solid; E.C.1.1.3.4 from Aspergillus niger) was

Table 3: Performance of different published EBFC systems utilizing DET or MET mechanisms.

anode	cathode	mechanism	OCP (V)	power density	reference
GOx-graphene/SWCNT co-gel	BOD-graphene/SWCNT co-gel	DET	0.61	190 $\mu W\cdot cm^{-2}$ 650 $\mu W\cdot cm^{-3}$	[72]
graphite/GOx/catalase/ubiquinone	graphite/PPO/quinhydrone	MET	0.27	24 $\mu W\cdot cm^{-3}$	[74]
CNT/GOx/catalase	CNT/laccase	DET	0.57	193 $\mu W\cdot cm^{-2}$ 161 $\mu W\cdot cm^{-3}$	[75]
Fc-MeOH/GOx CNPs	ABTS2-/BOD CNPs	MET	0.50	95 $\mu W\cdot cm^{-2}$	[76]
GOx/SWNT/Ppy composite	tyrosinase/CNPs/Ppy composite	DET	—	158 $\mu W\cdot cm^{-3}$	[77]
CDH/AuNPs	MvBOx/AuNPs	DET	0.57	1 $\mu W\cdot cm^{-2}$	[78]
GMC/GOx/GA	Pt	DET	0.48	22 $\mu W\cdot cm^{-2}$	[79]
CNTs/FcMe2-LPEI/Lactate	CNTs/Ar-pyr/BOx	MET	0.44	2.4 $\mu W\cdot cm^{-2}$	[80]
Foam-GOx	Pt	MET	0.32	31 $\mu W\cdot cm^{-2}$ 565 $\mu W\cdot cm^{-3}$	this work
Foam-GOx	Pt	DET	0.44	6.5 $\mu W\cdot cm^{-2}$ 120 $\mu W\cdot cm^{-3}$	this work

supplied by Sigma-Aldrich. Graphene nanoplatelets (GNPs) are multilayered graphene sheets that were supplied by KNANO (China) under the name of KNG-150. They are composed by more than ten carbon layers with 5–15 nm thickness and 1–20 μm diameter, showing an electrical conductivity of 12000 S·m^{-1} and a specific surface area of 41 m^2·g^{-1} (according to the manufacturer). Multiwalled carbon nanotubes (MWCNTs), with more than 95% of carbon content, were obtained from Dropsens S.A. (Spain) and used without further treatment. The average diameter of the tubes was 10 nm and the average length 1.5 μm. Acetic acid (ca. 99.5%) was obtained from Merck. Anhydrous D-glucose (99 %) was obtained from Scharlau. Peroxidase (HRP; type II, 120,000 U·g^{-1} solid; E.C.1.11.1.7 from horseradish) were purchased from Sigma Chemical Co., 2,2'-azino-bis(3-ethylbenzothiazoline-6-sulphonic acid) (ABTS) was obtained from Fluka. Trisodium phosphate dodecahydrate (ca. 98%), was furnished by Sigma and phosphoric acid (85%) by Carlo Erba. Bi-distilled water (18.2 MΩ·cm) was obtained from a Maxima Ultra Pure Water system from Elga. Chitosan with a medium molecular weight of 190–310 kDa, 75–85% deacetylated, was obtained from Aldrich.

Preparation of colloidal suspensions and films and foams

The preparation of the multicomponent bionanocomposites is shown in Figure 1. Two sets of aqueous mixtures of chitosan (CHI) and different proportions (Table 2) of SEP/HNTs/GNPs/MWCNTs were prepared at overall concentrations of 0.2% w/v and 8% w/v, respectively. First, the appropriate amounts of both nanoclays and GNPs/MWCNTs were dispersed in bi-distilled water and exposed to pulsed ultrasonic waves (VC750 Sonics Vibra-Cell, operating at 20 kHz) using a 13 mm standard probe. Separately, chitosan was slowly dissolved in an aqueous solution of 1% v/v acetic acid at 70 °C and added to the SEP/HNTs/GNPs/MWCNTs dispersion under magnetic stirring.

The bionanocomposite films were processed by solvent-casting from the 0.2% w/v dispersion on polyester Petri dishes and dried at 30 °C and 60% relative humidity (RH) in a CLIMA-CELL EVO Stability Chamber (Incubator model 111L).

The bionanocomposite foams were prepared by freeze-drying (Cryodos-80, Telstar) of the 8% w/v dispersion, which was cast in cylindrical plastic containers and plunged in liquid nitrogen.

Immobilization of glucose oxidase in halloysite nanotubes and their incorporation in bionanocomposite matrices

Glucose oxidase (100 mg) was dissolved in water (1 mL) and mixed with HNTs (200 mg). Then, the sample was vortexed and sonicated in an ultrasound bath until no aggregates of halloysite were visible. In order to ensure the complete infiltration of the HNT lumens by the GOx solution the samples were subject to alternating cycles of reduced pressure (approx. 70 Torr). The loaded HNT-GOx was separated from the solution by centrifugation, washing and finally dried overnight in a desiccator at 30 °C and stored at 4 °C until usage. HNT-GOx was added to the SEP/GNPs/MWCNTs/CHI mixtures (0.2% w/v and 8% w/v) described above, obtaining the compositions Film-1 and Foam-1 (Table 2). The resulting suspensions were processed by solvent-casting and freeze-casting to obtain the bioactive films (film-GOx) and the bioactive foams (foam-GOx), respectively, and were stored at 4 °C until usage.

Characterization techniques

The morphology of the prepared bionanocomposite films and foams was evaluated by scanning electron microscopy (SEM) using a SEM Philips XL 30 S-FEG microscope. Before examination, the samples were fractured in liquid nitrogen. The FTIR spectra of HNT-GOx samples were acquired with a BRUKER iFS spectrophotometer 66Vs. X-ray diffractograms were obtained with a D8-ADVANCE diffractometer (Bruker), using Cu Kα radiation. The voltage and current sources were set at 40 kV and 30 mA, respectively. Diffractograms were recorded at a goniometer speed of 0.5 s per step between 4° and 60° (2θ). The BET specific surface area and the pore size distribution (Barret–Joyner–Hallenda method) were determined from nitrogen adsorption/desorption isotherms obtained on a Micromeritics ASAP 2010 analyser. The samples were degassed at 120 °C under vacuum. The stability of the bionanocomposites in water was assessed by immersing a piece of the film in bi-distilled water for two months and noting the weight loss. The relative density (ρ_{rel}) of the bionanocomposite foams was estimated from the skeletal density using the following values: SEP = 2.3 g·mL^{-1}, HNTs = 2.2 g·mL^{-1}, GNPs = 2.3 g·mL^{-1}, MWCNTs = 2.1 g·mL^{-1}, chitosan = 0.2 g·mL^{-1}. The mechanical properties of the films and foams were assessed under ambient conditions by using a universal test machine (Instron Model 3345) equipped with a 5 kN load cell and at 1 mm·min^{-1} frame speed. At least three measurements were performed per sample. The electrical conductivity was determined by the four-point method, using a Solartron 1480 potentiostat (MultiStat). Elemental chemical analysis (CNHS Perkin Elmer 2400 analyzer) was carried out to estimate the amount of GOx loaded into the HNTs.

Biosensing test

Cyclic voltammetry (CV) was performed with a standard three-electrode electrochemical cell connected to a Solartron 1480 MultiStat potentiostat. A platinum wire was used as a counter electrode and Ag|AgCl (soaked in 1.0 M KCl) was used as a

reference electrode. In the biosensing tests, the working electrode was a film of 30 × 5 mm × 0.014 (3.49 mg, containing 0.028 mg of immobilized GOx) immersed in a potassium ferricyanide solution (0.2 mM) as mediator containing 0.1 M of phosphate buffered solution (pH 7). CV was performed in a potential range from −0.2 to 0.6 V at a scan rate of 5 mV·s^{-1}.

Biofuel cell test

Polarization curves were obtained from linear sweep voltammetry performed with a µStat 100 potentiostat (Dropsens, Spain) in a two-electrode configuration. The glucose/air biofuel cell was assembled by coupling the bioactive foam, as anode, to a Pt wire as cathode in a one-pot cell working in 0.1 M of glucose and 0.1 M PBS, at two different pH values (7 and 5.5) and saturated with air. The foam was connected to the potentiostat with a copper wire, glued with colloidal graphite and covered by an epoxy resin as isolating material. All tests were run three times at a scan rate of 1 mV·s^{-1} starting from the open-circuit potential (OCP, $I = 0$) to the short-circuit cell voltage ($I = I_{max}$). From the data of V$_{cell}$ as a function of I, the power (P) was calculated according to Equation 4.

$$P = I \cdot V_{cell} .\qquad (4)$$

Finally, the power density was obtained as a surface power density (µW·cm^{-2}) with the roughness factor (ECSA) calculated from the CV measurements, and as a volumetric power density (µW·mL^{-1}) considering a specific volume (0.02 cm^3), calculated from the specific density (1.9 g·mL^{-1}) [29].

Supporting Information

Supporting Information File 1

Additional experimental data.
[https://www.beilstein-journals.org/bjnano/content/supplementary/2190-4286-10-129-S1.pdf]

Acknowledgements

ORCID® iDs

Giulia Lo Dico - https://orcid.org/0000-0001-9841-4399
Bernd Wicklein - https://orcid.org/0000-0002-1811-6736
Lorenzo Lisuzzo - https://orcid.org/0000-0001-6954-2754
Giuseppe Lazzara - https://orcid.org/0000-0003-1953-5817
Pilar Aranda - https://orcid.org/0000-0003-2196-0476
Eduardo Ruiz-Hitzky - https://orcid.org/0000-0003-4383-7698

Preprint

References

1. Aono, M.; Bando, Y.; Ariga, K. *Adv. Mater. (Weinheim, Ger.)* **2012,** *24,* 150–151. doi:10.1002/adma.201104614
2. Ariga, K., Ed. *Manipulation of Nanoscale Materials: An Introduction to Nanoarchitectonics;* Royal Society of Chemistry: Cambridge, United Kingdom, 2012. doi:10.1039/9781849735124
3. Komiyama, M.; Yoshimoto, K.; Sisido, M.; Ariga, K. *Bull. Chem. Soc. Jpn.* **2017,** *90,* 967–1004. doi:10.1246/bcsj.20170156
4. Khan, A. H.; Ghosh, S.; Pradhan, B.; Dalui, A.; Shrestha, L. K.; Acharya, S.; Ariga, K. *Bull. Chem. Soc. Jpn.* **2017,** *90,* 627–648. doi:10.1246/bcsj.20170043
5. Ariga, K.; Mori, T.; Shrestha, L. K. *Chem. Rec.* **2018,** *18,* 676–695. doi:10.1002/tcr.201700070
6. Kryuchkova, M.; Fakhrullin, R. *Environ. Sci. Technol. Lett.* **2018,** *5,* 295–300. doi:10.1021/acs.estlett.8b00135
7. Ruiz-Hitzky, E.; Aranda, P.; Belver, C. Nanoarchitectures Based on Clay Materials. In *Manipulation of Nanoscale Materials: An Introduction to Nanoarchitectonics;* Ariga, K., Ed.; Royal Society of Chemistry: Cambridge, United Kingdom, 2012; pp 87–111. doi:10.1039/9781849735124-00087
8. Aranda, P.; Ruiz-Hitzky, E. *Chem. Rec.* **2018,** *18,* 1125–1137. doi:10.1002/tcr.201700113
9. Vinokurov, V. A.; Stavitskaya, A. V.; Glotov, A. P.; Novikov, A. A.; Zolotukhina, A. V.; Kotelev, M. S.; Gushchin, P. A.; Ivanov, E. V.; Darrat, Y.; Lvov, Y. M. *Chem. Rec.* **2018,** *18,* 858–867. doi:10.1002/tcr.201700089
10. Glotov, A.; Levshakov, N.; Stavitskaya, A.; Artemova, M.; Gushchin, P.; Ivanov, E.; Vinokurov, V.; Lvov, Y. *Chem. Commun.* **2019,** *55,* 5507–5510. doi:10.1039/c9cc01935a
11. Li, L.; Ma, W.; Higaki, Y.; Kamitani, K.; Takahara, A. *Langmuir* **2018,** *34,* 13361–13367. doi:10.1021/acs.langmuir.8b03107
12. Fu, L.; Yang, H.; Tang, A.; Hu, Y. *Nano Res.* **2017,** *10,* 2782–2799. doi:10.1007/s12274-017-1482-x
13. Lazzara, G.; Cavallaro, G.; Panchal, A.; Fakhrullin, R.; Stavitskaya, A.; Vinokurov, V.; Lvov, Y. *Curr. Opin. Colloid Interface Sci.* **2018,** *35,* 42–50. doi:10.1016/j.cocis.2018.01.002
14. Lvov, Y.; Wang, W.; Zhang, L.; Fakhrullin, R. *Adv. Mater. (Weinheim, Ger.)* **2016,** *28,* 1227–1250. doi:10.1002/adma.201502341
15. Cavallaro, G.; Lazzara, G.; Milioto, S.; Parisi, F.; Evtugyn, V.; Rozhina, E.; Fakhrullin, R. *ACS Appl. Mater. Interfaces* **2018,** *10,* 8265–8273. doi:10.1021/acsami.7b19361
16. Lo Dico, G.; Semilia, F.; Milioto, S.; Parisi, F.; Cavallaro, G.; Inguì, G.; Makaremi, M.; Pasbakhsh, P.; Lazzara, G. *Appl. Sci.* **2018,** *8,* 1455. doi:10.3390/app8091455
17. Tully, J.; Yendluri, R.; Lvov, Y. *Biomacromolecules* **2016,** *17,* 615–621. doi:10.1021/acs.biomac.5b01542
18. Lvov, Y. M.; Shchukin, D. G.; Möhwald, H.; Price, R. R. *ACS Nano* **2008,** *2,* 814–820. doi:10.1021/nn800259q

19. Shchukin, D. G.; Sukhorukov, G. B.; Price, R. R.; Lvov, Y. M. *Small* **2005,** *1,* 510–513. doi:10.1002/smll.200400120

20. Kumar-Krishnan, S.; Hernandez-Rangel, A.; Pal, U.; Ceballos-Sanchez, O.; Flores-Ruiz, F. J.; Prokhorov, E.; Arias de Fuentes, O.; Esparza, R.; Meyyappan, M. *J. Mater. Chem. B* **2016,** *4,* 2553–2560. doi:10.1039/c6tb00051g

21. Goda, E. S.; Gab-Allah, M. A.; Singu, B. S.; Yoon, K. R. *Microchem. J.* **2019,** *147,* 1083–1096. doi:10.1016/j.microc.2019.04.011

22. Sun, X.; Zhang, Y.; Shen, H.; Jia, N. *Electrochim. Acta* **2010,** *56,* 700–705. doi:10.1016/j.electacta.2010.09.095

23. Cavallaro, G.; Lazzara, G.; Milioto, S. *J. Phys. Chem. C* **2012,** *116,* 21932–21938. doi:10.1021/jp307961q

24. Pasbakhsh, P.; Chrichman, G. J., Eds. *Natural mineral nanotubes, properties and applications;* Apple Academic Press Inc.: Oakville, ON, USA; Waretown, NJ, USA, 2015. doi:10.1201/b18107

25. Fernandes, F. M.; Ruiz-Hitzky, E. *Carbon* **2014,** *72,* 296–303. doi:10.1016/j.carbon.2014.02.009

26. Ruiz-Hitzky, E.; Sobral, M. M. C.; Gómez-Avilés, A.; Nunes, C.; Ruiz-García, C.; Ferreira, P.; Aranda, P. *Adv. Funct. Mater.* **2016,** *26,* 7394–7405. doi:10.1002/adfm.201603103

27. Ruiz-Hitzky, E. *J. Mater. Chem.* **2001,** *11,* 86–91. doi:10.1039/b003197f

28. Ruiz-Hitzky, E.; Darder, M.; Alcântara, A. C. S.; Wicklein, B.; Aranda, P. Functional nanocomposites based on fibrous clays. In *Functional Polymer Composites with Nanoclays;* Lvov, Y.; Guo, B.; Fakhrullin, R., Eds.; RSC Smart Materials, Vol. 22; Royal Society of Chemistry: Cambridge, UK, 2017; pp 1–53. doi:10.1039/9781782626725-00001

29. González del Campo, M. M.; Darder, M.; Aranda, P.; Akkari, M.; Huttel, Y.; Mayoral, A.; Bettini, J.; Ruiz-Hitzky, E. *Adv. Funct. Mater.* **2018,** *28,* 1703048. doi:10.1002/adfm.201703048

30. Bertolino, V.; Cavallaro, G.; Lazzara, G.; Merli, M.; Milioto, S.; Parisi, F.; Sciascia, L. *Ind. Eng. Chem. Res.* **2016,** *55,* 7373–7380. doi:10.1021/acs.iecr.6b01816

31. Makaremi, M.; Pasbakhsh, P.; Cavallaro, G.; Lazzara, G.; Aw, Y. K.; Lee, S. M.; Milioto, S. *ACS Appl. Mater. Interfaces* **2017,** *9,* 17476–17488. doi:10.1021/acsami.7b04297

32. Wang, Y.; Qi, W.; Huang, R.; Su, R.; He, Z. *Adv. Mater. Interfaces* **2016,** *3,* 1500327. doi:10.1002/admi.201500327

33. Deuber, F.; Mousavi, S.; Federer, L.; Adlhart, C. *Adv. Mater. Interfaces* **2017,** *4,* 1700065. doi:10.1002/admi.201700065

34. Sun, J.; Yendluri, R.; Liu, K.; Guo, Y.; Lvov, Y.; Yan, X. *Phys. Chem. Chem. Phys.* **2017,** *19,* 562–567. doi:10.1039/c6cp07450b

35. Yang, Y.; Yang, X.; Tan, Y.; Yuan, Q. *Nano Res.* **2017,** *10,* 1560–1583. doi:10.1007/s12274-017-1476-8

36. Bhadra, J.; Popelka, A.; Abdulkareem, A.; Ahmad, Z.; Touati, F.; Al-Thani, N. *RSC Adv.* **2019,** *9,* 12496–12506. doi:10.1039/c9ra00936a

37. Ghimire, A.; Pattammattel, A.; Maher, C. E.; Kasi, R. M.; Kumar, C. V. *ACS Appl. Mater. Interfaces* **2017,** *9,* 42556–42565. doi:10.1021/acsami.7b13606

38. Kang, Z.; Jiao, K.; Yu, C.; Dong, J.; Peng, R.; Hu, Z.; Jiao, S. *RSC Adv.* **2017,** *7,* 4572–4579. doi:10.1039/c6ra26636c

39. Tiwari, J. N.; Vij, V.; Kemp, K. C.; Kim, K. S. *ACS Nano* **2016,** *10,* 46–80. doi:10.1021/acsnano.5b05690

40. Voiry, D.; Chhowalla, M.; Gogotsi, Y.; Kotov, N. A.; Li, Y.; Penner, R. M.; Schaak, R. E.; Weiss, P. S. *ACS Nano* **2018,** *12,* 9635–9638. doi:10.1021/acsnano.8b07700

41. El-Gendy, D. M.; Abdel Ghany, N. A.; Allam, N. K. *RSC Adv.* **2019,** *9,* 12555–12566. doi:10.1039/c9ra01539f

42. Wicklein, B.; Diem, A. M.; Knöller, A.; Cavalcante, M. S.; Bergström, L.; Bill, J.; Burghard, Z. *Adv. Funct. Mater.* **2018,** *28,* 1704274. doi:10.1002/adfm.201704274

43. Wicklein, B.; Kocjan, A.; Salazar-Alvarez, G.; Carosio, F.; Camino, G.; Antonietti, M.; Bergström, L. *Nat. Nanotechnol.* **2015,** *10,* 277–283. doi:10.1038/nnano.2014.248

44. Yan, J.; Wu, T.; Ding, Z.; Li, X. *Carbohydr. Polym.* **2016,** *136,* 1288–1296. doi:10.1016/j.carbpol.2015.10.049

45. Wu, Y.; Wang, Z.; Liu, X.; Shen, X.; Zheng, Q.; Xue, Q.; Kim, J.-K. *ACS Appl. Mater. Interfaces* **2017,** *9,* 9059–9069. doi:10.1021/acsami.7b01017

46. Żbik, M. S.; Raftery, N. A.; Smart, R. S. C.; Frost, R. L. *Appl. Clay Sci.* **2010,** *50,* 299–304. doi:10.1016/j.clay.2010.08.010

47. Svagan, A. J.; Berglund, L. A.; Jensen, P. *ACS Appl. Mater. Interfaces* **2011,** *3,* 1411–1417. doi:10.1021/am200183u

48. Darder, M.; López-Blanco, M.; Aranda, P.; Aznar, A. J.; Bravo, J.; Ruiz-Hitzky, E. *Chem. Mater.* **2006,** *18,* 1602–1610. doi:10.1021/cm0523642

49. Gibson, L. J.; Ashby, M. F. *Cellular Solids: Structure and Properties;* Cambridge University Press: Cambridge, UK, 1999.

50. Wicklein, B.; Aranda, P.; Ruiz-Hitzky, E.; Darder, M. *J. Mater. Chem. B* **2013,** *1,* 2911–2920. doi:10.1039/c3tb00580a

51. Padilla-Ortega, E.; Darder, M.; Aranda, P.; Figueredo Gouveia, R.; Leyva-Ramos, R.; Ruiz-Hitzky, E. *Appl. Clay Sci.* **2016,** *130,* 40–49. doi:10.1016/j.clay.2015.11.024

52. Xu, Y.; Sheng, K.; Li, C.; Shi, G. *ACS Nano* **2010,** *4,* 4324–4330. doi:10.1021/nn101187z

53. Obrey, K. A. D.; Wilson, K. V.; Loy, D. A. *J. Non-Cryst. Solids* **2011,** *357,* 3435–3441. doi:10.1016/j.jnoncrysol.2011.06.014

54. Shaari, N.; Kamarudin, S. K. *J. Power Sources* **2015,** *289,* 71–80. doi:10.1016/j.jpowsour.2015.04.027

55. Bai, H.; Zhang, H.; He, Y.; Liu, J.; Zhang, B.; Wang, J. *J. Membr. Sci.* **2014,** *454,* 220–232. doi:10.1016/j.memsci.2013.12.005

56. Vasileiou, A. A.; Kontopoulou, M.; Gui, H.; Docoslis, A. *ACS Appl. Mater. Interfaces* **2015,** *7,* 1624–1631. doi:10.1021/am5071255

57. Vasileiou, A. A.; Docoslis, A.; Kontopoulou, M.; Xiang, P.; Ye, Z. *Polymer* **2013,** *54,* 5230–5240. doi:10.1016/j.polymer.2013.07.034

58. Wicklein, B.; Darder, M.; Aranda, P.; Ruiz-Hitzky, E. *ACS Appl. Mater. Interfaces* **2011,** *3,* 4339–4348. doi:10.1021/am201000k

59. Wicklein, B.; Martín del Burgo, M. Á.; Yuste, M.; Darder, M.; Llavata, C. E.; Aranda, P.; Ortin, J.; del Real, G.; Ruiz-Hitzky, E. *Eur. J. Inorg. Chem.* **2012,** 5186–5191. doi:10.1002/ejic.201200579

60. Muguruma, H.; Hoshino, T.; Nowaki, K. *ACS Appl. Mater. Interfaces* **2015,** *7,* 584–592. doi:10.1021/am506758u

61. Darder, M.; Takada, K.; Pariente, F.; Lorenzo, E.; Abruña, H. D. *Anal. Chem. (Washington, DC, U. S.)* **1999,** *71,* 5530–5537. doi:10.1021/ac990759x

62. Yokoyama, K.; Kayanuma, Y. *Anal. Chem. (Washington, DC, U. S.)* **1998,** *70,* 3368–3376. doi:10.1021/ac9711807

63. Darder, M.; Aranda, P.; Hernández-Vélez, M.; Manova, E.; Ruiz-Hitzky, E. *Thin Solid Films* **2006,** *495,* 321–326. doi:10.1016/j.tsf.2005.08.285

64. Choi, H. N.; Kim, M. A.; Lee, W.-Y. *Anal. Chim. Acta* **2005,** *537,* 179–187. doi:10.1016/j.aca.2005.01.010

65. Wan, D.; Yuan, S.; Li, G. L.; Neoh, K. G.; Kang, E. T. *ACS Appl. Mater. Interfaces* **2010,** *2,* 3083–3091. doi:10.1021/am100591t

66. Zhu, N.; Han, S.; Gan, S.; Ulstrup, J.; Chi, Q. *Adv. Funct. Mater.* **2013,** *23,* 5297–5306. doi:10.1002/adfm.201300605
67. Papa, H.; Gaillard, M.; Gonzalez, L.; Chatterjee, J. *Biosensors* **2014,** *4,* 449–460. doi:10.3390/bios4040449
68. Marand, Z. R.; Shahtahmassebi, N.; Housaindokht, M. R.; Rounaghi, G. H.; Razavipanah, I. *Electroanalysis* **2014,** *26,* 840–848. doi:10.1002/elan.201300458
69. Ji, J.; Joh, H.-I.; Chung, Y.; Kwon, Y. *Nanoscale* **2017,** *9,* 15998–16004. doi:10.1039/c7nr05545e
70. Logan, B. E.; Hamelers, B.; Rozendal, R.; Schröder, U.; Keller, J.; Freguia, S.; Aelterman, P.; Verstraete, W.; Rabaey, K. *Environ. Sci. Technol.* **2006,** *40,* 5181–5192. doi:10.1021/es0605016
71. Falk, M.; Blum, Z.; Shleev, S. *Electrochim. Acta* **2012,** *82,* 191–202. doi:10.1016/j.electacta.2011.12.133
72. Campbell, A. S.; Jeong, Y. J.; Geier, S. M.; Koepsel, R. R.; Russell, A. J.; Islam, M. F. *ACS Appl. Mater. Interfaces* **2015,** *7,* 4056–4065. doi:10.1021/am507801x
73. Liu, Y.; Zhang, J.; Cheng, Y.; Jiang, S. P. *ACS Omega* **2018,** *3,* 667–676. doi:10.1021/acsomega.7b01633
74. Cinquin, P.; Gondran, C.; Giroud, F.; Mazabrard, S.; Pellissier, A.; Boucher, F.; Alcaraz, J.-P.; Gorgy, K.; Lenouvel, F.; Mathé, S.; Porcu, P.; Cosnier, S. *PLoS One* **2010,** *5,* e10476. doi:10.1371/journal.pone.0010476
75. Zebda, A.; Cosnier, S.; Alcaraz, J.-P.; Holzinger, M.; Le Goff, A.; Gondran, C.; Boucher, F.; Giroud, F.; Gorgy, K.; Lamraoui, H.; Cinquin, P. *Sci. Rep.* **2013,** *3,* 1516. doi:10.1038/srep01516
76. Trifonov, A.; Herkendell, K.; Tel-Vered, R.; Yehezkeli, O.; Woerner, M.; Willner, I. *ACS Nano* **2013,** *7,* 11358–11368. doi:10.1021/nn405218x
77. Min, K.; Ryu, J. H.; Yoo, Y. J. *Biotechnol. Bioprocess Eng.* **2010,** *15,* 371–375. doi:10.1007/s12257-009-3034-z
78. Falk, M.; Andoralov, V.; Blum, Z.; Sotres, J.; Suyatin, D. B.; Ruzgas, T.; Arnebrant, T.; Shleev, S. *Biosens. Bioelectron.* **2012,** *37,* 38–45. doi:10.1016/j.bios.2012.04.030
79. Garcia-Perez, T.; Hong, S.-G.; Kim, J.; Ha, S. *Enzyme Microb. Technol.* **2016,** *90,* 26–34. doi:10.1016/j.enzmictec.2016.04.010
80. Reid, R. C.; Jones, S. R.; Hickey, D. P.; Minteer, S. D.; Gale, B. K. *Electrochim. Acta* **2016,** *203,* 30–40. doi:10.1016/j.electacta.2016.04.012

A biomimetic nanofluidic diode based on surface-modified polymeric carbon nitride nanotubes

Kai Xiao[*1], Baris Kumru[1], Lu Chen[1,2], Lei Jiang[2], Bernhard V. K. J. Schmidt[1] and Markus Antonietti[1]

Full Research Paper

Address:
[1]Max Planck Institute of Colloids and Interfaces, Department of Colloid Chemistry, 14476 Potsdam, Germany and [2]Key Laboratory of Bio-inspired Smart Interfacial Science and Technology of Ministry of Education, School of Chemistry, Beihang University, 100191 Beijing, P.R. China

Email:
Kai Xiao[*] - xiaokai@iccas.ac.cn

* Corresponding author

Abstract

A controllable ion transport including ion selectivity and ion rectification across nanochannels or porous membranes is of great importance because of potential applications ranging from biosensing to energy conversion. Here, a nanofluidic ion diode was realized by modifying carbon nitride nanotubes with different molecules yielding an asymmetric surface charge that allows for ion rectification. With the advantages of low-cost, thermal and mechanical robustness, and simple fabrication process, carbon nitride nanotubes with ion rectification have the potential to be used in salinity-gradient energy conversion and ion sensor systems.

Introduction

Ion transport is the basis of energy and sensory systems in living organisms [1]. All biological signal transport and transduction processes, including pain, haptics, vision, audition, olfaction, and muscular movement, as well as energy conversion and consumption are associated with ion transport [2,3]. For example, a plant injured on one leaf by a nibbling insect can alert its other leaves to begin anticipatory defense responses by Ca^{2+} ion transport [4]. A very significant ion-transport mechanism based on Na^+ and K^+ across cell membranes results in the generation of the action potential, which plays a crucial role in the sensory system of intelligent life [5]. In the process of photosynthesis, light-driven passive ion transport results in a proton gradient across cell membranes, which enables the production of adenosine triphosphate (ATP) via ATP synthase [6]. All these passive and active ion transport processes in vivo occur in biological protein nanopores, which are very fragile. Therefore, it is challenging to reproduce a similar ion transport in vitro [7]. In the last decades, scientists from chemical and

material fields have attempted to achieve similar ion transport in solid-state nanopores or nanochannel systems, and other applied technologies [8-11].

The ion transport in solid-state materials has been studied with various nanostructures, i.e., 1D nanopores/nanochannels/nanotubes, 2D layered membranes, and 3D porous membranes, which can be fabricated from inorganic, organic, and polymer materials [12,13]. To date, three main ion-transport properties, namely, ion selectivity, ion rectification and ion pumping of biological ion channels have been successfully achieved in solid-state materials [14-16]. All these controllable active and passive ion transport mechanisms are based on the electrical double layer (EDL) effect [17,18]. In a charged nanochannel, only one ionic component can be transported across the nanochannel when the diameter of the nanochannel matches or falls below the Debye screening length because of the electrostatic interactions between the ions and the charged channel walls. As a result, positively charged nanochannels preferentially transport anions instead of cations, while the negatively charged nanochannels selectively transport cations [19-21]. This is the origin of ion selectivity. To realize ion rectification, asymmetric nanochannels and/or asymmetric surface-charge distributions are needed. In this case, the selected ions will be transported preferentially from one to the other side, which is the origin of ion rectification (or ion-diodes) [22]. Rectified ion transport is highly desired because it can suppress ion transport in unspecific directions, which plays a crucial role in accurate sensory systems and the generation of blue energy from salinity gradients [23,24].

We fabricated a carbon nitride nanotube membrane (CNNM) via an anodic aluminium oxide (AAO)-templated vapor deposition–polymerization process. Subsequently, the CNNMs were modified with 3-allyloxy-2-hydroxy-1-propanesulfonic acid or allylamine through a unilateral photo-functionalization process. The photo-functionalization allows for the spatial control over the process and, hence, the introduction of a gradient of charged grafted molecules. Thus, asymmetric membranes are formed and ion-diode properties are obtained.

Results and Discussion
Fabrication of carbon nitride nanotube membrane

Graphitic carbon nitride (g-CN) was chosen as it is formed from tri-*s*-triazine moieties interconnected via tertiary amines in a well-defined way without doping or modification, composed of only the two earth-abundant elements carbon and nitrogen. Moreover, it meets our requirements to fabricate negatively charged carbon nitride nanotubes and a fully condensed conjugated structure that stabilizes the π-electron system for a high

charge mobility [25]. The g-CN nanotube membrane (CNNM) was fabricated through vapor deposition–polymerization of melamine as the starting material (Figure 1a), which is a common way to obtain g-CN [25-27]. In this work, melamine and the AAO membrane with a pore diameter of 100 nm were placed in a tube furnace with N_2 flow (Figure 1b) [16]. The evaporation temperature was set to 573 K while the polymerization temperature was set to 773 K. Then, the evaporated precursor was deposited and polymerized in the porous AAO membrane, generating carbon nitride nanotubes. Figure 1c shows a schematic of a bare AAO membrane and the carbon nitride nanotubes formed in the AAO membrane. Similar to bulk g-CN fabricated by thermally induced polycondensation, the CNNM has a planar one-dimensional molecular structure based on NH-bridged tri-*s*-triazine units [25]. Meanwhile, the diameter of CNNMs can be well adjusted by controlling the amount of precursor (Figure S1, Supporting Information File 1). CNNMs fabricated by this approach possess a high nitrogen content with excellent chemical and thermal stability (Figures S2 and S3, Supporting Information File 1). It is also environmentally friendly, sustainable, and can be facilely synthesized on large scales with low cost [28,29].

Figure 2a shows the typical SEM image of the AAO membrane, CNNM@AAO, and the CNNM. After polymerization, there are carbon nitride nanotubes grown on the walls of the AAO nanochannels. The AAO substrate can be removed by immersion in 1 M hydrochloric acid to obtain the free-standing CNNM. The carbon nitride nanotubes have an external diameter of about 100 nm, and an inner diameter of about 60 nm. The chemical structure of carbon nitride nanotubes was further analyzed using FTIR (Figure 2b). The bare AAO substrate showed no obvious absorption peaks, while CNNM@AAO showed broad peaks between 3500 and 3000 cm^{-1}, which originate from the terminal amino groups. The typical stretching modes of CN heterocycles were found at 1200 to 1600 cm^{-1}, and the characteristic breathing mode of the triazine units was found at approximately 800 cm^{-1} after polymerization, thus indicating the formation of carbon nitride nanotubes [30-32].

Beyond that, high-resolution XPS spectra of C 1s and N 1s were illustrated in Figure 2c and Figure 2d, which further confirm the tri-*s*-triazine-based carbon nitride structure. The C 1s spectra can be deconvoluted into three peaks centered at 284.8, 286.4, and 287.9 eV, while N 1s spectrum can be deconvoluted into three peaks at 398.6, 399.7, and 400.9 eV. The C 1s peaks at 286.4 and 287.9 eV are associated to the major aromatic carbon species in the graphitic carbon nitride framework, representing the sp^2-hybridized carbon atoms in the N-containing aromatic ring. The N 1s peak in 398.6 eV is from
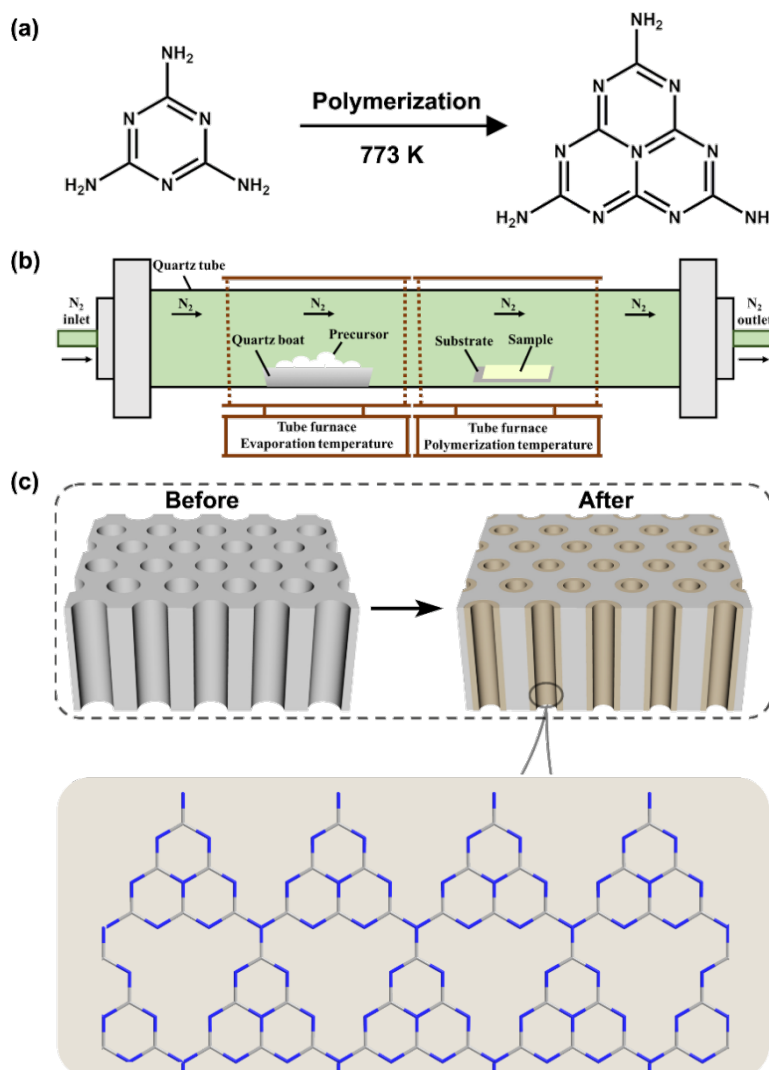
Figure 1: Fabrication process of carbon nitride nanotubes. (a) Synthetic route of polymeric carbon nitride nanotubes. (b) Schematic illustration of the fabrication process by vapor deposition–polymerization. (c) Schematic diagram of AAO substrate, carbon nitride nanotubes and molecular structure of the carbon nitride nanotubes.

the sp^2-hybridized nitrogen in the tri-*s*-triazine rings. The peak at 399.7 eV indicates the tertiary nitrogen N–C$_3$ groups. In addition, the terminal amino groups on the surface are also confirmed by the peak at 400.9 eV. All these results are consistent with graphitic carbon nitride powder reported before [28,33] indicating the formation of carbon nitride nanotubes.

Ion transport in carbon nitride nanotube membrane

As reported before [34,35], the graphitic carbon nitride fabricated by thermal polymerization has a negative surface charge in the initial state because of the incomplete polymerization or condensation with electron-rich –NH terminal groups. The negative surface charge is a crucial factor in ion transport. To

confirm that confinement effects as well as the surface charge control the ion-transport properties [36-38], we measured the conductance of KCl electrolyte both in bulk solution and across the carbon nitride nanotubes (Figure S4, Supporting Information File 1). Figure 3 showed the conductance as a function of salt concentration (KCl) both in bulk solution and across the CNNM. The conductivity of the bulk solution is proportional to the concentration of KCl, while the ionic conductance across the carbon nitride nanotubes remarkably deviates from the bulk value of 0.1 M to 10^{-6} M with a leveling of the current at approximately 0.35 µA. This indicates that the ion transport through the CNNM is fully governed by surface charges, which provides a possibility to control the ion transport by CNNMs.
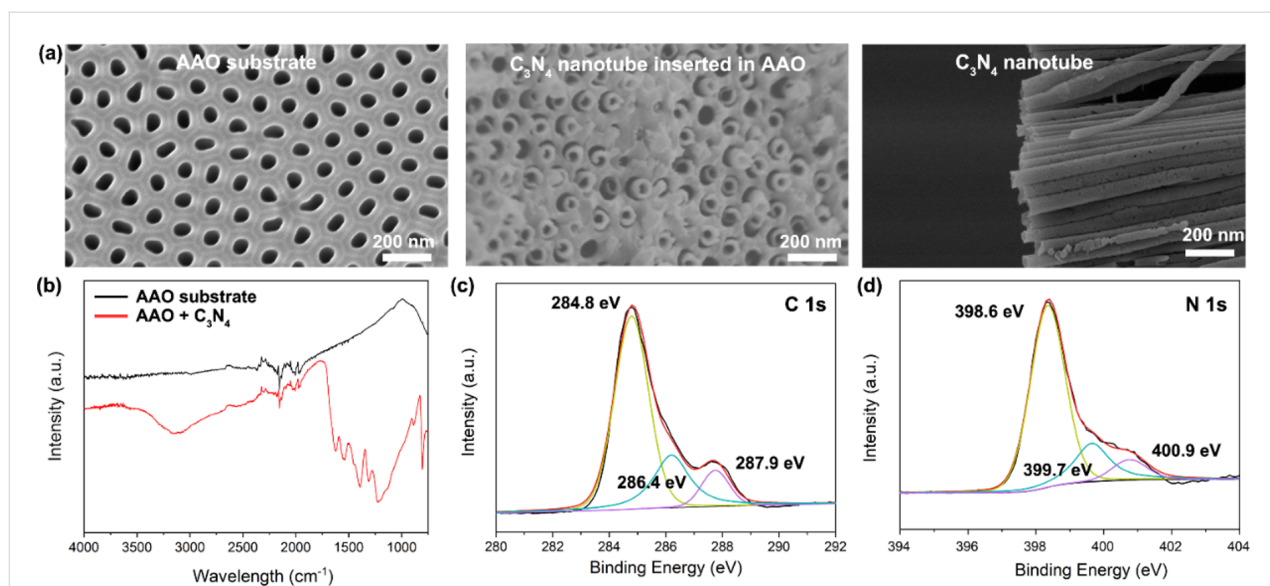
Figure 2: Carbon nitride nanotube properties. (a) SEM images of AAO substrate, carbon nitride nanotubes grown in the AAO substrate after polymerization, and carbon nitride nanotubes after removing the AAO substrate. (b) FTIR spectra before and after polymerization. (c) High-resolution XPS C 1s spectra of carbon nitride nanotubes, indicating two typical C 1s peaks at 284.8 and 287.9 eV. The former can be assigned to the sp^2-hybridized carbon atoms in the N-containing aromatic ring, while the latter is typically assigned to impurity carbon, such as graphitic C or grease. (d) High-resolution XPS N 1s spectra that are deconvoluted into three peaks, 398.6 eV (C=N–C), 399.7 eV (N–C$_3$), and 400.9 eV (C–NH–C and C–NH$_2$).
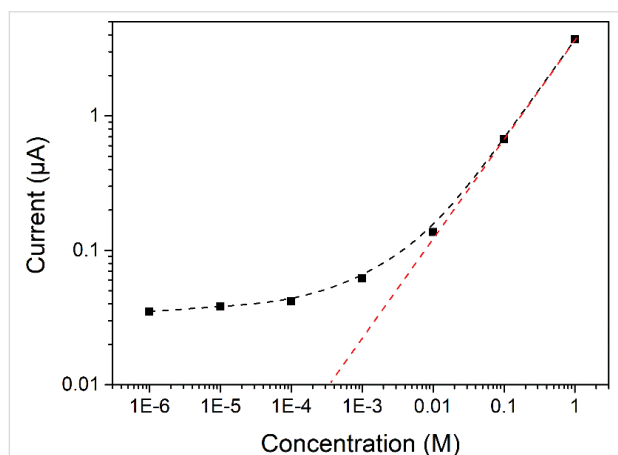
Figure 3: Conductance as a function of the salt concentration, indicating ion transportation controlled by surface charges in carbon nitride nanotubes (black squares). The red curve shows the data of the bulk solution (red curve).

Modification of the carbon nitride nanotube membrane

The current–voltage (*I*–*V*) measurements of the bare carbon nitride nanotubes showed that ion transport across the CNNM is symmetric. The CNNM shows no ion rectification because of its symmetric structure and surface-charge distribution (Figure S5, Supporting Information File 1). In order to obtain rectified ion transport, we modified the carbon nitride nanotubes unilaterally with a solution of 3-allyloxy-2-hydroxy-1-propanesulfonic acid sodium salt (AHPA) and with allylamine (AA)

(Figure 4a). As reported before [39,40], radicals can be created on the surface of g-CN through irradiation with visible light and different molecules can then be grafted to integrate various functionalities. The modification of CNNM with AHPA was confirmed by elemental mapping. As shown in Figure 4b, elemental mapping of the AHPA-modified membrane clearly shows the existence of sulfur atoms on the surface while unmodified side only contains carbon and nitrogen (Figure S6, Supporting Information File 1). The AHPA modification was also confirmed by FTIR spectra recorded before and after modification (Figure 4c). After modification, there is an obvious peak near 2950 cm^{-1}, which corresponds to the C–H bond stretching, originating from grafted AHPA molecules. In the case of the AA-modified membrane, FTIR spectra showed similar phenomena before and after modification (Figure 4c). The obtained results showed that AHPA and AA molecules are grafted successfully onto the CNNM.

Ion diode based on the modified carbon nitride nanotube membrane

Figure 5a shows the *I*–*V* curves before and after unilateral functionalization with AHPA. Before modification, the *I*–*V* curve is symmetric; while after AHPA modification, the ionic current at −0.5 V increased from −0.3 to −1.0 μA and the ionic current at +0.5 V only increased from 0.3 to 0.42 μA. This means the AHPA-modified CNNM shows an obvious ion rectification due to the unilateral introduction of negatively charged groups. Analogously, the AA-modified CNNM also showed asym-
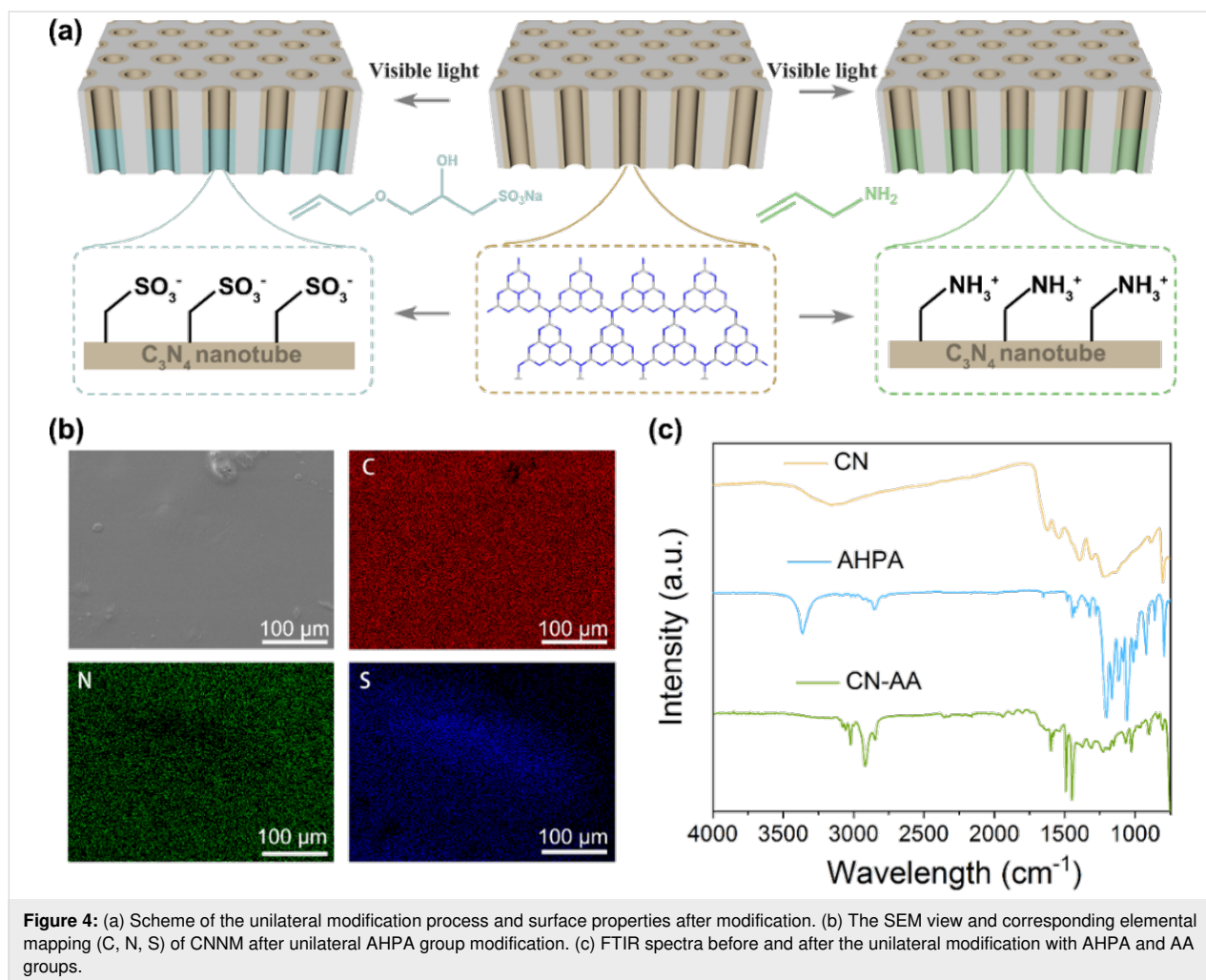
Figure 4: (a) Scheme of the unilateral modification process and surface properties after modification. (b) The SEM view and corresponding elemental mapping (C, N, S) of CNNM after unilateral AHPA group modification. (c) FTIR spectra before and after the unilateral modification with AHPA and AA groups.
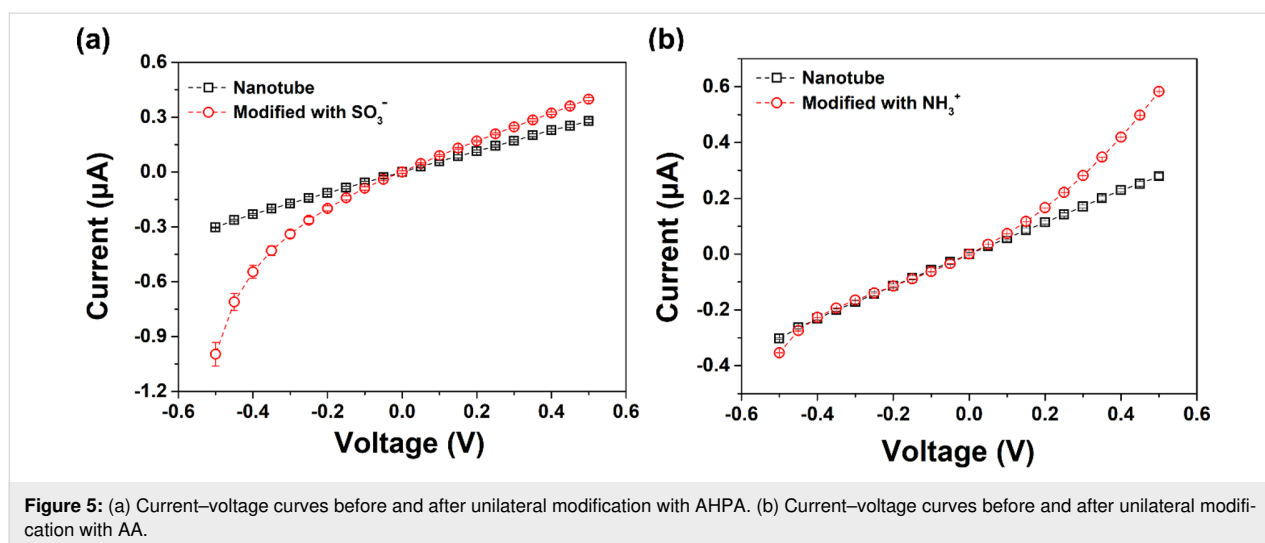

Figure 5: (a) Current–voltage curves before and after unilateral modification with AHPA. (b) Current–voltage curves before and after unilateral modification with AA.

metric ion transport. The ionic current at +0.5 V increased from 0.3 μA to 0.6 μA while ionic current at −0.5 V did not change after modification (Figure 5b). The asymmetric ion transport

can be ascribed to the asymmetric surface distribution of negatively charged amino groups. Overall, the deviation from the reference material is shifted towards negative values in the case

of AHPA modification and towards positive values in the case of AA modification. This can be attributed to the incorporation of oppositely charged functional groups. Thus, it is possible to tailor the direction of ion rectification via the photofunctionalization process and the choice of grafted molecules.

Conclusion

We fabricated a carbon nitride nanotube membrane by simple vapor deposition–polymerization and modified it via a photo-induced functionalization process to alter the ion transport properties. The carbon nitride nanotube membrane showed ion transport that was governed by surface charges of the electron-rich –NH terminal groups. After unilateral modification with AHPA and AA molecules, the symmetric surface charge distribution was altered, leading to ion rectification in the CNNM. With the advantages of low-cost, thermal and mechanical robustness, and simple fabrication process, the CNNM with ion rectification has the potential to be used in the energy generation through salinity gradients and ion sensor system.

Experimental

Materials: Unless otherwise noted, all of the commercial reagents were used as received. Allylamine (98%, Sigma-Aldrich), 3-allyloxy-2-hydroxy-1-propanesulfonic acid sodium salt solution (40 wt %, AHPA, Sigma-Aldrich) and melamine (purity >98.0%, Sigma-Aldrich). 60 μm thick AAO membranes with a pore width of 84 ± 16 nm were purchased from Heifei Puyuan Nano, China. Glass test tubes for vapor deposition–polymerization (VDP) were purchased from Merck Millipore.

Characterizations: The released CNNM was transferred to a quartz glass substrate and analyzed. X-ray photoelectron spectroscopy (XPS) was performed by an ESCALab220i-XL electron spectrometer from VG Scientific using 300W Al Kα radiation, while the base pressure was about 3×10^{-9} mbar. The binding energies were referenced to the C 1s line at 284.8 eV from adventitious carbon. A scanning electron microscope (SEM) JSM-7500F (JEOL) at an accelerating voltage of 3 kV was used to get the top view of the CNNs. X-ray diffraction (XRD) patterns were recorded with a Bruker D8 Advance instrument with Cu Kα radiation. Fourier transform infrared (FTIR) spectra were recorded with a Thermo Scientific Nicolet iS5 FTIR spectrometer.

Fabrication of CNNM: The carbon nitride nanotube membrane was fabricated by a VDP method described before [16]. Firstly, the commercial AAO membrane (diameter: 5 mm) was cleaned with ethanol and deionized water, then dried with nitrogen. Subsequently, the cleaned AAO and the precursor melamine were put on the bottom of the glass test tube. The samples were placed in the oven to heat to 773 K with a heating rate of 10 K/min, and then kept for 4 h to ensure polymerization. After the temperature naturally cooled down to ambient temperature, the AAO membrane turned from transparent white to brown, and yellowish carbon nitride power at the bottom of the test tube was obtained. To get a pure carbon nitride nanotube for TEM or SEM, the carbon nitride nanotube membrane was immersed in 1 M acid for chemical etching (72 h), then cleaned by deionized water and dried in an oven at 60 °C.

Modification: In a similar manner as described in our previous paper [39], 1 g of AHPA solution (40 wt % in water) and 1 g of deionized water were mixed (or 1 g of allylamine and 1 g of ethanol). The mixture was sonicated for 10 min, and nitrogen was flushed through the mixture for 3 min for the removal of dissolved oxygen. The CNNM was placed in a glass dish, then AHPA or AA solution was dropped onto the surface of the CNNM. The mixture was irradiated by 50 W LED daylight sources for the desired reaction time. Afterward, the mixture was vacuum-filtered, washed three times with water (3 × 50 mL), and washed once with acetone (20 mL).

Ion diode measurements: The setup for the measurement of the ion diode properties is shown in Figure S3 (Supporting Information File 1). The membrane was caught in a H-cell with electrolyte. A Ag/AgCl electrode was used to collect the ionic current. The *I–V* curves were adjusted to zero current at zero voltage to remove small offsets experienced between runs. All measurements were carried out at ambient temperature. The main transmembrane potential used in this work was stepped from −0.5 to +0.5 V at 0.05 V/step with 1 s/step (0.05 V/s). CNNMs before and after modification were mounted between two chambers of a custom-made H cell, which was filled with electrolyte. Ag/AgCl electrodes were used to collect the current and voltage signals. The ionic current was measured with a Keithley 6430 picoamperemeter (Keithley Instruments, Cleveland, OH).

Supporting Information

Supporting Information File 1
Additional experimental data.
[https://www.beilstein-journals.org/bjnano/content/supplementary/2190-4286-10-130-S1.pdf]

Acknowledgements

ORCID® iDs

Kai Xiao - https://orcid.org/0000-0001-9829-2707
Bernhard V. K. J. Schmidt - https://orcid.org/0000-0002-3580-7053

References

1. Hille, B. *Ion channels of excitable membranes,* 3rd ed.; Sinauer: Sunderland, MA, USA, 2001.
2. Blumwald, E.; Aharon, G. S.; Apse, M. P. *Biochim. Biophys. Acta, Biomembr.* **2000,** *1465,* 140–151. doi:10.1016/s0005-2736(00)00135-8
3. Holland, E.-M.; Braun, F.-J.; Nonnengässer, C.; Harz, H.; Hegemann, P. *Biophys. J.* **1996,** *70,* 924–931. doi:10.1016/s0006-3495(96)79635-2
4. Toyota, M.; Spencer, D.; Sawai-Toyota, S.; Jiaqi, W.; Zhang, T.; Koo, A. J.; Howe, G. A.; Gilroy, S. *Science* **2018,** *361,* 1112–1115. doi:10.1126/science.aat7744
5. Gadsby, D. C. *Nat. Rev. Mol. Cell Biol.* **2009,** *10,* 344–352. doi:10.1038/nrm2668
6. Steinberg-Yfrach, G.; Rigaud, J.-L.; Durantini, E. N.; Moore, A. L.; Gust, D.; Moore, T. A. *Nature* **1998,** *392,* 479–482. doi:10.1038/33116
7. Xiao, K.; Wen, L.; Jiang, L. *Small* **2016,** *12,* 2810–2831. doi:10.1002/smll.201600359
8. Yameen, B.; Ali, M.; Neumann, R.; Ensinger, W.; Knoll, W.; Azzaroni, O. *Chem. Commun.* **2010,** *46,* 1908–1910. doi:10.1039/b920870d
9. Qin, S.; Liu, D.; Wang, G.; Portehault, D.; Garvey, C. J.; Gogotsi, Y.; Lei, W.; Chen, Y. *J. Am. Chem. Soc.* **2017,** *139,* 6314–6320. doi:10.1021/jacs.6b11100
10. Pérez-Mitta, G.; Tuninetti, J. S.; Knoll, W.; Trautmann, C.; Toimil-Molares, M. E.; Azzaroni, O. *J. Am. Chem. Soc.* **2015,** *137,* 6011–6017. doi:10.1021/jacs.5b01638
11. Duan, C.; Majumdar, A. *Nat. Nanotechnol.* **2010,** *5,* 848–852. doi:10.1038/nnano.2010.233
12. Zhang, Z.; Wen, L.; Jiang, L. *Chem. Soc. Rev.* **2018,** *47,* 322–356. doi:10.1039/c7cs00688h
13. Kim, S. J.; Song, Y.-A.; Han, J. *Chem. Soc. Rev.* **2010,** *39,* 912–922. doi:10.1039/b822556g
14. Lin, C.-Y.; Combs, C.; Su, Y.-S.; Yeh, L.-H.; Siwy, Z. S. *J. Am. Chem. Soc.* **2019,** *141,* 3691–3698. doi:10.1021/jacs.8b13497
15. Zhang, M.; Guan, K.; Ji, Y.; Liu, G.; Jin, W.; Xu, N. *Nat. Commun.* **2019,** *10,* 1253. doi:10.1038/s41467-019-09286-8
16. Xiao, K.; Chen, L.; Chen, R.; Heil, T.; Lemus, S. D. C.; Fan, F.; Wen, L.; Jiang, L.; Antonietti, M. *Nat. Commun.* **2019,** *10,* 74. doi:10.1038/s41467-018-08029-5
17. Bocquet, L.; Charlaix, E. *Chem. Soc. Rev.* **2010,** *39,* 1073–1095. doi:10.1039/b909366b
18. Cheng, L.-J.; Guo, L. J. *Chem. Soc. Rev.* **2010,** *39,* 923–938. doi:10.1039/b822554k
19. Liu, Q.; Wen, L.; Xiao, K.; Lu, H.; Zhang, Z.; Xie, G.; Kong, X.-Y.; Bo, Z.; Jiang, L. *Adv. Mater. (Weinheim, Ger.)* **2016,** *28,* 3181–3186. doi:10.1002/adma.201505250
20. Xie, G.; Xiao, K.; Zhang, Z.; Kong, X.-Y.; Liu, Q.; Li, P.; Wen, L.; Jiang, L. *Angew. Chem., Int. Ed.* **2015,** *54,* 13664–13668. doi:10.1002/anie.201505269
21. Xiao, K.; Xie, G.; Zhang, Z.; Kong, X.-Y.; Liu, Q.; Li, P.; Wen, L.; Jiang, L. *Adv. Mater. (Weinheim, Ger.)* **2016,** *28,* 3345–3350. doi:10.1002/adma.201505842
22. Siwy, Z. S. *Adv. Funct. Mater.* **2006,** *16,* 735–746. doi:10.1002/adfm.200500471
23. Zhang, Z.; Sui, X.; Li, P.; Xie, G.; Kong, X.-Y.; Xiao, K.; Gao, L.; Wen, L.; Jiang, L. *J. Am. Chem. Soc.* **2017,** *139,* 8905–8914. doi:10.1021/jacs.7b02794
24. Yang, C.; Suo, Z. *Nat. Rev. Mater.* **2018,** *3,* 125–142. doi:10.1038/s41578-018-0018-7
25. Lin, L.; Ou, H.; Zhang, Y.; Wang, X. *ACS Catal.* **2016,** *6,* 3921–3931. doi:10.1021/acscatal.6b00922
26. Arazoe, H.; Miyajima, D.; Akaike, K.; Araoka, F.; Sato, E.; Hikima, T.; Kawamoto, M.; Aida, T. *Nat. Mater.* **2016,** *15,* 1084–1089. doi:10.1038/nmat4693
27. Wang, X.; Maeda, K.; Thomas, A.; Takanabe, K.; Xin, G.; Carlsson, J. M.; Domen, K.; Antonietti, M. *Nat. Mater.* **2009,** *8,* 76–80. doi:10.1038/nmat2317
28. Ong, W.-J.; Tan, L.-L.; Ng, Y. H.; Yong, S.-T.; Chai, S.-P. *Chem. Rev.* **2016,** *116,* 7159–7329. doi:10.1021/acs.chemrev.6b00075
29. Liu, J.; Wang, H.; Antonietti, M. *Chem. Soc. Rev.* **2016,** *45,* 2308–2326. doi:10.1039/c5cs00767d
30. Han, Q.; Wang, B.; Zhao, Y.; Hu, C.; Qu, L. *Angew. Chem., Int. Ed.* **2015,** *54,* 11433–11437. doi:10.1002/anie.201504985
31. Kroke, E. *Angew. Chem., Int. Ed.* **2014,** *53,* 11134–11136. doi:10.1002/anie.201406427
32. Ma, T. Y.; Dai, S.; Jaroniec, M.; Qiao, S. Z. *Angew. Chem., Int. Ed.* **2014,** *53,* 7281–7285. doi:10.1002/anie.201403946
33. Volokh, M.; Peng, G.; Barrio, J.; Shalom, M. *Angew. Chem., Int. Ed.* **2019,** *58,* 6138–6151. doi:10.1002/anie.201806514
34. Li, X.-H.; Wang, X.; Antonietti, M. *Chem. Sci.* **2012,** *3,* 2170. doi:10.1039/c2sc20289a
35. Xiao, K.; Giusto, P.; Wen, L.; Jiang, L.; Antonietti, M. *Angew. Chem., Int. Ed.* **2018,** *57,* 10123–10126. doi:10.1002/anie.201804299
36. Gao, J.; Guo, W.; Feng, D.; Wang, H.; Zhao, D.; Jiang, L. *J. Am. Chem. Soc.* **2014,** *136,* 12265–12272. doi:10.1021/ja503692z
37. Raidongia, K.; Huang, J. *J. Am. Chem. Soc.* **2012,** *134,* 16528–16531. doi:10.1021/ja308167f
38. Zhang, Z.; Kong, X.-Y.; Xiao, K.; Liu, Q.; Xie, G.; Li, P.; Ma, J.; Tian, Y.; Wen, L.; Jiang, L. *J. Am. Chem. Soc.* **2015,** *137,* 14765–14772. doi:10.1021/jacs.5b09918
39. Kumru, B.; Antonietti, M.; Schmidt, B. V. K. J. *Langmuir* **2017,** *33,* 9897–9906. doi:10.1021/acs.langmuir.7b02441
40. Kumru, B.; Cruz, D.; Heil, T.; Schmidt, B. V. K. J.; Antonietti, M. *J. Am. Chem. Soc.* **2018,** *140,* 17532–17537. doi:10.1021/jacs.8b08956

Janus-micromotor-based on–off luminescence sensor for active TNT detection

Ye Yuan[1,2], Changyong Gao[*2], Daolin Wang[2], Chang Zhou[2], Baohua Zhu[*1] and Qiang He[2]

Abstract

An active TNT (2,4,6-trinitrotoluene) catalytic sensor based on Janus upconverting nanoparticle (UCNP)-functionalized micromotor capsules, displaying "on–off" luminescence with a low limit of detection has been developed. The Janus capsule motors were fabricated by layer-by-layer assembly of UCNP-functionalized polyelectrolyte microcapsules, followed by sputtering of a platinum layer onto one half of the capsule. By catalytic decomposition of hydrogen peroxide to oxygen bubbles, the Janus UCNP capsule motors are rapidly propelled with a speed of up to 110 µm s^{-1}. Moreover, the Janus motors display efficient on–off luminescent detection of TNT. Owing to the unique motion of the Janus motor with bubble generation, the likelihood of collision with TNT molecules and the reaction rate between them are increased, resulting in a limit of detection as low as 2.4 ng mL^{-1} TNT within 1 minute. Such bubble-propelled Janus UCNP capsule motors have great potential for contaminated water analysis.

Introduction

Water pollution has become a worldwide social problem. For example, the explosive TNT (2,4,6-trinitrotoluene), which is a highly toxic substance, has been widely used in military applications. The United States Environmental Protection Agency (USEPA) has classified TNT as hazardous waste, as it is possibly carcinogenic and mutagenic. Consequently, TNT-contaminated water has become one of the most serious pollution problems in war and military testing areas [1-7]. To date, various approaches including mass spectroscopy [8], ion transfer spectroscopy [9], surface plasmon resonance [10],

molecularly imprinted polymers [6], and fluorescence polarization [11] have been proposed to detect TNT. However, most of these techniques have major limitations such as cumbersome pretreatment, complicated operation, long detection time and high cost. In recent years, owing to their simplicity, rare-earth-doped upconverting nanoparticles (UCNPs) have been developed for the detection of TNT [12]. Despite the advantages of UCNP-based TNT detection, it is still restricted by passive diffusion of TNT and UCNPs. Therefore, there is a significant need for the development of a fast and facile strategy to detect TNT that does not involve complicated sample pretreatment or expensive equipment.

Recently, synthetic micro/nanomotors have attracted tremendous attention because of their unique features and enormous potential applications in different fields [13-20]. Based on the concept of nanoarchitectonics [21,22], various kinds of micro/nanomotors have been fabricated, such as Janus capsule micromotors [23], tubular micromotors [24], helical nanomotors [25], nanowire motors [26], and nanorod motors [27]. Unlike inert particles that move by Brownian motion, micro/nanomotors can actively swim in solutions by converting energy from the environment (e.g., chemical fuel, light, acoustic or magnetic) into mechanical movement [28-37]. The active motion of micro/nanomotors has been proposed to improve reaction yields by overcoming the limitation of passive diffusion and enhancing the interaction between the reactants. However, self-propelled micromotors, to our knowledge, have never been explored for the detection of TNT.

Here, we report the first example of catalytic Janus capsule micromotors as luminescence quenching based sensors for active TNT detection. The Janus capsule micromotors were fabricated by depositing a thin platinum (Pt) film onto one hemisphere of the UCNP-functionalized hollow polyelectrolyte microcapsules. These as-prepared Janus micromotors can autonomously move by catalytic decomposition of hydrogen peroxide fuel into oxygen at a speed of up to 110 μm s^{-1} (22 body lengths per second). Meanwhile, the Janus microcapsules are able to actively adsorb and detect TNT based on the luminescence quenching of the UCNPs by TNT. The combination of efficient self-propulsion and TNT detection by these catalytic Janus micromotors demonstrates the potential for water pollutant analysis.

Results and Discussion

The Janus UCNP-functionalized hollow polyelectrolyte capsule micromotors were prepared via a template-assisted method as schematically shown in Figure 1a. Briefly, eight bilayers of poly(allylamine hydrochloride) (PAH) and poly(styrene sulfonate) (PSS) were alternately deposited onto the surface of 5 μm

silica particles by layer-by-layer (LbL) assembly [38-41]. The as-prepared particles were subsequently modified with amine-functionalized UCNPs through electrostatic interactions and then were dispersed on a glass slide to form a monolayer. After sputtering of a 20 nm thin film of Pt, the Janus UCNP-functionalized capsule motors were obtained by removing the silica cores with hydrofluoric acid.

To prepare the Janus UCNP capsule motors, NaYF$_4$:Yb^{3+}/Er^{3+} UCNPs were firstly synthesized following a previously published procedure with several modifications [42]. After treatment with poly(acrylic acid) (PAA), the surface of the UCNPs were functionalized with 3-aminopropyltriethoxysilane (APTES) to introduce the amine group. The nanostructure and morphology of the synthesized UCNPs were investigated by transmission electron microscopy (TEM). The TEM images in Figure 1b show that both the as-prepared UCNPs (inset image) and the APTES-modified UCNPs have good monodispersity and a hexagonal structure. The diameter of the APTES-UCNPs increased from 65 nm to 71 nm after modification with APTES. The chemical groups on the surface of the UCNPs were illustrated by Fourier-transform infrared (FTIR) spectroscopy. Figure 1c shows the FTIR spectra of the UCNPs and APTES-UCNPs. Compared with the FTIR spectrum of unmodified UCNPs, a notable transmission band peak at 1128 cm^{-1} (blue circle), attributable to the Si–O stretching vibration, can be seen in the FTIR spectra of APTES-UCNPs. These results indicate that the UCNPs were successfully modified with APTES. It has been demonstrated that the amine group is important to allow UCNPs to detect TNT. To verify the functionalization of the APTES-UCNPs with amine groups, the surface charge of the UCNPs before and after modification was measured. As shown in Figure 1d, the zeta potential changed from −22.08 to 17.3 mV, indicating the successful surface amine group functionalization. Moreover, the fluorescence emission spectrum shows that the surface functionalization did not affect the photoluminescence properties of the UCNPs (Figure 1e).

Furthermore, the structure and morphology of the Janus UCNP capsule motors were systematically characterized. The TEM images in Figure 1f show a microcapsule after functionalizing with UCNPs. It is evident that the APTES-UCNPs were uniformly dispersed on the surface of the microcapsule. After Pt sputtering and removal of the silica core, the Janus UCNP capsule motors were obtained. As shown in Figure 1g, the as-prepared APTES-UCNPs were partially covered with a Pt cap, displaying a Janus structure. The scanning electron microscopy (SEM) image in Figure 1h further confirms the asymmetric distribution of Pt on the one side of the Janus UCNP capsule motors. Due to the partial coverage of the Pt layer, the
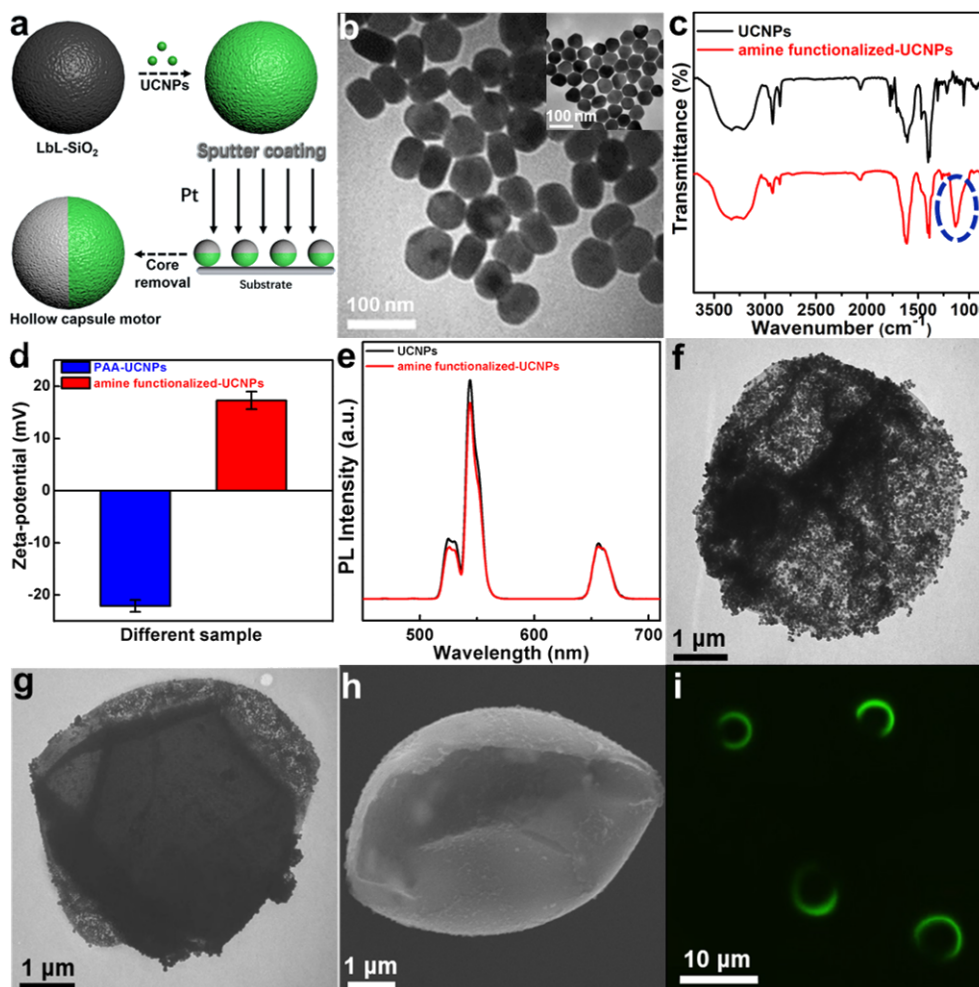
Figure 1: (a) Schematic representation of the fabrication process of Janus UCNP-modified polyelectrolyte capsule motors. (b) TEM images, (c) FTIR spectra, (d) zeta potential and (e) fluorescence emission spectrum of UNCPs with different surface functional groups. TEM images of UCNP-modified capsule (f) and Janus UCNP capsule motor (g). (h) SEM image of the Janus UCNP capsule motor. (i) Fluorescence microscope image of the Janus UCNP capsule motors.

Janus UCNP capsule motors show a semicircle shape under excitation with a 980 nm laser (Figure 1i). These results confirm that the Janus UCNP capsule motors were successfully prepared.

The autonomous motion of the Janus UCNP capsule motors was recorded by using microscopy. To better explore the movement behaviour of the Janus UCNP capsule motors, the corresponding motion trajectories, speed, and oxygen bubble frequency were studied systematically. The typical time-lapse images in Figure 2a–d (taken from the corresponding video in Supporting Information Files 1–4) show the trajectories of the motors in H_2O_2 solution with a concentration of 1%, 3%, 5% and 10% over a period of 1 s, respectively. It could be obviously seen that the Janus UCNP capsule motors swim in the H_2O_2 solution under the propulsion of oxygen bubbles that are

generated by the catalytic decomposition of H_2O_2 fuel on the Pt side. The dependence of the H_2O_2 fuel concentration on the average speed of the motors was investigated. As shown in the Figure 2e, the average speed of the motors increased with increasing concentration of H_2O_2. It can be found that the average speed of the Janus UCNP capsule motors increases from $\approx$13 µm s^{-1} ($\approx$2.6 body lengths s^{-1}) at 1% H_2O_2 to $\approx$110 µm s^{-1} ($\approx$22 body lengths s^{-1}) at 10% H_2O_2. By analysing the released oxygen bubbles, we also obtained the relationship between the bubble expulsion frequency and the speed of the Janus UCNP capsule motors (Figure 2f). We found that the bubble expulsion frequency exhibits a similar trend with the concentration of H_2O_2, indicating a positive correlation between the oxygen bubble expulsion frequency and the speed of the motors. Taken together, these results demonstrate that the obtained Janus UCNP capsule motors have desirable motion capability and
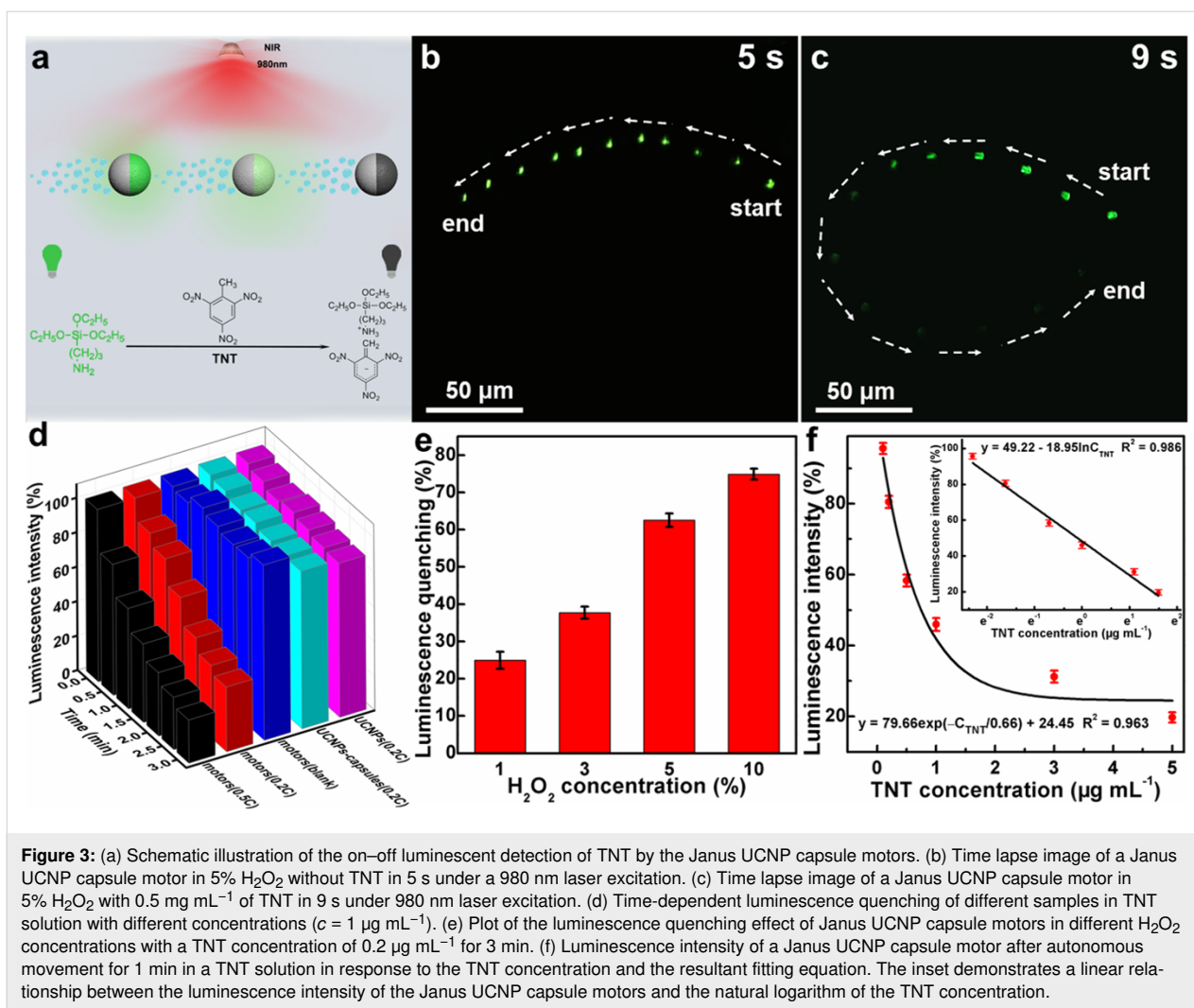
Figure 2: Images of the Janus UCNP capsule motors for different H_2O_2 concentrations: (a) 1%, (b) 3%, (c) 5% and (d) 10% after a period of 1 s. (e) Effect of the H_2O_2 concentration on the average speed of the Janus UCNP capsule motors. (f) Relationship of the oxygen bubble expulsion frequency of Janus UCNP capsule motors with different H_2O_2 concentration.
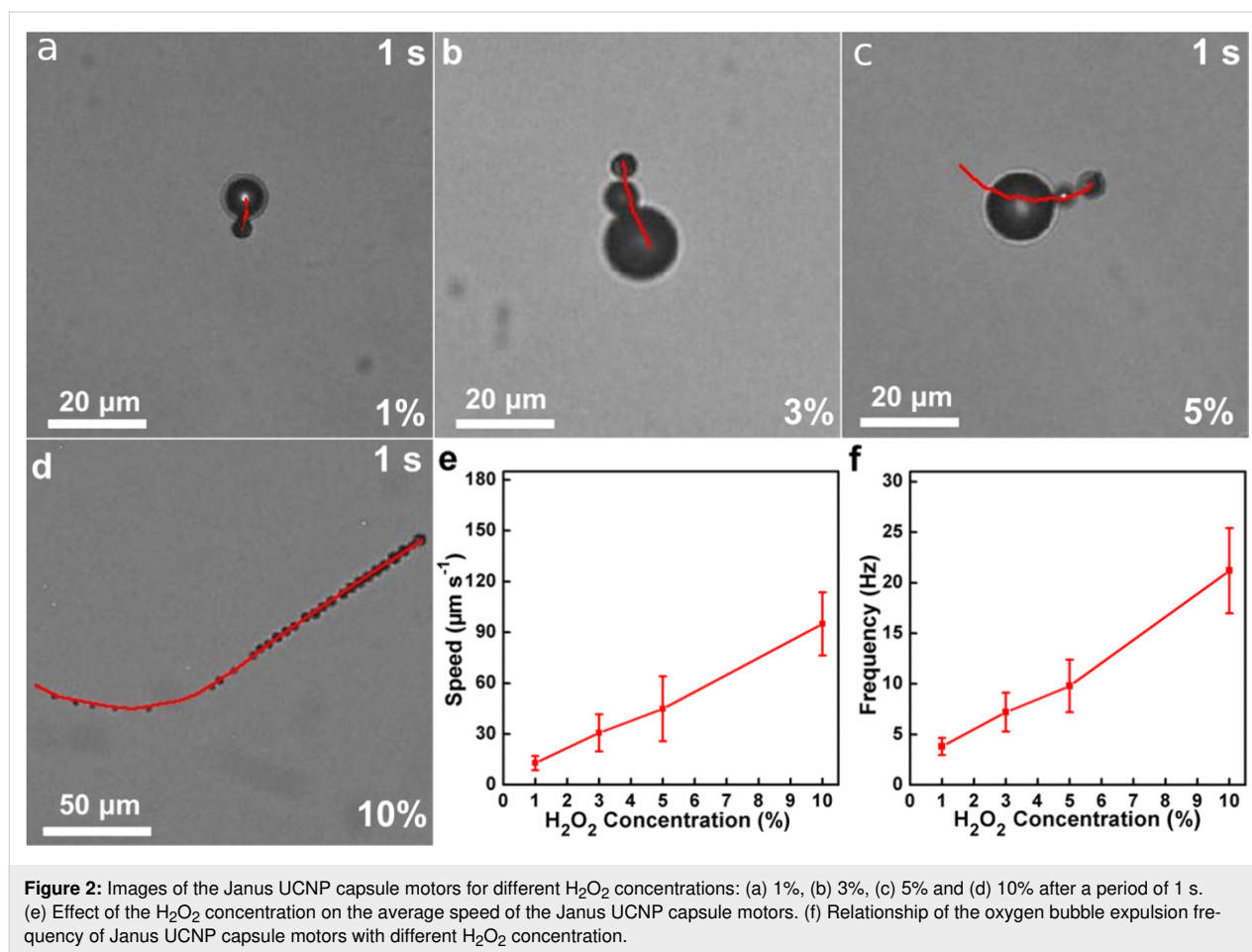
their movement speed can be controlled by adjusting the concentration of H_2O_2 and the expulsion frequency of the oxygen bubbles.

Figure 3a schematically illustrates the Janus UCNP capsule motor based, real time luminescence on–off detection of TNT. The luminescence quenching mechanism involves the Janus UCNP capsule micromotor and TNT. Owing to the active motion of the motors, the amino groups of the PAA chains modified on the surface of the UCNPs could chemically recognize the TNT molecules efficiently and form a Meisenheimer complex which has a strong absorption within the emission spectrum of the UCNPs. Due to the fluorescence resonance energy transfer from the excited UCNPs to the complex, the luminescence intensity of the Janus UCNP capsule motor is reduced, simplifying the visual detection of TNT. To assess the TNT detection capacity of the motors, they were dispersed in 5% H_2O_2 with and without TNT at pH 12. It was found that the upconversion luminescence of the Janus UCNP capsule motor exhibits no obvious change in movement in 5% H_2O_2 without TNT (Figure 3b and Video Supporting Information File 5). The time lapse image in Figure 3c (captured from the video in Sup-

porting Information File 6) demonstrates that the upconversion luminescence of the Janus UCNP capsule motor decreased gradually with via self-propelled movement in 5% H_2O_2 with 0.5 mg mL^{-1} of TNT, indicating that the green upconversion luminescence (543 nm) of the UCNPs was quenched by the presence of TNT.

The TNT sensing capability of these Janus UCNPs capsule motors was further evaluated by measuring the luminescence intensity. Figure 3d illustrates the time-dependent luminescence response of Janus UCNP capsule motors in TNT-contaminated H_2O_2. The motors were self-propelled for 3 min in 5% H_2O_2 containing 0.2 *c* (here, *c* = 1 µg mL^{-1}) TNT and showed instant luminescence quenching, while both the UCNPs and static Janus UCNP capsule motors displayed no obvious luminescence quenching under the same conditions. This finding demonstrates that the TNT detection efficiency of active Janus UCNP capsule motors is higher than that of the passive UCNPs and UCNP capsules owing to the continuous fluid mixing and the enhanced real time reactions between TNT and the Janus UCNP capsule motors [43]. Furthermore, the luminescence quenching effect of the Janus UCNP capsule motor is more

Figure 3: (a) Schematic illustration of the on–off luminescent detection of TNT by the Janus UCNP capsule motors. (b) Time lapse image of a Janus UCNP capsule motor in 5% H_2O_2 without TNT in 5 s under a 980 nm laser excitation. (c) Time lapse image of a Janus UCNP capsule motor in 5% H_2O_2 with 0.5 mg mL^{-1} of TNT in 9 s under 980 nm laser excitation. (d) Time-dependent luminescence quenching of different samples in TNT solution with different concentrations (c = 1 μg mL^{-1}). (e) Plot of the luminescence quenching effect of Janus UCNP capsule motors in different H_2O_2 concentrations with a TNT concentration of 0.2 μg mL^{-1} for 3 min. (f) Luminescence intensity of a Janus UCNP capsule motor after autonomous movement for 1 min in a TNT solution in response to the TNT concentration and the resultant fitting equation. The inset demonstrates a linear relationship between the luminescence intensity of the Janus UCNP capsule motors and the natural logarithm of the TNT concentration.

obvious in TNT solutions with higher concentration. We also found that the TNT detection efficiency of the Janus UCNP capsule motors increases with the increase of the H_2O_2 concentration (Figure 3e).

To determine the relationship between the TNT concentration and the luminescence quenching of the motors, they were dispersed in 5% H_2O_2 containing TNT with a concentration from 0 to 5 μg mL^{-1}. After motion for 1 min, the luminescence quenching of the Janus UCNP capsule motor was tested using a fluorescence spectrometer. As shown in Figure 3f, the luminescence quenching of the motor firstly presents a linear relationship with the increase of the TNT concentration and then decays exponentially. The specific relationship can be fitted to the formula y = 79.66 exp($-c_{TNT}$/0.66) + 24.45. The inset image in Figure 3d shows that a linear relationship exists between the luminescence intensity of the Janus UCNP capsule motors and the natural logarithm of the TNT concentration. The corresponding limit of detection (LOD) is calculated to be

2.4 ng mL^{-1} according to the equation LOD = (3SD)/k, where the SD is the standard deviation of the luminescence intensity of the Janus UCNP capsule motors and the k is the slope of the calibration curve (k = 18.95). Compared with the LOD of passive UCNPs (8.4 ng mL^{-1}), the TNT detection efficiency is enhanced by 3.5 times.

Conclusion

We have developed a micromotor-based active sensor for the detection of TNT based on the on–off luminescence of a Janus UCNP capsule motor. The Janus UCNP capsule motors were fabricated by layer-by-layer assembly combined with vacuum deposition. These Janus motors with a catalytic Pt layer can be propelled by oxygen bubbles at a speed of up to 110 μm s^{-1} in 10% H_2O_2 fuel. Owing to their active motion capability, the as-prepared Janus motor could quickly absorb TNT molecules. More importantly, the Janus UCNP capsule motor can effectively detect TNT based on the on–off luminescence of amine-functionalized UCNPs. Benefiting from the enhanced autono-

mous motion, the LOD of the Janus UCNP capsule motors (2.4 ng mL^{-1}) is 3.5 times better than that of static UCNPs within shorter analysis time. Such a micromotor could be used as a multifunctional platform integrating autonomous motion and TNT detection for efficient and rapid detection of environmental pollutants.

Experimental
Materials
Silica spheres with a diameter of 5 μm were obtained from Baseline Chrom Tech, Tianjin, China. Poly(styrene sulfonate) sodium salt (PSS, M_w = 70 000), poly(allylamine hydrochloride) (PAH, M_w = 70 000), poly(acrylic acid) (PAA, M_w = 1800), Y(NO$_3$)$_3$·6H$_2$O, Er(NO$_3$)$_3$·6H$_2$O, and Yb(NO$_3$)$_3$·6H$_2$O were purchased from Sigma-Aldrich. 2,4,6-Trinitrotoluene (TNT) was purchased from Best-reagent, Chengdu, China. 3-Aminopropyltriethoxysilane (APTES), ethylene glycol dimethacrylate (EGDMA) 2,2'-azobisisobutyronitrile (AIBN), 1-octadecene (ODE, 90%) and oleic acid (OA, 90%) were obtained from Aladdin Chemistry Co. Ltd. NaOH, NH$_4$F, ethanol, methanol, cyclohexane, trichloromethane, acetonitrile, NaCl, Na$_2$HPO$_4$, and NaH$_2$PO$_4$ were purchased from Tianjin Tianli Chemical Reagent Co. Ltd. Hydrofluoric acid (HF) and hydrogen peroxide (H$_2$O$_2$) were obtained from Beijing Chemical Works, China. All commercial materials were used without further purification.

Preparation of Janus UCNP capsule motors
NaYF$_4$:Yb/Er upconversion nanoparticles were firstly fabricated using a previously published method [42]. The obtained UCNPs (100 mg) were then mixed with PAA (300 mg) in 10 mL ethanol/chloroform (1:1) solution for 12 h at the room temperature. Then, the as-prepared PAA-UCNPs (80 mg) were added into 20 mL ethanol/acetonitrile (1:1) solution containing APTES (12.5 μL), EGDMA (25 μL), and AIBN (25 mg). After heating to 45 °C for 6 h, the amine-group-functionalized UCNPs were obtained.

To prepare Janus UCNP capsule motors, eight bilayers of PAH/PSS were deposited onto the surface of 5 μm silica particles through layer-by-layer assembly. Then, 1 mg of (PAH/PSS)$_8$-coated particles were mixed with 10 mg of amine-group-functionalized UCNPs for 1 h under continuous shaking, and excess UCNPs were removed by centrifugation. The Janus structure was prepared by depositing a monolayer of UCNP-coated silica particles on glass substrates and sputtering 20 nm of Pt onto the surface of the UCNP-coated silica particles, followed by peeling off the particles from the substrate. The silica cores were then dissolved by treating the particles with 0.5 M HF. The Janus UCNP capsule motors were obtained after three centrifugation/water washing steps.

Analysis of the movement of the Janus UCNP capsule motors
The movement studies were accomplished by dropping Janus UNCP capsule motors into hydrogen peroxide solutions of different concentration (1–10 vol %). The self-propelled motion of Janus UCNP capsule motors was recorded by using an Olympus BX53 fluorescence microscope. The trajectories of the motor movement were tracked by using the software of Image J and the motion velocity was analyzed using Origin 8 software.

Characterization
SEM imaging was carried out by dropping sample solutions onto the surface of silicon wafer. After drying, samples were observed using a Hitachi S-5200 microscope. For TEM observation, samples were dropped onto the carbon film of the copper grids and observed using a Hitachi H-7650 microscope. UV−vis absorption spectra were recorded using a Hitachi U-4100 spectrophotometer. FTIR spectra were collected in the wavelength range from 4000 to 500 cm^{-1} by a Thermo Fisher 4700 Fourier transform infrared spectrophotometer with the KBr method. Upconversion luminescence was measured using a HORIBA Jobin Yvon FluoroMax-4 spectrophotometer with a 980 nm diode laser at a power of 1 W cm^{-2} (Shanghai Laser & Optics Century Co. Ltd).

Supporting Information

Supporting Information File 1
The motion of a Janus UCNP capsule motor in 1% H$_2$O$_2$ solution.
[https://www.beilstein-journals.org/bjnano/content/supplementary/2190-4286-10-131-S1.mov]

Supporting Information File 2
The motion of a Janus UCNP capsule motor in 3% H$_2$O$_2$ solution.
[https://www.beilstein-journals.org/bjnano/content/supplementary/2190-4286-10-131-S2.mov]

Supporting Information File 3
The motion of a Janus UCNP capsule motor in 5% H$_2$O$_2$ solution.
[https://www.beilstein-journals.org/bjnano/content/supplementary/2190-4286-10-131-S3.mov]

Supporting Information File 4
The motion of a Janus UCNP capsule motor in 10% H$_2$O$_2$ solution.
[https://www.beilstein-journals.org/bjnano/content/supplementary/2190-4286-10-131-S4.mov]

ORCID® iDs

Ye Yuan - https://orcid.org/0000-0002-3018-4678
Changyong Gao - https://orcid.org/0000-0001-8137-7894
Baohua Zhu - https://orcid.org/0000-0003-1363-5657

References

1. Engel, Y.; Elnathan, R.; Pevzner, A.; Davidi, G.; Flaxer, E.; Patolsky, F. *Angew. Chem., Int. Ed.* **2010,** *49,* 6830–6835. doi:10.1002/anie.201000847
2. Dasary, S. S. R.; Singh, A. K.; Senapati, D.; Yu, H.; Ray, P. C. *J. Am. Chem. Soc.* **2009,** *131,* 13806–13812. doi:10.1021/ja905134d
3. Gao, D.; Zhang, Z.; Wu, M.; Xie, C.; Guan, G.; Wang, D. *J. Am. Chem. Soc.* **2007,** *129,* 7859–7866. doi:10.1021/ja070975k
4. Anderson, G. P.; Moreira, S. C.; Charles, P. T.; Medintz, I. L.; Goldman, E. R.; Zeinali, M.; Taitt, C. R. *Anal. Chem. (Washington, DC, U. S.)* **2006,** *78,* 2279–2285. doi:10.1021/ac051995c
5. Zhang, K.; Zhou, H.; Mei, Q.; Wang, S.; Guan, G.; Liu, R.; Zhang, J.; Zhang, Z. *J. Am. Chem. Soc.* **2011,** *133,* 8424–8427. doi:10.1021/ja2015873
6. Li, J.; Kendig, C. E.; Nesterov, E. E. *J. Am. Chem. Soc.* **2007,** *129,* 15911–15918. doi:10.1021/ja0748027
7. Li, R.; Yuan, Y.-P.; Qiu, L.-G.; Zhang, W.; Zhu, J.-F. *Small* **2012,** *8,* 225–230. doi:10.1002/smll.201101699
8. Cerruti, M.; Jaworski, J.; Raorane, D.; Zueger, C.; Varadarajan, J.; Carraro, C.; Lee, S.-W.; Maboudian, R.; Majumdar, A. *Anal. Chem. (Washington, DC, U. S.)* **2009,** *81,* 4192–4199. doi:10.1021/ac8019174
9. Matz, L. M.; Tornatore, P. S.; Hill, H. H. *Talanta* **2001,** *54,* 171–179. doi:10.1016/s0039-9140(00)00663-9
10. Kawaguchi, T.; Shankaran, D. R.; Kim, S. J.; Matsumoto, K.; Toko, K.; Miura, N. *Sens. Actuators, B* **2008,** *133,* 467–472. doi:10.1016/j.snb.2008.03.005
11. Gao, D.; Wang, Z.; Liu, B.; Ni, L.; Wu, M.; Zhang, Z. *Anal. Chem. (Washington, DC, U. S.)* **2008,** *80,* 8545–8553. doi:10.1021/ac8014356
12. Ma, Y.; Wang, S.; Wang, L. *TrAC, Trends Anal. Chem.* **2015,** *65,* 13–21. doi:10.1016/j.trac.2014.09.007
13. Wang, H.; Pumera, M. *Chem. Rev.* **2015,** *115,* 8704–8735. doi:10.1021/acs.chemrev.5b00047
14. Mei, Y.; Solovev, A. A.; Sanchez, S.; Schmidt, O. G. *Chem. Soc. Rev.* **2011,** *40,* 2109–2119. doi:10.1039/c0cs00078g
15. Gao, W.; Wang, J. *ACS Nano* **2014,** *8,* 3170–3180. doi:10.1021/nn500077a
16. Dong, R.; Cai, Y.; Yang, Y.; Gao, W.; Ren, B. *Acc. Chem. Res.* **2018,** *51,* 1940–1947. doi:10.1021/acs.accounts.8b00249
17. Zhang, Y.; Zhang, L.; Yang, L.; Vong, C. I.; Chan, K. F.; Wu, W. K. K.; Kwong, T. N. Y.; Lo, N. W. S.; Ip, M.; Wong, S. H.; Sung, J. J. Y.; Chiu, P. W. Y.; Zhang, L. *Sci. Adv.* **2019,** *5,* eaau9650. doi:10.1126/sciadv.aau9650
18. Peng, F.; Tu, Y.; Wilson, D. A. *Chem. Soc. Rev.* **2017,** *46,* 5289–5310. doi:10.1039/c6cs00885b
19. Su, Y.; Ge, Y.; Liu, L.; Zhang, L.; Liu, M.; Sun, Y.; Zhang, H.; Dong, B. *ACS Appl. Mater. Interfaces* **2016,** *8,* 4250–4257. doi:10.1021/acsami.6b00012
20. Liu, M.; Sun, Y.; Wang, T.; Ye, Z.; Zhang, H.; Dong, B.; Li, C. Y. *J. Mater. Chem. C* **2016,** *4,* 5945–5952. doi:10.1039/c6tc00971a
21. Ariga, K.; Ji, Q.; Nakanishi, W.; Hill, J. P.; Aono, M. *Mater. Horiz.* **2015,** *2,* 406–413. doi:10.1039/c5mh00012b
22. Ariga, K.; Li, J.; Fei, J.; Ji, Q.; Hill, J. P. *Adv. Mater. (Weinheim, Ger.)* **2016,** *28,* 1251–1286. doi:10.1002/adma.201502545
23. Gao, W.; D'Agostino, M.; Garcia-Gradilla, V.; Orozco, J.; Wang, J. *Small* **2013,** *9,* 467–471. doi:10.1002/smll.201201864
24. Jurado-Sánchez, B.; Wang, J.; Escarpa, A. *ACS Appl. Mater. Interfaces* **2016,** *8,* 19618–19625. doi:10.1021/acsami.6b05824
25. Huang, H.-W.; Sakar, M. S.; Petruska, A. J.; Pané, S.; Nelson, B. J. *Nat. Commun.* **2016,** *7,* 12263. doi:10.1038/ncomms12263
26. Fan, D.; Yin, Z.; Cheong, R.; Zhu, F. Q.; Cammarata, R. C.; Chien, C. L.; Levchenko, A. *Nat. Nanotechnol.* **2010,** *5,* 545–551. doi:10.1038/nnano.2010.104
27. Wang, W.; Li, S.; Mair, L.; Ahmed, S.; Huang, T. J.; Mallouk, T. E. *Angew. Chem., Int. Ed.* **2014,** *53,* 3201–3204. doi:10.1002/anie.201309629
28. Ma, X.; Hortelão, A. C.; Patiño, T.; Sánchez, S. *ACS Nano* **2016,** *10,* 9111–9122. doi:10.1021/acsnano.6b04108
29. Xu, T.; Gao, W.; Xu, L.-P.; Zhang, X.; Wang, S. *Adv. Mater. (Weinheim, Ger.)* **2017,** *29,* 1603250. doi:10.1002/adma.201603250
30. Mou, F.; Chen, C.; Ma, H.; Yin, Y.; Wu, Q.; Guan, J. *Angew. Chem., Int. Ed.* **2013,** *52,* 7208–7212. doi:10.1002/anie.201300913
31. Li, T.; Li, J.; Zhang, H.; Chang, X.; Song, W.; Hu, Y.; Shao, G.; Sandraz, E.; Zhang, G.; Li, L.; Wang, J. *Small* **2016,** *12,* 6098–6105. doi:10.1002/smll.201601846
32. Qiu, T.; Lee, T.-C.; Mark, A. G.; Morozov, K. I.; Münster, R.; Mierka, O.; Turek, S.; Leshansky, A. M.; Fischer, P. *Nat. Commun.* **2014,** *5,* 5119. doi:10.1038/ncomms6119
33. Xu, T.; Soto, F.; Gao, W.; Garcia-Gradilla, V.; Li, J.; Zhang, X.; Wang, J. *J. Am. Chem. Soc.* **2014,** *136,* 8552–8555. doi:10.1021/ja504150e
34. Tu, Y.; Peng, F.; Sui, X.; Men, Y.; White, P. B.; van Hest, J. C. M.; Wilson, D. A. *Nat. Chem.* **2017,** *9,* 480–486. doi:10.1038/nchem.2674

35. Zhang, L.; Zhang, H.; Liu, M.; Dong, B. *ACS Appl. Mater. Interfaces*
    2016, *8,* 15654–15660. doi:10.1021/acsami.6b04674

36. Liu, L.; Liu, M.; Su, Y.; Dong, Y.; Zhou, W.; Zhang, L.; Zhang, H.;
    Dong, B.; Chi, L. *Nanoscale* **2015,** *7,* 2276–2280.
    doi:10.1039/c4nr06621a

37. Liu, M.; Liu, L.; Gao, W.; Su, M.; Ge, Y.; Shi, L.; Zhang, H.; Dong, B.;
    Li, C. Y. *Nanoscale* **2015,** *7,* 4949–4955. doi:10.1039/c4nr07558g

38. Kotov, N. A.; Dekany, I.; Fendler, J. H. *J. Phys. Chem.* **1995,** *99,*
    13065–13069. doi:10.1021/j100035a005

39. Yan, X.; Li, J.; Möhwald, H. *Adv. Mater. (Weinheim, Ger.)* **2012,** *24,*
    2663–2667. doi:10.1002/adma.201200408

40. Volodkin, D.; Skirtach, A.; Möhwald, H. *Polym. Int.* **2012,** *61,* 673–679.
    doi:10.1002/pi.4182

41. Duan, L.; He, Q.; Wang, K.; Yan, X.; Cui, Y.; Möhwald, H.; Li, J.
    Angew. Chem., Int. Ed. **2007,** *46,* 6996–7000.
    doi:10.1002/anie.200700331

42. Gnanasammandhan, M. K.; Idris, N. M.; Bansal, A.; Huang, K.;
    Zhang, Y. *Nat. Protoc.* **2016,** *11,* 688–713. doi:10.1038/nprot.2016.035

43. Risso, F. *Annu. Rev. Fluid Mech.* **2018,** *50,* 25–48.
    doi:10.1146/annurev-fluid-122316-045003

Flexible freestanding MoS$_2$-based composite paper for energy conversion and storage

Florian Zoller[1,2], Jan Luxa[3], Thomas Bein[1], Dina Fattakhova-Rohlfing[2,4], Daniel Bouša[3] and Zdeněk Sofer[*3]

Full Research Paper

Address:
[1]Department of Chemistry and Center for NanoScience (CeNS), Ludwig-Maximilians-Universität München (LMU Munich), Geschwister-Scholl-Platz 1, 80539 Munich, Germany, [2]Faculty of Engineering and Center for Nanointegration Duisburg-Essen (CENIDE), University of Duisburg-Essen, Lotharstraße 1, 47057 Duisburg, Germany, [3]Department of Inorganic Chemistry, University of Chemistry and Technology Prague, Technická 5, 166 28 Prague 6, Czech Republic and [4]Forschungszentrum Jülich GmbH, Institute of Energy and Climate Research (IEK-1) Materials Synthesis and Processing, Wilhelm-Johnen-Straße, 52425 Jülich, Germany

Email:
Zdeněk Sofer[*] - zdenek.sofer@vscht.cz

* Corresponding author

Keywords:
flexible composites; hydrogen evolution reaction (HER); lithium ion batteries (LIBs); molybdenum disulfide; nanoarchitectonics; supercapacitors

Abstract

The construction of flexible electrochemical devices for energy storage and generation is of utmost importance in modern society. In this article, we report on the synthesis of flexible MoS$_2$-based composite paper by high-energy shear force milling and simple vacuum filtration. This composite material combines high flexibility, mechanical strength and good chemical stability. Chronopotentiometric charge–discharge measurements were used to determine the capacitance of our paper material. The highest capacitance achieved was 33 mF·cm^{-2} at a current density of 1 mA·cm^{-2}, demonstrating potential application in supercapacitors. We further used the material as a cathode for the hydrogen evolution reaction (HER) with an onset potential of approximately −0.2 V vs RHE. The onset potential was even lower (approximately −0.1 V vs RHE) after treatment with n-butyllithium, suggesting the introduction of new active sites. Finally, a potential use in lithium ion batteries (LIB) was examined. Our material can be used directly without any binder, additive carbon or copper current collector and delivers specific capacity of 740 mA·h·g^{-1} at a current density of 0.1 A·g^{-1}. After 40 cycles at this current density the material still reached a capacity retention of 91%. Our findings show that this composite material could find application in electrochemical energy storage and generation devices where high flexibility and mechanical strength are desired.

Introduction

The world's growing population has a nearly ever-increasing demand for energy. Due to the well-known problem of global warming, there are efforts to shift energy production from burning fossil fuels towards renewable energy sources. However, most of the established renewable energy sources are not suitable to meet the energy consumption requirements today. Hence, energy storage and conversion continues to be an important and urgent issue [1,2].

Lithium ion batteries (LIBs) are one of the most promising energy storage devices, combining high energy density and extremely low self-discharge. Nevertheless, in order to fulfill the (prospective) requirements and to extend their application to large energy storage systems or to the electromobility sector, an improvement in the energy storage capacity is necessary. Layered dichalcogenide materials such as molybdenum sulfide (MoS_2) are promising candidates for the replacement of the commercial anode material graphite. Apart from this specific application, chalcogenide materials also find numerous applications in various scientific fields [3-5]. During charge/discharge, MoS_2 undergoes a 4-electron process resulting in a theoretical specific capacity of 669 mA·h·g^{-1}, which is almost two times higher than that of graphite (372 mA·h·g^{-1}) [6].

However, poor electrical conductivity, capacity fading and large volume changes upon charge and discharge make the commercialization of MoS_2 in LIBs problematic [6,7]. In order to address this issue, the fabrication of MoS_2 composites and carbonaceous support materials (such as amorphous carbon [8], carbon nanofibers [7], carbon nanotubes [8] and graphene [9]) has already been demonstrated to be quite attractive. Typically, the electrodes are prepared by mixing these composites as active material with a polymeric binder, conductive carbon and an organic solvent to form a slurry, which is then coated onto a copper foil (current collector). The copper foil and the additives increase the overall weight, which dramatically decreases the gravimetric energy density. These electrodes are not applicable as anodes in flexible batteries due to the loss of contact between the active material and the current collector upon bending deformation [10]. However, there are promising reports on freestanding MoS_2/carbonaceous composite electrodes which have demonstrated attractive electrochemical performance [9-25].

Beside LIBs, supercapacitors (SCs) are seen as next-generation energy storage devices having a high specific power, fast charge–discharge rate and excellent cycling stability [2]. Freestanding, binder-free electrodes are also of great interest, as they can be used in flexible SCs [26]. In this regard, two-dimensional (2D) graphene has attained significant interest. Nevertheless, materials with higher performance are necessary [26,27]. MoS_2 is seen, due its layered graphene-analogous structure, as a promising alternative providing a large surface area, which is favorable for double-layer charge storage [27,28]. Moreover, Mo can occupy multiple oxidation states, which enables a pseudo-capacitive charge transfer by insertion of electrolyte ions, such as Li$^+$, Na$^+$, K$^+$ and H$^+$ [28,29]. Upon cycling, MoS_2 sheets can restack resulting in a decreased surface area, which is then followed by poor capacitive performance. Moreover, an appropriate heat management scheme has to be taken into account in real applications as it has been already shown for other nanomaterials [30,31]. Introducing support materials, such as graphene or carbon nanotubes (CNTs) can alleviate these problems and improve the performance of the materials [26].

Another popular related field in the context of energy storage and sustainable energy production is water splitting to produce hydrogen. The best catalysts for the hydrogen evolution reaction (HER) are unequivocally based on platinum and iridium, however the scarcity and the high cost of these materials are tremendous disadvantages for the production of hydrogen on an industrial scale [16]. Hence, it is necessary to develop new catalysts which are abundant, inexpensive and chemically robust [16]. MoS_2 is again a promising candidate. Theoretical and experimental studies have successfully demonstrated that nanoscale MoS_2 is more appropriate than the bulk phase equivalent. The surface of the bulk phase mainly consists of thermodynamically more stable basal sites, which are catalytically less active. In contrast, the sulfur edge sites of MoS_2 are highly catalytically active towards HER [32-34]. However, MoS_2 possesses only a low intrinsic conductivity, which hinders the charge transport [35]. Using MoS_2 together with conducting support materials, such as multiwalled carbon nanotubes (MWCNTs) has already been demonstrated to improve the catalytic properties [35].

Herein, we report on the synthesis of a freestanding MoS_2-based composite paper using a small addition of single-walled carbon nanotubes (SWCNTs) and shear-force milling in *N*-methyl-2-pyrrolidone (NMP). The paper was prepared simply by vacuum filtration of the slurry on top of a filter. The resulting material exhibits high flexibility and combines the high conductivity of SWCNTs and electrochemical potential of MoS_2. We also show that the material finds use as an anode in LIBs, supercapacitor electrodes and HER catalyst. The application for LIBs seems particularly promising as this composite material requires no additional binders, conductive additives or a current collector.

Results and Discussion

Characterization of morphology, composition and mechanical properties

The synthesized composite material based on MoS_2 and SWCNTs was prepared by shear-force milling of MoS_2 powder with SWCNTs. We then prepared a paper-like material by filtration of the mixture on top of a filter. The self-assembled material was denoted as MoS_2-based composite paper. A picture of the composite paper is shown in Figure 1.

We investigated the morphology of this compound material by scanning electron microscopy (SEM) with results shown in Figure 2. The morphology images of the top side of the composite paper (Figure 2a and 2b) show a homogeneous distribu-
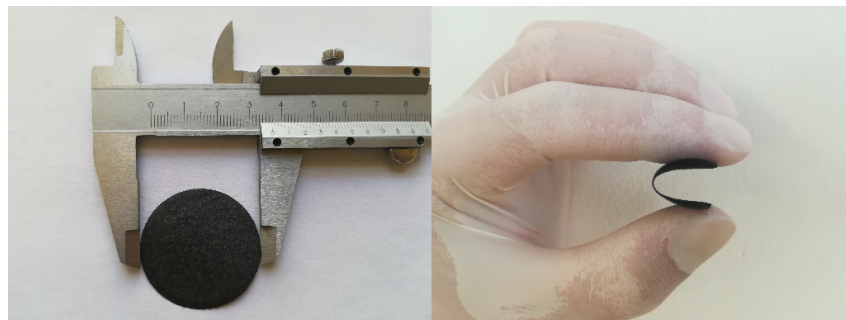

Figure 1: Image of the MoS_2-based composite paper showing its size and flexibility.
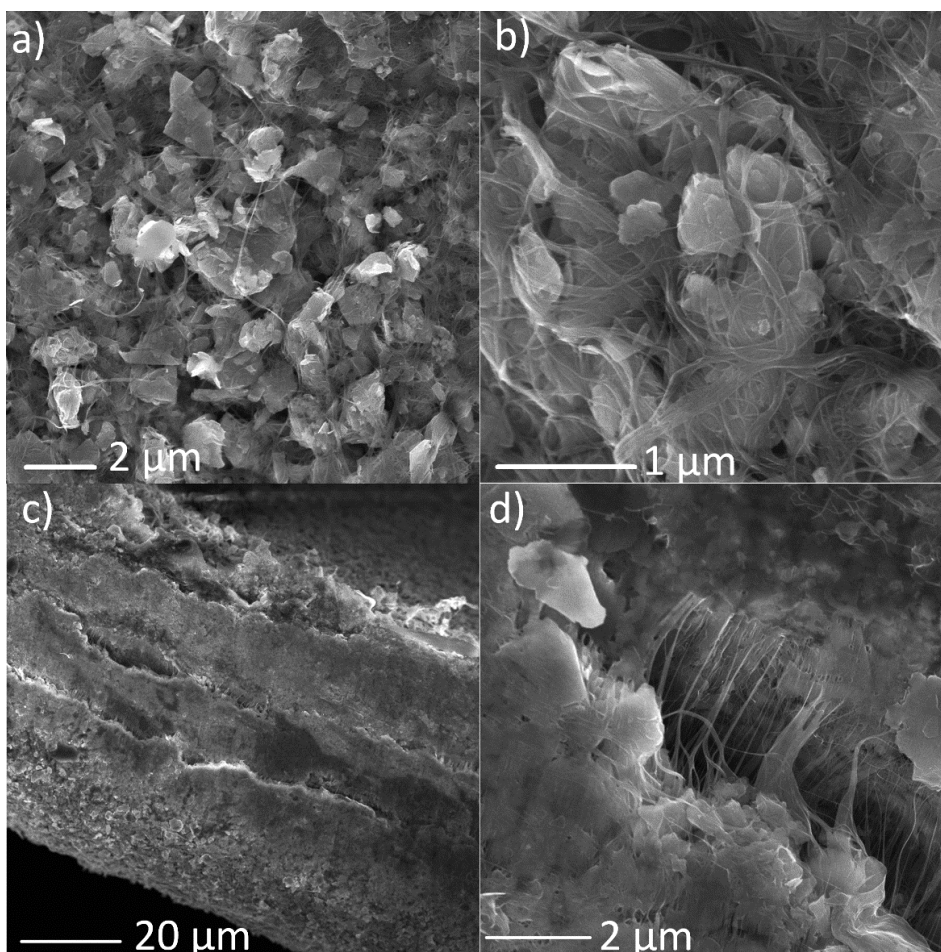

Figure 2: SEM micrographs of (a,b) plane and (c,d) cross-section images of the composite paper at different magnifications.

tion of SWCNTs among the MoS_2 sheets. SEM micrographs of the cross-section (Figure 2c and 2d) also illustrate that the SWCNTs significantly contribute to the flexibility and mechanical strength of the composite as they hold individual sheets together.

We also performed the composition characterization by energy-dispersive spectroscopy (EDS). The elemental composition maps (Supporting Information File 1, Figure S1) revealed a homogeneous distribution of elements. We have also identified (Supporting Information File 1, Table S1) that there was about 2.1 wt % of iron in the sample. This contamination originates from the carbon nanotubes, where iron usually serves as a catalyst for their growth [36].

X-ray photoelectron spectroscopy (XPS) was used to track the degree of degradation of the MoS_2 sheets. Components originating from MoS_2 and MoO_3 were identified in the core-level Mo 3d spectrum (Figure 3). The positions of the individual components are in agreement with previous reports for MoS_2 and MoO_3 [37,38]. The deconvolution revealed that the MoO_3 content was about ≈12 atom %. This degree of oxidation is lower than in the case of chemically exfoliated MoS_2, which is possibly due to a slightly lower degree of exfoliation [39]. Additionally, no oxidation was observed for sulfur as only states originating from sulfides were identified in the S 2p spectrum (Figure 3b) [40].

The chemical states of the SWCNTs could not be precisely determined due to the overlap with adventitious carbon. However, the conditions used during our experiment were highly unlikely to cause any chemical changes in the SWCNTs.

Additionally, the mechanical properties of prepared MoS_2-based composite paper were evaluated. The tensile strength and tensile ductility are important material parameters that influence material's final applicability. The tensile strength of the prepared material reached a value of 3.02 MPa while tensile

ductility was 7.74%. It should be mentioned that the preparation of paper solely from MoS_2 sheets is not possible since there is no material holding the individual MoS_2 sheets together. On the other hand, paper made of only SWCNT possesses a tensile strength of 5.95 MPa and tensile ductility of 2.45%. Therefore, incorporation of MoS_2 sheets into SWCNT paper results in decreased tensile strength and increased tensile ductility and the as-prepared MoS_2-based composite paper is able to undergo significant plastic deformation before rupture in the material occurs.

Electrochemical performance of freestanding MoS_2-based composite paper

First, we tested the MoS_2-based composite paper for applications in supercapacitors (SCs). The capacitance was measured by a chronoamperometry technique in KCl solution (1 M) using different charging–discharging current densities (1–5 mA·cm^{-2}) in a potential range determined by cyclic voltammetry (CV) shown in Supporting Information File 1, Figure S2. The CV curves demonstrate the rectangular shape pointing out the electric double-layer capacitance as the origin of capacitive behavior. The capacitance C in units of mF·cm^{-2} was calculated from the value of discharging current I, discharging time t, maximal voltage U and the area of the electrode that comes into contact with the electrolyte solution S. The calculation was performed using equation: $C = (2 \cdot I) / (S \cdot U/t)$.

The calculated values are summarized for each discharging current in Table 1. Charging–discharging curves of MoS_2-based composite paper obtained using the chronoamperometry mea-

Table 1: Capacitance of MoS_2-based composite paper measured using various discharging current densities.

Discharging current density (mA·cm^{-2})	1	2	3	4	5	6
Capacitance (mF·cm^{-2})	70	40	35	33	29	28

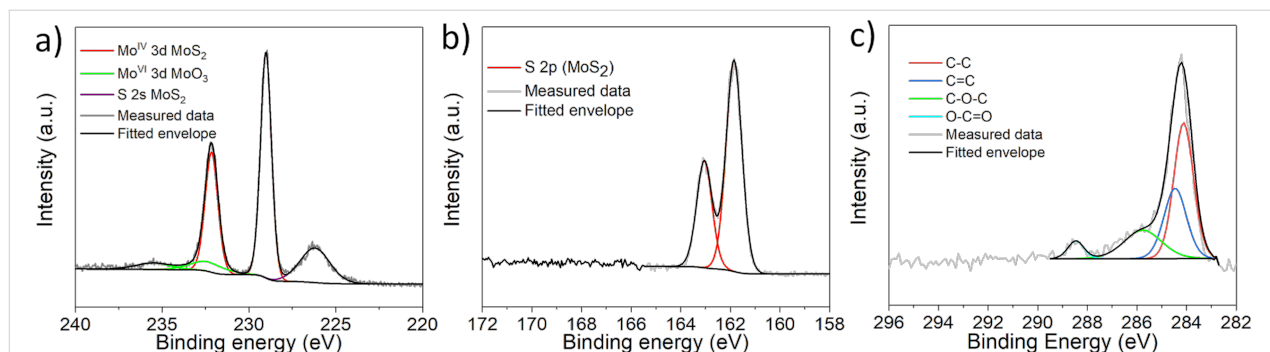**Figure 3:** Core-level X-ray photoelectron spectra of a) Mo 3d region, b) S 2p region, and c) C 1s region.
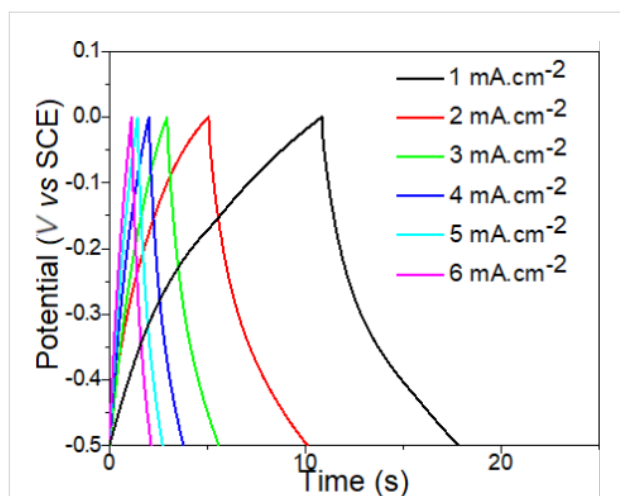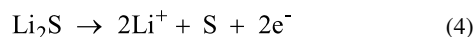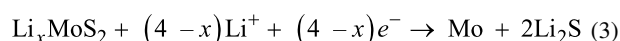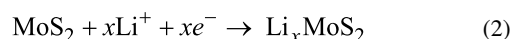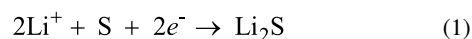
Figure 4: Charging–discharging curves of MoS_2-based composite paper obtained by chronoamperometry in 1M KCl solution using different current densities.

surement are shown in Figure 4. We also compared the capacitance of our composite MoS_2-based composite paper with other reported materials (see Table 2). The capacitance of our composite material exhibits a competitive value compared to other materials reported in the literature.

The freestanding MoS_2-based composite paper was also tested as an anode material for LIBs. Hence, the MoS_2-based composite paper was used directly as an anode without any binder, carbon additive or a Cu-foil current collector. Figure 5a shows the first four cycles of the cyclic voltammetry (CV) curves of the MoS_2-based composite paper. The measurements were performed at a scan rate of 0.1 $mV \cdot s^{-1}$ in the voltage range of 0.01–3.0 V vs Li/Li^+. In the initial cathodic scan, two dominant reduction peaks at around 1.0 and 0.3 V are detectable (Figure 5a). The first is associated with the insertion of lithium ions into the van der Waals spaces between the MoS_2 layers forming Li_xMoS_2 accompanied by a phase transformation from trigonal prismatic (2H) to octahedral (1T) (see the following Equation 2) [8,20,21]. The peak at ≈ 0.3 V corresponds to the conversion of the previously formed Li_xMoS_2 into metallic Mo and LiS_2 (see the following Equation 3) and the decomposition

of the electrolyte followed by the formation of a solid electrolyte interphase (SEI) layer [18,20]. The prominent anodic peak at ≈ 2.5 V results from the conversion of Li_2S to sulfur and lithium ions (see the following Equation 4) [20]. During the following discharge cycles the two peaks at ≈ 1.0 and ≈ 0.3 V diminish and three new reduction peaks at around 1.8, 1.1 and 0.3 V appear, which can be ascribed to the following reactions (Equations 1–3):

$$2Li^+ + S + 2e^- \rightarrow Li_2S \tag{1}$$

$$MoS_2 + xLi^+ + xe^- \rightarrow Li_xMoS_2 \tag{2}$$

$$Li_xMoS_2 + (4-x)Li^+ + (4-x)e^- \rightarrow Mo + 2Li_2S \tag{3}$$

$$Li_2S \rightarrow 2Li^+ + S + 2e^- \tag{4}$$

Hence, the reduction peak at ≈ 1.8 V and the oxidation peak at 2.5 V form together a reversible redox couple [20]. Starting with the second cycle, a shallow oxidation peak arises at ≈ 1.7 V which can be attributed to the partial oxidation of metallic Mo to MoS_2 [21,45].

Moreover, the electrochemical performance of the MoS_2-based composite paper is evaluated by galvanostatic discharge/charge measurements as well. The lithiation and delithiation plateaus (Figure 5b) obtained at a current density of 0.2 $A \cdot g^{-1}$ are consistent with the reduction and oxidation peaks gathered from the CV measurement.

In the first cycle, discharge and charge capacities of 870 and 684 $mA \cdot h \cdot g^{-1}$ were obtained, respectively. This corresponds to a coulombic efficiency of 79%, as shown in Figure 5b and Figure 5d. The irreversible initial capacity loss is mainly attributed to the formation of the SEI layer [8,17,20]. During the subsequent cycles, coulombic efficiencies of $\leq 97\%$ are reached, which implies a good cycling reversibility (Figure 5d). After 40 cycles a specific capacity of 675 $mA \cdot h \cdot g^{-1}$ is reached equaling a capacity retention of 78% compared to the initial

Table 2: Performance of various electrode materials in the literature compared to this work.

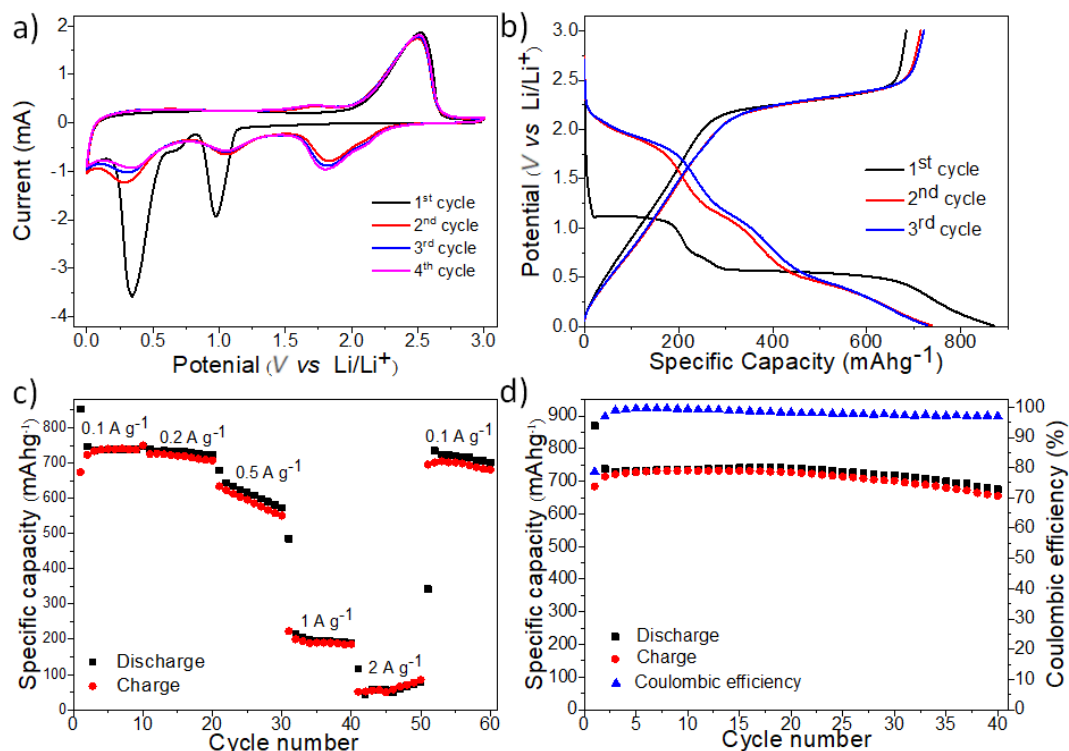| Ref.	Electrode material	Electrolyte	Capacitance ($mF \cdot cm^{-2}$)
this work	MoS_2-based composite paper	KCl	33
[41]	interdigital MWCNT electrode	PVA/KOH	107.3
[42]	CNT	PVDF-HFP/EMIMTFSI	2.88
[43]	graphene	PVA-H_2SO_4	2.32
[44]	graphene–CNT	KCl	2.8

Figure 5: Electrochemical analysis of the freestanding MoS$_2$-based composite paper. (a) CV curves at a scan rate of 0.1 V·s^{-1}, (b) discharge/charge voltage profiles at 0.2 A·g^{-1}, (c) reversible capacities at different current densities ranging from 0.1 to 2.0 A·g^{-1} and (d) cycling performance and coulombic efficiency at 0.2 A·g^{-1}.

cycle or 91% when compared to the second cycle. It should be noted that for the calculation of the specific capacitiy the total mass of the freestanding MoS$_2$-based composite paper electrode was used.
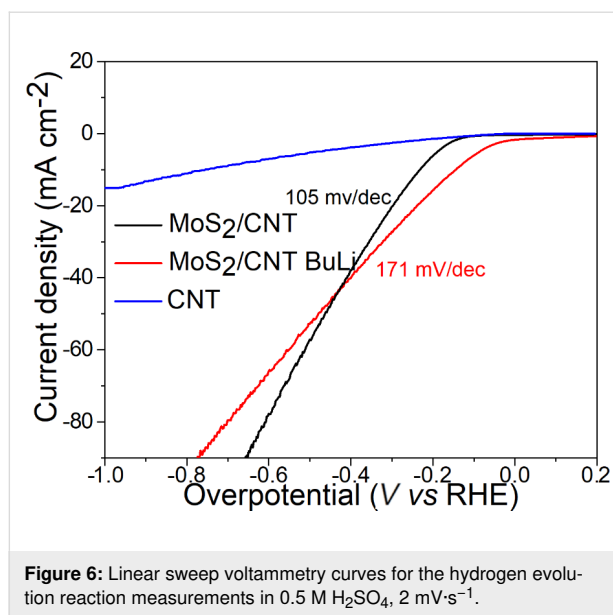
Moreover, the rate performance of the freestanding MoS$_2$-based composite paper electrodes was further investigated (Figure 5c). The composite delivers 740, 721, 596, 190 and 49 mA·h·g^{-1}, at current rates of 0.1, 0.2, 0.5, 1 and 2 A·g^{-1}, respectively. The slightly increasing capacity during the 2 A·g^{-1} step may be attributed to the high current rate activation of new Li$^+$ storage sites, originating from the opening up of blocked ends of SWCNTs [8]. Interestingly, when the current density was set back to 0.1 A·g^{-1} the capacity reached 681 mA·h·g^{-1} (80th cycle) equaling a capacity retention of 91% compared to the second cycle, also confirming the high structural stability of the freestanding MoS$_2$-based composite paper. The kinetic analysis of the MoS$_2$-based composite paper is described in Supporting Information File 1, Figure S2.

Finally, we tested the MoS$_2$-based composite paper as a catalyst for the hydrogen evolution reaction (HER). The results are shown in Figure 6. Apart from the pristine material, we also treated the paper with *n*-butyllithium (BuLi) solution to intro-

duce new active sites in the form of edge sites as well as defects. The pristine as-prepared material exhibited an onset potential of about −0.195 V vs RHE. On the other hand, BuLi-exfoliated MoS$_2$-based composite paper showed improved activity with an onset potential of about −0.095 V vs RHE. These differences clearly demonstrate that new sites were indeed introduced by the treatment. However, Figure 6 also demonstrates that BuLi-treated samples exhibited substantially higher (171 mV/dec) Tafel slope values than the pristine sample (105 mV/dec). This discrepancy could be caused by a loss of proper connection between the MoS$_2$ sheets and SWCNTs and a decrease in conductivity. This claim is supplemented by the fact that the paper material exhibited lower flexibility than the original one.

Conclusion

Using shear-force milling, we prepared a freestanding MoS$_2$-based composite paper material. This method is very simple and takes advantage of the fact that a paper-like material is self-assembled on top of a filter during vacuum filtration. The reported material exhibits high structural integrity and flexibility. The composite was tested in various electrochemical applications covering supercapacitors, anodes in lithium ion batteries and hydrogen evolution catalysis. In terms of supercapacitors,

Figure 6: Linear sweep voltammetry curves for the hydrogen evolution reaction measurements in 0.5 M H_2SO_4, 2 mV·s^{-1}.

our material exhibits a capacitance of 33 mF·cm^{-2} at a current density of 1 mA·cm^{-2}. This value is competitive with other reported materials based on carbon nanomaterials. This material can also be used as a hydrogen evolution reaction catalyst. The as-prepared materials exhibits an onset potential of approximately −0.195 V vs RHE and is capable of reaching current densities as high as 100 mA·cm^{-2}. Additionally, we treated the material with *n*-butyllithium to further enhance the HER activity. The resulting material exhibited a lower onset potential, however, the exfoliation of MoS_2 sheets resulted in a loss of connection between the MoS_2 sheets and SWCNTs. Ultimately, this led to a decrease in the conductivity, and consequently, substantial increase in the Tafel slope value. The MoS_2-based composite paper was also tested as a freestanding anode in LIBs without additives such as binders or conductive agents. After the initial loss of specific capacity due to the formation of the solid electrolyte interface, the composite delivers a specific capacity of 740 mA·h·g^{-1} at 0.1 A·g^{-1}. Moreover, the material retains 91% of its capacity after 40 cycles. A high capacity retention was also observed after the rate performance tests. These findings show that the reported material is also promising for application in flexible batteries.

Experimental
Materials
MoS_2 was purchased from Alfa Aesar, TUBALL^{TM} SWCNTs were purchased from OCSiAl, and *N*-methyl-2-pyrrolidone (NMP) was purchased from Sigma-Aldrich.

The PuriEL electrolyte (1.15 M LiPF$_6$ in ethylene carbonate/ethyl methyl carbonate/dimethyl carbonate (EC/EMC/DMC) = 2:2:6 v/v + 1.0 wt % fluoroethylene

carbonate (FEC), *soul*brain MI) and lithium metal (Rockwood) were used as received.

Preparation of MoS$_2$-based composite paper
125 mg of MoS_2 powder and 12.5 mg of SWCNTs were added to 80 mL of Ar-purged NMP. The suspension was then exfoliated under Ar atmosphere for 2 h at 16,000 rot/min using a high-energy shear-force disperser. After that, the mixture was vacuum-filtered on top of a nylon filter and washed with methanol several times. The use of methanol significantly shortens the time necessary for drying. The resulting material was then self-assembled into the form of a paper-like material. After drying under vacuum, the material was directly used.

Battery assembly and electrochemical measurements
The freestanding MoS_2-based composite paper was cut into round disks with a diameter of 18 mm (254.5 mm^2). They were directly used as an anode in ECC-PAT-Core (EL-Cell) battery test cells assembled in an argon-filled glove box using lithium metal both as the counter and reference electrode and an EL-CELL ECC1-01-0011-A/L glass fiber membrane as a separator. The used electrolyte consisted of a commercial mixture of 1.15 M LiPF$_6$ in EC/EMC/DMC at a 2:2:6 v/v and 1.0 wt % FEC.

The electrochemical measurements were performed at room temperature using an Autolab potentiostat/galvanostat (PGSTAT302N) with a FRA32M module or an Autolab multi-potentiostat M101 with a 8AUT.M101 module operated with Nova 1.11 software. The cyclic voltammograms were recorded in a potential range of 0.01–3.0 V vs Li/Li$^+$ using a scan rate ranging from 0.05 mV·s^{-1} to 1 mV·s^{-1}. The cells were charged and discharged galvanostatically at different *C* rates (0.1 to 2 A·g^{-1}) in a voltage range of 0.01–3.0 V vs Li/Li$^+$.

Supercapacitors
A disk with diameter of 14 mm was cut from the vacuum-assembled MoS_2-based composite paper material. Then it was placed into an electrochemical holder (InRedox, USA) which was placed in the middle of platinum basket (counter electrode). A saturated calomel reference electrode was used as the reference electrode and the measurements were performed in 1 M KCl solution. The exposed area was a disk with 0.94 mm diameter. In order to measure the charge–discharge curves, several charging–discharging currents (1–5 mA·cm^{-2}) were used to charge the material to −0.8 V vs SCE.

Hydrogen evolution reaction
For the HER measurements, the pristine sample was placed in an electrochemical holder (InRedox, USA) which was inserted

into the 0.5 M H_2SO_4 electrolyte with SCE and a carbon rod as the reference and counter electrodes, respectively. The scan rate was 2 mV·s^{-1}. For the *n*-butyllithium treated sample, the foil was left in *n*-butyllithium solution (2.5 M solution) for several days under inert Ar atmosphere. After that, water was added to the solution. The foil was then dried and used.

Characterization

The morphology was investigated using scanning electron microscopy (SEM) with a FEG electron source (Tescan Lyra dual beam microscope). The elemental composition and mapping were performed using an energy dispersive spectroscopy (EDS) analyzer (X-MaxN) with a 20 mm^2 SDD detector (Oxford Instruments) and AZtecEnergy software. A 10 kV beam was used for the measurements.

High-resolution X-ray photoelectron spectroscopy (XPS) was performed using an ESCAProbeP spectrometer (Omicron Nanotechnology Ltd, Germany) with a monochromatic aluminum X-ray radiation source (1486.7 eV). Wide-scan surveys of all elements were performed (0–1000 eV, step 0.5 eV) with subsequent high-resolution scans of the C 1s, S 2p and Mo 3d regions with a step of 0.05 eV.

The dynamic mechanical analysis was measured on a DMA DX04T (by RMI, Czech Republic) device. A sample with dimensions 7.600 mm (width), 0.173 mm (thickness) and 10.200 mm (active length) was loaded with a tensile longitudinal sinusoidal deformation with the amplitude of 0.02 mm and pretension of 0.03 mm. The temperature range was 20 to 200 °C with a heating rate of 2 °C·min^{-1} in air atmosphere. From the results, the values of the moduli and loss factor were evaluated as the second-order sliding average.

Supporting Information

Supporting Information File 1
Additional experimental results.
[https://www.beilstein-journals.org/bjnano/content/supplementary/2190-4286-10-147-S1.pdf]

Acknowledgements

ORCID® iDs

Thomas Bein - https://orcid.org/0000-0001-7248-5906
Zdeněk Sofer - https://orcid.org/0000-0002-1391-4448

Preprint

References

1. Hussain, A.; Arif, S. M.; Aslam, M.
   Renewable Sustainable Energy Rev. **2017,** *71,* 12–28.
   doi:10.1016/j.rser.2016.12.033
2. Sangeetha, D. N.; Selvakumar, M. *Appl. Surf. Sci.* **2018,** *453,* 132–140.
   doi:10.1016/j.apsusc.2018.05.033
3. *2016 11th International Conference on Advanced Semiconductor Devices & Microsystems (ASDAM),* Nov 13–16, 2016; .
4. Hardtdegen, H.; Mikulics, M.; Rieß, S.; Schuck, M.; Saltzmann, T.; Simon, U.; Longo, M. *Prog. Cryst. Growth Charact. Mater.* **2015,** *61,* 27–45. doi:10.1016/j.pcrysgrow.2015.10.001
5. Hardtdegen, H.; Rieß, S.; Schuck, M.; Keller, K.; Jost, P.; Du, H.; Bornhöfft, M.; Schwedt, A.; Mussler, G.; v.d. Ahe, M.; Mayer, J.; Roth, G.; Grützmacher, D.; Mikulics, M. *J. Alloys Compd.* **2016,** *679,* 285–292. doi:10.1016/j.jallcom.2016.04.013
6. Liu, H.; Su, D.; Zhou, R.; Sun, B.; Wang, G.; Qiao, S. Z.
   Adv. Energy Mater. **2012,** *2,* 970–975. doi:10.1002/aenm.201200087
7. Zhou, F.; Xin, S.; Liang, H.-W.; Song, L.-T.; Yu, S.-H.
   Angew. Chem., Int. Ed. **2014,** *53,* 11552–11556.
   doi:10.1002/anie.201407103
8. Zhang, Z.; Zhao, H.; Teng, Y.; Chang, X.; Xia, Q.; Li, Z.; Fang, J.; Du, Z.; Świerczek, K. *Adv. Energy Mater.* **2018,** *8,* 1700174.
   doi:10.1002/aenm.201700174
9. Chao, Y.; Jalili, R.; Ge, Y.; Wang, C.; Zheng, T.; Shu, K.; Wallace, G. G. *Adv. Funct. Mater.* **2017,** *27,* 1700234.
   doi:10.1002/adfm.201700234
10. Ren, J.; Ren, R.-P.; Lv, Y.-K. *Chem. Eng. J.* **2018,** *353,* 419–424.
    doi:10.1016/j.cej.2018.07.139
11. Wang, T.; Sun, C.; Yang, M.; Zhao, G.; Wang, S.; Ma, F.; Zhang, L.; Shao, Y.; Wu, Y.; Huang, B.; Hao, X. *J. Alloys Compd.* **2017,** *716,* 112–118. doi:10.1016/j.jallcom.2017.05.071
12. Kong, D.; He, H.; Song, Q.; Wang, B.; Lv, W.; Yang, Q.-H.; Zhi, L.
    Energy Environ. Sci. **2014,** *7,* 3320–3325. doi:10.1039/c4ee02211d
13. Rana, K.; Singh, J.; Lee, J.-T.; Park, J. H.; Ahn, J.-H.
    ACS Appl. Mater. Interfaces **2014,** *6,* 11158–11166.
    doi:10.1021/am500996c
14. Xie, D.; Tang, W. J.; Xia, X. H.; Wang, D. H.; Zhou, D.; Shi, F.; Wang, X. L.; Gu, C. D.; Tu, J. P. *J. Power Sources* **2015,** *296,* 392–399. doi:10.1016/j.jpowsour.2015.07.074
15. Wang, Y.; Ma, Z.; Chen, Y.; Zou, M.; Yousaf, M.; Yang, Y.; Yang, L.; Cao, A.; Han, R. P. S. *Adv. Mater. (Weinheim, Ger.)* **2016,** *28,* 10175–10181. doi:10.1002/adma.201603812
16. Zhang, Q.; Xu, Z.; Lu, B. *Energy Storage Mater.* **2016,** *4,* 84–91.
    doi:10.1016/j.ensm.2016.03.005
17. Malinský, P.; Cutroneo, M.; Macková, A.; Hnatowicz, V.; Szökölová, K.; Bohačová, M.; Luxa, J.; Sofer, Z. *Surf. Interface Anal.* **2018,** *50,* 1110–1115. doi:10.1002/sia.6475
18. Cutroneo, M.; Havranek, V.; Mackova, A.; Malinsky, P.; Torrisi, L.; Pérez-Hernández, J. A.; Roso, L.; Luxa, J.; Sofer, Z.; Böttger, R.
    Ion-beam lithography: A promising technique for the patterning of graphene oxide foil. In *AIP Conference Proceedings,* 2018.
    doi:10.1063/1.5053388
19. Wang, B.; Guo, R.; Zheng, M.; Liu, Z.; Li, F.; Meng, L.; Li, T.; Luo, Y.; Jiang, H. *Electrochim. Acta* **2018,** *260,* 1–10.
    doi:10.1016/j.electacta.2017.11.067

20. Zhao, H.; Wu, J.; Li, J.; Wu, H.; Zhang, Y.; Liu, H. *Appl. Surf. Sci.* **2018,** *462,* 337–343. doi:10.1016/j.apsusc.2018.08.110
21. Wang, W.; Yang, P.; Jian, Z.; Li, H.; Xing, Y.; Zhang, S. *J. Mater. Chem. A* **2018,** *6,* 13797–13805. doi:10.1039/c8ta03272f
22. Deng, Z.; Jiang, H.; Hu, Y.; Liu, Y.; Zhang, L.; Liu, H.; Li, C. *Adv. Mater. (Weinheim, Ger.)* **2017,** *29,* 1603020. doi:10.1002/adma.201603020
23. Deng, Y.; Ding, L.; Liu, Q.; Zhan, L.; Wang, Y.; Yang, S. *Appl. Surf. Sci.* **2018,** *437,* 384–389. doi:10.1016/j.apsusc.2017.12.020
24. Ma, X.; Liu, X.; Zhao, J.; Hao, J.; Chi, C.; Liu, X.; Li, Y.; Liu, S.; Zhang, K. *New J. Chem.* **2017,** *41,* 588–593. doi:10.1039/c6nj02238c
25. Bindumadhavan, K.; Srivastava, S. K.; Mahanty, S. *Chem. Commun.* **2013,** *49,* 1823–1825. doi:10.1039/c3cc38598a
26. Ge, Y.; Jalili, R.; Wang, C.; Zheng, T.; Chao, Y.; Wallace, G. G. *Electrochim. Acta* **2017,** *235,* 348–355. doi:10.1016/j.electacta.2017.03.069
27. Lamberti, A. *Mater. Sci. Semicond. Process.* **2018,** *73,* 106–110. doi:10.1016/j.mssp.2017.06.046
28. Choudhary, N.; Patel, M.; Ho, Y.-H.; Dahotre, N. B.; Lee, W.; Hwang, J. Y.; Choi, W. *J. Mater. Chem. A* **2015,** *3,* 24049–24054. doi:10.1039/c5ta08095a
29. Acerce, M.; Voiry, D.; Chhowalla, M. *Nat. Nanotechnol.* **2015,** *10,* 313–318. doi:10.1038/nnano.2015.40
30. Mikulics, M.; Kordoš, P.; Fox, A.; Kočan, M.; Lüth, H.; Sofer, Z.; Hardtdegen, H. *Appl. Mater. Today* **2017,** *7,* 134–137. doi:10.1016/j.apmt.2017.02.008
31. McGlen, R. J.; Jachuck, R.; Lin, S. *Appl. Therm. Eng.* **2004,** *24,* 1143–1156. doi:10.1016/j.applthermaleng.2003.12.029
32. Kamila, S.; Mohanty, B.; Samantara, A. K.; Guha, P.; Ghosh, A.; Jena, B.; Satyam, P. V.; Mishra, B. K.; Jena, B. K. *Sci. Rep.* **2017,** *7,* 8378. doi:10.1038/s41598-017-08677-5
33. Benck, J. D.; Hellstern, T. R.; Kibsgaard, J.; Chakthranont, P.; Jaramillo, T. F. *ACS Catal.* **2014,** *4,* 3957–3971. doi:10.1021/cs500923c
34. Zhang, G.; Liu, H.; Qu, J.; Li, J. *Energy Environ. Sci.* **2016,** *9,* 1190–1209. doi:10.1039/c5ee03761a
35. Cao, J.; Zhou, J.; Zhang, Y.; Liu, X. *Sci. Rep.* **2017,** *7,* No. 11242. doi:10.1038/s41598-017-11687-y
36. Homma, Y.; Kobayashi, Y.; Ogino, T.; Takagi, D.; Ito, R.; Jung, Y. J.; Ajayan, P. M. *J. Phys. Chem. B* **2003,** *107,* 12161–12164. doi:10.1021/jp0353845
37. Brown, N. M. D.; Cui, N.; McKinley, A. *Appl. Surf. Sci.* **1998,** *134,* 11–21. doi:10.1016/s0169-4332(98)00252-9
38. Spevack, P. A.; McIntyre, N. S. *J. Phys. Chem.* **1992,** *96,* 9029–9035. doi:10.1021/j100201a062
39. Luxa, J.; Vosecký, P.; Mazánek, V.; Sedmidubský, D.; Pumera, M.; Sofer, Z. *ACS Catal.* **2018,** *8,* 2774–2781. doi:10.1021/acscatal.7b04233
40. Ganta, D.; Sinha, S.; Haasch, R. T. *Surf. Sci. Spectra* **2014,** *21,* 19–27. doi:10.1116/11.20140401
41. Chen, Y.-T.; Ma, C.-W.; Chang, C.-M.; Yang, Y.-J. *Micromachines* **2018,** *9,* 242. doi:10.3390/mi9050242
42. Chen, H.; Zeng, S.; Chen, M.; Zhang, Y.; Li, Q. *Carbon* **2015,** *92,* 271–296. doi:10.1016/j.carbon.2015.04.010
43. El-Kady, M. F.; Kaner, R. B. *Nat. Commun.* **2013,** *4,* 1475. doi:10.1038/ncomms2446
44. Beidaghi, M.; Wang, C. *Adv. Funct. Mater.* **2012,** *22,* 4501–4510. doi:10.1002/adfm.201201292
45. Wu, M.; Xia, S.; Ding, J.; Zhao, B.; Jiao, Y.; Du, A.; Zhang, H. *ChemElectroChem* **2018,** *5,* 2263–2270. doi:10.1002/celc.201800520

Chiral nanostructures self-assembled from nitrocinnamic amide amphiphiles: substituent and solvent effects

Hejin Jiang[1,2], Huahua Fan[1,2], Yuqian Jiang[3], Li Zhang[*1] and Minghua Liu[*1,2]

Full Research Paper

Address:
[1]Beijing National Laboratory for Molecular Science (BNLMS), CAS Laboratory of Colloid, Interface and Chemical Thermodynamics, Institute of Chemistry, Chinese Academy of Sciences, Beijing 100190, China, [2]University of Chinese Academy of Sciences, Beijing 100049, China and [3]Laboratory for Nanosystem and Hierarchical Fabrication, CAS Center for Excellence in Nanoscience, National Center for Nanoscience and Technology, Beijing 100190, China

Email:
Li Zhang[*] - zhangli@iccas.ac.cn; Minghua Liu[*] - liumh@iccas.ac.cn

* Corresponding author

Abstract

Chiral nanostructures, such as α-helical proteins and double helix DNA, are widely found in biological systems and play a significant role in the biofunction of life. These structures are essentially fabricated through the covalent or noncovalent bonds between small chiral molecules. It is thus an important issue to understand how small chiral molecules can form chiral nanostructures. Here, using a series of isomeric nitrocinnamic amide derivatives, we have investigated the self-assembly behavior and the effect of the substituent position as well as the solvent on the formation of chiral nanostructures. It was found that totally different chiral nanostructures were formed due to the different positions of the nitro group on the cinnamic amide. Moreover, it was found that the chiral sense of the self-assembled nanostructures can be regulated by the solvent whereby helicity inversion was observed. This work provides a simple way to regulate the self-assembly pathway via molecular design and choice of solvent for the controlled creation of chiral nanostructures.

Introduction

The helical structure is widely found in biological systems and is considered to be a basic characteristic of living matter and perhaps even a requirement for life [1,2]. For example, the α-helix of peptides, the DNA double helix, and the triple helix of collagens are vital biological structures. It is an important issue to understand how such chiral nanostructures can be formed from simple small molecules. Nanoarchitectonics is a useful technology to create a new class of materials by controlled arrangement of structural nanoscale units such as atoms, molecules and assemblies [3-5]. It is also an efficient strategy to mimic helical structures [6-8]. Based on the concept of architectonics, amino acids [9-11], oligopeptides [12,13], saccharides

[14-16], steroids [17,18] and diaminocyclohexane derivatives [19,20] have been reported to self-assemble into helical structures, mimicking the natural helical structures found in biological systems. Generally speaking, the common feature of these building blocks is that chiral centers are contained. The synergy between various noncovalent interactions, including hydrogen bonding [21,22], π–π stacking [23,24], and hydrophobic interactions [25,26] provided by other moieties in self-assembly units, cause the chiral information to be accumulated and finally to express as helical structures. Then the question arises: will the chiral centers absolutely determine the chiral sense of the formed structures? Or do other noncovalent interactions have an influence on the chiral structures? Isomers with the same chiral center are good model compounds to investigate the effect of molecular structure on the chiral sense of self-assembled structures. In our previous study [27], three isomeric pyridine-containing L-glutamic amphiphiles have been found to self-assemble into different nanostructures including nanofibers, nanotwists and nanotubes, depending on the substituent position in the pyridine ring. However, we did not observe inversion in the helical sense of the formed self-assembled nanostructures due to the macroscopic chirality of nanofibers and nanotubes, which makes them difficult to be directly detected by a microscope.

On the other hand, helical architectures in many bimolecular systems have been shown to exhibit helicity inversion along with specific biofunctional transformations upon stimuli [28]. Thus, many attempts have been made towards understanding the reversal of handedness of helical biological systems. The chiral self-assembly gained from various noncovalent interactions is a very good biomimetic system due to the intrinsic dynamic nature of such materials and smart response to external stimuli. There are some works on the dynamic helical inversion in self-assembled structures triggered by the change of pH value [29,30], solvents [31,32], temperature [33,34], and photo-irradiation [35,36]. Inverse chiral nanostructures have exhibited their tunable functions in the field of asymmetric catalysts [37-39], chiral separation [40,41], and circular polarized luminescence [42,43]. In this case, tunable chiral functions can be found in the compounds with the same absolute configuration depending on the environmental conditions. Thus, more and more efforts should be made towards exploring self-assembled structures demonstrating helicity inversion, especially when the inversion directly occurs in nanostructures, i.e., chiral nanostructures with left-handed (right-handed) sense changed to right-handed (left-handed) upon external stimuli.

Based on these considerations, herein, we design three isomeric nitrocinnamic amide-containing L-glutamic amphiphiles, which differ in the position of the nitro group on the cinnamic amide,

and interestingly, we found that chiral structures with totally opposite helical sense can be obtained in the self-assembly of these L-glutamic amphiphiles, depending on the position of the nitro group. Furthermore, according to our previous study [43], the cinnamic amide assembly was closely related to the choice of solvent, and the photo-dimerization of the cinnamic amide moiety only occurred for methanol and ethanol. Other solvents could not be shown to induce this kind of transformation. We speculated that methanol or ethanol may affect the hydrogen bonding between the amide moieties, which differed from other kinds of solvents. In order to further confirm the specificity of methanol and investigate whether the solvent can cause the helicity inversion, in this study, we explore the self-assembly behavior of three nitrocinnamic amide-containing L-glutamic lipids in various solvents.

Results and Discussion
Self-assembly of NCLG
Three chiral amphiphile materials, named as 2NCLG, 3NCLG and 4NCLG (as an acronym related to the precursor nitrocinnamic L-glutamic acid (NCLG)), were designed and synthesized by covalently linking three *trans*-nitrocinnamic acids (2-NCA, 3-NCA and 4-NCA), respectively, to the organic lipid gelator *N*,*N*'-bis(octadecyl)-L-glutamic diamide (LGAm) (as shown in Figure 1). The difference between the three gelators is the substituent position of the nitro group on cinnamic acid. All of these gelators could be dissolved in organic solvents with heating, and the self-assembled molecules formed after cooling down to ambient temperature. At the same concentration (12 mg/mL), 2NCLG and 4NCLG formed white gels in EtOH, while 3NCLG precipitated in EtOH, as shown in Figure 1.

SEM characterization
Furthermore, the morphology of the 2NCLG, 3NCLG and 4NCLG assemblies in ethanol was analyzed by scanning electron microscopy (SEM). Figure 2 shows the detailed SEM images of the self-assembled structures. Upon SEM observation, 2NCLG self-assembled into a right-handed helical nanofiber with a helical pitch of about 250 nm and a width of approximately 70 nm, as shown in Figure 2a. As for 4NCLG assemblies, a similar right-handed helical nanofiber was obtained (Figure 2c). In contrast, a left-handed superhelical structure with a helical pitch of around 500 nm was observed in the 3NCLG system, which was formed by dozens of nanofibers. The nanohelix finally aggregated into microspherical structures (Figure 2b,d). Because of the wide field of view of the SEM illumination over the 3NCLG (Supporting Information File 1, Figure S1), the process of self-assembly was fast and the formed nanofiber structures tangled together into a superhelix. The superhelix then bundled together and formed microspherical structures. The microspherical structures finally aggregated
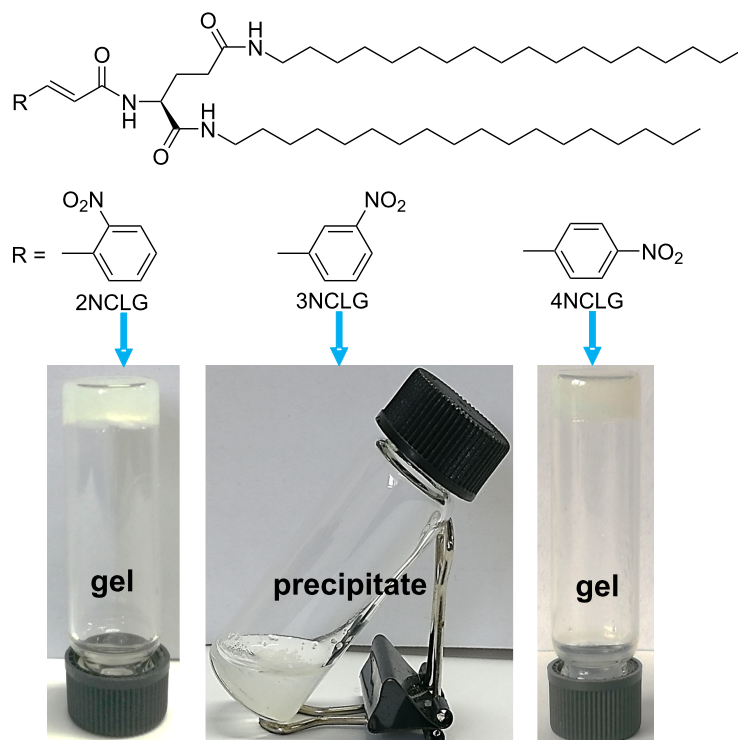
Figure 1: Molecular structure of three nitrocinnamic amide-containing L-glutamic amphiphiles and photographs of their self-assembled molecules in ethanol.
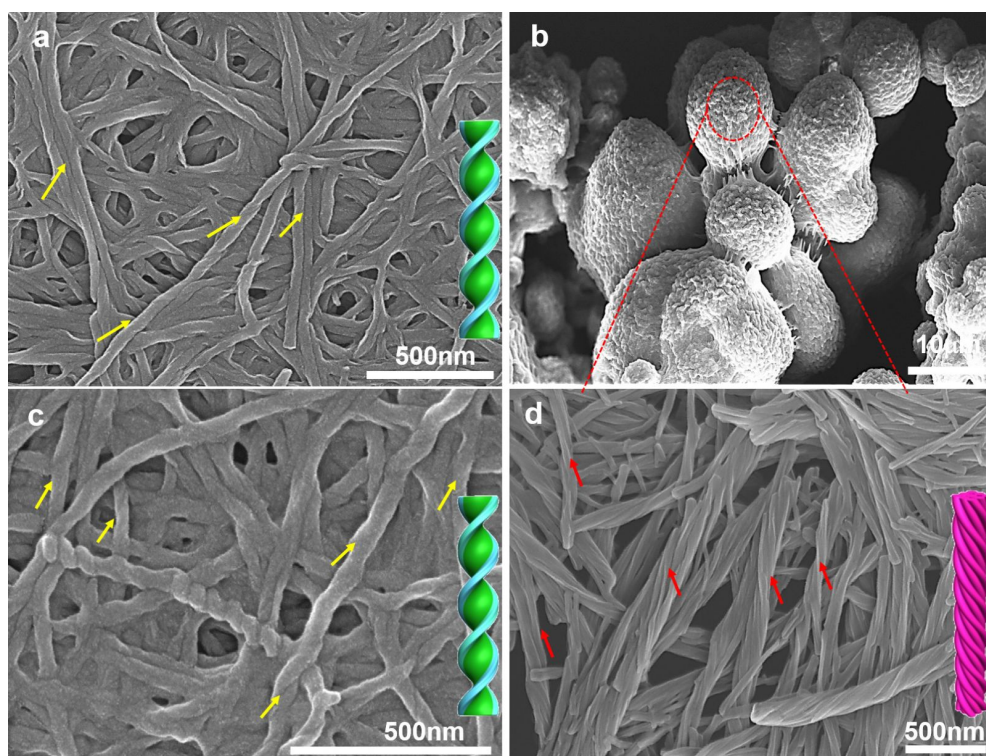

Figure 2: SEM images of NCLG assemblies in EtOH: (a) 2NCLG, (b,d) 3NCLG, and (c) 4NCLG self-assembled structures. The concentration is 12 mg/mL.

together and precipitated from the EtOH solvent. However, for the 2NCLG and 4NCLG structures, the process of self-assembly was slower than for 3NCLG and the nanofiber entangled together and formed 3D network gels. The SEM results reveal that the nanoscale chirality of the 3NCLG assembly is opposite to that of the 2NCLG and 4NCLG assemblies. It is suggested that the nanoscale chirality of the formed nanostructures did not strictly follow the chirality of the chiral carbon centers in glutamide. We speculate that the substituent position of NO_2 might affect the arrangement of molecules in the self-assembly process and subsequently lead to a different packing model of the NCLG compounds.

UV–vis and circular dichroism spectra

In order to further understand the different self-assembly behaviors among the NCLG molecules, the UV–vis spectra and circular dichroism (CD) spectra were investigated (Figure 3). Figure 3a shows the UV–vis spectra of NCLG solutions and assemblies in ethanol. It can be clearly observed that the 2NCLG, 3NCLG and 4NCLG solutions exhibited main absorp-

Figure 3: (a) UV–vis spectra of 2NCLG, 3NCLG, 4NCLG ethanol solutions and self-assembled molecules. (b) CD spectra of 2NCLG, 3NCLG and 4NCLG self-assembled molecules.

tion bands at approximately 249 nm, 263 nm and 306 nm, respectively, which can be ascribed to π–π* transitions. In addition, 2NCLG and 3NCLG showed a shoulder absorption peak at approximately 315 and 325 nm, respectively, while all the main absorption bands of the NCLG assemblies in ethanol showed a blue shift to 241 nm, 258 nm and 293 nm, respectively. This result suggests a H-like aggregation of NCLG molecules through π–π stacking. CD spectroscopy is considered to be a useful technique to monitor the supramolecular assembly. Consequently, distinct CD signals were obtained for the assemblies of the three NCLG molecules, as shown in Figure 3b. A negative Cotton effect at around 355 nm was observed for the 2NCLG gel, while a positive Cotton effect at about 300 nm and 370 nm appeared for the 3NCLG assembly. As for the 4NCLG system, a positive Cotton effect was detected at 371 nm and a negative one at 333 nm with a crossover at 348 nm. These CD bands were wider than the absorption bands of NCLG assemblies, which may be due to the chiral scattering [44]. Similar to previous reports [45], the hot solution of the three NGLG molecules was CD silent, while the distinct CD signals of the gels and precipitates supported the theory that the formation of assemblies and the chirality of ʟ-glutamic acid was transferred to the cinnamic amide moiety. In our previous work, the self-assembly of cinnamic acid derivatives was photo-responsive, while in this work, we found that the self-assembled molecules of the three gelators did not show photo-responsive properties under UV-light irradiation, in the CD spectra or in the morphology of the nanostructures. Supporting Information File 1, Figure S2 shows that the morphology of all the nanostructures remained intact, and the supramolecular chirality of the self-assembled molecules monitored by CD did not show inversion.

X-ray diffraction analysis

To understand the different structure of the three NCLG compounds, X-ray diffraction (XRD) measurements were further adopted to evaluate the assembled structures of the three gelators. As shown in Figure 4a, for 2NCLG xerogels, a series of sharp diffraction peaks were observed at 2θ = 2.51, 5.11, 10.21, 12.83 and 15.57, with a *d*-spacing ratio of 1:1/2:1/4:1/5:1/6. The diffraction pattern is related to the lamellar structure with the *d*-space of 3.50 nm. As for 4NCLG gels, the XRD pattern was almost similar to the 2NCLG assembly. A number of diffraction peaks occurred at 2θ = 2.51(100), 5.20(200), 10.23(400), 12.97(500) and 15.59(600), which clearly illustrated that the 4NCLG assembly also presented a lamellar structure. However, only 2θ = 5.56 and 10.74 diffraction peaks were observed for the 3NCLG assembly. Considering the structural similarity of the three NCLG molecules, we speculated that the first diffraction peak for 3NCLG did not appear. Then the lamellar structure with a *d*-spacing of ≈3.20 nm was obtained for the 3NCLG assemblies, although the order is lower than that of 2NCLG and
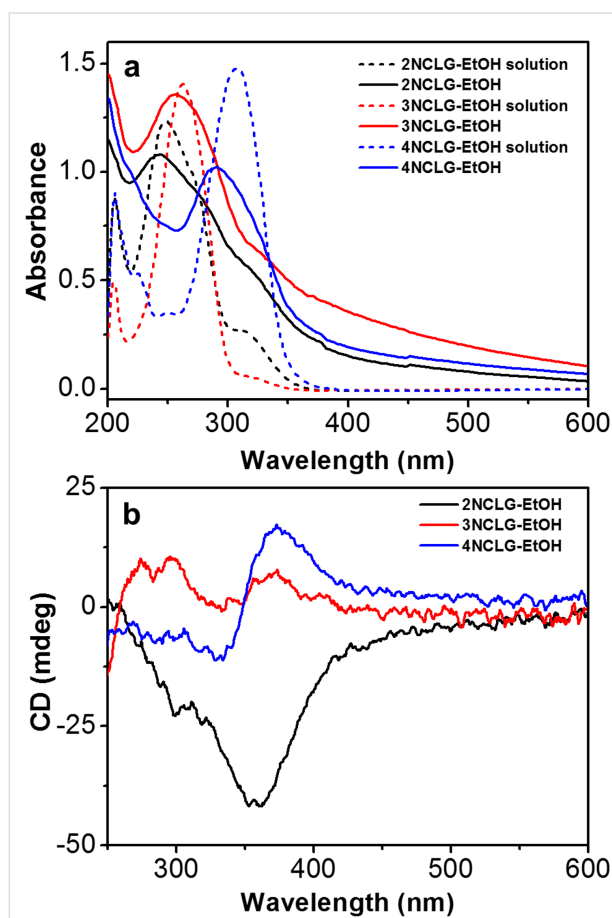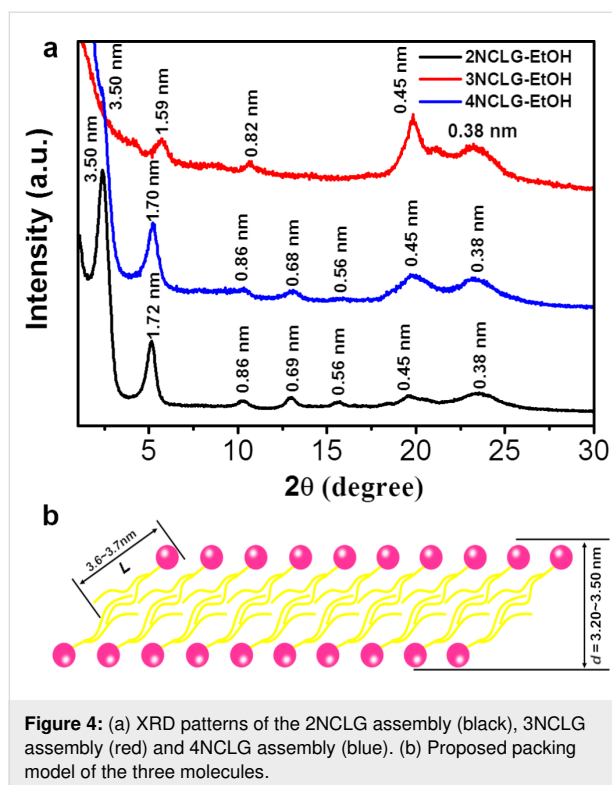
Figure 4: (a) XRD patterns of the 2NCLG assembly (black), 3NCLG assembly (red) and 4NCLG assembly (blue). (b) Proposed packing model of the three molecules.

4NCLG. Actually, the length (*L*) of the NCLG compounds is about 3.6–3.7 nm, as simulated by gaussview. The XRD pattern revealed that the *d*-spacing of the lamellar structure was 3.50 nm for 2NCLG and 4NCLG and 3.20 nm for 3NCLG, which is shorter than the length of two molecules (actually, even less than one molecular length) (Figure 4b). This result indicates that the NCLG assemblies might form a bilayer structure with high interdigitation of the alkyl chains, where the bilayer structure experiences a large tilt.

Fourier-transform infrared (FTIR) spectra

In order to elucidate the formation mechanism of the helicity and nanostructures of the self-assembled molecules, FTIR spectroscopy was employed to evaluate the formation mechanism of self-assembly. As shown in Figure 5, for the 2NCLG and 4NCLG assemblies, two absorption bands at ≈3330 cm^{-1} and ≈3284 cm^{-1} were observed, which can be ascribed to the N–H stretching vibration. While for 3NCLG, the shoulder absorption band showed a red shift to ≈3328 cm^{-1} and the main absorption band displayed a blue shift to ≈3302 cm^{-1}, which illustrated the weaker hydrogen bonding between 3NCLG molecules than that of 2NCLG and 4NCLG. The CH$_3$ and CH$_2$ stretching vibration bands of alkyl chains at ≈2955, 2920 and 2849 cm^{-1} showed no obvious change. The band at ≈1650 cm^{-1} was almost the same for all the three assemblies, which was assigned to the C=O stretching vibration of the amide I. However, the amide II band of the C–N–H bending vibration of the
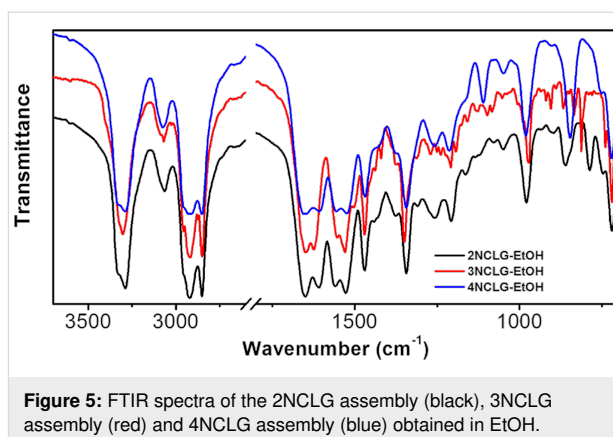

Figure 5: FTIR spectra of the 2NCLG assembly (black), 3NCLG assembly (red) and 4NCLG assembly (blue) obtained in EtOH.

2NCLG and 4NCLG assemblies was at ≈1560 cm^{-1}, while the band red-shifted to ≈1554 cm^{-1} for the 3NCLG assemblies. It also indicated that the hydrogen bonding between 3NCLG was weaker than the other two compounds. In addition, the absorption bands at ≈1520–1530 cm^{-1} and ≈1340–1350 cm^{-1} could be ascribed to the antisymmetric and symmetric stretching vibration of the nitro group, respectively. The absorption bands at ≈970–980 cm^{-1} were assigned to *trans*-vinylene C–H out-of-plane deformations and the ≈779–785 cm^{-1} absorption bands were attributed to *cis*-vinylenene C–H out-of-plane deformations. The detailed information of the FTIR spectra is given in Table 1.

Based on the data of FTIR spectra, we speculate that the helicity inversion of 3NCLG nanostructures might be due to the weak hydrogen bonding between 3NCLG molecules as compared to that of 2NCLG and 4NCLG. It also caused a relatively loose molecular packing of 3NCLG, which was also illustrated in the XRD patterns.

Next, we tried to simulate the packing model of the three NCLG compounds and two randomly adjacent molecules of NCLG were extracted from their crystals. As shown in Figure 6, it can be clearly observed that the packing model of the 2NCLG molecules was very similar to that of the 4NCLG molecules. Both of the molecules are misaligned in their crystal, which indicates that the bottom molecule is not directly below the upper one. Additionally, the length of intermolecular hydrogen bonds of 2NCLG and 4NCLG assemblies were found to be 1.2 Å and 2.0 Å, respectively. While for 3NCLG, the bottom molecule is right below the upper one and the length of intermolecular hydrogen bonds is 2.3 Å (i.e., longer than that of 2NCLG and 3NCLG). This result further demonstrated that the hydrogen bonding of the 3NCLG assembly was weaker than for the 2NCLG and 4NCLG assemblies. The difference in hydrogen bonding eventually led to different packing of the self-assembled molecules. The strong hydrogen bonding favored the

Table 1: Assignment and description of FTIR absorption bands of the three NCLG assemblies.

Frequency/cm^{-1}			Assignment and description
2NCLG	3NCLG	4NCLG	
3330	3328	3330	N–H stretching vibration
3284	3298	3284	N–H stretching vibration
2957	2955	2955	CH$_3$ asymmetric stretching vibration
2920	2920	2920	CH$_2$ asymmetric stretching vibration
2851	2849	2849	CH$_2$ symmetric stretching vibration
1651	1642	1650	amide I band (C–O) stretching vibration
1608	1610	1608	C=O stretching vibration in benzene ring
1561	1588	1559	amide II band (C–N–H) stretching vibration
1525	1549	1524	NO$_2$ antisymmetric stretch vibration
1344	1325	1344	NO$_2$ symmetric stretch vibration
979	971	979	*trans*-vinylene C–H out-of-plane deformation
785	779	none	*cis*-vinylene C–H out-of-plane deformation
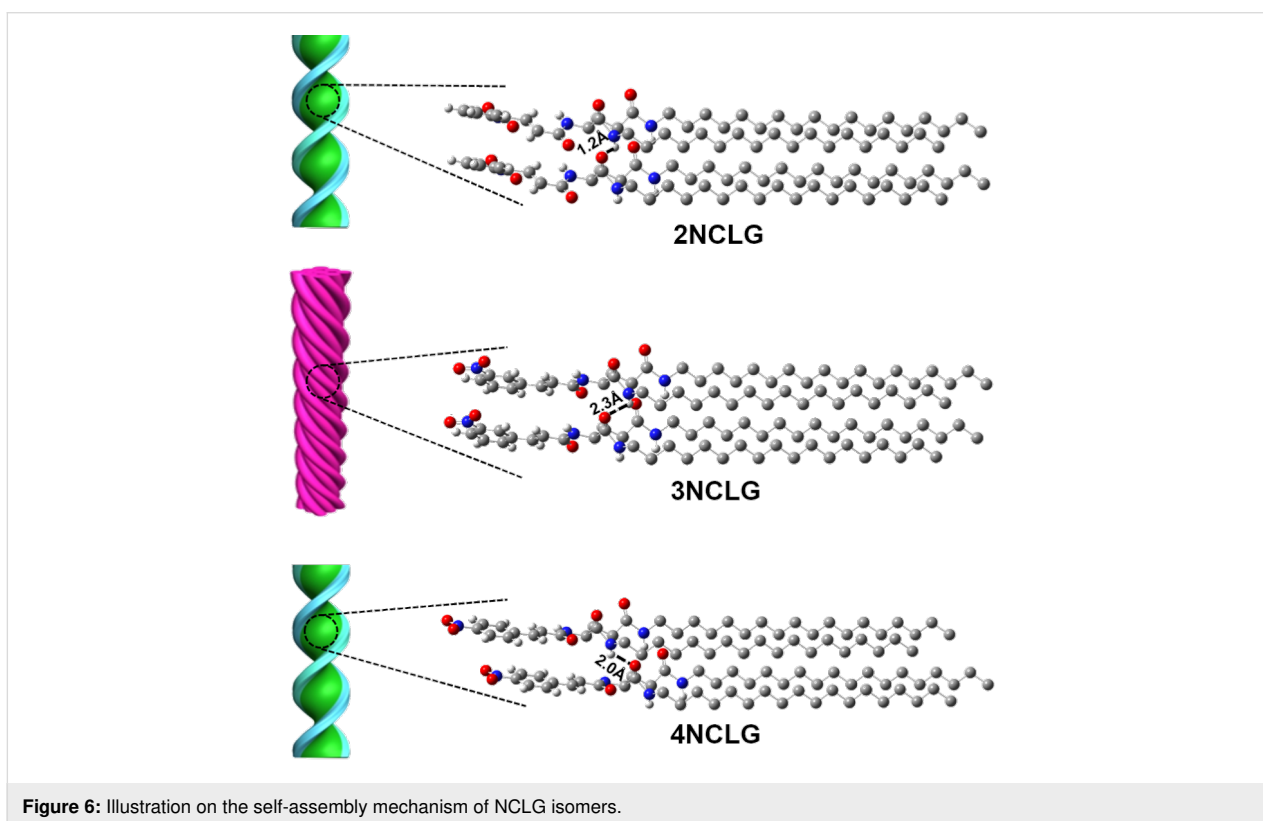
Figure 6: Illustration on the self-assembly mechanism of NCLG isomers.

formation of right-handed nanohelical structures, while the opposite chirality of the left-handed superhelix of 3NCLG was attributed to the weak hydrogen bonding in these assemblies.

Helicity inversion in self-assembly: effect of solvent

In addition, the effect of solvent on the 3NCLG self-assembly was also explored. The 3NCLG molecule could readily form transparent gels in DMF and THF when the concentration was above 8 mg/mL, while it formed a precipitate in methanol at the same concentration, likely indicating the different self-assembly behaviors of 3NCLG. Firstly, SEM was used to characterize the xerogels and dried precipitate, as shown in Figure 7. As we expected, the left-handed superhelix of 3NCLG precipitated in methanol was observed and the nanohelix (Figure 7a) further aggregated into microspherical structures (Figure 7b), which was likely due to the nanostructure of the ethanol assembly. However, both DMF organogels and THF organogels consist of
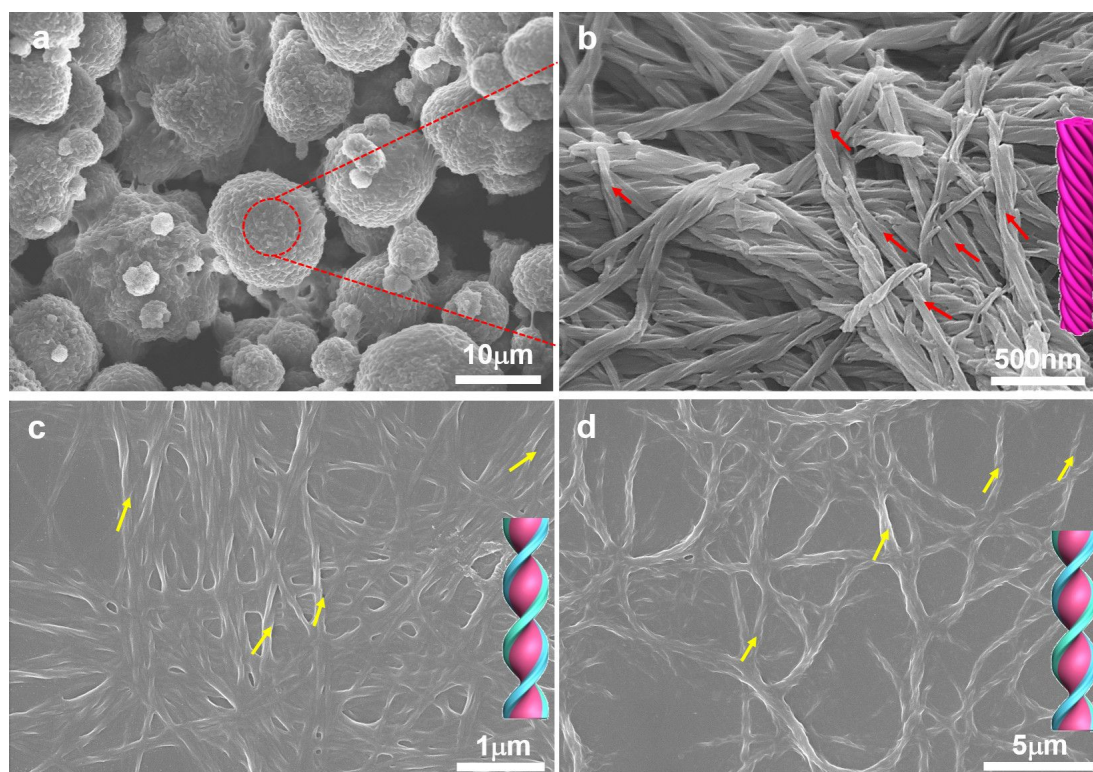
Figure 7: SEM images of the 3NCLG assembly in (a,b) MeOH, (c) DMF, and (d) THF. The concentration is 12 mg/mL.

right-handed helical nanostructures (Figure 7c and 7d). We speculated that the opposite chirality in DMF and THF assemblies to that of those in ethanol and methanol was also related to the intermolecular hydrogen bonding. Besides, 2NCLG formed right-handed nanohelix both in DMF and THF, which is the same as in ethanol. The 4NCLG gelator formed nanotube structures both in DMF and THF, which is different from the nanohelix that formed in ethanol (Supporting Information File 1, Figure S3). These results indicated that the choice of solvent had a significant effect on the formed nanostructures.

To support our speculation, the 3NCLG assemblies in DMF and THF were monitored by FTIR spectroscopy, as shown in Figure 8. We mainly focused on the N–H stretching vibration, the amide I stretching vibration and amide II bending vibration. For 3NCLG assemblies obtained in DMF and THF, the main absorption bands of the N–H stretching vibration were observed at ≈3292 cm^{-1} which showed a red shift from ≈3328 cm^{-1} compared to the N–H band of 3NCLG in ethanol. This result illustrates the stronger hydrogen bonding in 3NCLG DMF and THF assemblies. Moreover, the amide II, C–N–H bending vibration blue-shifted to ≈1562 cm^{-1} for 3NCLG in DMF and THF compared to 3NCLG in ethanol assemblies, which also proved that a relatively strong hydrogen bonding exists in the 3NCLG assemblies formed in DMF and THF. This
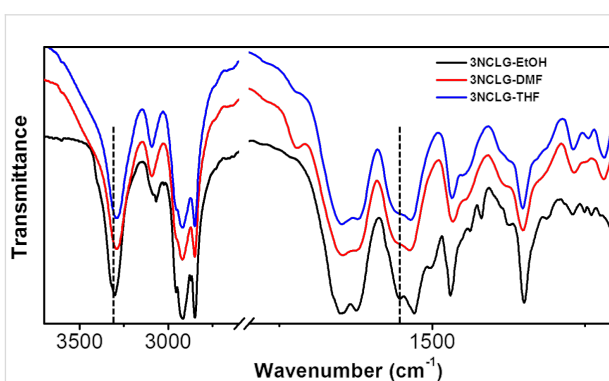
Figure 8: FTIR spectra of the 3NCLG assembly in ethanol (black), in DMF (red) and in THF (blue).

may be because the protic solvents ethanol and methanol could affect the hydrogen bonding between 3NCLG molecules. The result is that the 3NCLG self-assembled molecules obtained in ethanol and methanol present opposite helicity to those obtained in DMF and THF.

Conclusion

In conclusion, we found that the self-assembled structures of three isomeric nitrocinnamic amide derivatives showed variable helical sense depending on the substituted position of the

nitro group of the cinnamic amide. This varying helical sense occurred even though the molecular chirality of the three NCLG molecules was derived from the same source, i.e., L-glutamic acid. At the same time, the variation in the substituted position also led to different gelation abilities. Additionally, it was demonstrated that the chirality of a nanostructure can also be regulated by choice of solvents. The chiral inversion of these nanostructures was found to be related to the intermolecular hydrogen bonding of cinnamic amide amphiphiles.

Experimental
Chemicals and materials
*N*-(*tert*-Butoxycarbonyl)-L-glutamic acid (Boc-L-Glu) and 4-nitrocinnamic acid (4-NCA) were purchased from TCI. 1-Octadecylamine was bought from Alfa Aesar. 1-Hydroxy-benzotriazole (HOBt) was purchased from dams-beta. *Trans*-2-nitrocinnamic acid (2-NCA), *trans*-3-nitrocinnamic acid (3-NCA) and (*N*-(3-dimethylaminopropyl)-*N*'-ethylcarbodi-imide hydrochloride (EDC·HCl) were purchased from J&K. Dichloromethane, sodium bicarbonate (NaHCO$_3$) and hydro-chloric (HCl) and were supplied by Beijing Chemical Regent Company (China). Ethanol, *N*,*N*-dimethylformamide and tetra-hydrofuran were bought from Xilong Scientific. Milli-Q water (18.2 MΩ·cm) was used in all cases. All the chemicals and sol-vents were bought from commercial suppliers and used without further purification.

Synthesis of NCLG gelators
The synthesis and characterization of the precursors *N*,*N*'-bis-octadecyl-L-glutamic diamide (LGAm) has been reported previ-ously [46]. 2-NCA, 3-NCA and 4-NCA (0.59 g, 3.07 mmol) were respectively dispersed into 200 mL of dichloromethane with *N*,*N*'-bisoctadecyl-L-glutamine (LGAm; 1.0 g, 1.54 mmol). The mixture was then stirred for 30 min. Then, 1-hydroxy-benzotriazole (HOBt; 0.42 g, 3.07 mmol) and *N*-(3-dimethyl-aminopropyl)-*N*'-ethylcarbodiimide hydrochloride (EDC·HCl; 0.59 g, 3.07 mmol) were added to the reaction flask. The mix-ture was then stirred and heated under reflux for 3 days. The solvent was removed by filtration and the residue was washed with dichloromethane several times. The crude products were then heated to dissolve in ethanol (50 mL) and added into nearly saturated aqueous NaHCO$_3$ solution (500 mL) with stir-ring for 20 min. The sovent was then removed by filtration and the white product was washed with water. The dried product was dissolved in ethanol (50 mL) again by heating and the hot solution was then poured into aqueous HCl solution (500 mL). Finally, the dried product was purified by recrystallization four times in EtOH/THF to obtain the target compounds: 2NCLG
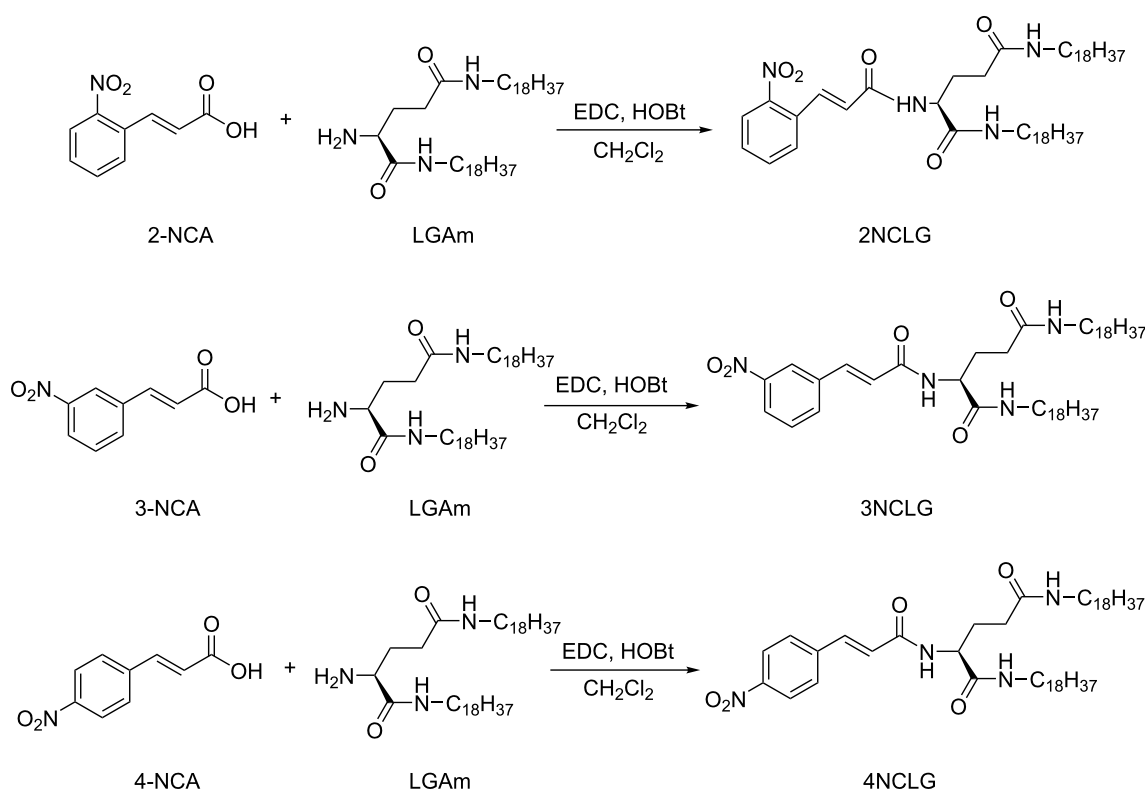
Scheme 1: Synthesis scheme of the target chiral compounds 2NCLG, 3NCLG and 4NCLG.

(0.71 g, 56% yield), 3NCLG (0.94 g, 74% yield) and 4NCLG (0.90 g, 71% yield) (Scheme 1).

2NCLG: ^{1}H NMR (500 MHz, DMSO-d_6, 100 °C, TMS) δ 0.83–0.94 (t, 6H), 1.20–1.50 (m, 60H), 1.36–1.50 (m, 4H), 1.80–1.90 (m, 1H), 1.93–2.00 (m, 1H), 2.10–2.20 (m, 2H), 3.12–3.17 (m, 4H), 4.33–4.44 (q, 1H), 6.73–6.82 (d, 1H), 7.35–7.43 (s, 1H), 7.53–7.66 (m, 2H), 7.68–7.81 (m, 3H), 7.96–8.07 (m, 2H); MALDI–TOF–MS *m/z*: [M]$^+$ calcd. for $C_{50}H_{88}N_4O_5$, 825.26; found, [M + Li]$^+$ 833.5, [M + Na]$^+$ 847.5.

3NCLG: ^{1}H NMR (500 MHz, DMSO-d_6, 100 °C, TMS) δ 0.83–0.93 (t, 6H), 1.19–1.50 (m, 60H), 1.36–1.50 (m, 4H), 1.78–1.90 (m, 1H), 1.93–2.04 (m, 1H), 2.10–2.19 (m, 2H), 3.03–3.17 (m, 4H), 4.34–4.44 (q, 1H), 6.90–7.00 (d, 1H), 7.34–7.44 (s, 1H), 7.50–7.60 (m, 2H), 7.62–7.74 (d, 1H), 7.90–8.02 (m, 2H), 8.14–8.22 (m, 1H), 8.34–8.40 (s, 1H); MALDI–TOF–MS *m/z*: [M]$^+$ calcd. for $C_{50}H_{88}N_4O_5$, 825.26 [M]$^+$; found, [M + Li]$^+$ 833.5, [M + Na]$^+$ 847.5.

4NCLG: ^{1}H NMR (500 MHz, DMSO-d_6, 100 °C, TMS) δ 0.80–0.93 (t, 6H), 1.16–1.50 (m, 60H), 1.36–1.52 (m, 4H), 1.81–1.93 (m, 1H), 1.93–2.04 (m, 1H), 2.09–2.29 (m, 2H), 3.03–3.16 (m, 4H), 4.33–4.43 (q, 1H), 6.88–6.98 (d, 1H), 7.33–7.45 (s, 1H), 7.48–7.62 (m, 2H), 7.76–7.85 (d, 2H), 7.95–8.07 (d, 1H), 8.17–8.28 (d, 2H); (MALDI–TOF–MS) *m/z*: [M]$^+$ calcd. for $C_{50}H_{88}N_4O_5$, 825.26; found, [M + Li]$^+$ 833.5, [M + Na]$^+$ 847.5.

General characterization

MALDI–TOF–MS was recorded on a Bruker Autoflex III instrument. Nuclear magnetic resonance (NMR) was characterized on a Bruker AVANCE III HD 500 machine. The gel and precipitate were cast onto single-crystal silica plates and then coated with a thin layer of Pt after drying to increase the contrast. After that, the morphology was observed with a Hitachi S-4800 FE-SEM operating at an accelerating voltage of 10 kV. UV–vis spectra were recorded with a Hitachi U-3900 spectrophotometer in quartz cuvettes (light path 0.1 mm and 1 cm). CD spectra were measured with a JASCO J-810 CD spectrophotometer in quartz cuvettes with a 0.1 mm path length over a range of 200–800 nm. XRD analysis was performed on a Rigaku D/Max-2500 X-ray diffractometer (Japan) with Cu Kα radiation (λ =1.5406 Å). The operating voltage was 40 kV and a current of 200 mA was used. The samples were cast on silicon substrates and dried in air for XRD measurements. Fourier-transform infrared (FTIR) spectroscopy was recorded with a Bruker TENSOR-27 spectrophotometer. The testing range was 400–4000 cm^{-1} and the wavenumber resolution was 4 cm^{-1} at room temperature.

Supporting Information

Supporting Information File 1
Additional experimental data.
[https://www.beilstein-journals.org/bjnano/content/supplementary/2190-4286-10-156-S1.pdf]

ORCID® iDs
Minghua Liu - https://orcid.org/0000-0002-6603-1251

References
1. Pauling, L.; Corey, R. B.; Branson, H. R. *Proc. Natl. Acad. Sci. U. S. A.* **1951,** *37,* 205–211. doi:10.1073/pnas.37.4.205
2. Watson, J. D.; Crick, F. H. C. *Nature* **1953,** *171,* 737–738. doi:10.1038/171737a0
3. Ariga, K.; Lee, M. V.; Mori, T.; Yu, X.-Y.; Hill, J. P. *Adv. Colloid Interface Sci.* **2010,** *154,* 20–29. doi:10.1016/j.cis.2010.01.005
4. Nakanishi, W.; Minami, K.; Shrestha, L. K.; Ji, Q.; Hill, J. P.; Ariga, K. *Nano Today* **2014,** *9,* 378–394. doi:10.1016/j.nantod.2014.05.002
5. Ariga, K.; Ji, Q.; Nakanishi, W.; Hill, J. P.; Aono, M. *Mater. Horiz.* **2015,** *2,* 406–413. doi:10.1039/c5mh00012b
6. Zhang, C.; Wang, S.; Huo, H.; Huang, Z.; Li, Y.; Li, B.; Yang, Y. *Chem. – Asian J.* **2013,** *8,* 709–712. doi:10.1002/asia.201201025
7. Gao, Y.; Hao, J.; Wu, J.; Zhang, X.; Hu, J.; Ju, Y. *Nanoscale* **2015,** *7,* 13568–13575. doi:10.1039/c5nr03699b
8. Gao, Y.; Hao, J.; Wu, J.; Li, Y.; Lin, Y.; Hu, J.; Ju, Y. *Soft Matter* **2016,** *12,* 8979–8982. doi:10.1039/c6sm02142e
9. Foster, J. A.; Edkins, R. M.; Cameron, G. J.; Colgin, N.; Fucke, K.; Ridgeway, S.; Crawford, A. G.; Marder, T. B.; Beeby, A.; Cobb, S. L.; Steed, J. W. *Chem. – Eur. J.* **2014,** *20,* 279–291. doi:10.1002/chem.201303153
10. Kumar, M.; Ing, N. L.; Narang, V.; Wijerathne, N. K.; Hochbaum, A. I.; Ulijn, R. V. *Nat. Chem.* **2018,** *10,* 696–703. doi:10.1038/s41557-018-0047-2
11. Goskulwad, S.; La, D. D.; Kobaisi, M. A.; Bhosale, S. V.; Bansal, V.; Vinu, A.; Ariga, K.; Bhosale, S. V. *Sci. Rep.* **2018,** *8,* 11220. doi:10.1038/s41598-018-29152-9
12. Zhao, Y.; Wang, J.; Deng, L.; Zhou, P.; Wang, S.; Wang, Y.; Xu, H.; Lu, J. R. *Langmuir* **2013,** *29,* 13457–13464. doi:10.1021/la402441w
13. Wang, Y.; Qi, W.; Huang, R.; Yang, X.; Wang, M.; Su, R.; He, Z. *J. Am. Chem. Soc.* **2015,** *137,* 7869–7880. doi:10.1021/jacs.5b03925
14. Yang, G.; Zhang, X.; Kochovski, Z.; Zhang, Y.; Dai, B.; Sakai, F.; Jiang, L.; Lu, Y.; Ballauff, M.; Li, X.; Liu, C.; Chen, G.; Jiang, M. *J. Am. Chem. Soc.* **2016,** *138,* 1932–1937. doi:10.1021/jacs.5b11733
15. Lidor-Shalev, O.; Pliatsikas, N.; Carmiel, Y.; Patsalas, P.; Mastai, Y. *ACS Nano* **2017,** *11,* 4753–4759. doi:10.1021/acsnano.7b01051
16. Karunakaran, S. C.; Cafferty, B. J.; Weigert-Muñoz, A.; Schuster, G. B.; Hud, N. V. *Angew. Chem., Int. Ed.* **2019,** *58,* 1453–1457. doi:10.1002/anie.201812808

17. Xing, P.; Tham, H. P.; Li, P.; Chen, H.; Xiang, H.; Zhao, Y. *Adv. Sci.*
    2018, *5,* 1700552. doi:10.1002/advs.201700552
18. Xing, P.; Li, Y.; Wang, Y.; Li, P.-Z.; Chen, H.; Phua, S. Z. F.; Zhao, Y.
    Angew. Chem., Int. Ed. **2018,** *57,* 7774–7779.
    doi:10.1002/anie.201802825
19. Kohno, K.; Morimoto, K.; Manabe, N.; Yajima, T.; Yamagishi, A.;
    Sato, H. *Chem. Commun.* **2012,** *48,* 3860–3862.
    doi:10.1039/c2cc18164a
20. Sethy, R.; Kumar, J.; Métivier, R.; Louis, M.; Nakatani, K.;
    Mecheri, N. M. T.; Subhakumari, A.; Thomas, K. G.; Kawai, T.;
    Nakashima, T. *Angew. Chem., Int. Ed.* **2017,** *56,* 15053–15057.
    doi:10.1002/anie.201707160
21. Gao, A.; Li, Y.; Lv, H.; Liu, D.; Zhao, N.; Ding, Q.; Cao, X.
    New J. Chem. **2017,** *41,* 7924–7931. doi:10.1039/c7nj01374d
22. Jones, C. D.; Simmons, H. T. D.; Horner, K. E.; Liu, K.;
    Thompson, R. L.; Steed, J. W. *Nat. Chem.* **2019,** *11,* 375–381.
    doi:10.1038/s41557-019-0222-0
23. Görl, D.; Zhang, X.; Stepanenko, V.; Würthner, F. *Nat. Commun.* **2015,**
    6, 7009. doi:10.1038/ncomms8009
24. Venkata Rao, K.; Miyajima, D.; Nihonyanagi, A.; Aida, T. *Nat. Chem.*
    2017, *9,* 1133–1139. doi:10.1038/nchem.2812
25. Zhang, L.; Wang, X.; Wang, T.; Liu, M. *Small* **2015,** *11,* 1025–1038.
    doi:10.1002/smll.201402075
26. Liu, M.; Zhang, L.; Wang, T. *Chem. Rev.* **2015,** *115,* 7304–7397.
    doi:10.1021/cr500671p
27. Duan, P.; Zhu, X.; Liu, M. *Chem. Commun.* **2011,** *47,* 5569–5571.
    doi:10.1039/c1cc10813a
28. Choi, J.; Majima, T. *Chem. Soc. Rev.* **2011,** *40,* 5893–5909.
    doi:10.1039/c1cs15153c
29. Pascal, S.; Besnard, C.; Zinna, F.; Di Bari, L.; Le Guennic, B.;
    Jacquemin, D.; Lacour, J. *Org. Biomol. Chem.* **2016,** *14,* 4590–4594.
    doi:10.1039/c6ob00752j
30. Kim, Y.; Li, H.; He, Y.; Chen, X.; Ma, X.; Lee, M. *Nat. Nanotechnol.*
    2017, *12,* 551–556. doi:10.1038/nnano.2017.42
31. Li, Y.; Li, B.; Fu, Y.; Lin, S.; Yang, Y. *Langmuir* **2013,** *29,* 9721–9726.
    doi:10.1021/la402174w
32. Nagata, Y.; Nishikawa, T.; Suginome, M.; Sato, S.; Sugiyama, M.;
    Porcar, L.; Martel, A.; Inoue, R.; Sato, N. *J. Am. Chem. Soc.* **2018,** *140,*
    2722–2726. doi:10.1021/jacs.7b11626
33. Fujiki, M. *J. Am. Chem. Soc.* **2000,** *122,* 3336–3343.
    doi:10.1021/ja9938581
34. Kulkarni, C.; Korevaar, P. A.; Bejagam, K. K.; Palmans, A. R. A.;
    Meijer, E. W.; George, S. J. *J. Am. Chem. Soc.* **2017,** *139,*
    13867–13875. doi:10.1021/jacs.7b07639
35. Cai, Y.; Guo, Z.; Chen, J.; Li, W.; Zhong, L.; Gao, Y.; Jiang, L.; Chi, L.;
    Tian, H.; Zhu, W.-H. *J. Am. Chem. Soc.* **2016,** *138,* 2219–2224.
    doi:10.1021/jacs.5b11580
36. Zhao, D.; van Leeuwen, T.; Cheng, J.; Feringa, B. L. *Nat. Chem.* **2017,**
    9, 250–256. doi:10.1038/nchem.2668
37. Wang, C.; Jia, G.; Zhou, J.; Li, Y.; Liu, Y.; Lu, S.; Li, C.
    Angew. Chem., Int. Ed. **2012,** *51,* 9352–9355.
    doi:10.1002/anie.201204850
38. Jiang, J.; Meng, Y.; Zhang, L.; Liu, M. *J. Am. Chem. Soc.* **2016,** *138,*
    15629–15635. doi:10.1021/jacs.6b08808
39. Yamamoto, T.; Murakami, R.; Komatsu, S.; Suginome, M.
    J. Am. Chem. Soc. **2018,** *140,* 3867–3870. doi:10.1021/jacs.8b00529
40. Shimomura, K.; Ikai, T.; Kanoh, S.; Yashima, E.; Maeda, K. *Nat. Chem.*
    2014, *6,* 429–434. doi:10.1038/nchem.1916
41. Sun, B.; Kim, Y.; Wang, Y.; Wang, H.; Kim, J.; Liu, X.; Lee, M.
    Nat. Mater. **2018,** *17,* 599–604. doi:10.1038/s41563-018-0107-4
42. Hashimoto, Y.; Nakashima, T.; Shimizu, D.; Kawai, T. *Chem. Commun.*
    2016, *52,* 5171–5174. doi:10.1039/c6cc01277a
43. Jiang, H.; Jiang, Y.; Han, J.; Zhang, L.; Liu, M. *Angew. Chem., Int. Ed.*
    2019, *58,* 785–790. doi:10.1002/anie.201811060
44. Cao, H.; Zhu, X.; Liu, M. *Angew. Chem., Int. Ed.* **2013,** *52,* 4122–4126.
    doi:10.1002/anie.201300444
45. Jin, X.; Jiang, J.; Liu, M. *ACS Nano* **2016,** *10,* 11179–11186.
    doi:10.1021/acsnano.6b06233
46. Zhu, X.; Li, Y.; Duan, P.; Liu, M. *Chem. – Eur. J.* **2010,** *16,* 8034–8040.
    doi:10.1002/chem.201000595

Layered double hydroxide/sepiolite hybrid nanoarchitectures for the controlled release of herbicides

Ediana Paula Rebitski, Margarita Darder and Pilar Aranda[*]

Abstract

In this work, organic–inorganic hybrid nanoarchitectures were prepared in a single coprecipitation step by assembling magnesium–aluminum layered double hydroxides (MgAl-LDH) and a sepiolite fibrous clay, with the simultaneous encapsulation of the herbicide 2-methyl-4-chlorophenoxyacetic acid (MCPA) as the MgAl-LDH retains its ion exchange properties. The synthetic procedure was advantageous in comparison to the incorporation of MCPA by ion exchange after the formation of the LDH/sepiolite nanoarchitecture in a previous step, as it was less time consuming and gave rise to a higher loading of MCPA. The resulting MCPA-LDH/sepiolite nanoarchitectures were characterized by various physicochemical techniques (XRD, FTIR and ^{29}Si NMR spectroscopies, CHN analysis and SEM) that revealed interactions of LDH with the sepiolite fibers through the silanol groups present on the outer surface of sepiolite, together with the intercalation of MCPA in the LDH confirmed by the increase in the basal spacing from 0.77 nm for the pristine LDH to 2.32 nm for the prepared materials. The amount of herbicide incorporated in the hybrid nanoarchitectures prepared by the single-step coprecipitation method surpassed the CEC of LDH (ca. 330 mEq/100 g), with values reaching 445 mEq/100 g LDH for certain compositions. This suggests a synergy between the inorganic solids that allows the nanoarchitecture to exhibit better adsorption properties than the separate components. Additionally, in the release assays, the herbicide incorporated in the hybrid nanoarchitectures could be completely released, which confirms its suitability for agricultural applications. In order to achieve a more controlled release of the herbicide and to act for several days on the surface of the soil, the hybrid nanoarchitectures were encapsulated in a biopolymer matrix of alginate/zein and shaped into spheres. In in vitro tests carried out in bidistilled water, a continuous release of MCPA from the bionanocomposite beads was achieved for more than a week, while the non-encapsulated materials released the 100% of MCPA in 48 h. Besides, the encapsulation may allow for better handling and transport of the herbicide.

Introduction

Nanoarchitectonics is a definition attributed to the development of materials with new functionalities based on a controlled arrangement of nanoscale structural units through their mutual interactions [1]. The term "nanoarchitectonics" coined at the "MANA" research center (Nanoscale Materials Division of the National Institute of Materials Science (NIMS) in Japan) is based on five main concepts: i) controlled self-organization, ii) chemical nanomanipulation, iii) field-induced material control, iv) new manipulations of atoms and molecules, and v) theoretical modeling and design [1,2]. Based on these premises a large number of nanoarchitectonic materials have been prepared including mesoporous solids, self-organized block-copolymers, supramolecular materials, and macromolecular systems of DNA and cells [2-5]. In this context, clay-based nanoarchitectonic materials have been developed over the years, starting from classical pillared clays and porous clay heterostructures (PCH) to more innovative materials involving the assembly of different types of nanoparticles and other species, and clays of different origin and morphology [6-11]. There are diverse methodologies and synthesis strategies to provide new functionalities to clays. Particularly useful for constructing nanoarchitectures is the use of organic–inorganic interphases as those provided by organoclays [12]. Besides typical 2D layered clays, fibrous (sepiolite, palygorskite) and tubular (halloysite, imogolite) clays are attracting growing

interest in the development of a large variety of functional nanomaterials and nanocomposites for application in diverse fields [13-15].

Sepiolite (Figure 1A) is a natural hydrated magnesium silicate with the ideal formula $[Si_{12}O_{30}Mg_8(OH,F)_4](H_2O)_4 \cdot 8H_2O$ [16,17], which exhibits high surface area and adsorption capacity due to the presence of silanol groups on the external surface of the clay fibers. These $\equiv$SiOH groups are arranged regularly along the structural edges of the fiber, being advantageous to produce functional nanoarchitectures. Thus, in recent years the number of publications related to the assembly of different types of nanoparticulated solids (e.g., metals, metal oxides, and graphene) and sepiolite or palygorskite has increased, yielding nanoplatforms useful in a large number of applications from catalysis, environmental remediation, energy production and storage to biomedicine [14,18]. The co-assembly of particles can be reached through several methods, from the direct assembly of the clay to diverse nanoparticulated solids to the in situ generation of nanoparticles in the presence of the clay [14]. One of the key points in these strategies is to reach a good disaggregation of the fibrous particles to favor the exposition of the clay surface for the assembly with other particles, either present in the medium or in the process of growing. Examples are the direct assembly of carbon nanotubes and sepi-

Figure 1: Schematic representations of (A) sepiolite and (B) layered double hydroxide structures, (C) molecular structure of 2-methyl-4-chlorophenoxyacetic acid (MCPA), and schemes of the synthesis of the hybrid MCPA-LDH/sepiolite nanoarchitectures by (D) ion exchange and (E) one-step coprecipitation.
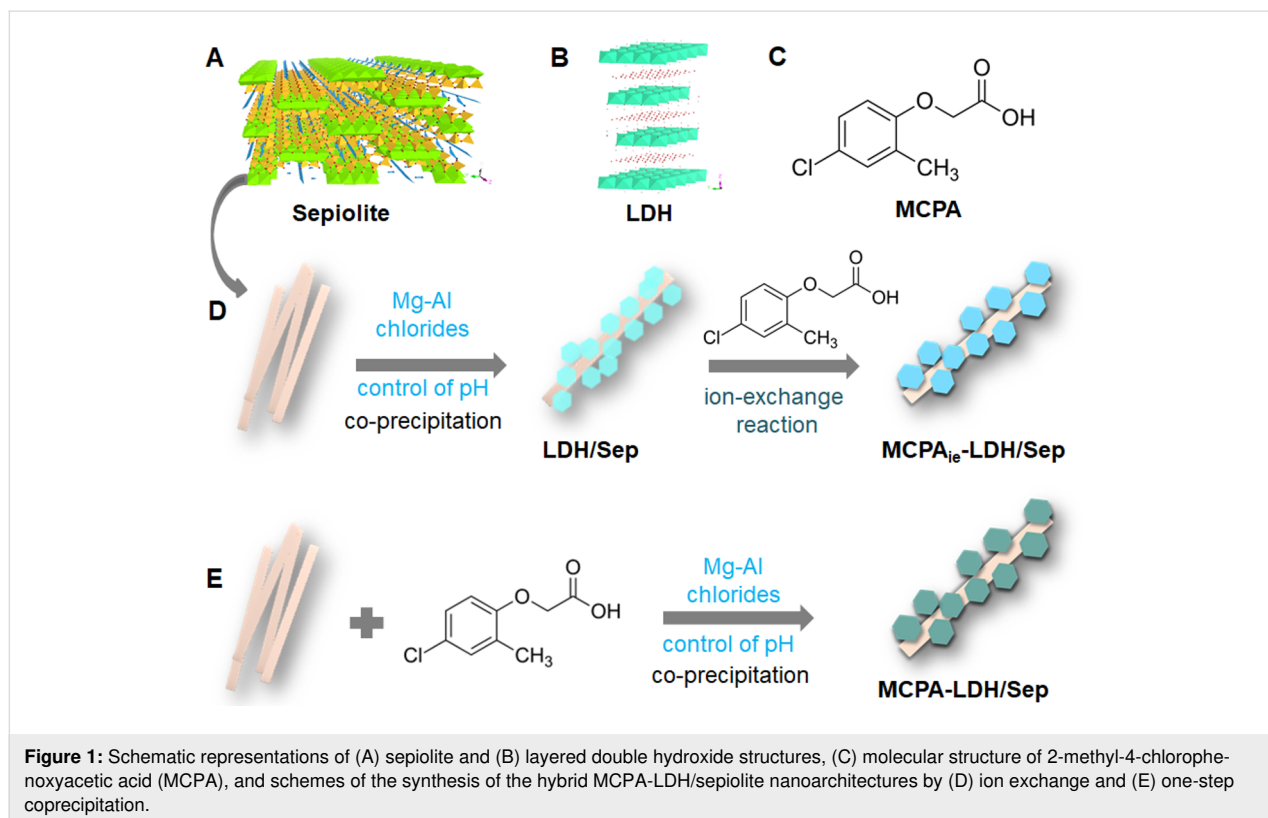
olite under ultrasonic irradiation [19] and the generation of layered titanosilicates in the presence of sepiolite [20]. In this context, the use of organic–inorganic interphases has proved highly effective to facilitate the co-assembly process, which favors the formation of more homogeneous and, in general, better organized nanoarchitectures [12].

Layered double hydroxides (LDH), often called anionic clays, are 2D solids of the general formula $[M(II)_{1-x}M(III)_x(OH)_2]^{x+}(A^{n-})_{x/n} \cdot mH_2O$ (Figure 1B), consisting of positively charged brucite-like layers that are balanced with anions and water molecules in the interlayer space [21]. Although there also exists in nature a Mg–Al layered double hydroxide, namely hydrotalcite, LDH materials can be easily prepared by coprecipitation from metal solutions at a controlled pH value. This procedure and other protocols of synthesis together with the possibility to stabilize solids involving a large variety of metal ions have provided a large variety of LDH compounds of interest in numerous applications as adsorbents of anionic pollutants, catalysts, additive of polymers, as components in diverse electrochemical devices (such as supercapacitors, sensors, and biosensors), in drug delivery and controlled-release formulations, or in non-viral gene transfection [21-26]. The fact that the stability of LDH varies with the pH value has proved advantageous in some of the above mentioned applications, in particular, for uses as host substrate in the immobilization of active species (e.g., drugs, pesticides, and DNA) for controlled-delivery applications [27-29]. LDH have been also used in the construction of different types of nanoarchitectonic materials. The used strategies included wet impregnation and layer-by-layer approaches to produce diverse type of multilayer heterostructures, e.g., ZnCr-LDH/TiO$_2$ films [30], in situ formation of the LDH in presence of other nanoparticles, e.g., sepiolite [31], and reconstruction of the LDH from parent "layered double oxides" in the presence of diverse species, e.g., silica nanoparticles [32].

Nanoarchitectonic materials involving the growth of LDH nanoparticles in the presence of fibrous clay silicates were patented several years ago [33]. Direct co-assembly of already formed particles of each component does not produce true nanoarchitectonic materials. Hence, it is necessary to grow the LDH in the presence of the fibrous clay [31]. In fact, the presence of silanol groups along the external surface of the silicate fibers act as anchoring points at which the LDH grows, forming LDH particles with their characteristic sandrose structure surrounding the clay fibers [31]. The resulting materials may show dual ion exchange behavior due to the anion and cation exchange properties of LDH and sepiolite components, respectively. This type of nanoarchitectonic materials could be of interest as adsorbents for the removal of pollutants from water,

for instance dyes [31] and, As(III) and As(V) species [34]. Moreover, they could be used as precursors for supported metal-oxide nanoparticles that could be of interest in catalysis [31]. MgAl-LDH/sepiolite nanoarchitectures have been also satisfactorily tested as nanofiller in Nafion membranes for fuel-cell applications [35]. With these premises, the current aim is to ascertain if it is possible to develop organic–inorganic hybrid materials using LDH-sepiolite nanoarchitectonic materials, as the presence of an organic counterpart could be of interest for introducing additional functionalities. Thus, in this first work, we have explored the incorporation of an anionic molecule, the herbicide 2-methyl-4-chlorophenoxyacetic acid (MCPA, Figure 1C), as it is expected to easily associate with the LDH. The resulting materials showed MCPA release properties that allow for the application of these systems for the controlled delivery of this herbicide. Hybrid nanoarchitectures were prepared profiting from the anion exchange properties of the MgAl-LDH/sepiolite and also by coprecipitation of the MgAl-LDH in the presence of an aqueous dispersion of sepiolite in which MCPA was also present. Differences in composition, structure and release behavior between the developed hybrid nanoarchitectures prepared by the two methods were examined and analyzed. In view to apply these materials in agriculture, the efficiency of formulations based on the hybrid nanoarchitectures was explored in in vitro tests of MCPA release, confirming the improvement of retention properties. For a better control in the MCPA release, the hybrid nanoarchitectures were also combined with mixtures of alginate–zein biopolymers [36] to improve the retention properties.

Results and Discussion
MCPA-LDH/sepiolite hybrid nanoarchitectures

The preparation of MgAl-LDH/sepiolite (LDH/Sep) hybrid nanoarchitectures was firstly achieved by ion exchange of MCPA herbicide anions with the chloride ions present in LDH/Sep nanoarchitectures previously prepared following the protocol reported elsewhere by Gomez-Avilés et al. [31] (Figure 1D). XRD patterns (Figure 2A) of both nanoarchitectures, as prepared and after the ion exchange reaction, showed the most intense peaks in the patterns of the pure sepiolite and the LDH. The differences in the position of the most intense peak ascribed to the LDH in the neat nanoarchitectures and most of the hybrid nanoarchitectures confirm the intercalation of MCPA in the LDH supported on the sepiolite fibers. The $d(003)$ reflection is shifted towards lower 2θ angles, resulting from an increase of the basal spacing from 0.77 to 2.15 nm, with values similar to those observed when MCPA is intercalated in the LDH [37,38]. FTIR spectra (Figure 2B) shows bands ascribed to the organic component in all of the hybrid nanoarchitectures, although, as occurs in the MCPA$_{ie}$-LDH
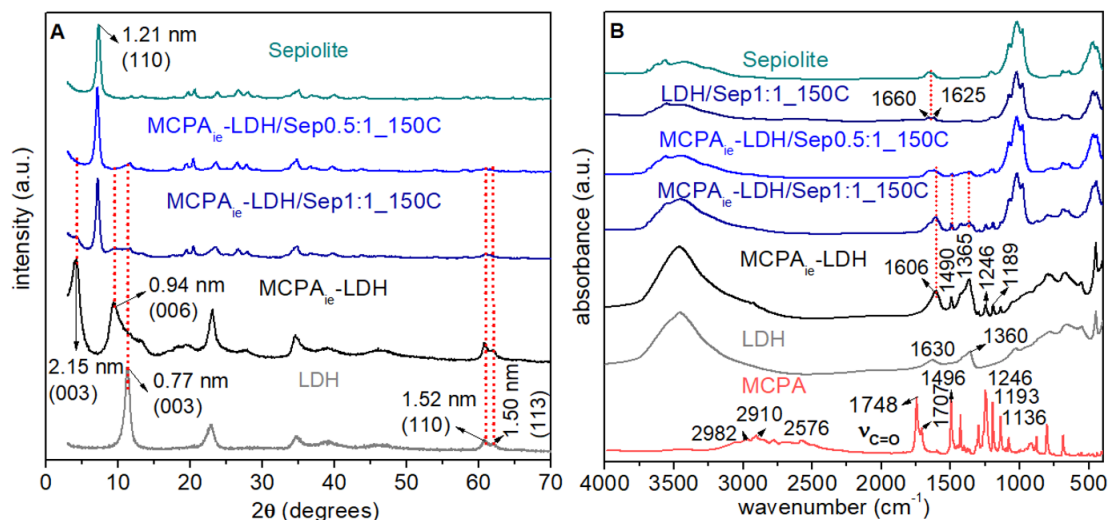
Figure 2: (A) XRD patterns and (B) FTIR spectra of individual components (sepiolite, LDH, and MCPA), MCPA$_{ie}$-LDH intercalation compound and the neat LDH/Sep and MCPA$_{ie}$-LDH/Sep hybrid nanoarchitectures.

intercalation compound, interactions with the inorganic substrate modified the position of the bands. This affects specially to the very intense bands at 1748 and 1707 cm^{-1} assigned to the $\nu_{C=O}$ vibration modes of the carboxylic group of MCPA, which are not observed in the spectra of both the MCPA$_{ie}$-LDH and the MCPA$_{ie}$-LDH/Sep1:1_150C hybrids (Figure 2B). They are shifted towards lower wavenumbers expected at around 1610 cm^{-1} (symmetric and asymmetric stretching vibration of ionized COO$^-$ groups) [39] as the carboxylic group should be present as carboxylate. In fact, the spectra show a large band in the range of 1630–1600 cm^{-1} due to the overlap of such bands with the one ascribed to δ_{HOH} vibration modes of water molecules adsorbed on the inorganic solids that appear at around 1630 cm^{-1} [40]. In addition around 1360 and 1365 cm^{-1}, in the initial LDH and in the MCPA$_{ie}$-LDH, a possible contamination with carbonate ions during the preparation of the materials is observed (Figure 2B) [41].

The amounts of MCPA present in each nanoarchitecture were determined by elemental chemical analysis (CHN) and expressed in relation to the amount of LDH present in the nanoarchitectures (Table 1). The expected anion exchange capacity (AEC) of the LDH is around 330 mEq/100 g LDH, and so the content in MCPA in the MCPA$_{ie}$-LDH intercalation compound suggests the ion exchange process is incomplete in the adopted experimental conditions. The content of MCPA in the MCPA$_{ie}$-LDH/Sep1:1_150C hybrid nanoarchitecture is similar to that of the MCPA$_{ie}$-LDH hybrid. However, the expected content for a complete ion exchange is reached in the MCPA$_{ie}$-LDH/Sep0.5:1_150C material. This effect could be ascribed to a lower degree of agglomeration of the LDH particles grown on the sepiolite fibers in the nanoarchitecture with lower content in LDH, which may favor a faster ion exchange reaction. In fact, in MCPA$_{ie}$-LDH/Sep0.3:1_150C, in which the sepiolite fibers are less covered, the amount of MCPA surpassed the ion exchange capacity of the LDH. This fact might be related to interaction of MCPA anions with hydrogen atoms of the silanol groups on the surface of sepiolite, acting as new points for MCPA adsorption. In fact, sepiolite may adsorb MCPA up to approx. 100 mg of MCPA per gram of sepiolite (see Figure S1, Supporting Information File 1).

Figure 3 shows images obtained by FE-SEM and TEM from the neat sepiolite and from the hybrid nanoarchitectures. The

Table 1: Amounts of MCPA in mEq/100 g of the hybrid and materials prepared by the ion exchange method.

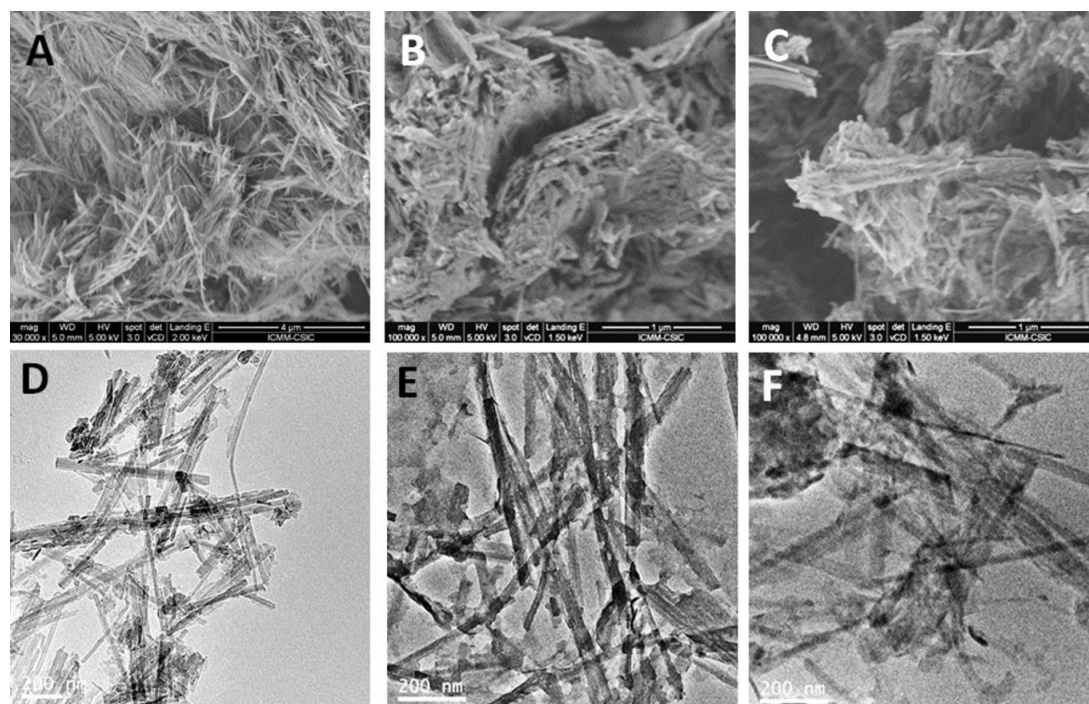| sample	LDH/Sep real ratio	MCPA-LDH/Sep real ratio	mEq of MCPA/100 g of LDH
MCPA$_{ie}$-LDH	—	—	278
MCPA$_{ie}$-LDH/Sep1:1_150C	0.94:1	0.90:1	269
MCPA$_{ie}$-LDH/Sep0.5:1_150C	0.47:1	0.45:1	325
MCPA$_{ie}$-LDH/Sep0.3:1_150C	0.28:1	0.27:1	452

Figure 3: FE-SEM images of (A) sepiolite, (B) LDH/Sep1:1_150C and (C) MCPA$_{ie}$-LDH/Sep1:1_150C nanoarchitectures; TEM images of (D) LDH/Sep0.5:1_150C, and the LDH/Sep1:1_150C nanoarchitecture (E) before and (F) after the ion exchange treatment with MCPA.

FE-SEM images show that the sepiolite fibers appear covered and compacted after the coprecipitation process to produce the corresponding nanoarchitecture. The aspect of the as prepared material and the material recovered after the intercalation of MCPA in the LDH component does not vary significantly. This fact is confirmed by TEM (Figure 3E,F), where it is possible to distinguish the presence of small flat particles attached to the fibers in both nanoarchitectures. These images also confirm that the ion exchange treatment is in fact a topotactic intercalation process that does not affect the nature of the LDH/sepiolite nanoarchitecture, confirming also the stability of this type of materials. In addition, FE-SEM and TEM images (Figure S2, Supporting Information File 1) show that the starting LDH and the MCPA$_{ie}$-LDH material exhibit small and uniform particles around 100 nm in diameter.

MCPA-LDH/sepiolite hybrid nanoarchitectures prepared via coprecipitation

MCPA-LDH intercalation compounds can be also produced by coprecipitation of the LDH in the presence of sepiolite and MCPA. The high pH value during the formation of MgAl-LDH facilitates the incorporation of MCPA as charge-compensating interlayer anion. The amount of adsorbed MCPA varies with the LDH/sepiolite ratio in the hybrid nanoarchitecture. Unexpectedly, large amounts of MCPA are taken up when the amount of LDH is reduced (Table 2). Moreover, it seems that the presence of large amounts of MCPA is accompanied by a lower yield of assembled LDH particles in the nanoarchitecture, which can be reduced to half for nanoarchitectures with a theoretical LDH/sepiolite composition of 0.5:1. In most of the prepared hybrid nanoarchitectures, the amount of MCPA exceeds the anionic exchange capacity of the LDH (ca. 330 mEq/100 g), which suggests that a part of the MCPA is adsorbed by another mechanism, perhaps on the external surface of the sepiolite clay or in interaction with the clay and the LDH particles. We have confirmed that at the pH value used in the synthesis process there is no precipitation of Al-MCPA or Mg-MCPA salts, although at lower pH values it is possible to produce precipitates in the presence of Al^{3+} ions. As reported in previous studies [42] and mentioned above, it has been demonstrated that sepiolite does not absorb large amounts of MCPA. However, we have observed that the adsorption of MCPA on sepiolite increases in the presence of Mg^{2+} and Al^{3+} salts at pH values below those required for the precipitation of the LDH (Table S1, Supporting Information File 1). This might occur during the coprecipitation of the LDH in the presence of MCPA. Given that this synthesis involves an organic molecule, the hybrid nanoarchitectures were heat-treated at 150 °C as in [31], and also at a lower temperature of 60 °C. Both thermal treatments resulted in similar materials, showing that lower temperatures could be used when less stable organic molecules are involved.

Table 2: LDH yield, LDH/Sep ratio and amount of MCPA incorporated in the hybrid nanoarchitectures prepared via coprecipitation.

sample	LDH yield (%)	LDH/Sep real ratio	mEq MCPA/100 g LDH
MCPA-LDH	89.7	—	303
MCPA-DH/Sep2:1_60C	84.0	1.68:1	336
MCPA-LDH/Sep2:1_150C	82.0	1.64:1	356
MCPA-LDH/Sep1:1_60C	81.0	0.81:1	385
MCPA-LDH/Sep1:1_150C	78.0	0.78:1	421
MCPA-LDH/Sep0.5:1_60C	78.0	0.39:1	433
MCPA-LDH/Sep0.5:1_150C	77.0	0.38:1	445
MCPA-LDH/Sep0.3:1_60C	54.4	0.18:1	1266
MCPA-LDH/Sep0.3:1_150C	41.4	0.19:1	1180

XRD patterns of the hybrid nanoarchitectures (Figure 4) confirmed that in all cases MCPA is intercalated in the interlayer space of the coprecipitated LDH, as indicated by the presence of the $d(003)$ reflection peak characteristic of the LDH structure at a 2θ angle around 4.5°. From that reflection, basal spacing values of 2.32 nm are deduced in the LDH present in the hybrid nanoarchitectures, which is similar to that determined in MCPA-LDH intercalation compounds prepared by both ion exchange and coprecipitation. The structure of sepiolite is maintained in all samples, independent of the proportion of LDH, while the most intense peak of the LDH decreased in intensity at the same time that the proportion of LDH/sepiolite is lowered. In addition, the LDH peaks $d(110)$ and $d(113)$ are observed in all the nanoarchitectures formed, confirming the formation of the LDH structure for all the studied LDH/sepiolite ratios.

The formation of true hybrid nanoarchitectures was confirmed by infrared and NMR spectroscopy. For this purpose, the spec-

tral region of the OH vibration bands of the Si–OH and Mg–OH groups was analyzed in detail. These bands appear at approximately 3720 and 3680 cm^{-1}, respectively, in the IR spectrum of pure sepiolite [43]. The band attributed to the OH vibration of the Mg–OH groups is observed in the hybrid nanoarchitectures with apparently the same intensity. In contrast, the intensity of the band at 3720 cm^{-1} associated with vibrations of Si–OH groups is attenuated in the hybrid nanoarchitectures, indicating that part of those silanol groups are in interaction with other species as observed in other modifications of sepiolite [44-47]. This perturbation originates from hydrogen interactions between the silanol groups of the silicate and LDH particles, inducing a shift of the associated IR band towards lower frequencies. In fact, the band practically becomes imperceptible, mainly in the MCPA-LDH/Sep hybrid nanoarchitectures after thermal treatment at the highest temperature (Figure 5A). Also, this band is not observed in samples containing the highest proportions of LDH with respect to sepiolite, where the LDH particles may be completely covering the sepiolite fibers. The chemical interactions between the LDH and sepiolite components in the LDH/Sep hybrid nanoarchitectures prepared by coprecipitation were also corroborated by ^{29}Si MAS NMR (Figure 5B). As previously reported [31], the spectrum of MgAl-LDH/Sep is different from that of pure sepiolite. The spectrum of neat sepiolite shows three Q^3 signals and one Q^2 signal. The latter one is associated with the silanol groups [48]. In the spectra of the MCPA-LDH/Sep0.5:1_60C and MCPA-LDH/Sep0.5:1_150C hybrid nanoarchitectures the Q^3 signals are slightly shifted to values around −92.3, −94.8 and −98.4 ppm, while the Q^2 signal is practically not detected (Figure 5B). In addition, a new Q^3 signal, is observed at −96.6 ppm, which could be associated with a new type of Si environment coming from the condensation of the silanol –OH groups on the surface of the sepiolite fibers with the hydroxy groups of the co-precipitated LDH particles, as previously reported for neat LDH/sepiolite nanoarchitectures [31]. The small differences observed in the FTIR and NMR spectra of hybrid nanoarchitectures prepared by consolidation at 60 and 150 °C
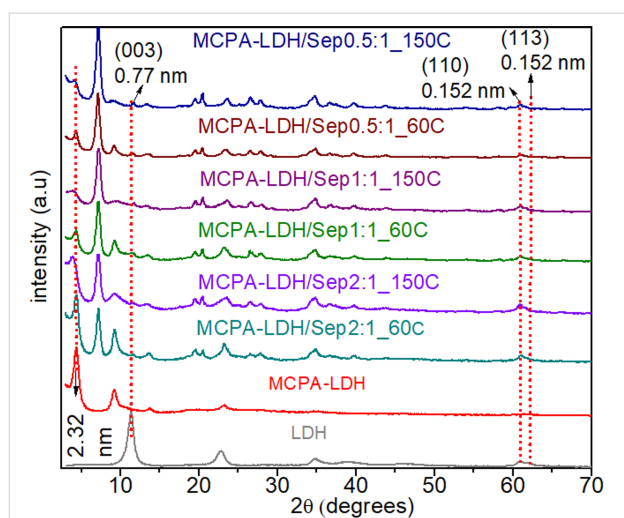
Figure 4: XRD patterns of hybrid nanoarchitectures prepared by coprecipitation of MgAl-LDH in the presence of sepiolite and MCPA at different theoretical LDH/sepiolite ratios (*x*:1).

Figure 5: (A) FTIR (3800 to 3600 cm^{-1} region) and (B) ^{29}Si MAS NMR spectra of neat sepiolite and hybrid nanoarchitectures prepared by coprecipitation of the MgAl-LDH in the presence of sepiolite and MCPA at different theoretical LDH/sepiolite ratios (*x*:1).
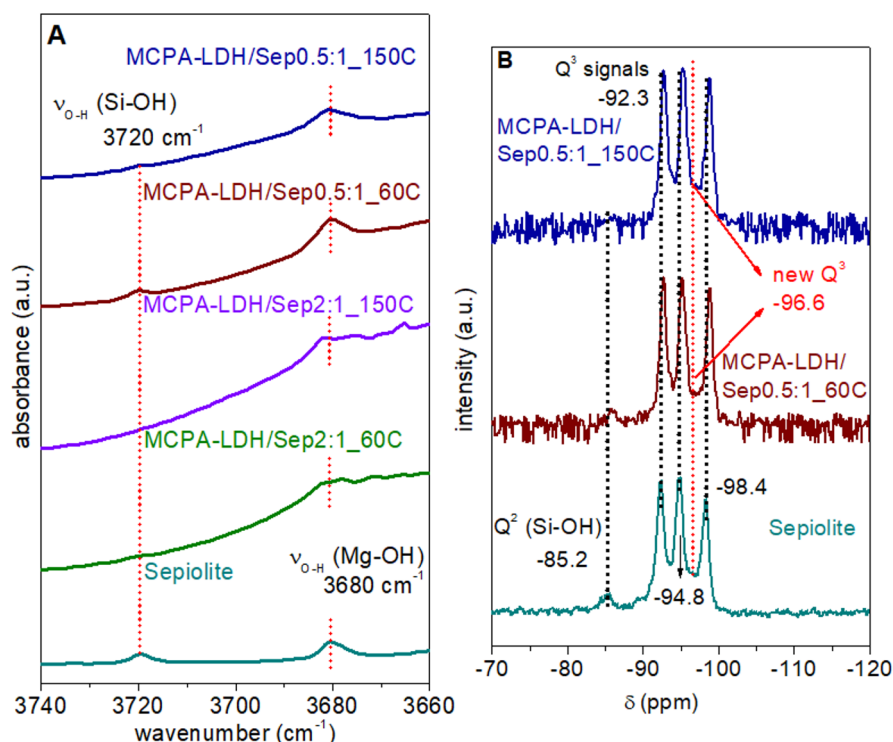
indicate the high stability of the prepared materials after both thermal treatments. This confirms the possibility of consolidating the hybrid nanoarchitectures at mild temperatures below 150 °C. FTIR spectroscopy also confirms the incorporation of MCPA through interaction with the LDH (Figure S3, Supporting Information File 1), as discussed for the hybrid nanoarchitectures prepared by ion exchange.

The FE-SEM images of the MCPA-LDH/Sep hybrid nanoarchitectures (Figure 6) confirm that sepiolite fibers are covered by LDH nanoparticles, which are more agglomerated in the hybrid nanoarchitectures containing higher amounts of LDH. In the structures with lower LDH content, the layered solid grows in particles of smaller size and TEM images clearly confirm that they remain attached to the silicate fibers (Figure 6F).

In vitro release of MCPA in water

The release of MCPA from the hybrid nanoarchitectures was evaluated in in vitro tests in deionized water (pH approx. 5.5), simulating the conditions of rain. The kinetics of the release depends on the nanoarchitecture composition (Figure 7), but in all cases an initial fast release is observed, followed by another zone showing slower kinetics. These two regimes could be due to the initial release of more accessible MCPA, most likely related to interparticle diffusion, while the second zone could be

due to diffusion of the intercalated herbicide molecules. The MCPA-LDH system showed the slowest release of MCPA, with around 35% lixiviated from the inorganic host after 8 h, being this value similar to those found for the release from MCPA$_{ie}$-LDH [49]. Other studies reported a complete release of the herbicide in a similar time [50]. In contrast, the release from the MCPA$_{ie}$-LDH/Sep1:1_150C hybrid nanoarchitecture, where the MCPA was incorporated by ion exchange showed a very rapid release, with practically 75% of the MCPA leached after the first 8 h. This result clearly confirms that the presence of the LDH as small nanoparticles attached to the fibrous clay may favor a rapid release of the intercalated species. In the hybrid nanoarchitectures prepared by coprecipitation and the same LDH/sepiolite ratio the release is slower. The slowest release occurred from the nanoarchitecture consolidated at 60 °C. A similar trend was observed when comparing the release from coprecipitated hybrid nanoarchitectures of other compositions consolidated at 60 and 150 °C (Figure S4, Supporting Information File 1). There is no clear explanation yet for this behavior. It might be ascribed to the different degree of hydration or the presence of OH$^-$ species in the systems consolidated at lower temperature, which determines a different mechanism of attack of H$^+$ to produce the degradation of the LDH and the subsequent release of entrapped MCPA. The fastest kinetics is observed with the lowest LDH content (Figure 7 and Figure S4,
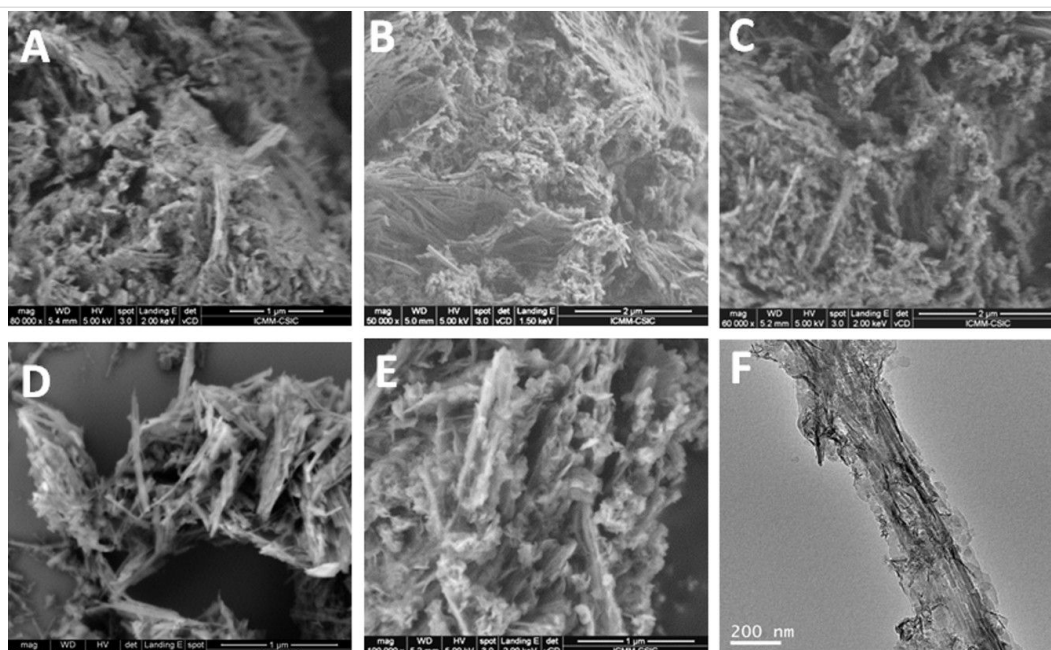
Figure 6: FE-SEM images of (A) MCPA-LDH/Sep2:1_150C, (B) MCPA-LDH/Sep1:1_150C, (C) MCPA-LDH/Sep0.5:1_60C, (D) LDH/Sep0.5:1_150C, and (E) MCPA-LDH/Sep0.5:1_150C hybrid nanoarchitectures prepared by coprecipitation from different LDH/sepiolite ratios; (F) TEM image of the MCPA-LDH/Sep0.5:1_60C hybrid nanoarchitecture.
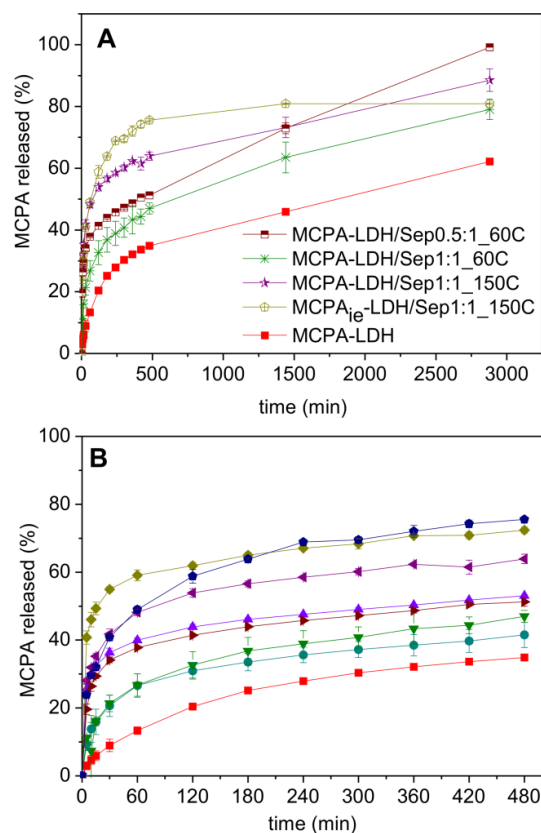
Figure 7: (A) In vitro release of MCPA from the hybrid formulations in deionized water (pH approx. 5.5), and (B) zoom of the same graph showing the release behavior in the first 500 min of the study.

Supporting Information File 1). This behavior is probably related to the fact that size and aggregation state of the LDH nanoparticles increase with the LDH content in the nanoarchitecture, slowing down the kinetics of the process. The measured release after 8 h of contact with water varies with values of around 50% for nanoarchitectures consolidated at 60 °C (e.g., 43 and 51% for the 1:1 and 0.5:1 LDH/Sep nanoarchitectures, respectively) to around 70% for nanoarchitectures consolidated at 150 °C (e.g., 73% for MCPA-LDH/Sep1.1_150C, Figure 7B). After 8 h the release evolves differently towards a steady state, and after 48 h only the MCPA-LDH/Sep0.5:1_60C system completely released MCPA. These results confirm that the release of the herbicide from the hybrid nanoarchitectures may be tuned by selecting the specific composition and characteristics of the system, which makes them of interest for agricultural purposes.

Given that the amount of initial release of MCPA in all the formulations is quite high, the encapsulation of the hybrid nanoarchitectures in a protective biopolymer matrix was proposed to afford a better control over the release of the herbicide. In a previous study [49], a biopolymer mixture of alginate and zein incorporating the MCPA$_{ie}$-LDH hybrid prepared by ion exchange was able to reduce the initial release of MCPA by approximately 10–15% in the first 8 h. In the current work, the MCPA-LDH/Sep0.5:1_60C nanoarchitecture was selected, as it releases 100% of the herbicide after a period of 48 h. The hybrid was dispersed in an alginate/zein matrix, with 17% of

zein with respect to the total biopolymer mass. The mixture was added dropwise to a $CaCl_2$ solution to produce bionanocomposite beads [36,49]. The encapsulation efficiency of the prepared bionanocomposite material was 51.2%, similar to that of other release systems based on the same encapsulation matrix [36].

In the bionanocomposite beads, the hydrophilicity of alginate is reduced by the presence of zein, contributing to a better control over the herbicide release. Figure 8 shows that release of MCPA from the A-Z@MCPA-LDH/Sep system is slower in the first 8 h than release from non-encapsulated systems, reaching approx. 40% after 48 h. A continuous study of the A-Z@MCPA-LDH/Sep0.5:1_60C formulation over 8 days was carried out, showing a release close to 70% in the presence of the biopolymer matrix. This result suggests that the bionanocomposite could reach 100% of MCPA release after about two weeks.

Figure 8: (A) In vitro release of MCPA encapsulated in the A-Z@MCPA-LDH/Sep bionanocomposite system over a period of 8 days in deionized water (pH 5.5), and (B) zoom of the same graph in the first 48 h of release.
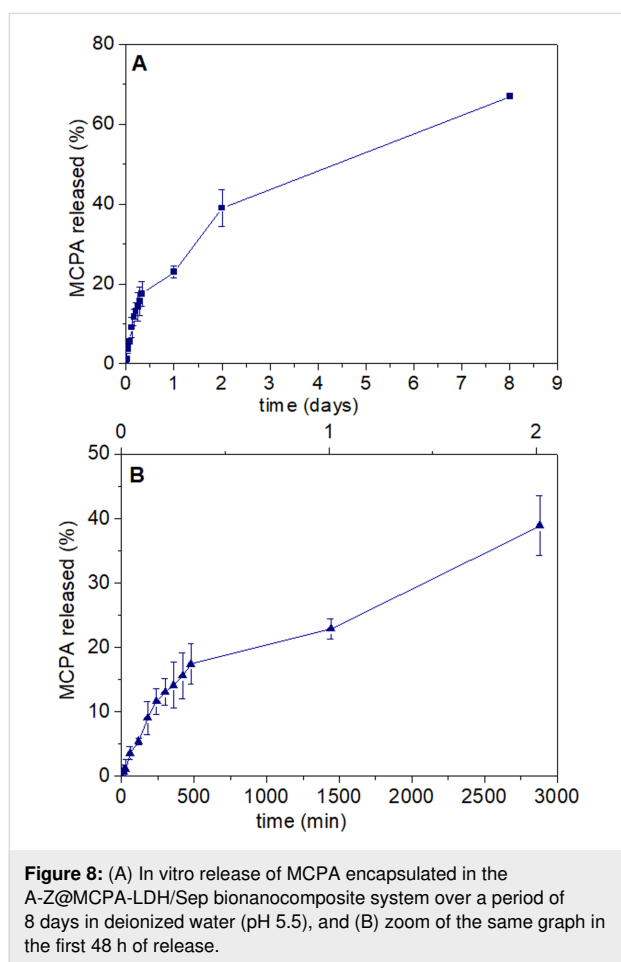
Conclusion

This work reports on two procedures to prepare hybrid LDH/sepiolite nanoarchitectonic materials in which the herbicide MCPA is intercalated in the inorganic layered compound. The stability of the prepared MgAl-LDH/sepiolite nanoarchitectures allows for the ion exchange of interlayer anions by the anionic MCPA species. Moreover, it is possible to produce hybrid MCPA-LDH/sepiolite nanoarchitectures in a single coprecipitation step. This last approach allows for the incorporation of higher amounts of MCPA than the ion exchange reaction with the additional advantage of being less time-consuming. FTIR and ^{29}Si NMR spectroscopic analysis corroborated that the LDH particles in the coprecipitated hybrid nanoarchitecture are chemically linked to the silanol groups that cover the silicate fibers, producing stable systems even using consolidation temperatures as low as 60 °C. The developed hybrid nanoarchitectures have been tested in vitro as systems for the controlled release of the incorporated organic species MCPA. In vitro tests carried out in deionized water showed that the herbicide release kinetics depended on the nanoarchitecture composition and the method of preparation. The materials with higher LHD content showed slower release rates. The herbicide could be completely released from the hybrid nanoarchitectures, confirming their suitability for the controlled release of pesticides in agriculture. To better control the release process, the hybrid nanoarchitectures can be encapsulated in a protective biopolymer matrix, such as alginate–zein, which delays the complete release up to several weeks. The presence of sepiolite in the hybrid nanoarchitectures could associate other active species to the formulation, profiting from the high capacity of this clay to adsorb numerous types of molecules. Finally, it is worthy to mention that the coprecipitation method opens the way to the production of other hybrid systems incorporating diverse organic and polymeric anionic species associated with nanometric LDH particles for controlled drug delivery and other applications.

Experimental
Starting reagents and materials
4-Chloro-2-methylphenoxyacetic acid (MCPA) was purchased from Sigma-Aldrich (M_W 200.62 g·mol^{-1}, 97% purity). Sepiolite from Vallecas-Vicálvaro (Spain) was provided by TOLSA S.A. as Pangel® S9, a commercial product of rheological grade that contains more than 95% pure sepiolite. Zein (Z) from maize, and alginate (A) were purchased from Sigma-Aldrich. Absolute ethanol was supplied by Panreac. Aqueous solutions were prepared from chemicals of analytical reagent grade: $AlCl_3 \cdot 6H_2O$ (>99%, Fluka), $MgCl_2 \cdot 6H_2O$ (99%, Carlo Erba), NaOH (≥98%, Fluka), $ZnCl_2$ (>98%, Fluka). Deionized water (resistivity = 18.2 MΩ·cm) was obtained with a Maxima Ultrapure Water from Elga.

Preparation of MCPA-LDH/sepiolite nanoarchitectures
MgAl-LDH/sepiolite (LDH/Sep) nanoarchitectures were prepared following the protocol described elsewhere [31]. In brief,

a solution of $MgCl_2$ and $AlCl_3$ (9.34 mmol and 4.68 mmol) was drop-wise added to a dispersion of 4 g of sepiolite in 350 mL of deionized water at a rate of 2 mL/min, while kept under N_2 flux to assure the removal of CO_2. At the same time, a solution of 1 M NaOH was added with the 800 Dosino automatic dispenser from Metrohm in order to maintain the pH value constant at 9. After the addition of the salts to reach LDH/sepiolite products with 1:1, 0.5:1 or 0.3:1 theoretical weight ratio, the system was kept under magnetic stirring under a N_2 flux for 24 h. The resulting LDH/Sep products were recovered by centrifugation, washed three times with deionized water, and dried at 150 °C under N_2 flux (100 mL/min) for 3 h to consolidate the nanoarchitectures. For comparison, a LDH solid was prepared in the same way but without the presence of sepiolite. The intercalation of MCPA by ion exchange was performed using a solution of the herbicide prepared by dissolving 1.5 g of MCPA in 125 mL of ionized water and adjusting its pH value to 7 with 1 M NaOH to assure the presence of the organic molecule as an anion. This solution was slowly added to a dispersion prepared with 0.5 g of the selected LDH/Sep nanoarchitecture, or the LDH, in 125 mL of deionized water, with a final pH of approximately 9. The system was then kept under magnetic stirring and N_2 flux for 72 h at room temperature. Subsequently, the solid was recovered by centrifugation, washed three times with water and dried at 60 °C overnight. The resulting materials were labeled as $MCPA_{ie}$-LDH, $MCPA_{ie}$-LDH/Sep1:1_150C, $MCPA_{ie}$-LDH/Sep0.5:1_150C and $MCPA_{ie}$-LDH/Sep0.3:1_150C.

In the same way, MCPA-LDH/sepiolite hybrid nanoarchitectures were prepared in one step by coprecipitation of the MgAl-LDH in presence of both sepiolite and MCPA. LDH formed on the surface of sepiolite fibers with intercalated herbicide anions instead of Cl^- ions. To this end, 4 g of sepiolite and 2.5 g of MCPA were dissolved in 350 mL of decarbonated deionized water. Again, the solution of $MgCl_2$ and $AlCl_3$ was varied in order to obtain hybrid nanoarchitectures with 2:1, 1:1, 0.5:1 and 0.3:1 theoretical LDH/Sep weight ratio. After the addition of the salts, the system was kept under magnetic stirring and N_2 flux for 24 h. The solid was washed and recovered by centrifugation and then subjected to a controlled heat treatment at 60 or 150 °C for 3 h under air flow (100 mL/min) to consolidate the nanoarchitectures prepared from MCPA-LDH/Sep. The hybrid nanoarchitectures were labeled as MCPA-LDH/Sep2:1_60, MCPA-LDH/Sep2:1_150C, MCPA-LDH/Sep1:1_60C, MCPA-LDH/Sep1:1_150C, MCPA-LDH/Sep0.5:1_60C and MCPA-LDH/Sep0.5:1_150C, MCPA-LDH/Sep0.3:1_60C and MCPA-LDH/Sep0.3:1_150C. Following a similar protocol, the LDH was also coprecipitated in the presence of only MCPA to produce the corresponding MCPA-LDH intercalated material, which in this case was dried at 60 °C.

Preparation of alginate–zein bionanocomposite beads

Alginate/zein beads were prepared following the following procedure adapted from Alcântara and co-workers [36]: i) The required amount of alginate to achieve a final total concentration of 2% in biopolymers was dissolved in 83 mL of water previously heated at 60 °C; ii) the required amount of zein (17% of the total biopolymer mass) and 34 mg of MCPA or the required amount of the MCPA-LDH or MCPA-LDH/Sep hybrids containing 34 mg of MCPA were incorporated into 20 mL of ethanol–water (80%,v/v); iii) the mixture was homogenized, and then slowly added to an alginate solution under magnetic stirring for approximately 30 min; iv) the formed gel was poured with a burette into a 5% $CaCl_2$ solution to form the bionanocomposite beads, which were kept under constant stirring for 15 min. At the end of the process, the beads were washed with deionized water to remove residual Ca^{2+} ions and finally dried at 40 °C overnight. In this way, the following alginate–zein (A-Z) bionanocomposite beads were prepared: A-Z@MCPA-LDH and A-Z@MCPA-LDH/Sep0.5:1_60C, incorporating the intercalation compound or the hybrid nanoarchitecture, respectively.

Characterization

Powder X-ray diffraction (XRD) data were collected on a Bruker D8 Advance diffractometer using a Cu Kα source, with a 2θ scan step of $2°·min^{-1}$ between 2 and 70°. The amount of the MCPA herbicide incorporated into the MCPA-LDH intercalation compounds and the MCPA-LDH/Sep hybrid nanoarchitectures was determined by CHN elemental chemical analysis using a LECO-CHNS-932 analyzer. Fourier transform infrared spectra (FTIR) were recorded from 4000 to 400 cm^{-1} with 2 cm^{-1} resolution in a Bruker IFS 66V-S spectrometer. Samples were prepared as pellets diluted in KBr or as pure samples pressed to form a tablet. ^{29}Si solid-state MAS spectroscopy at 79.49 MHz was carried out on a BRUKER AV-400-W spectrometer equipped with a 4 mm MAS NMR probe, with the samples rotating at a rate of approximately 10 kHz and using a π/2 pulse of recycle delay of 5.9 μs and 5.0 s. Chemical shifts are referenced to tetramethylsilane (TMS) at δ = 0 ppm. Surface morphology of the samples was studied with the field-emision scanning electronic microscope (FE-SEM) FEI-NOVA NanoSEM 230, and TEM images were performed on a JEOL 2100F STEM 200 kV microscope.

Release of MCPA in water

The release of MCPA from the MCPA-LDH hybrid, MCPA-LDH/Sep nanoarchitectures and the A-Z bionanocomposite materials was performed in 100 mL deionized water at pH 5.5, with the addition of the required quantity of material to provide 20 mg of MCPA. The experiment was maintained at room tem-

perature under slow magnetic stirring. At predetermined times, aliquots of 3 mL were analyzed and evaluated by UV spectrophotometry at 279 nm [51] to determine the concentration of the released herbicide. After the analysis, the collected solution was returned to the initial solution to keep the volume constant. All experiments were performed in triplicate.

Supporting Information

Supporting Information File 1
Additional experimental data.
[https://www.beilstein-journals.org/bjnano/content/
supplementary/2190-4286-10-163-S1.pdf]

Acknowledgements

ORCID® iDs
Ediana Paula Rebitski - https://orcid.org/0000-0003-4401-9347
Margarita Darder - https://orcid.org/0000-0002-7032-0419
Pilar Aranda - https://orcid.org/0000-0003-2196-0476

References

1. Aono, M.; Bando, Y.; Ariga, K. *Adv. Mater. (Weinheim, Ger.)* **2012,** *24,* 150–151. doi:10.1002/adma.201104614
2. Komiyama, M.; Yoshimoto, K.; Sisido, M.; Ariga, K. *Bull. Chem. Soc. Jpn.* **2017,** *90,* 967–1004. doi:10.1246/bcsj.20170156
3. Ariga, K., Ed. *Manipulation of Nanoscale Materials: An Introduction to Nanoarchitectonics;* Nanoscience & Nanotechnology Series, Vol. 24; Royal Society of Chemistry: Cambridge, United Kingdom, 2012. doi:10.1039/9781849735124
4. Khan, A. H.; Ghosh, S.; Pradhan, B.; Dalui, A.; Shrestha, L. K.; Acharya, S.; Ariga, K. *Bull. Chem. Soc. Jpn.* **2017,** *90,* 627–648. doi:10.1246/bcsj.20170043
5. Ariga, K.; Mori, T.; Shrestha, L. K. *Chem. Rec.* **2018,** *18,* 676–695. doi:10.1002/tcr.201700070
6. Galarneau, A.; Barodawalla, A.; Pinnavaia, T. J. *Nature* **1995,** *374,* 529–531. doi:10.1038/374529a0
7. Gil, A.; Korili, S. A.; Trujillano, R.; Vicente, M. A. V., Eds. *Pillared Clays and Related Catalysts;* Springer: New York, NY, U.S.A., 2010. doi:10.1007/978-1-4419-6670-4
8. Aranda, P.; Belver, C.; Ruiz-Hitzky, E. Inorganic heterostructured materials based on clay minerals. In *Materials and Clay Minerals;* Drummy, L. F., Ed.; CMS Workshop Lectures Series, Vol. 18; Clay Mineral Society: Chantilly, VA, U.S.A., 2014; pp 21–40. doi:10.1346/cms-wls-18-2
9. Ruiz-Hitzky, E.; Aranda, P.; Belver, C. Nanoarchitectures Based on Clay Materials. In *Manipulation of Nanoscale Materials: An Introductions to Nanoarchitectonics;* Ariga, K., Ed.; Nanoscience & Nanotechnology Series, Vol. 24; Royal Society of Chemistry: Cambridge, United Kingdom, 2012; pp 89–111. doi:10.1039/9781849735124-00087
10. Ruiz-Hitzky, E.; Aranda, P. *J. Sol-Gel Sci. Technol.* **2014,** *70,* 307–316. doi:10.1007/s10971-013-3237-9
11. Aranda, P.; Belver, C.; Ruiz-Hitzky, E. Nanoarchitectures by Sol–Gel from Silica and Silicate Building Blocks. In *The Sol-Gel Handbook: Synthesis, Characterization and Applications;* Levy, D.; Zayat, M., Eds.; Wiley-VCH Verlag GmbH: Weinheim, Germany, 2015; Vol. 1, pp 443–470. doi:10.1002/9783527670819.ch14
12. Aranda, P.; Darder, M.; Wicklein, B.; Rytwo, G.; Ruiz-Hitzky, E. Clay–Organic Interfaces for Design of Functional Hybrid Materials. In *Hybrid Organic–Inorganic Interfaces: Toward Advanced Functional Materials;* Delville, M. H.; Taubert, A., Eds.; Wiley-VCH Verlag GmbH: Weinheim, Germany, 2017; pp 1–84. doi:10.1002/9783527807130.ch1
13. Lvov, Y.; Guo, B.; Fakhrullin, R. F., Eds. *Functional Polymer Composites with Nanoclays;* Smart Materials Series, Vol. 22; Royal Society of Chemistry: Cambridge, United Kingdom, 2016. doi:10.1039/9781782626725
14. Aranda, P.; Ruiz-Hitzky, E. *Chem. Rec.* **2018,** *18,* 1125–1137. doi:10.1002/tcr.201700113
15. Vinokurov, V. A.; Stavitskaya, A. V.; Glotov, A. P.; Novikov, A. A.; Zolotukhina, A. V.; Kotelev, M. S.; Gushchin, P. A.; Ivanov, E. V.; Darrat, Y.; Lvov, Y. M. *Chem. Rec.* **2018,** *18,* 858–867. doi:10.1002/tcr.201700089
16. Brauner, K.; Preisinger, A. *Tschermaks Mineral. Petrogr. Mitt.* **1956,** *6,* 120–140. doi:10.1007/bf01128033
17. Santaren, J.; Sanz, J.; Ruiz-Hitzky, E. *Clays Clay Miner.* **1990,** *38,* 63–68. doi:10.1346/ccmn.1990.0380109
18. Aranda, P.; Ruiz-Hitzky, E. Nanoarchitectures based on sepiolite: assembly of nanoparticles. In *Surface Modification of Clays and Nanocomposites;* Beall, G.; Powell, C. E., Eds.; CMS Workshop Lectures Series, Vol. 20; Clay Minerals Society: Chantilly, VA, U.S.A., 2016; pp 87–100. doi:10.1346/cms-wls-20.7
19. Fernandes, F. M.; Ruiz-Hitzky, E. *Carbon* **2014,** *72,* 296–303. doi:10.1016/j.carbon.2014.02.009
20. Perez-Carvajal, J.; Aranda, P.; Ruiz-Hitzky, E. *J. Solid State Chem.* **2019,** *270,* 287–294. doi:10.1016/j.jssc.2018.11.018
21. Forano, C.; Hibino, T.; Leroux, F.; Taviot-Guého, C. Layered double hydroxides. In *Handbook of Clay Science;* Bergaya, F.; Theng, B. K. G.; Lagaly, G., Eds.; Elsevier: Oxford, United Kingdom, 2006; pp 1021–1095.
22. Forano, C.; Bruna, F.; Mousty, C.; Prevot, V. *Chem. Rec.* **2018,** *18,* 1150–1166. doi:10.1002/tcr.201700102
23. Wu, M. J.; Wu, J. Z.; Zhang, J.; Chen, H.; Zhou, J. Z.; Qian, G. R.; Xu, Z. P.; Du, Z.; Rao, Q. L. *Catal. Sci. Technol.* **2018,** *8,* 1207–1228. doi:10.1039/c7cy02314f
24. Zhao, M.; Zhao, Q.; Li, B.; Xue, H.; Pang, H.; Chen, C. *Nanoscale* **2017,** *9,* 15206–15225. doi:10.1039/c7nr04752e
25. Park, D.-H.; Hwang, S.-J.; Oh, J.-M.; Yang, J.-H.; Choy, J.-H. *Prog. Polym. Sci.* **2013,** *38,* 1442–1486. doi:10.1016/j.progpolymsci.2013.05.007
26. Leroux, F., Ed. Layered Double Hydroxide-based materials. *Recent Pat. Nanotechnol.* **2012,** *6,* 157–249.
27. Rives, V.; del Arco, M.; Martín, C. *Appl. Clay Sci.* **2014,** *88–89,* 239–269. doi:10.1016/j.clay.2013.12.002
28. Choi, G.; Eom, S.; Vinu, A.; Choy, J.-H. *Chem. Rec.* **2018,** *18,* 1033–1053. doi:10.1002/tcr.201700091
29. Nuruzzaman, M.; Rahman, M. M.; Liu, Y.; Naidu, R. *J. Agric. Food Chem.* **2016,** 1447–1483. doi:10.1021/acs.jafc.5b05214
30. Gunjakar, J. L.; Kim, T. W.; Kim, H. N.; Kim, I. Y.; Hwang, S.-J. *J. Am. Chem. Soc.* **2011,** *133,* 14998–15007. doi:10.1021/ja203388r

31. Gómez-Avilés, A.; Aranda, P.; Ruiz-Hitzky, E. *Appl. Clay Sci.* **2016,** *130,* 83–92. doi:10.1016/j.clay.2015.12.011
32. Djellali, M.; Aranda, P.; Ruiz-Hitzky, E. *Appl. Clay Sci.* **2019,** *171,* 65–73. doi:10.1016/j.clay.2019.02.004
33. Aranda, P.; Gómez Avilés, A.; Ruiz Hitzky, E. Materiales composites micro- y nano-estructurados basados en hidróxidos dobles laminares de tipo hidrotalcita y silicatos de la familia de las arcillas. Span. Patent ES2341637B1, May 23, 2011.
34. Tian, N.; Tian, X.; Liu, X.; Zhou, Z.; Yang, C.; Ma, L.; Tian, C.; Li, Y.; Wang, Y. *Chem. Commun.* **2016,** *52,* 11955–11958. doi:10.1039/c6cc05659h
35. Charradi, K.; Ahmed, Z.; Cid, R. E.; Aranda, P.; Ruiz-Hitzky, E.; Ocon, P.; Chtourou, R. *Int. J. Hydrogen Energy* **2019,** *44,* 10666–10676. doi:10.1016/j.ijhydene.2019.02.183
36. Alcântara, A. C. S.; Aranda, P.; Darder, M.; Ruiz-Hitzky, E. *J. Mater. Chem.* **2010,** *20,* 9495–9504. doi:10.1039/c0jm01211d
37. Inacio, J.; Taviot-Guého, C.; Forano, C.; Besse, J. P. *Appl. Clay Sci.* **2001,** *18,* 255–264. doi:10.1016/s0169-1317(01)00029-1
38. Cardoso, L. P.; Celis, R.; Cornejo, J.; Valim, J. B. *J. Agric. Food Chem.* **2006,** *54,* 5968–5975. doi:10.1021/jf061026y
39. Alromeed, A. A.; Scrano, L.; A. Bufo, S.; Undabeytia, T. *Pest Manage. Sci.* **2015,** *71,* 1303–1310. doi:10.1002/ps.3929
40. Pavlovic, I.; Barriga, C.; Hermosín, M. C.; Cornejo, J.; Ulibarri, M. A. *Appl. Clay Sci.* **2005,** *30,* 125–133. doi:10.1016/j.clay.2005.04.004
41. Miyata, S. *Clays Clay Miner.* **1975,** *23,* 369–375. doi:10.1346/ccmn.1975.0230508
42. Atçay, G.; Yurdakoç, K. *Acta Hydrochim. Hydrobiol.* **2000,** *28,* 300–304. doi:10.1002/1521-401x(200012)28:6<300::aid-aheh300>3.3.co;2-c
43. Ahlrichs, J. L. *Clays Clay Miner.* **1975,** *23,* 119–124. doi:10.1346/ccmn.1975.0230207
44. Casal, B.; Merino, J.; Serratosa, J.-M.; Ruiz-Hitzky, E. *Appl. Clay Sci.* **2001,** *18,* 245–254. doi:10.1016/s0169-1317(01)00030-8
45. Alcântara, A. C. S.; Darder, M.; Aranda, P.; Tateyama, S.; Okajima, M. K.; Kaneko, T.; Ogawa, M.; Ruiz-Hitzky, E. *J. Mater. Chem. A* **2014,** *2,* 1391–1399. doi:10.1039/c3ta14145d
46. Akkari, M.; Aranda, P.; Ben Rhaiem, H.; Ben Haj Amara, A.; Ruiz-Hitzky, E. *Appl. Clay Sci.* **2016,** *131,* 131–139. doi:10.1016/j.clay.2015.12.013
47. Akkari, M.; Aranda, P.; Ben Haj Amara, A.; Ruiz-Hitzky, E. *Beilstein J. Nanotechnol.* **2016,** *7,* 1971–1982. doi:10.3762/bjnano.7.188
48. de la Caillerie, J.-B. d.; Fripiat, J. J. *Catal. Today* **1992,** *14,* 125–140. doi:10.1016/0920-5861(92)80017-h
49. López-Capdevila, S.; Darder, M.; Aranda, P.; Ruiz-Hitzky, E. In *Actas de la Jornada Científica de la Sociedad Española de Arcillas;* Belver, C.; Cuevas, J.; Luque, J., Eds.; Socieda Española de Arcillas: Madrid, Spain, 2011; pp 23–24.
50. Bruna, F.; Celis, R.; Pavlovic, I.; Barriga, C.; Cornejo, J.; Ulibarri, M. A. *J. Hazard. Mater.* **2009,** *168,* 1476–1481. doi:10.1016/j.jhazmat.2009.03.038
51. Cardoso, L. P.; Valim, J. B. *J. Phys. Chem. Solids* **2006,** *67,* 987–993. doi:10.1016/j.jpcs.2006.01.015

Biocatalytic oligomerization-induced self-assembly of crystalline cellulose oligomers into nanoribbon networks assisted by organic solvents

Yuuki Hata[1], Yuka Fukaya[1], Toshiki Sawada[1,2], Masahito Nishiura[3] and Takeshi Serizawa[*1]

Address:
[1]Department of Chemical Science and Engineering, School of Materials and Chemical Technology, Tokyo Institute of Technology, 2-12-1 Ookayama, Meguro-ku, Tokyo 152-8550, Japan, [2]Precursory Research for Embryonic Science and Technology (PRESTO), Japan Science and Technology Agency (JST), 4-1-8 Honcho, Kawaguchi-shi, Saitama 332-0012, Japan and [3]DKS Co. Ltd., 5 Ogawaracho, Kisshoin, Minami-ku, Kyoto-shi, Kyoto 601-8391, Japan

Email:
Takeshi Serizawa[*] - serizawa@polymer.titech.ac.jp

* Corresponding author

Keywords:
cellulose oligomer; gel; nanoarchitectonics; nanoribbon networks; oligomerization-induced self-assembly; organic solvent

Abstract

Crystalline poly- and oligosaccharides such as cellulose can form extremely robust assemblies, whereas the construction of self-assembled materials from such molecules is generally difficult due to their complicated chemical synthesis and low solubility in solvents. Enzyme-catalyzed oligomerization-induced self-assembly has been shown to be promising for creating nanoarchitectured crystalline oligosaccharide materials. However, the controlled self-assembly into organized hierarchical structures based on a simple method is still challenging. Herein, we demonstrate that the use of organic solvents as small-molecule additives allows for control of the oligomerization-induced self-assembly of cellulose oligomers into hierarchical nanoribbon network structures. In this study, we dealt with the cellodextrin phosphorylase-catalyzed oligomerization of phosphorylated glucose monomers from D-glucose primers, which produce precipitates of nanosheet-shaped crystals in aqueous solution. The addition of appropriate organic solvents to the oligomerization system was found to result in well-grown nanoribbon networks. The organic solvents appeared to prevent irregular aggregation and subsequent precipitation of the nanosheets via solvation for further growth into the well-grown higher-order structures. This finding indicates that small-molecule additives provide control over the self-assembly of crystalline oligosaccharides for the creation of hierarchically structured materials with high robustness in a simple manner.

Introduction

Nanoarchitectonics is an emerging concept based on nanotechnology and other scientific fields, such as supramolecular chemistry, for constructing functional materials and systems in a bottom-up manner with the harmonization of mutual interactions [1-11]. Such harmonized mechanisms are found ubiquitously in biological systems consisting of a huge number of components; biomolecules, such as DNAs and peptides, and even living cells have therefore attracted considerable attention in nanoarchitectonics [1,4,11]. Achievements include nanopatterning [12], drug delivery [13], molecular sensing [14], nanodevices [15,16], and cell architectures [17,18]. On the other hand, crystalline poly- and oligosaccharides, such as cellulose and chitin, lag behind in nanoarchitectonics despite the superiority of their assemblies in terms of physicochemical stability and mechanical properties [19,20]. Plausible reasons are their complicated chemical synthesis [21] and low solubility in solvents [22,23], which prevent crystalline poly- and oligosaccharides from undergoing controlled self-assembly into ordered nanostructures in vitro. Nevertheless, naturally derived nanostructures (called nanocellulose [19,24,25] and nanochitin [20,26]) have demonstrated a robustness that makes them attractive for a wide range of applications. Therefore, the use of crystalline poly- and oligosaccharides as molecular building blocks has the potential to open new horizons in nanoarchitectonics.
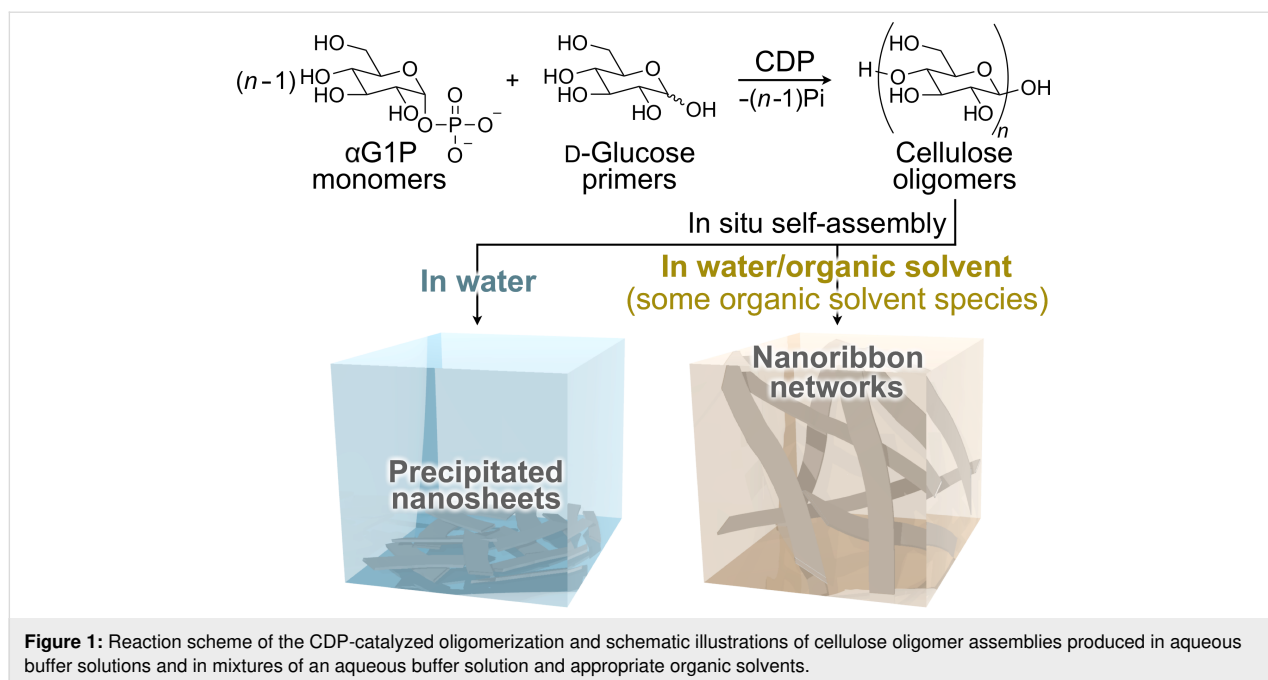
Oligomerization-induced self-assembly is a promising method for overcoming the above issues (i.e., the complicated chemical synthesis and the low solubility in solvents) with crystalline oligosaccharide nanoarchitectonics [21,27,28]. For example, the cellulase-catalyzed oligomerization of β-D-cellobiosyl fluoride monomers [29] and the cellodextrin phosphorylase (CDP)-catalyzed oligomerization of α-D-glucose 1-phosphate (αG1P) monomers from D-glucose [30,31] and cellobiose [32,33] primers have been demonstrated, where the synthesized cellulose oligomers (also known as cellodextrin) self-assemble in situ into unique nanostructures. In addition to the plain cellulose oligomer, cellulose oligomer derivatives bearing azido [34], alkyl [35], oligo(ethylene glycol) [36], vinyl [37,38], and amino [39,40] groups at the terminal have been successfully synthesized by using glucose derivatives as primers for the CDP-catalyzed oligomerization. By exploiting those enzyme-catalyzed oligomerization systems, various nanostructures, including nanofibrous assemblies [41], rectangular nanosheet-shaped lamellar crystals [30,31,39,42], distorted nanosheets with a bilayer structure [35], helical nanorods with a bilayer structure [35], and network structures composed of nanoribbon-shaped lamellar crystals [33,42-46] have been successfully constructed by changing the enzymatic reactions, tuning the self-assembly kinetics, introducing terminal functional groups,

and using additives. Among them, the strategy using additives has the advantages of versatility and convenience. Polymers [43,44] and colloidal particles [45] were shown to be useful additives. However, the potential of small-molecule additives for controlling the oligomerization-induced self-assembly of cellulose oligomers has yet to be investigated systematically, even though many more candidates are available for small molecules than for polymers and colloidal particles.

Herein, we show the formation of nanoribbon networks composed of crystalline cellulose oligomers via oligomerization-induced self-assembly assisted by organic solvents, which are widely used typical small molecules. The CDP-catalyzed oligomerization from D-glucose primers, which is known to produce rectangular nanosheets as precipitates in aqueous solution (Figure 1) [30,31], was used in this study. The oligomerization system in mixtures of an aqueous buffer solution and appropriate organic solvents was found to result in nanoribbon network structures for gel formation (Figure 1). It was suggested that the precipitation of the nanosheets was prevented effectively via solvation with the organic solvents through hydrogen bonding, allowing the formation of well-grown higher-order structures (i.e., nanoribbon networks). The observation demonstrates the significant effect of small-molecule additives for controlling the self-assembly of cellulose oligomers for the creation of hierarchically structured materials in a simple manner. This study will open a new scientific or technological world of nanostructured cellulose oligomers, which is different from that of naturally derived cellulosic materials [47-50].

Results and Discussion

Four kinds of common water-miscible organic solvents, namely, dimethyl sulfoxide (DMSO), *N,N*-dimethylformamide (DMF), acetonitrile (MeCN), and ethanol (EtOH), with different characteristics were used in this study. We addressed the CDP-catalyzed oligomerization from D-glucose primers, where the precipitated nanosheets are produced in aqueous solution [30,31]. The oligomerization reaction was conducted in the presence of organic solvents (5–25 vol %), while other conditions, such as αG1P monomer concentration (0.2 M), D-glucose primer concentration (0.05 M), CDP concentration (0.2 U mL^{-1}), temperature (60 °C), and incubation time (72 h), were as described in previous reports [31,42]. After the reaction, colorless solid products were observed in the solutions with relatively low organic solvent concentrations, suggesting the successful synthesis of water-insoluble cellulose oligomers under those conditions (Figure 2). Remarkably, the reaction mixtures with 10–20 vol % DMSO and 10 vol % EtOH were found to be in gel states after the reaction (Figure 2, photographs with yellow background).

Figure 1: Reaction scheme of the CDP-catalyzed oligomerization and schematic illustrations of cellulose oligomer assemblies produced in aqueous buffer solutions and in mixtures of an aqueous buffer solution and appropriate organic solvents.

Figure 2: Photographs of the reaction mixtures with organic solvents after the CDP-catalyzed oligomerization reaction. The blue, yellow, and white backgrounds denote the precipitate state, gel state, and trace amount of the products, respectively.

The apparent turbidity of the reaction mixtures decreased with increasing organic solvent concentrations for each organic solvent species (Figure 2). The observations were simply due to a reduction in the conversion of αG1P monomer into insoluble products (Figure 3), which was estimated from the insoluble product weights and the average degree of polymerization ($\overline{DP}$)

values calculated from the matrix-assisted laser desorption/ ionization time-of-flight (MALDI–TOF) mass spectra (see below). To check the possible denaturation of CDP by the organic solvents as an explanation for the decreased monomer conversions, circular dichroism (CD) spectra of CDP solutions containing 10 vol % MeCN or EtOH were measured after incu-

Figure 3: The αG1P monomer conversion into insoluble products with organic solvents.
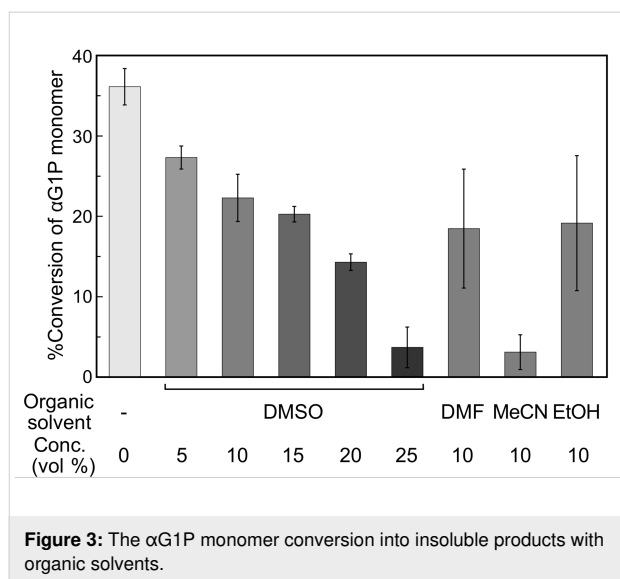
bation at 60 °C (Figure 4). Note that the light absorption of DMSO and DMF made the CD spectroscopy measurement impossible under the same conditions. Although incubation with the organic solvents for 6 h hardly affected the CD spectra (Figure 4a), incubation for 72 h led to a change in the spectra (Figure 4b), showing a change in the secondary structure of CDP. These results indicate that CDP was denatured gradually by the organic solvents during the oligomerization reaction, leading to decreasing enzymatic reaction rates for lower monomer conversions. On the other hand, although MeCN and EtOH caused different αG1P monomer conversions (Figure 3), they caused a similar change in the CD spectra of CDP. Each organic solvent species may lead to the denaturation of CDP in a different manner, while the difference could not be revealed

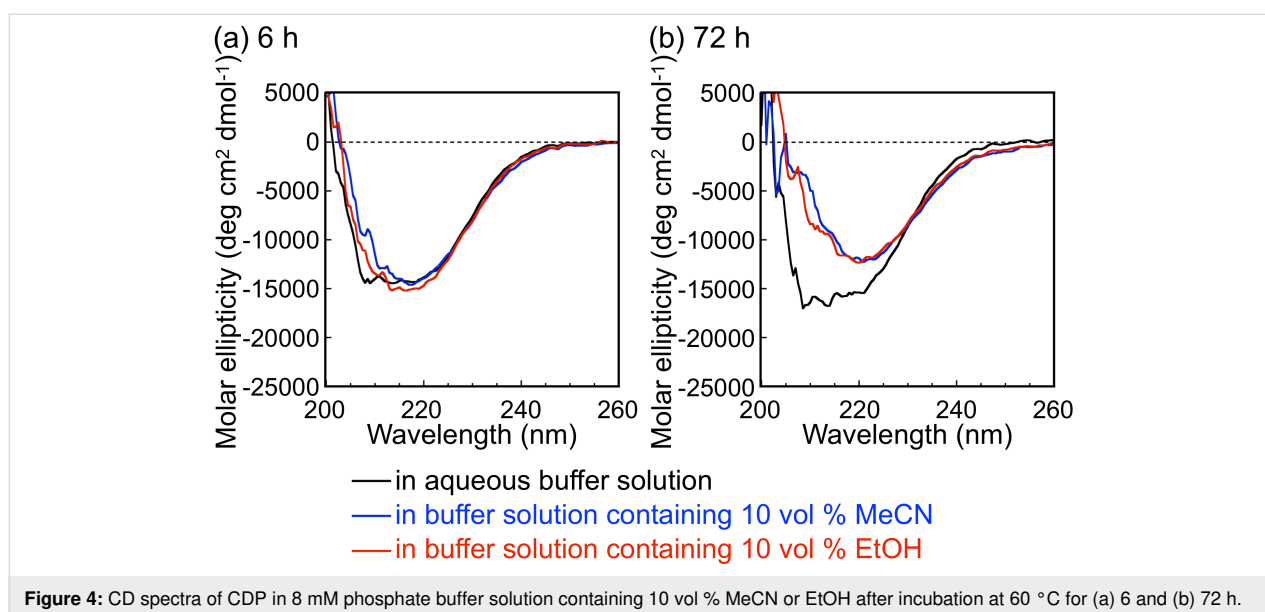by CD spectroscopy. Moreover, the organic solvents might affect the interaction between CDP and the substrates/products.

The chemical structure of the products was analyzed by ^{1}H NMR spectroscopy and MALDI–TOF mass spectrometry. The NMR spectra of the representative products showed proton signals for cellulose oligomers (Figure 5). In addition, the mass spectra further revealed the successful synthesis of cellulose oligomers (Figure 6). The $\overline{DP}$ values were calculated from both kinds of spectra to be 8–10, slightly lower than that of the oligomers synthesized in aqueous solution (i.e., 10) [31,42], depending on the organic solvent species and their concentrations (Table 1). The slight decrease in $\overline{DP}$ with the organic solvents was mainly attributed to the lower enzymatic reaction rates; a slower reaction would decrease the number of propagation steps for each molecular chain before solidification. Other factors, however, appeared to affect the $\overline{DP}$ (e.g., 10 vol % MeCN caused a relatively low monomer conversion yet a relatively high $\overline{DP}$, Figure 3 and Table 1). In addition, the population standard deviations (PSDs) of DP were calculated from the mass spectra and showed a trend of decreasing polydispersity with decreasing $\overline{DP}$ (Table 1), similar to the oligomerization in aqueous solution [42]. Although these results revealed a slight variation in the $\overline{DP}$ and polydispersity, our previous studies suggested that $\overline{DP}$ and polydispersity are not the dominant factors in the assembled structure of cellulose oligomers in the $\overline{DP}$ range of 7–10 [33,43-46]. Therefore, the gelation was considered not to be caused directly by the change in the DP, as discussed further below.

The crystal structure of the representative products was analyzed by X-ray diffraction (XRD) measurements and attenu-
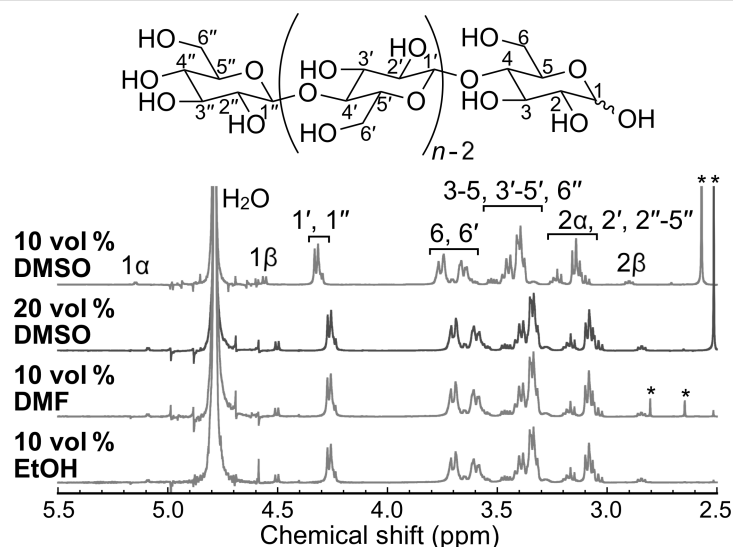

Figure 4: CD spectra of CDP in 8 mM phosphate buffer solution containing 10 vol % MeCN or EtOH after incubation at 60 °C for (a) 6 and (b) 72 h.

Figure 5: ^{1}H NMR spectra of the products with DMSO, DMF, and EtOH. The peaks with * are derived from the residual organic solvents.

Table 1: Summary of CDP-catalyzed oligomerization reaction with organic solvents.

species	organic solvent concentration (vol %)	state of product (inversion test)	$\overline{DP}$ (NMR)	$\overline{DP}$ (MALDI–TOF mass)	PSD of DP (MALDI–TOF mass)	allomorph (XRD and/or ATR-FTIR)	%χ_c (XRD)
no organic solvent	0	precipitate [31,42]	10 [31,42]	9	1.9	cellulose II [31,42]	52 [42]
DMSO	5	precipitate	–	9	1.4	–	–
DMSO	10	gel	8	8	1.2	cellulose II	60
DMSO	15	gel	–	8	1.1	–	–
DMSO	20	gel	8	8	1.0	cellulose II	64
DMSO	25	trace amount of product	–	8	1.1	–	–
DMF	10	precipitate	9	9	1.6	cellulose II	–
MeCN	10	precipitate	–	10	1.9	–	–
EtOH	10	gel	9	9	1.3	cellulose II	62

ated total reflection Fourier-transform infrared (ATR-FTIR) absorption spectroscopy. The XRD profiles showed three peaks at 2θ (θ is the Bragg angle) of 12.2, 19.9, and 22.1° (Figure 7), which corresponded to $1\overline{1}0$, 110, and 020 of the cellulose II allomorph, respectively [30]. In addition, the ATR-FTIR absorption spectra showed two characteristic peaks for the intrachain hydrogen-bonded hydroxyl groups in the cellulose II allomorph [51] at approximately 3441 and 3490 cm^{-1} (Figure 8). The cellulose II allomorph is the most stable allomorph of cellulose [19] and is typical of the cellulose oligomer assemblies formed in aqueous solution [31,42]. The degree of crystallinity (χ_c) values of the gelled products were calculated from the XRD profiles and found to be higher than those of the products in aqueous solution [42] (Table 1). The higher crystallinity with the organic solvents was attributed to the lower polydispersity in the DP, which would decrease the amount of

the amorphous-like assembled structures of the terminal residues of relatively long oligomer chains [42]. In other words, a higher uniformity of the chain lengths leads to higher integrity of the crystals.

Scanning electron microscopy (SEM) was used to uncover the nanomorphology of the gels. The images revealed a well-grown network structure composed of nanoribbon-shaped fibers (Figure 9), which were similar in shape to lamellar crystals of cellulose oligomers [42,52-54]. According to our examination, the cross-linking of the nanoribbons was apparently based on their physical contact, possibly through the hydrophobic effect and hydrogen bonding. We previously demonstrated nanoribbon network formation via oligomerization-induced self-assembly under macromolecular crowding conditions [43,44], which represent a solution state with high macromolec-
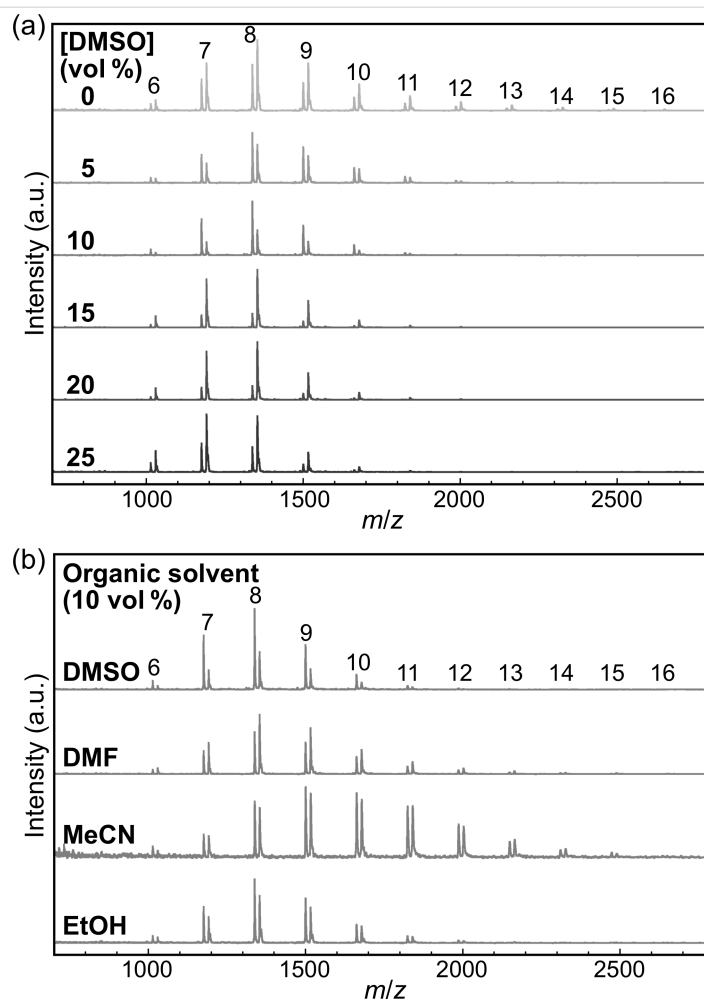
Figure 6: MALDI–TOF mass spectra of the products with (a) DMSO at various concentrations and (b) various organic solvents at 10 vol %. The numbers above the peaks denote the DP values of the cellulose oligomers. The spectra show two series of peaks corresponding to cellulose oligomers with sodium and potassium ion adducts.
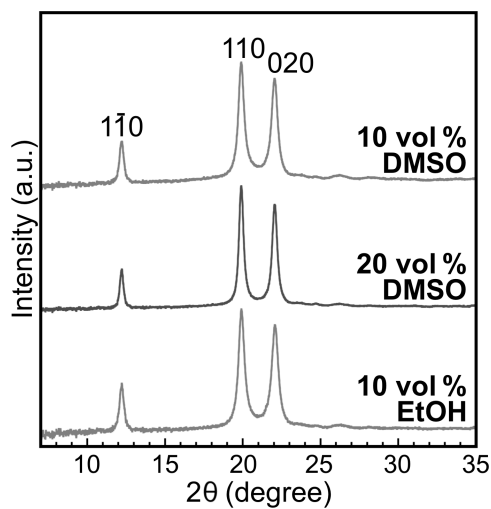
Figure 7: XRD profiles of the products with organic solvents. Miller indices for cellulose II are shown above the peaks.
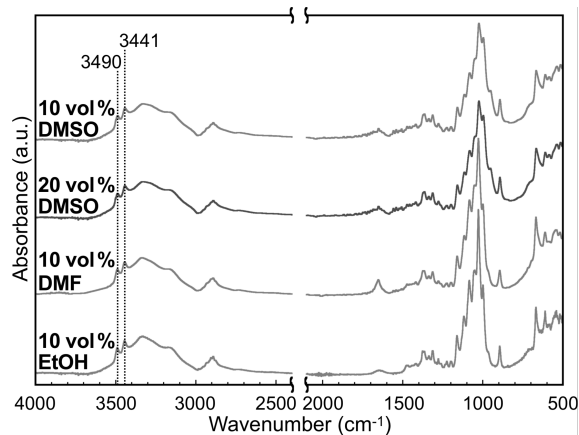
Figure 8: ATR-FTIR absorption spectra of the products with organic solvents. The numbers above the peaks denote the wavenumber.
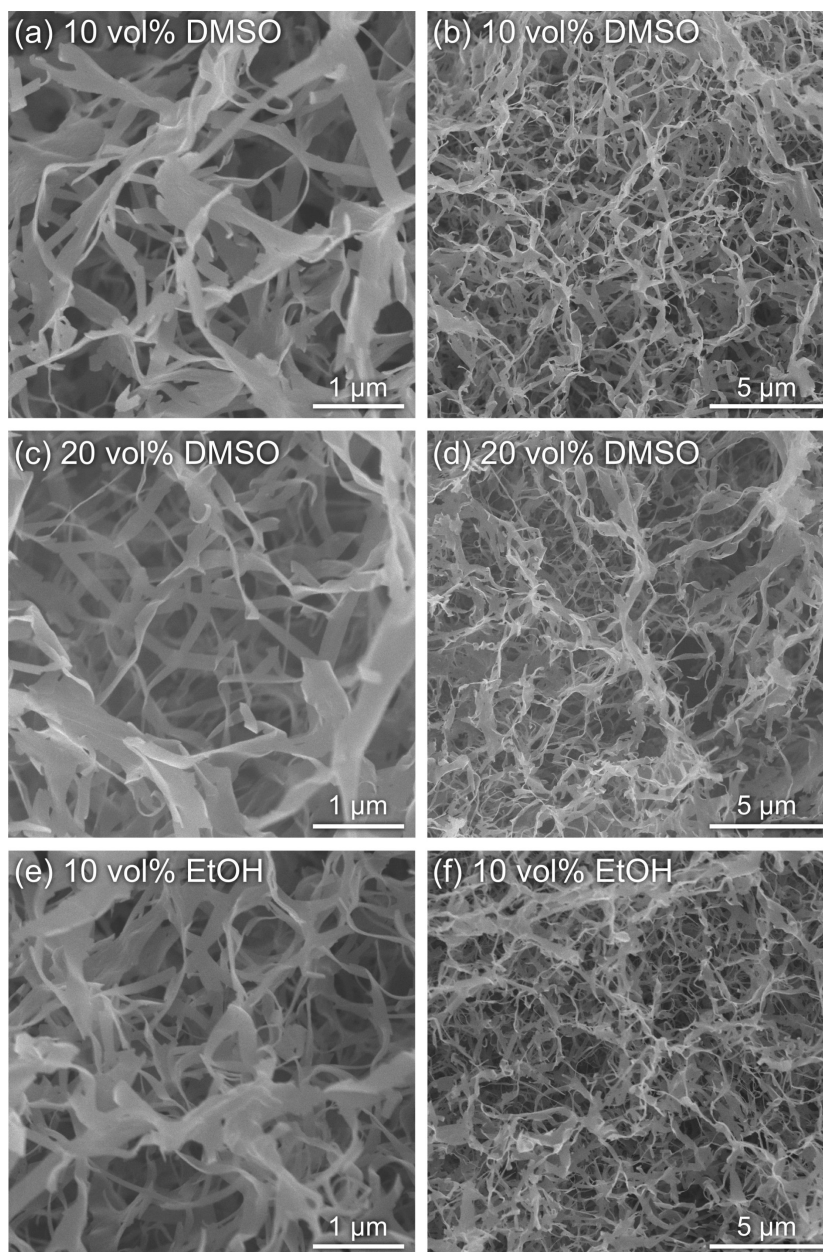
Figure 9: SEM images of the xerogels prepared from the gels synthesized with (a,b) 10 vol % DMSO, (c,d) 20 vol % DMSO, and (e,f) 10 vol % EtOH.

ular concentrations [55-57]. The crowding macromolecules with high molecular weights (typically more than 20k) induced high solution viscosity and depletion repulsion, which prevented the nanosheet-shaped lamellar crystals from aggregation and subsequent precipitation, enabling the formation of well-grown nanoribbon networks. On the other hand, the organic solvents used in this study were small molecules, indicating a different mechanism.

To gain insight into the mechanism underlying the nanoribbon network formation, we focused on the Kamlet–Taft solvent pa-

rameters, which are the most comprehensive and frequently used quantitative measure of solvent properties [58,59]. Among the three parameters, namely, the hydrogen bond donation ability (acidity) α, the hydrogen bond acceptor ability (basicity) β, and the dipolarity/polarizability π^*, β was found to be correlated. The organic solvents with relatively high β-values were found to induce the nanoribbon network formation (Table 2). This finding suggests that the precipitation of the nanosheet precursors was prevented effectively via solvation with the organic solvents mainly through hydrogen bonding from hydroxyl hydrogen on cellulose oligomers to the organic solvents,

Table 2: The Kamlet–Taft solvent parameters of the organic solvents used in this study [58].

Organic solvent	α	β	π*
DMSO	0	0.76	1.00
DMF	0	0.69	0.88
MeCN	0.19	0.40	0.75
EtOH	0.86	0.75	0.54

allowing further growth into higher-order structures (i.e., nanoribbon networks) in the bulk solution (Figure 10). This proposed mechanism would be reasonable considering that, in the case of a cellulose solvent series, β is the most significant parameter for dissolving cellulose via a mechanism involving interaction through hydrogen bonding with cellulose [60]. Such an attractive interaction with additive molecules is a novel driving force for controlling the oligomerization-induced self-assembly of cellulose oligomers. In summary, it was shown that organic solvents had the potential to induce the formation of well-grown higher-order structures of crystalline cellulose oligomer assemblies.

Figure 10: Schematic illustration of the proposed mechanism for dispersion stabilization of the nanosheet precursors via solvation with the organic solvents.
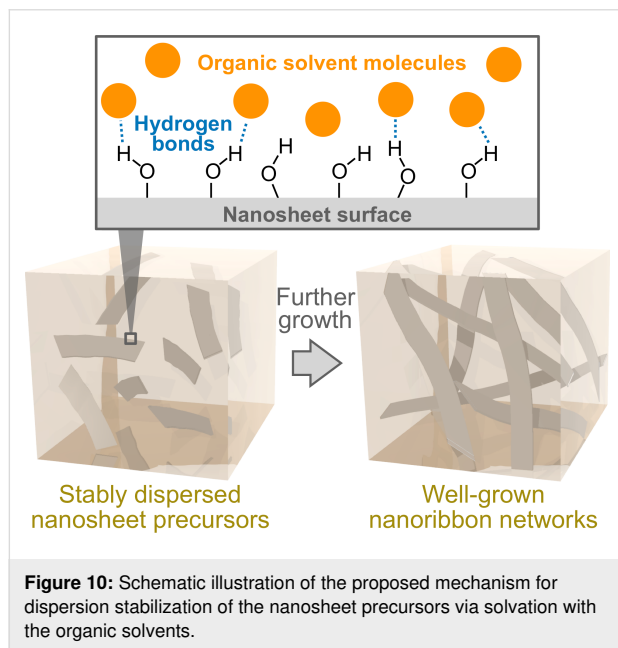
Conclusion

We showed that organic solvents provided control over the oligomerization-induced self-assembly of cellulose oligomers. The organic solvents with relatively high β-values prevented the irregular aggregation of the particulate nanostructures for the formation of well-organized higher-order structures. The main driving force was suggested to be the interaction of the organic solvent molecules with cellulose oligomers. Therefore, the use

of more strongly interacting molecules will allow more drastic changes in the assembled structures. Promising candidates include cellulose-dissolving solvents, represented by ionic liquids [23], which are known (or considered) to dissolve cellulose via direct interactions. Furthermore, the introduction of functional groups at the terminal of cellulose oligomers [34-40] significantly expands the variety of available molecular species that can interact with the oligomers. Consequently, the present study serves as inspiration for controlling the self-assembly of crystalline oligo- and polysaccharides via exploiting small-molecule additives, leading to advanced nanoarchitectonics for the creation of hierarchically structured materials with high robustness.

Experimental
Materials

αG1P disodium salt *n*-hydrate and 40% sodium deuteroxide (NaOD)/deuterium oxide (D_2O) solution were purchased from Wako Pure Chemical Industries. ProteoMass MALDI–MS standard, 1% trifluoroacetic acid, MeCN used for preparing MALDI–TOF mass spectrometry samples, 2,5-dihydroxybenzoic acid, and D_2O were purchased from Sigma-Aldrich. Dotite was purchased from Nisshin EM Corporation. All other reagents were purchased from Nacalai Tesque. Ultrapure water with a resistivity greater than 18.2 MΩ cm was supplied by a Milli-Q Advantage A-10 apparatus (Merck Millipore) and used throughout all experiments.

CDP-catalyzed oligomerization reaction

CDP from *Clostridium thermocellum* YM4 was prepared using a genetically engineered *Escherichia coli* according to a previous report [31]. For the synthesis of cellulose oligomers with organic solvents, αG1P monomer (0.2 M) and D-glucose primer (0.05 M) were incubated with CDP (0.2 U mL^{-1}) in 4-(2-hydroxyethyl)-1-piperazineethanesulfonic acid (HEPES; 0.5 M) buffer solutions containing organic solvents (DMSO, DMF, MeCN, or EtOH; 5, 10, 15, 20, or 25 vol %) at 60 °C for 72 h. Note that a HEPES buffer solution (1.5 M, pH 7.5) was used to prepare the reaction mixtures. To readily assess gelation, the vials containing the mixtures after the reaction were inverted. For SEM observations, the gelled products (1 mL) were purified by immersion in water at 4 °C for 1 week. The water was exchanged each day. For the other characterization techniques, the mixtures after the reaction (0.3 mL) were subjected to pipetting to obtain product dispersions. The resultant particulate products were purified with water/organic solvent mixtures (the organic solvent concentrations were the same as those in the reaction mixtures) by performing at least five centrifugation (20,400*g*)/redispersion cycles to remove more than 99.999% of the soluble fraction of the reaction mixtures. For MALDI–TOF mass spectrometry, the purified product

dispersions were stored at 4 °C until use. For the quantification of the insoluble products, a volume of the purified product dispersions was dried at 105 °C for 24 h, followed by weighing. For ¹H NMR spectroscopy, ATR-FTIR absorption spectroscopy, and XRD measurements, as much as possible of the supernatant after the final centrifugation was removed by pipette, followed by adding water to the products. The resultant product aqueous dispersions with residual organic solvents were lyophilized and then stored at 4 °C until use.

Characterization of the products

For NMR spectroscopy, the lyophilized products were dissolved in 4% $NaOD/D_2O$ to obtain product solutions (≥2% (w/v)). ¹H NMR spectra were recorded on an AVANCE III HD500 spectrometer (500 MHz, Bruker) at ambient temperature and calibrated using the signal of residual water ($\delta = 4.79$) as an internal standard. The $\overline{DP}$ was calculated using the following equation:

$$\overline{DP} = \frac{H_{1',1''}}{H_{1\alpha} + H_{1\beta}} + 1,$$ (1)

where $H_{1',1''}$, $H_{1\alpha}$, and $H_{1\beta}$ are the integrals of the corresponding protons (see the chemical structure of the cellulose oligomer in Figure 5).

For MALDI–TOF mass spectrometry, the purified product dispersions were mixed at a final concentration of 0.0033% (w/v) with 2,5-dihydroxybenzoic acid, trifluoroacetic acid, and MeCN at concentrations of 1.7 mg mL⁻¹, 0.02 vol %, and 50 vol %, respectively. The mixtures were deposited on an AXIMA 384-well plate and dried under ambient conditions. An AXIMA-performance instrument (Shimadzu) equipped with a nitrogen laser ($\lambda = 337$ nm) and pulsed ion extraction was used at an accelerating potential of 20 kV in linear positive ion mode to obtain mass spectra. The spectra were calibrated using peptide standards (ProteoMass MALDI–MS Standard) at 757.3997 (bradykinin fragment 1–7), 1533.8582 Da ($P_{14}R$), and 2465.1989 Da (ACTH fragment 18–39). The $\overline{DP}$ and the PSD of DP were calculated using the following equations:

$$\overline{DP} = \frac{\overline{M}_n - 18.0}{162} = \frac{\dfrac{\sum_i (N_i M_i)}{\sum_i N_i} - 18.0}{162}$$ (2)

$$\text{PSD of DP} = \sqrt{\frac{\sum_i N_i \left(i - \overline{DP}\right)^2}{\sum_i N_i}}$$ (3)

where $\overline{M}_n$ is the number average molecular weight, N_i is the peak area of *i*-mer species, and M_i is the molar mass of that species.

For XRD measurements, the lyophilized products were pressed into pellets using a hand press. A D8 DISCOVER instrument (Bruker) with Cu Kα radiation ($\lambda = 1.542$ Å) was operated under ambient conditions to obtain the transmission XRD patterns and transmitted X-ray intensities of the products using a two-dimensional (2D) detector and a scintillation counter, respectively. The 2D diffraction patterns were converted into 1D profiles in the 2θ range of 7–35°. The contribution of air scattering was subtracted from the 1D profiles based on the following equation:

$$I_{\text{cor}} = I_{\text{obs}} - t \cdot I_{\text{blank}}$$ (4)

where I_{cor} is the corrected intensity, I_{obs} is the observed intensity, t is the X-ray transmittance through the sample, and I_{blank} is the intensity measured without any sample. The amorphous cellulose halo obtained previously [42] was fitted to the 1D profiles in 2θ ranges adequately selected from 15–20° for each profile. The χ_c was estimated according to the following equation:

$$\chi_c = \frac{\int_{10°}^{35°} I_c(2\theta) d(2\theta)}{\int_{10°}^{35°} I(2\theta) d(2\theta)} \times 100$$ (5)

where $I_c(2\theta)$ is the diffraction intensity from the crystalline phase, and $I(2\theta)$ is the intensity from both the crystalline and amorphous phases.

For ATR-FTIR absorption spectroscopy, the lyophilized products in a powdery state were used. The spectra were recorded on an FT/IR-4100 instrument (JASCO) at a cumulative measurement number of 100 and a resolution of 2.0 cm⁻¹ under ambient conditions.

For SEM observations, the water solvent of the hydrogels after purification was exchanged stepwise with 10, 20, 30, 40, 50, 60, 70, 80 and 90 vol % EtOH, EtOH, EtOH/*tert*-butyl alcohol (1:1, v/v) and then *tert*-butyl alcohol by immersion. The obtained organogels were freeze-fractured using liquid nitrogen and a razor blade and then lyophilized. The obtained xerogels were mounted on substrates using Dotite and then coated with osmium. The fracture surface was observed by a field-emission scanning electron microscope (JSM-7500F, JEOL) at an accelerating voltage of 5 kV.

Analysis of the secondary structure of CDP

The secondary structure of CDP was analyzed by CD spectroscopy. CDP was dissolved in a 8 mM phosphate buffer solution containing 10 vol % MeCN or EtOH at a concentration where the absorbance of CDP at 280 nm was 0.1. The CDP solutions were incubated at 60 °C for 6 and 72 h. The CD spectra of the samples were recorded on a J-725 instrument (JASCO) at a path length of 2 mm, a scan rate of 100 nm min^{-1}, and a cumulative measurement number of 4.

Acknowledgements

ORCID® iDs

Yuuki Hata - https://orcid.org/0000-0003-1493-1896
Toshiki Sawada - https://orcid.org/0000-0001-7491-8357
Takeshi Serizawa - https://orcid.org/0000-0002-4867-8625

References

1. Zou, Q.; Liu, K.; Abbas, M.; Yan, X. *Adv. Mater. (Weinheim, Ger.)* **2016,** *28,* 1031–1043. doi:10.1002/adma.201502454
2. Ariga, K.; Li, J.; Fei, J.; Ji, Q.; Hill, J. P. *Adv. Mater. (Weinheim, Ger.)* **2016,** *28,* 1251–1286. doi:10.1002/adma.201502545
3. Malgras, V.; Ataee-Esfahani, H.; Wang, H.; Jiang, B.; Li, C.; Wu, K. C.-W.; Kim, J. H.; Yamauchi, Y. *Adv. Mater. (Weinheim, Ger.)* **2016,** *28,* 993–1010. doi:10.1002/adma.201502593
4. Komiyama, M.; Yoshimoto, K.; Sisido, M.; Ariga, K. *Bull. Chem. Soc. Jpn.* **2017,** *90,* 967–1004. doi:10.1246/bcsj.20170156
5. Khan, A. H.; Ghosh, S.; Pradhan, B.; Dalui, A.; Shrestha, L. K.; Acharya, S.; Ariga, K. *Bull. Chem. Soc. Jpn.* **2017,** *90,* 627–648. doi:10.1246/bcsj.20170043
6. Sawada, T. *Polym. J.* **2017,** *49,* 639–647. doi:10.1038/pj.2017.35
7. Komiyama, M.; Mori, T.; Ariga, K. *Bull. Chem. Soc. Jpn.* **2018,** *91,* 1075–1111. doi:10.1246/bcsj.20180084
8. Ariga, K.; Mori, T.; Shrestha, L. K. *Chem. Rec.* **2018,** *18,* 676–695. doi:10.1002/tcr.201700070
9. Sawada, T.; Serizawa, T. *Bull. Chem. Soc. Jpn.* **2018,** *91,* 455–466. doi:10.1246/bcsj.20170428
10. Azzaroni, O.; Ariga, K. *Mol. Syst. Des. Eng.* **2019,** *4,* 9–10. doi:10.1039/c9me90001b
11. Zhao, L.; Zou, Q.; Yan, X. *Bull. Chem. Soc. Jpn.* **2019,** *92,* 70–79. doi:10.1246/bcsj.20180248
12. Numajiri, K.; Kimura, M.; Kuzuya, A.; Komiyama, M. *Chem. Commun.* **2010,** *46,* 5127–5129. doi:10.1039/c0cc00044b
13. Zhu, G.; Zheng, J.; Song, E.; Donovan, M.; Zhang, K.; Liu, C.; Tan, W. *Proc. Natl. Acad. Sci. U. S. A.* **2013,** *110,* 7998–8003. doi:10.1073/pnas.1220817110
14. Zhu, Z.; Wu, C.; Liu, H.; Zou, Y.; Zhang, X.; Kang, H.; Yang, C. J.; Tan, W. *Angew. Chem., Int. Ed.* **2010,** *49,* 1052–1056. doi:10.1002/anie.200905570
15. Douglas, S. M.; Bachelet, I.; Church, G. M. *Science* **2012,** *335,* 831–834. doi:10.1126/science.1214081
16. Liu, M.; Fu, J.; Hejesen, C.; Yang, Y.; Woodbury, N. W.; Gothelf, K.; Liu, Y.; Yan, H. *Nat. Commun.* **2013,** *4,* 2127. doi:10.1038/ncomms3127
17. Matsuda, N.; Shimizu, T.; Yamato, M.; Okano, T. *Adv. Mater. (Weinheim, Ger.)* **2007,** *19,* 3089–3099. doi:10.1002/adma.200701978
18. Souza, G. R.; Molina, J. R.; Raphael, R. M.; Ozawa, M. G.; Stark, D. J.; Levin, C. S.; Bronk, L. F.; Ananta, J. S.; Mandelin, J.; Georgescu, M.-M.; Bankson, J. A.; Gelovani, J. G.; Killian, T. C.; Arap, W.; Pasqualini, R. *Nat. Nanotechnol.* **2010,** *5,* 291–296. doi:10.1038/nnano.2010.23
19. Moon, R. J.; Martini, A.; Nairn, J.; Simonsen, J.; Youngblood, J. *Chem. Soc. Rev.* **2011,** *40,* 3941–3994. doi:10.1039/c0cs00108b
20. Ifuku, S.; Saimoto, H. *Nanoscale* **2012,** *4,* 3308–3318. doi:10.1039/c2nr30383c
21. Kadokawa, J.-i. *Chem. Rev.* **2011,** *111,* 4308–4345. doi:10.1021/cr100285v
22. Chang, C.; Zhang, L. *Carbohydr. Polym.* **2011,** *84,* 40–53. doi:10.1016/j.carbpol.2010.12.023
23. Wang, H.; Gurau, G.; Rogers, R. D. *Chem. Soc. Rev.* **2012,** *41,* 1519–1537. doi:10.1039/c2cs15311d
24. Habibi, Y.; Lucia, L. A.; Rojas, O. J. *Chem. Rev.* **2010,** *110,* 3479–3500. doi:10.1021/cr900339w
25. Klemm, D.; Kramer, F.; Moritz, S.; Lindström, T.; Ankerfors, M.; Gray, D.; Dorris, A. *Angew. Chem., Int. Ed.* **2011,** *50,* 5438–5466. doi:10.1002/anie.201001273
26. Muzzarelli, R.; Mehtedi, M.; Mattioli-Belmonte, M. *Mar. Drugs* **2014,** *12,* 5468–5502. doi:10.3390/md12115468
27. Kobayashi, S.; Sakamoto, J.; Kimura, S. *Prog. Polym. Sci.* **2001,** *26,* 1525–1560. doi:10.1016/s0079-6700(01)00026-0
28. Shoda, S.-i.; Uyama, H.; Kadokawa, J.-i.; Kimura, S.; Kobayashi, S. *Chem. Rev.* **2016,** *116,* 2307–2413. doi:10.1021/acs.chemrev.5b00472
29. Kobayashi, S.; Kashiwa, K.; Kawasaki, T.; Shoda, S. *J. Am. Chem. Soc.* **1991,** *113,* 3079–3084. doi:10.1021/ja00008a042
30. Hiraishi, M.; Igarashi, K.; Kimura, S.; Wada, M.; Kitaoka, M.; Samejima, M. *Carbohydr. Res.* **2009,** *344,* 2468–2473. doi:10.1016/j.carres.2009.10.002
31. Serizawa, T.; Kato, M.; Okura, H.; Sawada, T.; Wada, M. *Polym. J.* **2016,** *48,* 539–544. doi:10.1038/pj.2015.125
32. Samain, E.; Lancelon-Pin, C.; Férigo, F.; Moreau, V.; Chanzy, H.; Heyraud, A.; Driguez, H. *Carbohydr. Res.* **1995,** *271,* 217–226. doi:10.1016/0008-6215(95)00022-I
33. Serizawa, T.; Fukaya, Y.; Sawada, T. *Langmuir* **2017,** *33,* 13415–13422. doi:10.1021/acs.langmuir.7b03653
34. Yataka, Y.; Sawada, T.; Serizawa, T. *Chem. Commun.* **2015,** *51,* 12525–12528. doi:10.1039/c5cc04378f
35. Yataka, Y.; Sawada, T.; Serizawa, T. *Langmuir* **2016,** *32,* 10120–10125. doi:10.1021/acs.langmuir.6b02679
36. Nohara, T.; Sawada, T.; Tanaka, H.; Serizawa, T. *Langmuir* **2016,** *32,* 12520–12526. doi:10.1021/acs.langmuir.6b01635
37. Wang, J.; Niu, J.; Sawada, T.; Shao, Z.; Serizawa, T. *Biomacromolecules* **2017,** *18,* 4196–4205. doi:10.1021/acs.biomac.7b01224

38. Adharis, A.; Petrović, D. M.; Özdamar, I.; Woortman, A. J. J.; Loos, K. *Carbohydr. Polym.* **2018**, *193*, 196–204. doi:10.1016/j.carbpol.2018.03.098

39. Nohara, T.; Sawada, T.; Tanaka, H.; Serizawa, T. *J. Biomater. Sci., Polym. Ed.* **2017**, *28*, 925–938. doi:10.1080/09205063.2017.1322248

40. Nohara, T.; Sawada, T.; Tanaka, H.; Serizawa, T. *Bull. Chem. Soc. Jpn.* **2019**, *92*, 982–988. doi:10.1246/bcsj.20190035

41. Lee, J. H.; Brown, R. M.; Kuga, S.; Shoda, S.; Kobayashi, S. *Proc. Natl. Acad. Sci. U. S. A.* **1994**, *91*, 7425–7429. doi:10.1073/pnas.91.16.7425

42. Hata, Y.; Sawada, T.; Marubayashi, H.; Nojima, S.; Serizawa, T. *Langmuir* **2019**, *35*, 7026–7034. doi:10.1021/acs.langmuir.9b00850

43. Hata, Y.; Kojima, T.; Koizumi, T.; Okura, H.; Sakai, T.; Sawada, T.; Serizawa, T. *ACS Macro Lett.* **2017**, *6*, 165–170. doi:10.1021/acsmacrolett.6b00848

44. Hata, Y.; Sawada, T.; Serizawa, T. *Polym. J.* **2017**, *49*, 575–581. doi:10.1038/pj.2017.22

45. Hata, Y.; Sawada, T.; Sakai, T.; Serizawa, T. *Biomacromolecules* **2018**, *19*, 1269–1275. doi:10.1021/acs.biomac.8b00092

46. Serizawa, T.; Fukaya, Y.; Sawada, T. *Polym. J.* **2018**, *50*, 799–804. doi:10.1038/s41428-018-0057-3

47. Cavallaro, G.; Lazzara, G.; Konnova, S.; Fakhrullin, R.; Lvov, Y. *Green Mater.* **2014**, *2*, 232–242. doi:10.1680/gmat.14.00014

48. Tran, A.; Hamad, W. Y.; MacLachlan, M. J. *ACS Appl. Nano Mater.* **2018**, *1*, 3098–3104. doi:10.1021/acsanm.8b00947

49. Lee, W. S.; Choi, J. *ACS Appl. Mater. Interfaces* **2019**, *11*, 19363–19371. doi:10.1021/acsami.9b03296

50. Kurečič, M.; Mohan, T.; Virant, N.; Maver, U.; Stergar, J.; Gradišnik, L.; Kleinschek, K. S.; Hribernik, S. *RSC Adv.* **2019**, *9*, 21288–21301. doi:10.1039/c9ra03399h

51. Nelson, M. L.; O'Connor, R. T. *J. Appl. Polym. Sci.* **1964**, *8*, 1311–1324. doi:10.1002/app.1964.070080322

52. Bittiger, H.; Husemann, E. *J. Polym. Sci., Part B: Polym. Lett.* **1972**, *10*, 549–553. doi:10.1002/pol.1972.110100712

53. Buleon, A.; Chanzy, H. *J. Polym. Sci., Polym. Phys. Ed.* **1978**, *16*, 833–839. doi:10.1002/pol.1978.180160508

54. Buffiere, J.; Abad, N.; Ahvenainen, P.; Dou, J.; Cocero, M. J.; Sixta, H. *ACS Sustainable Chem. Eng.* **2018**, *6*, 16959–16967. doi:10.1021/acssuschemeng.8b04296

55. Ellis, R. J. *Trends Biochem. Sci.* **2001**, *26*, 597–604. doi:10.1016/s0968-0004(01)01938-7

56. Nakano, S.-i.; Miyoshi, D.; Sugimoto, N. *Chem. Rev.* **2014**, *114*, 2733–2758. doi:10.1021/cr400113m

57. Hata, Y.; Sawada, T.; Serizawa, T. *J. Mater. Chem. B* **2018**, *6*, 6344–6359. doi:10.1039/c8tb02201a

58. Marcus, Y. *Chem. Soc. Rev.* **1993**, *22*, 409–416. doi:10.1039/cs9932200409

59. Jessop, P. G.; Jessop, D. A.; Fu, D.; Phan, L. *Green Chem.* **2012**, *14*, 1245–1259. doi:10.1039/c2gc16670d

60. Kuroda, K.; Satria, H.; Miyamura, K.; Tsuge, Y.; Ninomiya, K.; Takahashi, K. *J. Am. Chem. Soc.* **2017**, *139*, 16052–16055. doi:10.1021/jacs.7b08914

Nanoarchitectonics meets cell surface engineering: shape recognition of human cells by halloysite-doped silica cell imprints

Elvira Rozhina, Ilnur Ishmukhametov, Svetlana Batasheva, Farida Akhatova and Rawil Fakhrullin[*]

Address:
Institute of Fundamental Medicine and Biology, Kazan Federal University, Kreml uramı 18, Kazan 420008, Republic of Tatarstan, Russian Federation

Email:
Rawil Fakhrullin[*] - kazanbio@gmail.com

* Corresponding author

Keywords:
cell surface engineering; cell-recognising imprints; halloysite nanotubes; nanoarchtectonics

Abstract

Cell surface engineering, as a practical manifestation of nanoarchitectonics, is a powerful tool to modify and enhance properties of live cells. In turn, cells may serve as sacrificial templates to fabricate cell-mimicking materials. Herein we report a facile method to produce cell-recognising silica imprints capable of the selective detection of human cells. We used HeLa cells to template silica inorganic shells doped with halloysite clay nanotubes. The shells were destroyed by sonication resulting in the formation of polydisperse hybrid imprints that were used to recognise HeLa cells in liquid media supplemented with yeast. We believe that methodology reported here will find applications in biomedical and clinical research.

Introduction

Nanoarchitectonics has recently emerged as a "post-nanotechnology era" paradigm in the directed fabrication of functional materials [1]. It widely employs atom and molecule manipulation and self-organisation of nanoscale particles [2]. Engineering of cell surfaces with various nanoscale materials has been recognised as a powerful means to attenuate the intrinsic properties of microbial and eukaryotic cells [3]. In particular, nanostructured composite shells (both hard and soft) deposited onto live cells have been shown to render the cells with novel mechanic and chemical functionalities [4-6]. In line with the concepts of nanoarchitectonics, cell surface engineering relies on the self-assembly of miniature building blocks to form biomimetic soft or rigid shells to encapsulate live cells rendering them with additional functionalities [7]. In general, there are three principal routes to engineer the cell walls or membranes of live cells: 1) deposition of charged or neutral

polymers (that can be doped with nanoscale inorganic particles) [8,9]; 2) direct anchoring of inorganic nanoparticles to cell surfaces [10,11]; 3) fabrication of "hard" inorganic shells mimicking natural eggshells [12]. Synthetic polymers can be grafted onto the surface of individual cells using atom-transfer radical polymerization [13]. The versatility of cell surface engineering methods has led to intersections between these routes yielding functionalised cells with multiple functionalities [14]. Relatively solid microbial cells with cell walls as well as soft mammal cells (including human cells) were used in cell surface engineering [15]. Surface-engineered cells have found applications in whole-cell biocatalysis [16], cell therapy [17], magnetic cell delivery [18], fabrication of multicellular assemblies [19], cell protection [20,21], biosensors [22] and tissue engineering [23]. Shells derived from cells templates offer other fascinating opportunities due to their cell-mimicking geometries, for example, a novel class of bioinspired colloid particles was fabricated recently. Colloid antibodies were produced via the formation of solid silica shells doped with gold nanoparticles on bacterial cells. The cells were chemically decomposed, while the empty shells were broken by ultrasound and later used for shape-based recognition and killing of bacteria [24,25].

Inspired by the previous reports on the fabrication of colloidal cell imprints capable of microbial cell recognition [24,25], we have developed a nanoarchitectonics-based technology to produce imprints recognising human cells. To do so, we resorted on forming silica-based solid shells and reinforcing these shells with halloysite nanotubes. Halloysite, a naturally occurring biocompatible clay, is a promising candidate for the fabrication of various functional composite materials [26]. The anisotropic shape (hollow tubules having lengths from 300 nm to 1–2 µm, 50–70 nm diameter, and 20 nm lumen) and surface chemistry (outer surface of SiO_2, inner surface of Al_2O_3) make

these nanotubes ideal carriers for novel catalysts, polymer fillers, drug-delivery vehicles and tissue engineering scaffolds [27]. Halloysite nanotubes derived from various geological deposits differ in their mesoscopic structures [28], allowing to choose the clay nanotubes most suitable for a desired application. The positively charged nanotube lumen can be loaded with anionic molecules (including bioactive compounds), and the loading efficiency can be significantly increased by using vacuum pumping [29].

Halloysite has already shown its potential in cells surface engineering of microbial cells [30,31]. Here we used halloysite as a dopant for artificial silica shells deposited on viable human HeLa cells. Halloysite nanotubes were chosen as dopant because of their biocompatibilty and rather large lumen sizes suitable for loading various drugs and even enzymes [32]. In the future, the procedure developed here can be extended to other nanotubular particles such as boron nitride or imogolite nanotubes, which are also considered as safe materials for living organisms [33]. Recently, water-dispersed thermo-responsive boron nitride nanotubes were obtained by their functionalisation with poly(*N*-isopropylacrylamide), which can widen their biomedical applications [34]. After fabrication, the cells were bleached to produce hollow cell-shaped imprints. These imprints, in turn, were utilised to recognise HeLa cells in suspension. Importantly, the silica/halloysite imprints based on human cells were selective and did not interact with microbial cells of comparable sizes such as yeast cells.

Results and Discussion

Our experimental strategy is schematically depicted in Figure 1. Following the nanoarchitectonics paradigm [35], we produced composite inorganic shells around human HeLa cells, using a polyelectrolyte nanolayer as a means to facilitate the formation
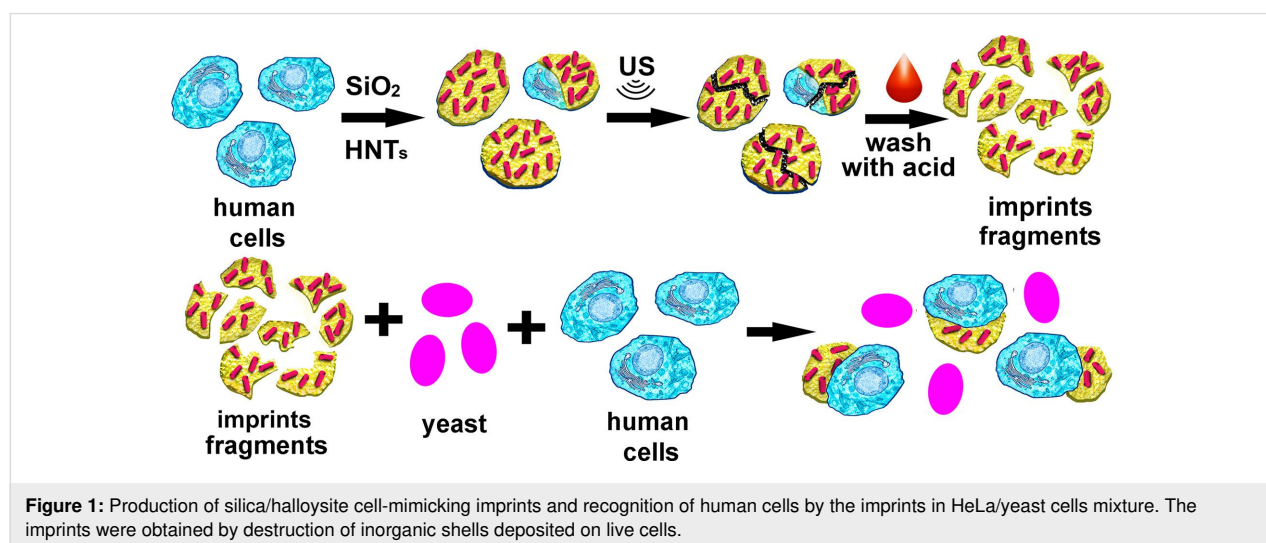

Figure 1: Production of silica/halloysite cell-mimicking imprints and recognition of human cells by the imprints in HeLa/yeast cells mixture. The imprints were obtained by destruction of inorganic shells deposited on live cells.

of silica/halloysite cell-mimicking imprints. Then the shells were disintegrated using sonication, while the cell debris was dissolved by acid washing to produce polydisperse silica/halloysite cells imprints. Next, these imprints were utilised to selectively recognise HeLa cells in cell growth media supplemented with yeast cells.

HeLa cells (having originally a negative zeta potential of ca. −10 mV) were first coated with a single layer of poly(acrylamide-*co*-diallyldimethylammonium chloride (P(AAm-*co*-DADMAC)) to reverse the surface charge of HeLa cells (the zeta potential after P(AAm-*co*-DADMAC deposition was ca. 46 mV). Positively charged cells were then subjected to a mixture of silicic acid derivatives (produced by mixing tetraethyl orthosilicate with HCl) and halloysite nanotubes (2.5 mg·mL^{-1}) for 10 min. In several experiments, halloysite-free silica shells were obtained following a previously published protocol [24,25]. Silica/halloysite-decorated HeLa cells were then imaged in situ with optical fluorescence microscopy. A typical image is shown in Figure 2A demonstrating the preserved cell morphology and characteristic nuclear DAPI stain. Next, we imaged the silica/halloysite-decorated HeLa cells with dark-field microscopy (Figure 2B,C) to confirm for-

mation and integrity of the inorganic layer. Dark-field microscopy at 1000× magnification is expected to resolve the rod-like shapes of halloysite [36]. This was confirmed in this study demonstrating the elongated tubular structures within the silica shells deposited around perinuclear areas, as shown in Figure 2C.

Scanning electron microscopy (SEM) was employed to investigate the morphology of the halloysite-doped and halloysite-free silica shells deposited onto HeLa cells. Suspended cells were deposited onto glass substrates, fixed with formaldehyde, sputter-coated with a thin gold layer and then imaged using a Hitachi SU8000 microscope. As shown in Figure 2D–F, the typical smooth surface topography of HeLa cells was changed drastically by the deposition of either pure or halloysite-doped silica. Analysing the cell diameter in the SEM images of intact and silica/halloysite-coated cells, we estimated the thickness of the inorganic shells (ca. 2 μm). In general, the shells were quite resilient and not prone to any mechanical damage unless subjected to a significant impact. This was indirectly confirmed in viability evaluation experiments. First, we tried to cultivate the cells in a regular way (24 h) by seeding them onto cell culture plates. Uncovered HeLa cells, as expected, were able to adhere
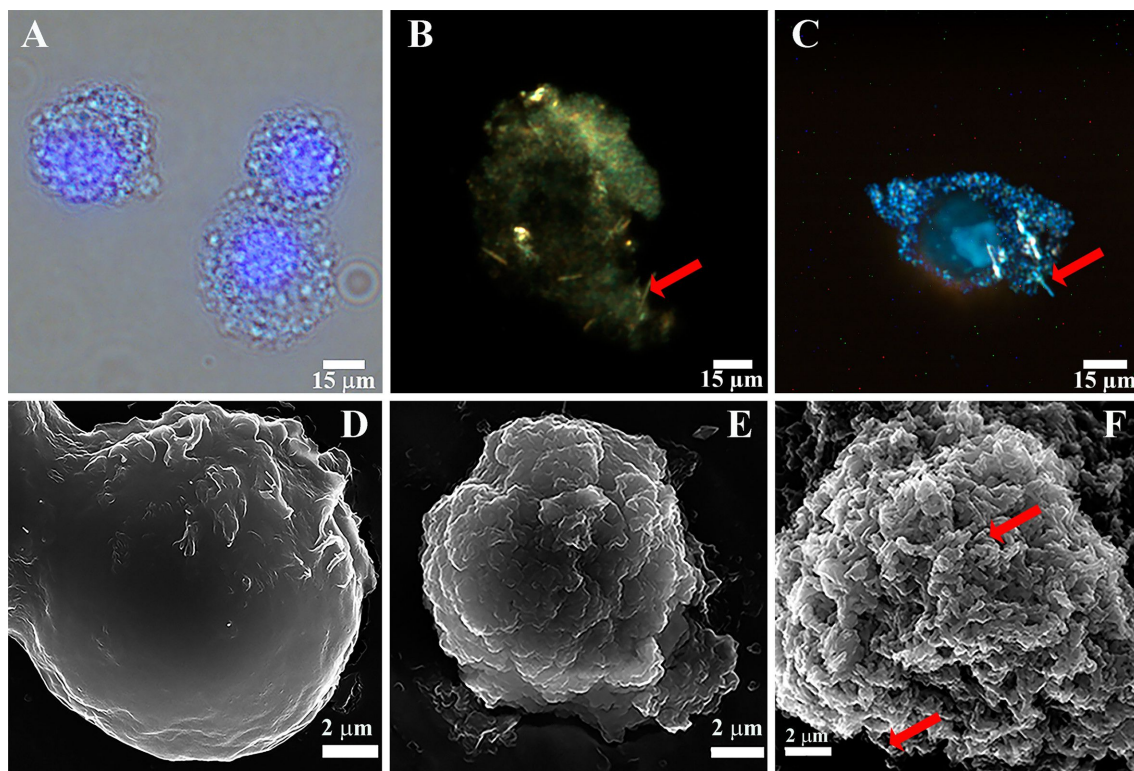
Figure 2: (A) optical/fluorescence microscopy image of live HeLa cells coated with halloysite-doped silica shells (nuclei are stained with DAPI); (B, C) dark-field microscopy images of live HeLa cells coated with halloysite-doped silica shells; scanning electron microscopy images of (D) intact HeLa cells, (E) HeLa cells coated with pure silica shells and (F) HeLa cells coated with halloysite-doped silica shells. Red arrows indicate halloysite nanotubes.

and subsequently colonise the substrates (Figure 3A,B), whereas the cells decorated with halloysite-doped silica shells did not adhere or proliferate, which was confirmed by optical microscopy (Figure 3C,D). One might expect that the deposition of silica/halloysite shells kills the HeLa cells, which lack any rigid cell protective structure such as cell walls in microbial cells [37], and that therefore no visual cell growth occurs. However, flow cytometry-based cell proliferation monitoring performed with cells stained with 5(6)-carboxyfluorescein diacetate *N*-succinimidyl ester (CFSE) dye has confirmed that cells coated with pure silica or silica/halloysite display a similar cell proliferation pattern as intact HeLa cells (Figure 3F,G), confirming the viability of the encapsulated cells. CFSE-labelled HeLa cells divide, thus the overall fluorescence intensity decreases. In case of silica-encapsulated HeLa cells there was a prominent decrease in fluorescence intensity during day 1 of the observation, which we attribute to the inhibition of proliferation by the silica shells. On day 3, however, the fluorescence intensity in silica-coated cells was even higher than in the control cells, apparently due to the partial destruction of the shells and the release of HeLa cells.

Although non-compromised viability is an important feature in any cell surface engineering investigation, in this study we were more concerned with the fabrication of imprints that are able to recognise human cells. To do so, we destroyed the cell-in-shell structures obtained by drying, resuspending in water and sonicating for 10 min. Then the organic cell debris was removed by treatment with aqueous HNO_3 and HCl mixture (3:1) and washed thoroughly with water. This procedure yielded polydisperse (100 nm to 1 μm) cell-templated imprints with diverse

morphology. Typical AFM and SEM images of the imprints are shown in Figure 4A–C. We have also used EDX spectroscopy to investigate the elemental composition of the silica/halloysite imprints (Figure 4D), confirming the typical elemental composition characteristic for halloysite. A strong peak of Al in the EDX image supports the presence of halloysite in the imprint, because Al is a major constituent of halloysite nanotubes.

The main goal of this study was to demonstrate the recognition of human cells by cell-templated imprints in a similar way as was reported previously for bacteria recognition [24,25]. To do so, we have mixed the imprints (0.1 g·mL^{-1}) with suspended HeLa cells (10^6 mL^{-1}) in growth media (Figure 4E). After 30 min of incubation, we found that more than 60% of the HeLa cells were recognised by the imprints. Additionally, for a better visualisation of the cell recognition events the imprints were labelled with rhodamine B and then added to DAPI-stained HeLa cells (Figure 4F). It is likely that the recognition event is facilitated by the nanostructured internal surface of the imprint built from halloysite nanotubes, which may increase the effective contact area between the cell surface and the imprint surfaces. In previous reports [24,25], the recognition event was apparently facilitated by the shape matching between the bacteria with rigid cell walls and the relatively uniform hollow imprints. In our study large-scale shape recognition is not likely to occur because HeLa cells are labile and do not keep the shape as well as bacteria do. We therefore believe that the recognition is based on a small-scale interaction between the inner surface of the imprints retaining the local cellular membrane shapes and cells. In this case, halloysite nanotubes may have a significant effect on the reproduction of the local cell
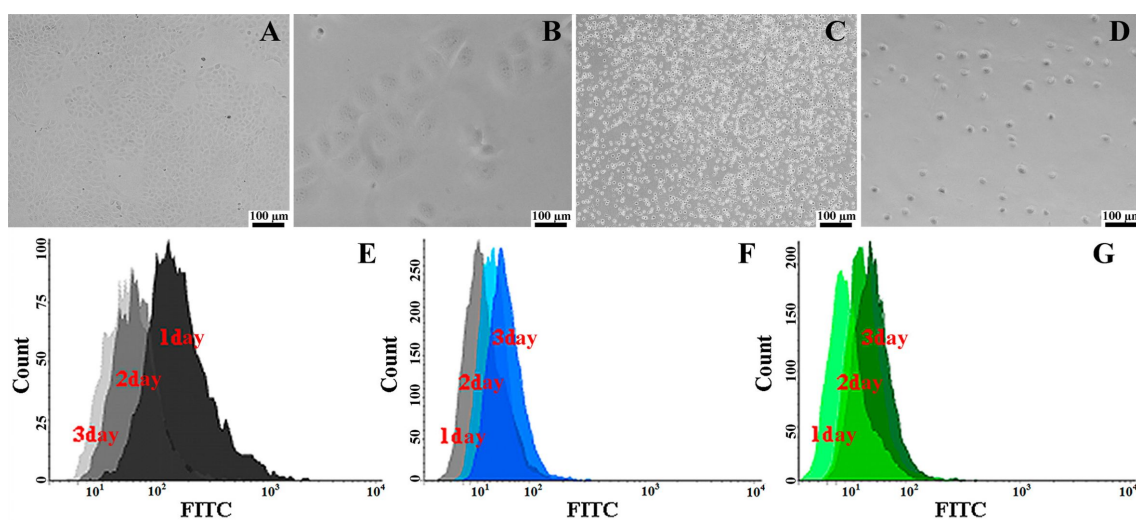

Figure 3: Optical microscopy images demonstrating the cultivation for 24 h of (A, B) substrate-attached intact HeLa cells and (C, D) HeLa cells coated with halloysite-doped silica shells; flow cytometry monitoring of cell division for three days of CFSE-stained (E) intact HeLa cells, (F) silica-coated HeLa cells and (G) HeLa cells coated with halloysite-doped silica shells.
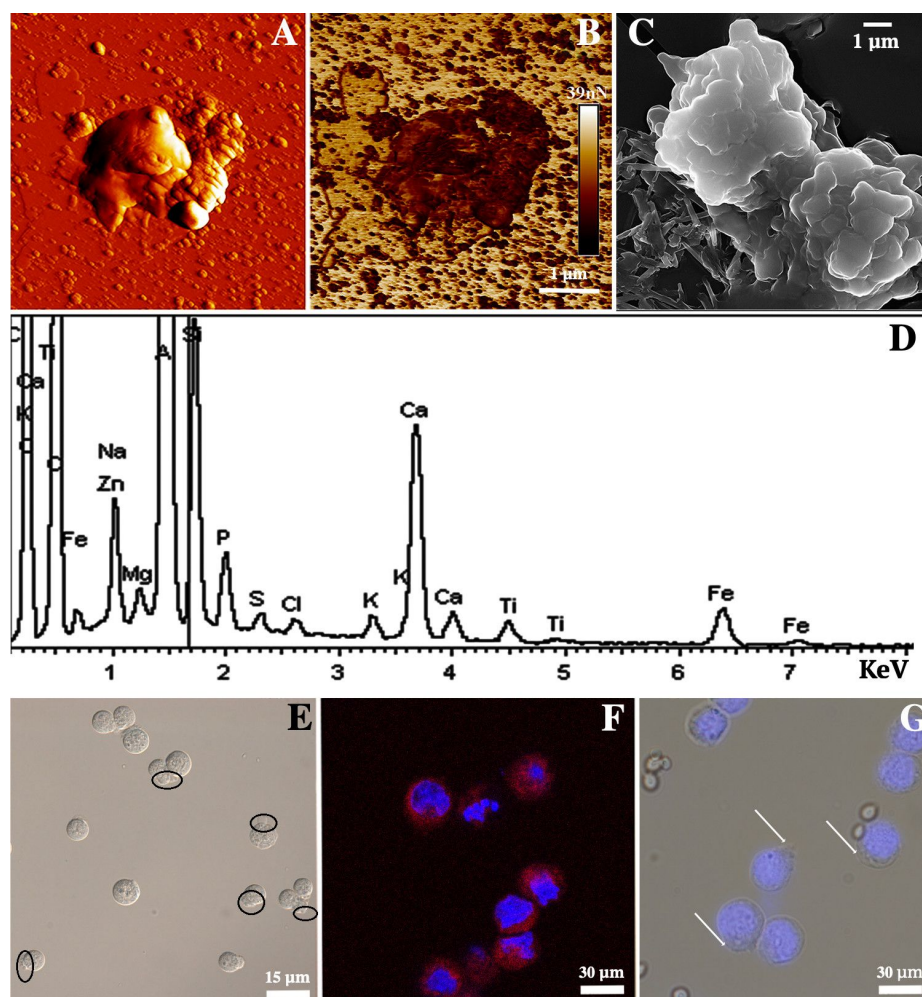
Figure 4: Atomic force microscopy (PeakForce Tapping mode) images of inorganic silica/halloysite imprints templated on HeLa cells: (A) topography image, (B) non-specific adhesion map; (C) scanning electron microscopy image of inorganic silica/halloysite imprints templated on HeLa cells; (D) EDX spectrum taken from the sample shown in (C), demonstrating the typical silica and halloysite elemental distribution; (E) optical and (F) confocal microscopy images demonstrating the recognition of HeLa cells with cell-templated imprints (cell nuclei stained with DAPI, imprints with rhodamine B in panel (F); (G) optical microscopy image of selective recognition of HeLa cells by the imprint in a mixture of human cells with yeast cells.

non-uniformities helping the subsequent recognition to happen. Finally, to demonstrate the selective recognition, we prepared mixtures of HeLa cells with yeast cells and then added HeLa cell-templated imprints. HeLa cells were pre-stained with a DAPI nuclear dye for better visualisation of mammal cells in a mixture with fungi cells. As shown in Figure 4G, only HeLa cells were recognised by the imprints, while yeast cells were ignored. Although this does not guarantee an equally effective recognition of other mammalian cells (i.e., in a mixture with HeLa cells), our results open new avenues for the fabrication of colloid particles capable of shape-based recognition of human cells. Viral and chemical transformation of cells induce changes in the architecture of the membrane [38], and tumor cells have many more microvilli than non-dividing normal cells [39]. These differences in the surfaces characteristics of cancer and

normal cells can potentially be used for designing new methods for the selective recognition of normal and tumor cells. Future research is needed to thoroughly investigate the capabilities of our method to template imprints and then recognise the target cells depending on species or cell type.

Experimental
Materials and reagents

Tetraethoxysilane (TEOS), poly(acrylamide-*co*-diallyldimethyl-ammonium chloride) (P(AAm-co-DADMAC), rhodamine B, poly(allylamine hydrochloride) (PAH) were purchased from Sigma-Aldrich. Millipore water (specific resistivity 18 MΩ·cm at 25 °C) was used in all experiments. Halloysite nanotubes (HNTs) of 95–98% purity were obtained from Applied Minerals Inc.

Cell culture

The human cervical carcinoma (HeLa) CCL-2 cell line was obtained from the American Type Culture Collection (ATCC, USA).The cells were cultured under standard culture conditions (5% CO_2 at 37 °C) in Dulbecco's modified Eagle's medium (DMEM) containing 10% heat-inactivated foetal bovine serum (FBS, Invitrogen, USA).

Fabrication of imprints using HeLa cell templates

The silica shells on individual HeLa cells were fabricated by biosilification [3]. To pre-functionalise the cells with P(AAm-*co*-DADMAC), the cells were trypsinised, collected, re-suspended in the medium to 10^6 cells·mL^{-1}and mixed with PAAm-*co*-DADMAC (1 wt %). After 10 min of incubation with the polycation solution, the cells were washed thrice with buffer to remove excess polyelectrolyte. Next, a thin silicon film was formed on the pre-functionalised cells. The working solution was prepared by mixing 1 part of TEOS with 0.1 parts of deionized H_2O and 0.01 parts of 1mM HCl for 20 min at room temperature, similarly to the approach described elsewhere [40]. The halloysite nanotubes were added to silicic acid derivatives to a final concentration of 2.5 mg·mL^{-1}. Then, the acid derivatives were mixed with the cells in serum-free medium (1:50 v/v) for 10 min on a rotator. The cells@SiO_2-HNTs were washed five times with Milli-Q water, and the sediment was dried for 12 h at 105 °C. Dried cells@-SiO_2-HNTs were re-suspended in Milli-Q water and crushed using an ultrasonic bath for 6–8 min. To remove the cell debris from the silica-halloysite imprints the cells@-SiO_2-HNTs fragments were centrifuged at 4500 rpm, the supernatant was removed, and 10 mL of a HNO_3 and HCl mixture (3:1) was added to the precipitate. After 30 min the silica-halloysite imprints were separated, washed three times with Milli-Q, and studied with AFM and SEM.

Cells recognition by imprints

The recognition of HeLa cells with imprints was visualised using bright-field optical microscopy (Axio Imager Z2, Carl Zeiss), and laser confocal microscopy (LSM 780: 405 nm and 633 nm lasers). For fluorescence microscopy imaging, inorganic cell imprints were incubated for 5 minutes in a solution of rhodamine B and then washed with distilled water until the water remained clear. After that, the inorganic imprints obtained from one million cells were placed in 1 mL of DMEM medium containing one million cells and incubated for 20–30 minutes. The nuclei of the cells were stained with 4′,6-diamidino-2-phenylindole (DAPI) according to the standard protocol. In order to check the specificity of the imprint binding to mammalian cells the imprints were placed in DMEM medium, containing one million Hela and one million yeast cells.

Characterisation

Scanning electron microscopy (SEM) imaging of samples sputter-coated with gold was performed with a Hitachi SU8000 microscope equipped with energy-dispersive X-ray (EDX) spectrometer. The interaction of cells with inorganic shapes was also recorded with an atomic-force microscope (Dimension Icon, Bruker, USA) operating in a PeakForce Tapping mode in air. The cells incubated with imprints for 15 minutes were washed with buffer; the precipitate was kept in glutaraldehyde (Sigma) for 1 hour, then washed with buffer and Milli-Q. Standard silicon nitride ScanAsyst-Air probes (Bruker) with resonance frequencies in the range of 70 to 95 kHz and spring constant in the range of 0.4 to 0.8 N m^{-1} (nominal length 115 μm, tip radius 2 nm) were used. The images were collected in air at 0.8–0.9 Hz scan rate and 512–1024 lines per scan. Topographic and nanomechanical characteristics were obtained. The data was processed using Nanoscope Analysis v.1.7. software (Bruker). For dark-field microscopy imaging HeLa cells were fixed and the nuclei were stained with DAPI. The Cytoviva® high annular aperture dark-field condenser attached to an Olympus BX51 upright microscope was used. The Olympus BX51 microscope was equipped with a fluorite 100× objective and Dage xL (Dage-MTI) CCD camera. Images were obtained using Exponent 7 software (Dage-MTI). The dark-field images were overlapped with transmission fluorescence images using the image processing software GIMP. Cell proliferative activity was examined by flow cytometry on the 1st, 2nd and 3rd day of cell co-incubation with imprints. The cells were stained with 5(6)-carboxyfluorescein diacetate *N*-succinimidyl ester (CFSE) (Invitrogen) as specified by the manufacturer and analysed using a BD FACS (USA) instrument.

ORCID® iDs

Elvira Rozhina - https://orcid.org/0000-0002-6237-3828
Rawil Fakhrullin - https://orcid.org/0000-0003-2015-7649

References

1. Ariga, K.; Ahn, E.; Park, M.; Kim, B.-S. *Chem. – Asian J.* **2019,** *14,* 2553–2566. doi:10.1002/asia.201900627

2. Ariga, K.; Ji, Q.; Nakanishi, W.; Hill, J. P.; Aono, M. *Mater. Horiz.* **2015,** *2,* 406–413. doi:10.1039/c5mh00012b

3. Park, J. H.; Hong, D.; Lee, J.; Choi, I. S. *Acc. Chem. Res.* **2016,** *49,* 792–800. doi:10.1021/acs.accounts.6b00087

4. Shi, P.; Zhao, N.; Coyne, J.; Wang, Y. *Nat. Commun.* **2019,** *10,* 2223. doi:10.1038/s41467-019-10231-y

5. Chen, Z.; Ji, H.; Zhao, C.; Ju, E.; Ren, J.; Qu, X. *Angew. Chem., Int. Ed.* **2015,** *54,* 4904–4908. doi:10.1002/anie.201412049

6. Guryanov, I.; Naumenko, E.; Konnova, S.; Lagarkova, M.; Kiselev, S.; Fakhrullin, R. *Nanomedicine: NBM* **2019,** *20,* 102038. doi:10.1016/j.nano.2019.102038

7. Hong, D.; Lee, H.; Ko, E. H.; Lee, J.; Cho, H.; Park, M.; Yang, S. H.; Choi, I. S. *Chem. Sci.* **2015,** *6,* 203–208. doi:10.1039/c4sc02789b

8. Jonas, A. M.; Glinel, K.; Behrens, A.; Anselmo, A. C.; Langer, R. S.; Jaklenec, A. *ACS Appl. Mater. Interfaces* **2018,** *10,* 16250–16259. doi:10.1021/acsami.8b01988

9. Emanet, M.; Fakhrullin, R.; Çulha, M. *ChemNanoMat* **2016,** *2,* 426–429. doi:10.1002/cnma.201600044

10. Maheshwari, V.; Fomenko, D. E.; Singh, G.; Saraf, R. F. *Langmuir* **2010,** *26,* 371–377. doi:10.1021/la9021195

11. Rozhina, E.; Batasheva, S.; Gomzikova, M.; Naumenko, E.; Fakhrullin, R. *Colloids Surf., A* **2019,** *565,* 16–24. doi:10.1016/j.colsurfa.2018.12.038

12. Fakhrullin, R. F.; Minullina, R. T. *Langmuir* **2009,** *25,* 6617–6621. doi:10.1021/la901395z

13. Kim, J. Y.; Lee, B. S.; Choi, J.; Kim, B. J.; Choi, J. Y.; Kang, S. M.; Yang, S. H.; Choi, I. S. *Angew. Chem., Int. Ed.* **2016,** *55,* 15306–15309. doi:10.1002/anie.201608515

14. Naumenko, E. A.; Dzamukova, M. R.; Fakhrullina, G. I.; Akhatova, F. S.; Fakhrullin, R. F. *Curr. Opin. Pharmacol.* **2014,** *18,* 84–90. doi:10.1016/j.coph.2014.09.009

15. Kim, B. J.; Cho, H.; Park, J. H.; Mano, J. F.; Choi, I. S. *Adv. Mater. (Weinheim, Ger.)* **2018,** *30,* 1706063. doi:10.1002/adma.201706063

16. Zhang, Y.; Zhang, S.; Sun, L.; Yang, Q.; Han, J.; Wei, Q.; Xie, G.; Chen, S.; Gao, S. *Chem. Commun.* **2017,** *53,* 3034–3037. doi:10.1039/c7cc00545h

17. Choi, D.; Lee, H.; Kim, H.-B.; Yang, M.; Heo, J.; Won, Y.; Jang, S. S.; Park, J. K.; Son, Y.; Oh, T. I.; Lee, E.; Hong, J. *Chem. Mater.* **2017,** *29,* 2055–2065. doi:10.1021/acs.chemmater.6b04096

18. Konnova, S. A.; Lvov, Y. M.; Fakhrullin, R. F. *Langmuir* **2016,** *32,* 12552–12558. doi:10.1021/acs.langmuir.6b01743

19. Fakhrullin, R. F.; Paunov, V. N. *Chem. Commun.* **2009,** *18,* 2511–2513. doi:10.1039/b902260k

20. Lee, J.; Choi, J.; Park, J. H.; Kim, M.-H.; Hong, D.; Cho, H.; Yang, S. H.; Choi, I. S. *Angew. Chem., Int. Ed.* **2014,** *53,* 8056–8059. doi:10.1002/anie.201402280

21. Park, J. H.; Kim, K.; Lee, J.; Choi, J. Y.; Hong, D.; Yang, S. H.; Caruso, F.; Lee, Y.; Choi, I. S. *Angew. Chem., Int. Ed.* **2014,** *53,* 12420–12425. doi:10.1002/anie.201405905

22. García-Alonso, J.; Fakhrullin, R. F.; Paunov, V. N.; Shen, Z.; Hardege, J. D.; Pamme, N.; Haswell, S. J.; Greenway, G. M. *Anal. Bioanal. Chem.* **2011,** *400,* 1009–1013. doi:10.1007/s00216-010-4241-3

23. Dzamukova, M. R.; Naumenko, E. A.; Rozhina, E. V.; Trifonov, A. A.; Fakhrullin, R. F. *Nano Res.* **2015,** *8,* 2515–2532. doi:10.1007/s12274-015-0759-1

24. Borovička, J.; Metheringham, W. J.; Madden, L. A.; Walton, C. D.; Stoyanov, S. D.; Paunov, V. N. *J. Am. Chem. Soc.* **2013,** *135,* 5282–5285. doi:10.1021/ja400781f

25. Borovička, J.; Stoyanov, S. D.; Paunov, V. N. *Nanoscale* **2013,** *5,* 8560–8568. doi:10.1039/c3nr01893h

26. Liu, M.; Fakhrullin, R.; Novikov, A.; Panchal, A.; Lvov, Y. *Macromol. Biosci.* **2019,** *19,* 1800419. doi:10.1002/mabi.201800419

27. Yendluri, R.; Lvov, Y.; de Villiers, M. M.; Vinokurov, V.; Naumenko, E.; Tarasova, E.; Fakhrullin, R. *J. Pharm. Sci.* **2017,** *106,* 3131–3139. doi:10.1016/j.xphs.2017.05.034

28. Cavallaro, G.; Chiappisi, L.; Pasbakhsh, P.; Gradzielski, M.; Lazzara, G. *Appl. Clay Sci.* **2018,** *160,* 71–80. doi:10.1016/j.clay.2017.12.044

29. Lisuzzo, L.; Cavallaro, G.; Pasbakhsh, P.; Milioto, S.; Lazzara, G. *J. Colloid Interface Sci.* **2019,** *547,* 361–369. doi:10.1016/j.jcis.2019.04.012

30. Konnova, S. A.; Sharipova, I. R.; Demina, T. A.; Osin, Y. N.; Yarullina, D. R.; Ilinskaya, O. N.; Lvov, Y. M.; Fakhrullin, R. F. *Chem. Commun.* **2013,** *49,* 4208–4210. doi:10.1039/c2cc38254g

31. Konnova, S. A.; Lvov, Y. M.; Fakhrullin, R. F. *Clay Miner.* **2016,** *51,* 429–433. doi:10.1180/claymin.2016.051.3.07

32. Tully, J.; Yendluri, R.; Lvov, Y. *Biomacromolecules* **2016,** *17,* 615–621. doi:10.1021/acs.biomac.5b01542

33. Lisuzzo, L.; Cavallaro, G.; Lazzara, G.; Milioto, S.; Parisi, F.; Stetsyshyn, Y. *Appl. Sci.* **2018,** *8,* 1068. doi:10.3390/app8071068

34. Kalay, S.; Stetsyshyn, Y.; Lobaz, V.; Harhay, K.; Ohar, H.; Çulha, M. *Nanotechnology* **2016,** *27,* 035703. doi:10.1088/0957-4484/27/3/035703

35. Komiyama, M.; Mori, T.; Ariga, K. *Bull. Chem. Soc. Jpn.* **2018,** *91,* 1075–1111. doi:10.1246/bcsj.20180084

36. Fakhrullina, G. I.; Akhatova, F. S.; Lvov, Y. M.; Fakhrullin, R. F. *Environ. Sci.: Nano* **2015,** *2,* 54–59. doi:10.1039/c4en00135d

37. Lee, H.; Hong, D.; Cho, H.; Kim, J. Y.; Park, J. H.; Lee, S. H.; Kim, H. M.; Fakhrullin, R. F.; Choi, I. S. *Sci. Rep.* **2016,** *6,* 38517. doi:10.1038/srep38517

38. Burger, M. M. *Proc. Natl. Acad. Sci. U. S. A.* **1969,** *62,* 994–1001.

39. Kolata, G. B. *Science* **1975,** *188,* 819–820. doi:10.1126/science.188.4190.819

40. Ramanathan, K.; Kamalasanan, M. N.; Malhotra, B. D.; Pradhan, D. R.; Chandra, S. *J. Sol-Gel Sci. Technol.* **1997,** *10,* 309–316. doi:10.1023/a:1018329518938

High-tolerance crystalline hydrogels formed from self-assembling cyclic dipeptide

Yongcai You[1], Ruirui Xing[2], Qianli Zou[*2], Feng Shi[*1] and Xuehai Yan[*2,3]

Abstract

Peptide-based supramolecular hydrogels, as a new type of biological nanoarchitectonic structure, hold great promise for a wide range of biomedical and nanotechnological applications, such as tissue engineering, drug delivery, and electronic and photonic energy storage. In this work, a cyclic dipeptide (CDP) cyclo-(Trp-Tyr) (C-WY), which has exceptional structural rigidity and high stability, is selected as a hydrogelator for the formation of supramolecular hydrogels. The unique hydrogen bonding in C-WY endows a high propensity for self-assembly and the resulting hydrogels are revealed to be crystalline. The crystalline hydrogels possess excellent mechanical capacity and superior tolerance to various harsh conditions, including in the presence of charged biopolymers, extreme acid/base environments, and changing thermal conditions. Such high tolerance enables the crystalline hydrogels to be applied in the complex and harsh environments of electrochemistry. In addition, this study demonstrates that the self-assembly of cyclic dipeptides results in highly robust hydrogels which can be applied for electrochemical applications such as electrochemical supercapacitors.

Introduction

On account of their high water content and highly tunable mechanical properties, hydrogels as soft nanoarchitectonics and soft matter are well-suited in extensive applications, such as tissue engineering, drug delivery, and electronic and photonic energy storage [1-10]. Self-assembled peptide materials have shown outstanding characteristics, such as excellent biocompatibility, structural flexibility, versatile functionality, and low immunogenicity [11-28]. Peptides can be deliberately engi-

neered to self-assemble into well-ordered hydrogels with adjustable mechanical and physicochemical properties [29-33]. Peptide-based supramolecular hydrogels have been widely used in biological and nanotechnology fields [34]. However, linear peptide-based hydrogels usually have several deficiencies, such as poor molecular rigidity, disabled mechanical modulus (storage or loss modulus), and poor environmental tolerance under thermal, acidic, or alkaline conditions [35-37]. Hence, new types of peptide hydrogels are highly needed to promote the practical applications of peptide hydrogels.

Cyclic dipeptides (CDPs), which are based on the basic structures of heterocyclic 2,5-diketopiperazines, are a special kind of dipeptides. They are the smallest cyclic peptides and contain six-membered heterocyclic lactam ring cores. CDPs exhibit exceptional structural rigidity, stability, as well as biological activity as compared to their linear counterparts [38-41]. There are many natural CDPs since they can be produced as secondary metabolites in many organisms. Hence, these are ideal raw materials for engineering functional architectures because of their unique biosecurity. Especially, CDPs contain four hydrogen-bonding sites, which provide a substantial tendency for self-assembly and the formation of gels. In addition, other weak forces, such as π–π stacking, hydrophobic effect, electrostatic interactions, and van der Waals forces, are also serviceable in driving molecular self-assembly of CDPs toward the formation of gels.

Gels prepared by CDP self-assembly integrate the advantages of low molecular weight gels, including the multiple functionalities, adjustable performance, and dynamic features. CDP-based gels have been developed as smart soft materials for a multitude of applications. However, most of the attention is focused on the amorphous assemblies in organic solvents and ionic liquids [42-46]. Although these CDP gels have good mechanical properties and deceased enzymatic degradation under physiological conditions, they still have some challenging problems such as inflexibility, low biosecurity and precipitation formation [47].

Herein, we investigate the self-assembly and application of a CDP, cyclo-(Trp-Tyr) (C-WY) (Scheme 1). C-WY contains a rigid six-member ring as a bridge, which increases the structural rigidity and stability. The abundant hydrogen bonds in C-WY endow a high propensity for self-assembly. In the previous example, the feasibility of C-WY peptide nanotubes as carriers of caspase 3 to silence shRNA delivery was verified. Based on these excellent characteristics of C-WY, it was selected as a hydrogelator for the formation of supramolecular hydrogels. The self-assembly of C-WY forms a hydrogel with crystal features and close-knit three-dimensional network structures. Importantly, the C-WY hydrogel exhibited adjustable rheological properties, excellent stability, and high tolerance under various conditions, including in the presence of charged biopolymers (poly-L-lysine (PLL), alginate (ALG), hyaluronic acid (HA)), extreme acid/base environments, and thermal conditions. Owing to the robustness of the hydrogel, the material also showed excellent performance as an electrochemical supercapacitor. Hence, self-assembled CDP hydrogels are promising for applications in complex and harsh environments.

Results and Discussion
Preparation and characterization of the hydrogel

C-WY was chosen as a model peptide to investigate the self-assembly of CDPs. A nontransparent hydrogel with a dense network of fibers was obtained simply by mixing a solution of C-WY in DMSO (2 mg, 20 µL) with water (480 µL) (Figure 1A). The hydrogen bonding interactions between the C-WY molecules were investigated by Fourier-transform infrared spectroscopy (FTIR). Compared with the peak of amide N–H stretching located at 3344 cm^{-1} of the unimolecular C-WY, the hydrogel has a red-shifted amide N–H stretching band located at 3317 cm^{-1}, indicating the formation of strong hydrogen bonds between C-WY molecules in the hydrogel (Figure 1B). Further characterization by scanning electron microscopy (SEM) and transmission electron microscopy (TEM) was performed to inspect the morphology of the hydrogel (Figure 1C,D). The fibers in the hydrogel are

Scheme 1: Schematic of the formation of self-assembled C-WY hydrogels and their applications in electrochemical supercapacitors.
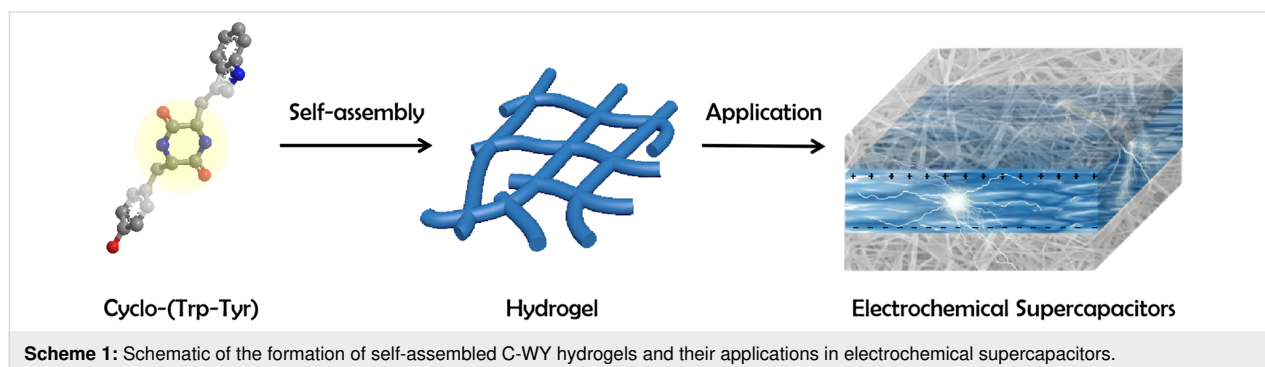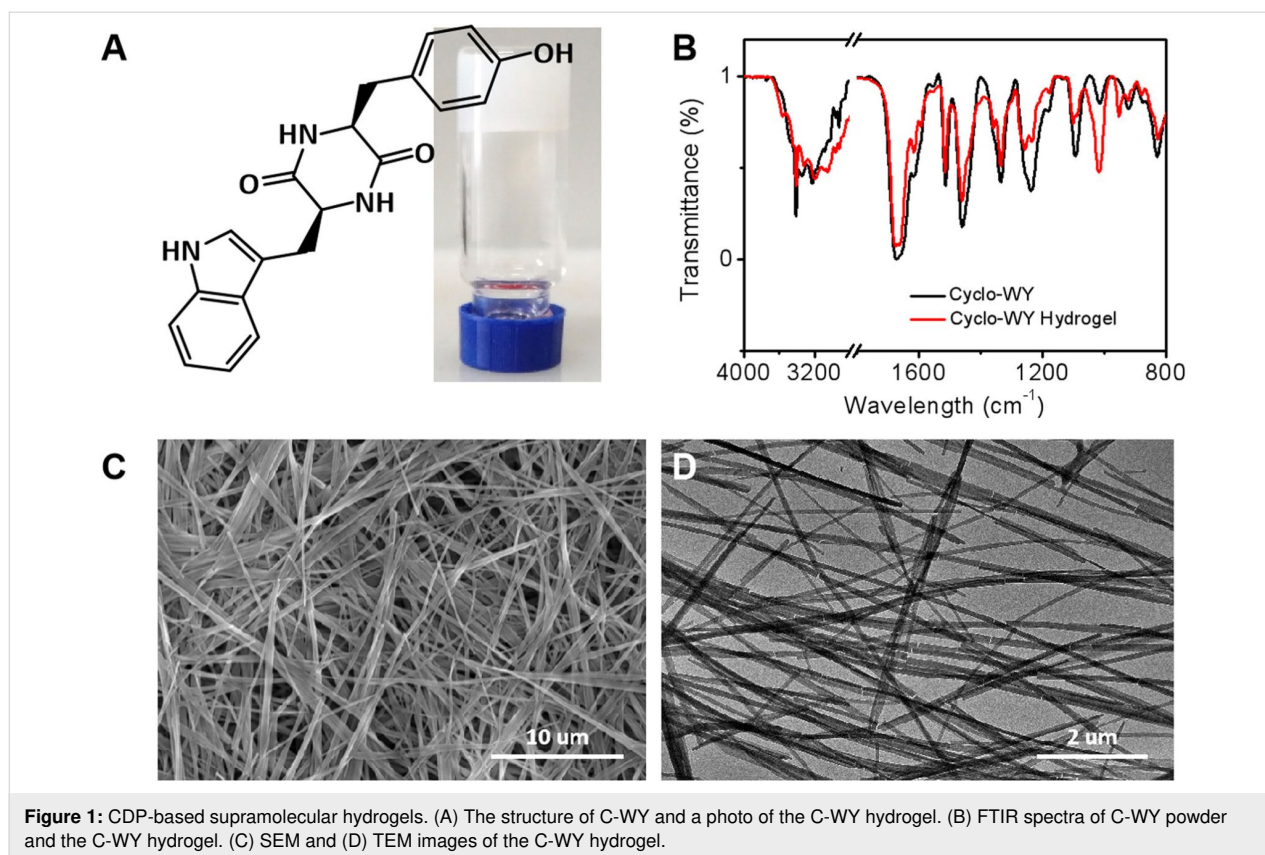
Figure 1: CDP-based supramolecular hydrogels. (A) The structure of C-WY and a photo of the C-WY hydrogel. (B) FTIR spectra of C-WY powder and the C-WY hydrogel. (C) SEM and (D) TEM images of the C-WY hydrogel.

100 ± 50 nm in width and dozens of micrometers in length. In addition, dense three-dimensional fibrous networks cross-linked by slender fibers were clearly observed. The cross-linked networks are beneficial to improving the stability of the hydrogels at extreme conditions [48]. The cross-linked networks are also the foundation for a range of biomedical and nanotechnological applications.

Interior structure and crystal pattern

The fibrillar structure and three-dimensional fibrous network of the C-WY hydrogel were further investigated by confocal laser scanning microscopy (CLSM) (Figure 2A). Thioflavin T (ThT) and nile red (NR), two specific dyes for hydrophobic domains and beta-sheet secondary structures, respectively, were used to obtain insights into the detailed interior structure of the hydrogel [49]. CLSM results confirmed that the C-WY hydrogel contains both hydrophobic domains (red regions) (Figure 2B) and beta-sheet secondary structures (blue regions) (Figure 2C). Intriguingly, the X-ray diffraction (XRD) results showed the presence of sharp peaks, indicating that the hydrogel has long-range, ordered, crystal patterns (Figure 2D). The crystal patterns were further confirmed by polarized optical microscopy (POM). POM images in cross-polarized light mode of a randomly selected fiber were taken ranging from 0° to 360° (Figure 2E). When the selected fiber was observed under a

cross-polarized angle of 0°, the sample was bright. In contrast, the sample turned dark when the cross-polarized angle was changed to 45°. The changing contrast behaviors between dark and bright changed periodically along with the angle changing by 45°. These results illustrate that the fibers in the hydrogel are intrinsically crystalline and thus have polarization properties.

Rheological properties

The rheological properties of hydrogels are key evaluation indicators for a variety of applications [50,51]. It is typically challenging for hydrogels based on linear peptides to maintain their original gel state for a long time or under shear force. Driven by a thermodynamic process, they tend to gradually form crystalline precipitations [34]. In order to investigate the rheological properties of the C-WY hydrogel, the storage (elastic, G') and loss (viscous, G'') modulus of the hydrogels aged for 48 h and 240 h were studied. The results showed that the mechanical capacity of the C-WY hydrogel enhanced along with time. Strain-induced shear-thinning and self-healing abilities of the hydrogel were detected through continuous step changes of oscillatory strain between 500% and 1% (at a constant frequency of 1 rad s^{-1}). Under a high magnitude strain (500%), the modulus of G'' values exceeded G' values, indicating the breaking of the hydrogel (Figure 3A). By decreasing the strain to 1%, the modulus of G'' falls below that of G', indicating the
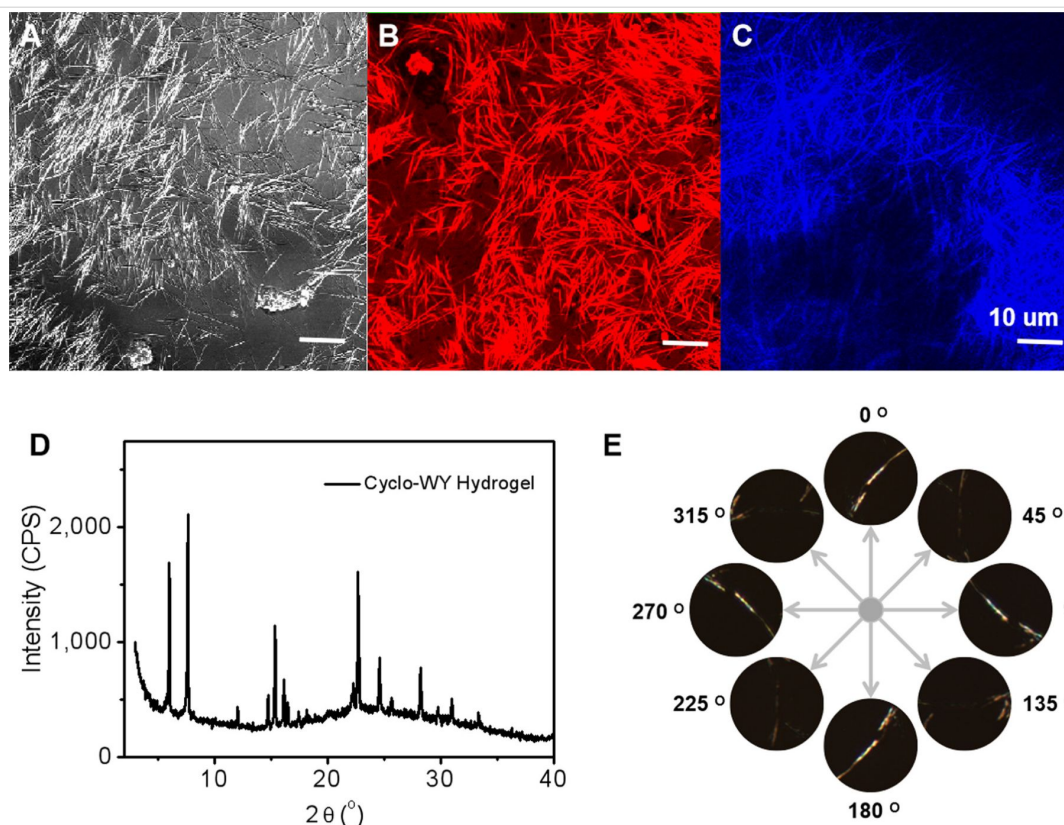
Figure 2: Interior structure and crystal pattern. (A) CLSM images of the C-WY hydrogel in light field. NR was used to indicate the formation of hydrophobic domains (red color, B) and ThT was used to indicate the beta-sheet secondary structures (blue color, C). (D) XRD pattern of the hydrogel. (E) POM images in cross-polarized light mode of samples taken at 0–360°.

recovery of the hydrogel (Figure 3B). These results illustrated that the recovery of the hydrogel is quick at both 48 h and 240 h, even at the fifth test cycle. As compared to that of 48 h, the C-WY hydrogel at 240 h showed a faster recovery speed. The strain-dependent oscillatory rheology results (at 240 h) showed a great anti-shear performance at stains ranging from about 0.1% to about 20%, indicating the shear-thinning behavior of the hydrogels. The hydrogel at 48 h was broken at a strain of more than 6% (Figure 3C). The hydrogels at both 48 h and 240 h exhibited broad linear viscoelastic regions ranging from 0.1–100 rad s^{-1} in frequency-dependent oscillatory shear rheology experiments (at a constant strain of 1%, Figure 3D). Meanwhile, the modulus (both G' and G'') was enhanced after aging for a longer time, indicating the improvement in the mechanical capacity of the hydrogels with time. Taken together, the rheological study indicates that the CWY hydrogels possess shear-thinning and self-healing behaviors, which are time-dependent and important for their applications.

Environmental tolerance

CDPs usually exhibit superior physical, chemical and thermal stability compared to their linear counterparts [52]. The hydrogels assembled from CDPs are therefore highly promising for

practical applications. In order to study the stability of the C-WY hydrogel, charged biopolymers, including positively charged PLL and negatively charged HA and ALG, were selected for co-incubation with the hydrogel. The mechanical properties, including modulus (G', G''), shear-thinning behavior, and self-healing capability, improved after the introduction of the biopolymers whether the biopolymers were positively or negatively charged (Figure 3C,D). Clearly, the electrostatic repulsion or attraction between the C-WY and biopolymers contributes to the enhancement of intermolecular interactions in the hydrogel, leading to the improvement of the rheological properties. The crystal structure remained unchanged (Figure 3E) and no obvious aggregation or precipitation was observed. Also, the microtopography of the hydrogel exhibited no obvious changes (Supporting Information File 1, Figure S1).

The environmental conditions, such as pH and temperature, play pivotal roles in practical application [53]. Also, the pH or temperature is closely related to the intermolecular forces in nanomaterials and thus always affects the stability of hydrogels. The morphology and mechanical properties of the C-WY hydrogels showed no significant change when they were incubated in acid or base solutions (pH 1 or pH 14) for 24 h (Sup-
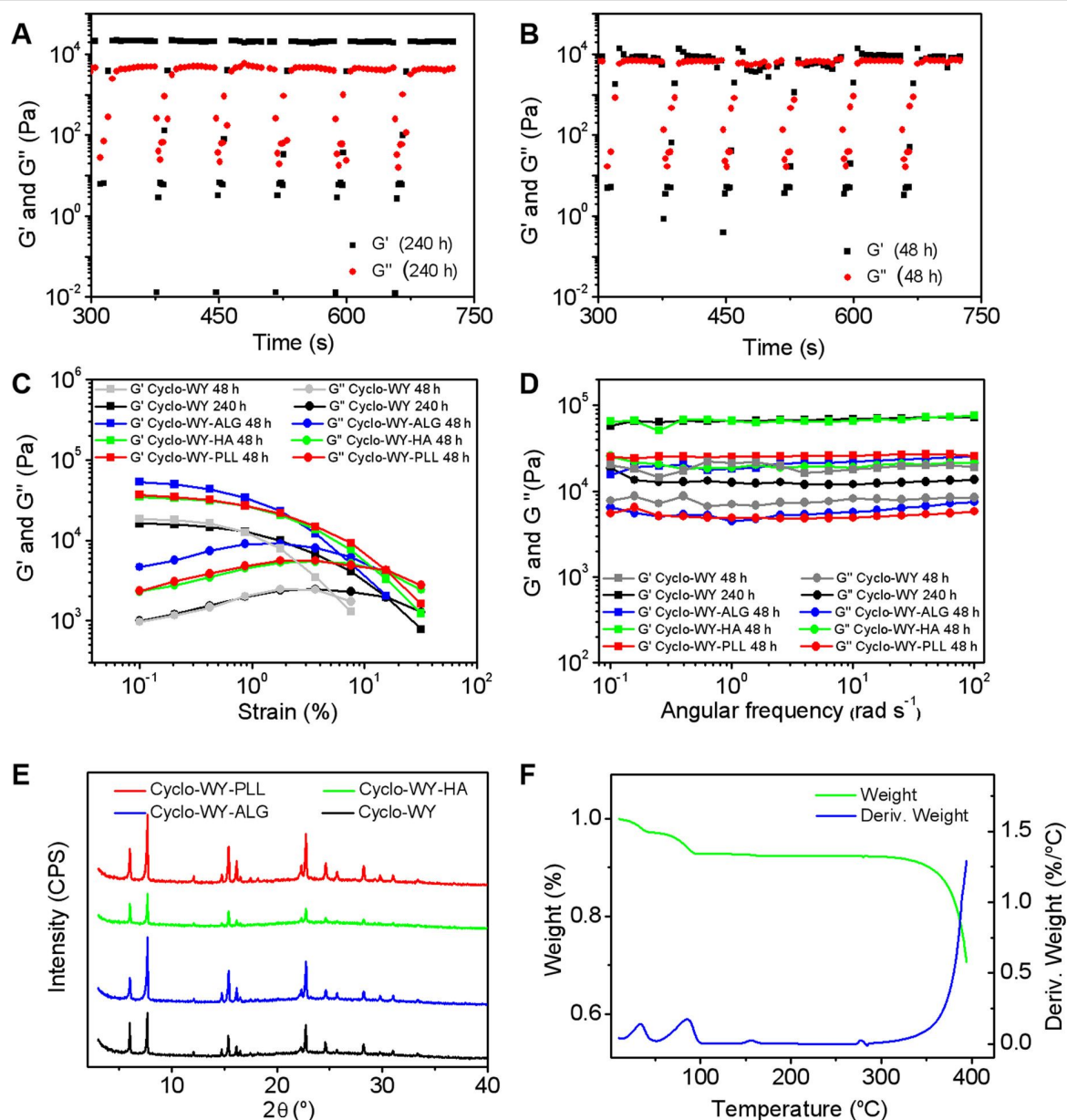
Figure 3: Rheological characterization and environmental tolerance. The self-healing capacity of the hydrogels at 48 h (A) and 240 h (B) demonstrated by the continuous step–strain experiments. Strain-dependent (C) and frequency-dependent (D) oscillatory shear rheology of the hydrogels under various conditions. (E) XRD patterns of hydrogels with various polymers. (F) TG curves of the C-WY hydrogel.

porting Information File 1, Figure S2 and S3). In addition, the thermogravimetric (TG) curves verified the robustness of the hydrogels for resisting temperatures ranging from 0 °C to about 350 °C. The TG curves of the hydrogels exhibited three thermal decomposition steps (Figure 3F). The first two temperature points were ≈40 °C and ≈95 °C, which should be mainly assigned to the loss of water. The third point was ≈350 °C, which should be assigned to the decomposition of C-WY molecules. The tolerance of hydrogels towards resisting biopolymers, pH and heat, may be due to the entangled fiber network and extensive intermolecular hydrogen bonds in the hydrogel.

In summary, the C-WY hydrogel was found to exhibit excellent environmental tolerance, including resistance to biopolymers, pH, and heat. Hence, the C-WY hydrogel is promising for applications in harsh environments, such as those of electrochemical supercapacitors.

Application in electrochemical supercapacitors

Inspired by the high stability in harsh environments, we next investigated the application of the C-WY hydrogel as a candidate material for electrochemical supercapacitors. Constraint

peptides are known for their superior chemical and stability compared to their linear counterparts. The hydrogels assembled from constraint C-WY peptides are therefore highly promising for application in bio-nanotechnology owing to their excellent stability from long-range ordered packing. Cyclic voltammetry (CV) curves of the hydrogel at different scan rates ranging from 10 to 40 mV were studied (Figure 4A). Typical capacitor shapes were observed in the curves, indicating that the C-WY hydrogel can be applied for electrochemical supercapacitors. In addition, the capacitive charge–discharge curves with galvanostatic current densities ranging from 25 to 200 mA/cm^2 showed that the hydrogel has excellent electrochemical stability (Figure 4B). These results indicate that hydrogels based on CDPs have commendable stability and thus can be applied as candidate components for supercapacitors.

Conclusion

In summary, we demonstrated that C-WY peptides can self-assemble into well-ordered fibrous networks based mainly on the inherent intermolecular hydrogen-bonding interactions. The hydrogel has a crystalline structure, excellent rheological properties, superior stability, and ideal robustness under various conditions, such as acidic or basic environments, or in the presence of charged biopolymers. Given its excellent electrochemical stability, the highly stable hydrogel was successfully demonstrated as an electrochemical supercapacitor. This study demonstrates that hydrogels based on self-assembly of CDPs can be valuable candidates for applications in harsh environments.

Supporting Information

Supporting Information File 1

Experimental section and additional figures.
[https://www.beilstein-journals.org/bjnano/content/supplementary/2190-4286-10-184-S1.pdf]

ORCID® iDs

Xuehai Yan - https://orcid.org/0000-0002-0890-0340

References

1. Jackman, J. A.; Cho, N.-J.; Nishikawa, M.; Yoshikawa, G.; Mori, T.; Shrestha, L. K.; Ariga, K. *Chem. – Asian J.* **2018,** *13,* 3366–3377. doi:10.1002/asia.201800935
2. Cringoli, M. C.; Kralj, S.; Kurbasic, M.; Urban, M.; Marchesan, S. *Beilstein J. Nanotechnol.* **2017,** *8,* 1553–1562. doi:10.3762/bjnano.8.157
3. Billiet, T.; Vandenhaute, M.; Schelfhout, J.; Van Vlierberghe, S.; Dubruel, P. *Biomaterials* **2012,** *33,* 6020–6041. doi:10.1016/j.biomaterials.2012.04.050
4. Zhao, L.; Zou, Q.; Yan, X. *Bull. Chem. Soc. Jpn.* **2019,** *92,* 70–79. doi:10.1246/bcsj.20180248
5. Hong, S.; Lee, H.; Lee, H. *Beilstein J. Nanotechnol.* **2014,** *5,* 887–894. doi:10.3762/bjnano.5.101
6. Pan, L.; Yu, G.; Zhai, D.; Lee, H. R.; Zhao, W.; Liu, N.; Wang, H.; Tee, B. C.-K.; Shi, Y.; Cui, Y.; Bao, Z. *Proc. Natl. Acad. Sci. U. S. A.* **2012,** *109,* 9287–9292. doi:10.1073/pnas.1202636109
7. Komiyama, M.; Yoshimoto, K.; Sisido, M.; Ariga, K. *Bull. Chem. Soc. Jpn.* **2017,** *90,* 967–1004. doi:10.1246/bcsj.20170156
8. Ariga, K.; Watanabe, S.; Mori, T.; Takeya, J. *NPG Asia Mater.* **2018,** *10,* 90–106. doi:10.1038/s41427-018-0022-9
9. Zhang, Y.; Zhang, H.; Zou, Q.; Xing, R.; Jiao, T.; Yan, X. *J. Mater. Chem. B* **2018,** *6,* 7335–7342. doi:10.1039/c8tb01487f
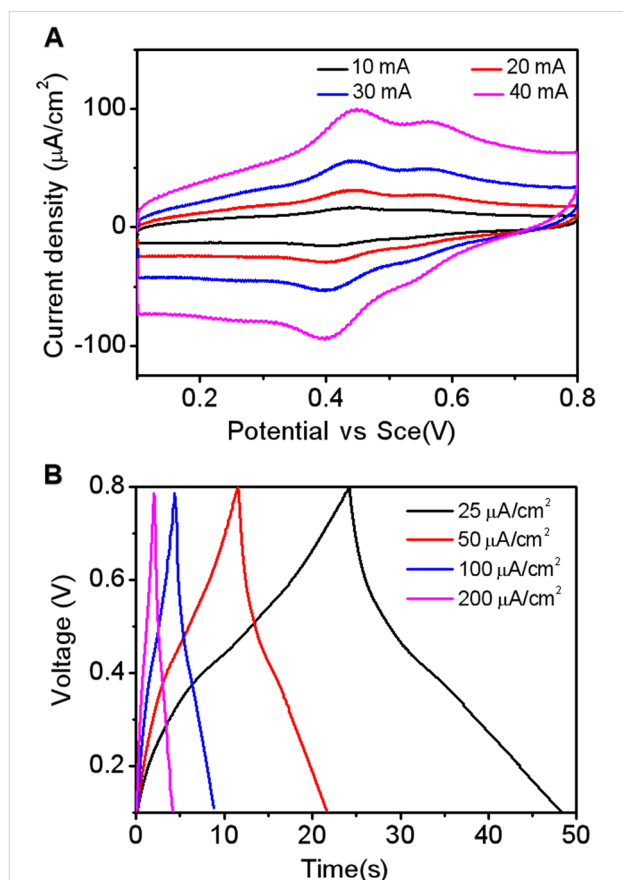

Figure 4: Characterization of hydrogels as supercapacitors. (A) Cyclic voltammograms at different scan rates. (B) Galvanostatic charge–discharge curves of C-WY hydrogels at different current densities.

10. Xing, R.; Liu, K.; Jiao, T.; Zhang, N.; Ma, K.; Zhang, R.; Zou, Q.; Ma, G.; Yan, X. *Adv. Mater. (Weinheim, Ger.)* **2016,** *28,* 3669–3676. doi:10.1002/adma.201600284

11. Shen, G.; Xing, R.; Zhang, N.; Chen, C.; Ma, G.; Yan, X. *ACS Nano* **2016,** *10,* 5720–5729. doi:10.1021/acsnano.5b07276

12. Xing, R.; Jiao, T.; Yan, L.; Ma, G.; Liu, L.; Dai, L.; Li, J.; Möhwald, H.; Yan, X. *ACS Appl. Mater. Interfaces* **2015,** *7,* 24733–24740. doi:10.1021/acsami.5b07453

13. Xing, R.; Li, S.; Zhang, N.; Shen, G.; Möhwald, H.; Yan, X. *Biomacromolecules* **2017,** *18,* 3514–3523. doi:10.1021/acs.biomac.7b00787

14. Wang, J.; Liu, K.; Xing, R.; Yan, X. *Chem. Soc. Rev.* **2016,** *45,* 5589–5604. doi:10.1039/c6cs00176a

15. Reches, M.; Gazit, E. *Curr. Nanosci.* **2006,** *2,* 105–111. doi:10.2174/157341306776875802

16. Zou, Q.; Abbas, M.; Zhao, L.; Li, S.; Shen, G.; Yan, X. *J. Am. Chem. Soc.* **2017,** *139,* 1921–1927. doi:10.1021/jacs.6b11382

17. Hamley, I. W. *Soft Matter* **2011,** *7,* 4122–4138. doi:10.1039/c0sm01218a

18. Hartgerink, J. D.; Beniash, E.; Stupp, S. I. *Science* **2001,** *294,* 1684–1688. doi:10.1126/science.1063187

19. Salaam, A. D.; Hwang, P.; McIntosh, R.; Green, H. N.; Jun, H.-W.; Dean, D. *Beilstein J. Nanotechnol.* **2014,** *5,* 937–945. doi:10.3762/bjnano.5.107

20. Liu, K.; Xing, R.; Zou, Q.; Ma, G.; Möhwald, H.; Yan, X. *Angew. Chem., Int. Ed.* **2016,** *55,* 3036–3039. doi:10.1002/anie.201509810

21. Zhang, S.; Marini, D. M.; Hwang, W.; Santoso, S. *Curr. Opin. Chem. Biol.* **2002,** *6,* 865–871. doi:10.1016/s1367-5931(02)00391-5

22. Abbas, M.; Zou, Q.; Li, S.; Yan, X. *Adv. Mater. (Weinheim, Ger.)* **2017,** *29,* 1605021. doi:10.1002/adma.201605021

23. Xing, R.; Yuan, C.; Li, S.; Song, J.; Li, J.; Yan, X. *Angew. Chem., Int. Ed.* **2018,** *57,* 1537–1542. doi:10.1002/anie.201710642

24. Li, G.; Li, S.; Sun, J.; Yuan, Z.; Song, A.; Hao, J. *Colloids Surf., A* **2018,** *558,* 57–64. doi:10.1016/j.colsurfa.2018.08.055

25. Cui, H.; Webber, M. J.; Stupp, S. I. *Biopolymers* **2010,** *94,* 1–18. doi:10.1002/bip.21328

26. Ren, X.; Zou, Q.; Yuan, C.; Chang, R.; Xing, R.; Yan, X. *Angew. Chem., Int. Ed.* **2019,** *58,* 5872–5876. doi:10.1002/anie.201814575

27. Yan, X.; Cui, Y.; Qi, W.; Su, Y.; Yang, Y.; He, Q.; Li, J. *Small* **2008,** *4,* 1687–1693. doi:10.1002/smll.200800960

28. Song, J.; Xing, R.; Jiao, T.; Peng, Q.; Yuan, C.; Möhwald, H.; Yan, X. *ACS Appl. Mater. Interfaces* **2018,** *10,* 2368–2376. doi:10.1021/acsami.7b17933

29. Ariga, K.; Li, J.; Fei, J.; Ji, Q.; Hill, J. P. *Adv. Mater. (Weinheim, Ger.)* **2016,** *28,* 1251–1286. doi:10.1002/adma.201502545

30. Abbas, M.; Xing, R.; Zhang, N.; Zou, Q.; Yan, X. *ACS Biomater. Sci. Eng.* **2018,** *4,* 2046–2052. doi:10.1021/acsbiomaterials.7b00624

31. Jayawarna, V.; Ali, M.; Jowitt, T. A.; Miller, A. F.; Saiani, A.; Gough, J. E.; Ulijn, R. V. *Adv. Mater. (Weinheim, Ger.)* **2006,** *18,* 611–614. doi:10.1002/adma.200501522

32. Chronopoulou, L.; Toumia, Y.; Cerroni, B.; Gentili, A.; Paradossi, G.; Palocci, C. *Colloids Surf., A* **2017,** *532,* 535–540. doi:10.1016/j.colsurfa.2017.04.003

33. Ma, D.; Zhou, N.; Zhang, T.; Hu, K.; Ma, X.; Gu, N. *Colloids Surf., A* **2017,** *522,* 97–104. doi:10.1016/j.colsurfa.2017.02.073

34. Mahler, A.; Reches, M.; Rechter, M.; Cohen, S.; Gazit, E. *Adv. Mater. (Weinheim, Ger.)* **2006,** *18,* 1365–1370. doi:10.1002/adma.200501765

35. Yan, C.; Altunbas, A.; Yucel, T.; Nagarkar, R. P.; Schneider, J. P.; Pochan, D. J. *Soft Matter* **2010,** *6,* 5143–5156. doi:10.1039/c0sm00642d

36. Yu, Z.; Xu, Q.; Dong, C.; Lee, S.; Gao, L.; Li, Y.; D'Ortenzio, M.; Wu, J. *Curr. Pharm. Des.* **2015,** *21,* 4342–4354. doi:10.2174/1381612821666150901104821

37. Adhikari, B.; Banerjee, A. *Soft Matter* **2011,** *7,* 9259–9266. doi:10.1039/c1sm06330h

38. Manchineella, S.; Govindaraju, T. *ChemPlusChem* **2017,** *82,* 88–106. doi:10.1002/cplu.201600450

39. Madhu, C.; Voshavar, C.; Rajasekhar, K.; Govindaraju, T. *Org. Biomol. Chem.* **2017,** *15,* 3170–3174. doi:10.1039/c7ob00167c

40. Jeziorna, A.; Stopczyk, K.; Skorupska, E.; Luberda-Durnas, K.; Oszajca, M.; Lasocha, W.; Górecki, M.; Frelek, J.; Potrzebowski, M. J. *Cryst. Growth Des.* **2015,** *15,* 5138–5148. doi:10.1021/acs.cgd.5b01121

41. Furukawa, T.; Akutagawa, T.; Funatani, H.; Uchida, T.; Hotta, Y.; Niwa, M.; Takaya, Y. *Bioorg. Med. Chem.* **2012,** *20,* 2002–2009. doi:10.1016/j.bmc.2012.01.050

42. Bellezza, I.; Peirce, M. J.; Minelli, A. *Trends Mol. Med.* **2014,** *20,* 551–558. doi:10.1016/j.molmed.2014.08.003

43. Hanabusa, K.; Matsumoto, Y.; Miki, T.; Koyama, T.; Shirai, H. *J. Chem. Soc., Chem. Commun.* **1994,** 1401–1402. doi:10.1039/c39940001401

44. Yan, X.; Su, Y.; Li, J.; Früh, J.; Möhwald, H. *Angew. Chem., Int. Ed.* **2011,** *50,* 11186–11191. doi:10.1002/anie.201103941

45. Hanabusa, K.; Matsumoto, M.; Kimura, M.; Kakehi, A.; Shirai, H. *J. Colloid Interface Sci.* **2000,** *224,* 231–244. doi:10.1006/jcis.1999.6672

46. Hoshizawa, H.; Suzuki, M.; Hanabusa, K. *Chem. Lett.* **2011,** *40,* 1143–1145. doi:10.1246/cl.2011.1143

47. Wang, P.; Zakeeruddin, S.; Exnar, I.; Gratzel, M. *Chem. Commun.* **2002,** *24,* 2972–2973. doi:10.1039/b209322g

48. Yang, M.; Xing, R.; Shen, G.; Yuan, C.; Yan, X. *Colloids Surf., A* **2019,** *572,* 259–265. doi:10.1016/j.colsurfa.2019.04.020

49. Wang, J.; Yuan, C.; Han, Y.; Wang, Y.; Liu, X.; Zhang, S.; Yan, X. *Small* **2017,** *13,* 1702175. doi:10.1002/smll.201702175

50. Yan, C.; Pochan, D. J. *Chem. Soc. Rev.* **2010,** *39,* 3528–3540. doi:10.1039/b919449p

51. Sun, J.; Guo, Y.; Xing, R.; Jiao, T.; Zou, Q.; Yan, X. *Colloids Surf., A* **2017,** *514,* 155–160. doi:10.1016/j.colsurfa.2016.11.062

52. Prasad, C. *Peptides* **1995,** *16,* 151–164. doi:10.1016/0196-9781(94)00017-z

53. Moreira, F. C.; Boaventura, R. A. R.; Brillas, E.; Vilar, V. J. P. *Appl. Catal., B* **2017,** *202,* 217–261. doi:10.1016/j.apcatb.2016.08.037

Review of advanced sensor devices employing nanoarchitectonics concepts

Katsuhiko Ariga[*1,2], Tatsuyuki Makita[2], Masato Ito[2], Taizo Mori[1,2], Shun Watanabe[2] and Jun Takeya[1,2]

Review

Address:
[1]WPI-MANA, National Institute for Materials Science, 1-1 Namiki, Tsukuba 305-0044, Japan and [2]Department of Advanced Materials Science, Graduate School of Frontier Sciences, The University of Tokyo, 5-1-5 Kashiwanoha, Kashiwa 277-8561, Japan

Email:
Katsuhiko Ariga[*] - ARIGA.Katsuhiko@nims.go.jp

* Corresponding author

Abstract

Many recent advances in sensor technology have been possible due to nanotechnological advancements together with contributions from other research fields. Such interdisciplinary collaborations fit well with the emerging concept of nanoarchitectonics, which is a novel conceptual methodology to engineer functional materials and systems from nanoscale units through the fusion of nanotechnology with other research fields, including organic chemistry, supramolecular chemistry, materials science and biology. In this review article, we discuss recent advancements in sensor devices and sensor materials that take advantage of advanced nanoarchitectonics concepts for improved performance. In the first part, recent progress on sensor systems are roughly classified according to the sensor targets, such as chemical substances, physical conditions, and biological phenomena. In the following sections, advancements in various nanoarchitectonic motifs, including nanoporous structures, ultrathin films, and interfacial effects for improved sensor function are discussed to realize the importance of nanoarchitectonic structures. Many of these examples show that advancements in sensor technology are no longer limited by progress in microfabrication and nanofabrication of device structures – opening a new avenue for highly engineered, high performing sensor systems through the application of nanoarchitectonics concepts.

Review
Introduction

Detection systems for various chemical, physical, environmental, and biological targets, so-called sensors, have been continuously explored [1-4]. Although their usefulness was recognized even in the early stages of modern science and technology, the importance of sensors has been recently re-evaluated in the context of current research developments. Today, sensors play an important role in technological advancement for various social demands. There are currently many strategies being

pursued for the production of functional materials [5-8], the detection of various risks [9-11], environmental remediation including pollution problems [12-14], energy production [15-17], energy and electricity storage [18-20], device technologies [21-23], and biomedical treatment [24-27], and the targets must be detected with high selectivity, high efficiency, environmental friendliness, and with low cost and low emission. Various fundamental areas of science and technology, such as organic synthesis [28-30], supramolecular organization [31-35], physical fabrication [36-38] and biotechnology [39-41], are expected to solve these problems where some additional factors have to be considered in order to achieve a high degree of control over the structure. This is accomplished by two major processes: (i) selective and sensitive recognition of external inputs (stimuli, substrates, etc.) and (ii) efficient logical conversion to outputs (response, energy, products, etc.). Good sensing systems have many contributions regarding the former part. This is why the importance of sensors has been re-recognized in modern sensor technology.

In recent decades, the development of sensor technologies has highly depended on advancements in microfabrication and nanofabrication of device structures. These so-called nanotechnological advancements enable us to prepare sensing devices with various advantageous features with an ultrasmall device size (thus requiring an ultrasmall amount of the target sample), highly integrated connection, and high sensitivity [42,43]. In addition to these nanotechnological advancements in device fabrication, sensing materials for molecular recognition have been continuously explored on the basis of supramolecular

chemistry with the aid of synthetic organic chemistry and materials science [44-46]. Therefore, further developments in sensors can be made by the combined efforts in nanotechnology and other research fields including supramolecular chemistry, organic synthesis, and materials sciences. In case of biosensors, contributions from biology play important roles [47-50]. These cross disciplinary collaborations that are necessary for sensor development fit well with the emerging concept of nanoarchitectonics [51,52], which involves a paradigm shift in research efforts to engineer functional materials and systems from nanoscale units through the fusion of nanotechnology with other research fields, including organic chemistry, supramolecular chemistry, materials science and biology. It can thus be said that the future developments of sensors can be supported by the field of nanoarchitectonics [53] (Figure 1).

The nanoarchitectonics concept was originally proposed by Masakazu Aono [54,55]. This conceptual methodology corresponds to the creation of functional materials from nanoscale units through combined processes, including organic synthesis, atomic/molecular manipulation, self-assembly, self-organization, stimuli-based arrangement, and biological treatment, depending on their necessity [56,57]. The high generality of the nanoarchitectonics concept can be applied to a wide range of research concepts, such as materials production [58-60], structure facilitation [61-65], catalysis [66,67], energy technology [68,69], environmental problems [70,71], biological investigation [72-75], and biomedical applications [76-78]. As compared with simple self-assembly processes, nanoarchitectonics is advantageous for architecting hierarchical structures and

Figure 1: Outline of the nanoarchitectonics concept and its contributions to sensor design and fabrication.
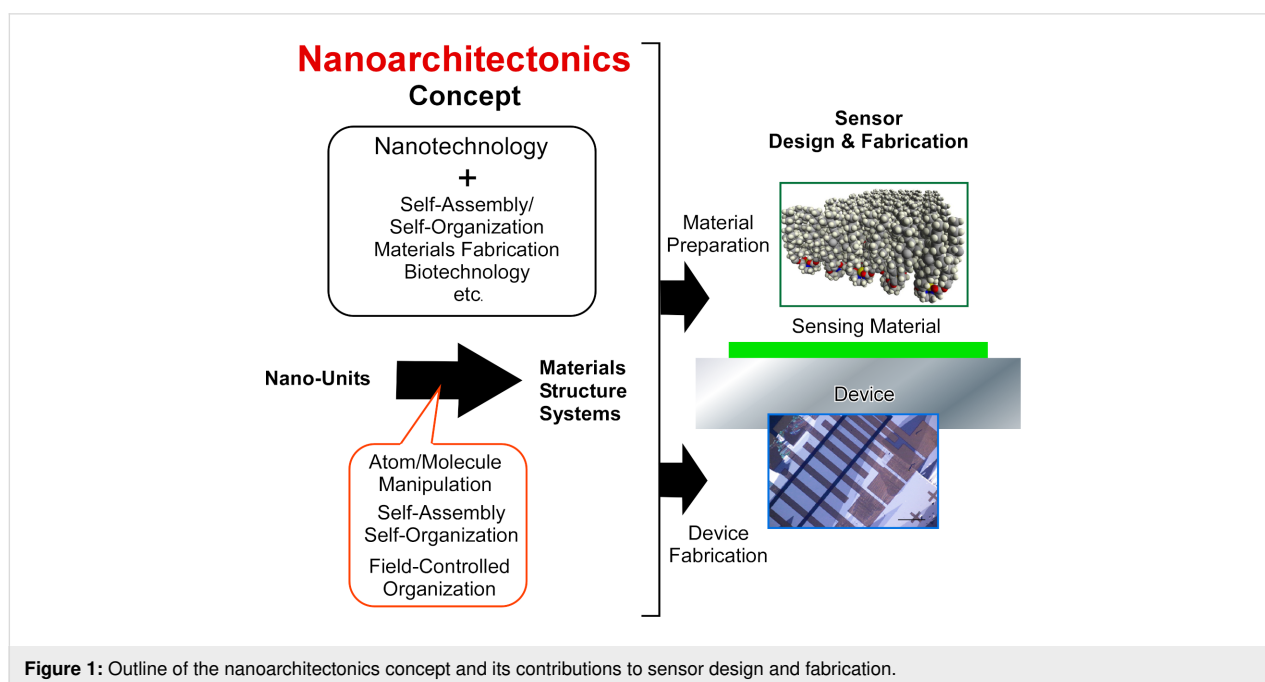
interfacing between materials and devices. In addition, the fabrication of sensor structures is one of the main outputs of nanoarchitectonics [79,80].

The nanoarchitectonics concept should also include uncertainties related to phenomena that occur on the nanoscale, where thermal and statistical fluctuations as well as quantum effects cannot be avoided [81]. The properties and functions on the nanoscale often result from the harmonization of various interactions. This feature is also found in many biological systems in which functional molecules harmonize under unavoidable thermal fluctuations. The nanoarchitectonics approach and biological processes thus share many of the same features [82]. Therefore, the design and fabrication of biosensors based on the nanoarchitectonics concept may have many particular advantages.

In this review article, we first discuss several examples of recent progress in sensor systems whose advanced nanoarchitectonic design and fabrication allowed for better performance. The examples are roughly classified according to the sensor target, such as chemical substances, physical conditions, and biological phenomena. In the following sections, advancements employing nanoarchitectonic motifs, including nanoporous structures, ultrathin films, and interfacial effects for sensor functions, are discussed. Based on these descriptions, we hope that we can impress the importance upon the advancements of sensor functions with nanoscale control, and especially the importance of nanoarchitectonics in the improvement of these concepts.

Recent examples of advanced sensors

Advancements in sensor capabilities, including sensitivity, selectivity and usability, can be accomplished by ultrafine design of device mechanisms and sensing material structures. Both the device and sensing material design can be accomplished with a combined concept, nanoarchitectonics, derived from nanotechnology (mainly for the device) and supramolecular chemistry and others (mainly for the sensing materials). For example, Osica recently reported sensor systems for selective acetone vapor detection [83,84]. The prepared systems are supported by two separate innovations, a membrane-type surface stress sensor as a novel nanomechanical device and a highly networked capsular nanoarchitecture of silica–porphyrin hybrid as the sensing material. Not limited to this particular case, innovations from both the device side and the materials side for improved sensors has been continuously pursued.

Sensors for chemical substances

Mainly due to the high demand to solve environmental problems, vapor sensors and gas-phase chemical sensors have been

actively researched. Tang and co-workers accomplished drastic improvement of sensitivity of H$_2$S gas detection by mechanical deformation of ultrathin single crystals of dinaphtho[3,4-*d*:3',4'-*d*']benzo[1,2-*b*:4,5-*b*']dithiophene in organic field effect transistors [85] (Figure 2). At the tensile state of the crystals, the sensitivity to H$_2$S gas at 1 ppm increased by 400% as compared to the original unstressed state. Upon exposure of the sensor crystals to H$_2$S gas, the adsorbed H$_2$S gas molecules induce a current between the source and drain. Changes in the intermolecular packing of the sensing organic crystals may cause more exposure of active sites to H$_2$S gas and dramatic shifts of mobility, resulting in unexpectedly high sensitivity. This example indicates that the delicate modulation of nanoarchitectures can improve chemical sensor capabilities.
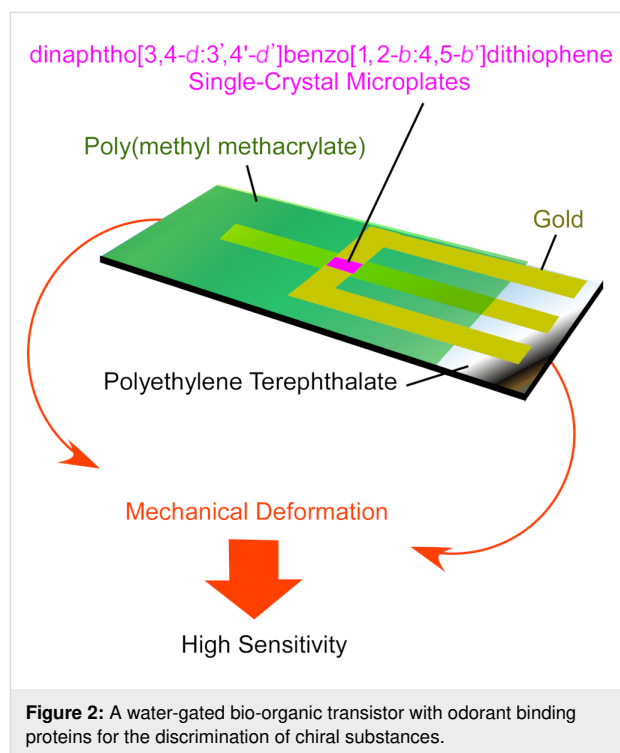
Figure 2: A water-gated bio-organic transistor with odorant binding proteins for the discrimination of chiral substances.

As an example of nanoarchitectonics effects between multiple components in sensing materials, Chen, Shi, and co-workers demonstrated highly sensitive resistance-based NO$_x$ gas sensors incorporating a dispersed composite of Co$_3$O$_4$ nanoparticles in black phosphorous thin films [86]. The composite structures were engineered by functionalization of black phosphorous nanosheets with branched polyethylenimine to which Co$_3$O$_4$ nanoparticles were included with a hydrothermal process. The sensor composite structures showed ultrahigh sensitivity and a fast response to NO$_x$ gas at room temperature in air, leading to a low detection limit even down to 10 ppb, probably due to the synergic effects of the unique electronic conduction of black phosphor and the heterostructure of the Co$_3$O$_4$ nanoparticles.

The inclusion of other processes, such as catalytic reactions and fluorescence quenching, often improves sensor capabilities through component nanoarchitectonics. Imanaka and co-workers used a combustion process induced by a precious-metal-free CeO_2–ZrO_2–ZnO catalyst for CO gas detection [87]. The semiconducting (p-type) La_2CuO_4-loaded CeO_2–ZrO_2–ZnO catalyst has a small heat capacity and dramatically increases the temperature of the Pt coil, resulting in a highly sensitive sensor signal. On the other hand, the n-type Sm_2CuO_4-loaded CeO_2–ZrO_2–ZnO catalyst is advantageous when rapid response and low temperature operation are required. The selection of nanoarchitectonic component materials in sensing units can be used to optimize sensing performance according to usage.

Luminescent xerogel-based sensors for amine vapors were reported by Hanabusa and co-workers [88]. The xerogels used in this sensor system were prepared with fluorescent gelators containing a tris(β-diketonato) complex with appropriate metals. The presence of amines can be found through fluorescence-quenching efficiencies of the thin layer films of the gel materials. The prepared films are most sensitive to the detection of tertiary amines.

The discrimination and sensing of chiral substances are regarded as a more difficult task because chiral molecules have identical properties except for their optical activity. As recently reported by Kondo et al., the use of chiral receptors is the key to discriminate chiral substances [89]. They used tetraamide-based receptors having chiral L-serine and L-threonine to discriminate enantiomers of *N*-acetyl amino acid anions through ratiometric fluorescence analysis. Torsi and co-workers adopted odorant binding proteins to discriminate chiral substances [90]. They immobilized odorant binding proteins to the gate of a water-gated bio-organic transistor (Figure 3). In this construction, the source and drain patterned substrate was covered with p-type poly[2,5-bis(3-tetradecylthiophen-2-yl)thieno[3,2-b]thiophene], a water droplet and a Au-plate modified with the odorant binding protein as a gate. Enantiomers of odorant carvone could be clearly discriminated by this sensing system. The capacitance changes may be caused by the binding of the odorant to the protein accompanied with the derivation of the free-energy and conformational changes. Such capacitance-modulated transistors would be useful for molecular sensing with weak interaction and faint differences.

Kim and co-workers fabricated sensor arrays that were engineered with fluorescence dyes and cucurbit[*n*]urils (*n* = 6, 7 and 8) as host systems [91]. The obtained sensors were used for sensing biogenic amines with the aid of principal component analysis. This nanoarchitectonics strategy could be applied for

Figure 3: Highly sensitive humidity sensor based on a triboelectric nanogenerator device where nanochannels in the membrane adsorb moisture, which results in the generation of internal stress.
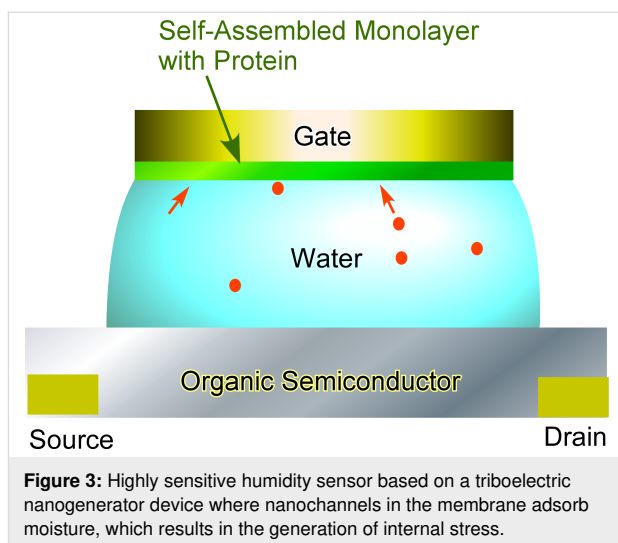
the sensing of various bio-related substances and may become useful for diagnostics of diseases such as cancer.

Sensors that are used to detect environmental risks mostly require detection of metal ions and toxic ions. Akamatsu et al. developed an optode-type sensor to visually detect cesium ions in domestic water and seawater [92] (Figure 4). The detection of radioactive cesium species becomes a serious demand after a nuclear plant explosion event, but radioactivity measurements do not always work with high areal resolution. The detection of cesium ions themselves with very high resolution would be useful together with radioactivity analysis. Cesium ion sensing using a film-type optode and nano-optode sensors would satisfy the former requirements. The optode sensors designed using nanoarchitectonic concepts incorporated a calix[6]arene derivative, responsive dye KD-M1337, and a cation exchanger sodium tetrakis[3,5-bis(trifluoromethyl)phenyl]borate. The binding of cesium ions to the calix[6]arene derivative shifts the equilibrium, resulting in color changes even in domestic water and seawater. Sonicating this optode mixture provides nano-optode sensor particles at a diameter of approximately 100 nm, which is a material capable of detection of cesium ions in sub-micromolar levels.

Use of 2D and layered materials in nanoarchitectonics for ion sensors is also investigated. Ruiz-Hitzky et al. reported the fabrication of potentiometric sensors for alkali-ion detection using clay materials intercalated with silacrown ethers, dimethylsila-14-crown-5 and dimethylsila-17-crown-6 [93]. The nanoengineered montmorillonite-based intercalation materials were included in poly(vinyl chloride)-based electrodes for potentiometric sensors towards alkali-metal ions in solution. Ultrasensitive sensors for mercury ions were prepared by Li et al. who engineered suspended atomically thin black phosphorus be-
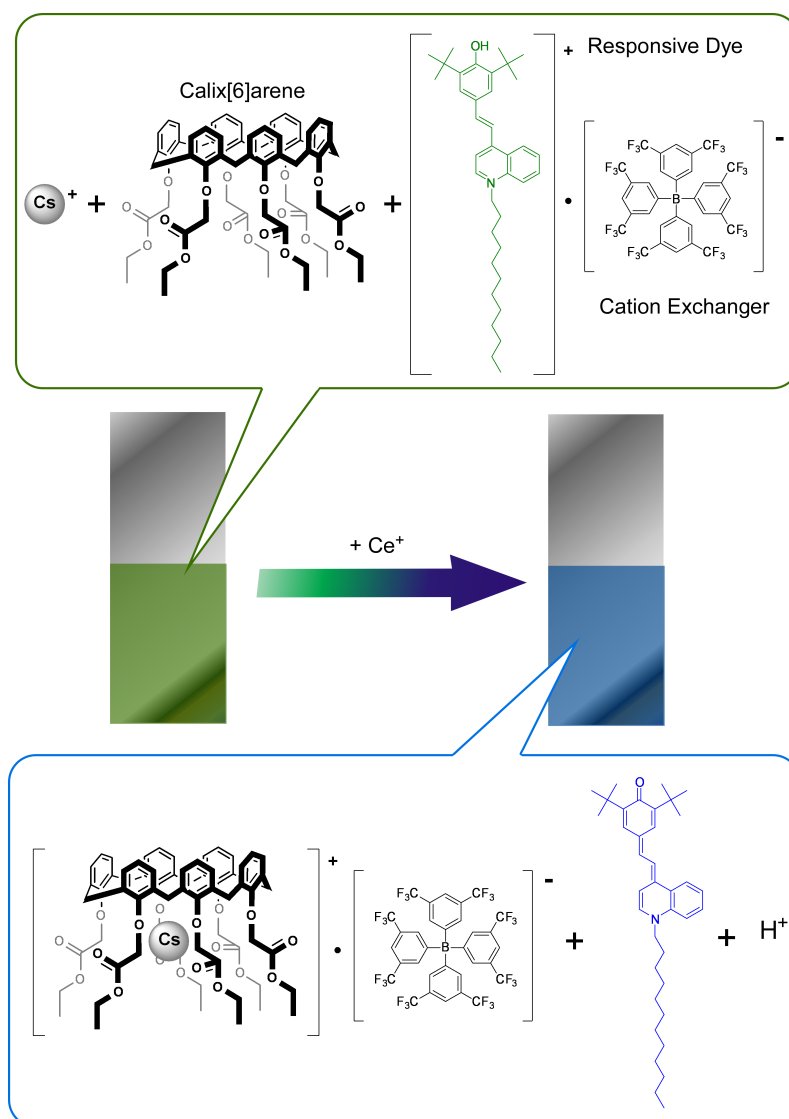
Figure 4: An optode sensor to visually detect cesium ions in domestic water and seawater, comprised of a calix[6]arene derivative, responsive dye KD-M1337, and cation exchanger.

tween the source and drain electrodes [94]. Due to the avoidance of substrate scattering, the sensors with bridged black phosphorus exhibit a much improved signal-to-noise ratio in mercury ion detection with a detection limit of 0.01 ppb and a very short detection time constant of 3 s. This nanoarchitectonic design can maximize the intrinsic potential of black phosphorus and other materials.

Sensors for physical conditions

Not limited to particular chemicals, the sensing of general external environments such as pH, humidity, pressure, and magnetic field is undoubtedly important. Spanu et al. reported sensitive pH sensors based on organic charge-modulated field-effect transistor structures with 6,13-bis(triisopropylsilylethynyl)-

pentacene [95]. The fabricated sensors have a super-Nernstian sensitivity and reference-less nature. This organic charge-modulated field-effect transistor mechanism is attributed to the variation of the threshold voltage in the organic field-effect transistor induced by charge variation upon the presence of a charge (protonation, etc.) on the sensing area. The sensitivity of the nanoengineered sensors is easily tunable by adjusting geometry-related parameters.

For practical uses, sensors are not always used in ideal conditions. Especially, their use in dynamic human life, including health monitoring and medical applications, require consideration of bending and deformation according to typical human motions. Someya and co-workers developed transparent

bending-insensitive pressure sensors [96]. They nanoengineered pressure sensor materials from composites of carbon nanotubes and graphene with a fluorinated copolymer, vinylidenefluoride-tetrafluoroethylene-hexafluoropropylene, and an ionic liquid, 1-butyl-3-methylimidazolium bis(trifluoromethanesulphonyl)imide, through an electrospinning process. The prepared sensor can only sense normal pressure without significant disturbance up to a bending radius of 80 μm. This sensor system could be applicable for demands requiring the evaluation of small normal pressures even on dynamic surfaces such as natural tissues and is expected to be useful for in situ biomedical digital monitoring, such as palpation for breast cancer.

Triboelectric nanogenerators to convert mechanical energy to electricity have recently been given much attention as self-powered systems. These systems can be designed using nanoarchitectonic principles with various sensing materials to form energy harvesting self-powered sensors [97,98]. Chen and co-workers introduced a perfluorosulfonic acid ionomer as a water-vapor-driven actuation material for a triboelectric nanogenerator device to realize a highly sensitive humidity sensor [99] (Figure 5). The reaction of the sensing materials to humidity results in electrical changes for sensing. The perfluorosulfonic acid ionomer membrane has perpendicularly extended nanochannels that can adsorb moisture. Under relatively high humidity conditions, the adsorption of water molecules expands the nanochannels resulting in internal stress generation. These changes can be sensitively detected by the triboelectric nanogenerator. At the same time, the collection of such electrical signals can work as energy harvesting devices from wind and raindrops. Similarly, Liao, Wang, and co-workers used a triboelectric nanogenerator system of thin films of fluorinated ethylene propylene to fabricate self-powered wind sensors operating in free-standing mode (anemometer triboelectric nanogenerator) and single-electrode mode (wind vane triboelectric nanogenerator) [100]. The former mode can be used for analysis of wind speed with less energy consumption and the latter one provides an accurate measurement for the wind direction. The wireless monitoring of these responses could contribute to large-scale climate monitoring.

Although various living creatures, including bacteria, insects, birds, and sharks, can sense magnetic fields for orientation and navigation, humans are basically insensitive to magnetic fields. The human detection of magnetic fields can be realized using electro-skin-type sensors for magnetic fields. Makarov and co-workers developed giant magnetoresistive sensors in foil form having high flexibility and mechanical durability [101]. For giant magnetoresistive materials, multilayer structures of Co/Cu and permalloy/Cu multilayers (permalloy = $Ni_{81}Fe_{19}$)

Figure 5: An electrolyte-gated organic field-effect transistor with anti-bisphenol A antibody. The addition of bisphenol A induces the removal of the antibody from the sensor surface, resulting in an increase in the drain current.
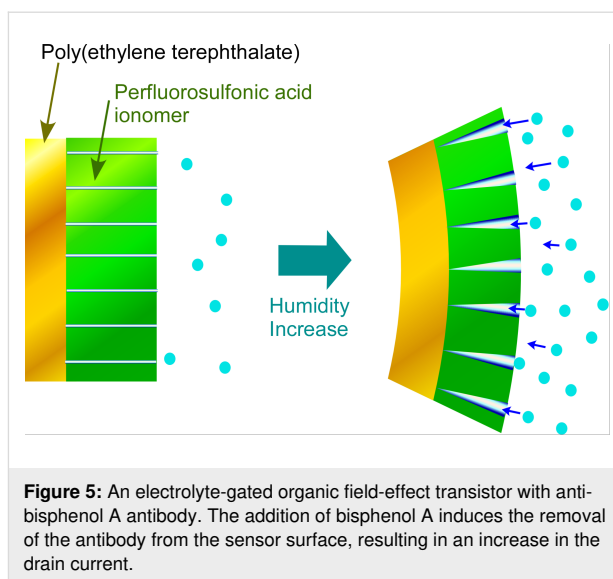
were engineered on ultrathin polyethylene terephthalate foils. The prepared sensors are extremely flexible (bending radii <3 μm) and light weight (≈3 g m^{-2}). They are wearable and act as a magneto-sensitive skin with navigation and touchless control capabilities.

Biosensors

Because biosensors can provide crucial contributions to human life, medical, and health monitoring, the development of biosensors has received significant attention. For example, for the detection of bisphenol A, which is suspected as an endocrine disruptor, Piro et al. produced a nanoarchitectonic electrolyte-gated organic field-effect transistor with poly(2,5-bis(3-tetradecylthiophen-2-yl)thieno[3,2-b]thiophene) as an organic semiconductor co-crystallized with an alkyl derivative of bisphenol A as a hapten [102] (Figure 6). Upon binding of the anti-bisphenol A antibody, the output current of the transistor first decreased. The addition of bisphenol A induced the removal of the antibody from the sensor surface through competitive binding, resulting in a capacitance increase accompanied with an increase of the drain current. The switching-on signal response of this system is in the nM range of concentration threshold for bisphenol A detection. This sensitivity is sufficient for the detection and monitoring of this persistent pollutant in drinking water.

As mentioned previously, the discrimination of chiral substances is a rather tough goal in sensor design. However, the detection of chiral amino acids is an unavoidable matter in technologies related to protein metabolism, food products and pharmaceuticals. Such difficult goals can be achieved through a nanoarchitectonics approach, namely molecular imprinting [103-105]. Qiu and co-workers developed sensors for chirality

Figure 6: A field-effect transistor with a monolayer of pentathiophene-type organic semiconductor for melamine detection where the monolayer structure of the semiconductive layer provides better sensor performance with long-term stability and high sensitivity.
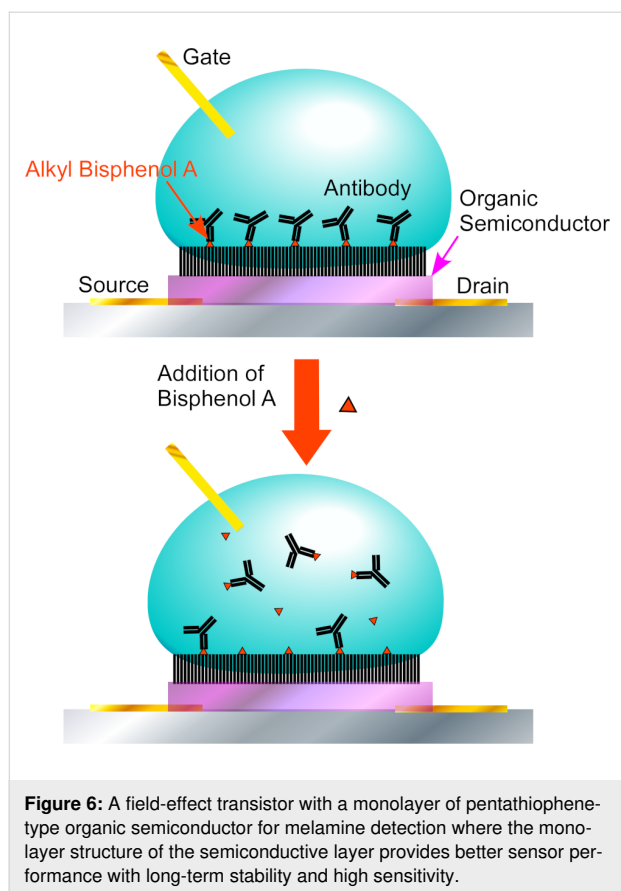
detection of amino acid guests using an organic electrochemical transistor with a poly(3,4-ethylenedioxythiophene)/poly(styrenesulfonate) (PEDOT/PSS) system modified with molecularly imprinted polymer films [106]. The selectivity factor of ʟ-tryptophan over ᴅ-tryptophan and that of ʟ-tyrosine over ᴅ-tyrosine were 11.6 and 14.5, respectively.

Life activities are also important targets in biosensor technology. Someya and co-workers developed a highly flexible organic amplifier to detect weak biosignals [107]. A highly conductive biocompatible gel composite made from multiwalled carbon nanotubes and aqueous hydrogel was integrated into a two-dimensional organic amplifier. The biocompatible nature of these nanoarchitectures is advantageous to favorably interface the bio-tissues and device electrodes. The dynamic motion of a living heart can be sensitively monitored without mechanical interference. This enables the direct evaluation of epicardial electrocardiogram signals with an amplification factor of 200. This idea can be expanded to various practical sensing demands such as temporal monitoring during medical surgery and long-term implantable monitoring. Ingebrandt and co-workers also reported biosensors to monitor electrophysiological activity of the cardiac cell line HL-1 [108]. The sensing system is based on organic electrochemical transistors with PEDOT/PSS materials

produced with a wafer-scale process, which is known to be useful for transducing and amplifying biological ionic signals.

In certain cases, device architectures and cell nanoarchitectures have to be well-matched for better sensor performance. Hsing and co-workers investigated the difference in sensing signals between tightly packed colorectal adenocarcinoma cells and leaky nasopharyngeal carcinoma cells using biosensors based on an organic electrochemical transistor [109]. The biosensor performance depends on the impedance of whole the system, including the transistor devices and monitored cells. Since cell packing affects the sensor signal, the optimum design of such cell sensors should be tuned according to cell packing. In order to evaluate the paracellular characteristics of tightly packed cells, a large-sized organic electrochemical transistor is advantageous. On the other hand, the high frequency related information of leaky cells can be effectively monitored by smaller organic electrochemical transistors.

Biosensors based on the electrical double layer gated AlGaN/GaN high electron mobility transistors were used to dynamically monitor changes in the transmembrane potential, as reported by Lee, Wang, and co-workers [110]. Here, circulating tumor cells of colorectal cancer together with cellular bioelectric signals were investigated. The proposed sensor design would also be useful for the rapid screening of diseases as a point-of-care diagnostic tool. Owens and co-workers developed organic field-effect transistor systems with PEDOT/PSS materials for the detection of lactate [111]. Enhanced lactate production was detected for cancer cells because of their promoted activity of glycolytic metabolism. These nanoengineered miniaturized biosensors would be useful for the continuous monitoring of tumor status in cancer patients.

Advancements in nanoarchitectonic motifs

In the previous sections, several examples of advanced sensor systems were reviewed according to sensing targets, chemical substances, physical conditions, and biological activities. The importance of a high degree of structural control (microscopic and nanoscopic levels) both for the sensing materials and the device structures can be found in most of the cases. Advanced sensors are certainly improved by application of nanoarchitectonics strategies. In the following sections, sensor designs are discussed on the basis of nanoarchitectonic structural motifs, such as nanoporous structures and extremely thin nanofilms as well as the highly enhanced molecular sensing capability at interfacial structures.

Porous structures

One of the most highly effective methods to improve the sensitivity of sensors is the enhancement of the surface (interfacial)

area for facile contact between the sensing target molecules and sensor device material. High surface area materials such as integrated structures and nanoporous materials can be obtained by molecular self-assembly [112-114] and template synthesis [115-119]. For example, various sensors with self-assembled fullerene materials and their carbonized materials as sensing structures were reported for aromatic gas vapors [120,121] and carbonized particles [122]. Mesoporous carbons were used for sensing of tannins in acidic aqueous environment with highly cooperative adsorption in the mesochannels [123]. The nanoarchitectonic construction of carbon nanocages with high surface mesoporous structures [124] was integrated with electrospun polymer fibers and resulted in a highly sensitive sensing material for aniline vapor [125]. Layer-by-layer structures of mesoporous carbon capsules can work as sensing membranes capable of selectively sensing through the doping of secondary sensing units [126].

As an emerging nanoporous material, metal–organic frameworks and porous coordination polymers have received much attention because of the various functional nanoporous structures that can be engineered through self-assembly from selected components [127-130]. Pan, Su, and co-workers fabricated metal–organic framework materials with microporous structure and switchable luminescence capability for sensitive water detection [131]. The metal–organic framework sensor was prepared from Zn and (5-(2-(5-fluoro-2-hydroxyphenyl)-4,5-bis(4-fluorophenyl)-1*H*-imidazol-1-yl)isophthalic acid) ligands, the latter of which shows a characteristic excited state intramolecular proton transfer. The adsorption of water molecules into the micropores induces interconversion between the hydrated and dehydrated phase, accompanied by the switching on and off of the excited state intramolecular proton transfer, resulting in sensitive switching between two-color photoluminescence. The sensing films consisting of paper and ZnO could realize a very sensitive water detection with a relative humidity of less than 1% and the detection of trace-level water of less than 0.05%. In addition, the interference from any small molecules other than water is also avoided. The precise nanoarchitectonic control of the structure results in high sensitivity and selectivity.

The nanoporous architectures of metal–organic frameworks can also serve as filters for molecular selection. Fan and co-workers prepared an electrical gas sensor for formaldehyde with high selectivity using the molecular sieving function of zeolitic imidazolate framework structures on ZnO nanorods [132]. Core–shell structures of zeolitic imidazolate frameworks and ZnO nanorods were prepared by direct growth of the framework on the ZnO nanorods. Limitation effects by the framework aperture provided improved selectivity for formaldehyde

over the other volatile organic compounds. This nanoarchitectonic strategy using molecular sieving effects of nanoporous frameworks can be applied to other targets of selected molecular size.

Ultrathin films

The immobilization of functional materials with ultrathin films such as self-assembled monolayers [133,134], Langmuir–Blodgett films [135-137], and layer-by-layer assembly [138-141] on sensors and related devices is a key nanoarchitectonics step for sensor fabrication. For example, Furusawa et al. immobilized nickel-nitrilotriacetic acid within a self-assembled monolayer on an organic field-effect transistor, which was used for the sensitive detection of small organic acid molecules, such as citric acid [142]. Hattori and co-workers fabricated an ATP/ADP sensitive image sensor by immobilization of apyrase as a self-assembled monolayer on a 128 × 128 pixel array semiconductor CCD-type pH imaging sensor [143]. Although the sensitivity of the prepared sensor is inferior to that of other fluorescence sensors, this sensor nanoarchitectonics approach does not require any labelling procedures. Therefore, it may be useful for the estimation of ATP discharge in damaged cells.

Ultrathin film nanoarchitectures are crucial not only for the facile contact between analytes and the sensor device but also with respect to the carrier mobility for semiconductor-based sensor devices. The enhancement of sensor performance on ultrathin films has been recognized in several recent research efforts. Guo and co-workers fabricated a field-effect transistor with monolayers and multilayers of pentathiophene-type organic semiconductor for melamine detection [144] (Figure 7). The used dialkoxyphenyl pentathiophene derivative has a semiconductive pentathiophene core sandwiched by two insulating C_{12} alkyl chains. Long-range ordered π-conjugated columns in densely packed arrays of the pentathiophene core confine charge carrier transport to one direction. The charge generation and transport can be effectively maximized by this carrier transport confinement. The fabricated field-effect transistor structure was integrated into a microfluidic device. The monolayer structure of the semiconductive layer provided better sensor performance with long-term stability and high sensitivity. The minimum detection limit for melamine was approximately 10 ppb.

The high performance of nanoarchitectonic semiconductive monolayers was also demonstrated by Chan and co-workers who successfully prepared semiconductor monolayer crystals of 2,9-didecyldinaphtho[2,3-b:2',3'-f]thieno[3,2-b]thiophene on the millimeter scale [145]. The semiconductor crystals encapsulated within poly(methyl methacrylate) exhibited a significantly high mobility (10.4 cm^2 V^{-1} s^{-1}). In multilayer structures,

Figure 7: Features of molecular recognition at interfacial media: (i) contacts of phases with different dielectric natures to result in huge enhancement of molecular recognition; (ii) connection of extremely different size events, enabling the manipulation of molecular receptors by macroscopic motion. Adapted with permission from [51] copyright 2015, The Royal Society of Chemistry.

the first layer on interface plays the main role in carrier transport and the layers above simply act as carrier suppliers. The crystal monolayer shows low anisotropy and thermally activated carrier transport. Such characteristics are different from the band-like carrier transport modes in thicker crystals. The fabricated sensor with ultrathin organic semiconductor crystals was an efficient NH_3 sensor with a detection limit on the 10 ppb level.

Specific effect of molecular sensing at interfaces

The high surface area nature of nanoporous materials and the ultrathin aspect of monolayer crystals are advantageous for improved sensor performance. These structural features can also be regarded as interfacial nanoarchitectonics. In this section, the scientific basis for molecular sensing (recognition and discrimination) specific to interfacial environments is briefly described and hints for future sensor designs are discussed. Interfacial environments provide two distinct features, (i) contacts of phases with different dielectric natures and (ii) connection of extremely different size events (both along the lateral direction and thickness direction, Figure 8).

Interfaces provide the potential of contact between two different media. Molecules with recognition capability (receptor mol-

ecules) prepared through organic synthesis are not always soluble in the aqueous phase and are not appropriate for sensing of water-soluble targets in solution phases. Placing such water-insoluble receptor molecules at a water-contacting interface is crucial to sense water-soluble substances such as important biomolecules. Not limited to this technical requirement, interfacial media have the benefit to greatly enhance molecular recognition capability [146,147].

Systematic research on the comparison of recognition efficiencies of a fixed molecular pair (guanidinium and phosphate) revealed that binding constants change significantly depending on interfacial types [148]. The binding constant between guanidinium and phosphate dispersed in aqueous media is only 1.4 M^{-1} [149]. This kind of molecular recognition based on hydrogen bonding and/or electrostatic interaction is weakened in polar media such as water phase. Chemical species with uneven charge distribution within a molecule are stabilized by solvation with polar solvent molecules, which is highly disadvantageous in the formation of host–guest complexes. However, the incorporation of guanidinium functionality into molecular assemblies such as aqueous micelles and lipid bilayers to place recognition sites at a mesoscopic interface increased the binding constants between guanidinium and phosphate to 10^2–10^4 M^{-1}

Figure 8: Mode of molecular recognition and sensing: (A) one most stable state between guest and host; (B) switching molecular binding by external stimuli; (c) tuning of receptor structures through continuously shifting molecular conformations for required demands. Adapted with permission from [52] copyright 2016, Springer Nature.
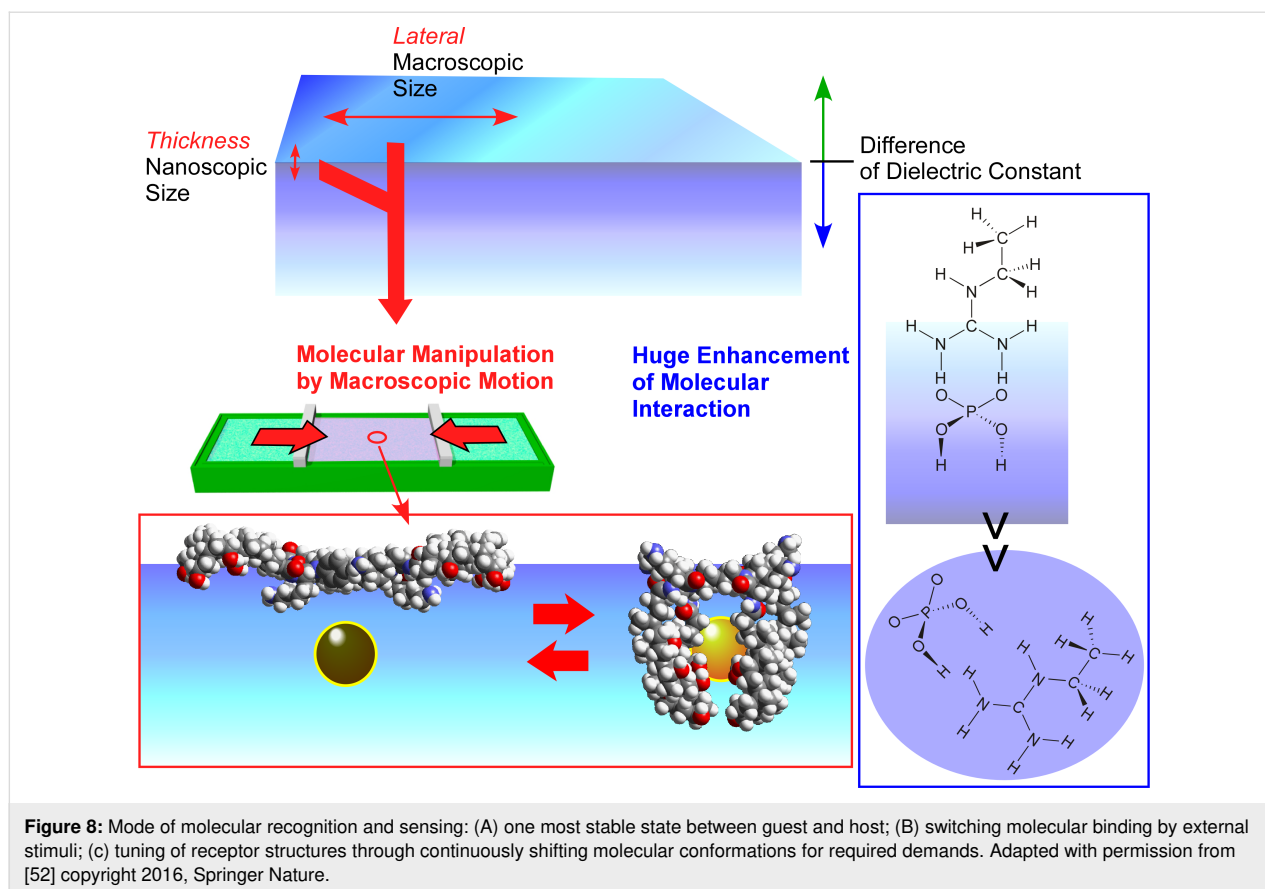
[148]. Furthermore, placing a guanidinium functionality at a macroscopic interface, such as air–water, results in a huge enhancement of the binding constant with aqueous phosphate to 10^6–10^7 M^{-1} [150,151]. These facts imply that the molecular sensing capability could be improved by selecting interfacial types and nanoarchitectonics of interfacial structures.

The above-mentioned specific features at the interfacial media were also proved by theoretical calculations based on quantum chemistry [152-154]. Even without direct contact, the low dielectric nature in nonpolar media located close to recognition sites provided positive effects. It is a plausible mechanism regarding how biological molecular recognition occurs in aqueous media [155]. The molecular recognition of small molecules can be accomplished at certain kind of interfacial environments such as cell membrane, inside surfaces of receptors and enzymes, and macromolecular interfaces at DNA and proteins. This mechanism for the enhancement of the molecular recognition capability at interfaces is surely applicable to other molecular recognition pairs and should also lead to highly efficient molecular recognition of various aqueous biomolecules including amino acids [156], peptides [157-159], sugars [160,161], nucleic acid bases [162,163], and nucleotides [164-166] at well-designed interfacial environments. In order to design and fabri-

cate sensors with better performance, interfacial nanoarchitectonics should be crucial factor.

Another feature specific to interfacial environments is the co-existence of extremely different sized structures. At dynamic interfaces, their lateral direction has macroscopic motional freedom but the structural changes in the thickness direction are confined to the nanometer scale. Therefore, macroscopic motions such as compression and expansion can be coupled with nanoscopic conformational changes of molecules embedded at dynamic interfaces [167-169]. For example, dihedral angles of binaphthyl units can be continuously tuned at the molecular level by dynamic compression and expansion of monolayers of tens of centimeters [170]. The digital switching of helicity of binaphthyl units is also possible through macroscopic motion [171]. Furthermore, the control of nanoscopic motions of molecular machines such as molecular catchers [172,173] and molecular motors [174,175] can be accomplished by macroscopic motions at the air–water interface.

The regulation of molecular conformation at interfacial media can be utilized for the tuning of molecular sensing. The structural tuning of an octacoordinate Na$^+$ complex of a cholesterol-substituted cyclen with twisting helicity at the air–water inter-

face was used to realize switching recognition selectivity between L- and D-amino acids [176,177]. Chiral sensing can be tuned by mechanical deformation of the receptor membrane at the interfacial environment. Two-dimensional deformation of cholesterol-substituted triazacyclononane monolayer was used to optimize the discrimination between uracil and thymine derivatives [178,179] that cannot be discriminated by naturally occurring DNA and RNA. Although the structural difference between uracil and thymine is only one methyl group, the difference in the binding constant between them is more than 60 times. A mechanically controlled indicator displacement assay for aqueous glucose detection based on fluorescence resonance energy transfer was also reported [180].

The mechanisms of molecular recognition and sensing are roughly summarized in Figure 9. The most basic mechanism

(Figure 9) is considered to form the most stable state between the guest and host [181-183]. Shinkai and co-workers proposed a breakthrough approach to switch molecular recognition using photo-isomerization of an azobenzene moiety in a receptor structure (Figure 9) [184,185]. This mechanism creates two (or more) states with different binding energies that are controlled by external stimuli. This can also be regarded as the origination of molecular function control by external stimuli. It shares working principles with molecular machines which are usually operated by switching between several states [186-188]. Unlike these pioneering approaches, the mechanical tuning of receptor molecules at interfacial media considers numerous candidates from continuously shifting molecular conformations (Figure 9) [189-191]. This method may use all available possibilities of flexible molecular structures. This methodology has not been fully applied in practical sensing systems so far.

Figure 9: Mode of molecular recognition and sensing: (A) one most stable state between guest and host; (B) switching molecular binding by external stimuli; (c) tuning of receptor structures through continuously shifting molecular conformations for required demands. Adapted with permission from [52] copyright 2016, Springer Nature.
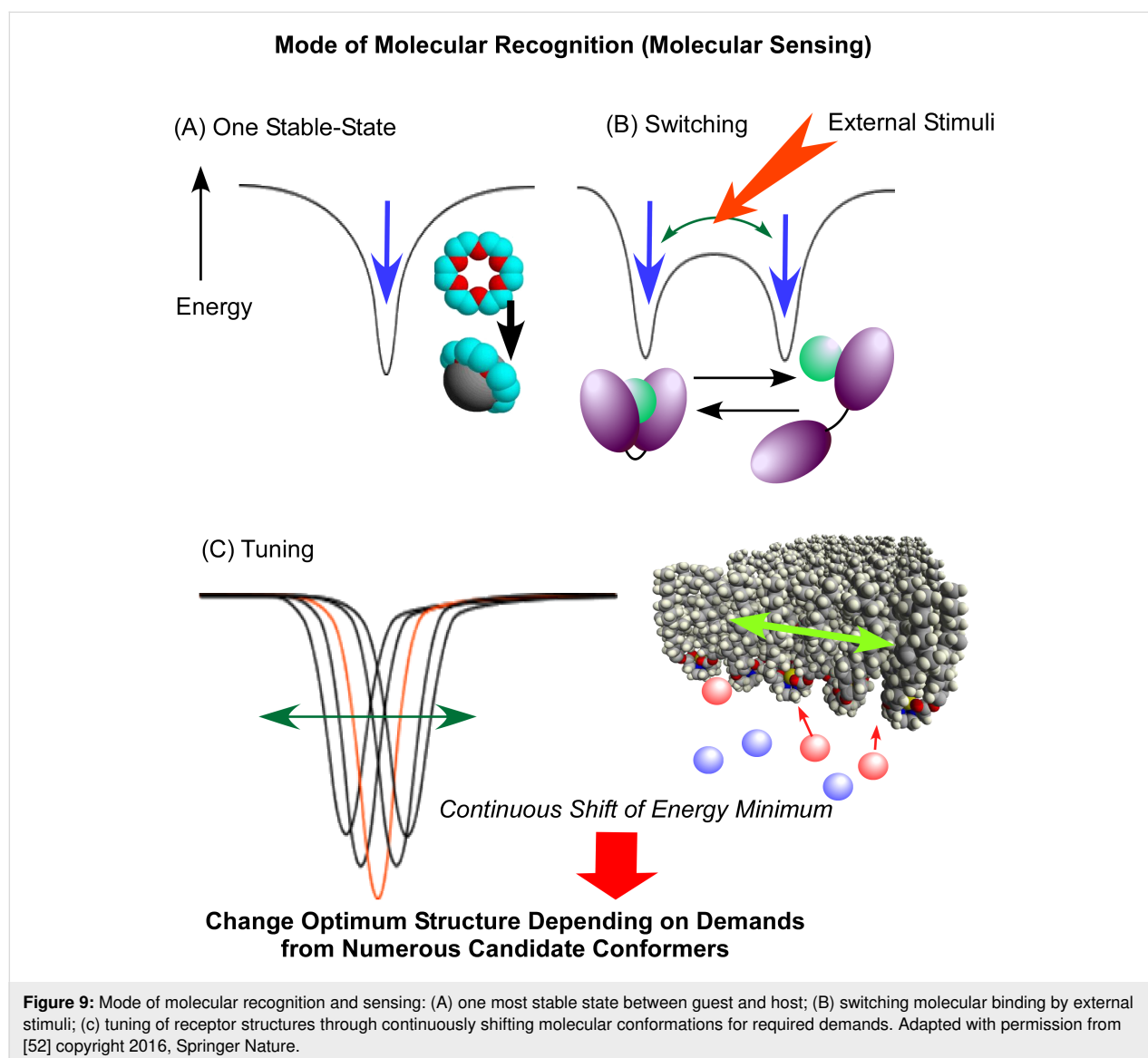
Conclusion

This review article introduces several examples of recent advanced sensors, classified according to the sensing targets (chemical substance, physical condition and biological phenomena) in the first part. In the second part, the importance of nanoarchitectured motifs, such as nanoporous structures, ultrathin films, and unusual interfacial effects, for improved sensor performance is discussed. Most of the examples illustrate the crucial role of the nanostructure in sensor design. Although fine structural control used to be an important task in device miniaturization and integration in past approaches, the importance of precise nanoscale control for sensor materials is widely recognized in recent developments. Molecular sieving effects for better selectivity by well-designed nanoporous structures and effective carrier transport within a well-packed ultrathin monolayer of organic semiconductors have become clear in recent research examples. Of course, further efforts regarding nanoscale design of sensing materials for better performance and selectivity have to be made. In many cases, sensor advancements can be implemented with the nanoarchitectonics methodologies.

However, some important mechanisms such as huge enhancements of molecular recognition efficiency and molecular tuning capability at interfaces still remain as basic milestones and have not been applied in practical sensor applications to date. Further advancements of sensors can be made by exploitation of the various flexible and dynamic natures of sensing materials where various interactions and effects have to be harmonized similar to the nanoarchitectonics strategy. In addition, dynamic harmonization of the interactions is also commonly observed in biological processes and systems. As discussed in some reviews, interfacing between electronic devices and ionic biosystems [192] and biocompatible device design [193] are crucial for future sensor devices. Therefore, investigation on dynamic nanoarchitectonics for sensor devices could lead to further advancements in bio-friendly sensor devices.

Of course, all important sensor activities cannot be described in this review. For example, sensors based on various advanced physical mechanisms such as plasmonic [194], dielectric sensing [195], surface-enhanced Raman scattering [196], Fabry–Pérot-based intraocular pressure [197], and/or novel nanostructured materials with exotic properties [198] undoubtedly have important contributions. In addition, mass-sensitive sensors, quartz and crystal microbalance [199] are are useful for many substances because mass changes and alteration of viscoelasticity such as phase transition [200] are common over all materials. Once developed, these technologies have to be translated into real-world applications for potential impact on daily life. A roadmap for this technology transfer cannot be easily predicted, but should include important factors such as miniaturization, wearable features, scalability, reliability, and sampling of analytes. This roadmap would be shortened by using new types of materials such as two-dimensional materials [201-204] and through introducing new methodologies such as mass-data analyses and machine learning [205,206]. Another important factor to accelerate progress would be process integration of top down microfabrication and bottom up self-organization to bridge materials and systems over a wide scale range. To combine all of these techniques and functional materials, the concept of nanoarchitectonics becomes a crucial bridge in this roadmap.

ORCID® iDs

Katsuhiko Ariga - https://orcid.org/0000-0002-2445-2955
Taizo Mori - https://orcid.org/0000-0002-6974-5137
Shun Watanabe - https://orcid.org/0000-0001-7377-6043

References

1. Imran, M.; Motta, N.; Shafiei, M. *Beilstein J. Nanotechnol.* **2018,** *9,* 2128–2170. doi:10.3762/bjnano.9.202
2. Zhang, Y.; Yuan, S.; Day, G.; Wang, X.; Yang, X.; Zhou, H.-C. *Coord. Chem. Rev.* **2018,** *354,* 28–45. doi:10.1016/j.ccr.2017.06.007
3. Dey, A. *Mater. Sci. Eng., B* **2018,** *229,* 206–217. doi:10.1016/j.mseb.2017.12.036
4. Sun, D.; Luo, Y.; Debliquy, M.; Zhang, C. *Beilstein J. Nanotechnol.* **2018,** *9,* 2832–2844. doi:10.3762/bjnano.9.264
5. Datta, K. K. R.; Reddy, B. V. S.; Ariga, K.; Vinu, A. *Angew. Chem., Int. Ed.* **2010,** *49,* 5961–5965. doi:10.1002/anie.201001699
6. Chaikittisilp, W.; Ariga, K.; Yamauchi, Y. *J. Mater. Chem. A* **2013,** *1,* 14–19. doi:10.1039/c2ta00278g
7. Jeevanandam, J.; Barhoum, A.; Chan, Y. S.; Dufresne, A.; Danquah, M. K. *Beilstein J. Nanotechnol.* **2018,** *9,* 1050–1074. doi:10.3762/bjnano.9.98
8. Irie, M.; Morimoto, M. *Bull. Chem. Soc. Jpn.* **2018,** *91,* 237–250. doi:10.1246/bcsj.20170365
9. Ishihara, S.; Labuta, J.; Nakanishi, T.; Tanaka, T.; Kataura, H. *ACS Sens.* **2017,** *2,* 1405–1409. doi:10.1021/acssensors.7b00591
10. Sarikhani, Z.; Manoochehri, M. *Bull. Chem. Soc. Jpn.* **2017,** *90,* 746–753. doi:10.1246/bcsj.20160407
11. Rasheed, T.; Bilal, M.; Nabeel, F.; Iqbal, H. M. N.; Li, C.; Zhou, Y. *Sci. Total Environ.* **2018,** *615,* 476–485. doi:10.1016/j.scitotenv.2017.09.126
12. Acharya, R.; Naik, B.; Parida, K. *Beilstein J. Nanotechnol.* **2018,** *9,* 1448–1470. doi:10.3762/bjnano.9.137
13. Zhang, X.; Jia, S.; Song, J.; Wu, S.; Han, X. *Bull. Chem. Soc. Jpn.* **2018,** *91,* 998–1007. doi:10.1246/bcsj.20180014
14. Shak, K. P. Y.; Pang, Y. L.; Mah, S. K. *Beilstein J. Nanotechnol.* **2018,** *9,* 2479–2498. doi:10.3762/bjnano.9.232

15. Hou, J.; Inganäs, O.; Friend, R. H.; Gao, F. *Nat. Mater.* **2018,** *17,* 119–128. doi:10.1038/nmat5063

16. Miyasaka, T. *Bull. Chem. Soc. Jpn.* **2018,** *91,* 1058–1068. doi:10.1246/bcsj.20180071

17. Guo, D.; Shibuya, R.; Akiba, C.; Saji, S.; Kondo, T.; Nakamura, J. *Science* **2016,** *351,* 361–365. doi:10.1126/science.aad0832

18. Chaikittisilp, W.; Hu, M.; Wang, H.; Huang, H.-S.; Fujita, T.; Wu, K. C.-W.; Chen, L.-C.; Yamauchi, Y.; Ariga, K. *Chem. Commun.* **2012,** *48,* 7259–7261. doi:10.1039/c2cc33433j

19. Watanabe, M.; Dokko, K.; Ueno, K.; Thomas, M. L. *Bull. Chem. Soc. Jpn.* **2018,** *91,* 1660–1682. doi:10.1246/bcsj.20180216

20. Kawai, T.; Nakao, S.; Nishide, H.; Oyaizu, K. *Bull. Chem. Soc. Jpn.* **2018,** *91,* 721–727. doi:10.1246/bcsj.20170420

21. Yamamura, A.; Watanabe, S.; Uno, M.; Mitani, M.; Mitsui, C.; Tsurumi, J.; Isahaya, N.; Kanaoka, Y.; Okamoto, T.; Takeya, J. *Sci. Adv.* **2018,** *4,* eaao5758. doi:10.1126/sciadv.aao5758

22. Ulaganathan, R. K.; Chang, Y.-H.; Wang, D.-Y.; Li, S.-S. *Bull. Chem. Soc. Jpn.* **2018,** *91,* 761–771. doi:10.1246/bcsj.20180016

23. Watanabe, Y.; Sasabe, H.; Kido, J. *Bull. Chem. Soc. Jpn.* **2019,** *92,* 716–728. doi:10.1246/bcsj.20180336

24. Ariga, K.; Lvov, Y. M.; Kawakami, K.; Ji, Q.; Hill, J. P. *Adv. Drug Delivery Rev.* **2011,** *63,* 762–771. doi:10.1016/j.addr.2011.03.016

25. Li, B. L.; Setyawati, M. I.; Chen, L.; Xie, J.; Ariga, K.; Lim, C.-T.; Garaj, S.; Leong, D. T. *ACS Appl. Mater. Interfaces* **2017,** *9,* 15286–15296. doi:10.1021/acsami.7b02529

26. He, H.; Xu, B. *Bull. Chem. Soc. Jpn.* **2018,** *91,* 900–906. doi:10.1246/bcsj.20180038

27. Kumar, J.; Liz-Marzán, L. M. *Bull. Chem. Soc. Jpn.* **2019,** *92,* 30–37. doi:10.1246/bcsj.20180236

28. Povie, G.; Segawa, Y.; Nishihara, T.; Miyauchi, Y.; Itami, K. *Science* **2017,** *356,* 172–175. doi:10.1126/science.aam8158

29. Sun, Z.; Matsuno, T.; Isobe, H. *Bull. Chem. Soc. Jpn.* **2018,** *91,* 907–921. doi:10.1246/bcsj.20180051

30. Sun, Z.; Ikemoto, K.; Fukunaga, T. M.; Koretsune, T.; Arita, R.; Sato, S.; Isobe, H. *Science* **2019,** *363,* 151–155. doi:10.1126/science.aau5441

31. Ruiz-Hitzky, E.; Darder, M.; Aranda, P.; Ariga, K. *Adv. Mater. (Weinheim, Ger.)* **2010,** *22,* 323–336. doi:10.1002/adma.200901134

32. Seiki, N.; Shoji, Y.; Kajitani, T.; Ishiwari, F.; Kosaka, A.; Hikima, T.; Takata, M.; Someya, T.; Fukushima, T. *Science* **2015,** *348,* 1122–1126. doi:10.1126/science.aab1391

33. Sawada, T.; Serizawa, T. *Bull. Chem. Soc. Jpn.* **2018,** *91,* 455–466. doi:10.1246/bcsj.20170428

34. Xing, R.; Yuan, C.; Li, S.; Song, J.; Li, J.; Yan, X. *Angew. Chem., Int. Ed.* **2018,** *57,* 1537–1542. doi:10.1002/anie.201710642

35. Dhiman, S.; George, S. J. *Bull. Chem. Soc. Jpn.* **2018,** *91,* 687–699. doi:10.1246/bcsj.20170433

36. Ringleb, F.; Andree, S.; Heidmann, B.; Bonse, J.; Eylers, K.; Ernst, O.; Boeck, T.; Schmid, M.; Krüger, J. *Beilstein J. Nanotechnol.* **2018,** *9,* 3025–3038. doi:10.3762/bjnano.9.281

37. Mori, T.; Tanaka, H.; Dalui, A.; Mitoma, N.; Suzuki, K.; Matsumoto, M.; Aggarwal, N.; Patnaik, A.; Acharya, S.; Shrestha, L. K.; Sakamoto, H.; Itami, K.; Ariga, K. *Angew. Chem., Int. Ed.* **2018,** *57,* 9679–9683. doi:10.1002/anie.201803859

38. Chen, R.; Kang, J.; Kang, M.; Lee, H.; Lee, H. *Bull. Chem. Soc. Jpn.* **2018,** *91,* 979–990. doi:10.1246/bcsj.20180042

39. Sung, B.; Kim, M.-H. *Beilstein J. Nanotechnol.* **2018,** *9,* 205–215. doi:10.3762/bjnano.9.22

40. Asanuma, H.; Murayama, K.; Kamiya, Y.; Kashida, H. *Bull. Chem. Soc. Jpn.* **2018,** *91,* 1739–1748. doi:10.1246/bcsj.20180278

41. Ariga, K.; Jia, X.; Song, J.; Hsieh, C.-T.; Hsu, S.-h. *ChemNanoMat* **2019,** *5,* 692–702. doi:10.1002/cnma.201900207

42. Einaga, Y. *Bull. Chem. Soc. Jpn.* **2018,** *91,* 1752–1762. doi:10.1246/bcsj.20180268

43. Kitamori, T. *Bull. Chem. Soc. Jpn.* **2019,** *92,* 469–473. doi:10.1246/bcsj.20180276

44. Xie, Y.; Ding, Y.; Li, X.; Wang, C.; Hill, J. P.; Ariga, K.; Zhang, W.; Zhu, W. *Chem. Commun.* **2012,** *48,* 11513–11515. doi:10.1039/c2cc36140j

45. Izawa, H.; Wada, M.; Nishino, S.; Sumita, M.; Fujita, T.; Morihashi, K.; Ifuku, S.; Morimoto, M.; Saimoto, H. *Bull. Chem. Soc. Jpn.* **2018,** *91,* 1220–1225. doi:10.1246/bcsj.20180128

46. Wang, Y.; Michinobu, T. *Bull. Chem. Soc. Jpn.* **2017,** *90,* 1388–1400. doi:10.1246/bcsj.20170294

47. Maduraiveeran, G.; Sasidharan, M.; Ganesan, V. *Biosens. Bioelectron.* **2018,** *103,* 113–129. doi:10.1016/j.bios.2017.12.031

48. Huang, R.; He, N.; Li, Z. *Biosens. Bioelectron.* **2018,** *109,* 27–34. doi:10.1016/j.bios.2018.02.053

49. Ferhan, A. R.; Jackman, J. A.; Park, J. H.; Cho, N.-J.; Kim, D.-H. *Adv. Drug Delivery Rev.* **2018,** *125,* 48–77. doi:10.1016/j.addr.2017.12.004

50. Li, B. L.; Wang, J.; Gao, Z. F.; Shi, H.; Zou, H. L.; Ariga, K.; Leong, D. T. *Mater. Horiz.* **2019,** *6,* 563–570. doi:10.1039/c8mh01232f

51. Ariga, K.; Ji, Q.; Nakanishi, W.; Hill, J. P.; Aono, M. *Mater. Horiz.* **2015,** *2,* 406–413. doi:10.1039/c5mh00012b

52. Ariga, K.; Minami, K.; Ebara, M.; Nakanishi, J. *Polym. J.* **2016,** *48,* 371–389. doi:10.1038/pj.2016.8

53. Ishihara, S.; Labuta, J.; Van Rossom, W.; Ishikawa, D.; Minami, K.; Hill, J. P.; Ariga, K. *Phys. Chem. Chem. Phys.* **2014,** *16,* 9713–9746. doi:10.1039/c3cp55431g

54. Ariga, K.; Ji, Q.; Hill, J. P.; Bando, Y.; Aono, M. *NPG Asia Mater.* **2012,** *4,* e17. doi:10.1038/am.2012.30

55. Ariga, K.; Nishikawa, M.; Mori, T.; Takeya, J.; Shrestha, L. K.; Hill, J. P. *Sci. Technol. Adv. Mater.* **2019,** *20,* 51–95. doi:10.1080/14686996.2018.1553108

56. Ariga, K.; Li, M.; Richards, G. J.; Hill, J. P. *J. Nanosci. Nanotechnol.* **2011,** *11,* 1–13. doi:10.1166/jnn.2011.3839

57. Ariga, K.; Li, J.; Fei, J.; Ji, Q.; Hill, J. P. *Adv. Mater. (Weinheim, Ger.)* **2016,** *28,* 1251–1286. doi:10.1002/adma.201502545

58. Ramanathan, M.; Shrestha, L. K.; Mori, T.; Ji, Q.; Hill, J. P.; Ariga, K. *Phys. Chem. Chem. Phys.* **2013,** *15,* 10580–10611. doi:10.1039/c3cp50620g

59. Nakanishi, W.; Minami, K.; Shrestha, L. K.; Ji, Q.; Hill, J. P.; Ariga, K. *Nano Today* **2014,** *9,* 378–394. doi:10.1016/j.nantod.2014.05.002

60. Ariga, K.; Malgras, V.; Ji, Q.; Zakaria, M. B.; Yamauchi, Y. *Coord. Chem. Rev.* **2016,** *320-321,* 139–152. doi:10.1016/j.ccr.2016.01.015

61. Sakakibara, K.; Hill, J. P.; Ariga, K. *Small* **2011,** *7,* 1288–1308. doi:10.1002/smll.201002350

62. Ariga, K.; Vinu, A.; Yamauchi, Y.; Ji, Q.; Hill, J. P. *Bull. Chem. Soc. Jpn.* **2012,** *85,* 1–32. doi:10.1246/bcsj.20110162

63. Ariga, K.; Yamauchi, Y.; Rydzek, G.; Ji, Q.; Yonamine, Y.; Wu, K. C.-W.; Hill, J. P. *Chem. Lett.* **2014,** *43,* 36–68. doi:10.1246/cl.130987

64. Ariga, K.; Watanabe, S.; Mori, T.; Takeya, J. *NPG Asia Mater.* **2018,** *10,* 90–106. doi:10.1038/s41427-018-0022-9

65. Sang, Y.; Liu, M. *Mol. Syst. Des. Eng.* **2019,** *4,* 11–28. doi:10.1039/c8me00068a

66. Abe, H.; Liu, J.; Ariga, K. *Mater. Today* **2016,** *19,* 12–18. doi:10.1016/j.mattod.2015.08.021

67. Ariga, K.; Ishihara, S.; Abe, H. *CrystEngComm* **2016,** *18,* 6770–6778. doi:10.1039/c6ce00986g

68. Kim, J.; Kim, J. H.; Ariga, K. *Joule* **2017,** *1,* 739–768. doi:10.1016/j.joule.2017.08.018

69. Khan, A. H.; Ghosh, S.; Pradhan, B.; Dalui, A.; Shrestha, L. K.; Acharya, S.; Ariga, K. *Bull. Chem. Soc. Jpn.* **2017,** *90,* 627–648. doi:10.1246/bcsj.20170043

70. Ariga, K.; Yamauchi, Y.; Ji, Q.; Yonamine, Y.; Hill, J. P. *APL Mater.* **2014,** *2,* 030701. doi:10.1063/1.4868177

71. Pandeeswar, M.; Senanayak, S. P.; Govindaraju, T. *ACS Appl. Mater. Interfaces* **2016,** *8,* 30362–30371. doi:10.1021/acsami.6b10527

72. Ariga, K.; Ji, Q.; McShane, M. J.; Lvov, Y. M.; Vinu, A.; Hill, J. P. *Chem. Mater.* **2012,** *24,* 728–737. doi:10.1021/cm202281m

73. Ariga, K.; Ji, Q.; Mori, T.; Naito, M.; Yamauchi, Y.; Abe, H.; Hill, J. P. *Chem. Soc. Rev.* **2013,** *42,* 6322–6345. doi:10.1039/c2cs35475f

74. Komiyama, M.; Yoshimoto, K.; Sisido, M.; Ariga, K. *Bull. Chem. Soc. Jpn.* **2017,** *90,* 967–1004. doi:10.1246/bcsj.20170156

75. Ariga, K.; Leong, D. T.; Mori, T. *Adv. Funct. Mater.* **2018,** *28,* 1702905. doi:10.1002/adfm.201702905

76. Ariga, K.; Kawakami, K.; Ebara, M.; Kotsuchibashi, Y.; Ji, Q.; Hill, J. P. *New J. Chem.* **2014,** *38,* 5149–5163. doi:10.1039/c4nj00864b

77. Pandey, A. P.; Girase, N. M.; Patil, M. D.; Patil, P. O.; Patil, D. A.; Deshmukh, P. K. *J. Nanosci. Nanotechnol.* **2014,** *14,* 828–840. doi:10.1166/jnn.2014.9014

78. Zhao, L.; Zou, Q.; Yan, X. *Bull. Chem. Soc. Jpn.* **2019,** *92,* 70–79. doi:10.1246/bcsj.20180248

79. Ariga, K.; Minami, K.; Shrestha, L. K. *Analyst* **2016,** *141,* 2629–2638. doi:10.1039/c6an00057f

80. Jackman, J. A.; Cho, N.-J.; Nishikawa, M.; Yoshikawa, G.; Mori, T.; Shrestha, L. K.; Ariga, K. *Chem. – Asian J.* **2018,** *13,* 3366–3377. doi:10.1002/asia.201800935

81. Aono, M.; Ariga, K. *Adv. Mater. (Weinheim, Ger.)* **2016,** *28,* 989–992. doi:10.1002/adma.201502868

82. Ariga, K. *Mater. Chem. Front.* **2017,** *1,* 208–211. doi:10.1039/c6qm00240d

83. Osica, I.; Imamura, G.; Shiba, K.; Ji, Q.; Shrestha, L. K.; Hill, J. P.; Kurzydłowski, K. J.; Yoshikawa, G.; Ariga, K. *ACS Appl. Mater. Interfaces* **2017,** *9,* 9945–9954. doi:10.1021/acsami.6b15680

84. Osica, I.; Melo, A. F. A. A.; Imamura, G.; Shiba, K.; Ji, Q.; Hill, J. P.; Crespilho, F. N.; Kurzydłowski, K. J.; Yoshikawa, G.; Ariga, K. *J. Nanosci. Nanotechnol.* **2017,** *17,* 5908–5917. doi:10.1166/jnn.2017.14388

85. Tang, K.; Song, Z.; Tang, Q.; Tian, H.; Tong, Y.; Liu, Y. *IEEE Electron Device Lett.* **2018,** *39,* 119–122. doi:10.1109/led.2017.2770181

86. Liu, Y.; Wang, Y.; Ikram, M.; Lv, H.; Chang, J.; Li, Z.; Ma, L.; Rehman, A. U.; Lu, G.; Chen, J.; Shi, K. *ACS Sens.* **2018,** *3,* 1576–1583. doi:10.1021/acssensors.8b00397

87. Rodlamul, P.; Tamura, S.; Imanaka, N. *Bull. Chem. Soc. Jpn.* **2019,** *92,* 585–591. doi:10.1246/bcsj.20180284

88. Sasaki, J.; Suzuki, M.; Hanabusa, K. *Bull. Chem. Soc. Jpn.* **2018,** *91,* 538–547. doi:10.1246/bcsj.20170409

89. Kondo, S.-i.; Sato, K.; Matsuta, Y.; Osawa, K. *Bull. Chem. Soc. Jpn.* **2018,** *91,* 875–881. doi:10.1246/bcsj.20180028

90. Mulla, M. Y.; Tuccori, E.; Magliulo, M.; Lattanzi, G.; Palazzo, G.; Persaud, K.; Torsi, L. *Nat. Commun.* **2015,** *6,* 6010. doi:10.1038/ncomms7010

91. Park, K. M.; Kim, J.; Ko, Y. H.; Ahn, Y.; Murray, J.; Li, M.; Shrinidhi, A.; Kim, K. *Bull. Chem. Soc. Jpn.* **2018,** *91,* 95–99. doi:10.1246/bcsj.20170302

92. Akamatsu, M.; Komatsu, H.; Matsuda, A.; Mori, T.; Nakanishi, W.; Sakai, H.; Hill, J. P.; Ariga, K. *Bull. Chem. Soc. Jpn.* **2017,** *90,* 678–683. doi:10.1246/bcsj.20170046

93. Ruiz-Hitzky, E.; Gómez-Avilés, A.; Darder, M.; Aranda, P. *Bull. Chem. Soc. Jpn.* **2018,** *91,* 608–616. doi:10.1246/bcsj.20170425

94. Li, P.; Zhang, D.; Jiang, C.; Zong, X.; Cao, Y. *Biosens. Bioelectron.* **2017,** *98,* 68–75. doi:10.1016/j.bios.2017.06.027

95. Spanu, A.; Viola, F.; Lai, S.; Cosseddu, P.; Ricci, P. C.; Bonfiglio, A. *Org. Electron.* **2017,** *48,* 188–193. doi:10.1016/j.orgel.2017.06.010

96. Lee, S.; Reuveny, A.; Reeder, J.; Lee, S.; Jin, H.; Liu, Q.; Yokota, T.; Sekitani, T.; Isoyama, T.; Abe, Y.; Suo, Z.; Someya, T. *Nat. Nanotechnol.* **2016,** *11,* 472–478. doi:10.1038/nnano.2015.324

97. Cao, R.; Pu, X.; Du, X.; Yang, W.; Wang, J.; Guo, H.; Zhao, S.; Yuan, Z.; Zhang, C.; Li, C.; Wang, Z. L. *ACS Nano* **2018,** *12,* 5190–5196. doi:10.1021/acsnano.8b02477

98. Askari, H.; Hashemi, E.; Khajepour, A.; Khamesee, M. B.; Wang, Z. L. *Nano Energy* **2018,** *53,* 1003–1019. doi:10.1016/j.nanoen.2018.09.032

99. Ren, Z.; Ding, Y.; Nie, J.; Wang, F.; Xu, L.; Lin, S.; Chen, X.; Wang, Z. L. *ACS Appl. Mater. Interfaces* **2019,** *11,* 6143–6153. doi:10.1021/acsami.8b21477

100. Wang, J.; Ding, W.; Pan, L.; Wu, C.; Yu, H.; Yang, L.; Liao, R.; Wang, Z. L. *ACS Nano* **2018,** *12,* 3954–3963. doi:10.1021/acsnano.8b01532

101. Melzer, M.; Kaltenbrunner, M.; Makarov, D.; Karnaushenko, D.; Karnaushenko, D.; Sekitani, T.; Someya, T.; Schmidt, O. G. *Nat. Commun.* **2015,** *6,* 6080. doi:10.1038/ncomms7080

102. Piro, B.; Wang, D.; Benaoudia, D.; Tibaldi, A.; Anquetin, G.; Noël, V.; Reisberg, S.; Mattana, G.; Jackson, B. *Biosens. Bioelectron.* **2017,** *92,* 215–220. doi:10.1016/j.bios.2017.02.020

103. Komiyama, M.; Mori, T.; Ariga, K. *Bull. Chem. Soc. Jpn.* **2018,** *91,* 1075–1111. doi:10.1246/bcsj.20180084

104. Lai, Y.; Deng, Y.; Yang, G.; Li, S.; Zhang, C.; Liu, X. *J. Biomed. Nanotechnol.* **2018,** *14,* 1688–1694. doi:10.1166/jbn.2018.2617

105. Takeuchi, T.; Sunayama, H. *Chem. Commun.* **2018,** *54,* 6243–6251. doi:10.1039/c8cc02923g

106. Zhang, L.; Wang, G.; Xiong, C.; Zheng, L.; He, J.; Ding, Y.; Lu, H.; Zhang, G.; Cho, K.; Qiu, L. *Biosens. Bioelectron.* **2018,** *105,* 121–128. doi:10.1016/j.bios.2018.01.035

107. Sekitani, T.; Yokota, T.; Kuribara, K.; Kaltenbrunner, M.; Fukushima, T.; Inoue, Y.; Sekino, M.; Isoyama, T.; Abe, Y.; Onodera, H.; Someya, T. *Nat. Commun.* **2016,** *7,* 11425. doi:10.1038/ncomms11425

108. Hempel, F.; Law, J. K.-Y.; Nguyen, T. C.; Munief, W.; Lu, X.; Pachauri, V.; Susloparova, A.; Vu, X. T.; Ingebrandt, S. *Biosens. Bioelectron.* **2017,** *93,* 132–138. doi:10.1016/j.bios.2016.09.047

109. Yeung, S. Y.; Gu, X.; Tsang, C. M.; Tsao, S. W.; Hsing, I.-m.
Sens. Actuators, A **2019,** *287,* 185–193.
doi:10.1016/j.sna.2018.12.032

110. Pulikkathodi, A. K.; Sarangadharan, I.; Chen, Y.-H.; Lee, G.-Y.;
Chyi, J.-I.; Lee, G.-B.; Wang, Y.-L. *Lab Chip* **2018,** *18,* 1047–1056.
doi:10.1039/c7lc01305a

111. Braendlein, M.; Pappa, A.-M.; Ferro, M.; Lopresti, A.; Acquaviva, C.;
Mamessier, E.; Malliaras, G. G.; Owens, R. M.
Adv. Mater. (Weinheim, Ger.) **2017,** *29,* 1605744.
doi:10.1002/adma.201605744

112. Cherumukkil, S.; Vedhanarayanan, B.; Das, G.; Praveen, V. K.;
Ajayaghosh, A. *Bull. Chem. Soc. Jpn.* **2018,** *91,* 100–120.
doi:10.1246/bcsj.20170334

113. Shimizu, T. *Bull. Chem. Soc. Jpn.* **2018,** *91,* 623–668.
doi:10.1246/bcsj.20170424

114. Liu, X.; Riess, J. G.; Krafft, M. P. *Bull. Chem. Soc. Jpn.* **2018,** *91,*
846–857. doi:10.1246/bcsj.20170431

115. Hu, M.; Reboul, J.; Furukawa, S.; Torad, N. L.; Ji, Q.; Srinivasu, P.;
Ariga, K.; Kitagawa, S.; Yamauchi, Y. *J. Am. Chem. Soc.* **2012,** *134,*
2864–2867. doi:10.1021/ja208940u

116. Chaikittisilp, W.; Torad, N. L.; Li, C.; Imura, M.; Suzuki, N.;
Ishihara, S.; Ariga, K.; Yamauchi, Y. *Chem. – Eur. J.* **2014,** *20,*
4217–4221. doi:10.1002/chem.201304404

117. Malgras, V.; Ji, Q.; Kamachi, Y.; Mori, T.; Shieh, F.-K.; Wu, K. C.-W.;
Ariga, K.; Yamauchi, Y. *Bull. Chem. Soc. Jpn.* **2015,** *88,* 1171–1200.
doi:10.1246/bcsj.20150143

118. Saptiama, I.; Kaneti, Y. V.; Oveisi, H.; Suzuki, Y.; Tsuchiya, K.;
Takai, K.; Sakae, T.; Pradhan, S.; Hossain, M. S. A.; Fukumitsu, N.;
Ariga, K.; Yamauchi, Y. *Bull. Chem. Soc. Jpn.* **2018,** *91,* 195–200.
doi:10.1246/bcsj.20170295

119. Sai-Anand, G.; Sivanesan, A.; Benzigar, M. R.; Singh, G.;
Gopalan, A.-I.; Baskar, A. V.; Ilbeygi, H.; Ramadass, K.; Kambala, V.;
Vinu, A. *Bull. Chem. Soc. Jpn.* **2019,** *92,* 216–244.
doi:10.1246/bcsj.20180280

120. Shrestha, L. K.; Shrestha, R. G.; Yamauchi, Y.; Hill, J. P.;
Nishimura, T.; Miyazawa, K.; Kawai, T.; Okada, S.; Wakabayashi, K.;
Ariga, K. *Angew. Chem., Int. Ed.* **2015,** *54,* 951–955.
doi:10.1002/anie.201408856

121. Bairi, P.; Minami, K.; Nakanishi, W.; Hill, J. P.; Ariga, K.;
Shrestha, L. K. *ACS Nano* **2016,** *10,* 6631–6637.
doi:10.1021/acsnano.6b01544

122. Bairi, P.; Minami, K.; Hill, J. P.; Ariga, K.; Shrestha, L. K. *ACS Nano*
2017, *11,* 7790–7796. doi:10.1021/acsnano.7b01569

123. Ariga, K.; Vinu, A.; Ji, Q.; Ohmori, O.; Hill, J. P.; Acharya, S.; Koike, J.;
Shiratori, S. *Angew. Chem., Int. Ed.* **2008,** *47,* 7254–7257.
doi:10.1002/anie.200802820

124. Ariga, K.; Vinu, A.; Miyahara, M.; Hill, J. P.; Mori, T.
J. Am. Chem. Soc. **2007,** *129,* 11022–11023. doi:10.1021/ja074870t

125. Kosaki, Y.; Izawa, H.; Ishihara, S.; Kawakami, K.; Sumita, M.;
Tateyama, Y.; Ji, Q.; Krishnan, V.; Hishita, S.; Yamauchi, Y.;
Hill, J. P.; Vinu, A.; Shiratori, S.; Ariga, K. *ACS Appl. Mater. Interfaces*
2013, *5,* 2930–2934. doi:10.1021/am400940q

126. Ji, Q.; Yoon, S. B.; Hill, J. P.; Vinu, A.; Yu, J.-S.; Ariga, K.
J. Am. Chem. Soc. **2009,** *131,* 4220–4221. doi:10.1021/ja9010354

127. Torad, N. L.; Hu, M.; Ishihara, S.; Sukegawa, H.; Belik, A. A.;
Imura, M.; Ariga, K.; Sakka, Y.; Yamauchi, Y. *Small* **2014,** *10,*
2096–2107. doi:10.1002/smll.201302910

128. Mei, L.; Shi, W.-q.; Chai, Z.-f. *Bull. Chem. Soc. Jpn.* **2018,** *91,*
554–562. doi:10.1246/bcsj.20170418

129. Li, J.; Wang, X.; Zhao, G.; Chen, C.; Chai, Z.; Alsaedi, A.; Hayat, T.;
Wang, X. *Chem. Soc. Rev.* **2018,** *47,* 2322–2356.
doi:10.1039/c7cs00543a

130. Azhar, A.; Li, Y.; Cai, Z.; Zakaria, M. B.; Masud, M. K.;
Hossain, M. S. A.; Kim, J.; Zhang, W.; Na, J.; Yamauchi, Y.; Hu, M.
Bull. Chem. Soc. Jpn. **2019,** *92,* 875–904. doi:10.1246/bcsj.20180368

131. Chen, L.; Ye, J.-W.; Wang, H.-P.; Pan, M.; Yin, S.-Y.; Wei, Z.-W.;
Zhang, L.-Y.; Wu, K.; Fan, Y.-N.; Su, C.-Y. *Nat. Commun.* **2017,** *8,*
15985. doi:10.1038/ncomms15985

132. Tian, H.; Fan, H.; Li, M.; Ma, L. *ACS Sens.* **2016,** *1,* 243–250.
doi:10.1021/acssensors.5b00236

133. Takimiya, K.; Nakano, M. *Bull. Chem. Soc. Jpn.* **2018,** *91,* 121–140.
doi:10.1246/bcsj.20170298

134. Suda, M. *Bull. Chem. Soc. Jpn.* **2018,** *91,* 19–28.
doi:10.1246/bcsj.20170283

135. Ariga, K.; Yamauchi, Y.; Mori, T.; Hill, J. P.
Adv. Mater. (Weinheim, Ger.) **2013,** *25,* 6477–6512.
doi:10.1002/adma.201302283

136. Seki, T. *Bull. Chem. Soc. Jpn.* **2018,** *91,* 1026–1057.
doi:10.1246/bcsj.20180076

137. Ariga, K.; Mori, T.; Li, J. *Langmuir* **2019,** *35,* 3585–3599.
doi:10.1021/acs.langmuir.8b01434

138. Ji, Q.; Honma, I.; Paek, S.-M.; Akada, M.; Hill, J. P.; Vinu, A.; Ariga, K.
Angew. Chem., Int. Ed. **2010,** *49,* 9737–9739.
doi:10.1002/anie.201004929

139. Rydzek, G.; Ji, Q.; Li, M.; Schaaf, P.; Hill, J. P.; Boulmedais, F.;
Ariga, K. *Nano Today* **2015,** *10,* 138–167.
doi:10.1016/j.nantod.2015.02.008

140. Ji, Q.; Qiao, X.; Liu, X.; Jia, H.; Yu, J.-S.; Ariga, K.
Bull. Chem. Soc. Jpn. **2018,** *91,* 391–397. doi:10.1246/bcsj.20170357

141. Rodrigues, V. C.; Moraes, M. L.; Soares, J. C.; Soares, A. C.;
Sanfelice, R.; Deffune, E.; Oliveira, O. N., Jr. *Bull. Chem. Soc. Jpn.*
2018, *91,* 891–896. doi:10.1246/bcsj.20180019

142. Furusawa, H.; Ichimura, Y.; Harada, S.; Uematsu, M.; Xue, S.;
Nagamine, K.; Tokito, S. *Bull. Chem. Soc. Jpn.* **2018,** *91,* 1020–1025.
doi:10.1246/bcsj.20180065

143. Endo, S.; Kato, R.; Sawada, K.; Hattori, T. *Bull. Chem. Soc. Jpn.*
2018, *91,* 304–310. doi:10.1246/bcsj.20170304

144. Chen, H.; Dong, S.; Bai, M.; Cheng, N.; Wang, H.; Li, M.; Du, H.;
Hu, S.; Yang, Y.; Yang, T.; Zhang, F.; Gu, L.; Meng, S.; Hou, S.;
Guo, X. *Adv. Mater. (Weinheim, Ger.)* **2015,** *27,* 2113–2120.
doi:10.1002/adma.201405378

145. Peng, B.; Huang, S.; Zhou, Z.; Chan, P. K. L. *Adv. Funct. Mater.* **2017,**
27, 1700999. doi:10.1002/adfm.201700999

146. Ariga, K.; Kunitake, T. *Acc. Chem. Res.* **1998,** *31,* 371–378.
doi:10.1021/ar970014i

147. Ariga, K.; Ito, H.; Hill, J. P.; Tsukube, H. *Chem. Soc. Rev.* **2012,** *41,*
5800–5835. doi:10.1039/c2cs35162e

148. Onda, M.; Yoshihara, K.; Koyano, H.; Ariga, K.; Kunitake, T.
J. Am. Chem. Soc. **1996,** *118,* 8524–8530. doi:10.1021/ja960991+

149. Springs, B.; Haake, P. *Bioorg. Chem.* **1977,** *6,* 181–190.
doi:10.1016/0045-2068(77)90019-0

150. Sasaki, D. Y.; Kurihara, K.; Kunitake, T. *J. Am. Chem. Soc.* **1991,** *113,*
9685–9686. doi:10.1021/ja00025a051

151. Sasaki, D. Y.; Kurihara, K.; Kunitake, T. *J. Am. Chem. Soc.* **1992,** *114,*
10994–10995. doi:10.1021/ja00053a065

152. Sakurai, M.; Tamagawa, H.; Furuki, T.; Inoue, Y.; Ariga, K.;
Kunitake, T. *Chem. Lett.* **1995,** *24,* 1001–1002.
doi:10.1246/cl.1995.1001

153. Sakurai, M.; Tamagawa, H.; Inoue, Y.; Ariga, K.; Kunitake, T. *J. Phys. Chem. B* **1997,** *101,* 4810–4816. doi:10.1021/jp9700591

154. Tamagawa, H.; Sakurai, M.; Inoue, Y.; Ariga, K.; Kunitake, T. *J. Phys. Chem. B* **1997,** *101,* 4817–4825. doi:10.1021/jp9700600

155. Ariga, K. *ChemNanoMat* **2016,** *2,* 333–343. doi:10.1002/cnma.201600053

156. Ikeura, Y.; Kurihara, K.; Kunitake, T. *J. Am. Chem. Soc.* **1991,** *113,* 7342–7350. doi:10.1021/ja00019a035

157. Cha, X.; Ariga, K.; Onda, M.; Kunitake, T. *J. Am. Chem. Soc.* **1995,** *117,* 11833–11838. doi:10.1021/ja00153a003

158. Cha, X.; Ariga, K.; Kunitake, T. *J. Am. Chem. Soc.* **1996,** *118,* 9545–9551. doi:10.1021/ja961526f

159. Ariga, K.; Kamino, A.; Cha, X.; Kunitake, T. *Langmuir* **1999,** *15,* 3875–3885. doi:10.1021/la981047p

160. Kurihara, K.; Ohto, K.; Tanaka, Y.; Aoyama, Y.; Kunitake, T. *J. Am. Chem. Soc.* **1991,** *113,* 444–450. doi:10.1021/ja00002a010

161. Ariga, K.; Isoyama, K.; Hayashida, O.; Aoyama, Y.; Okahata, Y. *Chem. Lett.* **1998,** *27,* 1007–1008. doi:10.1246/cl.1998.1007

162. Kurihara, K.; Ohto, K.; Honda, Y.; Kunitake, T. *J. Am. Chem. Soc.* **1991,** *113,* 5077–5079. doi:10.1021/ja00013a063

163. Kawahara, T.; Kurihara, K.; Kunitake, T. *Chem. Lett.* **1992,** *21,* 1839–1842. doi:10.1246/cl.1992.1839

164. Taguchi, K.; Ariga, K.; Kunitake, T. *Chem. Lett.* **1995,** *24,* 701–702. doi:10.1246/cl.1995.701

165. Ariga, K.; Kamino, A.; Koyano, H.; Kunitake, T. *J. Mater. Chem.* **1997,** *7,* 1155–1161. doi:10.1039/a700081b

166. Oishi, Y.; Torii, Y.; Kato, T.; Kuramori, M.; Suehiro, K.; Ariga, K.; Taguchi, K.; Kamino, A.; Koyano, H.; Kunitake, T. *Langmuir* **1997,** *13,* 519–524. doi:10.1021/la960112x

167. Ariga, K.; Mori, T.; Hill, J. P. *Adv. Mater. (Weinheim, Ger.)* **2012,** *24,* 158–176. doi:10.1002/adma.201102617

168. Ariga, K.; Mori, T.; Ishihara, S.; Kawakami, K.; Hill, J. P. *Chem. Mater.* **2014,** *26,* 519–532. doi:10.1021/cm401999f

169. Ariga, K.; Mori, T.; Nakanishi, W.; Hill, J. P. *Phys. Chem. Chem. Phys.* **2017,** *19,* 23658–23676. doi:10.1039/c7cp02280h

170. Ishikawa, D.; Mori, T.; Yonamine, Y.; Nakanishi, W.; Cheung, D. L.; Hill, J. P.; Ariga, K. *Angew. Chem., Int. Ed.* **2015,** *54,* 8988–8991. doi:10.1002/anie.201503363

171. Mori, T.; Ishikawa, D.; Yonamine, Y.; Fujii, Y.; Hill, J. P.; Ichinose, I.; Ariga, K.; Nakanishi, W. *ChemPhysChem* **2017,** *18,* 1470–1474. doi:10.1002/cphc.201601144

172. Ariga, K.; Terasaka, Y.; Sakai, D.; Tsuji, H.; Kikuchi, J.-i. *J. Am. Chem. Soc.* **2000,** *122,* 7835–7836. doi:10.1021/ja000924m

173. Ariga, K.; Nakanishi, T.; Terasaka, Y.; Tsuji, H.; Sakai, D.; Kikuchi, J.-i. *Langmuir* **2005,** *21,* 976–981. doi:10.1021/la0477845

174. Mori, T.; Komatsu, H.; Sakamoto, N.; Suzuki, K.; Hill, J. P.; Matsumoto, M.; Sakai, H.; Ariga, K.; Nakanishi, W. *Phys. Chem. Chem. Phys.* **2018,** *20,* 3073–3078. doi:10.1039/c7cp04256f

175. Mori, T.; Chin, H.; Kawashima, K.; Ngo, H. T.; Cho, N.-J.; Nakanishi, W.; Hill, J. P.; Ariga, K. *ACS Nano* **2019,** *13,* 2410–2419. doi:10.1021/acsnano.8b09320

176. Michinobu, T.; Shinoda, S.; Nakanishi, T.; Hill, J. P.; Fujii, K.; Player, T. N.; Tsukube, H.; Ariga, K. *J. Am. Chem. Soc.* **2006,** *128,* 14478–14479. doi:10.1021/ja066429t

177. Michinobu, T.; Shinoda, S.; Nakanishi, T.; Hill, J. P.; Fujii, K.; Player, T. N.; Tsukube, H.; Ariga, K. *Phys. Chem. Chem. Phys.* **2011,** *13,* 4895–4900. doi:10.1039/c0cp01990a

178. Mori, T.; Okamoto, K.; Endo, H.; Hill, J. P.; Shinoda, S.; Matsukura, M.; Tsukube, H.; Suzuki, Y.; Kanekiyo, Y.; Ariga, K. *J. Am. Chem. Soc.* **2010,** *132,* 12868–12870. doi:10.1021/ja106653a

179. Mori, T.; Okamoto, K.; Endo, H.; Sakakibara, K.; Hill, J. P.; Shinoda, S.; Matsukura, M.; Tsukube, H.; Suzuki, Y.; Kanekiyo, Y.; Ariga, K. *Nanoscale Res. Lett.* **2011,** *6,* 304. doi:10.1186/1556-276x-6-304

180. Sakakibara, K.; Joyce, L. A.; Mori, T.; Fujisawa, T.; Shabbir, S. H.; Hill, J. P.; Anslyn, E. V.; Ariga, K. *Angew. Chem., Int. Ed.* **2012,** *51,* 9643–9646. doi:10.1002/anie.201203402

181. Lehn, J.-M. *Angew. Chem., Int. Ed. Engl.* **1988,** *27,* 89–112. doi:10.1002/anie.198800891

182. Pedersen, C. J. *Angew. Chem., Int. Ed. Engl.* **1988,** *27,* 1021–1027. doi:10.1002/anie.198810211

183. Cram, D. J. *Angew. Chem., Int. Ed. Engl.* **1988,** *27,* 1009–1020. doi:10.1002/anie.198810093

184. Shinkai, S.; Manabe, O. *Top. Curr. Chem.* **1984,** *121,* 67–104. doi:10.1007/3-540-12821-2_3

185. Shinkai, S.; Ikeda, M.; Sugasaki, A.; Takeuchi, M. *Acc. Chem. Res.* **2001,** *34,* 494–503. doi:10.1021/ar000177y

186. Feringa, B. L. *Angew. Chem., Int. Ed.* **2017,** *56,* 11060–11078. doi:10.1002/anie.201702979

187. Sauvage, J.-P. *Angew. Chem., Int. Ed.* **2017,** *56,* 11080–11093. doi:10.1002/anie.201702992

188. Stoddart, J. F. *Angew. Chem., Int. Ed.* **2017,** *56,* 11094–11125. doi:10.1002/anie.201703216

189. Ariga, K. *Anal. Sci.* **2016,** *32,* 1141–1149. doi:10.2116/analsci.32.1141

190. Shirai, Y.; Minami, K.; Nakanishi, W.; Yonamine, Y.; Joachim, C.; Ariga, K. *Jpn. J. Appl. Phys.* **2016,** *55,* 1102A2. doi:10.7567/jjap.55.1102a2

191. Shrestha, L. K.; Mori, T.; Ariga, K. *Curr. Opin. Colloid Interface Sci.* **2018,** *35,* 68–80. doi:10.1016/j.cocis.2018.01.007

192. Nishizawa, M. *Bull. Chem. Soc. Jpn.* **2018,** *91,* 1141–1149. doi:10.1246/bcsj.20180064

193. Stauss, S.; Honma, I. *Bull. Chem. Soc. Jpn.* **2018,** *91,* 492–505. doi:10.1246/bcsj.20170325

194. Anker, J. N.; Hall, W. P.; Lyandres, O.; Shah, N. C.; Zhao, J.; Van Duyne, R. P. *Nat. Mater.* **2008,** *7,* 442–453. doi:10.1038/nmat2162

195. Tittl, A.; Leitis, A.; Liu, M.; Yesilkoy, F.; Choi, D.-Y.; Neshev, D. N.; Kivshar, Y. S.; Altug, H. *Science* **2018,** *360,* 1105–1109. doi:10.1126/science.aas9768

196. Vo-Dinh, T. *Sens. Actuators, B* **1995,** *29,* 183–189. doi:10.1016/0925-4005(95)01681-3

197. Narasimhan, V.; Siddique, R. H.; Lee, J. O.; Kumar, S.; Ndjamen, B.; Du, J.; Hong, N.; Sretavan, D.; Choo, H. *Nat. Nanotechnol.* **2018,** *13,* 512–519. doi:10.1038/s41565-018-0111-5

198. Sreekanth, K. V.; Alapan, Y.; ElKabbash, M.; Ilker, E.; Hinczewski, M.; Gurkan, U. A.; De Luca, A.; Strangi, G. *Nat. Mater.* **2016,** *15,* 621–627. doi:10.1038/nmat4609

199. Emir Diltemiz, S.; Keçili, R.; Ersöz, A.; Say, R. *Sensors* **2017,** *17,* 454. doi:10.3390/s17030454

200. Okahata, Y.; Kimura, K.; Ariga, K. *J. Am. Chem. Soc.* **1989,** *111,* 9190–9194. doi:10.1021/ja00208a009

201. Tan, S. M.; Poh, H. L.; Sofer, Z.; Pumera, M. *Analyst* **2013,** *138,* 4885. doi:10.1039/c3an00535f

202. Marvan, P.; Mazánek, V.; Sofer, Z. *Nanoscale* **2019,** *11,* 4310–4317. doi:10.1039/c8nr09294j

203. Kang, J.; Wells, S. A.; Sangwan, V. K.; Lam, D.; Liu, X.; Luxa, J.; Sofer, Z.; Hersam, M. C. *Adv. Mater. (Weinheim, Ger.)* **2018,** *30,* 1802990. doi:10.1002/adma.201802990

204. Lee, C. M.; Jin, C. H.; Ahn, C. H.; Cho, H. K.; Lim, J. H.; Hwang, S. M.; Joo, J. *Bull. Chem. Soc. Jpn.* **2019,** *92,* 1094–1099. doi:10.1246/bcsj.20190004

205. Liakos, K.; Busato, P.; Moshou, D.; Pearson, S.; Bochtis, D. *Sensors* **2018,** *18,* 2674. doi:10.3390/s18082674

206. Fonollosa, J.; Solórzano, A.; Marco, S. *Sensors* **2018,** *18,* 553. doi:10.3390/s18020553

The importance of design in nanoarchitectonics: multifractality in MACE silicon nanowires

Stefania Carapezzi[*1,2] and Anna Cavallini[1]

Full Research Paper

Open Access

Address:
[1]Department of Physics and Astronomy, University of Bologna, Viale Berti Pichat 6/2, 40127 Bologna, Italy and [2]DEI-ARCES, Viale del Risorgimento 2, 40125, Bologna, Italy

Email:
Stefania Carapezzi[*] - stefania.carapezzi@gmail.com

* Corresponding author

Abstract

Background: Mechanisms of self-assembly/self-organization are fundamental for the emergence of nanoarchitectonic systems composed by elemental units, and it is important to build a theoretical framework for them. Additionally, because the enhanced functionalities of these systems are related to their spatial morphologies, it is necessary to quantify the self-organized design through suited statistical analysis tools.

Results: We have investigated the self-assembly bundling process of nanowires fabricated by metal-assisted chemical etching (MACE). First, we have applied theoretical models in order to obtain a quantitative estimation of the driving forces leading to self-assembly. Then, we have studied the surfaces of the nanoarchitectures by means of multifractal analysis. We have found that these systems are not simple monofractals, but that the more complex paradigm of multifractality (different fractal dimensions across different scales) has to be applied to describe their morphology.

Conclusion: The multifractal analysis approach has proven its ability to discriminate among different MACE nanoarchitectures. Additionally, it has demonstrated its capacity to measure the degree of homogeneity of these surfaces. Finally, a correlation between the growth conditions and the capacity dimension of the nanowires was obtained.

Introduction

In the last years, huge progress was made regarding the study and the technological exploitation of materials endowed with new properties deriving from their nanoscale features. In this respect, the field of nanoarchitectonics [1,2] has attracted atten-tion as one of the most promising paradigmatic changes in nanotechnology. In general, the concept of nanoarchitectonics consists in the approach of building up large structures from nanoscaled units by self-assembly. This self-building is driven

by the reciprocal interactions among the units, where these interactions are such as van der Waals, electrostatic, magnetic, molecular, and entropic forces [3]. The technological advantage is that in comparison to the nanoscaled units these self-organized assemblies possess new functionalities. Atoms, molecules, or even nanoparticles or nanowires (NWs) can be used as basic units to self-arrange in new wholes.

NWs are among the most widely investigated nanoscaled objects. Especially semiconductor NWs offer the unique promise to boost the performance of semiconductor devices by quantum effects. In this respect, silicon NWs [4-7] are key elements in the field of nanotechnology, given that they can be integrated in the microelectronic industry, which is mainly Si-based. From a technological point of view, it is essential to explore the possibilities of a large-scale fabrication of NWs. The top-down approach [8] represents the main route to achieve this goal, because it allows for wafer-scale growth by an easy adaptation of microfabrication equipment already available in the industry. The top-down methods involve the use of both dry [9,10] and wet etching [11] to carve nanostructures from a substrate. Metal-assisted chemical etching (MACE) [12-15] has gained particular attention in this regard, because it is simple, of low cost and versatile. MACE is an anisotropic wet etching technique where the sculpting of the nanostructures is catalyzed by a discontinuous thin film of noble metal deposited on a substrate. The metal works as a local cathode where the reduction of oxidants occurs. The underneath semiconductor is the local anode where a charge-mediated nucleophilic substitution reaction takes place, which causes silicon atoms to be etched/removed from the substrate. The metal layer, which is not consumed during the process, simply sinks down while the uncovered parts of the substrate form the tips of the NWs. Indeed, no consummation occurs when gold is used, while other metals are partly dissolved in many instances. Because the fabrication step occurs in liquid ambient a final drying step is inherently involved. Under certain conditions of 1) high NW density and 2) high aspect-ratio of NWs, the surface tension between the residual fluid film and the NWs could induce a self-assembly [16,17] (see Figure 1). The process of the assembly of NWs induced by elastocapillary forces is complex. There are many factors that influence the assembly such as periodicity, height, cross section, and tensile strength of the NWs as well as evaporation rate and the surface tension of the fluid. Elastocapillary self-assembly of NWs is an extensively investigated versatile and scalable method to design complex and robust surface nanoarchitectures [18]. For tuning and selectivity of the design of NW assemblies other approaches should be considered [19].

In hierarchical nanoarchitectures generated by NWs or other elemental nanobjects the self-assembly/self-organization mech-
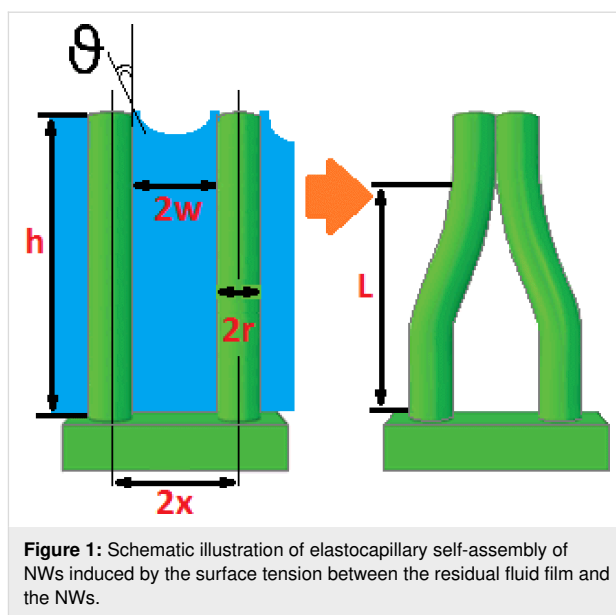
Figure 1: Schematic illustration of elastocapillary self-assembly of NWs induced by the surface tension between the residual fluid film and the NWs.

anisms are pivotal to generate the assembled structures. In fact, the direct fabrication of such structures by microfabrication or even nanofabrication approaches would be challenging or impossible, given the nanosized dimensions of the basic units. Because the spatial layout is self-driven in contrast to a hetero-directed placement, asymmetric interaction potentials and entropic forces can lead to different aggregation schemes from place to place and across the scales of the generated structures. The control over the spatial arrangement of the assembled elements is a key issue in nanoarchitectonics, because the emerging functionalities of the whole are linked to its geometry. As a fundamental step towards the full command of the nanoarchitectonic design it is thus necessary to characterize the self-generated morphologies, in order to be able to discriminate among them and possibly to relate them to growth procedures from one side and to physical properties from another side. In this regard, fractal analysis [20] is an analytical framework fit for the purpose. Indeed, self-assembled patterns derived from aggregative processes, which are omnipresent in nature, have been characterized by their fractal dimension [21-23] that contains information about their geometrical structure at multiple scales. However, sometimes the richness of the organization of shape is such that it is impossible to describe it by just one scaling law. In this latter case a shift to multifractal analysis is necessary.

In the present work we show the results of multifractal analysis of nanoarchitectured surfaces of MACE Si NWs. The spontaneous arrangements of the NWs were investigated by using atomic force microscopy (AFM). Among the scanning probe techniques, AFM shows a peculiar capability to quantitatively characterize features with nanoscaled dimensions. To gain

insight over the emergence of the organized nanoarchitectures we applied multifractal analysis to the AFM images. We have found that a single fractal dimension is not sufficient to describe the complex geometries of the NW systems. By examining the results of the multifractal analysis we have been able to highlight differences between the generated spatial patterns that we have correlated to the different growth conditions.

A Brief Survey of Multifractal Analysis

Let the fractal object F be a subset of the d-dimensional Euclidean space $\mathbb{R}^d$, which is the physical support of F, and be covered by a d-dimensional grid of length scale ε. The box-counting (BC) fractal dimension, or capacity, D_{BC} is defined as

$$D_{\mathrm{BC}}(F) \equiv -\lim_{\varepsilon \to 0} \frac{\ln N(\varepsilon)}{\ln \varepsilon} = \lim_{\varepsilon \to 0} \frac{\ln N(\varepsilon)}{\ln \frac{1}{\varepsilon}}, \quad (1)$$

where $N(\varepsilon)$ is the number of grid elements that overlap with F. Usually, D_{BC} is determined through the least squares linear fit of $\ln N(\varepsilon)$ as a function of ε. It is noteworthy to observe that Equation 1 represents a scaling rule that compares how much the detail (quantified by N) in a given pattern changes with the scale (ε), and it shows that for a (mono)fractal a single fractal dimension is able to characterize it across all the length scales [20]. For the deterministic fractals, which are mathematically constructed objects, the scale invariance holds for all scales. Well-known examples are Cantor set and Koch's curve [20]. Instead, natural objects and phenomena are intrinsically finite and their fractality, if any, can be determined only within a specific regime of length scales. These structures are called random fractals.

When the fractal analysis is applied to investigate shapes of natural objects, this is performed by analyzing their images. Thus, it is necessary to reframe the above concepts within the field of image analysis. The simplest type of digital image is a binary image, that is a squared (for the sake of simplicity) $S \times S$ discrete matrix M of pixels where each pixel can have black or white colour. In this case the fractal object will correspond to the set of the pixels of a given colour, for instance black, while all pixels corresponding to the other colour will be disregarded. To evaluate the dimension of D_{BC}, first a series of grids with different length scales will be overlaid to the image. Each grid is composed of $s_\varepsilon \times s_\varepsilon$ not overlapping boxes $G_\varepsilon(i,j)$, the size of which is the grid length scale ε, such that $M = \cup_{i,j=1,\dots s_\varepsilon} G_\varepsilon(i,j)$. Then it is useful to introduce a local measure $\mu_\varepsilon(i,j)$, which amounts to the number of pixels belonging to the fractal object and contained in the box $G_\varepsilon(i,j)$. It is evident that, when a single global exponent characterizes a

fractal object, the measure is uniform and $\mu_\varepsilon \propto \varepsilon^{-D_{\mathrm{BC}}}$. However, in case of multifractal objects the above does not apply anymore and the measure μ_ε varies at different locations.

The quantitative description of multifractality can be performed in different manners. One approach passes through the calculation of the Lipshitz-Hölder exponent α, which gives account of the pointwise singularity of the object, and its distribution $f(\alpha)$, known as the multifractal spectrum. One method to determine $f(\alpha)$ is the following [24]. The probability distribution of μ_ε is introduced as

$$P_\varepsilon(i,j) = \frac{\mu_\varepsilon(i,j)}{\sum_{i,j=1,\dots s_\varepsilon} \mu_\varepsilon(i,j)}, \quad (2)$$

from which a one-parameter family of normalized measures is constructed:

$$\mu'_\varepsilon(q;i,j) = \frac{\left[P_\varepsilon(i,j) \right]^q}{\sum_{i,j=1,\dots s_\varepsilon} \left[P_\varepsilon(i,j) \right]^q} \quad (3)$$

The parameter q works like a magnifying glass, enhancing 1) the regions of the fractal object with the lowest values of $P_\varepsilon(i,j)$ for $q < 1$ and 2) the regions with the highest values of $P_\varepsilon(i,j)$ for $q > 1$. The fractal dimension of the support of $\mu(q)$ is

$$f(q) = \lim_{\varepsilon \to 0} \frac{\sum_{i,j=1,\dots s_\varepsilon} \mu'_\varepsilon(q;i,j) \ln \mu'_\varepsilon(q;i,j)}{\ln \varepsilon}, \quad (4)$$

and the average value of the singularity strength

$$\alpha_\varepsilon(i,j) = \frac{\ln P_\varepsilon(i,j)}{\ln \varepsilon}$$

with respect to $\mu(q)$ is

$$\alpha(q) = \lim_{\varepsilon \to 0} \frac{\sum_{i,j=1,\dots s_\varepsilon} \mu'_\varepsilon(q;i,j) \ln P_\varepsilon(i,j)}{\ln \varepsilon}. \quad (5)$$

The mass exponent $\tau(q)$ is defined as

$$-\tau(q) = \lim_{\varepsilon \to 0} \frac{\chi_\varepsilon(q)}{\ln \varepsilon}, \quad (6)$$

given that

$$\chi_\varepsilon(q) \equiv \sum_{i,j=1,\dots s_\varepsilon} \left[P_\varepsilon(i,j) \right]^q$$

is the *q*-th power moment sum. $\tau(q)$ is linked to the multifractal spectrum by the Legendre transformation

$$\alpha(q) = -\frac{\mathrm{d}\tau(q)}{\mathrm{d}q} \text{ and } f(\alpha) = q\alpha(q) - \tau(q). \qquad (7)$$

It is also connected to the generalized fractal dimensions [25-27]

$$D(q) = \frac{1}{q-1} \lim_{\varepsilon \to 0} \frac{\ln \chi_\varepsilon(q)}{\ln \varepsilon}, \qquad (8)$$

because $\tau(q) = (q - 1)D(q)$. Thus, an alternative way to determine the multifractal spectrum is to calculate $D(q)$ from the above equation and to substitute it in Equation 7.

Results and Discussion
Elastocapillary self-assembly in MACE Si NWs

Figure 2 shows typical AFM images of the MACE Si NWs investigated in the present work. The procedure to grow the MACE samples is carried out as follows: (100)-oriented Si wafers are the substrates. As a first step, the native oxide is removed from their surfaces by UV-oxidizing (2 min) and then dipping them (5 min) in 5% HF. Subsequently, 2 nm thick Au layers are deposited on the cleaned surfaces by electron beam evaporation. These gold films do not coat the substrates uniformly. The uncovered parts of the Si surfaces become the seeds of the NWs in the subsequent etching step. For the etching step, the substrates are immersed in an aqueous solution of HF (5 M) and H_2O_2 (0.44 M). Two types of MACE Si NWs have been synthesised, with differences in 1) the doping of the source substrates and 2) the etching time. Longer etching times yield longer NWs. For one sample (labelled from now on SiNW1; Figure 2a) the source substrate was P-doped with a doping density of 10^{15} cm^{-3} and a NW length of 5 μm. For the other sample (labelled SiNW2; Figure 2b) the source substrate was As-doped with a doping density of about 10^{18} cm^{-3} and a NW length of 1.3 μm.

Figure 3a and Figure 3b are the masked images obtained applying a height threshold on the AFM measurements of Figure 2. The threshold divides the surface into two regions: the tips of NWs (black colour) and the remainder of the sample (white colour). The NW tips appear clustered in both samples, creating a very complex architecture over the surfaces. It is noteworthy to observe that this clustering has not been purposefully induced by design of the locations of NWs, but it is a spontaneous assembly occurring during the NW growth. Recently, a direct observation of MACE NWs bending and sticking together during the drying step has been reported [28]. The authors have found experimentally that the bending/bundling of NWs depended on their aspect ratio. It occurred for aspect ratios greater than 1:10, while it was not observed for an aspect ratio of about 1:5. Actually, many more factors have impact on the self-assembly of arrays of nano- and microstructures with high aspect ratios, when a liquid is evaporated off the surface [29,30]. Considering two adjacent NWs, first 1) the capillary force between them should be able to overcome the elastic force moving them back to the original straight position, in order to bring them into contact during the evaporation of the
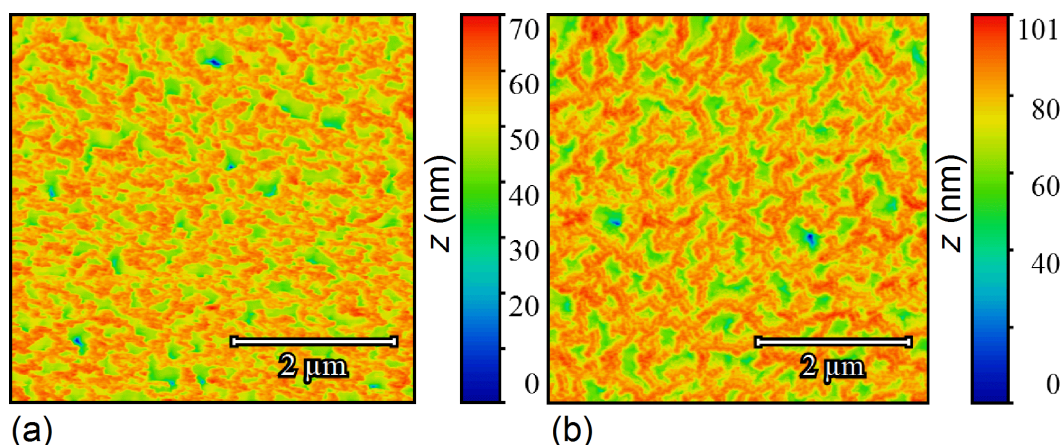

Figure 2: Representative AFM images of sample SiNW1 (a) and sample SiNW2 (b). The probed areas have a size of 5 × 5 μm². The AFM measurements have been performed by using a NT-MDT Solver Pro 4H microscope, using tapping mode in ambient atmosphere and at room temperature.
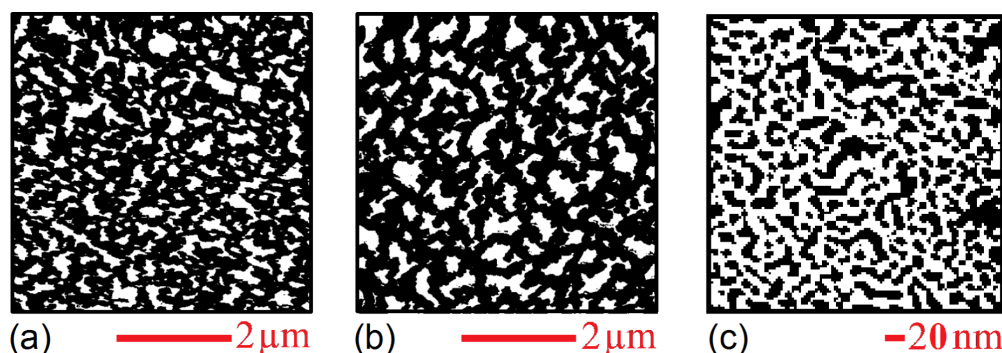
Figure 3: (a, b) Masks obtained by setting a threshold for the heights in the AFM images of SiNW1 and SiNW2 in Figure 2, in such a way that the black regions correspond to the tips of NWs. (c) Image obtained after binary-processing a SEM image adapted from [37] of a 2 nm Au layer deposited on a Si substrate by electron beam evaporation. The conditions during the growth of the gold thin film were similar to the ones during the growth of the samples SiNW1 and SiNW2. The black regions correspond to the uncovered silicon areas, while the white region represents the deposited Au. It is evident that by MACE processing the metal-coated substrate a spatially homogeneous arrangements of NWs would have been expected. On the contrary, in (a, b) the MACE-grown NWs are clustered.

liquid. Then a stable bundle will occur if 2) the adhesion force between the surfaces of the two NWs is larger than the elastic force. In order to theoretically confirm the self-assembly that occurred in both samples SiNW1 and SiNW2, we availed of literature [29,31] to model steps 1) and 2). Given a pillar-like structure of height h, clamped at one end, such that the other end is deflected by a length w, the magnitude of the elastic force acting on it can be calculated from the Euler–Bernoulli elementary beam theory [32], and it is given by

$$F_{\mathrm{el}} = \frac{3EIw}{h^3},\qquad(9)$$

where E is the Young modulus of the pillar and I is its area moment of inertia. The magnitude of the capillary force F_{C} between two cylindrical pillars when partially immersed in a liquid is [29]

$$F_{\mathrm{C}} = \frac{\pi \gamma_{\mathrm{liq}} r^2 \cos^2\theta}{\sqrt{x^2 - r^2}},\qquad(10)$$

where γ_{liq} is the liquid surface tension, θ is the contact angle between the liquid and the surface of the pillar, r is the radius of the pillar and $2x$ is the interdistance between the axes of the two pillars (see Figure 1). We have availed of the above Equations 9 and 10 to estimate the magnitudes of the elastic and capillary forces in our case. To this aim we have determined average values of 4.5 nm and of 7.5 nm for r and x, respectively. Considering the data reported in literature, we have considered not a single value but a range of values of a) E = 80–120 GPa [33] and of b) γ_{HF} from 0.5 mN/m [34] to 10.2 mN/m [35]. A value of $\theta = 70°$ has been found for silicon surfaces and HF [36]. The range of values for the capillary

force has thus been estimated to be 3–65 pN, which is orders of magnitude greater than the possible values of the elastic force, ranging from 0.9 to 1.4 fN for SiNW1, and from 53 to 80 fN for SiNW2. This confirms that under the growth conditions described here, F_{C} is greater than F_{el} and can bring the NWs into contact.

In order to find out whether the formed NW bundles are stable, we have calculated the critical aspect ratio [31] of the NWs of samples SiNW1 and SiNW2. The critical aspect ratio is a threshold value for the stability of the bundles. NWs with aspect ratios larger than the critical one will remain attached after bending towards each other and getting in contact. Given two collapsed pillars, such that the length of the non-contact portion is L (Figure 1b), a critical value of L can be estimated from [31]

$$\frac{9EIw^2}{L^4}\,\mathrm{d}L = \left(2\gamma_{\mathrm{sup}}c_0 - U_{\mathrm{c}}\right)\mathrm{d}L,\qquad(11)$$

where the term on the left-hand side is the decrease in strain energy if the non-contact region is increased by $\mathrm{d}L$, and the term on the right-hand side is the energy required to separate the surfaces of the two pillars by $\mathrm{d}L$. γ_{sup} is the surface energy of the pillar, c_0 is the contact width at equilibrium of the two pillars under no external force, and U_{c} is the stored elastic energy normalized to the contact length due to the deformation near the contact region. The values of c_0 and U_{c} are given by [31]

$$\frac{c_0}{2} = r_{\mathrm{c}} = \left(\frac{32r^2\gamma_{\mathrm{sup}}}{\pi E^*}\right)^{1/3}\qquad(12)$$

and

$$U_c = \frac{\pi E^* r^2}{32}\left(\frac{r_c}{r}\right)^4, \qquad (13)$$

given that $E^* = E/(1 - v^2)$ where v is the Poisson's ratio. By rearranging Equation 11 it is possible to derive the critical aspect ratio as

$$AR_{\mathrm{crit}} = \left[\frac{9E\pi w^2}{64(4\gamma_{\mathrm{sup}}r_c - U_c)}\right]^{1/4}, \qquad (14)$$

since $I = \pi r^4/4$ for a cylindrical pillar. Again, a range of values for γ_{sup} from 1 to 2.2 J/m^2 has been used according to literature [38], and a Poisson's ratio of 0.22. The values of AR_{crit} thus obtained range from 2.2 to 1.5, while the aspect ratios of the NWs are of 555 for sample SiNW1 and of 144 for sample SiNW2. This confirms theoretically the stability of the observed NW clusters. The process of self-assembly yielded the hierarchically structured MACE NW surfaces as shown in Figure 2. The complex spatial design thus achieved has been investigated by means of multifractal analysis.

Multifractal analysis applied to MACE NWs

In a previous section we gave a brief survey of the computational procedures involved into performing fractal and multifractal analysis. In both kinds of analysis, after the preliminary step of overlaying a grid of length scale ε to the image, it is crucial to establish a rule to assign a value to the local measure $\mu_\varepsilon(i,j)$ over each box of the grid. However, the recipe that has been given, $\mu_\varepsilon(i,j) \leftrightarrow$ number of pixels belonging to the fractal object and contained in the box (i,j) is meaningful only for binary images. Indeed, fractal objects that can be described by binary images are, for example, 2D contours or the 2D correspondent filled patterns (such as the regions of homogeneous colour of Figure 3). These fractals are clearly just a subset of the possible random fractal phenomena or structures that can be met in nature, where the complex features of real 3D morphologies cannot be rendered by binary images. In fact, the AFM images of Figure 2 are RGB images, where a colour scale connects the image colours to height values. It is noteworthy to observe that, once a suitable mapping is established to compute the local measure μ_ε for RGB or grey-scale images, the steps already described to calculate the fractal dimension, the multifractal spectrum or the generalized dimensions would be the same. In the present work we have chosen to use grey-scaled versions of the AFM images to perform the multifractal analysis, which has been implemented by means of the FracLac plugin [39] of the image analysis software ImageJ [40]. In fact,

in the grey-scaled AFM images the interval of heights actually measured is mapped onto grey-level values ranging from 0 (black) to 255 (white), which corresponds to a simple rescaling. The flow chart of the followed procedure has been schematically illustrated in Figure 4a,b. To calculate the local measure μ_ε for the grey-level images we availed of the differential box counting method: $\mu_\varepsilon(i,j) = \Delta_\varepsilon I(i,j) + 1$, given that $\Delta_\varepsilon I(i,j) = I_{\max} - I_{\min}$ is the difference in pixel intensities (grey-level values) over the box (i,j).

Figure 5 shows the D_q curves of different sampled areas of the surfaces of samples SiNW1 (a) and SiNW2 (b). First of all, these graphical spectra of D_q show that the nanoarchitectured surfaces generated by the self-assembly of NWs are indeed multifractal. Monofractals or objects that are not fractals tend to have flatter D_q curves than multifractals. Ideally, a D_q curve is flat for a monofractal because $D_q = D_0 \forall q$ [25]. With reference to Equation 8, it should be remembered that the generalized dimension is linked to the probability distribution $P_\varepsilon(i,j)$. The largeness of an element of such a distribution is directly related to the correspondent largeness of $\mu_\varepsilon(i,j)$ (see Equation 2). Thus, the parameter q is a kind of a resolution parameter that enhances 1) regions corresponding to higher μ_ε values for positive values of q, and 2) regions of lower μ_ε values for negative values of q. Keeping this in mind, and taking into account how we have defined above the local measure μ_ε, we observe that for sample SiNW1 the D_q values for each q are lower than the ones for sample SiNW2, or they are in the same range. That is, in sample SiNW2 there is a tendency to higher fractality for both areas with larger or smaller ranges of pixel intensities $\Delta_\varepsilon I$. This is related to the different growth conditions of sample SiNW1 and sample SiNW2.

In Table 1 are reported the D_0, D_1 and D_2 values of the sampled areas from sample SiNW1 and SiNW2. It can be proved that $D_q > D_{q'}$ if $q' > q$[25], and in fact we have found that $D_0 > D_1 > D_2$, where the difference between these values is an indication of the multifractality of the surfaces of samples SiNW1 and SiNW2. D_0 is the so called capacity (or box counting) dimension that would coincide with D_{BC} in a monofractal system. In our case we have found values of D_0 of about 1.84 for most of sampled areas of sample SiNW1, while a value of 1.72 was obtained in one case. In contrast, for sample SiNW2 we obtained values of about 1.73, again with a value of 1.86 obtained in one case. Such differences in capacity dimension for different areas of the same sample may be indicative of a certain degree of inhomogeneity in the final design of the NW patterns. Nevertheless, it is interesting to observe that the range of possible D_0 values seems to be approximately the same in both samples. It has to be noted that MACE Si NW samples have been characterized by simple fractal analysis in a previous
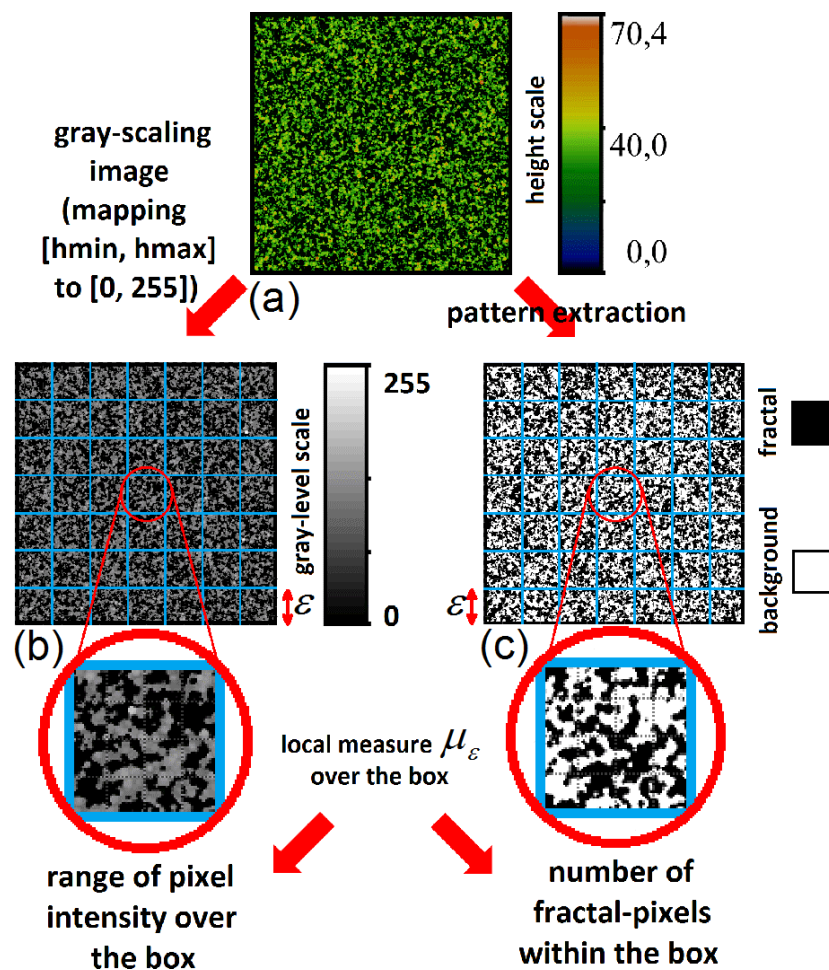
Figure 4: (a, b) Schematic of the differential box counting method applied to the AFM measurements. Each AFM image (a) is converted into a grey-scaled image (b). For a given grid of unit length ε laid down over the image (blue lattice), the local measure $\mu_\varepsilon(i,j)$ is computed as the range in intensity of all pixels belonging to the box. For the sake of comparison, the flow chart for the more common box counting method over binary images is illustrated in panels (a) and (c). From the AFM image (a) is extracted a silhouette or a mask (c). The region subject to fractal analysis is black (in the present case), while all remaining pixels are set to white. For a chosen grid, the local measure $\mu_\varepsilon(i,j)$ is then computed as the sum of black pixels within the box.
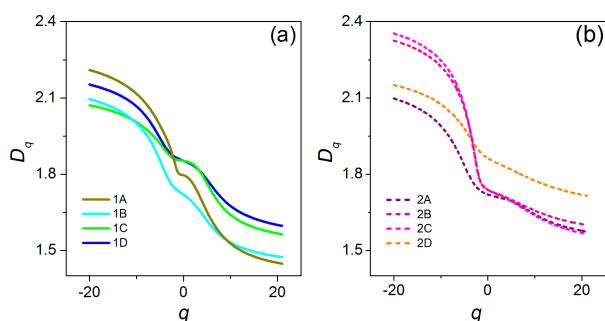
Figure 5: Curves of the generalized dimension D_q as a function of q for different probed areas of samples SiNW1 (a) and SiNW2 (b). The values of D_0, D_1 and D_2 for these areas have been reported in Table 1.

Table 1: Main parameters obtained from the multifractal analysis of the sampled areas of SiNW1 and SiNW2.

	SiNW1		
area	D_0	D_1	D_2
1A	1.7958	1.7854	1.7629
1B	1.7197	1.7054	1.6878
1C	1.8528	1.8486	1.8394
1D	1.8528	1.8453	1.8352
	SiNW2		
area	D_0	D_1	D_2
2A	1.7197	1.714	1.71
2B	1.8628	1.8526	1.8435
2C	1.7378	1.7289	1.7209
2D	1.7378	1.7296	1.7225

work [37], where a value of D_{BC} of about 1.9 has been found. However, it should be taken into account that in that case the analysis has been performed over binarized SEM images, where the patterns under study have been the regions corresponding to the tops of NWs, similar to the masked regions of Figure 3b,c. Thus, the complex 3D arrangements of the NWs have been completely ignored.

Finally, in Figure 6 the multifractal spectra $f(\alpha)$ of all the sampled areas of samples SiNW1 (a) and SiNW2 (b) are reported. Again, there is an indication of multifractality in both samples, given that in the case of an ideal monofractal $f(\alpha)$ would reduce to just a single point. In contrast to D_q, which represents the various dimensions of the distribution of the ranges of pixel intensity values over the whole imaged area, $f(\alpha)$ is the dimension obtained over different sub-regions that display the same α. Each curve $f(\alpha)$ shows the characteristic convex shape, peaked at $\alpha(0)$, where $f(\alpha(0)) = D_0$, as can be easily verified by Equations 6–8. The α values to the left of $\alpha(0)$ are associated with positive q values, the ones to the right of $\alpha(0)$ are associated with negative q values. Thus, the presence or the absence of symmetry of $f(\alpha)$ around its peak mirrors the same kind of symmetry/asymmetry in the distribution between regions with a large/small range of pixel intensity values. From Figure 6 it appears that $f(\alpha)$ spectra of the sampled areas of SiNW1 have a tendency to be symmetric. Instead of this, in the case of sample SiNW2 the intervals of α values of sub-areas with a smaller range of pixel intensity values (right part of the curve) are bigger than the ones for sub-areas with a larger range of pixel intensity values (left part of the curve). It can be suggested that for sample SiNW2 the multifractality is enhanced in sub-areas with smaller range of pixel intensity, that is of smaller height variation. In fact, it should be remembered that the pixel intensity is simply a rescaling of the measured height value. It is interesting to note that the property of symmetry/asymmetry of the $f(\alpha)$ spectrum applies to all areas of each sample, appearing to be an intrinsic feature.
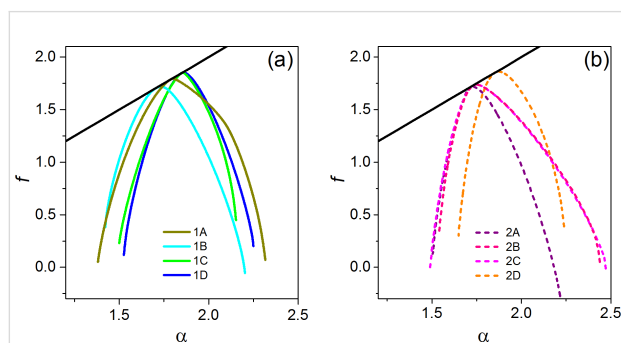

Figure 6: Multifractal spectra of sampled areas of MACE SiNW1 (a) and SiNW2 (b). The black line is the first diagonal.

Conclusion

In this work we have investigated the spontaneous spatial organization of nanoarchitectures of MACE Si NWs. First, we have applied theoretical models in order to estimate the driving forces leading to the self-assembly. Then we have availed of multifractal analysis to analyze the patterns. Our results confirm that fractal analysis would not be sufficient to capture the whole richness of the self-assembled structures. Differences in growth conditions result in differences in the generalized dimension and the multifractal spectrum. In contrast, when the same quantities are calculated over areas of the same sample the results show coherence, even if a minority of cases departs. This means that the nanoarchitectonic surfaces present locally some degree of inhomogeneity. This also highlights multifractal analysis as a powerful tool to "measure" the design of fractal-like nanoarchitectures. Finally, a correlation has been found between the growth conditions and the tendency to multifractality, which is more uniform across the MACE nanoarchitectures of sample SiNW1, while it is accentuated in the region formed by the tips of the nanowires of sample SiNW2.

ORCID® iDs

Stefania Carapezzi - https://orcid.org/0000-0002-9271-1189
Anna Cavallini - https://orcid.org/0000-0002-6949-2854

References

1. Ariga, K., Ed. *Manipulation of Nanoscale Materials;* Nanoscience & Nanotechnology Series; Royal Society of Chemistry: Cambridge, United Kingdom, 2012. doi:10.1039/9781849735124
2. Ariga, K.; Nishikawa, M.; Mori, T.; Takeya, J.; Shrestha, L. K.; Hill, J. P. *Sci. Technol. Adv. Mater.* **2019,** *20,* 51–95. doi:10.1080/14686996.2018.1553108
3. Bishop, K. J. M.; Wilmer, C. E.; Soh, S.; Grzybowski, B. A. *Small* **2009,** *5,* 1600–1630. doi:10.1002/smll.200900358
4. Cui, Y.; Duan, X.; Hu, J.; Lieber, C. M. *J. Phys. Chem. B* **2000,** *104,* 5213–5216. doi:10.1021/jp0009305
5. Cui, Y.; Lieber, C. M. *Science* **2001,** *291,* 851–853. doi:10.1126/science.291.5505.851
6. Hasan, M.; Huq, M. F.; Mahmood, Z. H. *SpringerPlus* **2013,** *2,* 151. doi:10.1186/2193-1801-2-151
7. Cavallini, A.; Carapezzi, S.; Castaldini, A.; Irrera, A. *Phys. B (Amsterdam, Neth.)* **2014,** *439,* 41. doi:10.1016/j.physb.2013.11.021
8. Hobbs, R. G.; Petkov, N.; Holmes, J. D. *Chem. Mater.* **2012,** *24,* 1975–1991. doi:10.1021/cm300570n
9. He, B.; Yang, Y.; Yuen, M. F.; Chen, X. F.; Lee, C. S.; Zhang, W. J. *Nano Today* **2013,** *8,* 265–289. doi:10.1016/j.nantod.2013.04.008
10. Carapezzi, S.; Castaldini, A.; Mancarella, F.; Poggi, A.; Cavallini, A. *ACS Appl. Mater. Interfaces* **2016,** *8,* 10443–10450. doi:10.1021/acsami.6b00600
11. Madou, M. J. Wet Chemical Etching and Wet Bulk Micromachining-Pools as Tools. *Fundamentals of Microfabrication and Nanotechnology,* 3rd ed.; Taylor & Francis Group: Boca Raton, FL, U.S.A., 2011; pp 215–318.

12. Huang, Z.; Geyer, N.; Werner, P.; de Boor, J.; Gösele, U.
Adv. Mater. (Weinheim, Ger.) **2011,** *23,* 285–308.
doi:10.1002/adma.201001784

13. Li, X. *Curr. Opin. Solid State Mater. Sci.* **2012,** *16,* 71–81.
doi:10.1016/j.cossms.2011.11.002

14. Han, H.; Huang, Z.; Lee, W. *Nano Today* **2014,** *9,* 271–304.
doi:10.1016/j.nantod.2014.04.013

15. Li, M.; Li, Y.; Liu, W.; Yue, L.; Li, R.; Luo, Y.; Trevor, M.; Jiang, B.;
Bai, F.; Fu, P.; Zhao, Y.; Shen, C.; Mbengue, J. M. *Mater. Res. Bull.*
2016, *76,* 436–449. doi:10.1016/j.materresbull.2016.01.006

16. Bai, F.; Li, M.; Song, D.; Yu, H.; Jiang, B.; Li, Y. *J. Solid State Chem.*
2012, *196,* 596–600. doi:10.1016/j.jssc.2012.07.029

17. Hill, J. J.; Haller, K.; Gelfand, B.; Ziegler, K. J.
ACS Appl. Mater. Interfaces **2010,** *2,* 1992–1998.
doi:10.1021/am100290z

18. De Volder, M.; Hart, A. J. *Angew. Chem., Int. Ed.* **2013,** *52,*
2412–2425. doi:10.1002/anie.201205944

19. Carapezzi, S.; Priante, G.; Grillo, V.; Montès, L.; Rubini, S.;
Cavallini, A. *ACS Nano* **2014,** *8,* 8932–8941. doi:10.1021/nn503629d

20. Mandelbrot, B. B. *The fractal geometry of nature;* W. H. Freeman and
Co., 1982.

21. Carrillo, J. L.; Mendoza, M. E.; Donado, F. *J. Stat. Mech.: Theory Exp.*
2005, P06001. doi:10.1088/1742-5468/2005/06/p06001

22. González-Gutiérrez, J.; Carrillo-Estrada, J. L.; Ruiz-Suárez, J. C.
J. Stat. Mech.: Theory Exp. **2013,** P12015.
doi:10.1088/1742-5468/2013/12/p12015

23. González-Gutiérrez, J.; Carrillo-Estrada, J. L.; Ruiz-Suárez, J. C.
J. Phys.: Conf. Ser. **2013,** *475,* 012003.
doi:10.1088/1742-6596/475/1/012003

24. Chhabra, A.; Jensen, R. V. *Phys. Rev. Lett.* **1989,** *62,* 1327–1330.
doi:10.1103/physrevlett.62.1327

25. Hentschel, H. G. E.; Procaccia, I. *Phys. D (Amsterdam, Neth.)* **1983,** *8,*
435–444. doi:10.1016/0167-2789(83)90235-x

26. Halsey, T. C.; Meakin, P.; Procaccia, I. *Phys. Rev. Lett.* **1986,** *56,*
854–857. doi:10.1103/physrevlett.56.854

27. Halsey, T. C.; Jensen, M. H.; Kadanoff, L. P.; Procaccia, I.;
Shraiman, B. I. *Phys. Rev. A* **1986,** *33,* 1141–1151.
doi:10.1103/physreva.33.1141

28. Kara, S. A.; Keffous, A.; Giovannozzi, A. M.; Rossi, A. M.; Cara, E.;
D'Ortenzi, L.; Sparnacci, K.; Boarino, L.; Gabouze, N.; Soukane, S.
RSC Adv. **2016,** *6,* 93649–93659. doi:10.1039/c6ra20323j

29. Chandra, D.; Yang, S. *Langmuir* **2009,** *25,* 10430–10434.
doi:10.1021/la901722g

30. Chandra, D.; Yang, S. *Acc. Chem. Res.* **2010,** *43,* 1080–1091.
doi:10.1021/ar100001a

31. Glassmaker, N. J.; Jagota, A.; Hui, C.-Y.; Kim, J. *J. R. Soc., Interface*
2004, *1,* 23–33. doi:10.1098/rsif.2004.0004

32. Hibbeler, R. C. *Mechanics of materials,* 3rd ed.; Prentice-Hall:
Englewood Cliffs, NJ, U.S.A., 1997.

33. Zhu, Y.; Xu, F.; Qin, Q.; Fung, W. Y.; Lu, W. *Nano Lett.* **2009,** *9,*
3934–3939. doi:10.1021/nl902132w

34. dos Santos, A. P.; Levin, Y. *J. Chem. Phys.* **2010,** *133,* 154107.
doi:10.1063/1.3505314

35. Hydrofluoric acid | HF - PubChem.
https://pubchem.ncbi.nlm.nih.gov/compound/14917#section=Heat-of-V
aporization&fullscreen=true (accessed Oct 10, 2019).

36. Hermansson, K.; Lindberg, U.; Hok, B.; Palmskog, G. Wetting
properties of silicon surfaces. In *TRANSDUCERS 91: 1991
International Conference on Solid-State Sensors and Actuators. Digest
of Technical Papers,* IEEE Publishing: Piscataway, U.S.A., 1991;
pp 193–196.

37. Fazio, B.; Artoni, P.; Antonia Iatì, M.; D'Andrea, C.; Lo Faro, M. J.;
Del Sorbo, S.; Pirotta, S.; Giuseppe Gucciardi, P.; Musumeci, P.;
Salvatore Vasi, C.; Saija, R.; Galli, M.; Priolo, F.; Irrera, A.
Light: Sci. Appl. **2016,** *5,* e16062. doi:10.1038/lsa.2016.62

38. Tran, R.; Xu, Z.; Radhakrishnan, B.; Winston, D.; Sun, W.;
Persson, K. A.; Ong, S. P. *Sci. Data* **2016,** *3,* 160080.
doi:10.1038/sdata.2016.80

39. FracLac for ImageJ.
https://rsb.info.nih.gov/ij/plugins/fraclac/FLHelp/Introduction.htm
(accessed Oct 10, 2019).

40. ImageJ. https://imagej.nih.gov/ij/ (accessed Oct 10, 2019).

License and Terms

Microbubbles decorated with dendronized magnetic nanoparticles for biomedical imaging: effective stabilization via fluorous interactions

Da Shi[1], Justine Wallyn[1], Dinh-Vu Nguyen[2], Francis Perton[2], Delphine Felder-Flesch[2], Sylvie Bégin-Colin[2], Mounir Maaloum[1] and Marie Pierre Krafft[*1]

Full Research Paper

Address:
[1]Institut Charles Sadron (CNRS), University of Strasbourg, 23 rue du Loess, 67034 Strasbourg, France and [2]Institut de Physique et de Chimie des Matériaux de Strasbourg (IPCMS), University of Strasbourg, 23 rue du Loess, 67034 Strasbourg, France

Email:
Marie Pierre Krafft[*] - krafft@unistra.fr

* Corresponding author

Abstract

Dendrons fitted with three oligo(ethylene glycol) (OEG) chains, one of which contains a fluorinated or hydrogenated end group and bears a bisphosphonate polar head ($C_nX_{2n+1}OEG_8Den$, X = F or H; n = 2 or 4), were synthesized and grafted on the surface of iron oxide nanoparticles (IONPs) for microbubble-mediated imaging and therapeutic purposes. The size and stability of the dendronized IONPs ($IONP@C_nX_{2n+1}OEG_8Den$) in aqueous dispersions were monitored by dynamic light scattering. The investigation of the spontaneous adsorption of $IONP@C_nX_{2n+1}OEG_8Den$ at the interface between air or air saturated with perfluorohexane and an aqueous phase establishes that exposure to the fluorocarbon gas markedly increases the rate of adsorption of the dendronized IONPs to the gas/water interface and decreases the equilibrium interfacial tension. This suggests that fluorous interactions are at play between the supernatant fluorocarbon gas and the fluorinated end groups of the dendrons. Furthermore, small perfluorohexane-stabilized microbubbles (MBs) with a dipalmitoylphosphatidylcholine (DPPC) shell that incorporates $IONP@C_nX_{2n+1}OEG_8Den$ (DPPC/Fe molar ratio 28:1) were prepared and subsequently characterized using both optical microscopy and an acoustical method of size determination. The dendrons fitted with fluorinated end groups lead to smaller and more stable MBs than those fitted with hydrogenated groups. The most effective result is already obtained with C_2F_5, for which MBs of ≈1.0 μm in radius reach a half-life of ≈6.0 h. An atomic force microscopy investigation of spin-coated mixed films of $DPPC/IONP@C_2X_5OEG_8Den$ combinations (molar ratio 28:1) shows that the IONPs grafted with the fluorinated dendrons are located within the phospholipid film, while those grafted with the hydrocarbon dendrons are located at the surface of the phospholipid film.

Introduction

Microbubbles (MBs), that is, micrometer-sized gas particles dispersed in an aqueous medium, are clinically used as contrast agents for ultrasound imaging, including molecular imaging, and actively investigated for surgical ablation, targeted drug and gene delivery [1-10]. They are also being examined for use, in conjunction with focused ultrasound, and under magnetic resonance imaging guidance, for achieving blood/brain and blood/tumor barrier crossing of drugs [11,12]. Medical MBs have a shell consisting of surfactants, phospholipids, or polymers and are usually stabilized by a fluorocarbon gas [13] that acts as an osmotic agent [14,15] and as a co-surfactant to phospholipids [16] and block co-polymers [17].

Nanoparticles can be attached to the bubble shells to extend their diagnostic and therapeutic potential by combining multi-modal imaging, drug or gene delivery, and/or enhancement and control of the acoustic signal for energy deposition, as is required for sonothrombolysis or ablation surgery. MBs incorporating iron oxide nanoparticles (IONPs) are sought after as dual contrast agents for ultrasound and magnetic resonance imaging [18-20] and drug delivery [21,22]. The shells of the presently available MBs that incorporate IONPs are often made of polymers. For example, ultrasmall superparamagnetic iron oxide nanoparticles were embedded in the wall of poly(butyl cyanoacrylate)-based MBs, allowing the blood–brain barrier penetration to be monitored [23]. Soft-shell colloids called liposheres have also been reported for enhanced gene and drug delivery [24]. These liposheres consist of gas-filled spheres coated by a film of soybean oil that encases the cargo of nanoparticles and is itself contained within a film of phospholipids [24]. Both polymer-shelled MBs and liposheres have some advantages and some limitations [25]. In both cases, the shells can be custom-made to enhance stability, circulation duration, drug-loading capacity and release rate, targeting the fusion with cell membranes [24]. Both types of constructs are generally more stable, but less echogenic than "true" gas microbubbles, due to the dampening effect of the polymer shell or oil contained in the phospholipid coating [24,25]. One important difficulty encountered in the preparation of such magnetic MBs is that IONPs rapidly aggregate in aqueous media [25]. Commercially available 50 nm magnetic IONPs coated with phospholipids allowed for the preparation of MBs that enabled transfection of neuroblastoma cells with a generic, fluorescent, small, interfering RNA under magnetic and ultrasound fields [26].

In the present work, we incorporated IONPs coated by dendritic phosphonates bearing oligo(ethylene glycol) (OEG) chains into the phospholipid shell of the MBs. OEG chains were selected in order to improve the dispersibility of the IONPs in water [27,28]. Dendritic phosphonates are effective anchoring agents

due to the covalent PO–metal bonds that stabilize aqueous dispersions of IONPs [27,29]. Such dendronized IONPs have been investigated for hyperthermia and magnetic resonance imaging owing to their increased stability in aqueous media and biocompatibility [27,28]. An even stronger anchoring agent consisting of a dendron structure bearing a bisphosphonate polar head provided increased colloidal stability in physiological media [30]. To the best of our knowledge, the implementation of dendronized IONPs in phospholipid-shelled MBs has not yet been reported. This approach is expected to combine some advantages over existing methods, including the ability to graft isolated IONPs instead of clusters at the MB surface, and allowing the microbubbles to go undetected, thus potentially minimizing the recourse to pegylated lipids.

We report here the preparation of perfluorohexane (*F*-hexane)-stabilized MBs with a shell of dipalmitoylphosphatidylcholine (DPPC) that incorporates IONPs grafted with OEG bisphosphonate-headed dendrons. Four dendrons were synthesized and investigated that feature two phosphonic acids and three OEG chains, including a longer one in the para position. The latter was fitted with a fluorinated (C_2F_5 or C_4F_9) or a hydrogenated (C_2H_5 or C_4H_9) end group ($C_nX_{2n+1}OEG_8Den$, X = F and H; n = 2 and 4, Figure 1). First, we present the synthesis and the characterization of the IONPs grafted with the selected dendrons ($IONP@C_nX_{2n+1}OEG_8Den$). Second, we report the adsorption kinetics of $IONP@C_nX_{2n+1}OEG_8Den$ at the interface between air or *F*-hexane-saturated air and water. Third, we discuss the size and stability characteristics of
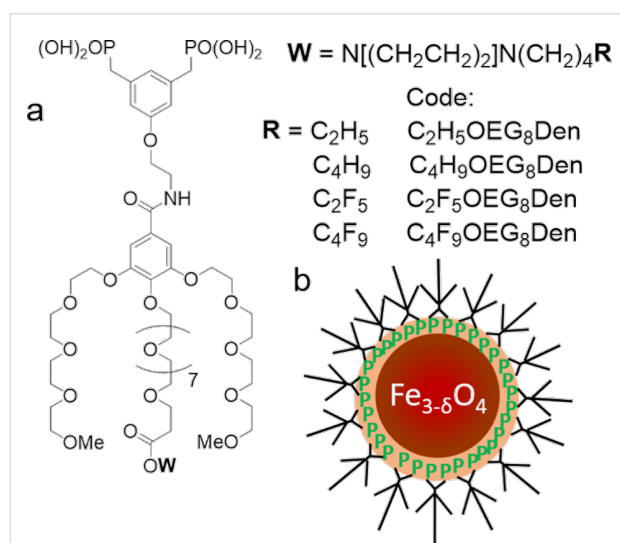

Figure 1: a) Molecular structure of the dendrons investigated ($C_nX_{2n+1}OEG_8Den$, X = F or H; n = 2 and 4); b) Schematic representation of a dendronized IONP showing the anchoring of the bisphosphonate function on the iron oxide.

F-hexane-stabilized DPPC-shelled MBs incorporating IONP@C$_n$X$_{2n+1}$OEG$_8$Den. Fourth, we report an atomic force microscopy (AFM) study that reveals that the location of the dendronized nanoparticles in the phospholipid film strongly depends on the nature of the terminal group.

Results and Discussion
Synthesis and grafting of dendrons on iron oxide nanoparticles

The OEG dendrons were synthesized as described in the Experimental section. Briefly, the piperazine scaffold was selected as an appropriate template to introduce the perfluoroalkylated or alkylated chain on a generation 1 bisphosphonic dendron bearing three OEG chains [31]. In order to facilitate the insertion and increase the visibility of the perfluoroalkylated (or alkylated) end group in the microbubble wall, the central OEG chain carrying the piperazine moiety was lengthened (Figure 1a). A multistep chemical sequence allowed for the production of bisphosphonate dendrons at a reasonable yield (55–80%). IONPs (mean diameter of 9.0 ± 0.9 nm) were synthesized by thermal decomposition of iron (II) stearate in the presence of oleic acid in dioctyl ether, which enables better control of the size, morphology and composition of the IONPs [32]. The four dendrons were grafted on the magnetic IONPs by direct exchange of the ligand (oleic acid) according to [33]. The excess dendron material was removed by ultrafiltration. The grafting of the dendrons on the IONPs was assessed by infrared spectroscopy (IR), which showed a significant reduction of the oleic acid alkyl bands (2926–2850 cm^{-1}) and the appearance of the OEG signal (1096 cm^{-1}) (Supporting Information File 1, Figure S1). The grafting of the dendrons on the IONPs was also confirmed by dynamic light scattering (DLS, Figure 2). The

Figure 2: Hydrodynamic diameter distributions of IONPs grafted with dendrons: C$_2$H$_5$OEG$_8$Den (38 ± 1 nm, black), C$_2$F$_5$OEG$_8$Den (37 ± 1 nm, red), C$_4$H$_9$OEG$_8$Den (95 ± 12 nm, orange), C$_4$F$_9$OEG$_8$Den (197 ± 15 nm, blue) in aqueous dispersions (Fe conc. 0.05 mg mL^{-1}).

hydrodynamic mean diameter of IONP@C$_2$X$_5$OEG$_8$Den (X = F or H) was ≈37 nm, which is significantly larger than the mean diameter of the oleic-acid-covered IONPs (≈10 nm, Supporting Information File 1, Figure S2). This can be ascribed to the fact that a corona of OEG chains is now present around the nanoparticle and captures molecules of water, which contributes to a further increase of the hydrodynamic radius. The mean diameter of the IONP@C$_4$X$_9$OEG$_8$Den materials was larger, namely ≈95 nm and ≈200 nm for X = H and F, respectively, revealing that aggregation occurs in aqueous media due to the hydrophobicity of the end group. Fortunately, this did not preclude performing the adsorption kinetics studies. Altogether, owing to their dendritic structure, the OEG chains were found to confer excellent dispersibility and stability to the IONPs [33].

Adsorption kinetics of dendronized nanoparticles at the gas/liquid interface

The adsorption of the dendronized IONPs at the air/water and *F*-hexane-saturated air/water interface was first investigated using bubble profile analysis tensiometry. As described in our earlier reports [34,35], we first confirmed that *F*-hexane taken alone, when introduced into the gaseous phase of the tensiometer bubble, adsorbs rapidly onto the interface, as indicated by the instant reduction of the interfacial tension σ by ≈4 mN m^{-1} (from 72 to 68 ± 0.5 mN m^{-1}, Supporting Information File 1, Figure S3). The concentration of Fe in the IONP dispersions was varied from 10^{-4} to 10^{-1} mol L^{-1}. The variations of the interfacial tension σ over time are collected in Figure 3 and Table 1. The results show that, not surprisingly, σ decreases with increasing Fe concentration in all cases. The lowest σ values were obtained for the IONPs grafted with the fluorinated dendrons, reflecting their higher hydrophobicity. We also observed that exposure to *F*-hexane has two important consequences on the adsorption of the dendronized IONPs. First, the adsorption process is accelerated, and second, the equilibrium interfacial tensions are significantly lowered.

We have reported similar effects of the fluorocarbon gas on the adsorption of a range of molecules, including phospholipids [36], polymers [17], proteins [37], biomarkers [38] and CeO$_2$ nanoparticles [39]. But the most important finding here is that the fluorocarbon gas affects the adsorption of the IONPs differently, depending on whether the dendron carries a fluorinated end group or not. The interfacial tension at equilibrium (σ$_{eq}$) of the dendronized IONP dispersions and characteristic times of adsorption (τ) of the latter for various Fe concentrations are collected in Table 1. The τ values were determined by fitting the adsorption profiles (Figure 3) to an exponential decay function. The variations of σ$_{eq}$ versus Fe concentration are plotted in Figure 4a. The differences (Δσ$_{eq}$) between σ$_{eq}$ of dendronized IONPs exposed to air and those exposed to *F*-hexane-saturated

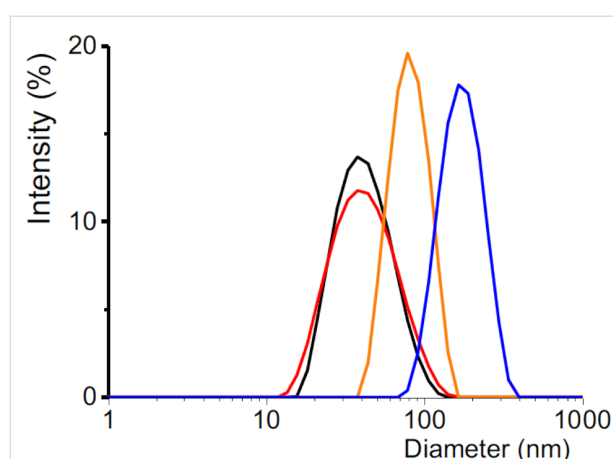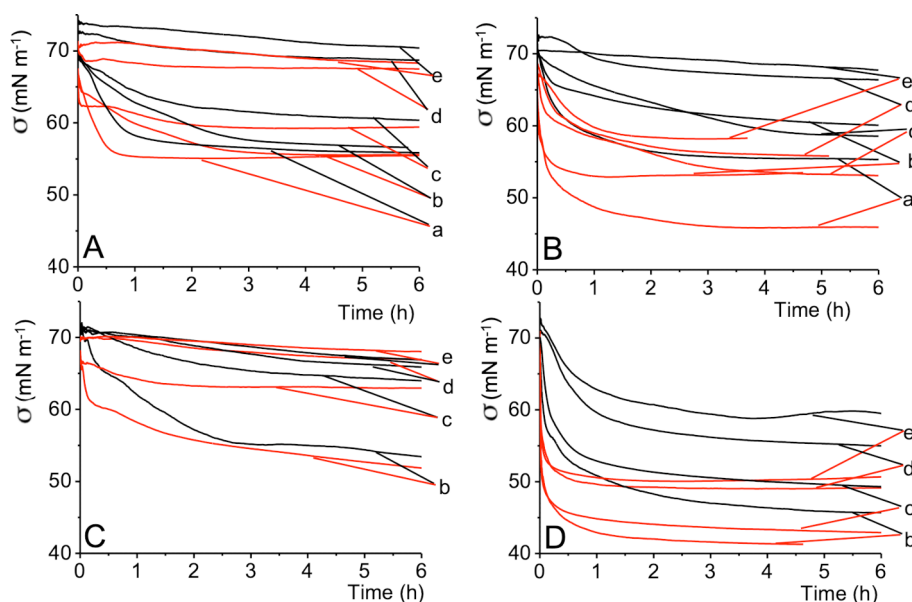**Figure 3:** Adsorption kinetics of IONPs grafted with various dendrons measured at 25 °C: A) $C_2H_5OEG_8Den$, B) $C_2F_5OEG_8Den$, C) $C_4H_9OEG_8Den$ and D) $C_4F_9OEG_8Den$, at various Fe concentrations: a) 0.1; b) 0.05; c) 10^{-2}; d) 10^{-3} and e) 10^{-4} mg mL^{-1}. The dendronized IONPs were exposed to air (black) or to *F*-hexane-saturated air (red).

Table 1: Characteristic adsorption time τ (h) and interfacial tension at equilibrium σ_{eq} (mN m^{-1}) of the IONPs grafted with hydrogenated or fluorinated dendrons.

| | $C_2H_5OEG_8Den$ | | | | $C_2F_5OEG_8Den$ | | | | $C_4H_9OEG_8Den$ | | | | $C_4F_9OEG_8Den$ | | | |
| | Air | | *F*-hexane | | Air | | *F*-hexane | | Air | | *F*-hexane | | Air | | *F*-hexane | |
Fe conc. (mol L^{-1})	τ	σ_{eq}	τ	σ_{eq}	τ	σ_{eq}	τ	σ_{eq}	τ	σ_{eq}	τ	σ_{eq}	τ	σ_{eq}	τ	σ_{eq}
1×10^{-1}	0.58 ± 0.05	56 ± 1	0.28 ± 0.03	55 ± 2	0.56 ± 0.05	55 ± 1	0.17 ± 0.02	46 ± 1	–	–	–	–	–	–	–	–
5×10^{-2}	1.36 ± 0.12	57 ± 2	1.11 ± 0.16	56 ± 2	1.11 ± 0.13	59 ± 2	0.56 ± 0.06	53 ± 1	1.25 ± 0.13	53 ± 2	1.11 ± 0.13	51 ± 1	0.28 ± 0.03	48 ± 2	0.03 ± 0.01	42 ± 2
1×10^{-2}	1.31 ± 0.20	60 ± 1	0.56 ± 0.14	59 ± 1	2.22 ± 0.26	58 ± 1	0.89 ± 0.11	53 ± 1	2.22 ± 0.30	65 ± 1	1.06 ± 0.12	64 ± 1	0.33 ± 0.03	49 ± 2	0.03 ± 0.01	42 ± 1
1×10^{-3}	2.08 ± 0.30	67 ± 3	0.42 ± 0.14	65 ± 1	2.22 ± 0.28	66 ± 1	0.56 ± 0.08	58 ± 2	8.61 ± 0.93	66 ± 1	4.72 ± 0.51	66 ± 2	0.92 ± 0.13	55 ± 1	0.06 ± 0.02	49 ± 1
1×10^{-4}	18.61 ± 1.87	70 ± 2	4.44 ± 0.39	68 ± 2	38.89 ± 3.90	66 ± 2	0.75 ± 0.10	58 ± 2	10.28 ± 1.08	65 ± 2	7.50 ± 0.62	67 ± 2	0.78 ± 0.23	60 ± 2	0.03 ± 0.02	52 ±3

air are plotted as a function of Fe concentration (Figure 4b). The $\Delta\sigma_{eq}$ are larger for the fluorinated dendrons than for their hydrogenated analogs (7.0 ± 1.3 vs 1.1 ± 1.0 mN m^{-1}).

These results indicate that in the presence of the fluorocarbon gas the surface excess of fluorinated dendrons is higher than for the hydrogenated analogs, or that the fluorinated dendrons form a more densely organized film at the interface. Either way,

these results strongly suggest the existence of fluorous interactions between the end groups of the dendrons and the supernatant fluorocarbon gas that facilitate the adsorption of the IONPs at the interface. The mutual interactions between fluorinated chains are known to be weak, yet effective attractive interactions can operate in water and organic solvents. For example, such interactions are responsible for the partition and segregation of *F*-alkyl chains, on which "fluorous" technolo-
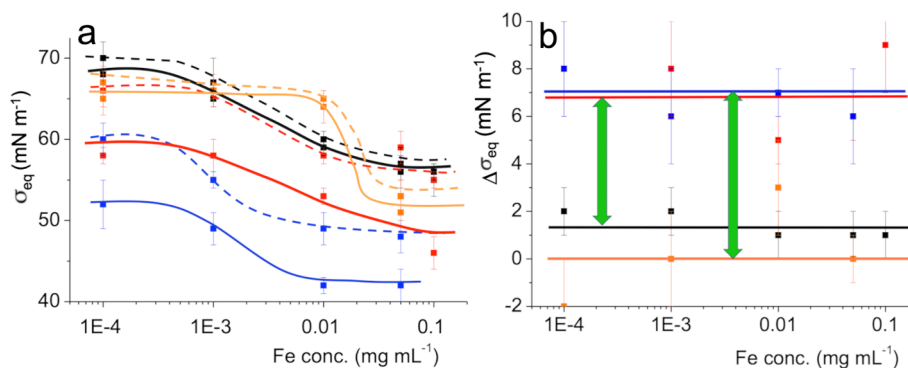
Figure 4: a) Variation of the interfacial tension at equilibrium (σ_{eq}, 25 °C) as a function of the Fe concentration in dispersions of IONPs grafted with dendrons ($C_2H_5OEG_8Den$: black; $C_2F_5OEG_8Den$: red; $C_4H_9OEG_8Den$: orange and $C_4F_9OEG_8Den$: blue) at the air (dashed line) and *F*-hexane-saturated air (solid line)/aqueous phase interface. b) Variation of the difference of the interfacial tension at equilibrium ($\Delta\sigma_{eq}$) measured under air and under *F*-hexane-saturated air versus Fe concentration for various IONPs (same color code). The green arrows highlight the difference in behavior between fluorinated and non-fluorinated dendrons.

gies are based that are used in many synthesis and separation processes [40]. However, studies of such interactions published to date are restricted to liquid/liquid and solid/liquid interfaces [41,42]. In contrast, the potential of fluorocarbon gases to develop attractive fluorous interactions at the gas/water interface has only recently been demonstrated [38]. It is noteworthy that the interactions between fluorinated chains are reinforced by very effective hydrophobic repulsion caused by the proximity of the water phase.

Figure 5 depicts the inverse of the characteristic adsorption time ($1/\tau$) as a function of the Fe concentration of the dendronized IONPs. The $1/\tau$ values increase with increasing Fe concentration (Figure 5a), except for the $C_4F_9OEG_8Den$ case, for which adsorption is only slightly increased (under air) or remains constant (under *F*-hexane). In all cases, the adsorption of the IONPs is accelerated by exposure to the *F*-hexane gas (solid lines). The magnitude of this effect depends on the degree of

fluoration of the dendron. The differences between the $1/\tau$ values measured under air and under *F*-hexane exposure ($\Delta 1/\tau$) are collected for each dendronized IONP in Figure 5b. The largest $\Delta 1/\tau$ values are obtained for the dendron fitted with the C_4F_9 end group, which indicates that the strength of the interactions between *F*-hexane and the terminal group increases with the number of fluorinated carbons of the latter.

Preparation and characterization of microbubbles incorporating dendronized iron oxide nanoparticles

Our microbubbles were prepared by mixing aqueous dispersions of DPPC and dendronized IONPs conditioned in vials that have a dead volume saturated with *F*-hexane, in a VialMix shaker (Experimental section). The size and stability characteristics of the *F*-hexane-stabilized microbubbles prepared with DPPC and dendronized IONPs were investigated by optical microscopy and ultrasound wave attenuation analysis. MBs
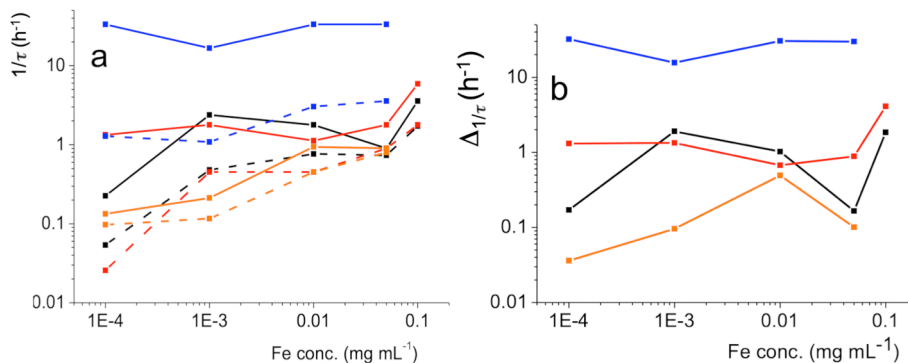
Figure 5: a) Variation of the inverse of the characteristic adsorption time ($1/\tau$) of the IONPs grafted with dendrons ($C_2H_5OEG_8Den$: black; $C_2F_5OEG_8Den$: red; $C_4H_9OEG_8Den$: orange; $C_4F_9OEG_8Den$: blue) at the air (dashed) and *F*-hexane-saturated air (solid line)/aqueous phase interface. b) Variation of the differences of $1/\tau$ measured under air and *F*-hexane-saturated air ($\Delta 1/\tau$) as a function of the Fe concentration (same color code).

stabilized by a shell of DPPC were investigated for comparison. Our acoustic device measures the variation of the attenuation coefficient of an ultrasound wave as a function of its frequency at the initial measuring time in the measuring cell (Experimental section). The change of the radius distributions over time is calculated from the attenuation curves. To this end, the bubble fraction is plotted against time allowing for the determination of the half-life of the bubbles [38]. The size and stability characteristics of the MBs incorporating the dendronized IONPs in their DPPC shell are provided in Table 2 and Figure 6.

The addition of dendronized IONPs led to a significant change in the MB mean radius and the size distribution for all the dendronized IONPs investigated, confirming their presence in the MB shell. A mean radius as small as 1.0 ± 0.2 μm was obtained with the fluorinated dendrons $C_2F_5OEG_8Den$ and $C_4F_9OEG_8Den$, which is comparable to that measured for a

non-dendronized DPPC shell. By comparison, the use of hydrogenated dendrons led to an increase in the MB mean radius. The stability of the MBs prepared with the fluorinated IONPs, given by the half-life of the corresponding bubbles, was also significantly higher than for those prepared with non-fluorinated NPs and, at least for $C_2F_5OEG_8Den$ (6.1 ± 0.9 h), comparable to that of DPPC (6.8 ± 0.5 h; Table 2 and Figure 7). These differences in behavior that depend on the fluorination of the dendron indicate that fluorous interactions exist between *F*-hexane in the gas core and the fluorinated NPs and play a significant role for the MB size and stability characteristics.

AFM analysis of spin-coated films of DPPC, dendronized iron oxide nanoparticles and their mixtures

With the aim to understand if the dendronized IONPs are incorporated within the DPPC shell of the MBs or located at the sur-

Table 2: Physical characteristics of the DPPC microbubbles with dendronized IONPs, the mean bubble radius derived by optical microscopy (R_{mean} (optical, μm)), the bubble radius obtained by the acoustical method (Raman (acoustical, μm)) and the determined half-life of the bubbles ($t_{1/2}$ (h)).

	DPPC	DPPC/ $C_2H_5OEG_8Den$	DPPC/ $C_2F_5OEG_8Den$	DPPC/ $C_4H_9OEG_8Den$	DPPC/ $C_4F_9OEG_8Den$
R_{mean} (optical, μm)	0.9 ± 0.1	1.6 ± 0.2	1.0 ± 0.2	1.4 ± 0.1	1.0 ± 0.2
R_{mean} (acoustical, μm)	0.8 ± 0.2	1.1 ± 0.2	0.9 ± 0.2	1.4 ± 0.2	1.2 ± 0.2
$t_{1/2}$ (h)	6.8 ± 0.5	3.6 ± 0.7	6.1 ± 0.9	1.3 ± 0.2	5.0 ± 0.9
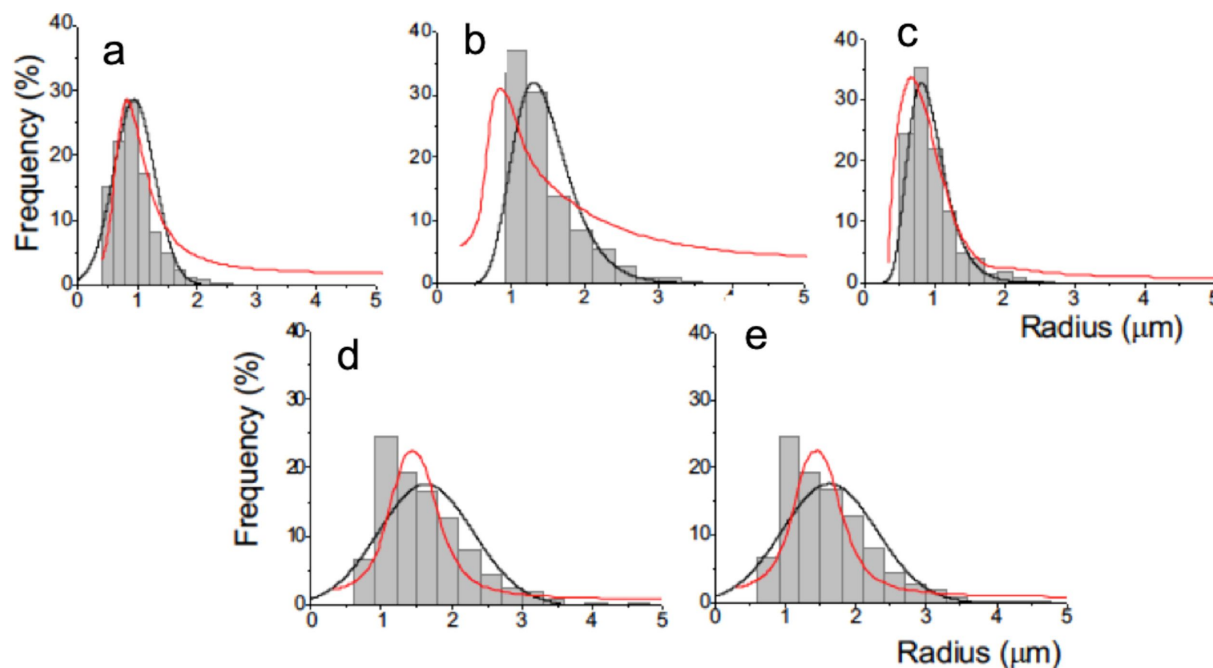
Figure 6: Size distributions of DPPC and DPPC/dendronized IONP-shelled microbubbles stabilized with *F*-hexane (grey line: Gaussian fit of the size histograms derived from optical microscopy; red line: distributions obtained by the acoustical method). a) DPPC alone; b–e) DPPC/ IONP@$C_nX_{2n+1}OEG_8Den$ mixtures with b) $C_2H_5OEG_8Den$; c) $C_2F_5OEG_8Den$; d) $C_4H_9OEG_8Den$, and e) $C_4F_9OEG_8Den$. The concentration of IONPs was 0.1 mg mL^{-1}; temperature 25 °C.

C$_2$F$_5$OEG$_8$Den, which is the dendron that led to the smallest and most stable MBs. The hydrocarbon analog C$_2$H$_5$OEG$_8$Den was also investigated for comparison. The DPPC concentration was set in order to obtain a discontinuous DPPC film (i.e., DPPC domains), allowing for the measurement of the film height.

The mean height of both IONP@C$_2$F$_5$OEG$_8$Den and IONP@C$_2$H$_5$OEG$_8$Den is 10.0 ± 1.7 nm, as determined by a statistical analysis of the particles (Figure 9). Usually, it is observed that the nanoparticles are convoluted by the AFM probe, which decreases the lateral resolution of the technique. Both IONP samples are well-dispersed with no indication of aggregation. The films of spin-coated DPPC form large monolayer and small bilayer domains (Figure 10a). The profile measured on the magnified image (Figure 10b and Figure 10c) shows that the heights of the monolayer and bilayer are 1.5 ± 0.3 nm and 5.0 ± 1.0 nm, respectively. These measurements are in agreement with earlier reports [43].

Figure 11A shows an AFM topography image of a mixed film composed of DPPC and IONP@C$_2$F$_5$OEG$_8$Den. The IONPs are embedded within the DPPC monolayer domains in which they

face of the shell (Figure 8), mixed films composed of phospholipid and nanoparticles were prepared by spin-coating on silicon wafers. The morphology of the films was investigated by AFM in the peak–force tapping mode. We therefore selected
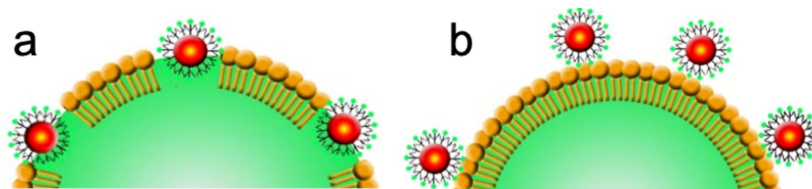
Figure 8: Schematic representation of dendronized IONPs a) incorporated within the MB DPPC shell and b) located at the surface of this shell.
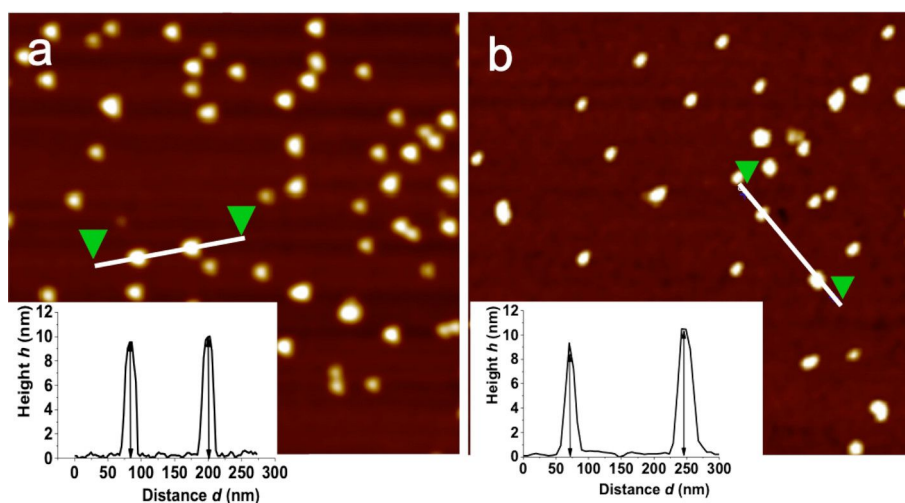
Figure 9: AFM topography images (1 × 1 μm) and height profiles of a) IONP@C$_2$F$_5$OEG$_8$Den and b) IONP@C$_2$H$_5$OEG$_8$Den. Dispersions of IONPs in ethanol (0.002 mg mL^{-1}) were spin-coated on silicon wafers.
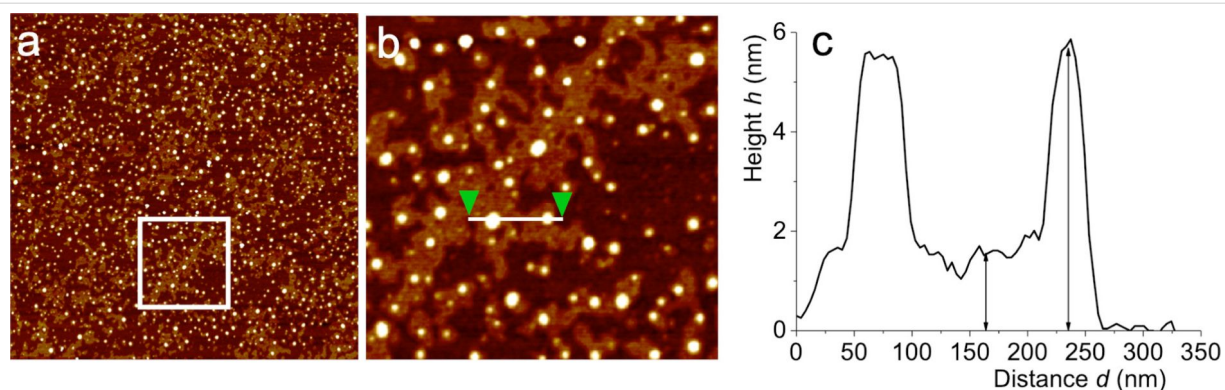
Figure 10: a) AFM topography image (4 × 4 µm) of a DPPC film spin-coated from an ethanol solution (0.5 mM); b) magnification (1 × 1 µm) of the square shown in a); c) height profile taken between the two green triangles in b).
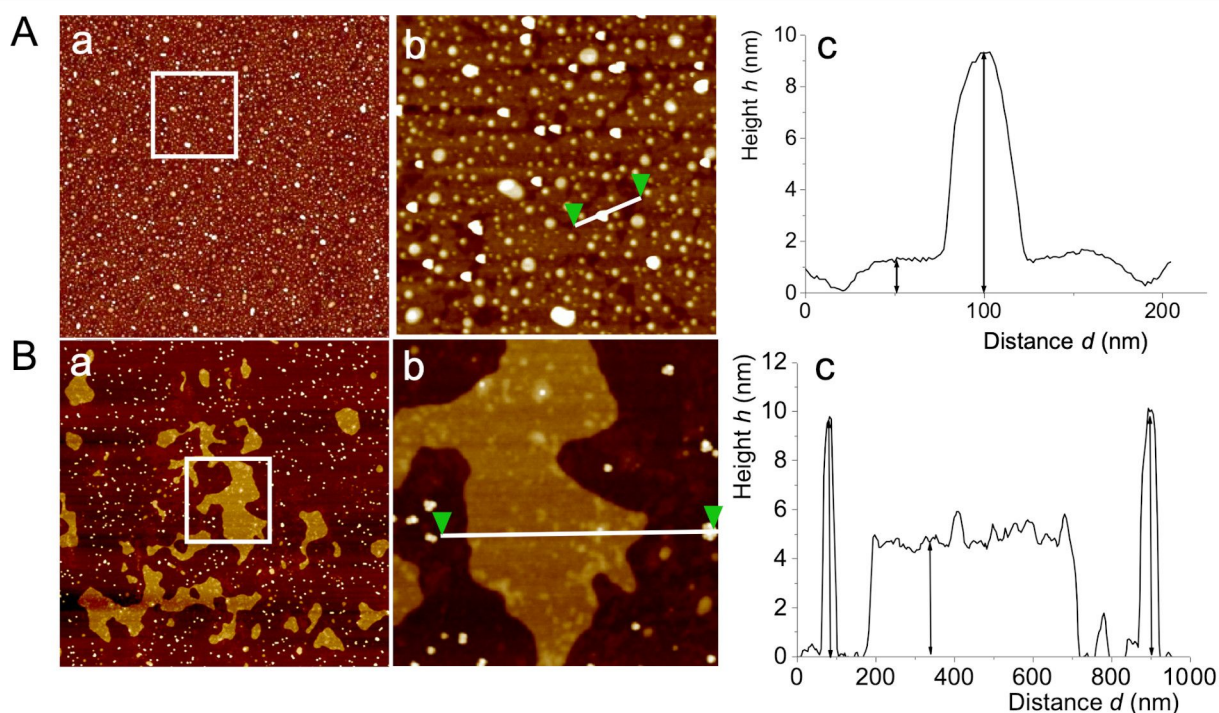
Figure 11: a) AFM topography image (4 × 4 µm) of the mixed spin-coated films composed of DPPC and IONP@C$_2$F$_5$OEG$_8$Den (Panel A) and IONP@C$_2$H$_5$OEG$_8$Den (Panel B); b) magnification images (1 × 1 µm) of the white square shown in a); c) height profiles taken between the two green triangles in the corresponding image in b). Co-dispersions of DPPC (0.5 mM) and IONPs (0.002 mg mL^{-1}) in ethanol were spin-coated on silicon wafers.

are well-dispersed, showing no tendency to aggregate. The profile (Figure 11Ac) measured on the magnified image (Figure 11Ab) clearly shows that the fluorinated IONPs are incorporated into the 1.5 nm thick DPPC monolayer. A different morphology is observed for the mixed film of DPPC and IONPs grafted with the hydrogenated dendron C$_2$H$_5$OEG$_8$Den. In this case, the domains formed by DPPC bilayers of ≈5 nm in height are omnipresent, while only a few domains of monolayers are observed (Figure 11Ba). It is seen that IONP@C$_2$H$_5$OEG$_8$Den are preferentially located in the regions of the wafer that are

devoid of phospholipid domains. The height profile measured on the magnification image (Figure 11Bb) shows two IONPs of ≈10 nm in height, clearly separated by a bilayer domain of ≈5 nm in height.

This difference can be explained by the fact that short fluorinated groups such as C$_2$F$_5$ can significantly increase the lipophilicity of molecules. This is the main reason why fluorine groups, such as CF$_3$ or C$_2$F$_5$, are incorporated into many drugs, as they significantly improve their biodistribution [44]. By

contrast, longer fluorinated chains, such as C_6F_{13} or C_8F_{17}, are well-known to confer a lipophobic character when grafted onto molecules and to induce phase separation in fluorocarbon/hydrocarbon mixtures [45,46]. These results tell us that the dendronized IONPs fitted with a C_2F_5 group have a higher affinity for the phospholipid film than those grafted with C_2H_5.

Conclusion

We report that small and highly stable magnetic MBs incorporating IONPs in their phospholipid shells can be obtained by using IONPs dendronized with OEG chains. The latter significantly increase the dispersibility of the nanoparticles in aqueous media.

We demonstrate that exposure to a supernatant fluorocarbon gas has a remarkable and considerable impact on the adsorption behavior of dendronized iron oxide nanoparticles and that the magnitude of this effect depends on the nature of the end group of the dendron grafted on the nanoparticles, which is either fluorinated or hydrogenated. Introducing a short fluorinated group at the end of the OEG chain is found to substantially increase the rate of adsorption of the nanoparticles at the interface with air and even more so when exposed to *F*-hexane-saturated air. A more compact film is observed when the film of nanoparticles is exposed to the fluorocarbon gas. This unexpected effect indicates that for the mixed film, at the interface, interactions develop between the fluorinated end group of the dendron and the fluorocarbon gas.

As a consequence of this new phenomenon, small and stable fluorocarbon-stabilized microbubbles with a half-life of ≈6 h can be obtained by admixing DPPC and iron oxide nanoparticles that are grafted with a C_2F_5-terminated dendron. The combined use of fluorinated dendrons and a supernatant fluorocarbon gas is a straightforward, effective method for preparing magnetic microbubbles that could facilitate the development of future applications in medicine.

Finally, the AFM analysis of the DPPC/iron oxide nanoparticles films indicates that the fluorinated dendronized iron oxide nanoparticles show a higher propensity to incorporate into phospholipid films than into hydrogenated ones, possibly due to the increased lipophilic character.

Experimental
Materials

1,2-Dipalmitoylphosphatidylcholine (DPPC) was purchased as a dry powder (99% purity) from Avanti Polar Lipids (Alabaster, AL) and used as received. Perfluorohexane (98% pure) was purchased from Fluorochem. Pluronic F-68 (a poly(ethylene oxide)−poly(propylene oxide) triblock copolymer, $M_W \approx 8300$,

purity >99%) and HEPES (*N*-(2-hydroxyethyl)piperazine-*N'*-2-ethanesulfonic acid) were purchased from Sigma-Aldrich (Lyon, France). A HEPES buffer solution (20 mmol L^{-1}) in a 150 mmol L^{-1} NaCl solution was prepared, and its pH was adjusted to 7.4 with 1 N NaOH. Water was purified using a Millipore system (surface tension 71.4 mN m^{-1} at 20 °C, resistivity 18.2 MΩ cm).

Synthesis of dendrons

The approach to the synthesis of the dendrons $C_2F_5OEG_8Den$ and $C_4F_9OEG_8Den$ is described in [47]. From the intermediate D2-2P, the piperazine unit was installed in two steps (Scheme 1): 1) deprotection of the *tert*-butyl group and 2) amide coupling by using HATU/DIPEA. Next, the removal of the carboxybenzyl group by hydrogenolysis allows for the introduction of the perfluoroalkyl chain via *N*-alkylation. Finally, treatment with trimethylsilyl bromide produced the desired fluorinated bisphosphonate dendron.

Characterization of $C_2F_5OEG_8Den$: ^{1}H NMR (500 MHz, CD$_3$OD) δ 7.25 (s, 2H), 6.84 (s, 1H), 6.79 (s, 2H), 4.22 (t, *J* = 4.5 Hz, 6H), 4.15 (t, *J* = 5.5 Hz, 2H), 3.87 (t, *J* = 4.7 Hz, 4H), 3.80 (t, *J* = 4.7 Hz, 2H), 3.76–3.50 (m, 52H), 3.33 (s, 6H), 3.12–3.09 (m, 2H), 3.03 (d, $^2J_{P-H}$ = 21.1 Hz, 4H), 2.65–2.62 (m, 2H), 2.27–2.16 (m, 2H), 1.88–1.82 (m, 2H), 1.68–1.62 (m, 2H) ppm; ^{13}C NMR (125 MHz, CD$_3$OD) δ 172.3, 169.5, 160.1, 153.8, 142.4, 136.6, 130.5, 115.3, 107.8, 73.6, 73.0, 71.9, 71.7–71.3 (several peaks), 70.8, 70.1, 68.5, 67.4, 62.2, 59.1, 57.3, 41.0, 39.6, 34.2, 24.2 ppm; ^{19}F NMR (282 MHz, CD$_3$OD) δ −86.9, −119.4 ppm; ^{31}P NMR (202 MHz, CD$_3$OD) δ 22.7 ppm.

Characterization of $C_4F_9OEG_8Den$: ^{1}H NMR (500 MHz, CD$_3$OD) δ 7.25 (s, 2H), 6.83 (s, 1H), 6.78 (s, 2H), 4.22 (t, *J* = 4.5 Hz, 6H), 4.14 (t, *J* = 5.6 Hz, 2H), 3.87 (t, *J* = 4.7 Hz, 4H), 3.80 (t, *J* = 4.6 Hz, 2H), 3.76–3.50 (m, 74H), 3.33 (s, 6H), 3.10–3.06 (m, 2H), 3.02 (d, $^2J_{P-H}$ = 21.0 Hz, 4H), 2.64–2.59 (m, 2H), 2.32–2.21 (m, 2H), 1.89–1.83 (m, 2H), 1.70–1.63 (m, 2H) ppm; ^{13}C NMR (125 MHz, CD$_3$OD) δ 172.3, 169.5, 160.1, 153.8, 142.4, 136.6, 130.5, 125.3, 115.3, 108.9, 79.3, 73.6, 73.0, 72.1, 71.9–71.3 (several peaks), 70.8, 70.0, 68.5, 67.4, 62.2, 59.1, 57.3, 52.9, 52.5, 43.7, 41.0, 39.6, 34.2, 30.8, 24.2, 18.7 ppm; ^{19}F NMR (470 MHz, CD$_3$OD) δ −82.6, −115.6, −125.3, −127.1 ppm; ^{31}P NMR (202 MHz, CD$_3$OD) δ 22.4 ppm.

Synthesis of dendronized iron oxide nanoparticles

The synthesis is adapted from an earlier report [33]. In a 100 mL two-necked flask, iron(II) stearate (2.2 mmol, 1.38 g), oleic acid (4.4 mmol, 1.24 g) and dioctyl ether (20 mL) were mixed together. The resulting solution was heated to 120 °C for

Scheme 1: Final steps of the synthesis of the dendrons $C_2F_5OEG_8Den$ and $C_4F_9OEG_8Den$. a) TFA/CH_2Cl_2, then piperazine-NCBz, HATU, DIPEA/ DMF; 99% (2 steps); b) H_2, Pd/C/ MeOH, then perfluoroalkyl iodide, K_2CO_3/CH_3CN; 80% for C_2F_5 and 55% for C_4F_9; c) $TMSBr/CH_2Cl_2$; 79% for C_2F_5 and 80% for C_4F_9.
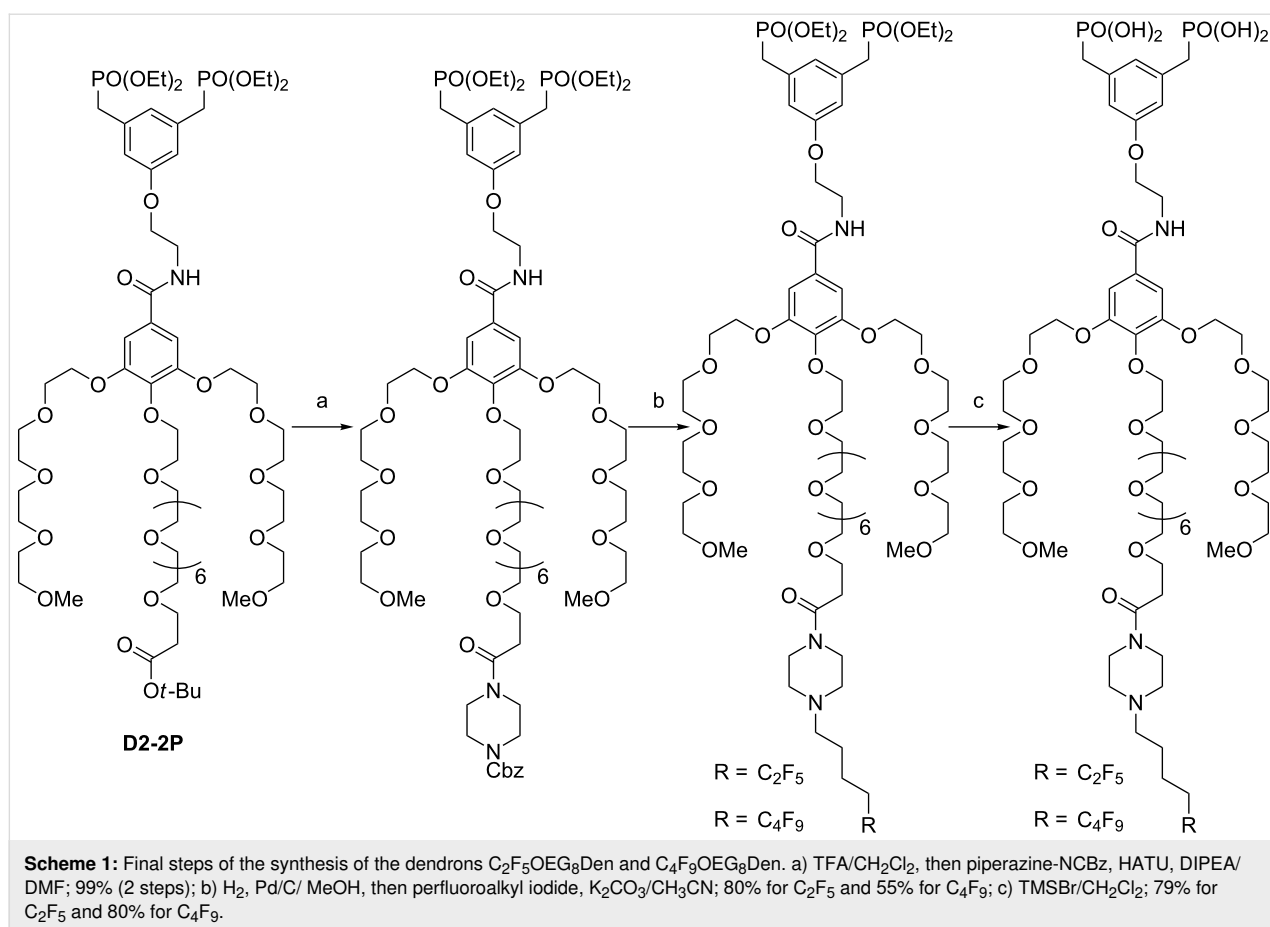
1 h under magnetic stirring without a reflux condenser. The magnetic stirrer was removed and the condenser was connected to the flask. The solution was heated up to 298 °C for 2 h at a heating rate of 5 °C min^{-1}. After cooling, a black suspension was collected and precipitated by addition of acetone. Finally, the nanoparticles were washed three times with a mixture of $CHCl_3$/acetone (1:4). In a 30 mL vial, a nanoparticle suspension in tetrahydrofuran (THF) (5 mg of iron) was introduced together with the appropriate dendron (7 mg). The vial was filled with 25 mL of THF and the mixture was magnetically stirred for 24 h. The resulting nanoparticles were centrifuged after addition of cyclohexane, dispersed in water and separated by ultrafiltration. The grafting of the fluorinated end-group was evidenced using HR-MAS.

Bubble profile analysis tensiometry

Axisymmetric bubble shape analysis was applied to a rising bubble of gas (air or *F*-hexane-saturated air) formed in a dispersion of dendronized IONPs in an aqueous phase (HEPES buffer). As described in [36], during the process of adsorption of the dendronized IONPs at the gas/liquid interface, the variation of the interfacial tension was acquired using a Tracker® tensiometer (Teclis, Civrieux d'Azergues, France). A 5 µL

bubble was formed at the end of a steel capillary that had a tip diameter of 1 mm. The rising bubble was saturated with *F*-hexane by purging a 1 mL syringe trice with *F*-hexane-saturated air sampled above liquid *F*-hexane. This syringe was then mounted immediately on the injection cell of the tensiometer, such that the rising bubble was formed. The pressure and concentration of the *F*-hexane-saturated vapor at 25 °C were set to 2.9×10^4 Pa and 11.66 mol m^{-3} [14]. IONP dispersions with Fe concentrations ranging from 0.1 to 10^{-4} mg mL^{-1} were obtained by diluting the 1 mg mL^{-1}-concentrated stem aqueous dispersions with HEPES buffer. The IONP@$C_4X_9OEG_8Den$ (X = F and H) aqueous dispersions were sonicated for 30 min (setting 5) before tensiometric measurement. The sonicator (Vibracell, Bioblock Scientific, Illkirch, France) was equipped with a 3 mm titanium probe and operated at 20 kHz with an output power of ≈600 W (duty cycle 40%).

Preparation of the microbubbles

DPPC (50 mmol L^{-1}) and Pluronic F-68 (DPPC/F-68 molar ratio 10:1) were dispersed in a non-degassed HEPES buffer solution (0.9 mL) in a sealed glass vial (inner diameter of 13 mm, length of 35 mm) by magnetic stirring for 3–6 h at 50 °C. Pluronic F-68 was added to facilitate phospholipid

dispersion and foam formation. 100 µL of the dendronized IONPs dispersion (Fe concentration of 1 mg mL^{-1}) were injected into the dispersion. The dispersions were sonicated under air in a sonication bath at 50 °C for 30 min. In the case of IONP@C$_4$X$_9$OEG$_8$Den (X = H or F), presonication (2 min, setting 5) under air was applied. N$_2$ was allowed to bubble through three vials containing F-hexane before being flushed above the aqueous phase into the sealed glass vial during 3 min in order to saturate the gas phase with F-hexane. The resulting dispersions were treated using a VialMix shaker (Bristol-Myers Squibb, New York, NY) for 45 s under F-hexane-saturated N$_2$ at room temperature. The resulting foam was immediately diluted to 10 mL of HEPES buffer. Size fractionation of the microbubbles was achieved by flotation for 60 min.

Optical microscopy

A few droplets (three to four) of the bubble dispersion were positioned in a concave glass slide and covered with a glass slide. The samples were observed using a Nikon Eclipse 90i microscope (transmission mode). Rapid image acquisition was obtained with a Lumenera Infinity 2 charge-coupled device (CCD) camera (Lumenera, Ottawa, Canada). The mean radii of the bubbles were determined using ImageJ on 5–10 slides.

Acoustic size determination

The method exploits the sound attenuation undergone by multi-frequency ultrasound waves that propagate through the aqueous bubble dispersion. Standard simple-harmonic resonator curves are fitted to measure the attenuation in order to infer the radii of the bubbles. A low-power emitter is used to avoid alteration of the bubble characteristics and stability. For further experimental details see [48]. Each measurement was repeated three times for different bubble preparations. The volume of the microbubble dispersion injected in the acoustic cell was 2 mL.

AFM topography analysis of mixed films of DPPC and dendronized IONPs

Thin films of DPPC, dendronized IONPs and DPPC/dendronized IONP mixtures were prepared by spin-coating on silicon wafers [49]. To this end, a dispersion of dendronized IONPs in water (1 mg L^{-1}) was freeze-dried and then dissolved in ethanol for preparing a dispersion with a concentration of 0.1 mg mL^{-1}. 40 µL of this dispersion was added to 2 mL of a 1 mM-concentrated DPPC ethanol solution in order to obtain a mixed DPPC/dendronized IONP spin-coated film that has the same DPPC/Fe molar ratio as that used for the preparation of the microbubbles (28:1). A 0.5 mM-concentrated mixed dispersion was obtained by diluting this 1 mM dispersion. Silicon wafers were cleaned for 30 min in a sonication bath containing ethanol/milli-Q water (1:1), followed by 2 min in a plasma

cleaner. A droplet (15 µL) of DPPC, dendronized IONPs or mixed DPPC/dendronized IONP dispersions was deposited on a silicon wafer and immediately spun for 1 min at 3000 rpm (Spin150 from SPS, Semiconductor Production Systems Europe). The spin-coated samples were placed under vacuum in a desiccator for 15–20 h to fully evaporate the solvents. The silicon wafers were stored at 4 °C until the AFM measurements. AFM images were obtained by scanning the spin-coated films using a Dimension AFM Icon (Bruker) instrument operated in peak–force tapping mode. Peak–force AFM is based on the peak–force tapping technology, in which the probe is oscillated in a similar way as in the tapping mode, but at far lower resonance frequency. Each time the tip and the sample are brought together, a force curve is captured. Ultrasharp silicon tips on a nitride lever were used (Bruker, ScanAsyst with a spring constant of 0.4 N m^{-1} and tip radius of ≈5 nm). During AFM imaging, the force was reduced in order to avoid dragging of molecules by the tip. The analysis of the images was conducted in the integrated software. At least three different samples were analyzed and several positions were scanned on the silicon wafer for each sample. The error on measurements along the z-axis was estimated at ±0.5 nm.

ORCID® iDs
Marie Pierre Krafft - https://orcid.org/0000-0002-3379-2783

References
1. Chong, W. K.; Papadopoulou, V.; Dayton, P. A. *Abdom. Radiol.* **2018,** *43,* 762–772. doi:10.1007/s00261-018-1516-1

2. Jain, A.; Tiwari, A.; Verma, A.; Jain, S. K. *Drug Delivery Transl. Res.* **2018,** *8,* 150–164. doi:10.1007/s13346-017-0448-6

3. Wang, S.; Hossack, J. A.; Klibanov, A. L. *J. Drug Targeting* **2018,** *26,* 420–434. doi:10.1080/1061186x.2017.1419362

4. Lindner, J. R. *Nat. Rev. Drug Discovery* **2004,** *3,* 527–533. doi:10.1038/nrd1417

5. Wheatley, M. A.; Forsberg, F.; Dube, N.; Patel, M.; Oeffinger, B. E. *Ultrasound Med. Biol.* **2006,** *32,* 83–93. doi:10.1016/j.ultrasmedbio.2005.08.009

6. Klibanov, A. L. *Med. Biol. Eng. Comput.* **2009,** *47,* 875–882. doi:10.1007/s11517-009-0498-0

7. Stride, E.; Edirisinghe, M. *Med. Biol. Eng. Comput.* **2009,** *47,* 809–811. doi:10.1007/s11517-009-0510-8

8. Rychak, J. J.; Klibanov, A. L. *Adv. Drug Delivery Rev.* **2014,** *72,* 82–93. doi:10.1016/j.addr.2014.01.009

9. Sirsi, S. R.; Borden, M. A. *Theranostics* **2012,** *2,* 1208–1222. doi:10.7150/thno.4306

10. Ferrara, K. W.; Borden, M. A.; Zhang, H. *Acc. Chem. Res.* **2009,** *42,* 881–892. doi:10.1021/ar8002442

11. Aw, M. S.; Paniwnyk, L.; Losic, D. *Expert Opin. Drug Delivery* **2016,** *13,* 1383–1396. doi:10.1080/17425247.2016.1192123

12. Song, K.-H.; Harvey, B. K.; Borden, M. A. *Theranostics* **2018,** *8,* 4393–4408. doi:10.7150/thno.26869

13. Schutt, E. G.; Klein, D. H.; Mattrey, R. M.; Riess, J. G. *Angew. Chem., Int. Ed.* **2003,** *42,* 3218–3235. doi:10.1002/anie.200200550

14. Kabalnov, A.; Bradley, J.; Flaim, S.; Klein, D.; Pelura, T.; Peters, B.; Otto, S.; Reynolds, J.; Schutt, E.; Weers, J. *Ultrasound Med. Biol.* **1998,** *24,* 751–760. doi:10.1016/s0301-5629(98)00033-7

15. Kabalnov, A.; Klein, D.; Pelura, T.; Schutt, E.; Weers, J. *Ultrasound Med. Biol.* **1998,** *24,* 739–749. doi:10.1016/s0301-5629(98)00034-9

16. Szíjjártó, C.; Rossi, S.; Waton, G.; Krafft, M. P. *Langmuir* **2012,** *28,* 1182–1189. doi:10.1021/la2043944

17. Ando, Y.; Tabata, H.; Sanchez, M.; Cagna, A.; Koyama, D.; Krafft, M. P. *Langmuir* **2016,** *32,* 12461–12467. doi:10.1021/acs.langmuir.6b01883

18. Yang, F.; Li, Y.; Chen, Z.; Zhang, Y.; Wu, J.; Gu, N. *Biomaterials* **2009,** *30,* 3882–3890. doi:10.1016/j.biomaterials.2009.03.051

19. Park, J. I.; Jagadeesan, D.; Williams, R.; Oakden, W.; Chung, S.; Stanisz, G. J.; Kumacheva, E. *ACS Nano* **2010,** *4,* 6579–6586. doi:10.1021/nn102248g

20. Liu, Z.; Lammers, T.; Ehling, J.; Fokong, S.; Bornemann, J.; Kiessling, F.; Gätjens, J. *Biomaterials* **2011,** *32,* 6155–6163. doi:10.1016/j.biomaterials.2011.05.019

21. Mulvana, H.; Eckersley, R. J.; Tang, M.-X.; Pankhurst, Q.; Stride, E. *Ultrasound Med. Biol.* **2012,** *38,* 864–875. doi:10.1016/j.ultrasmedbio.2012.01.027

22. Stride, E.; Porter, C.; Prieto, A. G.; Pankhurst, Q. *Ultrasound Med. Biol.* **2009,** *35,* 861–868. doi:10.1016/j.ultrasmedbio.2008.11.010

23. Lammers, T.; Koczera, P.; Fokong, S.; Gremse, F.; Ehling, J.; Vogt, M.; Pich, A.; Storm, G.; van Zandvoort, M.; Kiessling, F. *Adv. Funct. Mater.* **2015,** *25,* 36–43. doi:10.1002/adfm.201401199

24. Unger, E. C.; McCreery, T. P.; Sweitzer, R. H.; Caldwell, V. E.; Wu, Y. *Invest. Radiol.* **1998,** *33,* 886–892. doi:10.1097/00004424-199812000-00007

25. Nguyen, P. N.; Nikolova, G.; Polavarapu, P.; Waton, G.; Phuoc, L. T.; Pourroy, G.; Krafft, M. P. *RSC Adv.* **2013,** *3,* 7743–7746. doi:10.1039/c3ra40908b

26. Owen, J.; Crake, C.; Lee, J. Y.; Carugo, D.; Beguin, E.; Khrapitchev, A. A.; Browning, R. J.; Sibson, N.; Stride, E. *Drug Delivery Transl. Res.* **2018,** *8,* 342–356. doi:10.1007/s13346-017-0366-7

27. Basly, B.; Felder-Flesch, D.; Perriat, P.; Billotey, C.; Taleb, J.; Pourroy, G.; Begin-Colin, S. *Chem. Commun.* **2010,** *46,* 985–987. doi:10.1039/b920348f

28. Felder-Flesch, D. *Dendrimers in Nanomedicine,* 1st ed.; Jenny Stanford Publishing: New York, NY, U.S.A., 2016. doi:10.1201/9781315364513

29. Daou, T. J.; Pourroy, G.; Greneche, J. M.; Bertin, A.; Felder-Flesch, D.; Begin-Colin, S. *Dalton Trans.* **2009,** *23,* 4442–4449. doi:10.1039/b823187g

30. Casset, A.; Jouhannaud, J.; Garofalo, A.; Spiegelhalter, C.; Nguyen, D.-V.; Felder-Flesch, D.; Pourroy, G.; Pons, F. *Int. J. Pharm.* **2019,** *556,* 287–300. doi:10.1016/j.ijpharm.2018.12.024

31. Garofalo, A.; Parat, A.; Bordeianu, C.; Ghobril, C.; Kueny-Stotz, M.; Walter, A.; Jouhannaud, J.; Begin-Colin, S.; Felder-Flesch, D. *New J. Chem.* **2014,** *38,* 5226–5239. doi:10.1039/c4nj00654b

32. Sun, S.; Zeng, H.; Robinson, D. B.; Raoux, S.; Rice, P. M.; Wang, S. X.; Li, G. *J. Am. Chem. Soc.* **2004,** *126,* 273–279. doi:10.1021/ja0380852

33. Walter, A.; Billotey, C.; Garofalo, A.; Ulhaq-Bouillet, C.; Lefèvre, C.; Taleb, J.; Laurent, S.; Vander Elst, L.; Muller, R. N.; Lartigue, L.; Gazeau, F.; Felder-Flesch, D.; Begin-Colin, S. *Chem. Mater.* **2014,** *26,* 5252–5264. doi:10.1021/cm5019025

34. Nguyen, P. N.; Veschgini, M.; Tanaka, M.; Waton, G.; Vandamme, T.; Krafft, M. P. *Chem. Commun.* **2014,** *50,* 11576–11579. doi:10.1039/c3cc47840h

35. Shi, D.; Liu, X.; Counil, C.; Krafft, M. P. *Langmuir* **2019,** *35,* 10025–10033. doi:10.1021/acs.langmuir.8b03546

36. Nguyen, P. N.; Trinh Dang, T. T.; Waton, G.; Vandamme, T.; Krafft, M. P. *ChemPhysChem* **2011,** *12,* 2646–2652. doi:10.1002/cphc.201100425

37. Gazzera, L.; Milani, R.; Pirrie, L.; Schmutz, M.; Blanck, C.; Resnati, G.; Metrangolo, P.; Krafft, M. P. *Angew. Chem., Int. Ed.* **2016,** *55,* 10263–10267. doi:10.1002/anie.201603706

38. Yang, G.; O'Duill, M.; Gouverneur, V.; Krafft, M. P. *Angew. Chem., Int. Ed.* **2015,** *54,* 8402–8406. doi:10.1002/anie.201502677

39. Justeau, C.; Vela-Gonzalez, A. V.; Jourdan, A.; Riess, J. G.; Krafft, M. P. *ACS Sustainable Chem. Eng.* **2018,** *6,* 11450–11456. doi:10.1021/acssuschemeng.8b01471

40. Gladysz, J. A.; Curran, D. P.; Horváth, I. T., Eds. *Handbook of Fluorous Chemistry;* Wiley-VCH: Weinheim, Germany, 2004. doi:10.1002/3527603905

41. Luo, Z.; Zhang, Q.; Oderaotoshi, Y.; Curran, D. P. *Science* **2001,** *291,* 1766–1769. doi:10.1126/science.1057567

42. Dinh, L. V.; Gladysz, J. A. *Angew. Chem., Int. Ed.* **2005,** *44,* 4095–4097. doi:10.1002/anie.200500237

43. Jurak, M.; Chibowski, E. *Langmuir* **2007,** *23,* 10156–10163. doi:10.1021/la701220t

44. Wang, J.; Sánchez-Roselló, M.; Aceña, J. L.; del Pozo, C.; Sorochinsky, A. E.; Fustero, S.; Soloshonok, V. A.; Liu, H. *Chem. Rev.* **2014,** *114,* 2432–2506. doi:10.1021/cr4002879

45. Krafft, M. P.; Riess, J. G. *Chem. Rev.* **2009,** *109,* 1714–1792. doi:10.1021/cr800260k

46. Krafft, M. P.; Riess, J. G. *Chemosphere* **2015,** *129,* 4–19. doi:10.1016/j.chemosphere.2014.08.039

47. Nguyen, D.-V.; Hugoni, L.; Filippi, M.; Perton, F.; Shi, D.; Voirin, E.; Power, L.; Cotin, G.; Krafft, M. P.; Scherberich, A.; Lavalle, P.; Begin-Colin, S.; Felder-Flesch, D. *ChemPlusChem* **2019**. Submitted.

48. Rossi, S.; Waton, G.; Krafft, M. P. *Langmuir* **2010,** *26,* 1649–1655. doi:10.1021/la9025987

49. Simonsen, A. C.; Bagatolli, L. A. *Langmuir* **2004,** *20,* 9720–9728. doi:10.1021/la048683+

BEILSTEIN JOURNAL OF NANOTECHNOLOGY

Use of data processing for rapid detection of the prostate-specific antigen biomarker using immunomagnetic sandwich-type sensors

Camila A. Proença[1], Tayane A. Freitas[1], Thaísa A. Baldo[1], Elsa M. Materón[1,2], Flávio M. Shimizu[2,3], Gabriella R. Ferreira[4], Frederico L. F. Soares[1,5], Ronaldo C. Faria[*1] and Osvaldo N. Oliveira Jr.[*2]

Full Research Paper

Address:
[1]Chemistry Department, Federal University of São Carlos, CP 676, São Carlos 13565-905, São Paulo, Brazil, [2]São Carlos Institute of Physics, University of São Paulo, CP 369, São Carlos 13560-970, São Paulo, Brazil, [3]Brazilian Nanotechnology National Laboratory (LNNano), Brazilian Center for Research in Energy and Materials (CNPEM), Campinas 13083-970, São Paulo, Brazil, [4]Carlos Institute of Chemistry, University of São Paulo, São Carlos 13560-970, São Paulo, Brazil and [5]Chemistry Department, Federal University of Paraná, Curitiba, 81531-980, Paraná, Brazil

Email:
Ronaldo C. Faria[*] - rcfaria@ufscar.br; Osvaldo N. Oliveira Jr.[*] - chu@ifsc.usp.br

* Corresponding author

Abstract

Diagnosis of cancer using electroanalytical methods can be achieved at low cost and in rapid assays, but this may require the combination with data treatment for determining biomarkers in real samples. In this paper, we report an immunomagnetic nanoparticle-based microfluidic sensor (INμ-SPCE) for the amperometric detection of the prostate-specific antigen (PSA) biomarker, the data of which were treated with information visualization methods. The INμ-SPCE consists of eight working electrodes, reference and counter electrodes. On the working electrodes, magnetic nanoparticles with secondary antibodies with the enzyme horseradish peroxidase were immobilized for the indirect detection of PSA in a sandwich-type procedure. Under optimal conditions, the immunosensor could operate within a wide range from 12.5 to 1111 fg·L^{-1}, with a low detection limit of 0.062 fg·L^{-1}. Multidimensional projections combined with feature selection allowed for the distinction of cell lysates with different levels of PSA, in agreement with results from the traditional enzyme-linked immunosorbent assay. The approaches for immunoassays and data processing are generic, and therefore the strategies described here may provide a simple platform for clinical diagnosis of cancers and other types of diseases.

Introduction

The prostate-specific antigen (PSA) used in clinical diagnosis is present in normal prostatic secretions, but its concentration is often elevated in prostate cancer patients. In spite of its lack of specificity, PSA screening has contributed to a significant decline (45–70%) in prostate cancer mortality since the early 1990s [1]. To identify cancer biomarkers and to develop methodologies to quantify them at low cost is critical for early cancer diagnostics, while it also helps to understand cancer diseases [1]. Protein biomarkers are commonly measured using conventional immunoassays such as enzyme-linked immunosorbent assay (ELISA) [1], radioimmunoassay (RIA) [2], fluorescence methods [3], and chemiluminescence [4]. Unfortunately, these standard methodologies have high cost, long analysis times (around 18 h) and require pretreatment of samples [5,6]. Other approaches to produce immunosensors have therefore been studied, including electroanalytical methods [7,8] in which antibodies or antigens are immobilized on a suitable matrix and the specific antigen–antibody recognition leads to an electrical or electrochemical signal.

The choice of the molecular architecture for the electrochemical immunosensors is crucial for obtaining high sensitivity and specificity. The matrix on which the bioactive layer is deposited may contain metallic nanoparticles to enhance the electrochemical response [8,9], including magnetic nanoparticles (MNPs) that can be exploited for their catalytic properties [10] and magnetic separation in pre-concentrating the analyte [11-16]. The most common magnetic nanoparticles used for this purpose are magnetite (Fe_3O_4) nanoparticles, which have a stronger magnetism than other iron oxide nanoparticles [17]. These MNPs can be synthesized through various techniques, such as ultrasound irradiation, sol–gel methods, thermal decomposition, and co-precipitation [18-21]. In addition, they can be modified with biomolecules and other compounds to improve the sensing performance. Electrochemical immunosensors containing magnetic nanoparticles have been used to detect several cancer biomarkers [22-24]. Zhuo and co-workers detected carcinoembryonic antigen (CEA) and α-fetoprotein (AFP) with a three-layer immunosensor with Fe_3O_4 magnetic core modified with a Prussian blue (PB) interlayer and a gold shell. The enzymes horseradish peroxidase and glucose oxidase were immobilized to improve sensitivity, with linear ranges between 0.01 and 80.0 ng·mL^{-1} for CEA and from 0.014 to 142 ng·mL^{-1} for AFP, and detection limits of 4 pg·mL^{-1} and 7 pg·mL^{-1}, respectively [25]. PSA and interleukin 6 (IL-6) were measured with a microfluidic electrochemical immunoassay system, in which commercial magnetic particles were conjugated with secondary antibodies and horseradish peroxidase (HRP) [26]. These immunomagnetic nanoparticle-based microfluidic sensors with screen-printed carbon electrodes (INμ-SPCEs) showed limits of

detection of 0.23 pg·mL^{-1} for PSA and 0.30 pg·mL^{-1} for IL-6, measured in the serum of prostate cancer patients [26]. Immunosensors to detect PSA include magnetic nanoparticles modified with gold [27], nitrodopamine functionalized iron oxide nanoparticles [3,28], ferrocene [28] and others [29,30].

A major challenge regarding the use of immunosensors in real samples lies in the difficulty to analyze considerable amounts of data in a single analysis, especially owing to the expected variability of blood serum, saliva, urine and tissue samples. This has sparked interest in computational tools [31]. For instance, information visualization techniques have been used to enhance the distinguishing ability of biosensors [32-34]. Discrimination of blood serum samples from patients with distinct probability to develop pancreatic cancer was made possible with a multidimensional projection technique applied to immunosensing data [34]. In this paper, we describe an INμ-SPCE to detect PSA using amperometry. To the best of our knowledge, the limit of detection is the lowest in the literature. The high sensitivity is probably connected to the molecular architecture of the sensing device, in which polyclonal antibodies were immobilized onto magnetic nanoparticles to selectively capture PSA. Furthermore, a proof-of-principle experiment regarding the detection of PSA in healthy and prostate cancer cell lysates is demonstrated, where the data were discriminated using multidimensional projections within the PEx-Sensors software [32].

Results and Discussion
Analytical performance

The analytical performance of the INμ-SPCEs was evaluated using PSA standard solutions in PBS at concentrations ranging from 12.5 to 1111 fg·mL^{-1}. After capturing PSA with the bioconjugate (Ab$_2$-MNP-HRP) from the standard solution, 100 μL were injected into the microfluidic channel using an injection valve, and then incubated for 30 min on an anti-PSA-AuNP-SPCE surface. A sandwich-type structure was assembled following the incubation. The amperometric analytical signal was obtained using constant-potential amperometry at a working electrode potential of −200 mV vs pseudo-reference Ag/AgCl. The mixed solution containing H_2O_2 (1 μmol·L^{-1}) and hydroquinone (HQ, 10 μmol·L^{-1}) was injected into the electrochemical cell, and the signal was monitored. The HRP-Fe(III) immobilized on the MNPs was oxidized by H_2O_2 to form an intermediate (Fe^{4+}=O) and a porphyrin π-cation radical. The oxidized HRP was reduced by the mediator hydroquinone (HQ) forming benzoquinone (BQ), which was electrochemically reduced by accepting one electron from the electrode, with the enzyme returning to its native form. Figure 1A shows the cathodic peak current responses, with a linear dependence of the current on the logarithm of the PSA concentration

Figure 1: (A) Amperometric responses for a blank solution and PSA solutions at concentrations of: (a) 12.5, (b) 138, (c) 277, (d) 555, (e) 823 and (f) 1111 fg·mL^{-1} prepared in a calf serum medium. (B) Analytical curve for PSA standards, using MNPs, anti-Ab$_1$ and anti-Ab$_2$ at a concentration of 10 µg·mL^{-1}, and concentrations of 10 µmol·L^{-1} and 1 µmol·L^{-1} for HQ and H$_2$O$_2$, respectively.
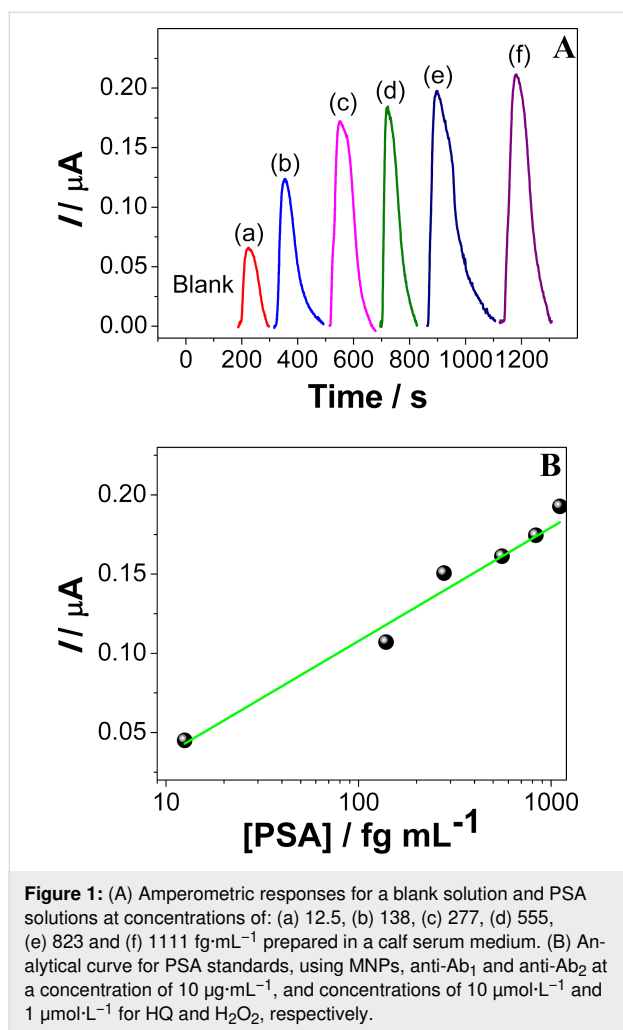
in Figure 1B, according to the linear regression equation: $I(\text{nA}) = 1.03 \cdot 10^{-6} + 7.2 \cdot 10^{-8} \log(x)$. The detection limit calculated using the IUPAC method [35,36] in Equation 1 is 0.062 fg·mL^{-1} :

$$\text{LD} = \frac{3 \cdot \text{SD}}{\text{slope}}, \tag{1}$$

where SD and slope are the standard deviation and slope of the calibration curve, respectively. To our knowledge, this limit of detection is the lowest found in the literature for immunosensors to detect PSA. The high sensitivity could be attributed to the use of MNPs (see characterization in Figure S1, Supporting Information File 1) decorated with Ab2 and HRP, which allowed for the capture, separation, and preconcentration of the analyte. It helped to acquire an amplified signal response and assisted the binding capacity of the antibody and antigen covalently immobilized on the electrode surface. Also, the monoclonal antibody provides high specificity to a single epitope, which is reflected in a low cross-reactivity. A comparison of

various sandwich-type immunosensors and immunoassays for detection of PSA in the literature is presented in Table 1.

Repeatability is a significant parameter for immunosensors. It was checked by using eight working electrodes in an array prepared under the same conditions, with the electrochemical response obtained at a given PSA concentration. The relative standard deviation in percent varied from 6% to 9%, with similar electrochemical responses for all immunosensors.

The detection mechanism for the immunosensors is likely an adsorption process, which is common for this type of sensor. We verified this hypothesis by modeling the amperometric responses for PSA antigen at concentrations from 12.5 to 1111 fg·mL^{-1} in Figure 2, where a Langmuir–Freundlich equation (Equation 2) was used to fit the data:

$$q = \frac{Q_m \left(K_a C_{\text{eq}} \right)^n}{\left(K_a C_{\text{eq}} \right)^n + 1}, \tag{2}$$

where Q_m is the adsorption capacity in nA, K_a is the adsorption affinity constant in milliliter per femtogram, C_{eq} is the concentration of the analyte in solution and n is a dimensionless index of heterogeneity, which varies between 0 and 1 for heterogeneous materials ($n = 1$ for homogeneous materials) [54]. Figure 2 shows the results with saturation of available sites with $Q_m = 339.85 \pm 32.15$ nA, which corresponds to ca. 64.4 fg·mL^{-1}, $n = 0.42 \pm 0.08$ and an affinity constant ($K_a = 0.45 \pm 0.09$ mL·fg^{-1}) characteristic of a polymer-based immunosensor [34,55]. This rather low value is expected for biosensors where the index n is characteristic of heterogeneous adsorption with polyclonal biomolecules that have many active sites with different degrees of affinity and selectivity.
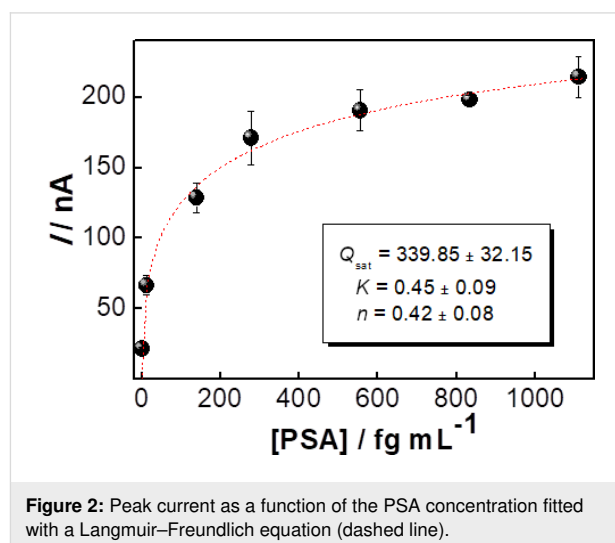

Figure 2: Peak current as a function of the PSA concentration fitted with a Langmuir–Freundlich equation (dashed line).

Table 1: Comparison of various sandwich-type immunosensors and immunoassays for the detection of PSA.

measurement method	linear range	detection limit	reference
amperometry	2–15 ng mL^{-1} and 15–120 ng mL^{-1}	1.1 ng·mL^{-1}	[37]
electrochemical impedance spectroscopy (EIS)	1–100 pg·mL^{-1}	1 pg·mL^{-1}	[38]
linear sweep voltammetry (LSV)	1–35 ng·mL^{-1}	0.76 pg·mL^{-1}	[39]
LSV	1–10 ng·mL^{-1}	1 ng·mL^{-1}	[40]
chemiluminescence	0.74 pg·mL^{-1} to 0.74 µg·L^{-1}	0.7 pg·mL^{-1}	[41]
amperometry	0–60 µg·L^{-1}	0.08 µg·L^{-1}	[5]
surface plasmon resonance	1–100 ng·mL^{-1}	1 ng·mL^{-1}	[42]
chronoamperometry	1×10^{-5} ng·mL^{-1} to 100 ng·mL^{-1}	0.002 pg·mL^{-1}	[43]
amperometry	50 fg·mL^{-1} to 40 ng·mL^{-1}	16.6 fg·mL^{-1}	[44]
EIS	1 pg·mL^{-1} to 100 ng·mL^{-1}	1 pg·mL^{-1}	[45]
EIS	0–10 ng·mL^{-1}	590 pg·mL^{-1}	[46]
EIS	0.05–5 ng·mL^{-1}	13 pg·mL^{-1}	[47]
EIS	0.01–10 ng·mL^{-1}	2 pg·mL^{-1}	[48]
chip enzyme immunoassay	3.2–50 ng·mL^{-1}	3.2 ng·mL^{-1}	[49]
electrochemical chemiluminescence (ECL)	0.0001–100 ng·mL^{-1}	0.1 pg·mL^{-1}	[50]
differential pulse voltammetry (DPV)	0.001–5 ng·mL^{-1}	0.31 pg·mL^{-1}	[51]
EIS	0.5 pg·mL^{-1} to 35 ng·mL^{-1}	5 pg·mL^{-1}	[52]
DPV	0.1 pg·mL^{-1} to 90 ng·mL^{-1}	10 fg·mL^{-1}	[52]
DPV	0.2–40 ng·mL^{-1}	0.020 ng·mL^{-1}	[53]
amperometry	12.5–1111 fg·mL^{-1}	0.062 fg·mL^{-1}	this work

Application of the immunosensor in real samples

The suitability of INµ-SPCEs for detecting PSA in real samples was tested with malignant (LNCap) and non-malignant (PNT-2) cells. In contact with cell lysates containing several proteins, the bioconjugate binds specifically to PSA (PSA-Ab$_2$-MNP-HRP), thus allowing for the capture, separation and preconcentration of PSA employing a magnet. Furthermore, detection is enhanced because of the presence of multiple immobilized HRP molecules. Figure 3 shows that a high amount of PSA is found in LNCap in comparison to PNT-2 using the immunosensor, in agreement with the standard ELISA method. The limit of quantification with the immunosensor is lower than the threshold established for the serum level found in patients with prostate cancer (above 3.6 ng·mL^{-1} stage A1) [56]. The samples were diluted in PBS for reaching the linear range, providing a response within the stipulated standards for the samples. Using the linear discrimination technique, the concentration is predicted for the real samples with 91.67% accuracy.

Information visualization applied to the immunosensing data

The sensitivity of the INµ-SPCEs could be exploited in distinguishing a diversity of samples by using multidimensional projection techniques. The whole amperograms in Figure 1A were processed with four multidimensional projection techniques, namely, principal component analysis (PCA), least

Figure 3: ELISA and INµ-SPCE results for PSA in control cell lysates (PNT-2) and prostate cancer cells (LNCap).
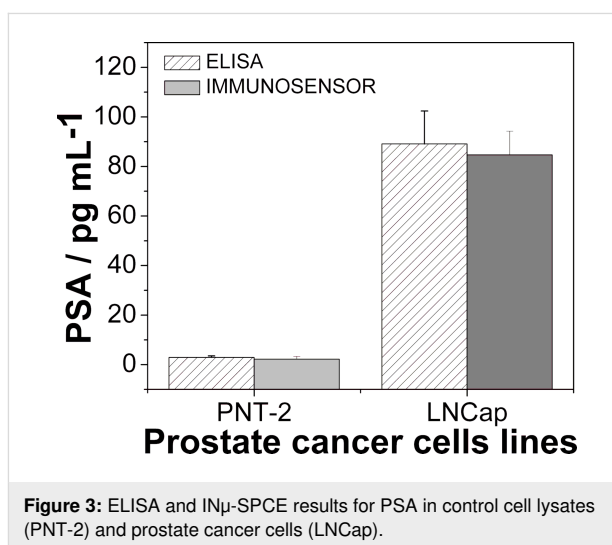
square projection (LSP), interactive document mapping (IDMAP) and Sammon's mapping (SM), and the silhouette coefficients, *S*, were calculated as summarized in Figure S2 (Supporting Information File 1). The samples can be discriminated very well in all cases because $S > 0.71$ [46], and the highest value was obtained with the IDMAP technique. From the parallel coordinates (PC) plot in Figure S3 (Supporting Information File 1), we notice that the initial values for the current hamper discrimination, and therefore these dimensions (corresponding to times) are marked as red boxes (i.e., $S < 0$) in

the upper part of the map. To improve discrimination, we adopted a feature-selection procedure [22] that consists in eliminating the dimensions that hamper discrimination. Figure 4 shows the parallel coordinates plot after feature selection, which leads to clear discrimination where the dimensions all contribute to detection, as represented by the blue boxes (i.e., *S* > 0).

The maps obtained with the various multidimensional projection techniques after feature selection are shown in Figure S4 (Supporting Information File 1). The silhouette coefficients *S* increased by about 20% in comparison to the values without feature selection. The *S* value for IDMAP was calculated using the following equation:

$$S_{\text{IDMAP}} = \frac{\delta\left(X_i, X_j\right) - \delta_{\min}}{\delta_{\max} - \delta_{\min}} - \delta\left(Y_i, Y_j\right), \quad (3)$$

where the minimum and maximum distances between the concentration values are given as $\delta_{\min}$ and $\delta_{\max}$, respectively, and $\delta(X_i, X_j)$ is the Euclidean distance between current responses for the PSA concentrations X_i and X_j [32]. IDMAP was found to give the highest *S* values and was used to project the data in Figure 5. One should note the large distance between the data points for PBS and those for the smallest concentration tested. This means that it is probably possible to detect PSA concentrations even lower than 12.5 fg·mL^{-1}. The projection is consistent with the PSA concentrations obtained with ELISA for PNT-2 and LNCap cells with values of 5 and 84–92 fg·mL^{-1}, respectively. This can be seen by the location of the sandwich-type immunosensing data for these cells in Figure 5.

Conclusion

In this paper, we leverage sensing technologies to achieve ultra-high sensitivity in detecting the prostate cancer biomarker PSA by using MNPs to capture PSA in a pre-concentration proce-

Figure 4: Parallel coordinates plot for PSA concentrations from 12.5 to 1111 fg·mL^{-1} after the feature-selection procedure. The *x*-axis represents time values, while the *y*-axis represents Euclidean distances related to the current.

Figure 5: IDMAP plot obtained from the data in Figure 1A for buffers containing different PSA concentrations and from Figure 3 for prostate cancer cells. In both cases, feature selection was applied before plotting the data.

dure for a sandwich-type immunomagnetic sensor. Electrochemical immunoassays with disposable microfluidic devices led to excellent linearity, reproducibility, and fast detection at low-cost, while showing excellent agreement with the standard method ELISA. Importantly, the approach for the immunoassays can be adapted for multiplex detection of biomarkers, in addition to PSA, by combining with other proteins. We also demonstrated that information visualization techniques, so far most commonly used for impedance spectroscopy sensing data, can be applied to amperometric results with a microfluidic sandwich-type immunosensor. The data processing allows for a more didactic interpretation of the results and improves separation between samples of patients with high levels of PSA from those who have lower concentrations.

Experimental
Materials
The reagents used were either of analytical or HPLC grade. Reduced L-glutathione (GSH, 99%), bovine serum albumin (BSA), $HAuCl_4 \cdot 3H_2O$ (99.9%), sodium borohydride (99%), horseradish peroxidase (HRP, M_W = 44000; 250–330 u·mg^{-1}), poly(diallydimethylammonium chloride) (PDDA, 20 wt % in H_2O), 1-(3-(dimethylamino)propyl)-3-ethylcarbodiimide hydrochloride (EDC), *N*-hydroxysulfosuccinimide (Sulfo-NHS), hydrogen peroxide (H_2O_2, 30%), Tween-20, and 2-(*N*-morpholino)ethanesulfonic acid hydrate (MES) were purchased from Sigma-Aldrich. Monoclonal (mouse) primary anti-human prostate specific antigen (PSA) antibody, natural human prostate-specific antigen (PSA), and standard and secondary anti-PSA antibodies were obtained from Abcam, Cambridge,

UK. Graphite-based ink was obtained from Henkel Electrodag, USA (reference code 423SS), silver chloride ink was purchased from Gwent electronic materials Ltd., UK (Product code C2130905D3), the cell lines PNT-2 and LNCap were acquired from the Banco de Células do Rio de Janeiro (BCRJ) (Rio de Janeiro, Brazil). For the synthesis of magnetic nanoparticles, sodium hydroxide (NaOH) with 97% purity and ferrous sulfate heptahydrate ($FeSO_4 \cdot 7H_2O$) with ≥99.6% purity were purchased from Vetec Química Fina Ltda (Rio de Janeiro, Brazil), and ferric chloride hexahydrate ($FeCl_3 \cdot 6H_2O$) with ≥98% purity was purchased from Sigma-Aldrich. Hydrochloric acid (HCl, 36.5–38.0% w/w) and NaCl with 99% purity were acquired from Labsynth (São Paulo, Brazil). Sodium citrate ($Na_3C_6H_5O_7$) with 99.8% purity was purchased from J.T Baker Chemical Company. All aqueous solutions were prepared with ultrapure water (18 MΩ·cm at 25 °C) obtained from a Milli-Q Direct-0.3 (Millipore) purification system.

Fabrication of sandwich-type electrochemical immunosensors
The multi-channel screen-printed array of electrodes was fabricated according to the procedures established by Faria and collaborators [57]. The experimental details are given in Supporting Information File 1. The fabrication of this sandwich-type immunosensor comprises four steps, as depicted in Figure 6: (1) deposition of monoclonal antibody on the carbon electrode, (2) bioconjugate modification using HRP and polyclonal antibody, (3) capture of biomarker by the bioconjugate, (4) sandwich formation by injection of the biomarker captured by Ab_2-MNP-HRP in the microfluidic system.
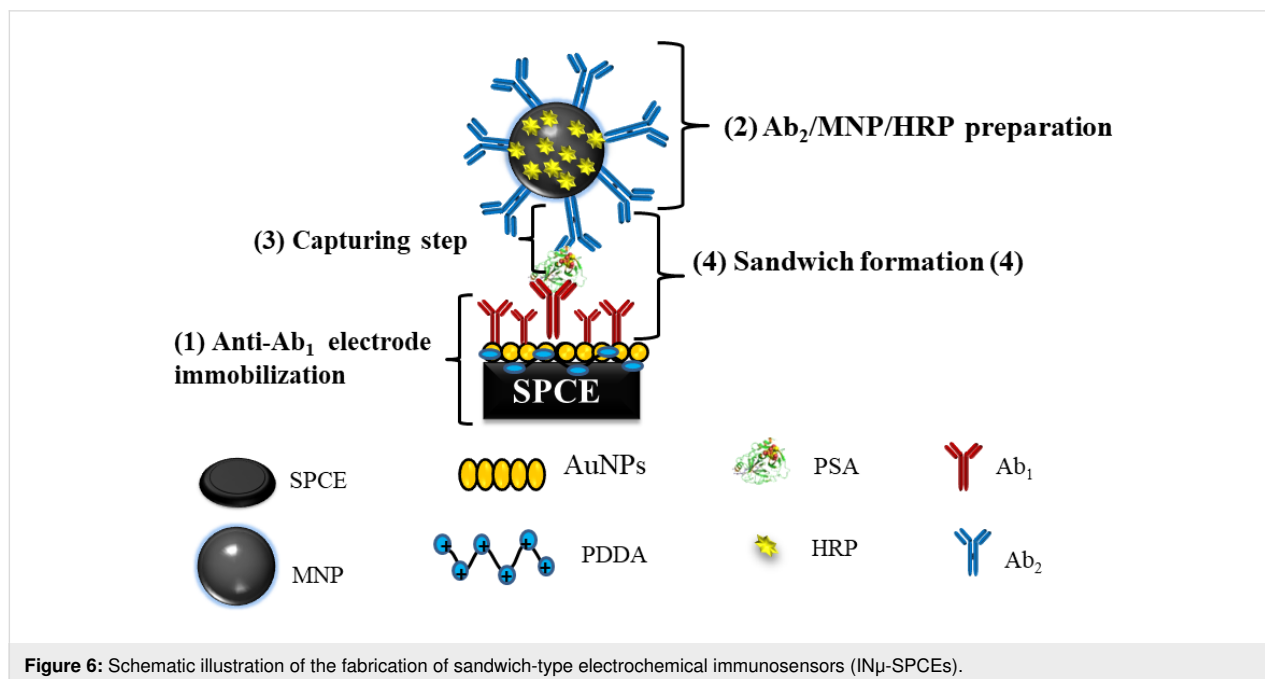

Figure 6: Schematic illustration of the fabrication of sandwich-type electrochemical immunosensors (INμ-SPCEs).

The first step included the deposition of a bilayer of poly(dial-lyldimethylammonium) (PDDA) and gold nanoparticles (AuNPs) decorated with glutathione, as illustrated in Figure 7. An aliquot of 5 µL of 2.0 mg·mL^{-1} of PDDA was added to each working electrode and kept for 20 min. The electrode surface was rinsed with Millipore water to remove excess of reagents. Then, 5.0 µL of gold nanoparticles modified with glutathione (AuNP-GSH, 46.68 µg·mL^{-1}) were dripped on the electrode and left for a period of 20 min. The carboxyl-terminated AuNP-GSH provided a chemical group suitable for covalent binding. Next, a volume of 5 µL EDC/NHS (0.4 mol·L^{-1} EDC and 0.1 mol·L^{-1} NHS) in water was added on the surface of INµ-SPCEs and kept for 10 min to activate the carboxyl groups from AuNP-GSH, therefore ensuring a stable covalent binding to the antibodies. The primary monoclonal antibodies (Ab1) were adsorbed on the electrode by adding 5 µL of a 10 µg·mL^{-1} solution in PBS 7.0, with adsorption occurring overnight. The electrodes were then washed with 1.0 mL PBS and incubated with 5 µL of bovine serum albumin (BSA) (2% w/w) diluted in PBS to avoid non-specific binding (NBS). Each step of the modification was monitored with polarization-modulated infrared reflection absorption spectroscopy (PM-IRRAS, see Figure S1F in Supporting Information File 1). The microfluidic cell was set up, and the electrodes were insulated using a polystyrene card with double-sided adhesive. The double-sided tape was used to delimit the electroactive area, which was fixed on the reference electrode under the arrangement of working electrodes and the auxiliary electrode. Also, the double-sided tape allowed for sealing of the microfluidic system.

The second step of the preparation of the sandwich immunosensors consisted in forming the bioconjugate complex of Ab$_2$ and HRP (Ab$_2$-MNP-HRP), as described by Uliana and co-workers [58]. Briefly, 2.0 mL (stock solution: 10 mg particles·mL^{-1}) of MNPs were placed in microtubes, which were then washed with 500 µL of 0.05 mol·L^{-1} MES buffer at pH 5.2 and separated magnetically. Later, the supernatant was discarded and washed thrice to give a final particle concentration of 40 mg·mL^{-1}. A 3 mg·mL^{-1} solution of EDC/NHS in 0.05 mol·L^{-1} MES buffer at pH 5.2 was added to the washed MNPs. It was shaken on a vortex-type stirrer for 5 min and on a rotary shaker for 30 min. Immediately after shaking, the particles were magnetically separated and washed with MES buffer again. The supernatant was then removed, and the washing procedure was repeated twice again. Subsequently, 250 µL of Ab$_2$ were added to the solution with a final concentration of 10 µg·mL^{-1}. The solution was vortexed and shaken on a custom-made rotary shaker for 24 h at room temperature. At this point, the solution was magnetically separated and washed with 600 µL PBS/0.05% Tween 20 buffer pH 7.4.

HRP was conjugated to the MNPs by adding 500 µL of 1.2 mg·mL^{-1} of the enzyme to the Ab$_2$-MNP complex. The mixture was left overnight on a rotary shaker. After 18 h of stirring, the bioconjugate complex was magnetically separated and then washed with 600 µL of PBS/0.05% Tween-20 and 0.1% BSA (four-fold). Later, 1.0 mL of glycine 1.0 mol·L^{-1} pH 8 was added to the solution. The solution was vortexed and stirred for 30 min at room temperature, followed by washing with
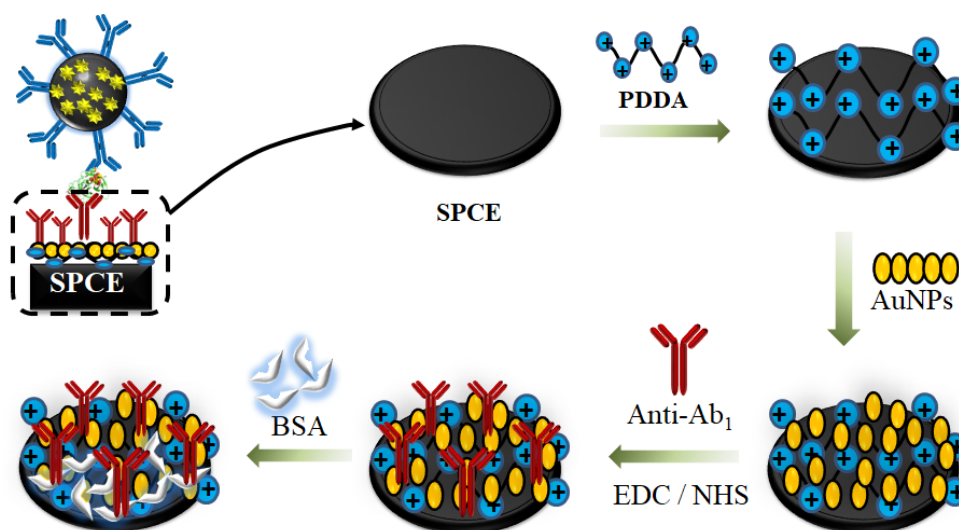
Figure 7: Electrode modification with 10 µg·mL^{-1} monoclonal antibody (Ab$_1$) using 5 µL of 2 mg·mL^{-1} PDDA and 5 µL of AuNP-GSH. To activate the carboxyl groups from AuNP-GSH and ensure a stable covalent binding of antibodies, EDC/NHS was used (0.4 mol·L^{-1} EDC and 0.1 mol·L^{-1} NHS). The electrodes were washed with 1.0 mL of PBS buffer pH 7.4 and incubated with 5 µL of bovine serum albumin (BSA) (2% w/w) diluted in phosphate-buffered saline (PBS), to avoid non-specific binding.

0.05% PBS/Tween-20 buffer, pH 7.4 and 2% BSA; and magnetic separation. Finally, the bioconjugate complex was resuspended with 250 µL of 0.05% PBS-Tween/20 buffer of pH 7.4 and 2% BSA giving a final particle concentration of 5 mg·mL^{-1}. These steps are summarized in Figure 8.

In the third step, shown in Figure 9, 20 µL of Ab$_2$-MNP-HRP were added to 320 µL PBS buffer at pH 7.4. For the standard calibration, 20 µL of the antigen-enriched calf serum were added to the composite bioconjugate complex mixture. The mixture was then incubated at 37 °C for 30 min, and dilutions were required to decrease the protein concentration. The devices were also evaluated with real samples, including culture medium of cancerous and control cells (lineage of LNCap and PNT-2 cells, respectively). The cell lines PNT-2 and

LNCap were acquired from the Banco de Células do Rio de Janeiro (BCRJ, Rio de Janeiro, Brazil). The samples were diluted to a 1:30000 ratio. The resulting conjugate, Ab$_2$-MNP-HRP-protein, was magnetically separated and washed with 400 µL of 0.5% BSA and 20 mol·L^{-1} of PBS buffer pH 7.4. It was then resuspended to 125 µL.

In the fourth and last step, the bioconjugate complex was used to form the sandwich-type immunosensor, with 125 µL of the final solution used in the immunoassay to fill a 100 µL sample loop. This was performed in a microfluidic system with a flow rate of 100 µL·min^{-1}. The complex was injected with a syringe and the flow was stopped for 30 min. In the amperometric detection step, the biomarker quantification was performed by an indirect method through the electrochemical response of the

Figure 8: Preparation of the bioconjugate complex of Ab$_2$ and HRP (Ab$_2$-MNP-HRP).

Figure 9: Illustration of the PSA capturing step.
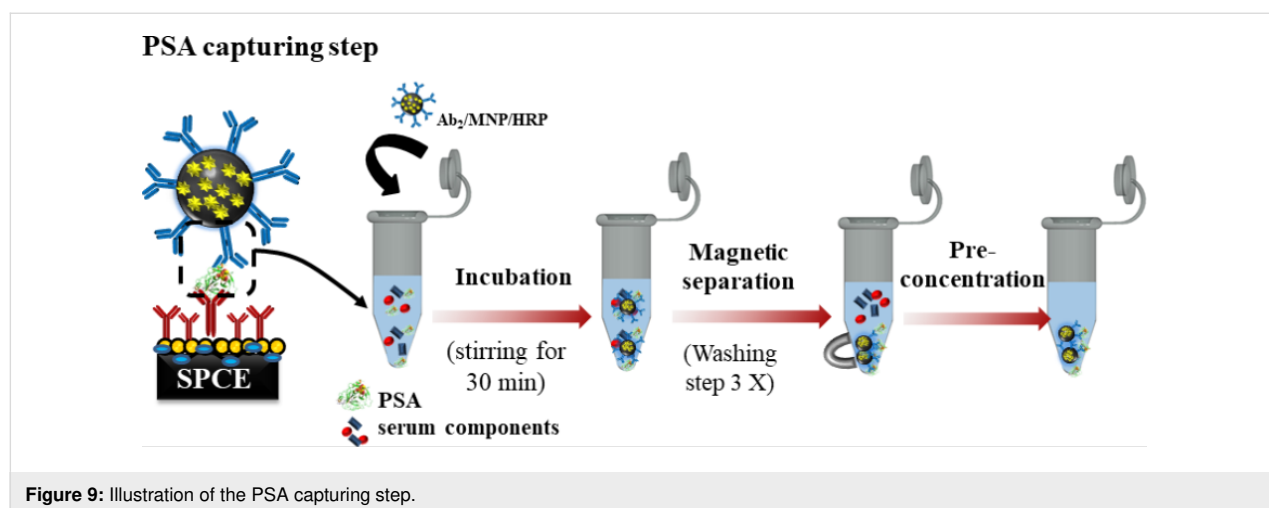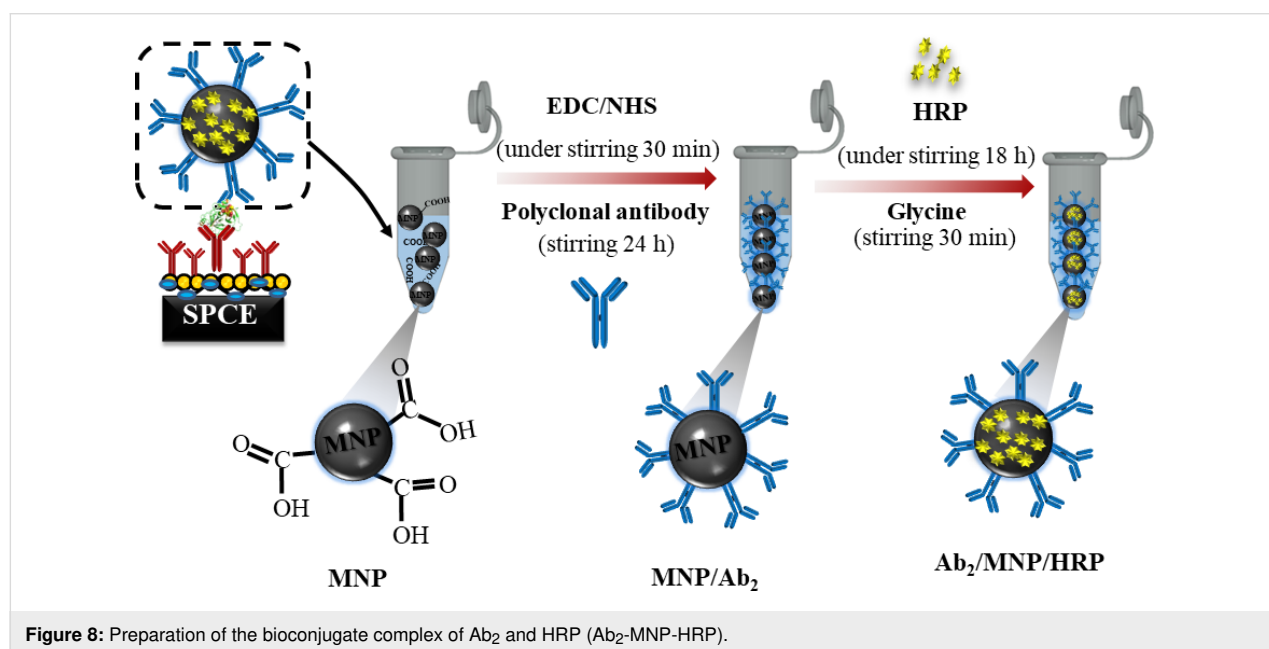
marker in the MNPs. It was monitored by injecting a solution containing 1.0 µmol·L^{-1} of H$_2$O$_2$ and 10 µmol·L^{-1} of hydroquinone (HQ) in the microfluidic system. The amperometric measurements were performed using a DropSens µStat 8000 multi-potentiostat/galvanostat. The multichannel screen-printed array contained eight working carbon electrodes combined with one pseudo-reference electrode (Ag/AgCl) and one auxiliary electrode (carbon). The microfluidic system was set up with an injection pump (NE-1000 programmable Single Syringe Pump, New Era Pump System, Farmingdale, USA) and an injection valve with a sample loop of 100 µL.

Data treatment with information visualization methods

The distinction of real samples is certainly challenging when various samples are analyzed, and false positives may occur. This has prompted researchers to use statistical and computational methods to treat the sensing data [31], in some cases with conjunction with machine learning approaches [31,59]. Here we employed multidimensional projection techniques based on linear and nonlinear multidimensional scaling (MDS) approaches such as principal component analysis (PCA) [60], Least squares projection (LSP) [61], Sammon's mapping (SM) [62] and interactive document mapping (IDMAP) [63] implemented in the software as projection explorer sensors (PEx-Sensors) [32,64]. The amperogram data (current as a function of the time) were dimensionally reduced by PCA and FastMap [65] and then projected with PCA, LSP, IDMAP, and SM techniques. The dissimilarities between samples were converted to Euclidean distances with the whole rising current curves being transformed into single data points as observed in the projection plots. Three independent sets of measurements were utilized on this analysis. A full description of these techniques and PEx-sensors can be found in [32].

This type of analysis provides a map for pattern recognition among samples. It has been applied to biosensing data, mainly with IDMAP, which includes an algorithm to minimize the global error through a pairwise error function [63]. Herein, we combined the projections with parallel coordinates maps to perform feature selection with the exclusion of dimensions found to be deleterious for discrimination of similar data points, analogously to [66]. The performance upon applying the different projection techniques was evaluated by calculating the silhouette coefficient, *S*, defined as the average of the distances between each data instance and all other points belonging to the same group, and the minimum distance between each data instance and other instances belonging to other groups [67]. *S* values vary between −1 and 1. According to Rousseeuw, values above 0.71 indicate that a strong discrimination was obtained [68].

Supporting Information

Supporting Information features detailed information on the synthesis of magnetic iron oxide nanoparticles, electrode fabrication, and sample preparation. Also, the characterization of MNPs and electrode surfaces by using Fourier-transform infrared spectroscopy (FTIR), field-emission scanning electron microscopy (FE-SEM), energy-dispersive X-ray spectroscopy (EDX), and polarization-modulated infrared reflection absorption spectroscopy (PM-IRRAS, Figure S1) is described. The Silhouette coefficients calculated for IDMAP, Sammon's mapping (SM), principal component analysis (PCA), and least square projection (LSP) multidimensional projection techniques to analyze the PSA concentration of immunosensor before (All) and after (FS) feature selection (Figure S2) are provided as well. The parallel coordinates plot for PSA concentrations from 12.5 to 1111 fg·mL^{-1} are given in Figure S3, while plots of three multidimensional projection techniques, i.e., PCA, LSP, and SM are shown in Figure S4.

Supporting Information File 1

Additional procedures and figures.
[https://www.beilstein-journals.org/bjnano/content/supplementary/2190-4286-10-210-S1.pdf]

ORCID® iDs

Camila A. Proença - https://orcid.org/0000-0001-8438-4651
Tayane A. Freitas - https://orcid.org/0000-0002-2086-5576
Thaísa A. Baldo - https://orcid.org/0000-0002-3212-0571
Frederico L. F. Soares - https://orcid.org/0000-0002-8555-2095
Ronaldo C. Faria - https://orcid.org/0000-0003-1094-9597

References

1. Saini, S. *Cell. Oncol.* **2016,** *39,* 97–106.
   doi:10.1007/s13402-016-0268-6
2. Liedtke, R. J.; Batjer, J. D. *Clin. Chem.* **1984,** *30,* 649–652.
3. Wang, X.; Zhao, M.; Nolte, D. D.; Ratliff, T. L. *Biosens. Bioelectron.*
   2011, *26,* 1871–1875. doi:10.1016/j.bios.2010.02.009
4. Ellis, W. J.; Vessella, R. L.; Noteboom, J. L.; Lange, P. H.;
   Wolfert, R. L.; Rittenhouse, H. G. *Urol.* **1997,** *50,* 573–579.
   doi:10.1016/s0090-4295(97)00251-3
5. Panini, N. V.; Messina, G. A.; Salinas, E.; Fernández, H.; Raba, J.
   Biosens. Bioelectron. **2008,** *23,* 1145–1151.
   doi:10.1016/j.bios.2007.11.003

6. Zani, A.; Laschi, S.; Mascini, M.; Marrazza, G. *Electroanalysis* **2011,** *23,* 91–99. doi:10.1002/elan.201000486

7. Meng, W.; Zhang, W.; Zhang, J.; Chen, X.; Zhang, Y. *Anal. Methods* **2019,** *11,* 2183–2189. doi:10.1039/c9ay00064j

8. Liu, L.; Zhao, G.; Dong, X.; Li, X.; Wei, Q.; Cao, W. *Anal. Methods* **2018,** *10,* 4917–4925. doi:10.1039/c8ay01533c

9. Kim, D.-J.; Lee, N.-E.; Park, J.-S.; Park, I.-J.; Kim, J.-G.; Cho, H. J. *Biosens. Bioelectron.* **2010,** *25,* 2477–2482. doi:10.1016/j.bios.2010.04.013

10. Pankhurst, Q. A.; Connolly, J.; Jones, S. K.; Dobson, J. *J. Phys. D: Appl. Phys.* **2003,** *36,* R167–R181. doi:10.1088/0022-3727/36/13/201

11. Wen, W.; Yan, X.; Zhu, C.; Du, D.; Lin, Y. *Anal. Chem. (Washington, DC, U. S.)* **2017,** *89,* 138–156. doi:10.1021/acs.analchem.6b04281

12. Liébana, S.; Brandão, D.; Alegret, S.; Pividori, M. I. *Anal. Methods* **2014,** *6,* 8858–8873. doi:10.1039/c4ay01373e

13. Proença, C. A.; Baldo, T. A.; Freitas, T. A.; Materón, E. M.; Wong, A.; Durán, A. A.; Melendez, M. E.; Zambrano, G.; Faria, R. C. *Anal. Chim. Acta* **2019,** *1071,* 59–69. doi:10.1016/j.aca.2019.04.047

14. Aqil, A.; Vasseur, S.; Duguet, E.; Passirani, C.; Benoît, J. P.; Roch, A.; Müller, R.; Jérôme, R.; Jérôme, C. *Eur. Polym. J.* **2008,** *44,* 3191–3199. doi:10.1016/j.eurpolymj.2008.07.011

15. Hatch, G. P.; Stelter, R. E. *J. Magn. Magn. Mater.* **2001,** *225,* 262–276. doi:10.1016/s0304-8853(00)01250-6

16. Park, J.; Lim, H. B. *Food Chem.* **2014,** *160,* 112–117. doi:10.1016/j.foodchem.2014.03.047

17. Teja, A. S.; Koh, P.-Y. *Prog. Cryst. Growth Charact. Mater.* **2009,** *55,* 22–45. doi:10.1016/j.pcrysgrow.2008.08.003

18. Ferreira, G. R.; Segura, T.; de Souza, F. G., Jr.; Umpierre, A. P.; Machado, F. *Eur. Polym. J.* **2012,** *48,* 2050–2069. doi:10.1016/j.eurpolymj.2012.09.003

19. Mascolo, M.; Pei, Y.; Ring, T. *Materials* **2013,** *6,* 5549–5567. doi:10.3390/ma6125549

20. Yu, S.; Chow, G. M. *J. Mater. Chem.* **2004,** *14,* 2781–2786. doi:10.1039/b404964k

21. Neves, J. S.; de Souza, F. G., Jr.; Suarez, P. A. Z.; Umpierre, A. P.; Machado, F. *Macromol. Mater. Eng.* **2011,** *296,* 1107–1118. doi:10.1002/mame.201100050

22. Ahmadi, A.; Shirazi, H.; Pourbagher, N.; Akbarzadeh, A.; Omidfar, K. *Mol. Biol. Rep.* **2014,** *41,* 1659–1668. doi:10.1007/s11033-013-3014-4

23. Li, J.; Gao, H.; Chen, Z.; Wei, X.; Yang, C. F. *Anal. Chim. Acta* **2010,** *665,* 98–104. doi:10.1016/j.aca.2010.03.020

24. Tang, D.; Yuan, R.; Chai, Y. *J. Phys. Chem. B* **2006,** *110,* 11640–11646. doi:10.1021/jp060950s

25. Zhuo, Y.; Yuan, P.-X.; Yuan, R.; Chai, Y.-Q.; Hong, C.-L. *Biomaterials* **2009,** *30,* 2284–2290. doi:10.1016/j.biomaterials.2009.01.002

26. Chikkaveeraiah, B. V.; Mani, V.; Patel, V.; Gutkind, J. S.; Rusling, J. F. *Biosens. Bioelectron.* **2011,** *26,* 4477–4483. doi:10.1016/j.bios.2011.05.005

27. Chuah, K.; Lai, L. M. H.; Goon, I. Y.; Parker, S. G.; Amal, R.; Justin Gooding, J. *Chem. Commun.* **2012,** *48,* 3503. doi:10.1039/c2cc30512g

28. Li, H.; Wei, Q.; He, J.; Li, T.; Zhao, Y.; Cai, Y.; Du, B.; Qian, Z.; Yang, M. *Biosens. Bioelectron.* **2011,** *26,* 3590–3595. doi:10.1016/j.bios.2011.02.006

29. Tang, D.; Yuan, R.; Chai, Y. *Anal. Chem.* **2008,** *80,* 1582–1588. doi:10.1021/ac702217m

30. Beveridge, J. S.; Stephens, J. R.; Williams, M. E. *Annu. Rev. Anal. Chem.* **2011,** *4,* 251–273. doi:10.1146/annurev-anchem-061010-114041

31. Paulovich, F. V.; De Oliveira, M. C. F.; Oliveira, O. N., Jr. *ACS Sens.* **2018,** *3,* 1433–1438. doi:10.1021/acssensors.8b00276

32. Paulovich, F. V.; Moraes, M. L.; Maki, R. M.; Ferreira, M.; Oliveira Jr., O. N.; de Oliveira, M. C. F. *Analyst* **2011,** *136,* 1344. doi:10.1039/c0an00822b

33. Moraes, M. L.; Petri, L.; Oliveira, V.; Olivati, C. A.; de Oliveira, M. C. F.; Paulovich, F. V.; Oliveira, O. N., Jr.; Ferreira, M. *Sens. Actuators, B* **2012,** *166-167,* 231–238. doi:10.1016/j.snb.2012.02.046

34. Thapa, A.; Soares, A. C.; Soares, J. C.; Awan, I. T.; Volpati, D.; Melendez, M. E.; Fregnani, J. H. T. G.; Carvalho, A. L.; Oliveira, O. N., Jr. *ACS Appl. Mater. Interfaces* **2017,** *9,* 25878–25886. doi:10.1021/acsami.7b07384

35. Thompson, M.; Ellison, S. L. R.; Wood, R. *Pure Appl. Chem.* **2002,** *74,* 835–855. doi:10.1351/pac200274050835

36. Manso, J.; Mena, M. L.; Yáñez-Sedeño, P.; Pingarrón, J. *J. Electroanal. Chem.* **2007,** *603,* 1–7. doi:10.1016/j.jelechem.2007.02.004

37. Liu, S.; Zhang, X.; Wu, Y.; Tu, Y.; He, L. *Clin. Chim. Acta* **2008,** *395,* 51–56. doi:10.1016/j.cca.2008.04.031

38. Barton, A. C.; Davis, F.; Higson, S. P. J. *Anal. Chem. (Washington, DC, U. S.)* **2008,** *80,* 6198–6205. doi:10.1021/ac800491m

39. Qu, B.; Chu, X.; Shen, G.; Yu, R. *Talanta* **2008,** *76,* 785–790. doi:10.1016/j.talanta.2008.04.026

40. Escamilla-Gómez, V.; Hernández-Santos, D.; González-García, M. B.; Pingarrón-Carrazón, J. M.; Costa-García, A. *Biosens. Bioelectron.* **2009,** *24,* 2678–2683. doi:10.1016/j.bios.2009.01.043

41. Zheng, Y.; Chen, H.; Liu, X.-P.; Jiang, J.-H.; Luo, Y.; Shen, G.-L.; Yu, R.-Q. *Talanta* **2008,** *77,* 809–814. doi:10.1016/j.talanta.2008.07.038

42. Huang, L.; Reekmans, G.; Saerens, D.; Friedt, J.-M.; Frederix, F.; Francis, L.; Muyldermans, S.; Campitelli, A.; Hoof, C. V. *Biosens. Bioelectron.* **2005,** *21,* 483–490. doi:10.1016/j.bios.2004.11.016

43. Chu, Y.; Wang, H.; Ma, H.; Wu, D.; Du, B.; Wei, Q. *RSC Adv.* **2016,** *6,* 84698–84704. doi:10.1039/c6ra13841a

44. Feng, J.; Li, Y.; Li, M.; Li, F.; Han, J.; Dong, Y.; Chen, Z.; Wang, P.; Liu, H.; Wei, Q. *Biosens. Bioelectron.* **2017,** *91,* 441–448. doi:10.1016/j.bios.2016.12.070

45. Arya, S. K.; Bhansali, S. *Biosens. J.* **2011,** *1,* 102.

46. Jang, H. D.; Kim, S. K.; Chang, H.; Choi, J.-W. *Biosens. Bioelectron.* **2015,** *63,* 546–551. doi:10.1016/j.bios.2014.08.008

47. Mao, K.; Wu, D.; Li, Y.; Ma, H.; Ni, Z.; Yu, H.; Luo, C.; Wei, Q.; Du, B. *Anal. Biochem.* **2012,** *422,* 22–27. doi:10.1016/j.ab.2011.12.047

48. Li, Y.; Han, J.; Chen, R.; Ren, X.; Wei, Q. *Anal. Biochem.* **2015,** *469,* 76–82. doi:10.1016/j.ab.2014.09.022

49. Adel Ahmed, H.; Azzazy, H. M. E. *Biosens. Bioelectron.* **2013,** *49,* 478–484. doi:10.1016/j.bios.2013.05.058

50. Shi, H.-W.; Zhao, W.; Liu, Z.; Liu, X.-C.; Wu, M.-S.; Xu, J.-J.; Chen, H.-Y. *Talanta* **2016,** *154,* 169–174. doi:10.1016/j.talanta.2016.03.059

51. Fan, D.; Li, N.; Ma, H.; Li, Y.; Hu, L.; Du, B.; Wei, Q. *Biosens. Bioelectron.* **2016,** *85,* 580–586. doi:10.1016/j.bios.2016.05.063

52. Kavosi, B.; Salimi, A.; Hallaj, R.; Moradi, F. *Biosens. Bioelectron.* **2015,** *74,* 915–923. doi:10.1016/j.bios.2015.07.064

53. Salimi, A.; Kavosi, B.; Fathi, F.; Hallaj, R. *Biosens. Bioelectron.* **2013,** *42,* 439–446. doi:10.1016/j.bios.2012.10.053

54. Soares, J. C.; Soares, A. C.; Pereira, P. A. R.; Rodrigues, V. da C.; Shimizu, F. M.; Melendez, M. E.; Scapulatempo Neto, C.; Carvalho, A. L.; Leite, F. L.; Machado, S. A. S.; Oliveira, O. N. *Phys. Chem. Chem. Phys.* **2016,** *18,* 8412–8418. doi:10.1039/c5cp07121f

55. Soares, A. C.; Soares, J. C.; Shimizu, F. M.; Melendez, M. E.; Carvalho, A. L.; Oliveira, O. N., Jr. *ACS Appl. Mater. Interfaces* **2015,** *7,* 25930–25937. doi:10.1021/acsami.5b08666

56. Kuriyama, M.; Obata, K.; Miyagawa, Y.; Nishikawa, E.; Koide, T.; Takeda, A.; Komeda, Y.; Kanbayashi, T.; Nakano, M.; Miyake, K. *Int. J. Urol.* **1996,** *3,* 462–467. doi:10.1111/j.1442-2042.1996.tb00577.x

57. Afonso, A. S.; Uliana, C. V.; Martucci, D. H.; Faria, R. C. *Talanta* **2016,** *146,* 381–387. doi:10.1016/j.talanta.2015.09.002

58. Uliana, C. V.; Peverari, C. R.; Afonso, A. S.; Cominetti, M. R.; Faria, R. C. *Biosens. Bioelectron.* **2018,** *99,* 156–162. doi:10.1016/j.bios.2017.07.043

59. Shimizu, F. M.; Pasqualeti, A. M.; Todão, F. R.; de Oliveira, J. F. A.; Vieira, L. C. S.; Gonçalves, S. P. C.; da Silva, G. H.; Cardoso, M. B.; Gobbi, A. L.; Martinez, D. S. T.; Oliveira, O. N., Jr.; Lima, R. S. *ACS Sens.* **2018,** *3,* 716–726. doi:10.1021/acssensors.8b00056

60. Jolliffe, I. T. Principal Component Analysis and Factor Analysis. *Principal Component Analysis;* Springer Series in Statistics; Springer New York: New York, NY, U.S.A., 1986; pp 115–128. doi:10.1007/978-1-4757-1904-8_7

61. Paulovich, F. V.; Nonato, L. G.; Minghim, R.; Levkowitz, H. *IEEE Trans. Visualization Comput. Graphics* **2008,** *14,* 564–575. doi:10.1109/tvcg.2007.70443

62. Sammon, J. W. *IEEE Trans. Comput.* **1969,** *C-18,* 401–409. doi:10.1109/t-c.1969.222678

63. Minghim, R.; Paulovich, F. V.; de Andrade Lopes, A. Content-based text mapping using multi-dimensional projections for exploration of document collections. In *Proceedings of the Society of Photo-Optical Instrumentation Engineers (SPIE),* San Jose, CA, U.S.A.; 60600S. doi:10.1117/12.650880

64. Soares, T.; Uliana, C. H.; Zanoni, J. N. Glutathione promoves myenteric neuroprotection in the jejunum of diabetic rats. In *Proceedings of the International neurogastroenterology and motility meeting,* 2012, Bologna, Italy; pp 43–190. doi:10.1111/j.1365-2982.2012.01997.x

65. Faloutsos, C.; Lin, K.-I. FastMap: A fast algorithm for indexing, data-mining and visualization of traditional and multimedia datasets. In *Proceedings of the 1995 ACM SIGMOD international conference on Management of data,* San Jose, U.S.A.; pp 163–174. doi:10.1145/568271.223812

66. Daikuzono, C. M.; Shimizu, F. M.; Manzoli, A.; Riul, A., Jr.; Piazzetta, M. H. O.; Gobbi, A. L.; Correa, D. S.; Paulovich, F. V.; Oliveira, O. N., Jr. *ACS Appl. Mater. Interfaces* **2017,** *9,* 19646–19652. doi:10.1021/acsami.7b04252

67. Tan, P.-N.; Steinbach, M.; Kumar, V. Instructor's Solution Manual. *Introduction to Data Mining;* Pearson Addison-Wesley, 2006.

68. Rousseeuw, P. J. *J. Comput. Appl. Math.* **1987,** *20,* 53–65. doi:10.1016/0377-0427(87)90125-7

Small protein sequences can induce cellular uptake of complex nanohybrids

Jan-Philip Merkl[*1,2,3], Malak Safi[1,4], Christian Schmidtke[2,3], Fadi Aldeek[1,5], Johannes Ostermann[2,6], Tatiana Domitrovic[7,8], Sebastian Gärtner[2,9], John E. Johnson[8], Horst Weller[2,3,6] and Hedi Mattoussi[1]

Letter

Address:
[1]Department of Chemistry and Biochemistry, Florida State University, 95 Chieftan Way, Tallahassee, Florida 32306, United States, [2]Institute of Physical Chemistry; University of Hamburg, Grindelallee 117, 20146 Hamburg, Germany, [3]The Hamburg Center for Ultrafast Imaging, University of Hamburg, Luruper Chaussee 149, 22761 Hamburg, Germany, [4]Laboratoire Physique des Solides, UMR 8502, Université de Paris Sud bât 510, 91405 Orsay Cedex, France, [5]Altria Center for Research and Technology, 601 E Jackson Street, Richmond, VA, 23219, United States, [6]Center for Applied Nanotechnology (CAN) GmbH, Grindelallee 117, 20146 Hamburg, Germany, [7]Instituto de Microbiologia Paulo de Goes, Universidade Federal do Rio de Janeiro, 310. Lab I014, 21941-902, Rio de Janeiro, Brazil, [8]The Scripps Research Institute, Department of Integrative Structural and Computational Biology, MB31, La Jolla, California 92037, United States and [9]Universitätsklinikum Hamburg Eppendorf, 20246, Martinistraße 52, 20251 Hamburg, Germany

Email:
Jan-Philip Merkl[*] - janphilip.merkl@gmail.com

* Corresponding author

Keywords:
bioconjugation; cellular uptake; nanoparticle hybrids; polymer encapsulation; self-assembly

Abstract

In this letter, we report on the ability of functional fusion proteins presenting a lytic gamma peptide, to promote interactions with HeLa cells and delivery of large hybrid nanostructures.

Introduction

Developing hybrid nanostructures made of more than one component nanomaterial, combined with biomolecules is a highly sought goal in biomedical science, and can find applications in multimodal imaging and therapeutics [1,2]. Although interest in developing such hybrid nanostructures by, for example, combining plasmonic and fluorescent, or magnetic and fluorescent nanoparticles have attracted much attention for the development of bioassays, their use as cellular labelling platforms has

been less explored [2,3]. A few demonstrations describing the use of such hybrid nanostructures in cell labelling have been recently reported. In one study, Jana and co-workers reported the design of fluorescent and plasmonic nanohybrids by covalent attachment of luminescent quantum dots (QDs) and Au nanorods. Further functionalization with glucose, using glutaraldehyde coupling chemistry, yielded nanohybrids that could subsequently be used for the staining of cell membranes [4]. In two separate studies, Chan and co-workers described two interesting hybrid systems. In the first, a charge driven self-assembly of AuNPs and different-colour QDs into multicolour, non-blinking nanohybrids was introduced. These nanohybrids were then coupled to various proteins, and among them the human transferrin protein was found to induce the highest intracellular uptake following 24 h incubation of these hybrids with cell cultures [5]. In the second, functional colloidal superstructures assembled using DNA linkers elicited a reduction in the response of macrophages to these hybrid materials combined with an improvement in their in vivo tumour accumulation [6]. Weil and co-workers described the use of multimodal platforms, made of diamond dots combined with gold nanoparticles, as imaging probes of live cell cultures [7]. We have recently characterized a hybrid system consisting of self-assembled gold nanoparticles (AuNPs) and polymer-encapsulated QDs. These constructs were further functionalized with polyhistidine-tagged proteins, yielding functional conjugates that exhibit fluorescent and plasmonic properties [8].

Over the last two decades several groups have investigated mechanisms for intracellular-uptake and in vivo biodistribution of various nanomaterials [9-11]. Due to the complexity of nanostructured materials combined with the intricacy of cell biology, it has been proven very difficult to develop a good understanding of what controls the processes involved in the intracellular uptake and ensuing distribution of various nanomaterials [9]. Several studies have consistently found that NPs are very often taken up by endocytosis, and once inside the cells they remain trapped within endosomal compartments [10,12]. A few other studies reported that a sizable fraction of the delivered nanoparticles can end up in the cytoplasm, by either circumventing endocytosis through the use of virus-derived peptide sequences, or non-disruptively penetrating the cellular membranes [13]. Escape from endosomal vesicles of once endocytosed nanoparticles have also been discussed [12,14,15].

More recently, there have been a few reports discussing the use of luminescent Eu-loaded hydroxyapatite nanocrystals for rapid HeLa cancer cell imaging [9,11,16], or the nanostructure self-assembly driven by amino acid coordination to increase the biological stability and tumour accumulation of curcumin [17]. Overall, there is a consensus that using colloidally stable nano-

particles is crucial for understanding and controlling cellular uptake, because materials that are prone to aggregation show higher non-specific interactions with biological fluids and cell membranes [18,19].

Here, we report on the use of a lytic gamma peptide (γ-peptide) derived from the *Nudaurelia Capensis Omega* virus (NωV), which was genetically fused onto maltose binding protein appended with 6-histidine tag, (His$_6$-MBP-γ), to promote the intracellular delivery of hybrid QD-AuNP assemblies [20,21]. This peptide is produced during viral capsid maturation and is thought to enable cellular internalization of the virus. It has been shown that the MBP-fused γ-peptide is able to disrupt artificial liposomes [20,21]. Recently, we have used this His$_6$-MBP-γ to promote the uptake of QDs by mammalian cells [22]. Here, we expand this approach to test the peptide capacity to promote the intracellular uptake of more complex hybrid nanostructures made of self-assembled QDs and AuNPs.

Results and Discussion

The biologically active plasmonic–fluorescent hybrids were formed using a self-assembly route which relies on direct metal-coordination interactions. Here, amine-to-gold and imidazole-to-gold coordination were applied to couple QDs and AuNPs, or to conjugate His$_6$-MBP-γ onto the AuNPs, respectively [8,23]. AuNPs stabilized with zwitterion-modified lipoic acid (LA-ZW-AuNPs) were selected for this study, due to their compact size, enhanced colloidal stability, and reduced non-specific interactions in biological media [22,24-31]. The central QDs used to build up the hybrid assemblies were prepared via encapsulation within a polymer coating made of an amine-functionalized polyisoprene-*block*-polyethylene oxide (PI-*b*-PEO-NH$_2$). The lateral amine groups allowed attachments to AuNPs, which then served for the immobilization of a few His$_6$-MBP-γ, as schematically shown in Figure 1A.

To demonstrate the potential utility of this nanohybrid system in biology, colloidal stability studies in culture media were first carried out. We found no sign of aggregation build up for at least 5 hours, as verified using dynamic light scattering measurements, where mono-modal autocorrelation function along with a single intensity vs hydrodynamic size peak (i.e., Laplace transform profile) were acquired (see Figure 1B) [17]. The hydrodynamic diameter of the entire nanohybrid is approx. 90 nm; this is larger than the values measured for LA-ZW-AuNPs ($D_H \approx 10$ nm) and for QD-NH$_2$ ($D_H \approx 30$ nm) and the dimension of the MBP (an ellipsoidal with overall dimensions of ≈3 × 4 × 6.5 nm) [8,32]. In a control experiment, using citrate-stabilized AuNPs in a similar assay, the hybrid self-assembly precipitated within few minutes. This behaviour is attributed to the nature of the citrate coating (weak stabilizer),

Figure 1: (A) Schematic representation of the nanohybrids (not to scale). The central QD (red, yellow, blue = core/shell/shell) is embedded in a cross-linked polymer micelle, consisting of a hydrophobic block (red) and an amphiphilic block (PEO). Interaction of the QDs with AuNPs (purple) is driven by the amine functional group. Gold nanoparticles are His-conjugated to His$_6$-MBP-γ. The entire nanohybrid has a hydrodynamic diameter of ≈90 nm. (B) Profiles of the intensity autocorrelation function, collected from a dispersion of the nanohybrids in Dulbecco's Modified Eagle Medium (DMEM) media, at various time intervals over a period of 5 h. The profiles are unchanged, indicating colloidal stability. (C) Binding of the nanohybrids (presenting MBP-γ) onto an amylose column; the fluorescent and pinkish band reflect the presence of QDs and AuNPs. (D) A representative epifluorescence image of fixed HeLa cells after incubation with the nanohybrids at c(QD) = 100 nM and 14 His$_6$-MBP-γ equiv/AuNP, scale bar = 50 μm. (E) Confocal microscopy images of HeLa cells incubated with nanohybrids for 1 h; c(QD) = 50 nM and 7 His$_6$-MBP-γ equiv/AuNP. 60× magnification was used. Scale bar = 20 μm. (Top panels) data correspond to nanohybrids containing His$_6$-MBP (no γ-peptide); (bottom panels) correspond to nanohybrids with His$_6$-MBP-γ. Shown are differential interference contrast (DIC), 4′,6-Diamidino-2-phenylindol (DAPI), Cy5-red, and yellow QD channels, along with the merged images. Figure 1A adapted with permission from [8], copyright 2016 American Chemical Society.

and further proves that using LA-ZW-AuNPs enhances their colloidal stability of the whole assembly, yielding a platform suitable for investigating interactions with cells. Further details on the stability under additional conditions are provided in Supporting Information File 1.

We first tested the biological activity of the His$_6$-MBP-γ in the hybrids, as done in reference [30]. We found that once uploaded onto an amylose-filled column, the nanohybrid stayed tightly bound to the column even after several washes with buffer. The bimodal character of the hybrid is reflected in the pinkish colour of the AuNPs and the fluorescence of the QDs of the immobilized band in the amylose column (see Figure 1C). The band could be readily released by adding a few mL (10–20) of maltose solution. This release is promoted by the stronger affinity of maltose (the substrate for MBP) to the bound His$_6$-MBP-γ. Overall, this experiment clearly proves that the nanohybrids contain MBP and that the bound MBP stays functional [8,23,28]. Further details are available in Supporting Information File 1.

After confirming the structural integrity and colloidal stability of the nanohybrids, we then proceeded to probe their interactions with HeLa cell cultures. For this, dispersions made of consisting of 100 nM QD solution, 2 equivalents of LA-ZW-AuNP per QD and 14 equivalents His$_6$-MBP-γ per AuNPs, were incubated with the cell culture for 1 h. Following rinsing the culture was imaged using epifluorescence and confocal fluorescence microscopy. A pronounced intracellular uptake of the hybrids was observed, as indicated by the significant fluorescence staining of the cells (see Figure 1D). Additional confocal images collected from two sets of cultures, one incubated with nanohybrids prepared with His$_6$-MBP-γ and the other with His$_6$-MBP (gamma-free MBP), and serving as control. Only the culture incubated with nanohybrids prepared with His$_6$-MBP-γ yielded pronounced intracellular staining; the control cultures did not show any cellular uptake (see Figure 1D and Figures S3 and S4 in Supporting Information File 1). In addition, the distribution of the QD staining (shown in Figure 1E, top panels) is not fully overlapped with the endosomal compartments counterstained with a red dye.

We tested the effects of decreasing the overall concentration of the nanohybrids or the number of MBP-γ per nanohybrid assembly on the staining levels of the cells. We found that reducing the overall concentration of the overall hybrids, the QD-to-AuNP molar ratio in the hybrids, the incubation time to 30 min, resulted in significantly lower levels of intracellular QD staining. Flow cytometry measurements showed that under these modified conditions approx. 20% of the cells are labelled with the nanohybrids. In comparison, no signal was measured from cells incubated with nanohybrids prepared in the absence of His$_6$-MBP-γ (Figure S5 in Supporting Information File 1).

To gain further insight into the distribution of QD stain, we visualized the cell cultures incubated with a lower nanohybrid concentration and lower MBP-γ loading of per nano-assembly, using confocal microscopy (Figure 1E). A close examination of the images allows us to distinguish three different colour distributions: the cell nuclei shown in blue (stained with DAPI), the endosomal compartments counterstained in red (labelled with Cy5-transferin), and QDs in yellow. The images clearly indicate that QDs and Cy5-transferrin do not co-localize. In addition, the dark signals observed in bright field mode, coincide with the yellow fluorescence emitted when we switch to fluorescence mode. This indicates that these spot signals are assemblies of multiple hybrid particles, containing AuNPs and encapsulated QDs [3]. Similar features were reported in a recent publication of the Jana group [4]. Due to the colloidal stability of these constructs as verified by DLS, we assume that the appearance of these rather large structures/patterns is due to the *cellular fate* of these structures rather than appearance in solution. The confocal microscopy data were further exploited to generate a z-stack, to visualize the fluorescence distribution of the nanocomposites side-by-side with that of the Cy5 dye and cell nuclei. The 3D-stack, shown in Figure 2A, confirms that distribution of the internalized nanohybrids (yellow staining) is distinct from that of the endosomes (counterstained in red). This provides further confirmation of the data shown in Figure 1E, demonstrating that the nanohybrids are not trapped within endocytic vesicles.

The respective signals were further identified using spectral resolution of the emission associated with the three chromophores. The spectral scan of one confocal plane (in Figure 2B) shows different locations for the nanohybrids (yellow), endosomal marker (red), and cell nuclei (blue). Spectral unmixing was also applied to a region, where the QD fluorescence staining is close to the Cy5-transferrin associated with the endosomal marker (Figure 2C). The two stainings corresponding to the nanohybrids and Cy-5-transferrin do not share the same compartments. Clearly, these findings combined show that the nanocomposites, when internalized, are found in sub-
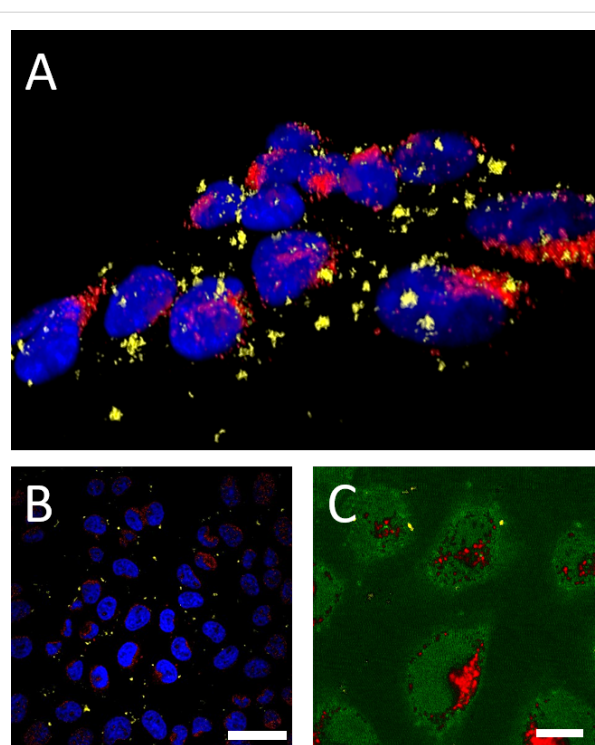
Figure 2: Confocal z-stack image of HeLa cells. (A) Volume view of the confocal z-stack showing blue: DAPI, red: endosomal marker Cy5, yellow: QD signal. (B) Spectral scan of one confocal plane (same colour code, scale bar 50 µm) (C) spectral unmixing of QD fluorescence (575 nm) and Cy5-spectrum (red) highlighting no superposition between the QD and the Cy5 signal, scale bar 10 µm.

cellular compartments that are distinct from those stained with the Cy5-transferrin. These results are in good agreement with our previous findings reported in reference [22]. These results suggest that the mechanism of cellular uptake promoted by the gamma peptide may not be driven by endocytosis [22]. Nonetheless, the distribution of the QD fluorescence is still different from that expected for a pure cytosolic delivery, where a more homogeneous distribution of the signal would be expected [33]. Whether these findings are due to the cellular response on the NP-based structure of the hybrid, or they reflect the typical cellular fate of a non-enveloped virus is a question that cannot be easily addressed. However, it is worth noting that even a small amount of γ-peptide (an average of ≈7 γ-peptide per nanohybrid) can promote the uptake of nanohybrids, which hydrodynamic size exceeds both the QD construct of our previous study (d(QD-LA) ≈ 10–15 nm [22]) or the virus particle itself (*d* ≈ 40 nm [21]).

Experimental

In brief, the functionalized polymer-encapsulated quantum dots were left to incubate with partially capped gold nanoparticles. This conjugate was subsequently functionalized with His$_6$-MBP-γ using self-assembly processes. For controls His$_6$-MBP

was used. The processes are described in more detail in Supporting Information File 1. In reference [8] further details on the hybrid characterization can be found.

Supporting Information

Expression of the fusion protein His$_6$-MBP-gamma, particle synthesize, hybrid assembly and characterization, DLS characterization and colloidal stability assessment, cellular incubation, amylose column, HeLa cellular culture, epifluorescence z-stack, epifluorescence control experiments, flow cytometry, further instrumentation.

Supporting Information File 1

Additional experimental data.
[https://www.beilstein-journals.org/bjnano/content/
supplementary/2190-4286-10-238-S1.pdf]

Acknowledgements

ORCID® iDs

Jan-Philip Merkl - https://orcid.org/0000-0003-4856-967X

Preprint

A non-peer-reviewed version of this article has been previously published as a preprint doi:10.3762/bxiv.2019.111.v1

References

1. Sailor, M. J.; Park, J.-H. *Adv. Mater. (Weinheim, Ger.)* **2012,** *24,* 3779–3802. doi:10.1002/adma.201200653
2. Bigall, N. C.; Parak, W. J.; Dorfs, D. *Nano Today* **2012,** *7,* 282–296. doi:10.1016/j.nantod.2012.06.007
3. Stender, A. S.; Marchuk, K.; Liu, C.; Sander, S.; Meyer, M. W.; Smith, E. A.; Neupane, B.; Wang, G.; Li, J.; Cheng, J.-X.; Huang, B.; Fang, N. *Chem. Rev.* **2013,** *113,* 2469–2527. doi:10.1021/cr300336e
4. Basiruddin, S.; Maity, A. R.; Saha, A.; Jana, N. R. *J. Phys. Chem. C* **2011,** *115,* 19612–19620. doi:10.1021/jp206641k
5. Song, F.; Tang, P. S.; Durst, H.; Cramb, D. T.; Chan, W. C. W. *Angew. Chem., Int. Ed.* **2012,** *51,* 8773–8777. doi:10.1002/anie.201201872
6. Chou, L. Y. T.; Zagorovsky, K.; Chan, W. C. W. *Nat. Nanotechnol.* **2014,** *9,* 148–155. doi:10.1038/nnano.2013.309
7. Liu, W.; Naydenov, B.; Chakrabortty, S.; Wuensch, B.; Hübner, K.; Ritz, S.; Cölfen, H.; Barth, H.; Koynov, K.; Qi, H.; Leiter, R.; Reuter, R.; Wrachtrup, J.; Boldt, F.; Scheuer, J.; Kaiser, U.; Sison, M.; Lasser, T.; Tinnefeld, P.; Jelezko, F.; Walther, P.; Wu, Y.; Weil, T. *Nano Lett.* **2016,** *16,* 6236–6244. doi:10.1021/acs.nanolett.6b02456
8. Merkl, J.-P.; Schmidtke, C.; Aldeek, F.; Safi, M.; Feld, A.; Kloust, H.; Mattoussi, H.; Lange, H.; Weller, H. *J. Phys. Chem. C* **2016,** *120,* 25732–25741. doi:10.1021/acs.jpcc.6b05204
9. Nazarenus, M.; Zhang, Q.; Soliman, M. G.; del Pino, P.; Pelaz, B.; Carregal-Romero, S.; Rejman, J.; Rothen-Rutishauser, B.; Clift, M. J. D.; Zellner, R.; Nienhaus, G. U.; Delehanty, J. B.; Medintz, I. L.; Parak, W. J. *Beilstein J. Nanotechnol.* **2014,** *5,* 1477–1490. doi:10.3762/bjnano.5.161
10. Iversen, T.-G.; Skotland, T.; Sandvig, K. *Nano Today* **2011,** *6,* 176–185. doi:10.1016/j.nantod.2011.02.003
11. Wilhelm, S.; Tavares, A. J.; Dai, Q.; Ohta, S.; Audet, J.; Dvorak, H. F.; Chan, W. C. W. *Nat. Rev. Mater.* **2016,** *1,* 16014. doi:10.1038/natrevmats.2016.14
12. Treuel, L.; Jiang, X.; Nienhaus, G. U. *J. R. Soc., Interface* **2013,** *10,* 1742–1762. doi:10.1098/rsif.2012.0939
13. Sousa, A. A.; Hassan, S. A.; Knittel, L. L.; Balbo, A.; Aronova, M. A.; Brown, P. H.; Schuck, P.; Leapman, R. D. *Nanoscale* **2016,** *8,* 6577–6588. doi:10.1039/c5nr07642k
14. Cabane, E.; Zhang, X.; Langowska, K.; Palivan, C. G.; Meier, W. *Biointerphases* **2012,** *7,* 9. doi:10.1007/s13758-011-0009-3
15. Delehanty, J. B.; Mattoussi, H.; Medintz, I. L. *Anal. Bioanal. Chem.* **2009,** *393,* 1091–1105. doi:10.1007/s00216-008-2410-4
16. Kataoka, T.; Abe, S.; Tagaya, M. *ACS Appl. Mater. Interfaces* **2019,** *11,* 8915–8927. doi:10.1021/acsami.8b22740
17. Li, Y.; Zou, Q.; Yuan, C.; Li, S.; Xing, R.; Yan, X. *Angew. Chem., Int. Ed.* **2018,** *57,* 17084–17088. doi:10.1002/anie.201810087
18. Safi, M.; Courtois, J.; Seigneuret, M.; Conjeaud, H.; Berret, J.-F. *Biomaterials* **2011,** *32,* 9353–9363. doi:10.1016/j.biomaterials.2011.08.048
19. Walkey, C. D.; Olsen, J. B.; Song, F.; Liu, R.; Guo, H.; Olsen, D. W. H.; Cohen, Y.; Emili, A.; Chan, W. C. W. *ACS Nano* **2014,** *8,* 2439–2455. doi:10.1021/nn406018q
20. Canady, M. A.; Tihova, M.; Hanzlik, T. N.; Johnson, J. E.; Yeager, M. *J. Mol. Biol.* **2000,** *299,* 573–584. doi:10.1006/jmbi.2000.3723
21. Domitrovic, T.; Matsui, T.; Johnson, J. E. *J. Virol.* **2012,** *86,* 9976–9982. doi:10.1128/jvi.01089-12
22. Safi, M.; Domitrovic, T.; Kapur, A.; Zhan, N.; Aldeek, F.; Johnson, J. E.; Mattoussi, H. *Bioconjugate Chem.* **2017,** *28,* 64–74. doi:10.1021/acs.bioconjchem.6b00609
23. Aldeek, F.; Muhammed, M. A. H.; Palui, G.; Zhan, N.; Mattoussi, H. *ACS Nano* **2013,** *7,* 2509–2521. doi:10.1021/nn305856t
24. Ashraf, S.; Park, J.; Bichelberger, M. A.; Kantner, K.; Hartmann, R.; Maffre, P.; Said, A. H.; Feliu, N.; Lee, J.; Lee, D.; Nienhaus, G. U.; Kim, S.; Parak, W. J. *Nanoscale* **2016,** *8,* 17794–17800. doi:10.1039/c6nr05805a
25. Han, H.-S.; Martin, J. D.; Lee, J.; Harris, D. K.; Fukumura, D.; Jain, R. K.; Bawendi, M. *Angew. Chem., Int. Ed.* **2013,** *52,* 1414–1419. doi:10.1002/anie.201208331

26. García, K. P.; Zarschler, K.; Barbaro, L.; Barreto, J. A.; O'Malley, W.; Spiccia, L.; Stephan, H.; Graham, B. *Small* **2014,** *10,* 2516–2529. doi:10.1002/smll.201303540

27. Moyano, D. F.; Saha, K.; Prakash, G.; Yan, B.; Kong, H.; Yazdani, M.; Rotello, V. M. *ACS Nano* **2014,** *8,* 6748–6755. doi:10.1021/nn5006478

28. Zhan, N.; Palui, G.; Grise, H.; Tang, H.; Alabugin, I.; Mattoussi, H. *ACS Appl. Mater. Interfaces* **2013,** *5,* 2861–2869. doi:10.1021/am302788q

29. Zhan, N.; Palui, G.; Mattoussi, H. *Nat. Protoc.* **2015,** *10,* 859–874. doi:10.1038/nprot.2015.050

30. Aldeek, F.; Safi, M.; Zhan, N.; Palui, G.; Mattoussi, H. *ACS Nano* **2013,** *7,* 10197–10210. doi:10.1021/nn404479h

31. Perng, W.; Palui, G.; Wang, W.; Mattoussi, H. *Bioconjugate Chem.* **2019,** *30,* 2469–2480. doi:10.1021/acs.bioconjchem.9b00549

32. Sburlino, J. C.; Lu, G. Y.; Quiocho, F. A. *J. Biol. Chem.* **1991,** *266,* 5202–5219.

33. Kapur, A.; Medina, S. H.; Wang, W.; Palui, G.; Ji, X.; Schneider, J. P.; Mattoussi, H. *ACS Omega* **2018,** *3,* 17164–17172. doi:10.1021/acsomega.8b02918

Molecular architectonics of DNA for functional nanoarchitectures

Debasis Ghosh, Lakshmi P. Datta and Thimmaiah Govindaraju[*]

Abstract

DNA is the key biomolecule central to almost all processes in living organisms. The eccentric idea of utilizing DNA as a material building block in molecular and structural engineering led to the creation of numerous molecular-assembly systems and materials at the nanoscale. The molecular structure of DNA is believed to have evolved over billions of years, with structure and stability optimizations that allow life forms to sustain through the storage and transmission of genetic information with fidelity. The nanoscale structural characteristics of DNA (2 nm thickness and ca. 40–50 nm persistence length) have inspired the creation of numerous functional patterns and architectures through noncovalent conventional and unconventional base pairings as well as through mutual templating-interactions with small organic molecules and metal ions. The recent advancements in structural DNA nanotechnology allowed researchers to design new DNA-based functional materials with chemical and biological properties distinct from their parent components. The modulation of structural and functional properties of hybrid DNA ensembles of small functional molecules (SFMs) and short oligonucleotides by adapting the principles of molecular architectonics enabled the creation of novel DNA nanoarchitectures with potential applications, which has been termed as templated DNA nanotechnology or functional DNA nanoarchitectonics. This review highlights the molecular architectonics-guided design principles and applications of the derived DNA nanoarchitectures. The advantages and ability of functional DNA nanoarchitectonics to overcome the trivial drawbacks of classical DNA nanotechnology to fulfill realistic and practical applications are highlighted, and an outlook on future developments is presented.

Review

Introduction

The development of functional molecular systems and materials on a nanoscale through custom design and engineering of molecular organization is a highly attractive concept in materials science [1,2]. Exploitation of biomolecules and their in-built information for molecular recognition to engineer ordered assemblies and coassemblies of SFMs is termed as molecular architectonics [3,4]. The construction of molecular architectures through the controlled assembly of designed molecular units with fascinating properties and functions is central to all materials and bioengineering processes [1-4]. The use of biomolecules or synthetic systems with biomolecular components is capable of aiding the judicious regulation of molecular assembly parameters and properties to construct novel functional architectures in the scheme of molecular architectonics [1,2]. Among all biomolecules, DNA, with a well-defined structure, is the epitome of molecular recognition and a robust system for molecular and materials engineering. The molecular stability, predictable sequence specificity, molecular recognition properties, and the formation of regular and defined structures of DNA made it possible to custom the design and to engineer a range of molecular architectures [5-9]. In DNA, two polydeoxyoligonucleotides (single-stranded DNA, ssDNA) are held together by complementary or conventional Watson–Crick (WC) base pairing interactions (Figure 1). In WC base pairing interactions, adenine (A) and thymine (T) form a doubly hydro-

gen-bonded base pair (A=T), while guanine (G) and cytosine (C) form a triply hydrogen-bonded base pair (G≡C) [10]. The hydrogen bonding-mediated base pairing geometry is conditional on the conformation of the glycoside bonds and interactive hydrogen bonding sites. Apart from WC hydrogen bonding, unconventional hydrogen bonding, electrostatic, and metal ion interactions play a significant role in the formation of noncanonical DNA architectures (Figure 1) [5]. The noncanonical hydrogen bonding interactions are responsible for the formation of a range of higher-ordered DNA structures. In particular, the double-stranded DNA duplex is a perfect nanoscale molecular architecture with a 2 nm thick rigid structure and a persistence length of ca. 40–50 nm. Moreover, ssDNA sequences can be used as molecular glue to construct diverse and well-defined nanoarchitectures. In this context, Seeman and co-workers introduced the disruptive idea of using DNA as a molecular building block to design and construct nanosystems and materials, which paved the way for the celebrated area of DNA nanotechnology [11]. Nevertheless, the nanoscale structural features of DNA have inspired the design of diverse functional architectures utilizing both conventional and unconventional base pairing along with the mutually templating interactions of SFMs and metal ions [12]. The field of DNA nanotechnology has evolved over the years from using DNA tiles and blocks to employing SFMs and their assemblies as templates to
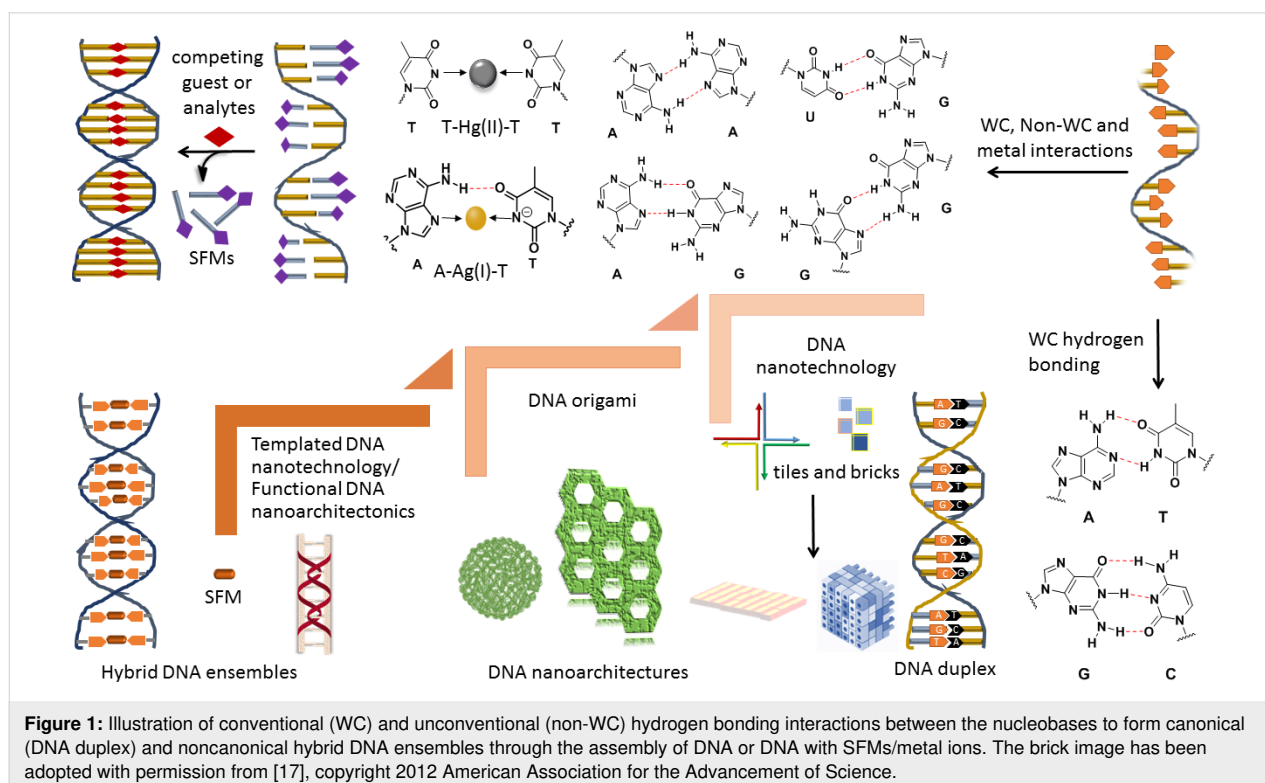

Figure 1: Illustration of conventional (WC) and unconventional (non-WC) hydrogen bonding interactions between the nucleobases to form canonical (DNA duplex) and noncanonical hybrid DNA ensembles through the assembly of DNA or DNA with SFMs/metal ions. The brick image has been adopted with permission from [17], copyright 2012 American Association for the Advancement of Science.

control the molecular organization on the nanoscale to generate complex DNA architectures or origami and hybrid ensembles, respectively, through the judicious exploitation of conventional and nonconventional base pairing interactions [12,13].

The field of DNA nanotechnology was further advanced by the DNA origami concept introduced by Rothemund and co-workers [14,15]. Intertwining and congregation of more than one DNA strand to produce DNA tiles or bricks, which staple in a programmed fashion to form crystalline assembly structures with well-defined geometries, constitute the guiding principles of specific nucleobase pairing-driven DNA nanostructures (DNA nanotechnology) [16,17]. In other words, DNA origami involves the programmed folding of long DNA sequences to generate defined but complex shapes on the nanoscale. Despite the expeditious advancements in the field of DNA nanotechnology, utilization of long DNA sequences, complex computer-based design strategies, reproducibility, and the high cost involved in the entire process have become the limiting factors in the realization of practical applications. In this context, the emerging field of SFM-templated or mutually templated DNA nanotechnology (functional DNA nanoarchitectonics) is considered the state-of-art to construct hybrid DNA nanoarchitectures with assured functional properties and practical applications [12,13,18-21]. In functional DNA nanoarchitectonics, short oligonucleotides (ssDNA) with sequences of less than persistence length (ca. 40–50 nucleotides) are co-organized with SFMs or their assemblies to generate hybrid DNA ensembles [18,20]. The short oligonucleotides are inexpensive to synthesize in-house or commercially available, and their coassembly with SFMs assures to generate novel nanoarchitectures with functional properties and applications. Although the field of classical DNA nanotechnology exploited the supramolecular bottom-up self-assembly, the functional features can be integrated through mutually templated coassembly of SFMs and short ssDNA sequences in the emerging field of functional DNA nanoarchitectonics [22]. Remarkably, engineering molecular coassemblies of SFMs and ssDNA to generate functional DNA nanoarchitectures represents a seamless relationship between the molecular architectonics and nanoarchitectonics. The field of nanoarchitectonics has been introduced and pioneered by Aono and Ariga at NIMS, Japan, who reported numerous self-assembly approaches to construct a range of nanoarchitectures [23-30].

The understanding and controlling of noncovalent interactions on the molecular level to engineer the assembly and coassembly of molecular components is a challenging task. Therefore, molecular architectonics of biomolecules with designer SFMs is an interesting and reliable approach wherein biomolecules with in-built information for molecular recognition guide the func-

tional assembly and coassembly of SFMs. In essence, the molecular architectonics of DNA with SFMs to construct nanoarchitectures covers molecules to (nano)materials to functional applications. Typically, SFMs are suitably functionalized functional molecules with excellent optoelectronic properties that undergo π-stacking and support the co-organization of oligonucleotides to form hybrid DNA ensembles [18,20]. These hybrid DNA ensembles can be employed for a range of applications in the fields of materials science, nanotechnology, sensors, molecular or nanoelectronics, diagnostics, drug delivery, and biomedical sciences.

The remarkable molecular fidelity and sequence-specific molecular recognition make DNA the ideal candidate in the scheme of molecular architectonics to design and construct functional DNA nanoarchitectures. In this review, we attempted to cover the molecular architectonics of DNA, which comprises programmed self-assembly (DNA nanotechnology) and coassembly (templated DNA nanotechnology/functional DNA nanoarchitectonics) to produce diverse molecular and nanoarchitectures. The functional DNA nanoarchitectonics, encompassing the formation of functional hybrid DNA ensembles through coassembly of organic molecules (SFMs) and short oligonucleotides, is envisioned to overcome the limitations associated with classical DNA nanotechnology to realize practical applications [13]. The various design approaches of DNA self-assembly and coassembly that have been utilized to form novel nanostructures with a range of applications, from materials to biomedicine, are covered. The judicious exploitation of canonical and noncanonical base pairing interactions supported by various other noncovalent interactions for the creation of molecular and nanoarchitectures of DNA are highlighted. Overall, the aim of this article was to provide a brief overview on the molecular architectonics of DNA with respect to the historical perspective, the evolution of the celebrated area of DNA nanotechnology, and recent advancements in the form of functional DNA nanoarchitectonics to realize practical applications.

Classical DNA nanotechnology: programmed molecular self-assembly of DNA

The use of DNA as a building block for the construction of nanomaterials typically involves exploitation of the WC base pairing and predictability of the structural outcome owing to sequence specificity [31,32]. The DNA hybridization through WC base pairing (A=T and G≡C) effectively facilitates the programmability of the molecular self-assembly of DNA. In a standard WC base pairing-driven assembly, two complementary DNA strands anneal together to form a duplex structure. In a DNA hybridization process, the oligonucleotides with complementary base sequences are dissolved in a buffer solution and subject-

ed to annealing, which involves a cycle of heating the solution followed by cooling [31]. Seeman and co-workers envisioned the construction of 3D nanoarchitectures by utilizing DNA as a structural building block and hybridization (base pairing) as the 'glue' [33,34]. The initial attempts with ssDNA were compromised due to the lack of rigidity within ssDNA molecular systems. However, the higher-order double-stranded DNA systems exhibited higher rigidity as compared to ssDNA. The selection of the correct base pairing sequence and order enabled the assembly of DNA with balanced rigidity and flexibility within the nanomaterial systems. The maintenance of an exact stoichiometry and long annealing period were the major criteria to achieve defect-free architectures from long DNA sequences. Rothemund, Yan, and co-workers introduced the concept of assembling so-called scaffold and staple strands to construct functional geometric architectures [15,35]. In this process of DNA assembly, the long scaffold strand can adapt different geometries upon interaction with multiple staple strands. The advantages of this concept are that the preservation of exact stoichiometric ratios of ssDNA sequences is not necessary and that the assembly can be performed faster. The introduction of staple strands to the scaffold initiates the local folding, and further addition of multiple staple strands leads to strand displacement, thereby healing the mismatches in long DNA scaffold strands.
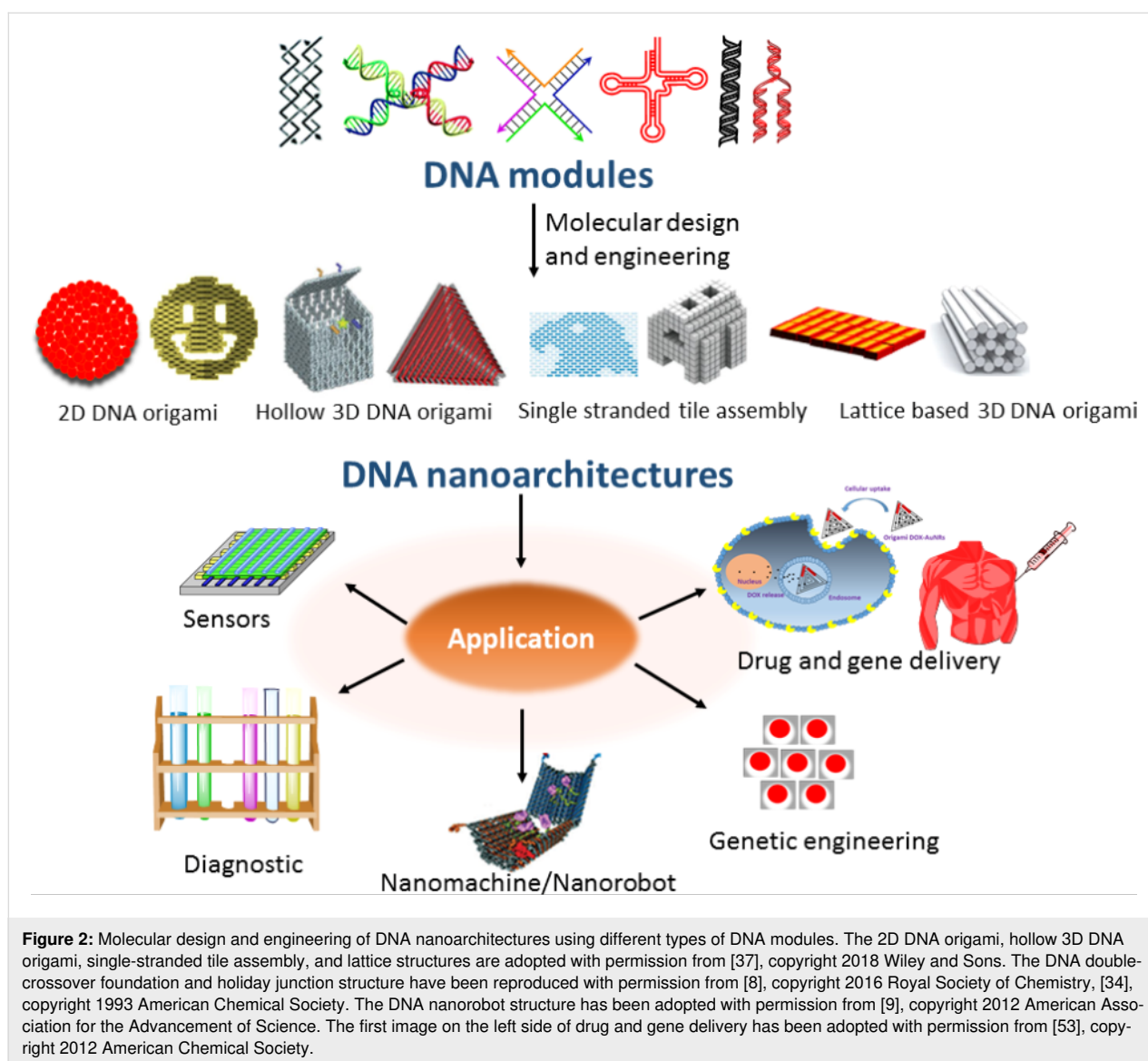
The sticky end cohesion method to create nanostructured ensembles is a radically different concept for DNA assembly [36]. The partial complementary feature of DNA used in this approach results in single-stranded overhang regions, so-called sticky ends. The binding interaction between two different but complementary sticky ends guides the sequential assembly of building blocks. The weak interactions, viz., hydrogen bonding and electrostatic interactions, act as driving forces for the assembly of building blocks to form ordered structures of DNA. Further, the self-assembly can be regulated by varying the extent of base pairing in double-stranded DNA or overhang regions of the building blocks. DNA nanotechnology has hugely benefitted from the recombinant DNA technology, which enabled the construction of complex architectonics through DNA origami [37]. The self-recognition characteristics of DNA allows the development of a wide array of DNA-based nanoarchitectures by employing an array of designer sequences and motifs. In the earliest designs, the Holliday junction structure of DNA was used to create nanostructured DNA materials [38,39]. The structural analysis of the self-assembled nanomaterials synthesized using junctional building blocks showed a compromised stability due to the sequence symmetry. The elimination of sequence symmetry is one of the most important criteria in DNA nanotechnology [40,41]. Exclusion of symmetry is equally important in DNA-based sequence and motif design. In the design of DNA nanomotifs, double-crossover tiles are designed specifically from ssDNA sequences. These double-crossover tiles have paved the way for the programmable construction of robust DNA nanoarchitectures with well-defined structural and functional properties. Moreover, the programed assembly of both single-stranded and double-stranded DNA can lead to the generation of a variety of nanoarchitectures with potential biological applications (Figure 2).

Diversity in DNA nanoarchitectures

The structural diversity of DNA nanoarchitectures is the most attractive feature of DNA nanotechnology. From the application perspective, DNA nanotechnology can be divided into static and dynamic categories [42,43]. In static DNA nanotechnology, the DNA strands are immobilized within particular geometries, patterns, or crystals that facilitate the positional assembly of nanoparticles along the DNA nanostructures [42]. The dynamic DNA nanotechnology includes DNA nanomachines with potential applications ranging from sensing to delivery and robotics [43]. Inspired by the complementary base pairing-directed DNA hybridization, 1D, 2D, and 3D DNA nanoarchitectures can be constructed through three major methods: i) DNA tile-based construction, ii) DNA origami, and iii) nanoparticle-templated procedures. The tile-based method relies on multiple crossover junctions, which utilize a small number of short DNA sequences and impart enough rigidity to assemble nanoarchitectures. The designed short DNA strands initiate the formation of double- and triple-crossover building block structures, which are further utilized to make diverse architectures through a combinatorial approach. Mao and co-workers exploited the tile-based strategy for the construction of three-point star motifs using three different DNA sequences [44]. In this design, each arm corresponded to a double-crossover motif and its assembly led to the formation of 3D wireframe polyhedrons, depending on the concentration and curvature of the motifs. The curvature and flexibility could be modulated through incorporation of hairpin loops. Zhang and co-workers reported new strategies for the design of DNA wireframe nanostructures wherein the single-stranded tile (SST) method facilitated the formation of tubular structures of variable dimensions [45].

As discussed earlier, the pioneering work by Rothemund and others opened the era of DNA origami that aided the construction of unique and most complex architectures [46]. The rectangular DNA origami was gaining momentum in recent times, which involved studies on molecular engineering of DNA using rectangular tiles connected via dangling DNA strands [47,48]. Yan and co-workers reported the construction of rectangular DNA origami nanoarchitectures in which the parallel strands

Figure 2: Molecular design and engineering of DNA nanoarchitectures using different types of DNA modules. The 2D DNA origami, hollow 3D DNA origami, single-stranded tile assembly, and lattice structures are adopted with permission from [37], copyright 2018 Wiley and Sons. The DNA double-crossover foundation and holiday junction structure have been reproduced with permission from [8], copyright 2016 Royal Society of Chemistry, [34], copyright 1993 American Chemical Society. The DNA nanorobot structure has been adopted with permission from [9], copyright 2012 American Association for the Advancement of Science. The first image on the left side of drug and gene delivery has been adopted with permission from [53], copyright 2012 American Chemical Society.

were assembled in a zigzag fashion along the DNA helical axis [46]. Endo and co-workers paved the way for creating X-shaped, Y-shaped, and asterisk-shaped structures using 2D and 3D DNA origami tiles [49,50]. The groups of Endo and Sungiyama showed that 2D origami architectures could be used as building blocks for the construction of 3D DNA origami [50]. Apart from creating a wide range of architectural shapes, DNA origami is anticipated to have possible applications in the fields of biosciences, the design of protein scaffolds, and plasmonics [51-53]. Shih and co-workers utilized DNA origami nanotechnology for the structural determination of plasma membrane proteins [54]. They reported the construction of detergent-resistant 0.8 µm-long liquid crystalline DNA nanotubes organized from a 7.3 kb scaffold strand and >170 short oligonucleotide-long staple strands. The liquid crystalline matrices of six helix DNA origami bundles induced a weak

alignment of proteins within the plasma membrane. The solubilization and weak alignment of proteins within plasma membrane are crucial to measure the residual dipolar couplings (RDCs), and the RDCs are crucial to obtain NMR structural information on membrane-bound proteins. As reported, DNA origami-based liquid crystalline media can overcome detergent-related compatibility problems to accurately measure RDCs.

DNA nanomachines or nanorobots are highly innovative and advanced versions of DNA-based molecular designs, which are intended to act and perform as machines with respect to internal or external stimuli. The pioneering design and development of DNA-based molecular machines was introduced by Seeman and co-workers in 1999 [55]. In this early and seminal work, it was shown that branched motifs of DNA can be exploited as switchable mechanical machines. DNA double-crossover (DX) tiles

were used to fabricate the molecular devices. The crossover points of the tiles were separated by a helical turn, which triggered the switchable motion of the device through B-to-Z-form transition, and the relative changes in position and transformation were monitored by the fluorescence resonance energy transfer (FRET) technique. Zhao and co-workers reported the design and construction of a DNA origami-based nanorobot for the cargo delivery of payloads into cancer cells [56]. The autonomous DNA nanorobot was constructed using a nucleolin-binding DNA aptamer and was loaded with thrombin protease. The nucleolin protein was overexpressed in tumor-associated endothelial cells, which triggered the mechanical opening of the DNA nanomachine, followed by the release of the cargo protease from the inner cavity to the targeted area. In vivo studies in mice demonstrated that the intravenously injected nanorobot could effectively deliver thrombin to tumor-associated blood vessels. The targeted delivery and nonimmunogenicity of the nanorobot made it a promising candidate for drug delivery in cancer therapeutics. The group of Krishnan reported the construction of a DNA nanodevice to quantitatively determine the activity and location of chloride ion channels and transport under pH stimuli [57]. In another work, they reported the construction of a DNA-based reporter nanomachine for quantitative imaging of lysosome [58]. This two-ion measurement (2-IM) method could image both pH and chloride ion variations in lysosomes. The 2-IM analysis was conducted on primary skin fibroblast cells derived from healthy and Neiman–Pick-diseased patients. The results showed significant differences in the lysosomal population in cells between the diseased and the healthy state. The group of Andersen reported a DNA nanobox with controllable lid, and its dynamic nature potentially facilitated the stimuli-responsive release of cargo molecules into the targeted area [59]. In another interesting design, DNA origami nanorobots were implanted into living systems and executed DNA-based biocomputing via dynamic cell-associated interactions [60]. An alteration of the physiological pH can be indicative of a diseased condition, and therefore monitoring physiological pH values with high sensitivity is required. Our group designed a molecular beacon (LMB) DNA device appended with a FRET pair as pH sensing probe in cells [19]. The remarkable feature of the LMB probe was the structural transition from a closed (molecular beacon) state to an open (A-motif) state in a pH-responsive manner within artificial vesicles and living cells. The DNA device was made up of 24 nucleobases, of which 12 adenine nucleobases were present within the loop region, and a closed molecular beacon structure was formed *via* two stretches of five complementary base pairs. Cy3 and Cy5 dyes acted as donor–acceptor FRET pair systems that were ligated at the 5' and 3' end of the duplex stem structure, respectively. Under normal physiological conditions, the closed hairpin structure of the LMB probe facilitated juxtaposi-

tion of the two dyes, followed by efficient FRET. In acidic pH, the N1 of adenine became protonated, which triggered the structural transition of the LMB device from a closed to an open state through reverse Hoogsteen base pairing and electrostatic interactions. The pH-responsive structural transition of LMB from a closed to an open state altered the FRET response, which was exploited for sensing of acidic pH (3–5.5) with a low step size (0.2–0.3) within synthetic vesicles that mimicked the intracellular environment. The in cellulo study in HeLa cells demonstrated the efficient cellular uptake of the DNA device without the need for a vector and provided efficient sensing of changes in the intracellular acidic pH value. In recent years, DNA thin film-based biosensors received significant interest for the detection of biologically relevant analytes, such has forensic samples [61,62]. The design of active electrochemical DNA sensors involves critical optimization of the sensor platforms. The length of the target oligonucleotide sequence and the selective use of dopants significantly dominate the sensing efficacy [63]. In this context, electrochemical DNA sensors were developed by noncovalent layer-by-layer assemblies of phenothiazine dyes and DNA for the detection of damaged DNA [64]. Apart from biological samples, the identification of volatile organic compounds is another important field gaining the attention of researchers. Hairpin DNA and peptide sequences were integrated in a sensor design strategy to develop an optoelectronic nose for the selective detection of volatile organic components [65].

DNA tetrahedron nanostructures

The structural analogy to virus particles makes DNA polyhedrons highly appealing architectures with biomimetic functional relevance. Among all polyhedrons, tetrahedrons are the simplest architectural scaffolds to construct and modulate structural and functional patterns. The tetrahedron with regular edges and acmes is a perfect architectural shape for the construction of DNA nanoarchitectures. The virus-mimetic feature of the DNA tetrahedron accounts for the facile cellular uptake via a caveolin-dependent pathway, while the rigid and sharp-edged features bestow the thermal and enzymatic stability. The construction of a DNA tetrahedron was first attempted by Turberfield and co-workers, wherein short oligonucleotide sequences were used for the bottom-up assembly process [66]. In addition to short oligonucleotide sequences, DNA tiles were also used to build DNA tetrahedrons. In another approach, DNA tetrahedron cages were prepared for efficient cellular uptake and imaging of live cells [67]. Human embryonic kidney (HEK) cells were cultured with a range of fluorescently tagged DNA tetrahedrons, and the subcellular localization was monitored. An organelle-staining study indicated the localization of the tetrahedrons within the cytoplasm and demonstrated efficient cellular uptake of DNA tetrahedrons without the need for any

transfection agents or procedures. One of the advantages of DNA tetrahedrons is that the edges can be covalently modified with several active functionalities or biomolecules. The groups of Shangguan and Tan reported on the biofunctionalization of metal nanoparticles using aptamer-appended DNA tetrahedron nanostructures [68]. The aptamer-appended tetrahedron structures were constructed using three 55 nucleotide-long carboxylic acid-linked DNA strands and a tumor-targeting 87 nucleotide-long aptamer. The carboxylic acid groups of the DNA tetrahedron facilitated the interaction with oleic acid-coated iron oxide nanoparticles via a ligand exchange reaction. The aptamer–DNA tetrahedron-functionalized iron oxide nano-particle system was capable of selectively targeting the cancer cells and, potentially, to act as an MRI contrast agent. The programmability of the DNA tetrahedrons provided an opportunity to conjugate other functional nucleic acid sequences, viz., DNA, siRNA, or DNAzymes, to serve as potential diagnostic or therapeutic (theranostic) nanoagents. Xu and co-workers demonstrated the derivation of a DNA tetrahedral electrolumi-nescence (ECL) biosensor probe for a functional biosensing assay (Figure 3) [69]. The ECL biosensor platform was constructed based on a DNA tetrahedral scaffold embedded with Ru(bpy)$_3^{2+}$-conjugated silica nanoparticles. The DNA tetrahedron geometry acted as a capture DNA that repelled the nonspecific DNA entanglement along the ECL platform and stimulated the hybridization of glucose oxidase (GOD) enzyme-conjugated DNA (GOD-S). In a programmable cyclic amplifi-cation pathway, the target DNA triggered the release of GOD-S that catalyzed glucose to form hydrogen peroxide, followed by changing the ECL signal. The ECL sensing solution was made up of tripropylamine (TPrA) and glucose (10 mM). The concen-tration of target DNA could easily be assessed by quantifying the ECL quenching via formation of hydrogen peroxide. Kim and co-workers developed an innovative approach of intercala-tion of the anticancer drug doxorubicin within the DNA tetrahe-dron that showed improved therapeutic efficacy in drug-resis-tant breast cancer cells [70]. The doxorubicin-encapsulated DNA tetrahedron system exhibited enhanced cellular uptake and outflanked the drug efflux process in multidrug-resistant cancer cells. The biocompatible features, natural degradability, and low immunogenicity made the DNA tetrahedron a poten-tial carrier platform for the delivery of drug cargos. Lee and co-workers showed that self-assembled DNA tetrahedron nanoarchitectures with narrow size distribution could deliver
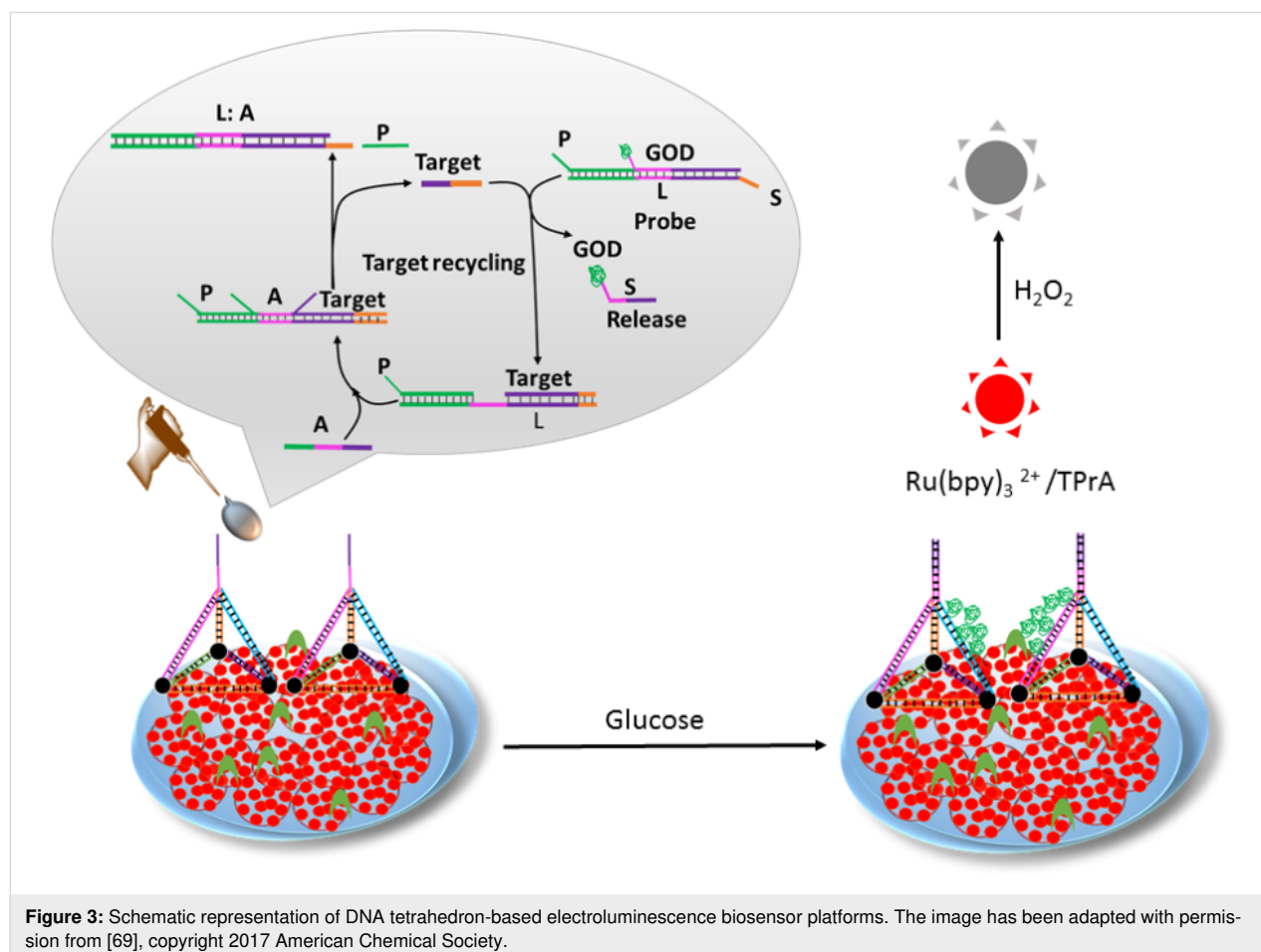

Figure 3: Schematic representation of DNA tetrahedron-based electroluminescence biosensor platforms. The image has been adapted with permis-sion from [69], copyright 2017 American Chemical Society.
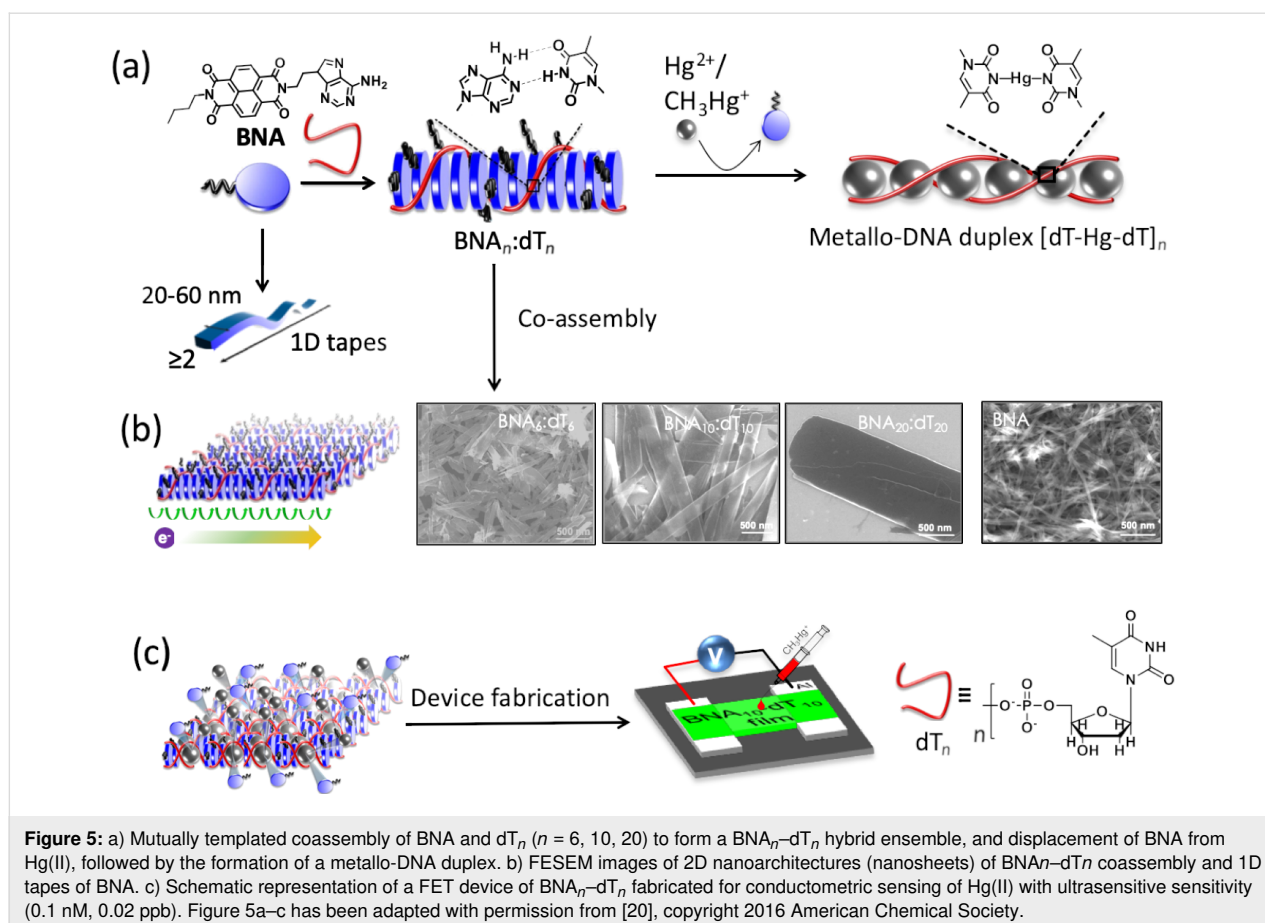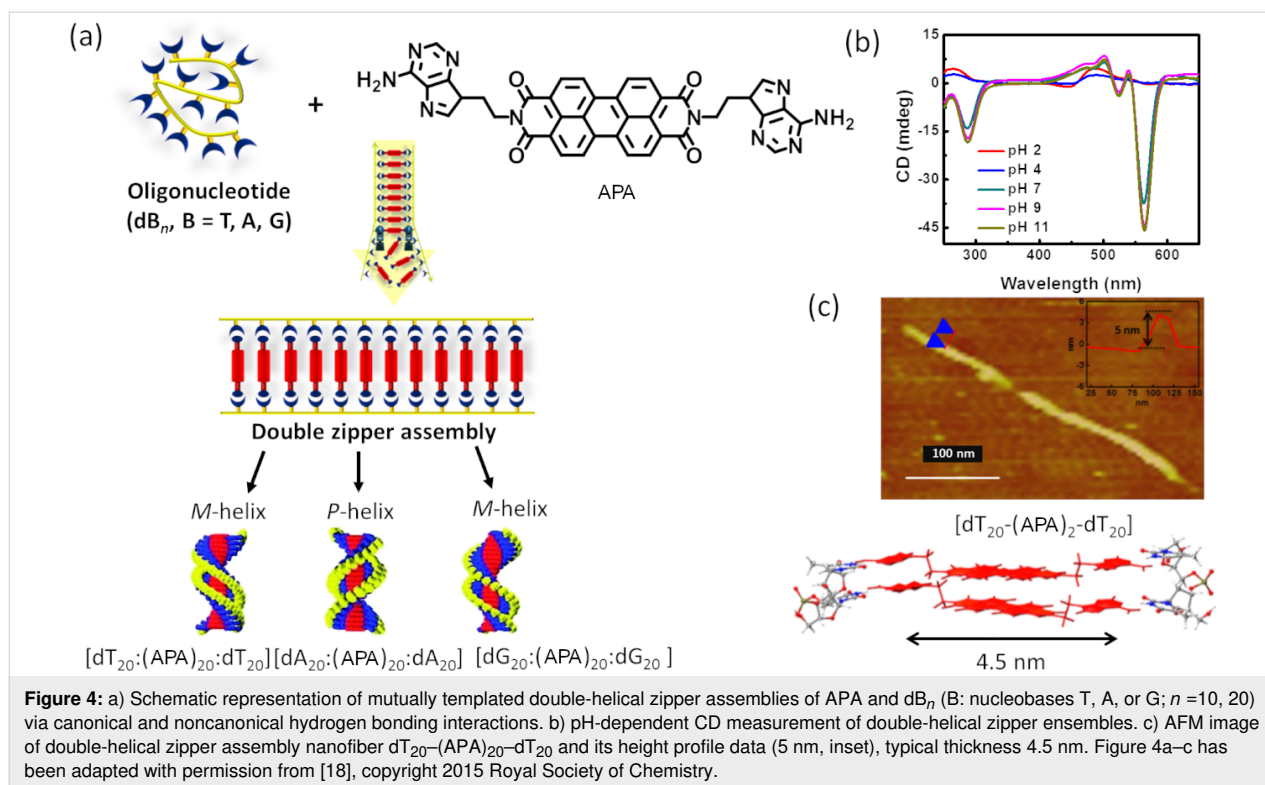
siRNA into tumor cells [71]. The programmable DNA strands were functionalized with tumor-targeting folate ligands. The nanoarchitecture consisted of six DNA strands having a total of 186 WC base pairs. The complementary overhang regions at the 3′ ends self-assembled to form tetrahedron nanoarchitectures. The edges of the tetrahedron were found to be thirty base pairs long and the height was ≈8 nm. The middle of each edge consisted of a nick with an overhang region whose sequence was exactly complementary to the siRNA sequence, and, typically, six siRNAs could be annealed with the tetrahedron unit. To ascertain the in vivo transfection efficiency of the siRNA-loaded DNA tetrahedron nanoarchitecture, pharmacokinetic profiling and organ biodistribution assays were conducted in xenograft tumor-bearing mice. The siRNA-conjugated DNA tetrahedron nanoarchitecture system was administered to mice by tail vein injection, and the quantitative accumulation was monitored by fluorescence molecular tomography imaging, combined with computed tomography. The imaging data showed accumulation of siRNA-loaded tetrahedrons at the tumor surface 25 min after injection. The siRNA-mediated gene silencing feature was monitored by performing an in vivo firefly luciferase gene expression analysis. The remarkable feature of this study was the one-step synthesis of hybrid DNA–siRNA tetrahedron nanoarchitectures and cation-free gene transfection ability.

Small-molecule-templated DNA nanoarchitectures

The molecular self-assembly of DNA through sequence-specific base pairing is extensively used to create complex nanoarchitectures with variable size and shape in the field of classical DNA nanotechnology. In spite of the possibility of creating complex nanoarchitectures through advanced design and programming, the use of long DNA sequences, high manufacturing cost, and reproducibility of the derived nanoarchitectures are some of the major concerns to be addressed in classical DNA nanotechnology or DNA origami for practical applications. In this context, the emerging field of templated DNA nanotechnology, or functional DNA nanoarchitectonics, is particularly appealing to overcome the trivial drawbacks of DNA nanotechnology in its original form [1,20,25]. The molecular architectonics of SFMs and DNA has enormous potential for the design and construction of SFM-mediated and mutually templated hybrid DNA ensembles and nanoarchitectures with assured functional properties and applications [13,20]. In particular, functional DNA nanoarchitectonic involves the coassembly of suitably designed SFMs and short oligonucleotides supported by canonical and noncanonical hydrogen bonding interactions. Apart from hydrogen bonding, aromatic π–π stacking, electrostatic, metal ion, and host–guest interactions facilitate the molecular coassembly of SFMs and short oligo-
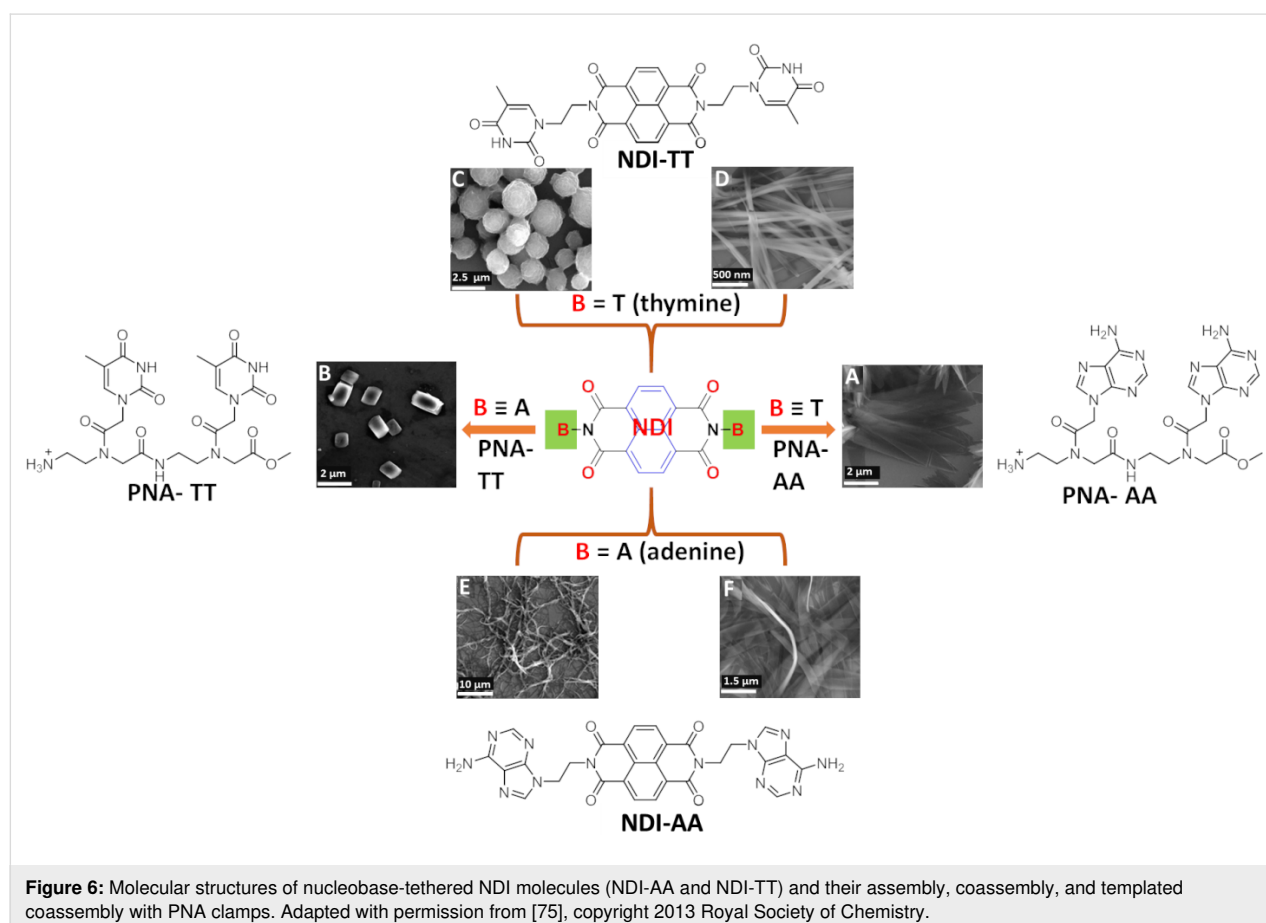
nucleotides. The π-conjugated arylenediimides with interesting optoelectronic properties, such as naphthalenediimide (NDI) and perylenediimide (PDI), are attractive SFMs to support zipper assembly of DNA via π stacking and hydrogen bonding interactions. Our group has successfully demonstrated the molecular architectonics of nucleobase-conjugated arylenediimides and short oligonucleotides through conventional and unconventional base pairing interactions to construct well-defined nanoarchitectures with definite applications [18]. In a unique design, a symmetrically functionalized adenine-conjugated PDI derivative (APA) was designed to interact with thymine via canonical and noncanonical hydrogen bonding, and with guanine via noncanonical hydrogen bonding interactions. The PDI was functionalized with adenine, owing to its unique ability to form hydrogen bonds with other complementary and noncomplementary nucleobases. The canonical hydrogen bonding interaction with oligothymidine resulted in the formation of hybrid DNA ensembles of the type $dT_n–(APA)_n–dT_n$, $n = 10$, 20, through double-helical zipper assembly (Figure 4a). Further studies revealed that the interaction of APA with dG_{10} and dT_{10} resulted in the formation of M-type double-helical zipper assemblies, while with dA_{10}, the formation of a P-type helix was preferred. pH-dependent circular dichroism (CD) measurements showed the collapse of the double-helical zipper assemblies at pH < 6 (Figure 4b). Remarkably, the nanofiber (molecular) structure of the individual double-helical zipper assembly $dT_{20}–(APA)_{20}–dT_{20}$, extended end-to-end through aromatic interactions, was visualized by AFM (Figure 4c). The left-handedness of the double-helical assembly $dT_{20}–(APA)_{20}–dT_{20}$ observed in AFM correlated with the CD data. The stimuli-responsiveness of the SFM-supported chirality-imprinted double-helical assembly systems points at potential drug delivery systems for small molecular and gene-based drugs.

Mercury is one of the most toxic heavy metals, with a severe impact on human health already at ultralow concentrations [20,72-74]. Selective binding of Hg(II) with thymine is a highly feasible interaction to be exploited for its detection. We utilized the mercury–thymine interaction to develop ultrasensitive detection methods for mercury at subnanomolar concentrations [20]. This design strategy utilizes homothymine (oligothymidine) sequences for the selective and sensitive detection of mercury, and thereby unambiguously circumvents the limitations associated with the earlier reports of DNA-based sensor systems. In our creation strategy, novel DNA nanoarchitectures were designed and developed for the sensing of mercury at subnanomolar levels, wherein adenine-conjugated naphthalenediimide (BNA) forms a mutually templated assembly with oligothymidine (dT_n, $n = 6$, 10, 20, Figure 5a). The $BNA_n–dT_n$ coassembly led to the formation of 2D nanosheets of variable dimensions depending on the dT_n chain length

Figure 4: a) Schematic representation of mutually templated double-helical zipper assemblies of APA and dB_n (B: nucleobases T, A, or G; n =10, 20) via canonical and noncanonical hydrogen bonding interactions. b) pH-dependent CD measurement of double-helical zipper ensembles. c) AFM image of double-helical zipper assembly nanofiber dT_{20}–$(APA)_{20}$–dT_{20} and its height profile data (5 nm, inset), typical thickness 4.5 nm. Figure 4a–c has been adapted with permission from [18], copyright 2015 Royal Society of Chemistry.

Figure 5: a) Mutually templated coassembly of BNA and dT_n (n = 6, 10, 20) to form a BNA_n–dT_n hybrid ensemble, and displacement of BNA from Hg(II), followed by the formation of a metallo-DNA duplex. b) FESEM images of 2D nanoarchitectures (nanosheets) of $BNAn$–dTn coassembly and 1D tapes of BNA. c) Schematic representation of a FET device of BNA_n–dT_n fabricated for conductometric sensing of Hg(II) with ultrasensitive sensitivity (0.1 nM, 0.02 ppb). Figure 5a–c has been adapted with permission from [20], copyright 2016 American Chemical Society.

(Figure 5b). Oligothymidine (dT$_n$) mutually templated with BNA was used for the first time to improve the detection sensitivity for mercury, which involved the thermodynamically and entropically favored displacement of BNA owing to the formation of metallo-DNA duplexes (dT–Hg–dT)$_n$ (Figure 5a). The displacement of BNA caused significant changes in the morphological, chiroptical, and electrical conductivity properties of the system, which was used for the dual-responsive detection of ultralow concentrations (subnanomolar level) of mercury. The BNA$_n$–dT$_n$ coassembly material was used to fabricate a field-effect transistor (FET) for the detection of mercury (Figure 5c). Remarkably, both chiroptical and conductometric measurement-based data provided subnanomolar detection of mercury (≥0.1 nM, 0.02 ppb), which was 100 times lower than the permitted maximum quantity of mercury in water (≈10 nM, ≈2 ppb), as per the United States Environmental Protection Agency (USEPA). The AFM-based measurement also showed excellent transport properties of individual BNA$_n$–dT$_n$ nanoarchitectures (nanosheets), which also provided highly sensitive detection of mercury. The displacement of BNA in BNA$_n$–dT$_n$ by Hg(II) resulted in a change of morphology of the nanoarchitectures from nanosheets to 1D tapes. This unique strategy demonstrated the design and potential application of SFM-sup-

ported DNA nanoarchitectures in sensors and bio-optoelectronics. In another study, we reported a molecular architectonic of adenine (A)- and thymine (T)-appended naphthalenediimide derivatives (NDI-AA and NDI-TT, respectively), with peptide nucleic acid (PNA) dimers (clamps) via WC and Hoogsteen base pairing interactions (Figure 6) [75]. The hydrogen bonding interactions, along with hydrophobic interactions, imparted by the nucleobases and the NDI core, facilitated the formation of versatile nano- and microarchitectures. The morphological evaluation showed the formation of petals, fibres, ribbons, and porous spheres by NDI-AA and NDI-TT under different conditions. This study demonstrated the existence of unusual Hoogsteen interactions among the nucleobases that formed 9-membered hydrogen-bonded ring structures instead of an 8-membered WC structure. The chiral ssDNA could host a multitude of diverse molecules and was capable of altering the handedness of the host–guest assembly systems [76]. Switchable helicity was observed when diaminopurine-conjugated naphthalene derivatives interacted as guest molecules within oligothymidine. The helicity of the coassembly systems was found to change with the solutions' pH value. The reversal of helicity was observed at lower pH, where the right-handed B-DNA form effectively transformed to left handed Z-DNA due to pro-

Figure 6: Molecular structures of nucleobase-tethered NDI molecules (NDI-AA and NDI-TT) and their assembly, coassembly, and templated coassembly with PNA clamps. Adapted with permission from [75], copyright 2013 Royal Society of Chemistry.

tonation of the guest derivative. Similar experiments performed with adenine and cytosine templates did not show such a reversal of helicity. This report is a typical example for the design of DNA-triggered switchable functional nanoarchitectures.

Reprograming the molecular self-assembly of DNA through noncovalent incorporation of organic molecules can potentially modify and expand the structural diversity and functionality of the resulting nanoarchitectures. In a recent work by Sleiman and co-workers, cyanuric acid (CA) with hydrogen-bonding faces, analogous to three thymine functions, was exploited to modulate the assembly of ssDNA to form unique nanofiber architectures [77]. The novelty of this work lies in the use of a small molecule, CA, that promoted the self-assembly-driven reprograming of polyadenine strands into a noncanonical motif. The interactions between adenine and CA were consistent with the formation of hexameric rosette architectures, and CA facilitated the cooperative growth of polyadenine strands with a very high aspect ratio.
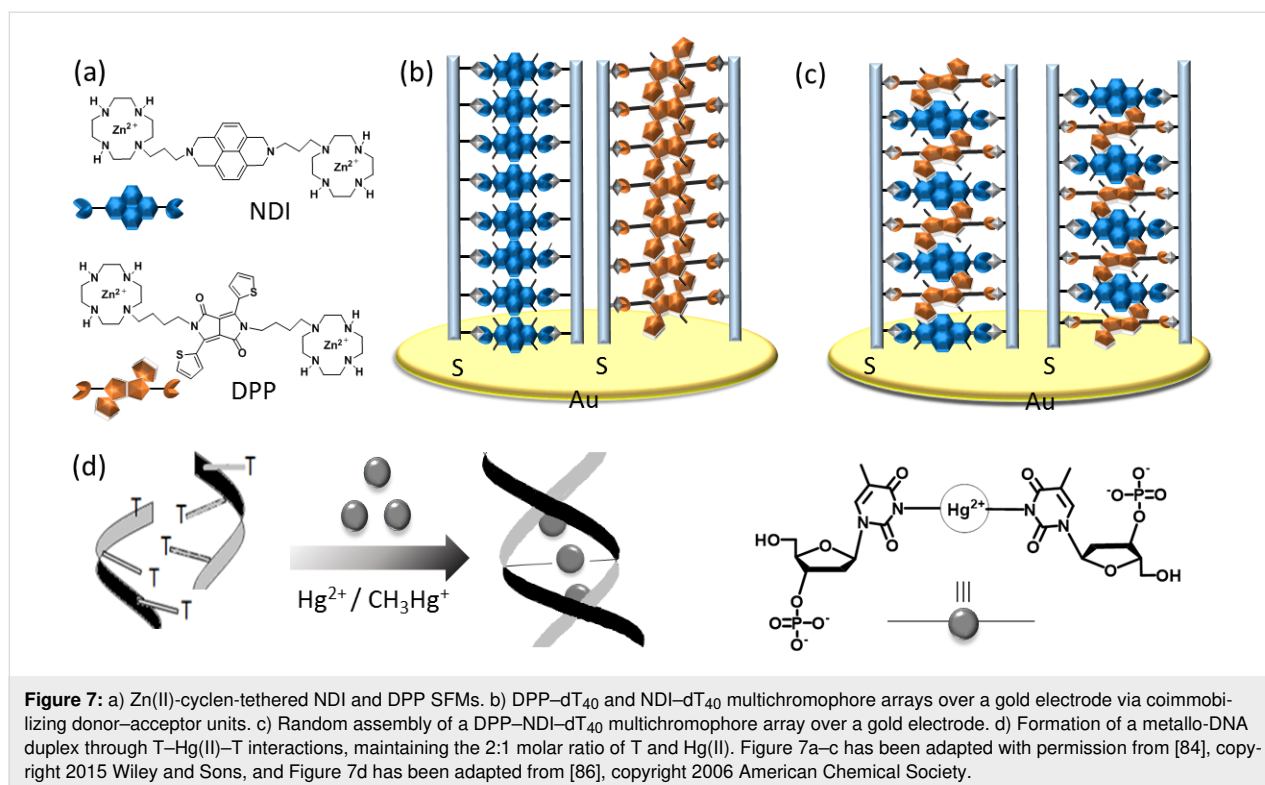
The secondary structure of biomolecules depends on weak noncovalent interactions, especially ionic interactions, between oppositely charged moieties or surfaces. In fact, ionic or electrostatic interactions can play an important role in the scheme of templated DNA nanoarchitectonics. Similarly, fundamental DNA binding interactions of small molecules, viz., intercalation and groove binding, can be used to construct small molecule–DNA ensembles. Williams and co-workers reported a distinct binding mechanism based on the so-called phosphate clamp, wherein the DNA backbone phosphate groups were used for the interaction with small functional molecules [78]. Essentially, the interaction of cationic small molecules with the anionic periphery of DNA led to the formation of electrostatically stable small molecule–DNA ensembles. The aromatic molecules with cationic functionalities were capable of imparting dual stabilization through π stacking and electrostatic interactions. Ulrich and co-workers reported the interaction of aromatic molecules bisfunctionalized with guanidinium moieties and ssDNA in aqueous solution [79]. The cationic guanidinium moieties interacted with the anionic phosphodiester backbone of DNA, while aromatic π stacking played a significant role in the molecular assembly in aqueous solution. In another study, isophthalamide and dipicolinamide molecules were shown to act as synthetic small-molecule vectors for the transfection of plasmid DNA [80]. The dipicolinamide molecules acted as an anion (phosphate) binder and exhibited channel forming properties, thereby becoming an efficient biomaterial for the binding and delivery of cargo DNA. *Escherichia coli* was chosen as representative bacterium for transfection studies. The dipicolinamide-guided transfection with plasmid DNA was found to

stimulate the growth of *E. coli*, which confirmed the good transfection efficiency of the small-molecule (dipicolinamide) vector.

Izawa and co-workers reported the use of anthracene derivatives to drive the self-assembly of ssDNA into helical nanofibers [81]. The weak interactions between thymidylic acid-conjugated anthracenes and complementary oligoadenylic acid resulted in the formation of helical J-aggregates via A–T base pairing interactions. The characterizations performed using spectroscopic and microscopic methods suggested the binary self-assembly between the anthracene derivatives and 20-meric oligodeoxyadenylic acid where the transition dipolar axis of the anthracene derivatives was aligned in a head-to-tail fashion. The UV–vis and CD spectroscopy data showed cooperative changes in the binary self-assembly in response to the temperature. Shimizu and co-workers reported the synthesis of nucleotide-tethered oligo(*p*-phenylene vinylene), (2,1-ethenediyl-1,4-phenylenemethylene)bis(2′-deoxy-3′-thymidylic acid), and examined the complementary interaction with 20-meric oligodeoxyadenylic acid in water [82]. The binary self-assembly between the oligo(*p*-phenylene vinylene) and oligodeoxyadenylic acid in water resulted in the formation of right-handed helical stacks of different diameters, based on the residual stoichiometry of the two components. However, the interaction with noncomplementary 20-meric oligothymidylic acid did not produce any self-assembled structure in water. In another study, the interaction between a thymidine bolaamphiphile dTp–20–dTp and a series of oligoadenylic acids d(A)$_n$ (n = 2, 4, 6, 8, 10, 20, 40) was found to form nanofibers with a double-helical structure [83]. The binary self-assembly interaction between the bolaamphiphile and the oligoadenylic acids dTp–20–dTp/d(A)$_n$, n = 2, 4, 6, 8, 10, 20, 40, strictly depended on the chain length of the oligoadenylic acid. Through the presence of equal amounts of adenine and thymine within the ensembles, it was possible to form hydrogels in water upon incubation for several days. However, an increase in oligoadenylic acid chain length resulted in changes in hydrogel color and rigidity.

Metal–base pair interactions-guided design of DNA nanoarchitectures

Metal–base pair interaction-driven molecular architectonics are one of the major alternatives to hydrogen bonding (WC and non-WC)-supported base pair interactions for the development of functional DNA nanoarchitectures. Nakamura and co-workers reported the construction of metal–ssDNA coassembly systems wherein Zn(II)-bis(cyclen)-conjugated NDI and diketopyrrolopyrrole (DPP)-based multichromophore units were used for mutual templating of short oligonucleotides (Figure 7a) [84]. In their previous reports, Zn(II)-bis(cyclen)-

Figure 7: a) Zn(II)-cyclen-tethered NDI and DPP SFMs. b) DPP–dT$_{40}$ and NDI–dT$_{40}$ multichromophore arrays over a gold electrode via coimmobilizing donor–acceptor units. c) Random assembly of a DPP–NDI–dT$_{40}$ multichromophore array over a gold electrode. d) Formation of a metallo-DNA duplex through T–Hg(II)–T interactions, maintaining the 2:1 molar ratio of T and Hg(II). Figure 7a–c has been adapted with permission from [84], copyright 2015 Wiley and Sons, and Figure 7d has been adapted from [86], copyright 2006 American Chemical Society.

conjugated NDI were shown to guide the formation of multichromophore arrays via binding with dT$_n$, and the lengths of the multichromophore arrays were found to be dependent on the dT$_n$ chain length and temperature [85]. The multichromophoric array of NDI and oligo-dT$_n$ assembled over a gold substrate showed photocurrent generation due to electron conduction because of the π-stacked array of the NDI assembly. In their next design approach, two separate zinc binding systems, Zn(II)-bis(cyclen)–NDI and Zn(II)-bis(cyclen)–DPP, were decorated using oligothymidine (dT$_{40}$) as a scaffold via interaction of Zn(II)-bis(cyclen) with thymidine residues. The ensemble behaved as a donor–acceptor heterojunction system where DPP acted as a donor moiety and NDI as an acceptor moiety. One of the advantages of this system was that the DNA–multichromophore organization could be aligned vertically over the gold electrode, which facilitated exothermic charge separation and suppressesed the ground-state charge transfer (CT) complexation between DPP and NDI, followed by the generation of a photocurrent (Figure 7b). However, the randomly assembled array of DPPNDI–dT$_{40}$ immobilized across the gold electrode was unable to generate any photocurrent response owing to ground-state CT complexation of DPP with NDI in their random arrangement (Figure 7c). Tanaka, Ono, and co-workers reported the generation of mercury-mediated base pairing T–Hg(II)–T band metallo-DNA duplex structures (Figure 7d) [86]. Lu and co-workers exploited the T–Hg(II)–T metal–base pairing to control the DNAzyme activity through allosteric

interactions [87]. For the first time, we showed the mercury-mediated displacement of SFM (BNA) from the BNA$_n$–dT$_n$ hybrid ensemble to form a metallo-DNA duplex of homothymidine sequences, and this transformation was used as a chiroptical and conductometric sensor platform for the ultrasensitive detection of mercury at a subnanomolar level (vide supra) [20,72]. The remarkable outcome of our design strategy was attributed to the ultrasensitive detection of mercury through FET device fabrication, which overcame the limitations of earlier reports on DNA-based Hg(II) detection.

Chromophore conjugation-guided DNA architectonics

The introduction of organic chromophores within the nucleic acid system is one of the distinct approaches to generate functional DNA architectures [88]. Porphyrins are well-known macrocyclic organic chromophores acting as light harvesting systems that can be efficiently compacted within the spatial arrangements of DNA double-helical assemblies [88]. Meunier [89], Hélène [90], and co-workers reported the utility of porphyrin-tethered DNA as artificial nucleases. Murashima, Sugimoto, and co-workers adopted a novel approach to design DNA nanoarchitectures by substituting the nucleobases of DNA with porphyrins [91]. The tetraphenylporphyrin-modified nucleotide was inserted into the center of a 13-mer oligonucleotide sequence in an automated DNA synthesizer through phosphoramidite chemistry. The annealing of porphyrin-tethered oligo-

nucleotides with complementary oligonucleotides resulted in the formation of a B-form DNA duplex. The conformational distortion effect due to the intercalation of porphyrin was neutralized via stabilization of the ensemble by stacking interactions that created the B-form duplex structure. Sitaula, Reed, and co-workers reported the ligation of a porphyrin derivative by a 19-nucleotide DNA sequence [92]. The porphyrin units were ligated by DNA via direct amidation, and the covalent attachment allowed the insertion of an array of porphyrin segments along the nucleotide sequence. Recently, a transmembrane lipid bilayer nanopore comprised of folded DNA became the center of attraction by mimicking natural protein pores. Howorka and co-workers reported the synthesis of porphyrin-conjugated DNA nanopores as a simple and effective strategy to span through the bilayer system [93]. The nanopore consisted of six hexagonally packed DNA double-helical assemblies that were preserved by double-crossover strands (Figure 8a). The two porphyrin units were positioned at the terminal of a helical bundle that improved the directional insertion of the nanobarrel across the bilayer. AFM images showed that the assembled morphology of the hexagonally packed nanobarrels was made up of porphyrin-tethered DNA (Figure 8b). Stulz and co-workers designed a porphyrin-tethered single-DNA duplex as a transmembrane ion channel [94]. Their minimalistic design approach involved the attachment of six porphyrin units along the oligonucleotide sequence that facilitated the movement of ions through the channel. The schematic of molecular dynamics simulation data (Figure 8c) showed the movement of ions through the lipid–nanopore interface via the formation of a toroidal pore. The binding of porphyrin-tethered nanopores with

giant unilamellar vesicles was analyzed by confocal microscopy (Figure 8d). The inherent fluorescent signal of porphyrin showed their presence across the lipid vesicle. Further investigations on ionic current traces demonstrated that the lipid membrane insertion and gating behavior of the nanopore resembled natural protein channels (Figure 8e). Embodiment of the porphyrin within the DNA system played dual roles, viz., imparting hydrophobic effects and characteristic optical responses to monitor the insertion mechanism. Notably, the position of conjugation and the number of porphyrin units were crucial parameters that significantly affected the insertion process. Asanuma and co-workers incorporated six methyl red chromophores into a double-helical DNA through D- and L-threoinol linkers to analyze the molecular exciton theory of heterodimeric chromophores [95]. NMR studies revealed the antiparallel orientation of the two dyes across the duplex strand. Further studies indicated that the increment in dye number could dramatically affect the spectroscopic behavior and the solution properties of the dye.

DNA–metal nanoparticle architectures

Interactions of DNA with nanoparticles are an attractive area for the fabrication of functional DNA nanoarchitectures [96]. The surface properties of the nanoparticles are greatly influenced by the functionalization with DNA. The crystallization of nanoparticles can be easily programed by the selection of designer DNA sequences. In fact, DNA-mediated assembly is widely used to synthesize hybrid lattices of gold nanoparticles and protein-based capsid particles [97,98]. The methylation of DNA is one of the epigenetic modifications that include the ad-
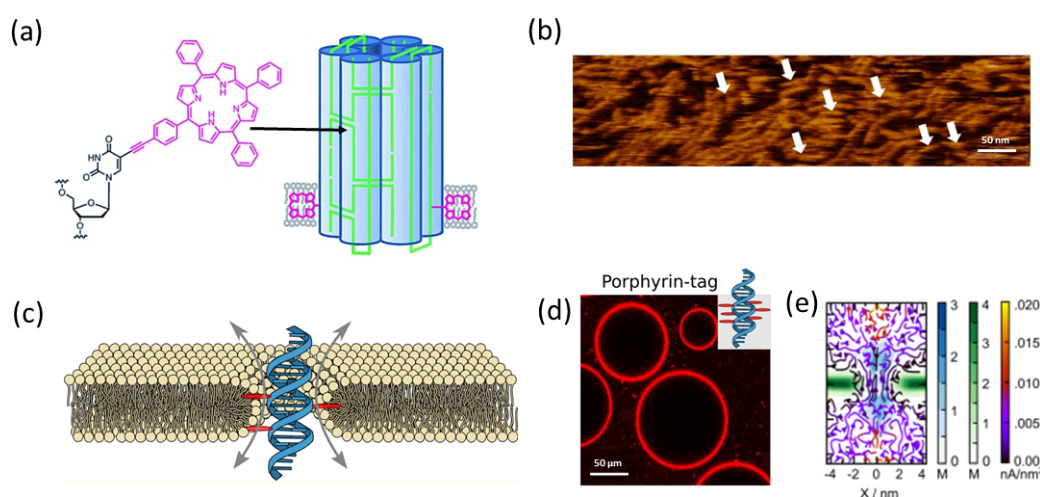

Figure 8: a) Schematic representation of a porphyrin-appended DNA nanopore base lipid anchor. b) AFM image of a nanopore assembly. c) Schematic design of a membrane-spanning porphyrin-tagged DNA duplex. d) Fluorescence confocal image highlighting the interaction of porphyrin-tethered DNA with lipid membrane. e) Molecular dynamics simulation to analyze steady-state local densities of porphyrin–DNA-anchored lipid chains and their current flow. Figure 8a and Figure 8b were adapted from [93], distributed under a Creative Commons Attribution license, copyright 2013 by the authors. Figure 8c–e was adapted with permission from [94], copyright 2016 American Chemical Society.

dition of a methyl group to cytosine, and this modification controls the genetic programing in living system. The epigenetically reprogrammed methylation landscape in cells is a marker for several types of cancer. The cancer pathology is characterized by different methylation patterns, which include the net loss of global methylation throughout the genome sequence, while the regulatory or promoter regions of DNA involve a high rate of methylation. The differences in genomic distribution of methylation greatly influence the solution properties of DNA, and this concept has been exploited by Trau and co-workers to analyze the different interaction patterns of methylated and nonmethylated DNA with gold nanoparticles [22]. The consistent and high methylation level of genomes makes the DNA more hydrophobic, while the distinct methylation in cancer genomes shows much lower hydrophobicity. The changes in solvation properties of DNA drastically affect the affinity towards metal nanoparticles. Based on these aspects, the authors have efficiently evaluated the affinity of genomic DNA towards metal nanoparticles depending on the methylation pattern and extent of methylation throughout the genome. In particular, this constituted a promising sensor-free diagnostic platform for the detection of cancer. Chen and co-workers showed that the interaction of DNA with dithiothreitol (DTT)-conjugated gold nanoclusters (Au NCs) results in the formation of 'raspberry-like' particles with potential gene delivery application [99]. The novelty of the 'raspberry-like' structures lay in their biocompatible 'shield', which protected the capped DNA from enzymatic degradation. Gianneschi and co-workers documented the synthesis of crystalline gold nanowires from DNA block copolymer micelles [100]. The block copolymer micelles were synthesized through ring-opening polymerization, followed by the integration of DNA oligonucleotides in a postpolymerization modification process. The DNA acted as a polar head group, while the whole polymer system acted as a template for nanowire synthesis. The miniaturization of devices is of central importance in electronics and has galvanized significant research in materials science. The need for the miniaturization of devices at the nanoscale interface has led to the exploration of new material systems and building blocks, while relinquishing the use of traditional silicon-based materials also played a key role. Biomolecular nanolithography is a newer approach to create nanopatterned surfaces using biomolecules as scaffolds [101,102]. The interesting features of this technique are the combination of two separate scales, the nanoscale and the biomacromolecular interface, to produce functional architectures. In this context, the well-defined structural organization, anionic properties, and polymeric nature qualify DNA and RNA as potential candidates for scaffolding purposes. Employing the nanolithography technique, precise DNA nanostructures can be constructed, and these DNA nanoarchitectures exhibit remarkable molecular recognition properties at the

nanoscale. Hutchison and co-workers reported the use of DNA as a scaffold for nanoscale patterning of metal nanoparticles over a DNA surface [103]. The electrostatic interaction with the ligand stabilized the metal nanoparticles, and the backbone phosphate groups of DNA triggered the formation of different nanoarchitectures, such as ribbons, linear chains, and branched structures. Patolsky and co-workers documented the photochemical covalent attachment of gold nanoparticles to DNA surfaces, which resulted in the formation of a gold nanowire [104]. The synthesis of DNA gold nanowires was followed by the incorporation of psoralen-functionalized gold nanoparticles across double-stranded DNA. Psoralen acted as an intercalator that led to photochemical crosslinking of the components within the DNA matrix. The photoinduced [2+2] cycloaddition of the thymine residues of DNA in the psoralen-functionalized gold nanoparticle matrix resulted in the formation of conductive nanorings or nanowires. Willner and co-workers reported a novel nanoarchitectonic consisting of a DNA-crosslinked CdS nanoparticle array on an electrode surface that generated an efficient photocurrent upon irradiation [105]. The electrostatic interaction of $[Ru(NH_3)_6]^{3+}$ with the DNA-bound CdS nanoparticle system supported tunneling of the conduction band electrons, followed by the generation of photocurrents. Similarly, λ-DNA was used as a biogenic template for the generation of silver nanowires and the synthesis of palladium nanoparticle clusters [106,107].

Conclusion and Outlook

The disruptive idea of using DNA as a material building block (DNA nanotechnology) has brought a revolution to the broad areas of nanoscience and nanotechnology. A large number of research groups have been involved in the rational design of DNA-based nanomaterials, origami, nanomachines, and devices. The unique structural features enabled by predictable sequence-specific interactions have made DNA a versatile component for programmable molecular architectonics to construct diverse molecular and nanoarchitectures. In DNA nanotechnology, robust design and programming protocols have led to the creation of 1D, 2D, and 3D nanoarchitectures using well-defined tiles and bricks. Remarkably, complex DNA architectures in terms of shape and size could be achieved through the concept of DNA origami. While DNA nanotechnology (and origami) is extremely creative in its original form and produced complex nanoarchitectures of virtually any shape and size through standard and robust DNA self-assembly, potential applications of these materials are yet be realized. In this context, templated DNA nanotechnology or functional DNA nanoarchitectonics have been conceived to overcome the limitations of classical DNA nanotechnology. In this simple and novel approach, molecular architectonics of suitably tethered SFMs, or their assemblies, and ssDNA produced hybrid DNA ensembles

with functional properties and practical applications. Mutually templated coassemblies of SFMs and ssDNA were orchestrated through conventional (WC) and unconventional (non-WC) hydrogen bonding-, aromatic π–π stacking-, electrostatic-, and metal coordination-based interactions. Notably, novel functional DNA nanoarchitectures were produced through the coassembly of inexpensive short ssDNA sequences (oligonucleotides) and SFMs that ensured practical applications. The solution-based molecular architectonics approach to design and construct SFM-tethered hybrid DNA ensembles opened up new possibilities in the fields of materials science, nanoscience, nanotechnology, and biomedicine. Organic chemistry played a key role in the design and synthesis of SFMs suitable for the coassembly with ssDNA to cater for specific applications, ranging from novel materials design, optoelectronics, sensors, diagnostics, and drug delivery to therapy. The outlook for the emerging field of functional DNA nanoarchitectonics lies in the controlled and programmed coassembly (molecular architectonics) through mutual templating of SFMs or other designer units and ssDNA to generate novel molecular and nanoarchitectures with emergent properties and practical applications in the domains of health, energy, and environment.

Acknowledgements

Funding

ORCID® iDs

Thimmaiah Govindaraju - https://orcid.org/0000-0002-9423-4275

References

1. Avinash, M. B.; Govindaraju, T. *Acc. Chem. Res.* **2018,** *51,* 414–426. doi:10.1021/acs.accounts.7b00434
2. Roy, B.; Govindaraju, T. *Bull. Chem. Soc. Jpn.* **2019,** *92,* 1883–1901. doi:10.1246/bcsj.20190215
3. Avinash, M. B.; Govindaraju, T. *Adv. Mater. (Weinheim, Ger.)* **2012,** *24,* 3905–3922. doi:10.1002/adma.201201544
4. Avinash, M. B.; Govindaraju, T. *Nanoscale* **2014,** *6,* 13348–13369. doi:10.1039/c4nr04340e
5. Suseela, Y. V.; Narayanaswamy, N.; Pratihar, S.; Govindaraju, T. *Chem. Soc. Rev.* **2018,** *47,* 1098–1131. doi:10.1039/c7cs00774d
6. Ariga, K.; Li, J.; Fei, J.; Ji, Q.; Hill, J. P. *Adv. Mater. (Weinheim, Ger.)* **2016,** *28,* 1251–1286. doi:10.1002/adma.201502545
7. Winfree, E.; Liu, F.; Wenzler, L. A.; Seeman, N. C. *Nature* **1998,** *394,* 539–544. doi:10.1038/28998
8. Lee, D. S.; Qian, H.; Tay, C. Y.; Leong, D. T. *Chem. Soc. Rev.* **2016,** *45,* 4199–4225. doi:10.1039/c5cs00700c
9. Douglas, S. M.; Bachelet, I.; Church, G. M. *Science* **2012,** *335,* 831–834. doi:10.1126/science.1214081
10. Blackburn, G. M.; Gait, M. J.; Loakes, D.; Williams, D. M., Eds. *Nucleic Acids in Chemistry and Biology;* Royal Society of Chemistry: Cambridge, United Kingdom, 2007. doi:10.1039/9781847555380
11. Seeman, N. C. *Nature* **2003,** *421,* 427–431. doi:10.1038/nature01406
12. Govindaraju, T., Ed. *Templated DNA Nanotechnology,* 1st ed.; Jenny Stanford Publishing: New York City, NY, U.S.A., 2019. doi:10.1201/9780429428661
13. Roy, B.; Ghosh, D.; Govindaraju, T. Functional Molecule–Templated DNA Nanoarchitectures. In *Templated DNA Nanotechnology,* 1st ed.; Govindaraju, T., Ed.; Jenny Stanford Publishing: New York City, NY, U.S.A., 2019; pp 69–106. doi:10.1201/9780429428661-3
14. Maune, H. T.; Han, S.-p.; Barish, R. D.; Bockrath, M.; Goddard, W. A., III; Rothemund, P. W. K.; Winfree, E. *Nat. Nanotechnol.* **2010,** *5,* 61–66. doi:10.1038/nnano.2009.311
15. Rothemund, P. W. K. *Nature* **2006,** *440,* 297–302. doi:10.1038/nature04586
16. Seeman, N. C. *Nano Lett.* **2001,** *1,* 22–26. doi:10.1021/nl000182v
17. Ke, Y.; Ong, L. L.; Shih, W. M.; Yin, P. *Science* **2012,** *338,* 1177–1183. doi:10.1126/science.1227268
18. Narayanaswamy, N.; Suresh, G.; Priyakumar, U. D.; Govindaraju, T. *Chem. Commun.* **2015,** *51,* 5493–5496. doi:10.1039/c4cc06759b
19. Narayanaswamy, N.; Nair, R. R.; Suseela, Y. V.; Saini, D. K.; Govindaraju, T. *Chem. Commun.* **2016,** *52,* 8741–8744. doi:10.1039/c6cc02705a
20. Pandeeswar, M.; Senanayak, S. P.; Govindaraju, T. *ACS Appl. Mater. Interfaces* **2016,** *8,* 30362–30371. doi:10.1021/acsami.6b10527
21. Roy, B.; Ramesh, M.; Govindaraju, T. DNA-Based Nanoswitches and Devices. In *Templated DNA Nanotechnology,* 1st ed.; Govindaraju, T., Ed.; Jenny Stanford Publishing: New York City, NY, U.S.A., 2019; pp 365–408. doi:10.1201/9780429428661-11
22. Sina, A. A. I.; Carrascosa, L. G.; Liang, Z.; Grewal, Y. S.; Wardiana, A.; Shiddiky, M. J. A.; Gardiner, R. A.; Samaratunga, H.; Gandhi, M. K.; Scott, R. J.; Korbie, D.; Trau, M. *Nat. Commun.* **2018,** *9,* 4915. doi:10.1038/s41467-018-07214-w
23. Aono, M.; Bando, Y.; Ariga, K. *Adv. Mater. (Weinheim, Ger.)* **2012,** *24,* 150–151. doi:10.1002/adma.201104614
24. Komiyama, M.; Yoshimoto, K.; Sisido, M.; Ariga, K. *Bull. Chem. Soc. Jpn.* **2017,** *90,* 967–1004. doi:10.1246/bcsj.20170156
25. Ariga, K.; Mori, T.; Nakanishi, W.; Hill, J. P. *Phys. Chem. Chem. Phys.* **2017,** *19,* 23658–23676. doi:10.1039/c7cp02280h
26. Komiyama, M.; Mori, T.; Ariga, K. *Bull. Chem. Soc. Jpn.* **2018,** *91,* 1075–1111. doi:10.1246/bcsj.20180084
27. Zhao, L.; Zou, Q.; Yan, X. *Bull. Chem. Soc. Jpn.* **2019,** *92,* 70–79. doi:10.1246/bcsj.20180248
28. Ariga, K.; Nishikawa, M.; Mori, T.; Takeya, J.; Shrestha, L. K.; Hill, J. P. *Adv. Mater. (Weinheim, Ger.)* **2019,** *20,* 51–95. doi:10.1080/14686996.2018.1553108
29. Ariga, K.; Leong, D. T.; Mori, T. *Adv. Funct. Mater.* **2018,** *28,* 1702905. doi:10.1002/adfm.201702905
30. Khan, A. H.; Ghosh, S.; Pradhan, B.; Dalui, A.; Shrestha, L. K.; Acharya, S.; Ariga, K. *Bull. Chem. Soc. Jpn.* **2017,** *90,* 627–648. doi:10.1246/bcsj.20170043
31. Simmel, F. C. *Angew. Chem., Int. Ed.* **2008,** *47,* 5884–5887. doi:10.1002/anie.200801982
32. Li, Z.; Wang, J.; Li, Y.; Liu, X.; Yuan, Q. *Mater. Chem. Front.* **2018,** *2,* 423–436. doi:10.1039/c7qm00434f

33. Seeman, N. C. *J. Theor. Biol.* **1982,** *99,* 237–247.
    doi:10.1016/0022-5193(82)90002-9
34. Fu, T. J.; Seeman, N. C. *Biochemistry* **1993,** *32,* 3211–3220.
    doi:10.1021/bi00064a003
35. Yan, H.; LaBean, T. H.; Feng, L.; Reif, J. H.
    Proc. Natl. Acad. Sci. U. S. A. **2003,** *100,* 8103–8108.
    doi:10.1073/pnas.1032954100
36. Seeman, N. C. *Chem. Biol.* **2003,** *10,* 1151–1159.
    doi:10.1016/j.chembiol.2003.12.002
37. Nummelin, S.; Kommeri, J.; Kostiainen, M. A.; Linko, V.
    Adv. Mater. (Weinheim, Ger.) **2018,** *30,* 1703721.
    doi:10.1002/adma.201703721
38. Endo, M.; Sugiyama, H. *ChemBioChem* **2009,** *10,* 2420–2443.
    doi:10.1002/cbic.200900286
39. Lin, C.; Liu, Y.; Rinker, S.; Yan, H. *ChemPhysChem* **2006,** *7,*
    1641–1647. doi:10.1002/cphc.200600260
40. Seeman, N. C. *Trends Biotechnol.* **1999,** *17,* 437–443.
    doi:10.1016/s0167-7799(99)01360-8
41. He, Y.; Tian, Y.; Chen, Y.; Deng, Z.; Ribbe, A. E.; Mao, C.
    Angew. Chem., Int. Ed. **2005,** *44,* 6694–6696.
    doi:10.1002/anie.200502193
42. Yang, Z.; Liu, H.; Liu, D. *NPG Asia Mater.* **2015,** *7,* e161.
    doi:10.1038/am.2015.2
43. Liu, H.; Liu, D. *Chem. Commun.* **2009,** 2625–2636.
    doi:10.1039/b822719e
44. He, Y.; Ye, T.; Su, M.; Zhang, C.; Ribbe, A. E.; Jiang, W.; Mao, C.
    Nature **2008,** *452,* 198–201. doi:10.1038/nature06597
45. Zhang, F.; Jiang, S.; Wu, S.; Li, Y.; Mao, C.; Liu, Y.; Yan, H.
    Nat. Nanotechnol. **2015,** *10,* 779–784. doi:10.1038/nnano.2015.162
46. Han, D.; Pal, S.; Nangreave, J.; Deng, Z.; Liu, Y.; Yan, H. *Science*
    2011, *332,* 342–346. doi:10.1126/science.1202998
47. Kuzuya, A.; Komiyama, M. *Nanoscale* **2010,** *2,* 310–322.
    doi:10.1039/b9nr00246d
48. Tørring, T.; Voigt, N. V.; Nangreave, J.; Yan, H.; Gothelf, K. V.
    Chem. Soc. Rev. **2011,** *40,* 5636–5646. doi:10.1039/c1cs15057j
49. Endo, M.; Hidaka, K.; Kato, T.; Namba, K.; Sugiyama, H.
    J. Am. Chem. Soc. **2009,** *131,* 15570–15571. doi:10.1021/ja904252e
50. Endo, M.; Yang, Y.; Sugiyama, H. *Biomater. Sci.* **2013,** *1,* 347–360.
    doi:10.1039/c2bm00154c
51. Michelotti, N.; Johnson-Buck, A.; Manzo, A. J.; Walter, N. G.
    Wiley Interdiscip. Rev.: Nanomed. Nanobiotechnol. **2012,** *4,* 139–152.
    doi:10.1002/wnan.170
52. Kaminska, I.; Bohlen, J.; Mackowski, S.; Tinnefeld, P.; Acuna, G. P.
    ACS Nano **2018,** *12,* 1650–1655. doi:10.1021/acsnano.7b08233
53. Jiang, Q.; Song, C.; Nangreave, J.; Liu, X.; Lin, L.; Qiu, D.;
    Wang, Z.-G.; Zou, G.; Liang, X.; Yan, H.; Ding, B. *J. Am. Chem. Soc.*
    2012, *134,* 13396–13403. doi:10.1021/ja304263n
54. Douglas, S. M.; Chou, J. J.; Shih, W. M. *Proc. Natl. Acad. Sci. U. S. A.*
    2007, *104,* 6644–6648. doi:10.1073/pnas.0700930104
55. Mao, C.; Sun, W.; Shen, Z.; Seeman, N. C. *Nature* **1999,** *397,*
    144–146. doi:10.1038/16437
56. Li, S.; Jiang, Q.; Liu, S.; Zhang, Y.; Tian, Y.; Song, C.; Wang, J.;
    Zou, Y.; Anderson, G. J.; Han, J.-Y.; Chang, Y.; Liu, Y.; Zhang, C.;
    Chen, L.; Zhou, G.; Nie, G.; Yan, H.; Ding, B.; Zhao, Y.
    Nat. Biotechnol. **2018,** *36,* 258–264. doi:10.1038/nbt.4071
57. Saha, S.; Prakash, V.; Halder, S.; Chakraborty, K.; Krishnan, Y.
    Nat. Nanotechnol. **2015,** *10,* 645–651. doi:10.1038/nnano.2015.130
58. Leung, K.; Chakraborty, K.; Saminathan, A.; Krishnan, Y.
    Nat. Nanotechnol. **2019,** *14,* 176–183.
    doi:10.1038/s41565-018-0318-5
59. Andersen, E. S.; Dong, M.; Nielsen, M. M.; Jahn, K.; Subramani, R.;
    Mamdouh, W.; Golas, M. M.; Sander, B.; Stark, H.; Oliveira, C. L. P.;
    Pedersen, J. S.; Birkedal, V.; Besenbacher, F.; Gothelf, K. V.;
    Kjems, J. *Nature* **2009,** *459,* 73–76. doi:10.1038/nature07971
60. Amir, Y.; Ben-Ishay, E.; Levner, D.; Ittah, S.; Abu-Horowitz, A.;
    Bachelet, I. *Nat. Nanotechnol.* **2014,** *9,* 353–357.
    doi:10.1038/nnano.2014.58
61. Wang, M.; Zhang, S.; Ye, Z.; Peng, D.; He, L.; Yan, F.; Yang, Y.;
    Zhang, H.; Zhang, Z. *Microchim. Acta* **2015,** *182,* 2251–2258.
    doi:10.1007/s00604-015-1569-6
62. Yáñez-Sedeño, P.; Agüí, L.; Pingarrón, J. M. Biosensors in Forensic
    Analysis. In *Forensic Science: A Multidisciplinary Approach;* Katz, E.;
    Halámek, J., Eds.; Wiley-VCH Verlag: Weinheim, Germany, 2016;
    pp 215–262. doi:10.1002/9783527693535.ch11
63. Booth, M. A.; Harbison, S. A.; Travas-Sejdic, J. *Biosens. Bioelectron.*
    2011, *28,* 362–367. doi:10.1016/j.bios.2011.07.051
64. Evtugyn, G. A.; Stepanova, V. B.; Porfireva, A. V.; Zamaleeva, A. I.;
    Fakhrullin, R. R. *J. Nanosci. Nanotechnol.* **2014,** *14,* 6738–6747.
    doi:10.1166/jnn.2014.9345
65. Gaggiotti, S.; Hurot, C.; Weerakkody, J. S.; Mathey, R.; Buhot, A.;
    Mascini, M.; Hou, Y.; Compagnone, D. *Sens. Actuators, B* **2020,** *303,*
    127188. doi:10.1016/j.snb.2019.127188
66. Goodman, R. P.; Schaap, I. A. T.; Tardin, C. F.; Erben, C. M.;
    Berry, R. M.; Schmidt, C. F.; Turberfield, A. J. *Science* **2005,** *310,*
    1661–1665. doi:10.1126/science.1120367
67. Walsh, A. S.; Yin, H.; Erben, C. M.; Wood, M. J. A.; Turberfield, A. J.
    ACS Nano **2011,** *5,* 5427–5432. doi:10.1021/nn2005574
68. Li, J.; Hong, C.-Y.; Wu, S.-X.; Liang, H.; Wang, L.-P.; Huang, G.;
    Chen, X.; Yang, H.-H.; Shangguan, D.; Tan, W. *J. Am. Chem. Soc.*
    2015, *137,* 11210–11213. doi:10.1021/jacs.5b05650
69. Feng, Q.-M.; Guo, Y.-H.; Xu, J.-J.; Chen, H.-Y.
    ACS Appl. Mater. Interfaces **2017,** *9,* 17637–17644.
    doi:10.1021/acsami.7b04553
70. Kim, K.-R.; Kim, D.-R.; Lee, T.; Yhee, J. Y.; Kim, B.-S.; Kwon, I. C.;
    Ahn, D.-R. *Chem. Commun.* **2013,** *49,* 2010–2012.
    doi:10.1039/c3cc38693g
71. Lee, H.; Lytton-Jean, A. K. R.; Chen, Y.; Love, K. T.; Park, A. I.;
    Karagiannis, E. D.; Sehgal, A.; Querbes, W.; Zurenko, C. S.;
    Jayaraman, M.; Peng, C. G.; Charisse, K.; Borodovsky, A.;
    Manoharan, M.; Donahoe, J. S.; Truelove, J.; Nahrendorf, M.;
    Langer, R.; Anderson, D. G. *Nat. Nanotechnol.* **2012,** *7,* 389–393.
    doi:10.1038/nnano.2012.73
72. Makam, P.; Shilpa, R.; Kandjani, A. E.; Periasamy, S. R.; Sabri, Y. M.;
    Madhu, C.; Bhargava, S. K.; Govindaraju, T. *Biosens. Bioelectron.*
    2018, *100,* 556–564. doi:10.1016/j.bios.2017.09.051
73. Huang, C.-C.; Yang, Z.; Lee, K.-H.; Chang, H.-T.
    Angew. Chem., Int. Ed. **2007,** *46,* 6824–6828.
    doi:10.1002/anie.200700803
74. Lee, J.-S.; Han, M. S.; Mirkin, C. A. *Angew. Chem., Int. Ed.* **2007,** *46,*
    4093–4096. doi:10.1002/anie.200700269
75. Narayanaswamy, N.; Avinash, M. B.; Govindaraju, T. *New J. Chem.*
    2013, *37,* 1302–1306. doi:10.1039/c3nj00060e
76. Janssen, P. G. A.; Ruiz-Carretero, A.; González-Rodríguez, D.;
    Meijer, E. W.; Schenning, A. P. H. J. *Angew. Chem., Int. Ed.* **2009,** *48,*
    8103–8106. doi:10.1002/anie.200903507
77. Avakyan, N.; Greschner, A. A.; Aldaye, F.; Serpell, C. J.; Toader, V.;
    Petitjean, A.; Sleiman, H. F. *Nat. Chem.* **2016,** *8,* 368–376.
    doi:10.1038/nchem.2451

78. Komeda, S.; Moulaei, T.; Woods, K. K.; Chikuma, M.; Farrell, N. P.; Williams, L. D. *J. Am. Chem. Soc.* **2006,** *128,* 16092–16103. doi:10.1021/ja062851y

79. Paolantoni, D.; Rubio-Magnieto, J.; Cantel, S.; Martinez, J.; Dumy, P.; Surin, M.; Ulrich, S. *Chem. Commun.* **2014,** *50,* 14257–14260. doi:10.1039/c4cc05706f

80. Atkins, J. L.; Patel, M. B.; Daschbach, M. M.; Meisel, J. W.; Gokel, G. W. *J. Am. Chem. Soc.* **2012,** *134,* 13546–13549. doi:10.1021/ja304816e

81. Iwaura, R.; Ohnishi-Kameyama, M.; Iizawa, T. *Chem. – Eur. J.* **2009,** *15,* 3729–3735. doi:10.1002/chem.200802537

82. Iwaura, R.; Hoeben, F. J. M.; Masuda, M.; Schenning, A. P. H. J.; Meijer, E. W.; Shimizu, T. *J. Am. Chem. Soc.* **2006,** *128,* 13298–13304. doi:10.1021/ja064560v

83. Iwaura, R.; Yoshida, K.; Masuda, M.; Ohnishi-Kameyama, M.; Yoshida, M.; Shimizu, T. *Angew. Chem., Int. Ed.* **2003,** *42,* 1009–1012. doi:10.1002/anie.200390257

84. Nakamura, M.; Tsuto, K.; Jomura, A.; Takada, T.; Yamana, K. *Chem. – Eur. J.* **2015,** *21,* 11788–11792. doi:10.1002/chem.201501955

85. Nakamura, M.; Okaue, T.; Takada, T.; Yamana, K. *Chem. – Eur. J.* **2012,** *18,* 196–201. doi:10.1002/chem.201102216

86. Miyake, Y.; Togashi, H.; Tashiro, M.; Yamaguchi, H.; Oda, S.; Kudo, M.; Tanaka, Y.; Kondo, Y.; Sawa, R.; Fujimoto, T.; Machinami, T.; Ono, A. *J. Am. Chem. Soc.* **2006,** *128,* 2172–2173. doi:10.1021/ja056354d

87. Liu, J.; Lu, Y. *Angew. Chem., Int. Ed.* **2007,** *46,* 7587–7590. doi:10.1002/anie.200702006

88. Stulz, E. *Acc. Chem. Res.* **2017,** *50,* 823–831. doi:10.1021/acs.accounts.6b00583

89. Casas, C.; Lacey, C. J.; Meunier, B. *Bioconjugate Chem.* **1993,** *4,* 366–371. doi:10.1021/bc00023a011

90. Boutorine, A. S.; Brault, D.; Takasugi, M.; Delgado, O.; Hélène, C. *J. Am. Chem. Soc.* **1996,** *118,* 9469–9476. doi:10.1021/ja960062i

91. Murashima, T.; Hayata, K.; Saiki, Y.; Matsui, J.; Miyoshi, D.; Yamada, T.; Miyazawa, T.; Sugimoto, N. *Tetrahedron Lett.* **2007,** *48,* 8514–8517. doi:10.1016/j.tetlet.2007.09.147

92. Sitaula, S.; Reed, S. M. *Bioorg. Med. Chem. Lett.* **2008,** *18,* 850–855. doi:10.1016/j.bmcl.2007.11.033

93. Burns, J. R.; Göpfrich, K.; Wood, J. W.; Thacker, V. V.; Stulz, E.; Keyser, U. F.; Howorka, S. *Angew. Chem., Int. Ed.* **2013,** *52,* 12069–12072. doi:10.1002/anie.201305765

94. Göpfrich, K.; Li, C.-Y.; Mames, I.; Bhamidimarri, S. P.; Ricci, M.; Yoo, J.; Mames, A.; Ohmann, A.; Winterhalter, M.; Stulz, E.; Aksimentiev, A.; Keyser, U. F. *Nano Lett.* **2016,** *16,* 4665–4669. doi:10.1021/acs.nanolett.6b02039

95. Fujii, T.; Kashida, H.; Asanuma, H. *Chem. – Eur. J.* **2009,** *15,* 10092–10102. doi:10.1002/chem.200900962

96. Jones, M. R.; Seeman, N. C.; Mirkin, C. A. *Science* **2015,** *347,* 1260901. doi:10.1126/science.1260901

97. Elghanian, R.; Storhoff, J. J.; Mucic, R. C.; Letsinger, R. L.; Mirkin, C. A. *Science* **1997,** *277,* 1078–1081. doi:10.1126/science.277.5329.1078

98. Mirkin, C. A.; Letsinger, R. L.; Mucic, R. C.; Storhoff, J. J. *Nature* **1996,** *382,* 607–609. doi:10.1038/382607a0

99. Zhang, L.; Li, Z.; Jing, J.; Ding, H.; Chen, Z. *Part. Part. Syst. Charact.* **2019,** *36,* 1800517. doi:10.1002/ppsc.201800517

100. Chien, M.-P.; Gianneschi, N. C. *Small* **2011,** *7,* 2041–2046. doi:10.1002/smll.201101014

101. Rundqvist, J.; Hoh, J. H.; Haviland, D. B. *Langmuir* **2006,** *22,* 5100–5107. doi:10.1021/la052306v

102. Kershner, R. J.; Bozano, L. D.; Micheel, C. M.; Hung, A. M.; Fornof, A. R.; Cha, J. N.; Rettner, C. T.; Bersani, M.; Frommer, J.; Rothemund, P. W. K.; Wallraff, G. M. *Nat. Nanotechnol.* **2009,** *4,* 557–561. doi:10.1038/nnano.2009.220

103. Warner, M. G.; Hutchison, J. E. *Nat. Mater.* **2003,** *2,* 272–277. doi:10.1038/nmat853

104. Patolsky, F.; Weizmann, Y.; Lioubashevski, O.; Willner, I. *Angew. Chem., Int. Ed.* **2002,** *41,* 2323–2327. doi:10.1002/1521-3773(20020703)41:13<2323::aid-anie2323>3.0.co; 2-h

105. Willner, I.; Patolsky, F.; Wasserman, J. *Angew. Chem.* **2001,** *113,* 1913–1916. doi:10.1002/1521-3757(20010518)113:10<1913::aid-ange1913>3.0.c o;2-p

106. Braun, E.; Eichen, Y.; Sivan, U.; Ben-Yoseph, G. *Nature* **1998,** *391,* 775–778. doi:10.1038/35826

107. Richter, J.; Seidel, R.; Kirsch, R.; Mertig, M.; Pompe, W.; Plaschke, J.; Schackert, H. K. *Adv. Mater. (Weinheim, Ger.)* **2000,** *12,* 507–510. doi:10.1002/(sici)1521-4095(200004)12:7<507::aid-adma507>3.0.co;2 -g

License and Terms